THÈSE

En vue de l'obtention de

L'HABILITATION À DIRIGER LES RECHERCHES DE L'UNIVERSITÉ DE TOULOUSE

Délivré par : *l'Université Toulouse 3 Paul Sabatier (UT3 Paul Sabatier)*

Présentée et soutenue le *07/06/2023* **par :**

Guillaume Daviller

Computational Fluid Dynamics Applied to Aeroacoustics: From Numerical Methods to Flow Physics Analysis

JURY

E. Lamballais	Professeur - Université de Poitiers	Rapporteur
J.-C. Robinet	Professeur - Arts et Métiers ParisTech	Rapporteur
P. Sagaut	Professeur - Université Aix-Marseille	Rapporteur
P. Jordan	Directeur de Recherche CNRS - PPRIME	Membre du Jury
C. Bailly	Professeur - Ecole Centrale de Lyon	Membre du Jury
E. Piot	Directrice de Recherche - ONERA	Membre du Jury
F. Nicoud	Professeur - Université de Montpellier	Membre du Jury
C. Airiau	Professeur - Université de Toulouse III	Membre du Jury

École doctorale et spécialité :
MEGEP : Dynamique des fluides

Unité de Recherche :
Centre Européen de Recherche et de Formation Avancée en Calcul Scientifique

Correspondant :
Christophe Airiau

Abstract

This manuscript aims to present an overview of my research activities since my Ph.D. defended in 2010. These works result from the collaboration with CERFACS and CNRS (IMFT) researcher to supervise students (Ph.D., Post-Docs, and trainees). The main thread of this research project is the Computational Fluid Dynamics (CFD), dedicated to the aeroacoustics applied to aeronautics and aerospace fields. The final objective of this program is to improve our knowledge in order to develop efficient CFD software to reduce the environmental impact of aircraft, helicopters, or rockets.
With the aim to improve the physical models in CFD solver to help design, the analysis, understanding and high-fidelity predictions of compressible turbulent flows are the key points of these research activities in aeroacoustics. Aeroacoustics problems are by definition time dependent. As a consequence, my research interest focuses on the use of the Large-Eddy Simulation (LES) methodology to solve both turbulent flow and acoustics fields in complex geometries. Moreover, as most of the flows encountered are characterized by high Reynolds numbers, the use of High-Performance Computing (HPC) is also mandatory to reduce the restitution time.

The research I conduct with my students and collaborators using numerical and theoretical tools cover many topics such as:

- High-order numerical methods
- Adaptive mesh refinement
- Turbulence modeling for boundary conditions
- Noise source mechanisms

In the first part of this manuscript, a summary of the key achievements in some of these selected fields is given. Following the state of the art, a series of syntheses concerning the above-mentioned topics are given. New research activities are also presented thereafter. These research works are supported by publications given in the second part (20 peer review journal papers, H factor: 8). The last part of the manuscript presents my *Curriculum Vitae* and the list of the 11 Ph.D. students, 8 post-doctorates and 10 master trainees I have supervised. The Academic and Industrial collaborations I have been involved in and which have funded these works are also presented. Finally, the courses I have taught are detailed.

Dedication and acknowledgements

Je remercie tout d'abord les membres du jury d'avoir accepté d'évaluer mes travaux et en particulier Messieurs Éric Lamballais, Jean-Christophe Robinet et Pierre Sagaut pour avoir accepté le rôle de rapporteur de ce manuscrit.

J'ai une pensée particulière pour mes directeurs de thèses, Pierre Comte et Peter Jordan, avec qui cette aventure a commencé.

Je remercie également Thierry Poinsot, Jean-François Boussuge et Catherine Lambert pour m'avoir fait confiance et permis d'intégrer l'équipe CFD du Cerfacs. Ce laboratoire est unique et permet de s'épanouir dans le domaine si particulier de la mécanique des fluides numériques. J'en profite pour remercier l'ensemble de mes collègues, sans qui ces travaux n'auraient pas pu aboutir. Je tiens également à souligner le travail exceptionnel des équipes Administration et Informatique du Cerfacs pour leur disponibilité et leur soutien permanent.

Je tiens également à remercier mes collègues de l'ONERA, Guillaume Puigt et Hugues Deniau, qui ont participé activement à plusieurs des études présentées dans ce manuscrit. Je remercie également l'ensemble de mes collaborateurs académiques et industriels.

Je pense également à tous les stagiaires, doctorants et post-doctorants avec qui j'ai eu la chance de travailler et de réaliser l'ensemble de mes travaux.

Finalement, un grand merci à ma famille et mes amis pour leur aide et leur soutien sans faille depuis toutes ces années.

Table of Contents

Page

Nomenclature

Acronyms

ACARE Advisory Council for Aeronautics Research in Europe

AI Artificial Intelligence

AMR Adaptive Mesh Refinement

AMR Adaptive Mesh Refinement

ANR Agence Nationale de la Recherche

APE Acoustics Perturbation Equation

ATER Attaché Temporaire d'Enseignement et de Recherche

BBSAN BroadBand Shock-Associated Noise

BPR By-Pass Ratio

CAA Computational AeroAcoustics

CAE Computer-Assisted Engineering

CERFACS Centre Européen de Recherche et de Formation Avancée en Calcul Scientifique

CFD Computational Fluid Dynamics

CFL Courant-Friedrichs-Lewy

CNRS Centre National de la Recherche Scientifique

CROR Contra-Rotating Open Rotor

DFG Deutsche Forschungsgemeinschaft

DNC Direct Noise Computation

DNS Direct Numerical Simulation

DOF Degree Of Freedom

EPIC Établissement public à caractère industriel et commercial

FP Flux Points

FP7 Seventh Framework Programme

FRAE Fondation de Recherche pour l'Aéronautique et l'Espace

FSS Free-Shock Separation

FUI Fonds Unique Interministériel

FWH Ffowcs Williams and Hawking

GDR Groupement De Recherche

GNN Graph Neural Network

IMFT Institut de Mécanique des Fluides de Toulouse

IROQUA Initiative de Recherche pour l'Optimisation acoustiQUe Aéronautique

LES Large-Eddy Simulation

LIKE Losses In Kinetic Energy

LMFA Laboratoire de Mécanique des fluides et d'Acoustique

LODI Local One-Dimensional and Inviscid

NPR Nozzle Pressure Ratio

NRI-NSCBC Non Reflecting Inlet Navier-Stokes Characteristics Boundary Condition

NSCBC Navier-Stokes Characteristics Boundary Condition

OASPL OverAll Sound Pressure Level

OGV Outlet Guiding Vanes

PIV Particle Image Velocimetry

PRACE Partnership for Advanced Computing in Europe

QOI Quantity of Interest

RANS Reynolds-Average Navier-Stokes

RK Runge-Kutta

rms root mean square

RSS Restricted Shock Separation

RT Raviart-Thomas

RTRA Réseau Thématique de Recherche Avancée

SDRT Spectral Difference method using Raviart-Thomas elements

SNGR Stochastic Noise Generation and Radiation

SP Solution Points

SPL Sound Pressure Level

STAE Sciences et Technologie pour l'Aéronautique et l'Espace

TIC Truncated Ideal Contour

UHBR UltraHigh Bypass Ratio

URANS Unsteady Reynolds-Averaged Navier-Stokes

WMLES Wall Modeled LES

List of Tables

List of Figures

CHAPTER 1

Research activities

This first chapter is devoted to the summary of my research activities in the field of computational fluid dynamics to study compressible turbulence and aeroacoustic problems. The objectives which have driven the research work presented in this manuscript were to develop efficient numerical methods in order to analyze, understand and predict aeroacoustic phenomena. This research effort was conducted in close collaboration with colleagues from IMFT, LMFA, ONERA, Sherbrooke University (Canada), and also from Airbus and Safran as the ultimate goal is to provide design methods to the industry. The work was funded by European (FP7, H2020, CleanSky), national projects (ANR), and ANRT (Cifre).

1.1 Introduction

With the aim to contribute to Computer-Assisted Engineering (CAE), computational fluid dynamics (CFD) covers a wide range of disciplines. Indeed, the numerical study of flow physics requires knowledge of applied mathematics, physics, and computer sciences. The particular area of aeroacoustics aggregates all the problems encountered in CFD in order to obtain an accurate and efficient prediction of the noise radiated by a turbulent flow.

The discipline of aeroacoustics, well known by the fluid mechanics community, is born in 1952 with the pioneering works of Sir James Lighthill [1, 2][1]. The Navier-Stokes equation was rearranged by the author into a wave equation in order to study jet noise source mechanisms in a medium at rest. The so-called Lighthill's acoustic analogy was extended later by Ffowcs Williams and Hawking [4] for moving surfaces in arbitrary motion and Goldstein [5] for the

[1]Preliminary work on propeller vortex sound was also done in Russia in 1946 [3]

noise propagation in ducts. Numerous variants of Lighthill's analogy were developed in order to identify sound source mechanisms, as for example, those of Powell [6] and Howe [7, 8] using the vorticity. An exhaustive list of the different acoustic analogies can be found in [9]. However, although the acoustic analogies allow to couple the generation with the propagation of the noise, they do not allow to explain the source mechanisms which drive the sound generation in most of the flows encountered in aeronautics or aerospace.

There are mainly 3 phenomena that are responsible for the noise sources studied in aeroacoustics. First, there is the *impulsive noise* which results from the motion of a moving surface, such as helicopter rotors or turbine engine fans. Second, the *turbulence noise*, which exists in all flow motion and which is the most complex to explain due to the unsteady three-dimensional randomly nature of turbulent flows. Finally, the last phenomenon is the *combustion noise*. It comes from the combustion itself (*direct combustion noise*) and from the interaction of non-acoustics waves with obstacles or moving surfaces (*indirect combustion noise*).

This research project is motivated by characterizing the various noise sources encountered in next-generation propulsion systems and aircraft. However, the extreme degree of complexity in terms of geometry and flow field in systems like Ultra-High Bypass Ratio (UHBR) turbofans, Contra-Rotating Open Rotors (CROR), and airframe devices, means that investigating the three noise phenomena defined above represents a significant challenge. As an example, the relative weights of noise sources from present aircraft engine parts and airframe at take-off and approach are given in Fig. 1.1 [10]. Noise emissions of current aircraft are dominated by fan noise, jet noise, and airframe noise depending on the engine regime. In 2011, the Advisory Council for Aeronautics Research in Europe (ACARE) has proposed to reduce the perceived noise by 65% by 2050.

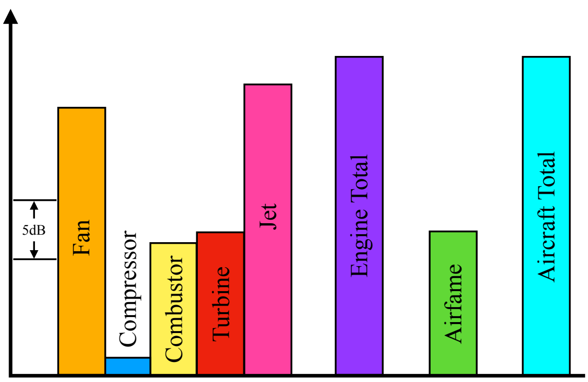

(a) Take-off

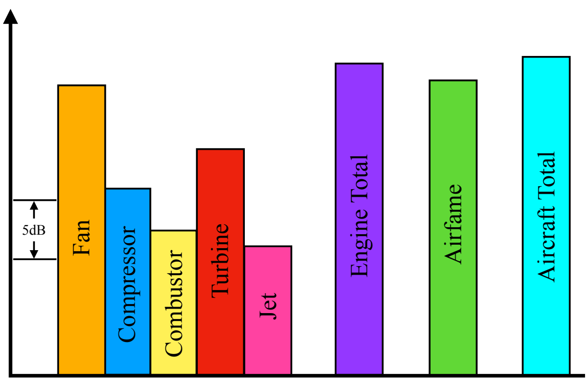

(b) Approach

Figure 1.1. Relative weights of noise sources at take-off and approach, from [10]

UHBR and CROR are the two next engine architectures identified in order to reduce fuel consumption and noise emissions [11]. For each of these future engines, it is expected that the balance of noise sources will be modified. In particular, it is possible that turbomachinery noise mechanisms become predominant. An illustration of an UHBR architecture is shown in Fig. 1.2 where main flow features and noise sources are summarized. In such configuration, the fan diameter is increased and the nacelle length is decreased, as well as the number of turbine stages, to reduce mass and drag. Therefore, the main noise sources, which were the broadband jet noise [12–14] and rotor/stator interaction tonal noise, will decrease in favor of secondary noise sources such as fan self-noise, tip noise, inlet turbulence interaction noise.

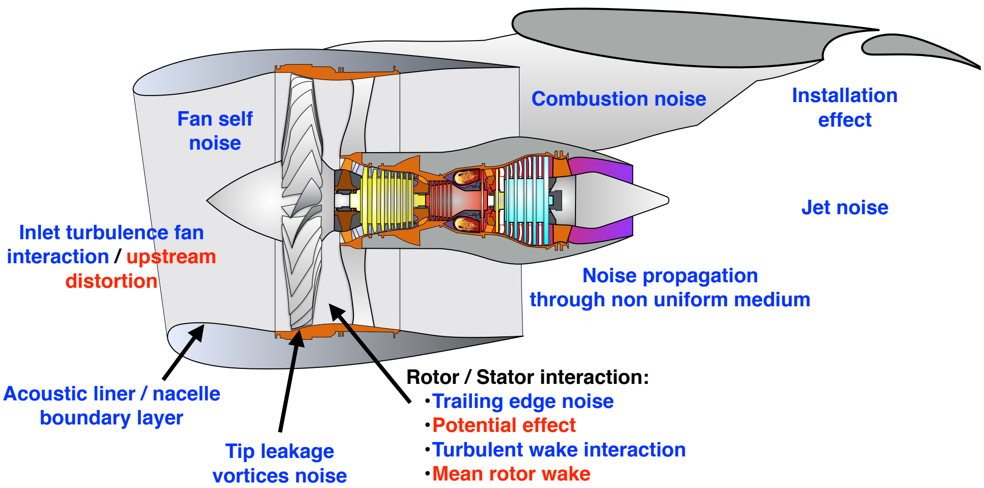

Figure 1.2. UHBR noise sources (red indicates the tonal noise sources and blue the broadband noise sources)

Indeed, as described by Peake and Parry [15], in most flight conditions, the transition to turbulence occurs on both blades and vanes, and wall-pressure fluctuations grow in their boundary layer and diffract at the trailing edge yielding the trailing-edge noise. The fan may also ingest upstream atmospheric turbulence and large-scale turbulent distortion and therefore triggers some inlet turbulence-interaction noise. Turbulent wakes are also shed by the rotor blades and impact on the downstream Outlet Guiding Vanes (OGV) yielding the wake turbulence interaction noise. Because of the rotating fan and its necessary tip gap, tip leakage vortices form in the tip clearance and possibly impact the downstream OGV or even on the next blade if the flow rate is low enough. A turbulent boundary layer also grows along the nacelle that is chopped by the rotor blades. Both contributions (tip vortices and nacelle turbulent boundary layer) contribute to the so-called tip noise. Moreover, the combustion noise [16, 17] contribution will be also more important. However, this type of turbofan architecture will lead to an increase in the related problem of installation noise due to the vicinity of the engine exit with the aircraft wing [18]. Moreover, a shorter nacelle and turbine impose to develop more efficient acoustic liners in order to reduce fan noise [19].

On the other hand, CRORs represent a serious alternative to UHBR turbofan as this architecture allows reduced fuel consumption and better propulsive efficiency. As described by Moreau and Roger [20], they are characterized by tonal noise. Indeed, as illustrated in Fig. 1.3, there is no nacelle to dampen the noise in such unducted engine as in classical turbofan. Together with installation effects caused by the pylon and the core engine sources, three main broadband noise contributions can be observed. Due to the high chord-based Reynolds numbers for most flight conditions, the transition to turbulence still occurs on all blades. Turbulent wall-pressure fluctuations will grow in the boundary layer and diffract at the trailing edge yielding trailing-edge noise. The front rotor then sheds turbulent wakes that impinge on the downstream rear-rotor blades. Possible atmospheric turbulence and large-scale flow structures can also contribute to the ingestion of turbulence in the CROR. Both source mechanisms trigger the turbulence-interaction noise. Finally, at the tip of the blades of both rotors, tip vortices form. The front-rotor tip vortex can then interact with the rear rotor yielding to tip vortex interaction noise.

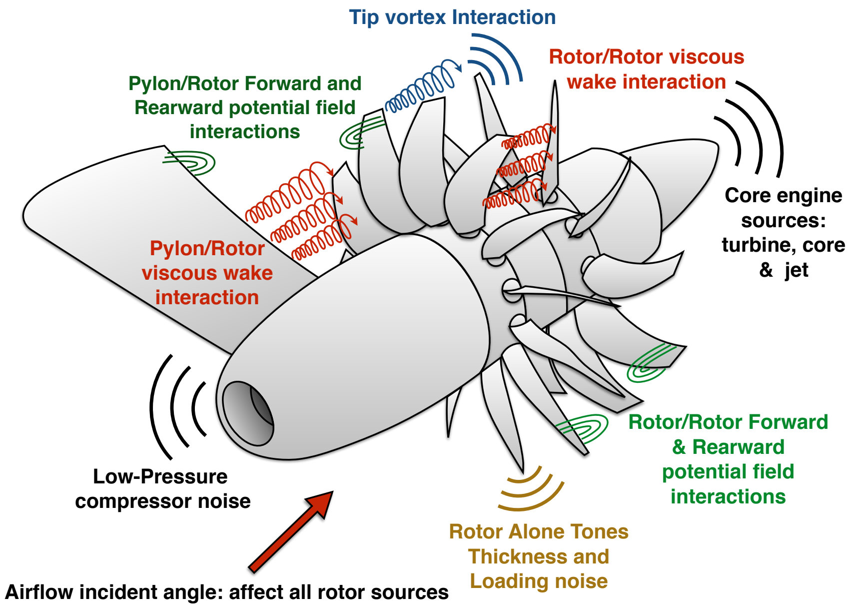

Figure 1.3. CROR noise sources

The noise generated by the aircraft itself, the airframe noise, represents the last airplane noise source to investigate. Airframe noise contributes to half of the noise emission during the approach and landing phase, since the use of the high BPR turbofan engines. As shown in Fig. 1.4, airframe noise results from the interaction of the aerodynamic fluctuation of the airflow surrounding the aircraft with the discontinuities of the aircraft structures, mainly the landing gears and the high-lift devices. As underlined by Dobrzynski [21], landing gear noise is essentially broadband, originates from flow separation of the different elements composing the landing gear itself, or from interactions of turbulent wake flow with downstream gear element. However, some high frequencies tonal components occur due to small components or cavities. Moreover, the installation effect on the landing gear noise is of importance since it results in a modification of the acoustic sources and noise directivity [22]. On the other hand, when high-lift devices are deployed as illustrated in Fig. 1.4, the noise emission is characterized by an additional broadband noise with tonal components. The main noise source mechanisms come from the slat leading-edge flow unsteadiness, the vortex shedding from slat trailing-edges, and the wing trailing-edge scattering of boundary-layer turbulent kinetic energy into acoustic energy.

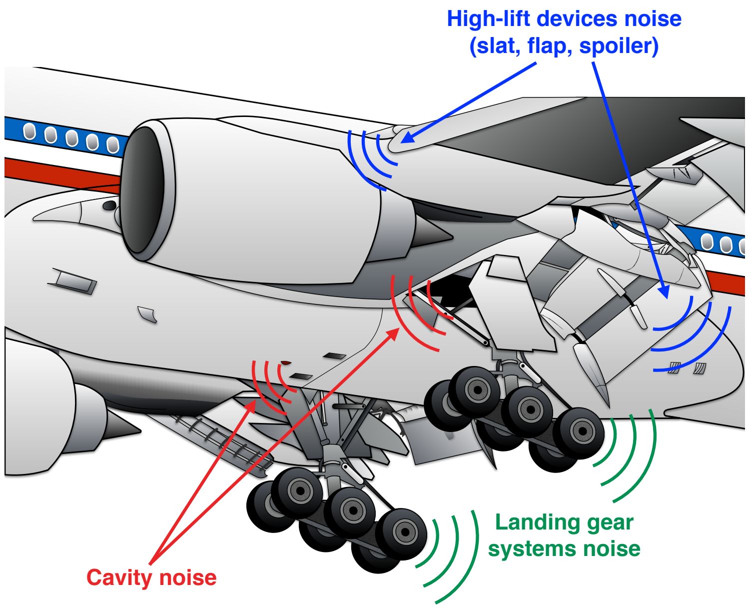

Figure 1.4. Airframe noise sources

As underlined by Casalino *et al.* [23], the design of aircraft noise reduction technologies requires studying each of these noise sources. However, tackling numerically such complex geometries and flow configurations together requires multiphysics and multi-component analyses using advanced numerical techniques through High-Performance Computing (HPC). Indeed, due to the time-dependent nature of aeroacoustics problems, Computational AeroAcoustics (CAA) involves CPU time-consuming simulations. CAA is a recent research area, having started in the 90′s [24] with the progress in computational resources. First numerical applications were performed on academic problems (mixing layer, single jet...) in the early 2000′s [25, 26], twenty years ago. The last decade or the "second golden age of aeroacoustics" [27], was then dedicated to improve methods for noise prediction problems on more realistic geometry. The recent capability of CFD solver to simulate full turbofan engine [28, 29] or full aircraft airframe noise [30] combined with the reality of the exascale computing (Frontier system at Oak Ridge National Laboratory, 2022) suggests that the "third golden age of aeroacoustics" [31] has begun.

To better understand all the difficulties involved in Computational AeroAcoustics simulations, it is first very important to keep in mind the acoustics fluctuations particularities in comparison with the aerodynamic field [32]. The issues relevant to CAA were first underlined by Tam [33] and Lele [34] at the end of the 90′s. In particular, there is a large difference between the energy levels of the sound and the unsteady flow fluctuations [35]. Indeed, acoustic wave amplitudes are about 10^4 to 10^5 time lower than those of the amplitude of the mean flow field. For example, a pressure perturbation of $p' = 1$Pa leads to a measured sound intensity of 93.97dB[2]. Moreover, there are also large disparities in the length scales, as the wavelength of an acoustic wave is about 10^2 time larger than the shear thickness observed in a free shear flow. The resulting noise radiated by a turbulent flow is then generally characterized by a large spectral bandwidth, with a factor of about 10^3 between the lower and larger frequencies to take into account. Finally, whereas aerodynamic fluctuations are only convected in the streamwise direction of the flow field, acoustics waves propagate at sound speed over very large distances in all spatial directions.

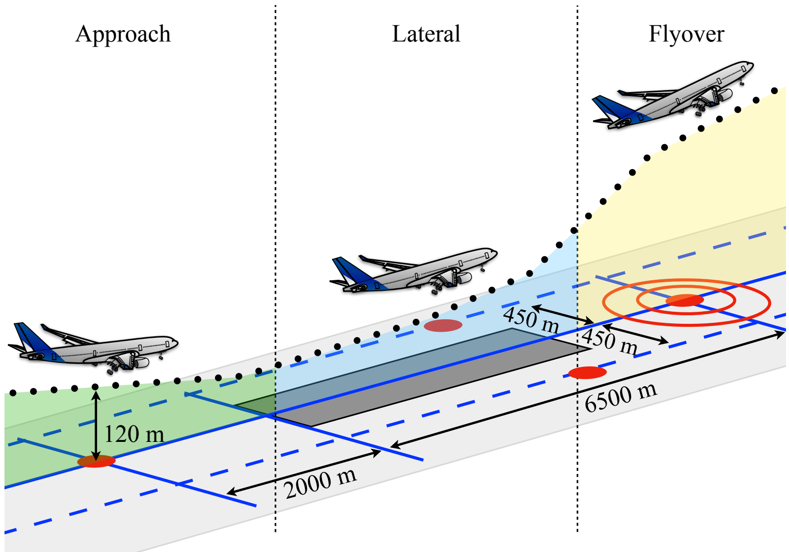

Figure 1.5. Aircraft noise certification reference measurement points

As a consequence, the realization of a Direct Noise Computation (DNC) of a given flow field, meaning that both aerodynamic fields and acoustic fluctuations characteristics will be calculated simultaneously, impose strong numerical constraints on the algorithms of discretization, on the meshes and on the boundary conditions, but not only. Indeed, in order to perform such simulations to predict aircraft noise certification, for example, acoustic fluctuations must be transported over several hundred meters up to the measurement points, as illustrated in Fig. 1.5. This would imply huge computational domains where compressible Navier-Stokes or Lattice Boltzmann equations will be solved, which is feasible, but not efficient for obvious CPU cost

[2]Note that the maximum level of exposition in France is fixed at 80dB

reasons. Therefore, noise prediction algorithms used nowadays in CAA are of hybrid type, meaning that flow and noise sources are computed on restricted computational domains using CFD solvers first. Then the noise sources, recorded on a volume or a surface surrounding the main flow field, are propagated using transport methods (solving Linearized Euler Equation for example) and/or using analytical methods up to the far-field target location. Regarding the far-field noise prediction, there is a consensus accepted by the CAA community since the two last decades around the use of Ffowcs Williams and Hawking (FWH) integral acoustics method coupled with Large-Eddy Simulations (LES) [36–38]. The most popular FWH formalisms are the advanced time formulation developed by Casalino [39] (Farassat 1A [40]) for penetrable surface and moving observer in a medium at rest and the formulation 1C from Najafi-Yasdi *et al.* [41] when considering a convective flow. Nevertheless, alternatives hybrid methods are also used, such as those based on the use of Reynolds-Averaged Navier-Stokes (RANS) simulations coupled with Stochastic Noise Generation and Radiation (SNGR) [42] or Acoustics Perturbation Equation (APE) [43]. Unsteady Reynolds-Averaged Navier-Stokes (URANS) coupled with FWH is also widely used to predict tonal turbomachinery noise in industry [44–46]. Noise prediction approaches for CAA are summarized in Fig. 1.6. Readers interested in a comprehensive review of these methods should refer to the following books [9, 47].

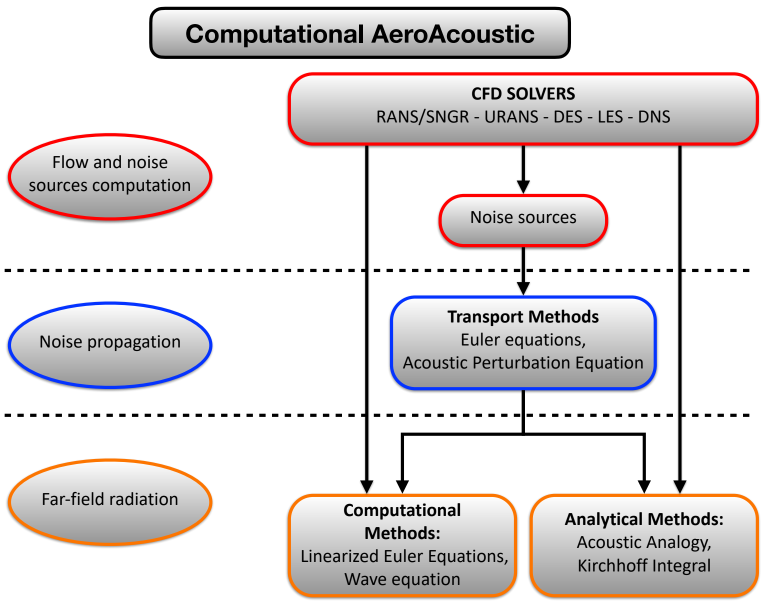

Figure 1.6. Noise prediction methods

The work we will describe address the problem of the prediction of turbulent noise sources using high-fidelity LES. Indeed, while the CPU cost of LES remains relatively high for CAA, this approach allows to simulate high Reynolds number turbulent flow, while it remains unaffordable using Direct Numerical Simulation (DNS). Moreover, LES or Wall Modeled LES (WMLES) approaches provide a better description of the flow compared to Detached Eddy Simulation

(DES) [48, 49] or LBM very large eddy simulation (VLES) [31]. In fact, DES and VLES are more dedicated to industrial flow predictions and are less useful when dealing with analysis and understanding of noise source mechanisms in turbulent flow [50]. Indeed, regarding the jet-noise problem tackled using LES in the chapter 5 of this manuscript, the importance of the mesh discretization [51] and of the nozzle-exit boundary layer state [52, 53] together with numerical methods and boundary conditions [47] were shown to be critical issues to deal with in order to obtain a correct prediction of the turbulent jet and radiated sound. In fact, as mentioned before, the *turbulence noise* is problematic because, as Jordan [54] states: "*The theory is thus not equipped to access the dynamics that underpin the fluctuating shearing motions that drive the sound field*". As a consequence, it is necessary to correctly resolve the Navier-Stokes equations in the region containing the noise sources downstream of the nozzle exit up to 15 jet diameter with a reasonable CPU cost, as underlined by Brès *et al.* [53]. Therefore, to carry out this work, a collaboration between researchers with different skills in mathematics, physics, and computer sciences is necessary.

To achieve these objectives, the publications associated with this research project are organized[3] into a series of chapters, presented as follows. As the starting point of CAA studies is to solve compressible Navier-Stokes equations on complex geometries, it is natural to begin with the development of a high-order numerical method on unstructured meshes, introduced in chapter 2. In this paper [55], a stable formulation of the Spectral Difference (SD) method on tetrahedral grids is proposed. This discontinuous approach allows increasing locally the number of degrees of freedom within each cell of the mesh by using a high-order polynomial representation. Indeed, the idea is to preserve good HPC properties as the SD method avoids large stencils on unstructured grids while keeping low dispersion and dissipation properties, which are essential in CAA. The continuity of the solution at cell interfaces is then ensured using a Riemann solver. Another key aspect of the SD method is the ability to locally increase the grid resolution using both spatial mesh refinement (h-refinement) and the degree of the polynomial approximation (p-refinement).

Because of the importance of the local mesh resolution to obtain an accurate flow prediction, whether in a near-wall or in a free shear flow, chapter 3 proposes a mesh adaptation strategy. Taking the example of the pressure losses prediction of an industrial swirled fuel injector used for helicopter engines, the paper [56] describes a methodology based on a h-refinement approach to obtain a high-quality mesh. This static Adaptive Mesh Refinement (AMR) approach is based on the definition of a sensor which considers the total dissipation of the kinetic energy as Quantity of Interest (QOI). In this paper, by combining experiment and LES, it is shown that both pressure losses and flow field are correctly predicted only with a few mesh refinement steps performed

[3]The arrangement is not chronological.

during the simulation. Moreover, it is demonstrated that this methodology does not depend on the type of mesh. This work has laid the foundation for a user-independent method of mesh generation and was extended to the prediction of side-loads in rocket nozzle [57] (not included in the manuscript) and to the acoustics prediction of a tip-leakage vortex flow [58] (discussed later).

The work described above has highlighted the importance of mesh resolution near the walls as well as the input conditions. In chapter 4, which comprises two papers, we propose boundary conditions to address aeroacoustics simulations of high Reynolds numbers flows using LES. The first paper [59] proposes a generalized non-reflecting inlet boundary condition. The method is based on the Navier-Stokes Characteristic Boundary Condition (NSCBC) [60] and allows injecting simultaneously turbulence and acoustic waves while guaranteeing the non-reflection of the outgoing acoustic waves. This method allows the simulations to converge more quickly without drifting from the imposed mean target value, thus correcting the limitation of classical formulations. In the second paper [61], WMLES approach based on a high-order method is developed in the formalism of finite volume schemes. The approach is validated by simulating turbulent channel flows. In particular, the turbulent intensities measured in the logarithmic region of the boundary layer are in agreement with DNS data. This methodology has been applied in the case of an isothermal subsonic round jet [62] (conference paper not included in the manuscript). The sound pressure levels predicted using LES with wall modeling were found in good agreement compared with the experiment.

After developing the numerical method, the meshing technique, and the modeling of the boundary conditions, chapter 5 addresses the jet noise problem using LES with two papers, where results are first carefully validated against available experimental data. In the first [63], the temperature effects on the noise source mechanisms of a realistic subsonic high by-pass-ratio (BPR) dual-stream jet including a central plug is carried out. It is observed that the aerodynamic jet behavior is mostly driven by the secondary stream whereas only the jet core length is reduced when the primary stream is heated, as for a single jet. However, an additional acoustic source is found when the primary jet is cold. This source has an upstream directivity and results from the interaction of trapped waves in the jet core interacting with the central plug. In the second paper [64], the signatures of the BroadBand Shock-Associated Noise (BBSAN) in a supersonic round jet is investigated. Thanks to a wavelet-based methodology, characteristic patterns of shock cell noise that travel upstream were identified and analyzed.

Finally, chapter 6 presents two new scientific activities and includes two papers. These two activities are focused on turbomachinery noise and are a logical continuation of previous aeroacoustics studies on jet noise. The first paper [58] deals with the aeroacoustics of the tip clearance flow, which is a particular noise source of the fan noise. This work used the methodology presented in chapter 3 and boundary conditions from chapter 4 in order to recover the complex structure of the tip leakage vortex flow. In the second part, which includes the recent paper from Gentil *et al.* [65], a theoretical analysis of the composition noise due to waves of chemical composition, which is part of the indirect combustion noise mechanism, is given. The theory, based on an entropy decomposition, is verified by comparing the model predictions with direct numerical simulations of nozzle flows.

A summary of each chapter of the manuscript is presented in the following sections to provide a comprehensive overview of the main contributions of this research project. Readers interested in more details are invited to explore the chapters.

1.2 High order numerical method

Chapter 2 presents an extension of the Spectral Difference (SD) method on unstructured tetrahedral grids. The SD method is a fairly recent high-order discontinuous method introduced by Kopriva and Kolias [66] in 1996 and extended to simplex cells to handle complex geometries by Liu *et al.* [67] in 2006. The SD method principle is to define a polynomial of degree p to represent the solution and one of degree $p+1$ for the flux on each element of the mesh, ensuring the consistency of the formulation at an order of accuracy of $p+1$. The discontinuity at the cell interfaces is then solved using a Riemann solver. Contrary to the Discontinuous Galerkin method which is based on an integral formulation, the SD method solves the strong form of Euler [68] and Navier-Stokes [69] equations on triangular and hexahedral meshes [70]. Unfortunately, the SD method was found unstable for triangular cells for an order of accuracy strictly greater than two [71] and thus capable of handling CFD problems using only unstructured quadrangle/hexahedral grids. However, recent work of Balan *et al.* [72] has provided a breakthrough by proposing an alternative formulation based on the use of Raviart-Thomas (RT) elements [73] for the flux approximation on triangles linearly stable up to the fourth-order, the SDRT method. The development of a stable SDRT on tetrahedral grids has then begun with an extension of this work for $p=4$ and $p=5$ (ie 5^{th} and 6^{th} order, respectively), using a Fourier analysis-based optimization process to define stable Flux Points (FP) positions for Euler and Navier-Stokes simulations by Veilleux *et al.* [74] (not included in the manuscript). The interested reader by a detailed description of the SDRT formulation on triangles is also invited to refer to the Ph.D. thesis of A. Veilleux [75].

The SDRT scheme on tetrahedral cells is first given in the reference domain $\mathcal{T}_e$, illustrated in Fig. 1.7, to make easier the implementation [76, 77].

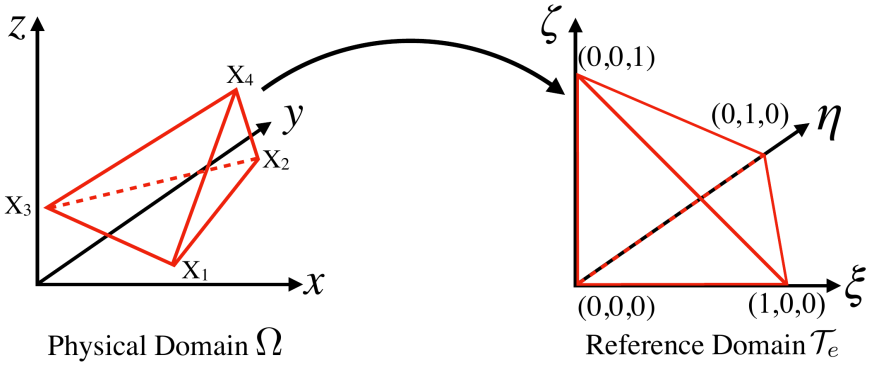

Figure 1.7. Transformation of a tetrahedron in the reference domain

The 3D scalar conservation equation 1.1 in the reference domain is:

$$\frac{\partial \hat{u}(\boldsymbol{\xi}, t)}{\partial t} + \hat{\nabla} \cdot \hat{\mathbf{f}} = 0 \tag{1.1}$$

where $\hat{\nabla}$ is the differential operator in the reference domain, $\boldsymbol{\xi} = (\xi, \eta, \zeta)$ are the coordinates in the reference domain. $\hat{u}$ and $\hat{\mathbf{f}}$ are the solution and the flux vector in the reference domain defined by:

$$\hat{u} = |J| u \tag{1.2}$$

and

$$\hat{\mathbf{f}} = |J| J^{-1} \mathbf{f}(u, \nabla u) \tag{1.3}$$

with J, the Jacobian matrix which allows the transformation from the physical (x, y, z) to the reference domain (ξ, η, ζ), u the state variable and $\mathbf{f}$ the flux vector in the physical domain Ω, which is expressed as:

$$\mathbf{f} = \mathbf{f}^i(u) - \mathbf{f}^v(u, \nabla u) \tag{1.4}$$

where $\mathbf{f}^i$ is the inviscid flux and $\mathbf{f}^v$ the viscous flux.

In order to ensure the consistency of the formulation (meaning that solution and flux divergence will both be polynomials of degree p), the solution $\hat{u}$ must be approximated by a polynomial of degree p, whereas the flux vector $\hat{\mathbf{f}}$ must be approximated by a polynomial of degree $p+1$ in the RT space. Indeed, the RT space is by definition the smallest polynomial space, which guarantees a divergence of degree p. The number of degrees of freedom (DOF)

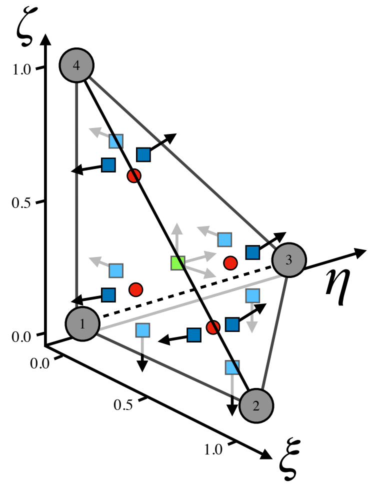

Figure 1.8. Points distribution in the tetrahedral reference element for $p = 1$: SP (●), interior FP (■)), face FP (■)

N_{SP} needed to support the solution polynomial approximation of degree p is:

$$N_{SP} = \frac{(p+1)(p+2)(p+3)}{6}, \tag{1.5}$$

Similarly, N_{FP} is the number of DOF needed to represent a flux vector-valued function in the RT space:

$$N_{FP} = \frac{1}{2}(p+1)(p+2)(p+4), \tag{1.6}$$

In the SD method, the solution $\hat{u}_h$ is defined at Solution Points (SP) whereas fluxes $\hat{\mathbf{f}}$ are computed in another set of points called Flux Points (FP). SP (●) and FP (■) distribution for $p = 1$ on a reference tetrahedron is presented in Fig. 1.8. They are denoted ξ_j and ξ_k respectively in the following. Regarding the SDRT scheme in the reference tetrahedron, the solution $\hat{u}$ is first approximated by a polynomial of degree p, $\hat{u}_h$, expanded using a modal representation based on the Φ orthonormal Proriol-Koornwinder-Dubiner (PKD) [78–80] basis:

$$\hat{u}_h(\boldsymbol{\xi}) = \sum_{m=1}^{N_{SP}} \sum_{j=1}^{N_{SP}} \hat{u}_j \; \left(\Phi_m(\boldsymbol{\xi}_j)\right)^{-1} \; \Phi_m(\boldsymbol{\xi}) \tag{1.7}$$

Then the solution values at solution points are extrapolated to flux points as:

$$\hat{u}_h(\boldsymbol{\xi}_k) = \sum_{m=1}^{N_{SP}} \hat{u}_j \; \left(\Phi_m(\boldsymbol{\xi}_j)\right)^{-1} \; \Phi_m(\boldsymbol{\xi}_k) \tag{1.8}$$

and the inviscid flux function is approximated by $\hat{\mathbf{f}}_h^i$ in the RT space as a linear combination of scalar flux values $\hat{f}_k^i$ and of vector-valued $\boldsymbol{\psi}_k$ interpolation basis functions:

$$\hat{\mathbf{f}}_h^i(\boldsymbol{\xi}) = \sum_{k=1}^{N_{FP}} \hat{f}_k^i \boldsymbol{\psi}_k(\boldsymbol{\xi}), \tag{1.9}$$

For flux points located at the interior of the element (in Fig. 1.8), the scalar flux value is obtained from the scalar product between the flux vector and a normal vector. Since interior flux points are not located on an edge or a face, by definition, the choice of this normal vector is quite arbitrary. Then, for flux points located on faces (in Fig. 1.8), two different values of the flux are available, coming from the solution extrapolation step performed independently on each cell. A unique scalar flux value $\hat{f}_k^i$ is thus defined using a standard numerical flux function $\left(\hat{\mathbf{f}}_k^i \cdot \hat{\mathbf{n}}_k\right)^*$, given as a solution of a Riemann problem using two extrapolated quantities, one on each side of the interface.

$$\hat{f}_k^i = \begin{cases} \hat{\mathbf{f}}_k^i \cdot \hat{\mathbf{n}}_k = |J| J^{-1} \mathbf{f}_k^i(u_h(\boldsymbol{\xi}_k)) \cdot \hat{\mathbf{n}}_k, & \boldsymbol{\xi}_k \in \mathcal{T}_e \setminus \partial\mathcal{T}_e \\ \\ \left(\hat{\mathbf{f}}_k^i \cdot \hat{\mathbf{n}}_k\right)^* = \left(\mathbf{f}_k^i \cdot |J| (J^{-1})^\top \hat{\mathbf{n}}_k\right)^*, & \boldsymbol{\xi}_k \in \partial\mathcal{T}_e \end{cases} \tag{1.10}$$

where $\left(\hat{\mathbf{f}}_k^i \cdot \hat{\mathbf{n}}_k\right)^*$ is the standard numerical inviscid flux in the reference element and $u_h(\boldsymbol{\xi}_k) = \frac{1}{|J|}\hat{u}_h(\boldsymbol{\xi}_k)$ is the approximated solution in the physical domain.

The computation of the viscous flux $\mathbf{f}^v$ is based on a centered formulation [70, 81]. The procedure is given in detail in the Ph.D. thesis of A. Veilleux [75]. Finally, the flux values are given by:

$$\hat{f}_k = \begin{cases} |J| J^{-1}(\mathbf{f}_k^i - \mathbf{f}_k^v) \cdot \hat{\mathbf{n}}_k, & \boldsymbol{\xi}_k \in \mathcal{T}_e \setminus \partial\mathcal{T}_e \\ \\ \left(\mathbf{f}_k^i \cdot |J| (J^{-1})^\top \hat{\mathbf{n}}_k\right)^* - \mathbf{f}_k^v \cdot |J| (J^{-1})^\top \hat{\mathbf{n}}_k, & \boldsymbol{\xi}_k \in \partial\mathcal{T}_e \end{cases} \tag{1.11}$$

The flux polynomial approximation can then be derived at solution points:

$$\hat{\nabla} \cdot \hat{\mathbf{f}}(u) = \left(\hat{\nabla} \cdot \hat{\mathbf{f}}_h\right)(\boldsymbol{\xi}_j) = \hat{f}_k \left(\hat{\nabla} \cdot \boldsymbol{\psi}_k\right)(\boldsymbol{\xi}_j) \tag{1.12}$$

The final spatially semi-discretized form of the hyperbolic equation are:

$$\frac{d\hat{u}_j^{(i)}}{dt} + \sum_{k=1}^{N_{FP}} \hat{f}_k^{(i)} \left(\hat{\nabla} \cdot \boldsymbol{\psi}_k\right)(\boldsymbol{\xi}_j) = 0, \quad j \in [\![1, N_{SP}]\!], \quad i \in [\![1, N_{cell}]\!]. \tag{1.13}$$

and the solution can be time-integrated using any standard time integration scheme (Runge-Kutta scheme for instance).

According to the literature [55, 72], the solution points location has no influence on the scheme stability for triangles or tetrahedra. However, the FP location is the parameter of interest to determine stable SDRT formulations. In order to use hybrid meshes, it was decided to place the FP on edges or faces exactly at the position of FP located on adjacent cells. This is illustrated for FP on triangle and quadrilateral's edge in Fig. 1.9 (a). In this case, the Gauss-Chebyshev quadrature rule is used to compute points location [70], leading to a stable formulation.

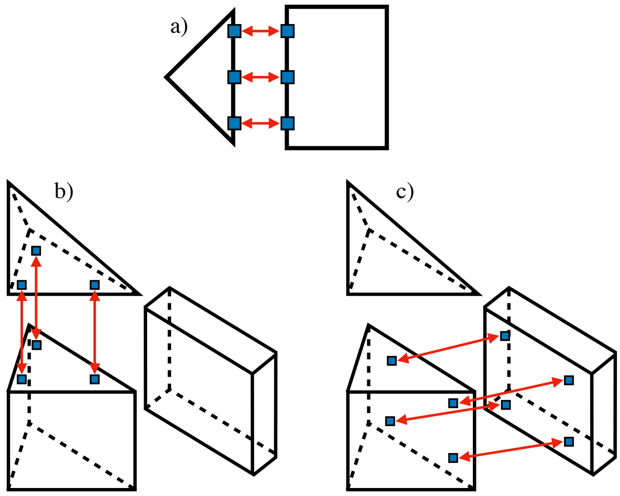

Figure 1.9. Flux points distribution for hybrid mesh implementation (■)

In a similar manner, FP located on a tetrahedron face must be placed at the location of FP on the triangular face of a prismatic element (Fig. 1.9 (b)). In this case, the Williams-Shunn-Jameson quadrature rule [82] is used. For the FP on the prismatic square face, they must be defined in the same place as on a hexahedron face, as shown in Fig. 1.9 (c), using also Gauss-Chebyshev points. So the remaining flux points to place are the interior flux points and are thus the parameter of interest to determine a stable SDRT scheme on tetrahedra.

For this purpose, a linear stability analysis based on a Fourier analysis is used [83]. To do so, the discrete numerical solution is assumed under the form of a planar harmonic wave:

$$
\begin{aligned}
\hat{\mathbf{U}}^{i_1,i_2,i_3} &= \tilde{\mathbf{U}} \exp\Big(I\mathbf{k}\left(i_1\mathbf{x} + i_2\mathbf{y} + i_3\mathbf{z}\right)\Big) \\
&= \tilde{\mathbf{U}} \exp\Big(I\kappa\left(i_1 \cos\vartheta_1 \sin\vartheta_2 + i_2 \sin\vartheta_1 \sin\vartheta_2 + i_3 \cos\vartheta_2\right)\Big),
\end{aligned} \tag{1.14}
$$

with $\kappa = k\Delta x$ the grid frequency, k the wave number of the harmonic wave and $(\vartheta_1, \vartheta_2)$ its orientation angles.

Injecting this wave in a linear advection equation leads to the semi-discrete equation:

$$\frac{d\tilde{\mathbf{U}}}{dt} = \frac{||\mathbf{c}||}{\Delta x}\,\mathbf{M}_\mathrm{z}\,\tilde{\mathbf{U}} \tag{1.15}$$

where the discrete spatial operator is fully represented by the matrix $\mathbf{M}_\mathrm{z}$.

The matrix $\mathbf{M}_\mathrm{z}$ depends on:

- the SP location
- the FP location
- the advection angle $\theta \in [0, 2\pi]$
- the grid frequency $\kappa \in [-\pi, \pi]$
- the harmonic plane orientation $\vartheta \in [-\pi, \pi]$

The location of SP and FP on edges are fixed whereas different interior flux point locations are investigated by varying $\theta, \kappa, \vartheta$. The complete spectrum of the SDRT spatial operator $\lambda_{\mathbf{M}_\mathrm{z}}$ is obtained by computing the eigenvalues of $\mathbf{M}_\mathrm{z}$ over the grid frequency $\kappa \in [-\pi, \pi]$ considering $(\vartheta_1, \vartheta_2) \in [0, 2\pi]$. From this eigenvalue analysis it is possible to determine the behavior of the SDRT spatial discretization. Indeed:

$$\begin{cases} \text{if} \quad \max(\mathrm{Re}(\lambda_{\mathbf{M}_\mathrm{z}})) = 0, & \text{spatially conservative scheme} \\ \text{if} \quad \max(\mathrm{Re}(\lambda_{\mathbf{M}_\mathrm{z}})) < 0, & \text{spatially stable (or dissipative) scheme} \\ \text{if} \quad \max(\mathrm{Re}(\lambda_{\mathbf{M}_\mathrm{z}})) > 0, & \text{spatially unstable scheme} \end{cases} \tag{1.16}$$

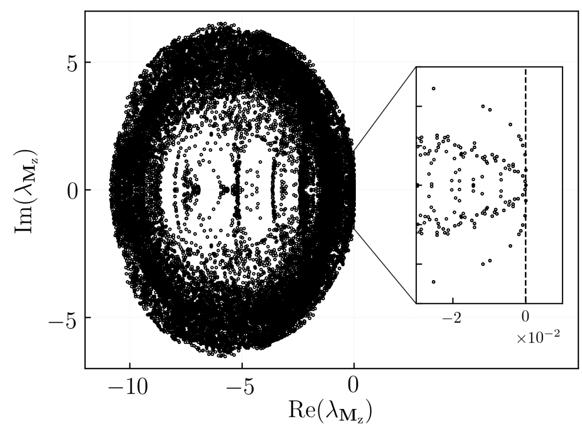

(a) $p = 1$

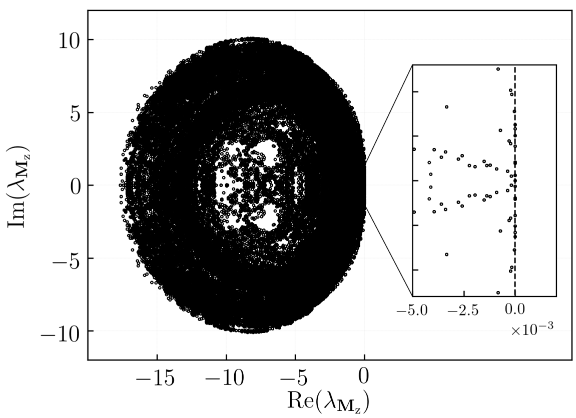

(b) $p = 2$

Figure 1.10. Spectrum of matrix $\mathbf{M}_\mathrm{z}$ for stable SDRT schemes on tetrahedral elements

Results of the Fourier analysis using the Shunn-Ham quadrature rule for the interior FP location [84] are shown in Fig. 1.10 for advection angles $(\theta_1, \theta_2) \in (0, \pi/8, \pi/4)^2$. For both $p = 1$ and $p = 2$, it is found $\mathrm{Re}(\lambda_{\mathbf{M}_z}) \leq 0$, indicating a stable SDRT scheme up to the 3^{rd} order of accuracy.

Performing the same linear stability analysis for a coupled time-space discretization using different Runge-Kutta (RK) methods give the Courant-Friedrichs-Lewy (CFL) stability limits of the SDRT scheme [55]. The results are resumed in table 1.1 for the standard explicit 4-stage RK algorithm (denoted RKs4), the 4-step Strong Stability Preserving RK method at 3^{rd} order [85] (denoted **SSP4**) and the low storage, low dissipative and low dispersive RK scheme from Bogey and Bailly [86] (denoted RKo6).

Temporal scheme	$p = 1$	$p = 2$
SSP4	0.33	0.21
RKs4	0.25	0.15
RKo6	0.38	0.23

Table 1.1. CFL stability limits for SDRT schemes on tetrahedra coupled with different temporal schemes

This SDRT scheme for tetrahedral grids is then validated with a DNS of the Taylor-Green Vortex (TGV) at a Reynolds number of $Re = \rho_{\text{inf}} U_{\text{inf}} L/\mu_{\text{inf}} = 1600$ using ***JAGUAR*** solver. This test case is detailed by Carton de Wiart *et al.* [87] and used in the 5^{th} International Workshop on High-Order CFD Methods [88]. The computational domain is a periodic cube, shown in Fig. 1.11 (a), containing initially eight vortices a $t = 0$. Three different meshes (M_1, M_2 and M_3) composed of about 0.66×10^6, 1.5×10^6 and 3.0×10^6 tetrahedral cells are considered, respectively. The SDRT scheme is combined with the RKo6 temporal scheme and a Roe Riemann solver in this case. A reference solution from a pseudo-spectral finite difference code at fourth order is used to validate the results [87]. This solution is obtained on a Cartesian grid with 512^3 DOF. The different grid characteristics are summarized in tab. 1.2.

Scheme	Mesh	Number of Elements	DOF Number	$\Delta t(sec)$
SDRT	M_1	0.66×10^6	6.6×10^6	$4.5 \cdot 10^{-5}$
	M_2	1.5×10^6	15.7×10^6	$3.5 \cdot 10^{-5}$
	M_3	3.0×10^6	30.7×10^6	$3.0 \cdot 10^{-5}$
Spectral	-	133×10^6	134×10^6	-

Table 1.2. Computational conditions for the TGV test case with $p = 2$

Taylor-Green Vortex is an unsteady flow of a decaying vortex. It is widely used to obtain an initial condition for turbulence transition studies as it is an unstable flow that generates small eddies, followed by a decay phase similar to homogeneous turbulence. Fig. 1.11 (a) shows the coherent turbulent structures obtained at the end of the computation at $t = 20L/U_\infty$, using the Q-criterion for $p = 2$. The temporal evolution of the kinetic dissipation rate $\varepsilon(t) = \mathrm{d}E_k/\mathrm{d}t(t)$

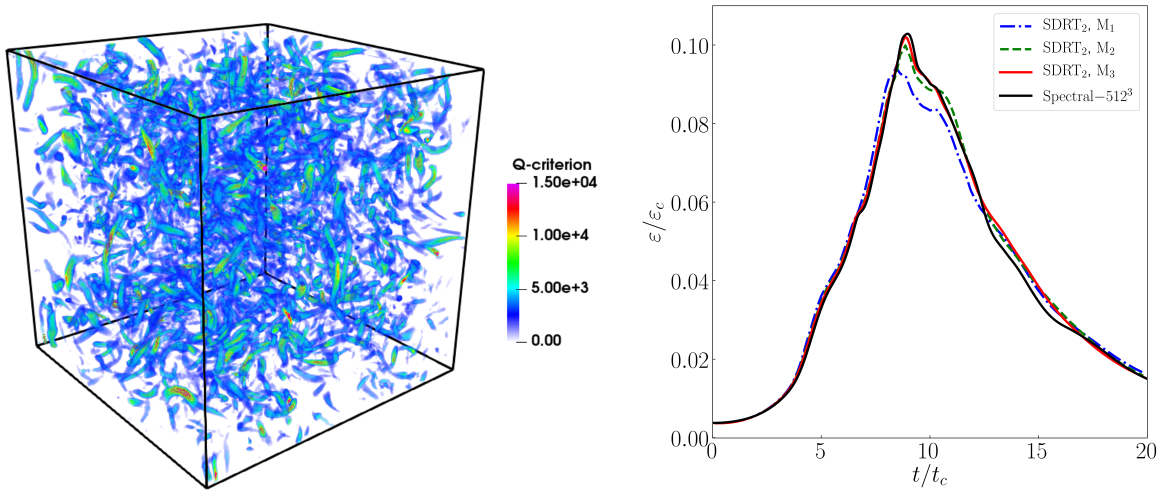

(a) Volume rendering of the Q-criterion at $t_f = 20t_c$ **(b)** Kinetic energy dissipation rate

Figure 1.11. Taylor-Green Vortex test case for SDRT $p = 2$

is depicted in Fig. 1.11 (b). It can be observed that results using the third-order SDRT on M_2 and M_3 grids are in good agreement with the reference data, whereas the peak of kinetic energy dissipation rate is underestimated on the coarse M_1 grid. The improvement in the accuracy of the solution as the mesh is refined can be observed at the peak, where the maximum value is particularly well predicted using the mesh M_3.

The development and validation of the SDRT scheme for tetrahedral cells at 2^{nd} and 3^{th} order of accuracy was the first step in order to perform LES on complex geometries using SD. Indeed, for automatic mesh generation and adaptive mesh refinement, tetrahedrons are one of the most used elements on unstructured meshes. In what follows, a mesh adaptation strategy is proposed for this LES framework with the goal of providing a user-independent method for generating meshes.

1.3 Adaptive mesh refinement

The paper included in chapter 3 presents a joint experimental and numerical study performed using LES to enable accurate prediction of both velocity profiles and pressure losses across a realistic swirled injector used in industrial combustion chambers. This study starts from the fact that most of the LES solvers fail to predict correctly the pressure drops through the swirled injector with more than 20% of error [90] whereas velocity profiles at swirler exhausts are usually well predicted for both reacting [91, 92] and non-reacting [93, 94] flows. A view of a modern combustion chamber is given in Fig. 1.12 (a). It allows to illustrate the complexity of such industrial geometry, composed of 15 radial swirl injectors. Dilution and cooling holes

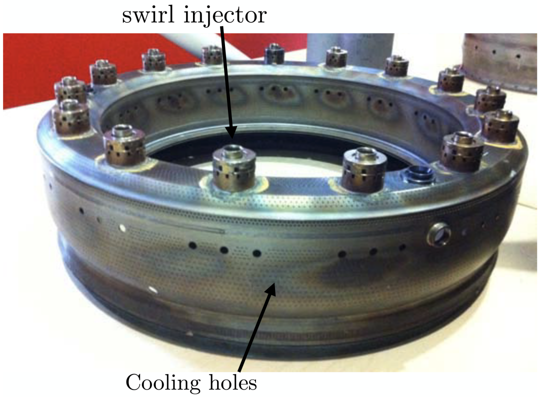

(a) combustion chamber

(b) swirl injector

Figure 1.12. Annular combustion chamber of a helicopter engine, from [89]

(multi-perforated) are also visible on the combustion chamber wall. The swirl injector, shown in Fig. 1.12 (b), has two counter-rotating passages for air with eight tangential vanes. In order to characterize the pressure losses with accuracy, a swirl injector is isolated on the test rig depicted in Fig. 1.13 where the velocity field is measured using Particle Image Velocimetry (PIV) and the pressure loss using a differential pressure sensor (one probe is located on the wall of the upstream plenum and the other in the atmosphere).

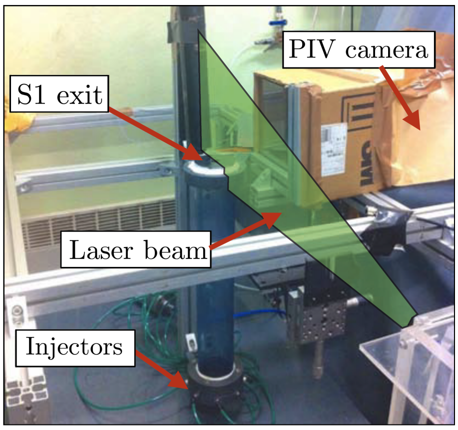

(a) Experimental workbench

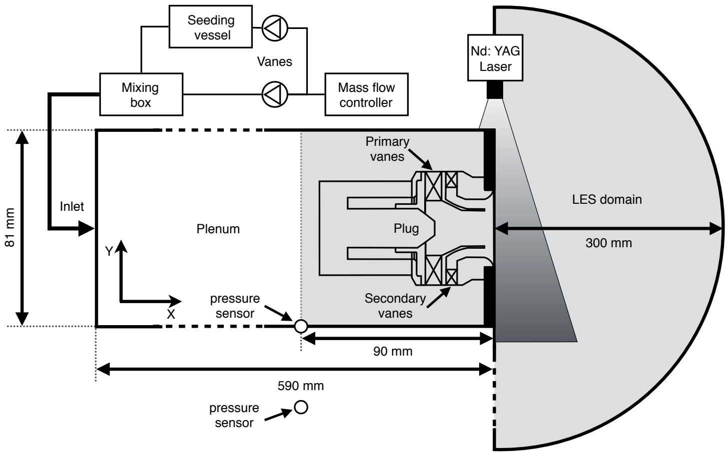

(b) schematic view

Figure 1.13. Experimental setup, The longitudinal (xOy) PIV plane is highlighted. The shaded area corresponds to the CFD domain

Thanks to a non-reactive LES using ***AVBP*** solver, a view of the instantaneous structures of the flow resulting from the passage of the air through the swirler is shown in Fig. 1.14. This allows a better understanding of the complexity not only of the flow but also of the internal geometry and thus of the mesh to be generated. The flow inside the swirler is dominated by a Precessing Vortex Core (PVC) followed at the exit of the swirler by a breakdown zone where multiple smaller turbulent structures develop. From this illustration, it is easier to identify the areas where pressure drops are mainly induced. Indeed, the strong changes in flow direction combined with the sudden expansion of the swirler passages are the regions where losses occur.

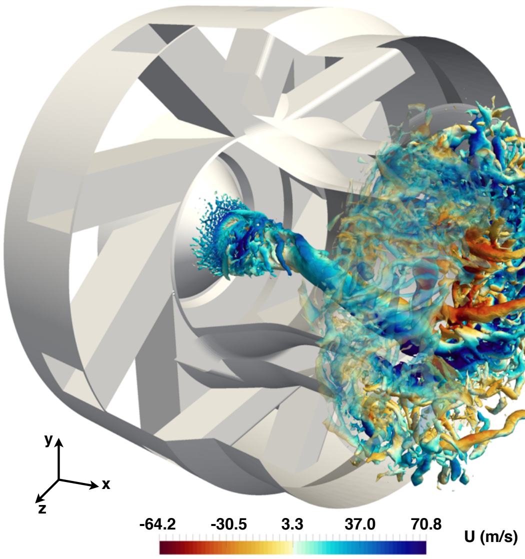

Figure 1.14. Instantaneous flow structures in a swirler identified using Q-criterion $Q = 1.67 \times 10^4 (U_b/D)^2$ colored by axial velocity for a mass flow rate $\dot{m} = 4.29\,\mathrm{g} \cdot \mathrm{s}^{-1}$

In the purpose of identifying these regions, it is necessary to define a criterion that represents the physics of the problem. In this case, it means to identify the mechanism responsible for the losses. As mentioned by Denton [95], entropy production due to fluid friction irreversibilities is one of the main sources of loss for most of adiabatic flows. The entropy transport equation for compressible flows can be written as:

$$\frac{\partial \rho s}{\partial t} + \frac{\partial \rho u_j s}{\partial x_j} = \frac{1}{T} \left(\tau_{ij} \frac{\partial u_i}{\partial x_j} + \frac{\partial}{\partial x_j} \left(\lambda \frac{\partial T}{\partial x_j} \right) \right) \tag{1.17}$$

and the entropy production term due to viscous effect, ie the mechanical irreversibility, is the viscous dissipation Φ:

$$\Phi = \tau_{ij} \frac{\partial u_i}{\partial x_j} = \frac{\mu}{2} \left(\frac{\partial u_i}{\partial x_j} + \frac{\partial u_j}{\partial x_i} - \frac{2}{3} \frac{\partial u_k}{\partial x_k} \right)^2 \tag{1.18}$$

Assuming an incompressible and adiabatic flow, it is then possible to make a direct link between the pressure losses and the dissipation from the conservative equation of kinetic energy E_c:

$$\frac{\partial E_c}{\partial t} + \frac{\partial}{\partial x_j} \left(u_j P_t \right) = \frac{\partial \left(\tau_{ij} u_i \right)}{\partial x_j} + \Phi \tag{1.19}$$

with the total pressure $P_t = P + E_c$.

Without external forces, the integration of the equation 1.19 over a volume Δ for a steady flow leads to the definition of the pressure losses ΔP_t:

$$Q_v \Delta P_t = \int_{\Delta} \Phi dV \tag{1.20}$$

where Q_V is the volume flow rate and ΔP_t is the pressure loss.

This analysis highlights that a Quantity of Interest (QOI) to consider in order to improve the pressure losses prediction is the dissipation field Φ. Moreover, this is always valid considering compressible flows as the work lost is proportional to entropy production [96, 97]. In order to be able to generate LES meshes automatically, the static Adaptive Mesh Refinement (AMR) strategy proposed is based on a $h-$refinement method thanks to the MMG3D library [98]. As a consequence, the resulting mesh is independent of the initial mesh.

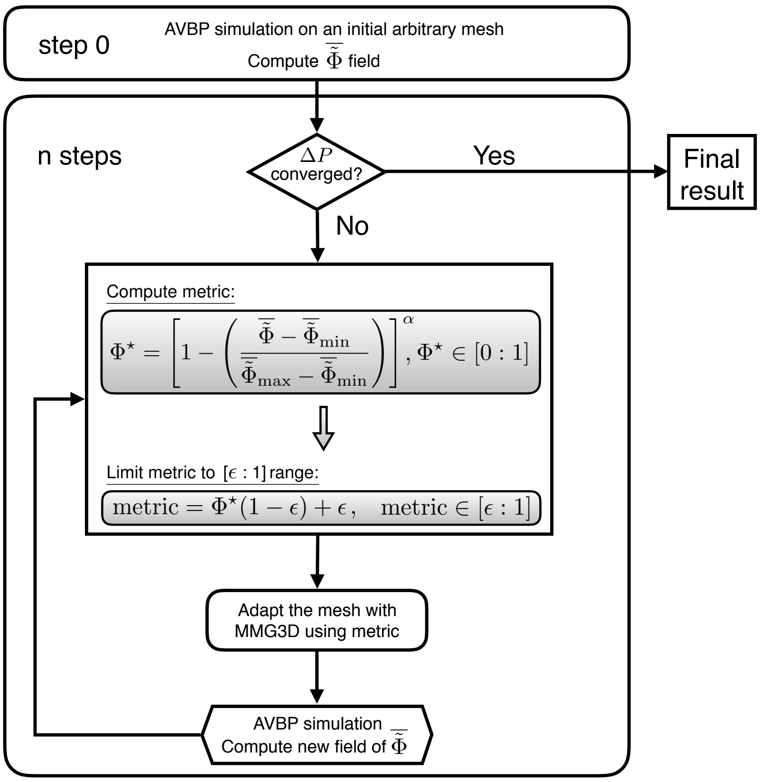

Figure 1.15. Mesh adaptation algorithm

Thus, it is proposed to consider the time-averaged dissipation rate $\overline{\tilde{\Phi}}$ in a LES formalism, ie including the subgrid-scale (SGS) model contribution, leading to the following QOI:

$$\overline{\tilde{\Phi}} = \overline{(\mu + \mu_t)\left(\frac{\partial \tilde{u}_i}{\partial x_j} + \frac{\partial \tilde{u}_j}{\partial x_i} - \frac{2}{3}\frac{\partial \tilde{u}_k}{\partial x_k}\right)^2} \tag{1.21}$$

Where μ is the kinematic viscosity and μ_t is the turbulent viscosity from the SGS model. Operators $\tilde{.}$ and $\bar{.}$ represent the LES filtered variables and the time-average, respectively.

The iterative AMR algorithm used is detailed in Fig. 1.15. From a first LES, if the target pressure losses are not reached, then a metric is built based on the dimensionless field $\Phi^\star$ and a new mesh is generated, followed by another LES. Note that the parameter α is a magnifying factor allowing to smooth singularities and ϵ fixes the maximum refinement (the metric is used as a multiplicative factor to reduce the cells size of the mesh). In general, it has been observed that only a few mesh refinements steps (1 to 3) are sufficient to reach the target.

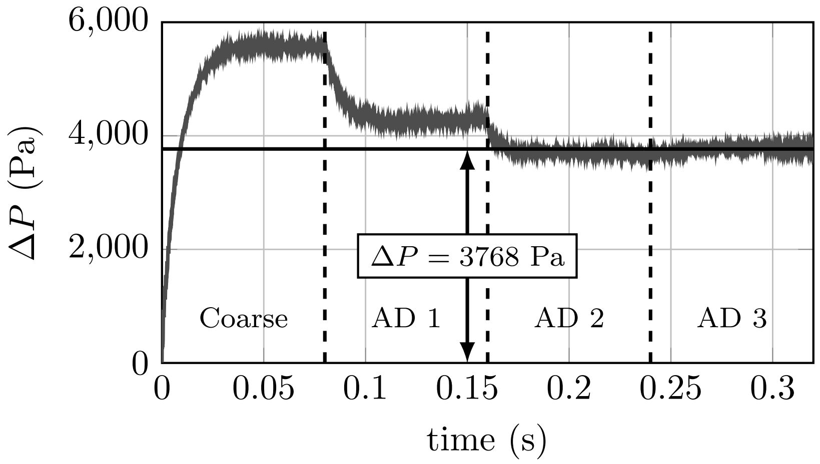

Figure 1.16. Evolution of the pressure loss computed with LES as a function of time and comparison with the target experimental value (straight solid line) for a mass flow rate $\dot{m} = 4.29\,\mathrm{g} \cdot \mathrm{s}^{-1}$

Indeed, the temporal evolution of the instantaneous pressure loss measured in the LES for a mass flow rate of $\dot{m} = 4.29\,\mathrm{g} \cdot \mathrm{s}^{-1}$ in Fig. 1.16 shows a convergence of the pressure losses in 3 steps. While the error on the first coarse mesh was 46%, it decreased to 10% on the second (AD1) and less than 1% on the third (AD2). The study is then completed by a last LES (AD3) which confirms the mesh convergence with again a good agreement with the experimental pressure losses.

The QOI based on the total dissipation, also called “LIKE”, for Losses In Kinetic Energy, has been also used successfully to study side-loads in rocket nozzle using LES by Daviller *et al.* [6] (not included in the manuscript) by decreasing the computational cost of 20% and generalized to wall-modeled turbomachinery LES by Odier *et al.* [99] by combining it with the normalized wall distance y^+. Moreover, the mesh refinement method, based on MMG3D, is available via the *PyHip* [100] package, distributed from PyPI server.

Finally, the realization of these studies would not have been possible without non-reflective boundary conditions and efficient wall modeling. These issues are addressed in the next chapter.

1.4 Boundary conditions

The need to develop new approaches to tackle boundary modeling problems for compressible flows solvers is a critical issue well identified: "*A basic difficulty for boundary conditions in Navier-Stokes codes is the lack of complete theoretical background*" [101]. Indeed, one of the origins of the problem lies in the fact that "*boundary conditions must provide an information on all resolved scales of motion taking into account that the three Kovasznay modes exist at all scales, and that different conditions should be applied on each of the modes* [102][4]. The chapter 4 contains two papers dedicated to boundary conditions for LES of compressible flows. The first presents a generalization of the inlet Navier-Stokes Characteristics Boundary Condition (NSCBC) of Poinsot and Lele [104] for subsonic flows. A novel non-reflective formulation is proposed in order to inject both turbulence and acoustics, avoiding the drift of the mean inlet velocities while allowing a faster convergence of the simulation. The second paper presents a combination of high order-methods with wall models in order to compute wall-bounded flows at high Reynolds numbers using LES.

1.4.1 Compressible non-reflecting boundary conditions

The following study discusses how to simultaneously inject three-dimensional turbulence and acoustic waves while being non-reflective for the outgoing acoustic waves. The method uses the non-linear characteristics boundary conditions [104]. The reader interested in an exhaustive review of different approaches to modeling artificial boundary conditions for compressible flows can refer to [105]. The objective is to develop a boundary condition that satisfy the three properties:

- P1: Perfectly non-reflecting inlet and well-posed boundary condition formulation for Navier-Stokes equations
- P2: injection of plane acoustic wave
- P3: injection of three-dimensional turbulence

[4] In 1953, Kovasznay introduced the decomposition of compressible fluctuations into three physical modes (vortical, acoustic and entropy) based on a linearized theory [103]

The compressible Navier-Stokes equations in conservative form are considered:

$$\frac{\partial U}{\partial t} + \frac{\partial \mathbf{F}_i^c}{\partial x_i} + \frac{\partial \mathbf{F}_i^d}{\partial x_i} = 0 \tag{1.22}$$

where

$$\mathbf{U} = \begin{bmatrix} \rho \\ \rho u_j \\ \rho E \end{bmatrix}, \quad \mathbf{F}_i^c = \begin{bmatrix} \rho u_i \\ \rho u_i u_j + p\delta_{ij} \\ \rho u_i(\rho e_s + p) \end{bmatrix}, \quad \mathbf{F}_i^d = \begin{bmatrix} 0 \\ \tau_{ij} \\ \tau_{ik} u_k - q_i \end{bmatrix}, \quad j = 1, 2, 3, \tag{1.23}$$

are respectively the vector of conservative variables, the convective flux, and the viscous and diffusive flux. τ is the viscous stress tensor, q_i the heat flux vector, e_s and E the sensible and total energies, respectively:

$$e_s = \int_{To}^{T} C_v dT \ \text{ and } \ E = e_s + \frac{1}{2}\left(u^2 + v^2 + w^2\right) \tag{1.24}$$

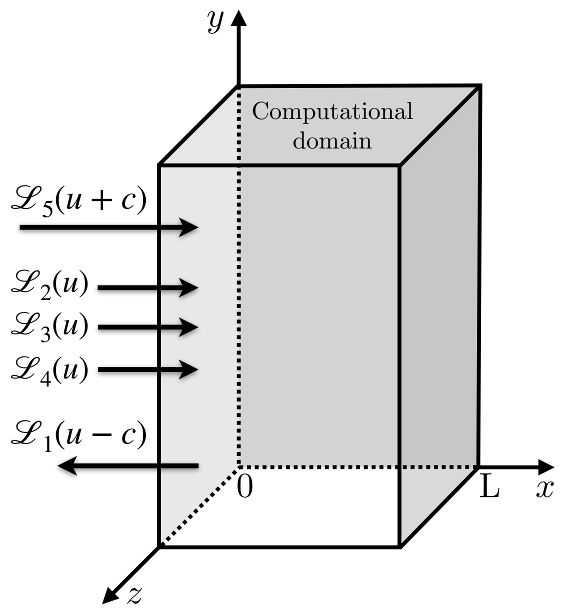

Figure 1.17. Characteristic waves at a subsonic inlet $x = 0$

For a subsonic inlet in the yOz plane, depicted in Fig. 1.17, the target velocity components to impose are (u^t, v^t, w^t). Eq. 1.22 expressed in terms of waves propagating in the $\vec{x}$ direction becomes:

$$\frac{\partial U}{\partial t} + D_i + \frac{\partial \mathbf{F}_y^c}{\partial y} + \frac{\partial \mathbf{F}_z^c}{\partial z} + \frac{\partial \mathbf{F}_i^d}{\partial x_i} = 0 \tag{1.25}$$

where

$$\mathbf{D_i} = \begin{pmatrix} d_1 \\ ud_1 + \rho d_2 \\ vd_1 + \rho d_3 \\ wd_1 + \rho d_4 \\ \dfrac{u_k u_k}{2} d_1 + \dfrac{d_5}{\gamma - 1} + \rho u_i d_{j+1} \end{pmatrix} \tag{1.26}$$

and

$$\mathbf{d}_i = \begin{pmatrix} \dfrac{1}{c^2}\left[\mathcal{L}_2 + \dfrac{1}{2}(\mathcal{L}_5 + \mathcal{L}_1)\right] \\ \dfrac{1}{2\rho c}(\mathcal{L}_5 - \mathcal{L}_1) \\ \mathcal{L}_3 \\ \mathcal{L}_4 \\ \dfrac{1}{2}(\mathcal{L}_5 + \mathcal{L}_1) \end{pmatrix} = \begin{pmatrix} \dfrac{\partial(\rho u)}{\partial x} \\ u\dfrac{\partial u}{\partial x} + \dfrac{1}{\rho}\dfrac{\partial p}{\partial x} \\ u\dfrac{\partial v}{\partial x} \\ u\dfrac{\partial w}{\partial x} \\ \rho c^2 \dfrac{\partial u}{\partial x} + u\dfrac{\partial p}{\partial x} \end{pmatrix} \tag{1.27}$$

with $\mathcal{L}_i$'s the amplitudes of characteristic waves illustrated in Fig. 1.17 propagating at $u - c$, u and $u - c$ ($c = \sqrt{\gamma p/\rho}$ is the speed of sound). As a consequence, the four incoming waves $\mathcal{L}_2$, $\mathcal{L}_3$, $\mathcal{L}_4$ and $\mathcal{L}_5$ must be imposed (the outgoing wave $\mathcal{L}_1$ is given by the field inside the computational domain) to ensure a well-posed problem. From the principle of NSCBC, the local one-dimensional and inviscid (LODI) equations provide an estimation of $\mathcal{L}_i$'s:

$$\begin{cases} \dfrac{\partial \rho}{\partial t} + \dfrac{1}{c^2}\left(\mathcal{L}_2 + \dfrac{1}{2}(\mathcal{L}_5 + \mathcal{L}_1)\right) = 0 \\ \dfrac{\partial u}{\partial t} + \dfrac{1}{2\rho c}(\mathcal{L}_5 - \mathcal{L}_1) = 0 \\ \dfrac{\partial v}{\partial t} + \mathcal{L}_3 = 0 \\ \dfrac{\partial w}{\partial t} + \mathcal{L}_4 = 0 \\ \dfrac{\partial p}{\partial t} + \dfrac{1}{2}(\mathcal{L}_5 + \mathcal{L}_1) = 0 \end{cases} \tag{1.28}$$

Assuming an isentropic subsonic inlet, the classical NSCBC conditions with the injection of both acoustic waves and turbulence [104] lead to:

$$
\begin{cases}
\mathcal{L}_2 = 0 \\
\mathcal{L}_3 = -\dfrac{\partial v^t}{\partial t} + 2K(v - v^t) \\
\mathcal{L}_4 = -\dfrac{\partial w^t}{\partial t} + 2K(w - w^t) \\
\mathcal{L}_5 = \rho c \left(-2\dfrac{\partial u_a^t}{\partial t} - 2\dfrac{\partial u_v^t}{\partial t} + 2K\left[u - (\bar{u} + u_a^t + u_v^t)\right] \right)
\end{cases}
\tag{1.29}
$$

with $\bar{u}$ the target mean velocity, u_a^t the target acoustic fluctuation and u_v^t the target vortical fluctuation, leading to $u^t = \bar{u} + u_a^t + u_v^t$. K is a relaxation coefficient that corresponds to the cut-off frequency $f_c = K/4\pi$ [106]. However, in order to avoid drifting of the mean target velocity to impose $\bar{u}$, a large value of K must be used, which leads to a reflecting boundary because no waves lower than f_c can leave the domain.

By combining results from Polifke *et al.* [107] with the work of Prosser [108], the formulation of $\mathcal{L}_5$ can be extended to become totally non-reflecting by including the outgoing acoustic waves that propagate upstream within the computational domain and reach the inlet with the velocity u^-:

$$
\mathcal{L}_5 = \rho c \left(-2\frac{\partial u_a^t}{\partial t} - \frac{\partial u_v^t}{\partial t} + 2K\left[u - (\bar{u} + u_a^t + u_v^t + u^-)\right] \right)
\tag{1.30}
$$

This formulation called NRI-NSCBC (Non-Reflecting Inlet NSCBC) satisfy the property P1 as the relaxation term remains zero (except if non-acoustic term are present at the inlet). Moreover, properties P2 and P3 are satisfied as terms to inject acoustic waves $2\partial u_a^t/\partial t$ and turbulence $\partial u_v^t/\partial t$ are exact (note that factor 2 must be removed for vorticity injection [109]).

The originality of this formulation lies in the evaluation of the acoustic velocity u^-. Indeed, to evaluate this outgoing wave velocity, Polifke *et al.* [107] used the Plane Wave Masking approach, which consists in introducing a series of cutting planes near a boundary. This method, although efficient, remains expensive in terms of memory and CPU usage and is not suitable for complex geometries on unstructured multi-element meshes. It is proposed in this work to use the exact formulation for u^-, coming from the LODI Eq. 1.28:

$$\frac{\partial u}{\partial t} = -\frac{1}{2\rho c}(\mathcal{L}_5 - \mathcal{L}_1) \tag{1.31}$$

Considering the decomposition of the velocity into right and left going waves $u = u^+ + u^-$, this leads to:

$$\frac{\partial u^+}{\partial t} = -\frac{1}{2\rho c}\mathcal{L}_5 \quad \text{and} \quad \frac{\partial u^-}{\partial t} = \frac{1}{2\rho c}\mathcal{L}_1 \tag{1.32}$$

As a consequence, u^- can be easily evaluated locally at each point of the inlet boundary from the time integral of the acoustic wave $\mathcal{L}_1$:

$$u^- = \frac{1}{2\rho c}\int_0^t \mathcal{L}_1 dt \tag{1.33}$$

The NRI-NSCBC formulation was validated on various test cases, including analytical solutions, detailed in the first paper of chapter 4 [59]. Using the ***AVBP*** compressible solver, a reactive DNS of a slot-burner configuration is performed. A stoichiometric, premixed methane/air flame is forced at the inlet by turbulence and acoustic wave using NRI-NSCBC and compared with NSCBC (with a relaxation coefficient $K = 10^5$ s^{-1}). The physical domain used for the simulation is shown in Fig. 1.18 (a). It consists in a bi-periodic spatial channel of $n_x \times n_y \times n_z = 512 \times 256 \times 256$ cells where fresh gases (at $u = 10$ m/s and $T = 300$ K) are surrounded by burnt gases (at $u = 0.1$ m/s and $T = 2256$ K) injected using a double hyperbolic tangent. The resulting flame is observed using an isosurface of temperature $T = 1600$ K.

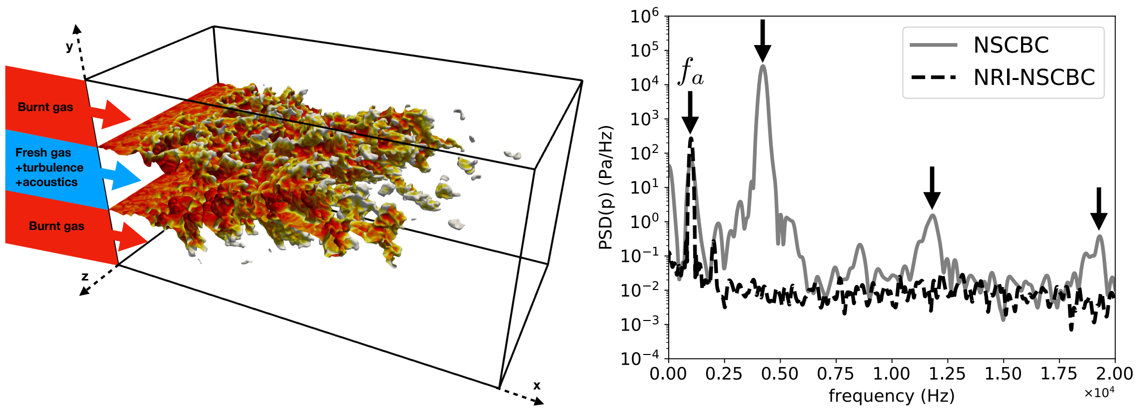

(a) Isosurface of $T = 1600$ K **(b)** Pressure spectra at inlet

Figure 1.18. Slot-burner configuration

The fresh gases are perturbed at the inlet by a turbulence level of 1 m/s and an acoustic wave at $f_a = 1$ kHz. The response of the flame to the acoustics forcing is observed on the pressure spectra measured at the inlet in Fig. 1.18 (b). Whereas the spectrum obtained using NRI-NSCBC exhibits the expected result with only a discrete peak at f_a, the spectrum observed using the classical NSCBC shows three additional spurious modes at $f = 4350$Hz, $f = 12500$Hz and $f = 19500$ Hz. These three modes correspond to the longitudinal 1/4 wave, 3/4 wave, and 5/4 wave eigenmodes of the computational domain and are forced by the boundary conditions.

The result obtained on this classical thermoacoustics case to study Flame Transfer Functions (FTF) shows that the NRI-NSCBC boundary conditions allow to obtain the expected solution with precision. In order to tackle realistic geometries at high Reynolds numbers, it is also mandatory to consider wall-model boundary conditions for LES.

1.4.2 Wall modeling

The second paper [61] presents an extension of the compressible wall model of Bocquet *et al.* [110] in order to perform aeroacoustic simulations of jet noise. Wall Model LES (WMLES) approaches allow to reduce the prohibitive computational cost required to solve turbulent boundary layers at high Reynolds numbers. To do this, WMLES resolves only energy-containing eddies in the outer region of the flow [5]. Following the work on Finite Difference schemes by Kawai & Larsson [113] and on Spectral Differences by Lodato *et al.* [114], a wall modeling approach is proposed for the sixth-order Finite Volumes compact scheme of Fosso *et al.* [115] in the industrial ***elsA*** software.

The Navier-Stokes equations 1.22 in integral conservation form over a cell volume Ω is:

$$\frac{\partial}{\partial t}\int_{\Omega}\mathbf{U}d\Omega + \int_{\partial\Omega}\mathbf{F}^c(\mathbf{U})\cdot\vec{n}\mathrm{d}S + \int_{\partial\Omega}\mathbf{F}^d(\nabla\mathbf{U},\mathbf{U})\cdot\vec{n}\mathrm{d}S = 0 \tag{1.34}$$

The Finite Volume high-order computation of the convective fluxes at a cell interface $i+1/2$ is obtained by solving the implicit compact relation:

$$\alpha_{i+1/2}\tilde{\mathbf{U}}_{i-1/2} + \tilde{\mathbf{U}}_{i+1/2} + \beta_{i+1/2}\tilde{\mathbf{U}}_{i+3/2} = \sum_{l=-1}^{2} a_l\overline{\mathbf{U}}_{i+l} \tag{1.35}$$

with $\tilde{\mathbf{U}}$ and $\overline{\mathbf{U}}$ the averaged value of $\mathbf{U}$ at cell interfaces and in the volume Ω, respectively, defined as:

$$\tilde{\mathbf{U}} = \frac{1}{|\partial\Omega|}\int_{\partial\Omega}\mathbf{U}\mathrm{d}S \quad \text{and} \quad \overline{\mathbf{U}} = \frac{1}{|\Omega|}\int_{\Omega}\mathbf{U}\mathrm{d}\Omega \tag{1.36}$$

[5] Many approaches exist in the literature. Interested readers can refer to [111, 112]

The stability of the scheme is ensured using the sixth-order seven-points stencil compact filter from Lele [116]:

$$\alpha_f \hat{\mathbf{U}}_{i-1} + \hat{\mathbf{U}}_i + \alpha_f \hat{\mathbf{U}}_{i+1} = \sum_{l=-3}^{3} \beta_l \overline{\mathbf{U}}_{i+l} \tag{1.37}$$

with $\hat{\mathbf{U}}$ the filtered variables. In the following, this filter is also used as an implicit SGS model for LES [117, 118]. A complete description of the numerical algorithm implemented in the ***elsA*** software to address CAA can be found in [119].

The application of the wall model is given in Fig. 1.19. From a point M above the wall, the instantaneous velocity $\tilde{u}$, pressure $\tilde{p}$ and temperature $\tilde{T}$ from LES are given to the wall model in order to estimate the wall shear stress $\tau_w = \mu_w \partial U/\partial y|_{y=0}$ and the wall heat flux $\Phi_w = -\lambda \partial T/\partial y|_{y=0}$. In this work, it was chosen to estimate these two quantities using quasi-analytical wall models because of their negligible computational cost.

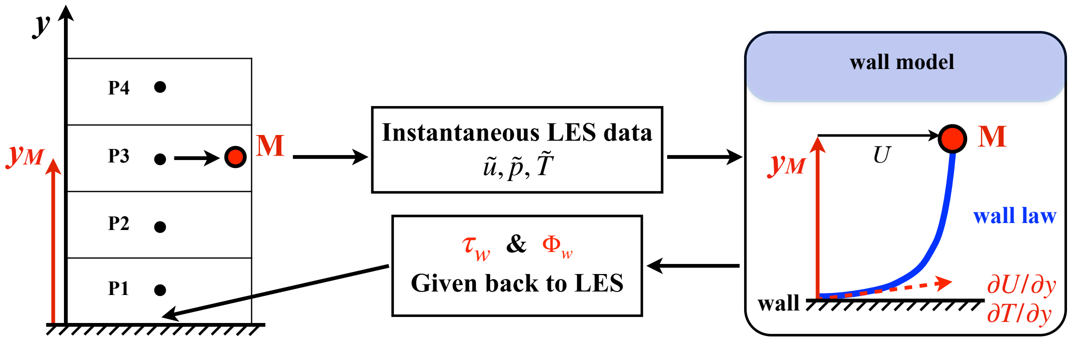

Figure 1.19. Wall model principle

The wall model is described by the system of equations 1.38 in wall units. It is based on the hypothesis that there are no pressure variations in the wall-normal directions. Eq. 1.38a is first integrated into the wall-normal direction to obtain the density at the wall $\rho_w = p/(RT_w)$.

$$\begin{cases} \dfrac{\partial p}{\partial y} = 0 & \text{(1.38a)} \\[2ex] u^+ = \dfrac{U}{u_\tau} = \dfrac{1}{\kappa}\ln(1+\kappa y^+) + \left(B - \dfrac{1}{\kappa}\ln\kappa\right)\left(1 - \exp\left(-\dfrac{y^+}{11}\right) - \dfrac{y^+}{11}\exp(-0.33y^+)\right) & \text{(1.38b)} \\[2ex] T^+ = -\dfrac{(T-T_w)\rho_w C_p u_\tau}{\Phi_w} = P_r y^+ \exp(\Gamma) + \Big(2.12\ln(1+y^+) + f(P_r)\Big)\exp(\dfrac{1}{\Gamma}) & \text{(1.38c)} \end{cases}$$

The wall shear stress τ_w is evaluated using the Reichardt law [120] given by eq. 1.38b where

U is the wall model input velocity in the local coordinate frame and $y^+ = \rho_w u_\tau y/\mu_w$ (μ_w is the dynamic molecular viscosity at the wall computed using Sutherland law). The von Kármán constant is $\kappa = 0.41$ and $B = 5.25$. The friction velocity $u_\tau = \sqrt{\tau_w/\rho_w}$ is then evaluated by inverting eq. 1.38b using a Newton algorithm.

In the case of an isothermal wall[6], the wall heat heat flux Φ_w is given by the Kader law [121] in eq. 1.38c, with P_r the Prandtl number, $\Gamma = -10^{-2}(P_r y^+)^4/(1 + 5P_r^3 y^+)$ and $f(P_r) = (3.85P_r^{1/3} - 1.3)^2 + 2.12 \ln P_r$.

Since equations 1.38b and 1.38c are valid only for incompressible flows, the Van Driest transformation [122] (eq. 1.39) is used to extend them to compressible flows, according to Morkovin's hypothesis [123][7]:

$$u^+_{VD} = \int_0^{u^+} \sqrt{\frac{\rho}{\rho_w}}\, du^+ = \frac{1}{\kappa} \ln y^+ + B \tag{1.39}$$

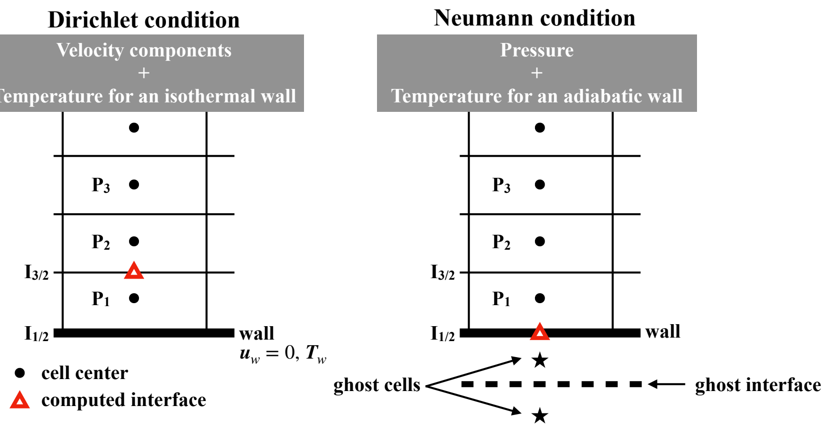

Figure 1.20. Near-wall discretization

The coupling of the wall model (eq. 1.38) with the spatial high order scheme (eq. 1.35) is resumed in Fig. 1.20. The velocity satisfied a Dirichlet condition (as well as the temperature for an isothermal wall) and the no-slip condition $\boldsymbol{u}_w = 0$ is imposed at the wall. In this case, the velocity vector at the first cell interface above the wall is computed using a second-order centered scheme. However, the pressure satisfy a Neumann condition (as well as the temperature for an adiabatic wall) and two ghost cells are then needed to apply the four points implicit scheme (eq. 1.35)[8].

[6] $\Phi_w = 0$ for an adiabatic wall

[7] Morkovin's hypothesis assumes that the compressibility effects due to pressure and density fluctuations are negligible compared to the mean variation of the density and viscosity of the fluid for flows up to Mach number $M < 5$

[8] Note that three ghost cells are needed to apply the implicit filter given by eq. 1.37

The WMLES approach was first validated on a temporal bi-periodic turbulent channel flow characterized by a Mach number $M = 0.2$ and a friction Reynolds number $Re_\tau = u_\tau h/\nu_w = 2000$ (with h the half height of the channel and ν_w the kinematic viscosity at wall) and compared to the DNS of Hoyas and Jiménez [124]. A view of the instantaneous turbulent coherent structures developing in the channel and identified using the Q-criterion is shown in Fig. 1.21.

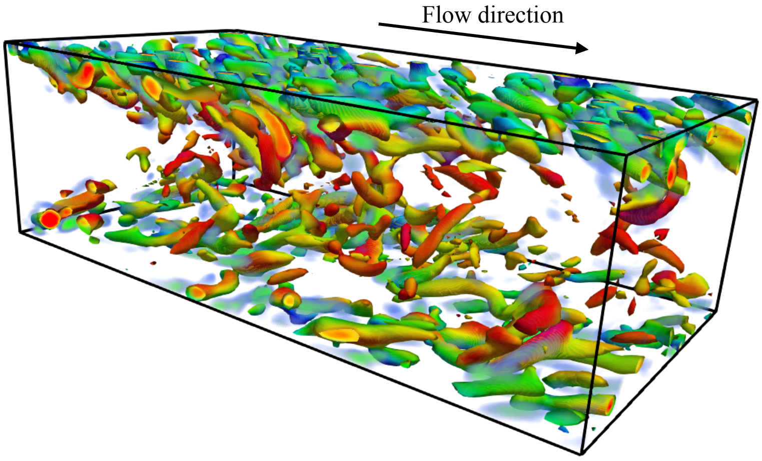

Figure 1.21. Isosurface of Q-criterion in a channel at $Re_\tau = 2000$ colored by the velocity magnitude using the WMLES approach ($[n_x \times n_y \times n_z] = [127 \times 41 \times 65]$)

The statistical results in wall units obtained for the mean u^+ and rms u'^+ axial velocities, as well as the Reynolds shear stress $-u'v'^+$, are plotted in Fig. 1.22. A Cartesian mesh composed of $[n_x \times n_y \times n_z] = [64 \times 41 \times 65]$ point is used in this case leading to a grid spacing in wall unit of $x^+ = 200$, $y^+ = 100$ and $z^+ = 100$. Moreover, the influence of the point M location is investigated considering four points P_1, P_2, P_3 and P_4 located at $y_M^+ = 50$, 150, 250 and 300 in wall units (see Fig. 1.19). Indeed, it has been shown in Finite Differences [113, 125] that selecting a computational point M located further than the first point P_1 over the wall improved the results due to the under-resolution of the LES.

In Fig. 1.22, the best agreement with the DNS data is found for LES using points P_3 and P_4, for $y^+ > 150$. It can be observed that despite the fact that the points P_1 and P_2 are located on the mean velocity profile in Fig. 1.22 (a), the amplitude of the mean and rms profiles are underpredicted over all the channel half-heigh using P_1 whereas u^+ is overpredicted in the logarithmic region using P_2. Regarding the CPU cost, the DNS is performed with a mesh composed of $[n_x \times n_y \times n_z] = [6144 \times 633 \times 4608]$ points and needs 6×10^6 CPU hours using 2048 processors [124]. On the other hand, the LES mesh contains 1×10^5 times fewer points than in the DNS, and simulations were performed using 1 CPU core during 192h. These results demonstrate the ability of the WMLES approach proposed in this study to perform LES of flows at high Reynolds numbers, such as jet flows.

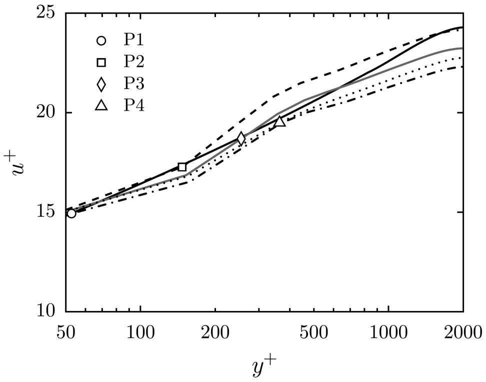

(a) Mean streamwise velocity u^+

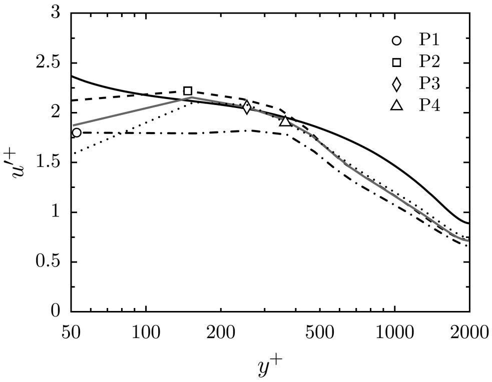

(b) rms streamwise velocity u'^+

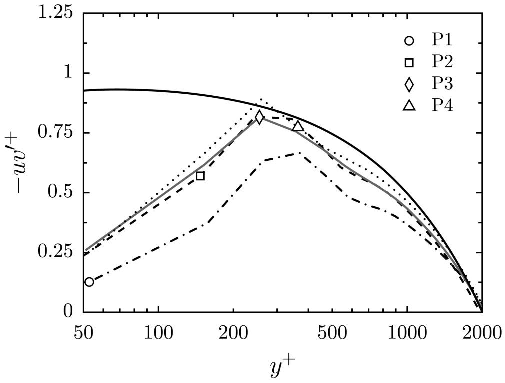

(c) Reynolds shear stress $-u'v'^+$

Figure 1.22. Representation in wall units as a function of the wall distance y^+ of (a) the mean longitudinal velocity profile $u^+ = \langle u \rangle / u_\tau$ (b) rms streamwise velocity $u'^+ = \langle u'u' \rangle^{1/2} / u_\tau$ (c) Reynolds shear stress $-u'v'^+ = \langle u'v' \rangle^{1/2} / u_\tau$. Results are represented using black solid lines (——) for the DNS [124], dashed-dotted (-·-··) for LES using P1, dashed lines (- - -) for LES using P2, grey solid lines (——) for LES using P3, dotted lines (······) for LES using P4

The WMLES is then used to study the noise radiated by an isothermal subsonic round jet at Mach number $M = U_j/c = 0.6$ and Reynolds number $Re_D = U_j D_j/\nu = 5.7 \times 10^5$ corresponding to the experiment of Cavalieri *et al.* [126], with D_j and U_j the jet diameter and velocity, respectively. The computational domain corresponds to a "O-H" type mesh and contains 83 million points, including 2.4 million points in the jet nozzle (all the numerical details are given in Le Bras *et al.* [127], not included in the manuscript). In order to compare the results, an LES without wall-model is also performed. The vorticity field and associated acoustic radiation (pressure fluctuations) are displayed in Fig. 1.23. The shear-layer development downstream of the nozzle lip seems to be fully turbulent, as expected considering the initial

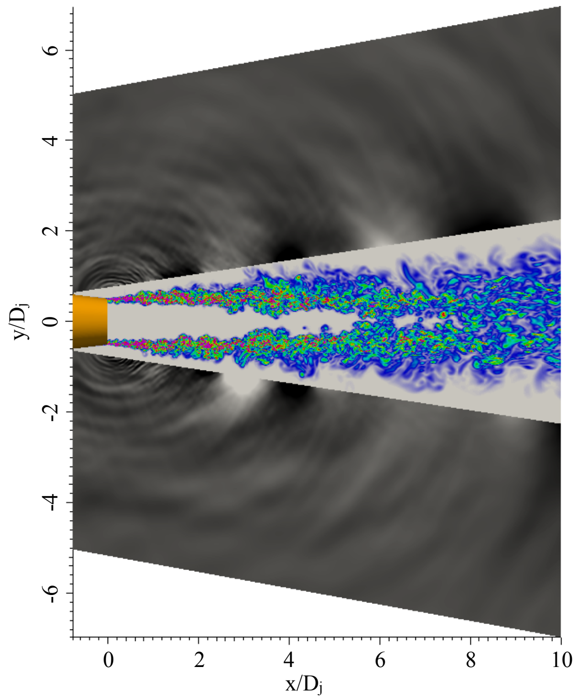

Figure 1.23. Jet at $M = 0.6$ and $Re = 5.7 \times 10^5$: vorticity magnitude and pressure fluctuations in the xOy plane

conditions of the experiments. Indeed, vortical structures are found immediately at the nozzle exit section, with both small and large structures, in agreement with the jet Reynolds number.

The radial profiles of the mean velocity field and rms values in the nozzle exit plane, depicted in Fig. 1.24, are in agreement with the experiment and confirm these observations. In particular, the boundary-layer thickness differs by less than 5% difference from the measurements in both simulations (with and without wall model). However, the intensity of the rms peak near the wall is overestimated without wall model ($\langle u'u' \rangle^{1/2}_{max} = 20\%$) whereas it is comparable to the experimental value ($\langle u'u' \rangle^{1/2}_{max} = 11\%$) in the WMLES ($\langle u'u' \rangle^{1/2}_{max} = 14\%$).

The impact of the WMLES on the Sound Pressure Level (SPL) measured in the far-field at $r = 35D_j$ is shown in Fig. 1.25 for angles of $\theta = 30°$ and $\theta = 90°$ thanks to the Ffowcs-Williams and Hawkings (FW-H) analogy (***Antares*** library [128]). SPL obtained in the WMLES are in agreement with the experiment whereas it is overestimated by 5dB in the case without wall model. This last result demonstrates that WMLES improves significantly jet noise prediction at high Reynolds numbers. Indeed, the importance of turbulent conditions at the nozzle exit on jet acoustic fields is well recognized by the LES jet noise community [53, 129][9].

[9] Many experimental studies were also dedicated to this subject since 1964 (see [130, 131] for example)

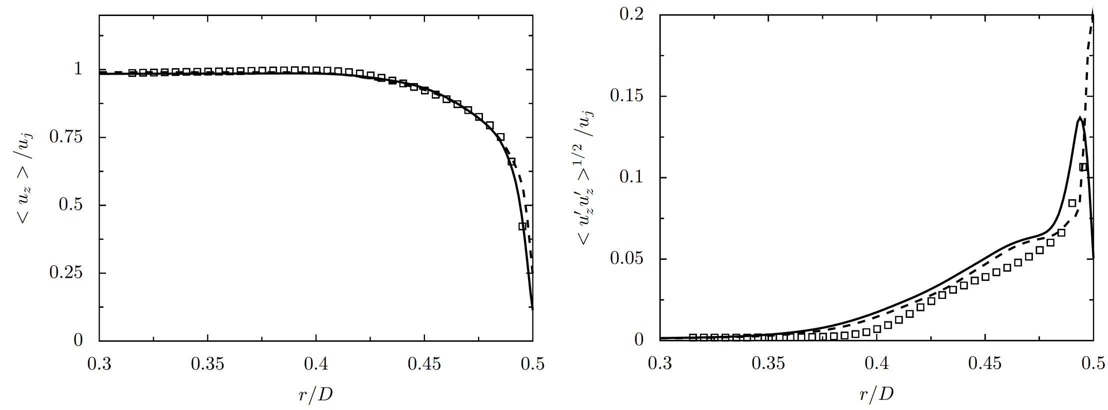

(a) Mean streamwise velocity $\langle U \rangle / U_j$ **(b)** rms streamwise velocity $\langle u'u' \rangle / U_j$

Figure 1.24. Jet at $M = 0.6$ and $Re = 5.7 \times 10^5$: Boundary layer profiles at the nozzle exit, —— WMLES, - - - LES and □ experiment [126]

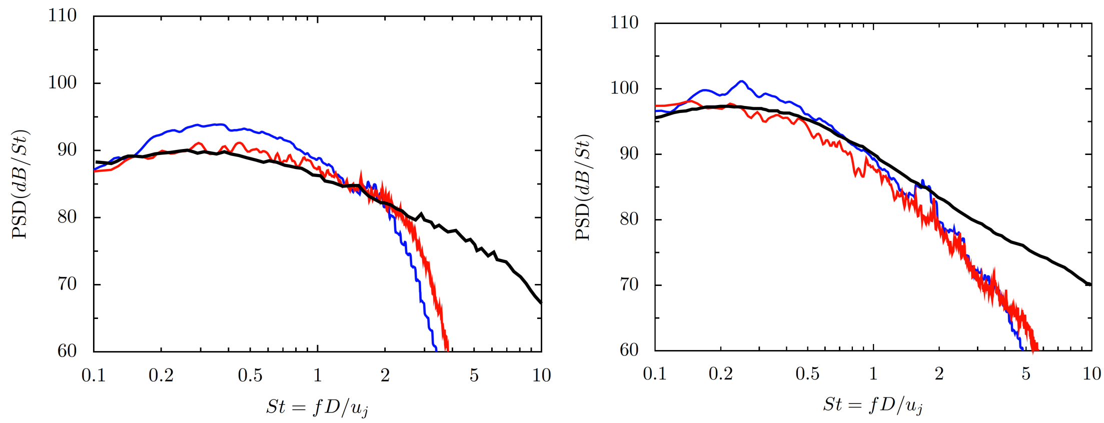

(a) SPL at $\theta = 90°$ **(b)** SPL at $\theta = 30°$

Figure 1.25. Jet at $M = 0.6$ and $Re = 5.7 \times 10^5$: Far-field pressure spectra at $35D_j$, —— WMLES, —— LES and —— experiment [126]

These last works in the framework of numerical methods and modeling of compressible flows now allow the study of noise source mechanisms on more realistic configurations and more complex flows.

1.5 Jet noise source mechanisms

As mentioned in the introduction of this manuscript, jet noise problem is at the origin of research in aeroacoustics for 70 years. Until now, the physical mechanisms by which the sound is generated from the turbulent motion of the jet remain not understood[10]. Moreover, as

[10] Readers interested in this topic are invited to refer to the work conducted by Jordan [54]

mentioned in the introduction of this manuscript and illustrated in Fig. 1.1 (a), jet noise is the dominant noise source at take-off on the current generation of engines. Consequently, the study of this phenomenon is still a major challenge, both from a scientific point of view in order to understand and explain it, and from an industrial point of view in order to accurately predict the nuisances of future aircraft engines at the design stage. Two papers dedicated on jet noise are included in chapter 5. In the first, temperature effects in subsonic jet noise are discussed on a realistic dual stream jet characterized by a BPR close to 9, which is a geometry representative of a real turbofan engine. The objective is to have a thorough description of the flow and noise radiated by a non-potential jet flow, with particular attention to the temperature effects caused by the primary stream. The second paper investigates the particular case of supersonic jet noise with a focus on the broadband shock-associated noise (BBSAN) source mechanisms in an under-expanded jet flow. In this work, the characteristic signature of the BBSAN is identified using a wavelet-based analysis.

1.5.1 Subsonic jet flow

In Biolchini *et al.* [63], the numerical high fidelity LES counterpart of the EXEJET experimental program [132] is conducted in order to investigate flow field and noise radiated by the jet flow from an axisymmetric BPR-9 nozzle. The baseline experimental configuration considered is shown in Fig. 1.26 (a) in the CEPRA19 anechoic test chamber [133]. A detailed view of the dual-stream nozzle with the central plug is depicted in Fig. 1.26 (b). In order to study temperature effects on both flow and acoustic fields, two operating points at take-off conditions without flight effect are considered.

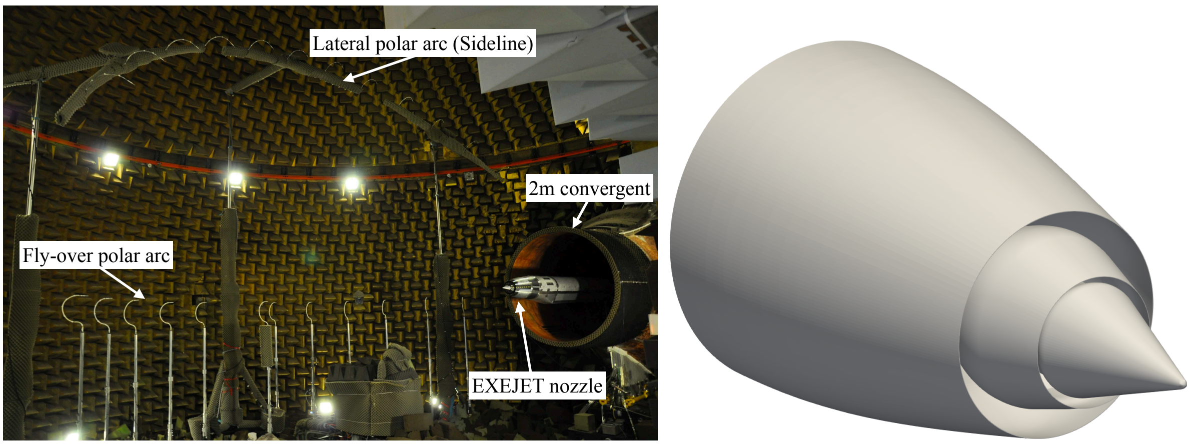

(a) CEPRA19 **(b)** EXEJET nozzle

Figure 1.26. EXEJET nozzle in anechoic test chamber of CEPRA19 [133]

To have a fair comparison, the acoustic Mach number for primary and secondary streams are kept constants, namely $M^p = U_j^p/c_0 = 1.07$ and $M^s = U_j^s/c_0 = 0.84$, respectively, while the temperature of the primary stream differs. c_0 is the ambient speed of sound, subscript $._j$ denotes the jet, superscripts $.^p$ and $.^s$ the primary and secondary stream, respectively. The first operating point has a hot primary stream with a static temperature of $T_j^p = 776$ K, leading to a temperature ratio $T_j^p/T_j^s = 2.7$. This dual stream jet, denoted T800 in the following, is characterized by a primary jet Mach number $M_j^p = U_j^p/c_j = 0.65$ and a diameter-based Reynolds number of $Re^p = U_j^p D^p/\nu^p = 5.5 \times 10^5$. The second dual stream jet, denoted T400, is characterized by a cold primary stream at $T_j^p = 405$ K ($T_j^p/T_j^s = 1.4$). Therefore, the decrease in temperature at constant velocity U_j^p leads to an increase in the Mach $M_j^p = 0.89$ and Reynolds $Re^p = 1.7 \times 10^6$ numbers of the T400 primary stream. The flow properties are given in Tab. 1.26.

	Primary stream				Secondary stream			
jet	M^{p}	$M_{\mathrm{j}}^{\mathrm{p}}$	$T_{\mathrm{j}}^{\mathrm{p}}$ (K)	Re^{p}	M^{s}	$M_{\mathrm{j}}^{\mathrm{s}}$	$T_{\mathrm{j}}^{\mathrm{s}}$ (K)	Re^{s}
T800	1.07	0.65	776	5.5×10^5	0.84	0.82	286	3.8×10^6
T400	1.07	0.89	405	1.7×10^6	0.84	0.82	286	3.8×10^6

Table 1.3: Flow properties of the two jets T800 & T400

The compressible LES are performed using the ***elsA*** software on a structured grid composed of 256×10^6 hexahedral cells with the high-order WMLES approach developed in the previous chapter (numerical methods, mesh and simulation stages are described in [63]). A visualization of the instantaneous vorticity and pressure fluctuation field of the T800 case is presented in Fig. 1.27 (a) while a 3D rendering view of the Mach number is given in Fig. 1.27 (b).

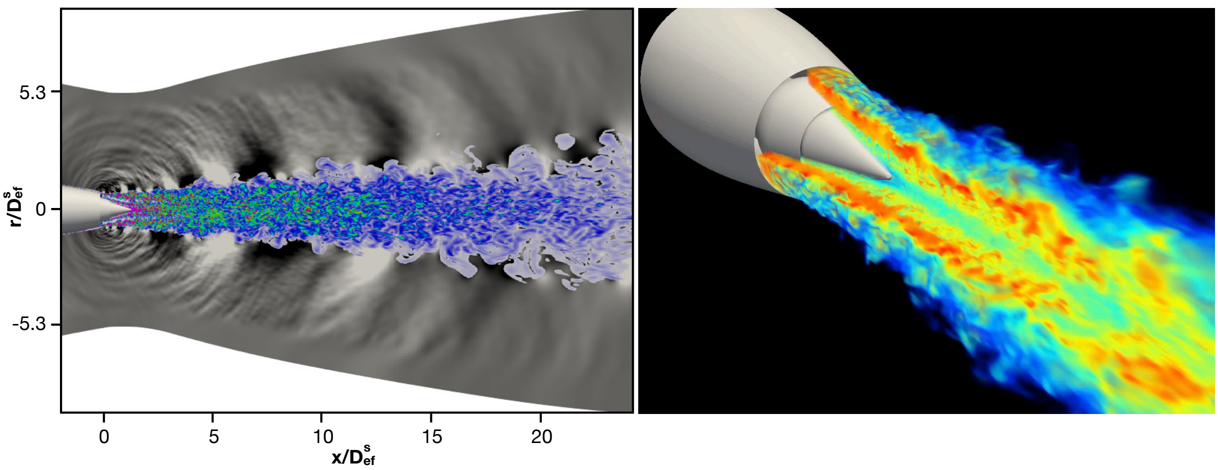

(a) Vorticity & acoustic fields **(b)** Mach number

Figure 1.27. Instantaneous view of the T800 dual stream jet

It can be observed that the flow field presents a high turbulent activity and mixing layers merge rapidly downstream the nozzle, for $x/D^s_{ef} \geq 5$. D^s_{ef} is the effective secondary stream diameter defined as $D^s_{ef} = \sqrt{D^{s2}_j - D^{p2}_j(x = x^s_{ep})}$, with x^s_{ep} the axial coordinate of the secondary flow exhaust plane. Regarding the acoustic field, low frequencies acoustic waves propagating downstream are observed. Similar observations are done for the T400 case. Indeed, as shown in the first paper of the chapter 5, the flow of this dual stream nozzle is mainly driven by the secondary stream due to the high BPR, and the difference in the flow field due to temperature effects are restricted to the primary stream for $x/D^s_{ef} \leq 5$[11].

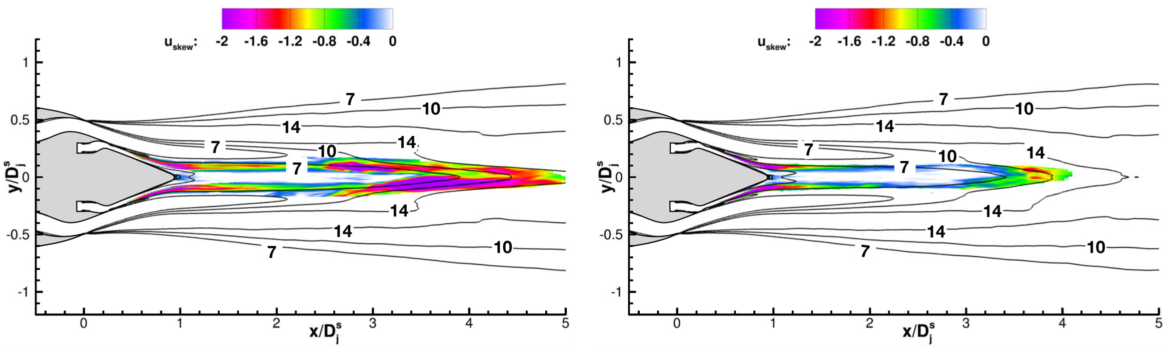

(a) T400 **(b)** T800

Figure 1.28. Axial velocity skewness $u_{skew} = \langle u'u'u' \rangle / \langle u'u' \rangle^{3/2}$. Isolines indicate level of $\langle u'u' \rangle^{1/2} / U^s_j \times 10^{-2}$ m/s

However, it is possible to identify acoustic production regions when looking at high-order statistics, such as skewness $u_{skew} = \langle u'u'u' \rangle / \langle u'u' \rangle^{3/2}$ in Fig. 1.28. Indeed, the intermittency[12] of turbulent jet noise is characterized by localized bursts caused by large-scale structures [14]. Moreover, it has been shown by Bogey [136, 137] for single round jet, that large values of skewness (using axial velocity fluctuations) can be related to low frequencies acoustic production. The skewness fields of T400 and T800 configurations indicate that the shear layers between the primary and secondary stream as well as the end of the jet core are the most intermittent areas in these two dual stream jets. Nevertheless, the area of negative skewness values in the T400 configuration is larger than in the T800 case. Therefore, more intermittent events at low frequencies should be observed in the T400 case.

The far-field acoustic radiation is computed using a FWH analogy. Overall sound pressure level (OASPL) and SPL at $\theta = 30°$ and $\theta = 130°$ of T400 and T800 case are compared in Fig. 1.29.

[11] As observed experimentally on single round jets by Lau [134], an increase of the temperature leads to shorter jet core length due to a higher turbulent intensity

[12] Methods for studying intermittency are described in Schneider *et al.* [135]

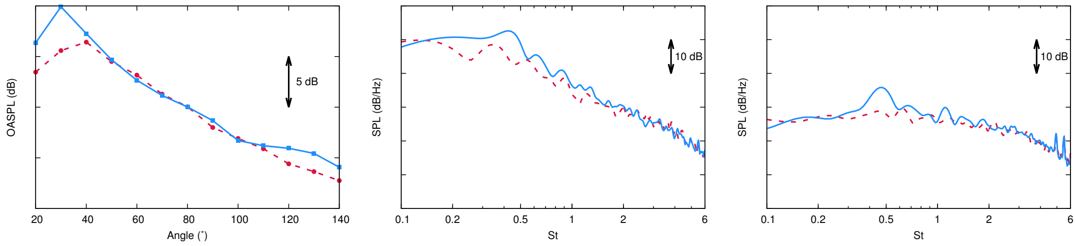

(a) OASPL **(b)** SPL at $\theta = 30°$ **(c)** SPL at $\theta = 130°$

Figure 1.29. Acoustic directivity and pressure spectra in far-field normalized to an observer distance of $r = 1$m for T400 —— and T800 - - -

In Fig. 1.29 (a), it can be observed that the temperature change on the primary stream has no influence on the OASPL for angles between $50° \leq \theta \leq 110°$. However, in the case of the T400, higher acoustic levels up to 4 dB are observed for small angles ($\theta < 50°$) and upstream acoustic radiation ($\theta > 110°$). For small angles, this difference can be explained by the higher intermittency observed in the T400 case. This is confirmed by the higher SPL in low frequencies at $\theta = 30°$ in Fig. 1.29 (b). However, for $\theta = 130°$ (Fig. 1.29 (b)) an extra bump about 8 dB at Strouhal number St $= fD^s_{ef}/U^s_j = 0.46$ is observed. In order to explain the physical mechanism responsible for this additional tonal acoustic radiation, a frequency-wavenumber decomposition of the pressure signal on the jet axis is performed. The diagrams obtained are depicted in Fig. 1.30. It can be observed that for both cases, a strong energetic band identifying the Kelvin-Helmholtz instability waves and characterized by a group velocity close to the convection velocity of $u_c = 0.7U^p_j$ is present.

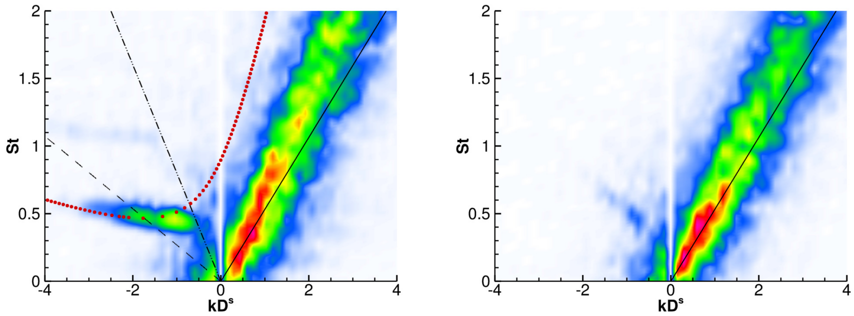

(a) T400 **(b)** T800

Figure 1.30. Frequency-wavenumber diagram of the pressure on jet axis. The contours are distributed logarithmically over two order of the energy magnitude. Lines represent waves celerity related to the dispersion relation $k = \omega/c$, where c is the wave celerity, ω is the frequency and k the wave number. —— $u_c = 0.7U^p_j$, -··-· $-c_0$, - - - $u_c - c_0$ and ······ cylindrical soft duct model from Towne *et al.* [138]

However, in the T400 case, another band with a negative phase velocity bounded by the

$-c_0$ and $u_c - c_0$ group velocities is observed at a frequency $\mathrm{St} = 0.46$. This corresponds to the signature of acoustic trapped waves in the jet core [138, 139]. Moreover, this frequency band is correctly predicted by the vortex-sheet model given by Towne *et al.* [138].

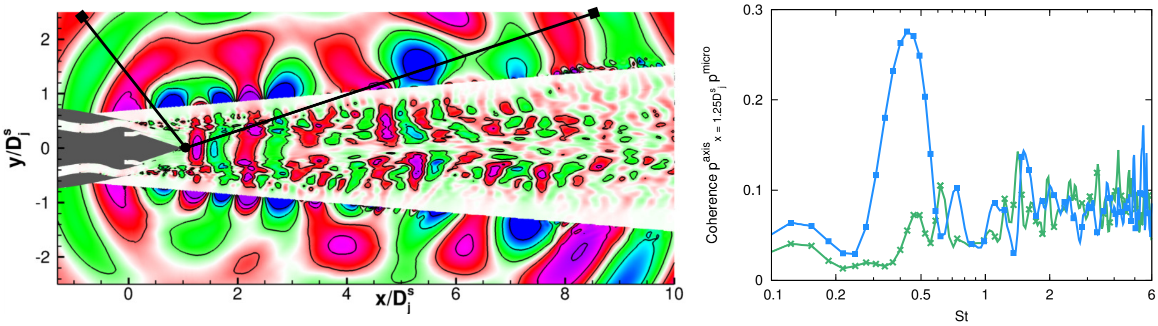

(a) Filtered pressure at $St = 0.46$ **(b)** Coherence function

Figure 1.31. T400 case: (a) Instantaneous filtered pressure field at $St = 0.46$. Dynamic range inside the flow comes from -1000 to 1000 Pa and from -20 to 20 Pa outside the flow. (b) Coherence function (C_{pp}) between pressure for probes at $x = 1.25D_j^s$ and acoustic pressure at two positions : —■— $r = 2.5D_j^s$ et $x = -0.9D_j^s$ ($\theta = 130°$) ; —×— $r = 2.5D_j^s$ and $x = 9D_j^s$ ($\theta = 30°$)

Finally, the additional tonal noise radiated in the far-field of the T400 jet for high angles is explained using the coherence function on the filtered fluctuating pressure field at $\mathrm{St} = 0.46$ shown in Fig. 1.31 (a). Indeed, whereas no acoustics radiation up to the far-field from the trapped waves is observed in potential round jets [138], in the T400 case the peak observed in Fig. 1.29 (c) is due to the interaction of the trapped wave k^- with the central plug of the EXEJET nozzle. This is confirmed by the peak observed on the coherence function at $\mathrm{St} = 0.46$ in Fig. 1.31 (b) for a probe located close to the plug tip and another one at $\theta = 130°$ in the farfield.

The conclusion of this study is that the methods implemented in this research program allow us to investigate subsonic jet noise on realistic dual-stream configurations at take-off and identify acoustics sources. In the following paper, this work is extended to cruise flight conditions and supersonic jet noise.

1.5.2 Supersonic jet flow

Whereas aircraft noise is dominated at take-off by broadband subsonic jet noise, cabin noise perceived by passengers in cruise conditions can be due to another component, the broadband shock-associated noise (BBSAN)[13]. In fact, due to the ambient conditions at cruise altitude

[13] Since the pioneering work of Powell [140] in 1953 on screech tones and Harper-Bourne and Fisher [141] who discovered broadband shock-associated noise in 1973, supersonic jet noise generation process is still a research topic of interest [142, 143]

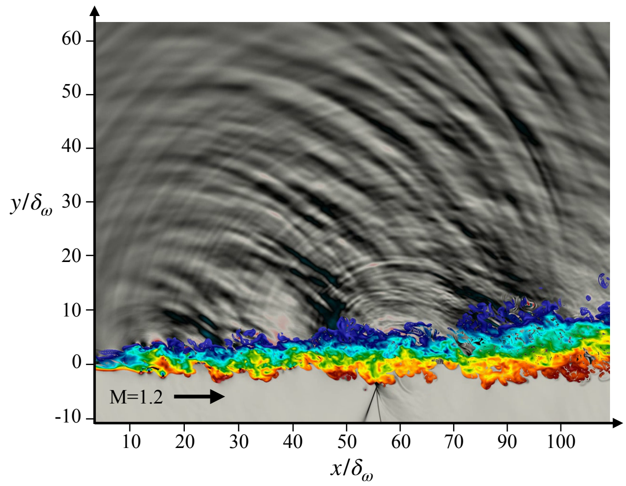

Figure 1.32. 3D DNS of a shock mixing layer interaction, xOy plane, from Daviller *et al.* [144]. The imposed compression wave in the mixing layer is drawn using numerical Schlieren (bottom) and the acoustic field (top) is shown using fluctuating pressure. The shear layer is depicted using vorticity contours colored by the Mach number.

(around 36 000 feet), the secondary stream of the turbofan becomes imperfectly expanded and so slightly supersonic. As a consequence, a series of compression and expansion waves appears downstream of the secondary flow exhaust. BBSAN results from the interaction of these diamond-shaped shock cells with the turbulent structures which develop in jet shear layers.

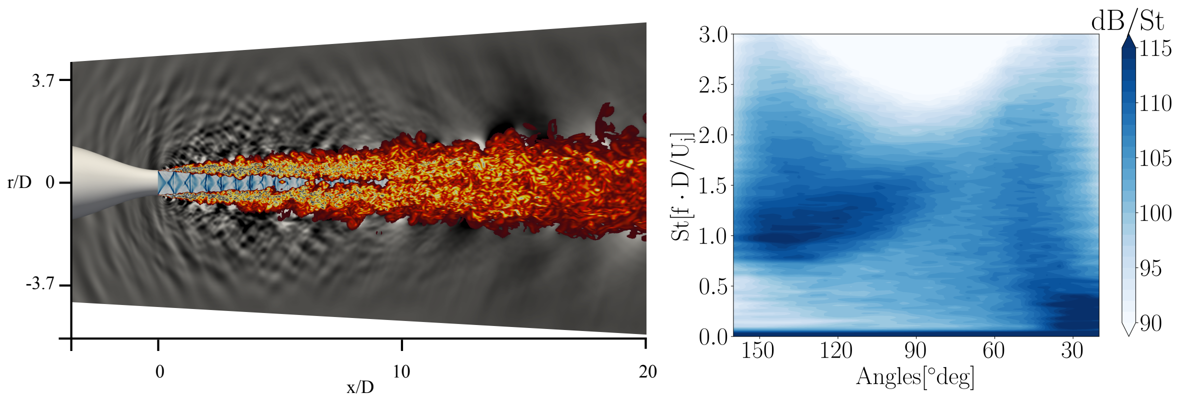

(a) Instantaneous flow

(b) SPL far-field directivity at $r/D_j = 53$

Figure 1.33. LES of under-expanded single jet at $M_j = 1.15$ and $Re_j = 1.25 \times 10^6$. In picture (a) the train of shock cells downstream the nozzle is depicted using a numerical Schlieren (blue), the turbulent structures of the jet are shown using the vorticity magnitude (color), and the acoustic field using the fluctuating pressure (in gray)

As a results, an intense high-frequency noise that mainly radiates upstream is generated [33]. The illustration given in Fig. 1.32 shows the two acoustic components resulting from the interaction of an isolated oblique compression-expansion wave and a three-dimensional mixing layer at Mach number $M = 1.2$ and Reynolds number $Re_{\delta_\omega=2000}$ computed using DNS [144][14]. Indeed, it can be observed in the resultant acoustic field the low-frequency mixing noise propagating downstream and the upstream radiated high-frequency acoustic waves due to the shock-turbulence interaction. This work, beginning in 2012 during the ANR JESSICA is extended to a non-screeching supersonic under-expanded single jet in the paper of Pérez Arroyo *et al.* [64]. Using ***elsA*** software, compressible LES of a jet at Mach number $M_j = 1.15$ and Reynolds number $Re_j = 1.25 \times 10^6$ is carried out.

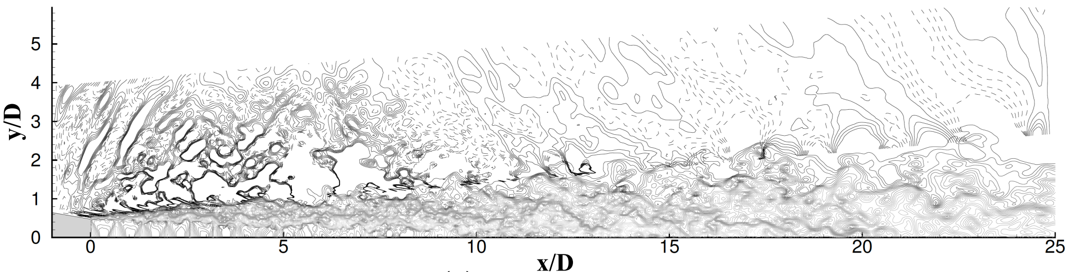

(a) Original flow

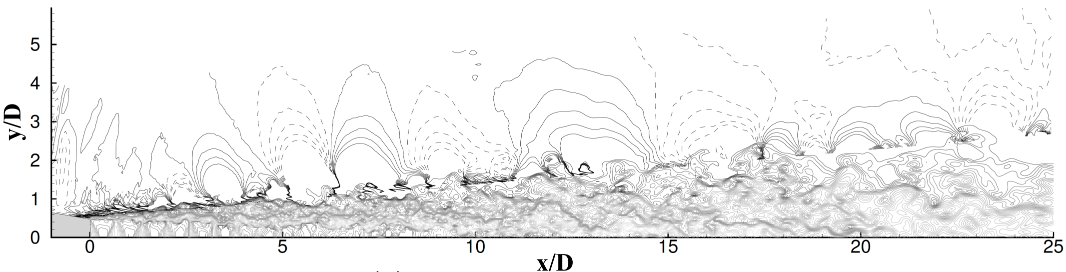

(b) hydrodynamic component

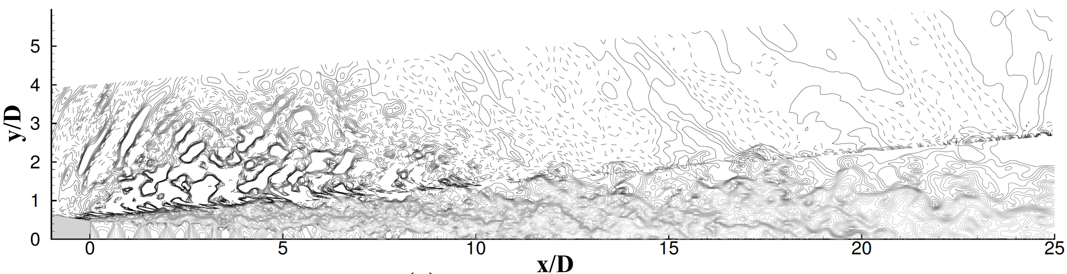

(c) acoustic component

Figure 1.34. Hydrodynamic-acoustic filtering of fluctuating pressure ($-150 \leq p'(\mathrm{Pa}) \leq 150$), from [146]

The jet flow field and the acoustic radiated are shown in Fig. 1.33 (a) as well as the

[14] The computational domain is discretized by using $776 \times 392 \times 80$ points and extends within the range $L_x \times L_y \times L_z = 200\delta_\omega \times 95\delta_\omega \times 10\delta_\omega$. Numerical methods are described in Daviller *et al.*[145]

far-field directivity in Fig. 1.33 (b). On the latter, the shock-cell noise corresponds to the high-frequencies at Strouhal number St > 0.6 and upstream angles $\theta \geq 90°$, whereas the mixing noise is found for St < 0.5 at low angles ($\theta \leq 60°$).

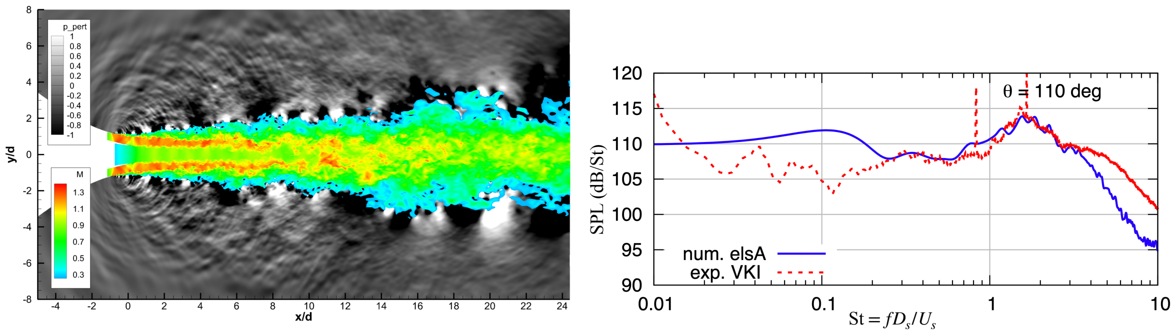

(a) Instantaneous flow

(b) SPL at $r/D_s = 30$ and $\theta = 110°$

Figure 1.35. LES of an under-expanded dual jet

A first investigation is done using the Fourier-based acoustic-hydrodynamic filtering proposed by Tinney and Jordan [147] and results are shown in Fig. 1.34 (from the book chapter [146] not included in the manuscript). The filtered subsonic hydrodynamic and acoustic components are shown in Fig. 1.34 (b) and (c), respectively, and can be compared to the original two-dimensional fluctuating pressure field in Fig. 1.34 (a). It can be observed, although this separation is not exact, that this filtering procedure allows the separation of the acoustic radiation from the hydrodynamic region in the irrotational near-field of the jet. In particular, a wavepacket [14, 148] representative of the large-scale organized motions signature is observed in Fig. 1.34 (b).

However, this phase-velocity filtering does not allow to identify possible signatures associated with events characteristic of the shock-mixing layer interaction in the reconstructed jet flow field. Indeed, no conclusions regarding the shock-cell noise generation or acoustics that propagates upstream can be done. In order to extract the signature of the BBSAN, a wavelet-based conditional averaging procedure is implemented. The idea is to characterize the role of intermittent disturbances that occurs in the jet flow and lead to noise generation. Indeed, contrary to the Fourier transform, the wavelet decomposition used in this study allows to identify space-time localized source activities [149].

In the following, this approach is applied to a supersonic under-expanded dual stream jet [150, 151] more representatives of the nowadays turbofan engines installed in commercial aircraft (this analysis is a part of the Ph.D. of C. Pérez Arroyo [152], not included in the manuscript). The cold coaxial jet (without a central plug) considered is characterized by a subsonic primary flow at Mach number $M_p = 0.89$ and a Reynolds number $Re_p = 0.57 \times 10^6$ enclosed by a supersonic secondary stream at Mach number $M_s = 1.2$ and a Reynolds number $Re_s = 1.66 \times 10^6$. The Nozzle Pressure Ratio (NPR) of the two concentric convergent nozzles is set to 1.675 and 2.45, respectively. Finally, ambient conditions are considered ($T_\infty = 283$ K and $P_\infty = 101325$ Pa). Instantaneous flow and acoustic fields are depicted in Fig. 1.35 (a) using Mach number and fluctuating pressure, respectively. Oblique shock cells can be observed at the exit of the secondary and primary nozzles in the secondary stream. Moreover, the SPL in the far-field computed from ***elsA*** simulation using FWH analogy for an upstream observer at $\theta = 110°$ is shown in Fig. 1.35 (b). An overall good agreement with the experiment is observed, especially regarding the frequency range of the BBSAN peak ($1 \leq \mathrm{St} \leq 3$).

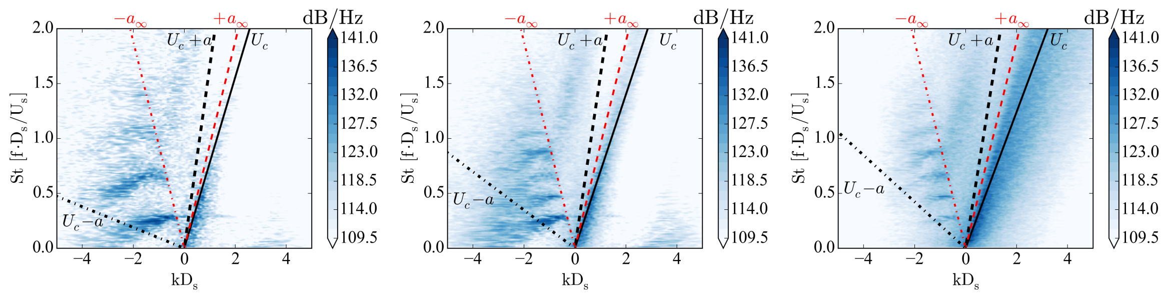

(a) Primary jet axis **(b)** Primary jet lipline **(c)** Secondary jet lipline

Figure 1.36. Supersonic dual stream jet: Frequency-wavenumber diagrams of the pressure

In order to characterize the spatio-temporal dynamics of this dual jet flow field, a frequency-wavenumber decomposition of the pressure is performed on the dual stream jet axis and on each jet liplines in Fig. 1.36 (primary and secondary). As previously observed on a subsonic dual stream jet (see Fig. 1.30), the energy band in the right half-plane of both figures correspond to downstream propagating Kelvin-Helmholtz instability waves while the waves in the left half-plane with negative phase velocity are representative of upstream traveling waves. On the primary jet axis, in Fig. 1.36 (a), two energetic bands at $\mathrm{St} = 0.3, 0.6$ are observed whereas five energetic bands with negative phase velocity at $\mathrm{St} = 0.3, 0.5, 0.7, 0.9, 1.1$ are present on the primary and secondary jet liplines in Fig. 1.36 (b) and (c), respectively. On the jet axis, the waves observed could be attributed to a set of trapped acoustics waves generated at the end of the potential core of the primary jet. Indeed, the Mach number and temperature ratio of the primary stream satisfy the conditions for observing such phenomena [138]. However, the waves traveling upstream on primary and secondary jet liplines could be attributed to the shock-cell noise from the supersonic secondary stream.

The previous frequency-wavenumber decomposition allows to filter the signal into upstream

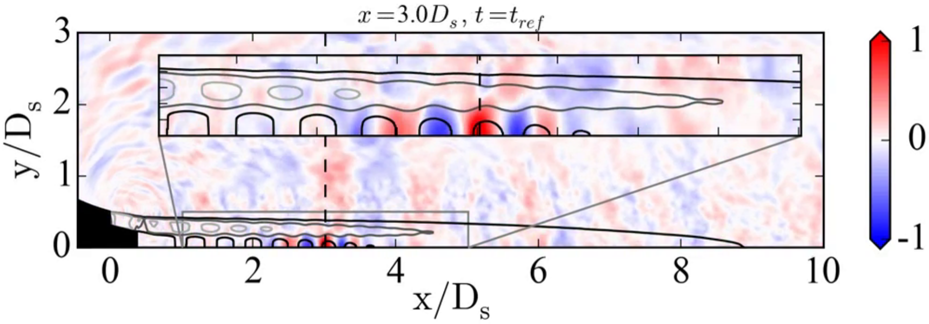

(a) $\{p^-; p\}$ Axis

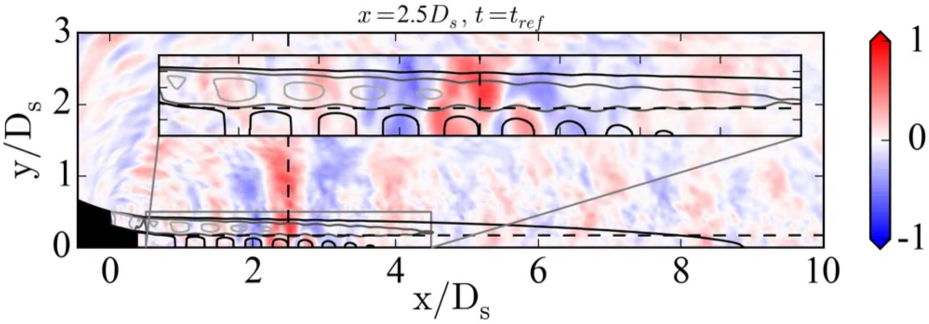

(b) $\{p^+; p\}$ Primary lipline

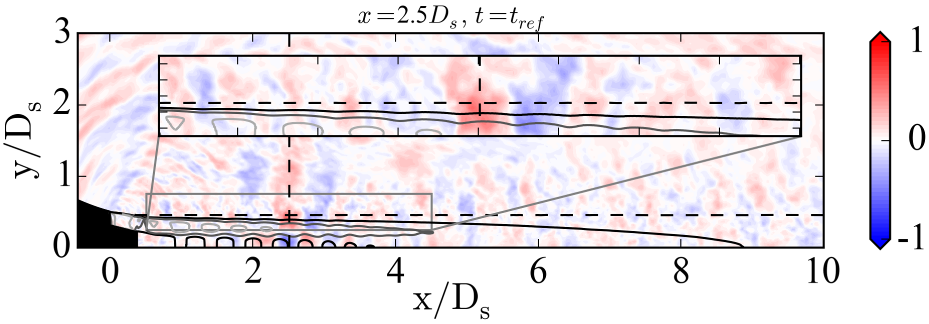

(c) $\{p^-; p\}$ Secondary lipline

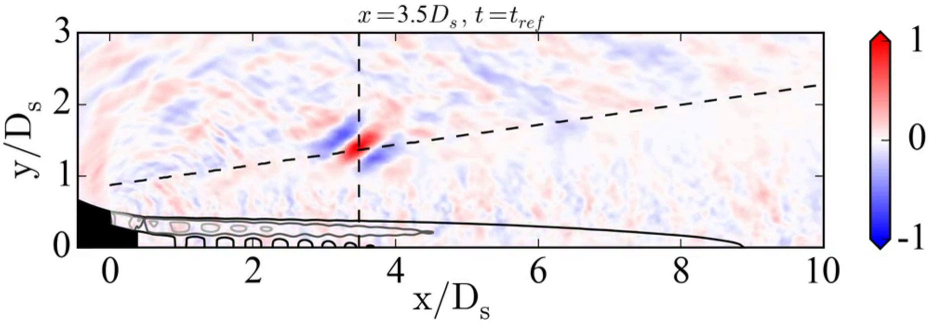

(d) $\{p^-; p\}$ Near-field

Figure 1.37. Normalized two-dimensional cross-conditioning maps. Solid lines represent the Mach number contours $M = 1$. The intersection of the dashed lines represents the location in space of the reference point.

p^- and downstream p^+ traveling waves, respectively. These reconstructed signals are then used as reference signals for event identification in the wavelet identification procedure. The signatures resulting from the conditional averaging obtained in a two-dimensional cut where the reference events are detected are shown in Fig. 1.37. The auto-conditioning of the negative traveling pressure waves p^- on the jet axis is displayed in Fig. 1.37 (a) at $\mathrm{St} = 0.6$ for events localized at $x/D_s = 3$. This signature is characteristic of the trapped waves convected upstream inside the potential core. It can be also observed a phase opposition with waves present in the secondary stream. On the contrary, the signature detected using p^+ in the shear layer of the primary jet at $x/D_s = 2.5$ for $\mathrm{St} = 0.9$ in Fig. 1.37 (b) is characterized by down-traveling waves which extend radially from the jet axis up to the near-field, representative of the mixing noise. Looking at the pressure fluctuations captured using the pressure signal p^- for $\mathrm{St} = 0.9$ in the shear layer of the secondary jet at $x/D_s = 2.5$ in Fig. 1.37 (c) allows to observe upstream convected waves that may have been generated from the shock/mixing layer interaction. Finally, the two-dimensional auto-conditioning of the negative traveling pressure p^- in the near-field is shown in Fig. 1.37 (d). The events are detected at $x/D_s = 3.5$ for $\mathrm{St} = 1.4$. The signature calculated is representative of the shock-cell noise and presents an acoustic wave shape propagating upstream and originating around $x/D_s \approx 5$.

Following the work done on the subsonic dual stream jet, the wavelet-based methodology used in this work allows to analyze temporal signature of a supersonic jet. In particular, the characteristics patterns identified can be associated with spatio-temporal wavepacket coherent structures [142]. However, the additional complexity of considering a secondary supersonic stream requires further investigations on more realistic configurations including a central plug and hot primary stream as illustrated in Fig. 1.38.

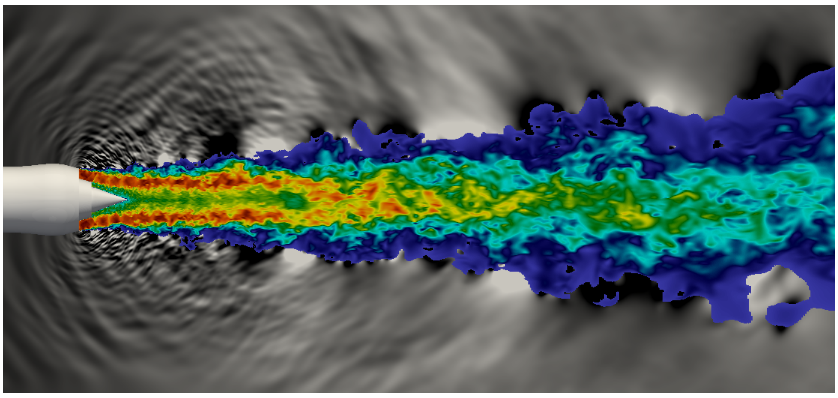

Figure 1.38. Realistic supersonic dual stream jet including a central plug and a hot primary stream from Daviller & Deniau [153], Mach number & pressure fluctuations fields

1.6 New research activities

Since the objectives of this work are focused on understanding and predicting aerodynamic noise phenomena using CFD, chapter 6 discusses two new activities devoted to fan noise and core noise in turbomachinery. Indeed, as underlined in the introduction, the "green" fuel-efficient design of future UHBR engine architectures could result in increased combustion noise and fan noise as illustrated in Fig. 1.39.

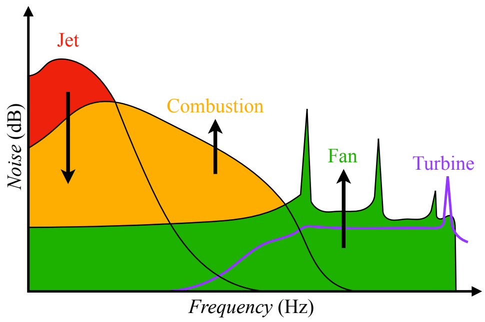

Figure 1.39. Turbofan engine SPL & UHBR trend, from Férand PhD thesis [154]

In the first paper, WMLES is used to study the tip leakage flow of an academic single airfoil and define the appropriate numerical methods to use. The second paper addresses indirect combustion noise related to fuel chemistry using a joint theoretical and numerical analysis.

1.6.1 Turbomachinery aeroacoustics

The work presented in Lamidel *et al.* [58] was motivated by the study of the fan noise contribution, which is expected to be amplified on future UHBR turbofan engines for all flight conditions [155]. Indeed, an increase of the fan noise with the height of the gap between the fan and casing wall of the nacelle was observed [156, 157]. This is mainly due to secondary flows such as the unsteady tip leakage vortex flow developing from the blade tips, as depicted in Fig. 1.40. The resolution of the flow in the gap represents the critical issue of this work. Indeed, as the size of the gap is of the order of a millimeter, it is not taken into account in the simulations [158] or is under-resolved (about 10 cells) to save CPU time [28, 159].

In order to define the numerical best practices to capture efficiently both aerodynamics and acoustics of such phenomenon in turbofan, it was chosen to consider an isolated non-rotating NACA5510 airfoil. This configuration, shown in Fig. 1.41, allows getting rid of the rotation effects. The experiment, performed at LMFA [160], is characterized by a Mach number $M = 0.2$ and a Reynolds number based on the chord $Re = 9.3 \times 10^5$. The gap height considered is $s = 10$ mm. The objectives of this study are to answer the questions of inflow conditions, mesh resolution, and wall modeling on the tip leakage vortex flow prediction using WMLES. The simulations presented thereafter are performed using the ***AVBP*** solver. Instantaneous

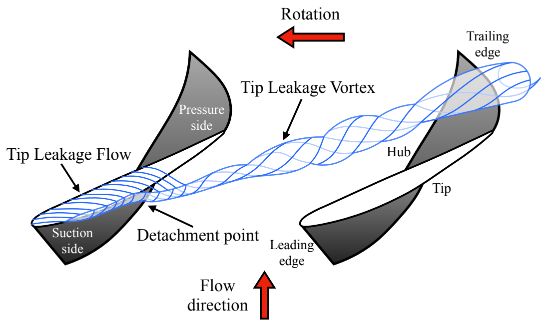

Figure 1.40. Tip flow phenomenology (casing wall view of fan blades)

views of the flow field are shown in Fig. 1.42. This configuration leads to the generation of a tip separation vortex at the leading edge of the pressure side and a tip leakage vortex on the suction side but also to an induced vortex downstream generated by the circulation of the tip leakage vortex, as shown in Fig. 1.42 (a). The vorticity and dilatation fields reveal the influence of the mixing layers from the rectangular jet of the convergent in Fig. 1.42 (b). As shown in the first paper of chapter 6, removing the convergent and imposing the inflow profile from a RANS simulation allows to reduce the CPU cost of 20% but results in spurious noise generation and an underestimation of the mean axial velocity of the tip leakage vortex.

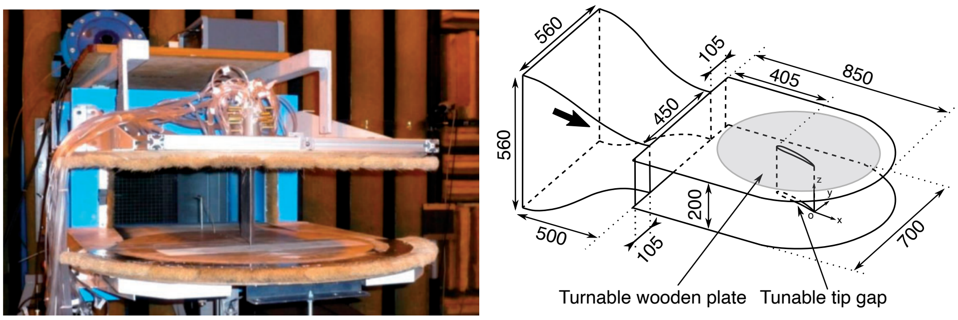

(a) (b)

Figure 1.41. LMFA experimental single airfoil set-up, from Jacob *et al.* [160]

However, as observed in Fig. 1.43 (b), taking into account the full experimental set-up in the WMLES is not sufficient to capture the tip leakage vortex structure with accuracy. In fact, although the gap is discretized using 20 tetrahedra, the acceleration at the center of the tip leakage vortex is not recovered compared to the PIV data in Fig. 1.43 (a). In order to put the cell in the tip leakage vortex area, the AMR strategy developed in chapter 3 (see also section 1.3) is used with a metric based on the time-averaged dissipation field $\overline{\tilde{\Phi}}$. However, in order to limit the size of the new mesh, only the regions including the tip leakage vortex, the wake, and the vicinity of the airfoil surface are refined. After adaptation the gap is discretized using about 35 cells and the computational cost is increased by 25%. As a comparison, Koch *et al.* [161] have discretized the gap using 46 cells for a wall-resolved LES on

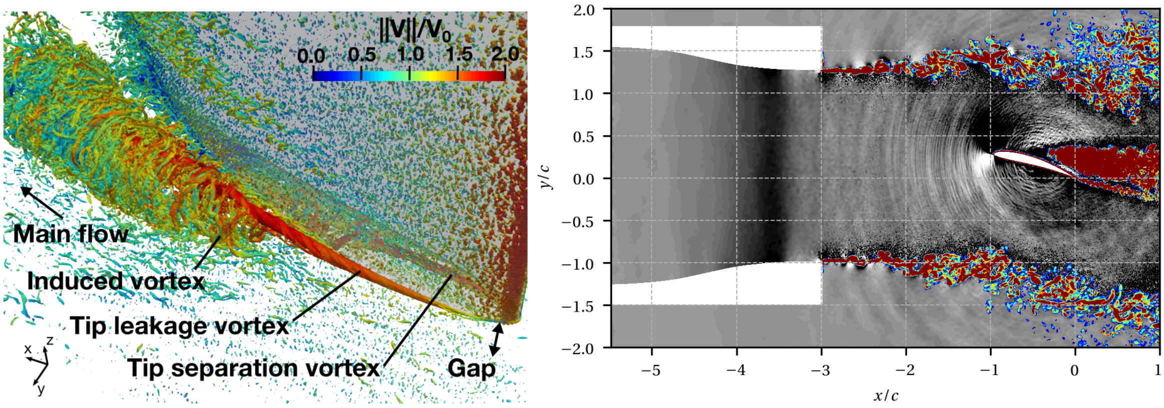

(a) Q criterion (suction side) **(b)** Vorticity and dilatation fields at $z/c = 0.1$

Figure 1.42. Instantaneous view of the tip leakage flow field

the same configuration. Compared to PIV results (see Fig. 1.43 (a)), the adapted mesh allows to capture the tip leakage vortex topology with less than 15% of error, as observed in Fig. 1.43 (c).

The spectral signature of the tip leakage flow on the airfoil suction side (77.5% of the chord, $z = 11.5$ mm) and in the farfield ($y = 2$ m, $\theta = 90°$) are given in Fig. 1.44 (a) and (b), respectively. Results from WMLES using adapted mesh are compared with the experiment of Jacob *et al.* [160] and wall-resolved LES of Koch *et al.* [161] and Boudet *et al.* [162]. PSD of the wall pressure fluctuations from the WMLES in Fig. 1.44 (a) is in agreement with the experiment, validating the use of a wall law for the study of the tip leakage flows.

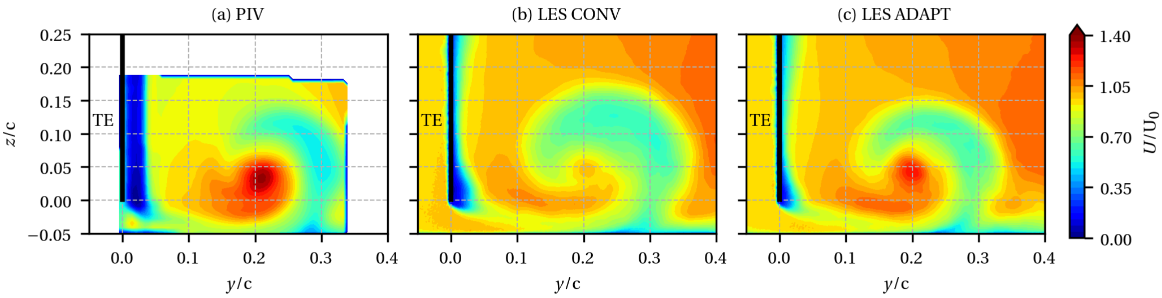

Figure 1.43. Streamwise mean velocity at the NACA 5510 trailing edge $x/c = 0.01$

Regarding the noise radiated in the far-field in Fig. 1.44 (b), the acoustic propagation is done using the pressure signal recorded on the airfoil surface and the solid FWH formulation (loading noise contribution only). The noise predicted using WMLES is globally in agreement with the experiment and other simulations, although the noise level is weak. However, the lack of thickness and quadrupole noise contribution in the FWH formulation can explain the

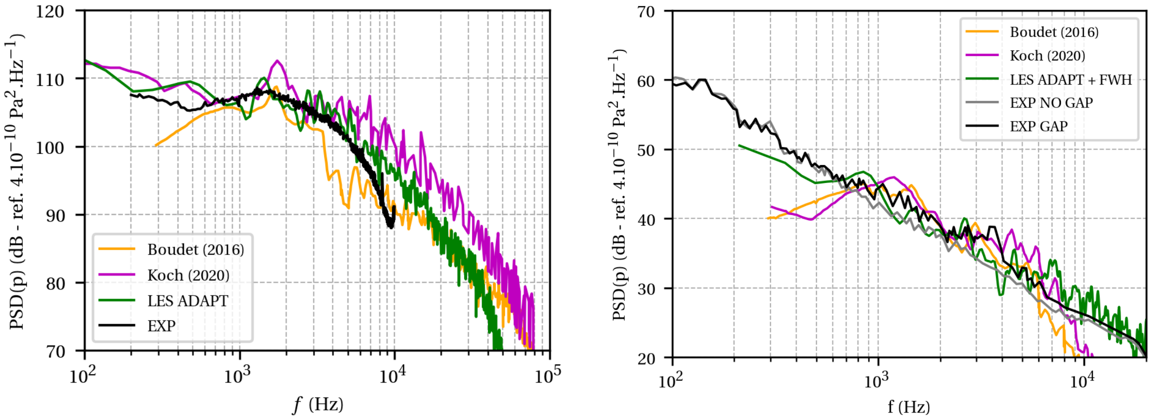

(a) Wall pressure fluctuation

(b) Farfield pressure fluctuation

Figure 1.44. Spectral signature of the Tip Leakage Flow

differences with the experiment, in particular for frequencies between 3 kHz and 4 kHz.

This first activity on the acoustics of turbomachinery, carried out jointly with the LMFA, has made it possible to define the numerical ingredients necessary for the study of fan noise. In particular, it has been observed that careful attention to the modeling of the inflow conditions is essential. In addition, due to the complexity of the flow at the fan tip, the use of AMR is mandatory together with a wall model in order to reduce the CPU cost of these simulations.

1.6.2 Combustion noise

The second part of chapter 6 aims to address the *combustion noise* issue, which represents a non-negligible sound source of the total engine noise (see Fig. 1.39). Combustion noise originates from flame unsteadiness in the combustion chamber and is characterized by two distinct mechanisms of generation and propagation: the *direct* and *indirect* noise, respectively, illustrated in Fig. 1.45. Whereas the first mechanism is due to the generation of pressure waves by the heat release fluctuations in the combustion chamber [163–165], the second is produced by the acceleration of inhomogeneities in vorticity, temperature or mixture composition through turbine stages [17, 166, 167].

In the recent work of Gentil *et al.* [65], a theoretical analysis of the composition noise is proposed, based on the linearized Euler equation and a decomposition of the entropy between temperature and mixture composition for heterogeneous species mixture flow. The validation of this model is done by comparing analytical solution and DNS using ***AVBP*** solver considering inviscid flows through two-dimensional nozzles.

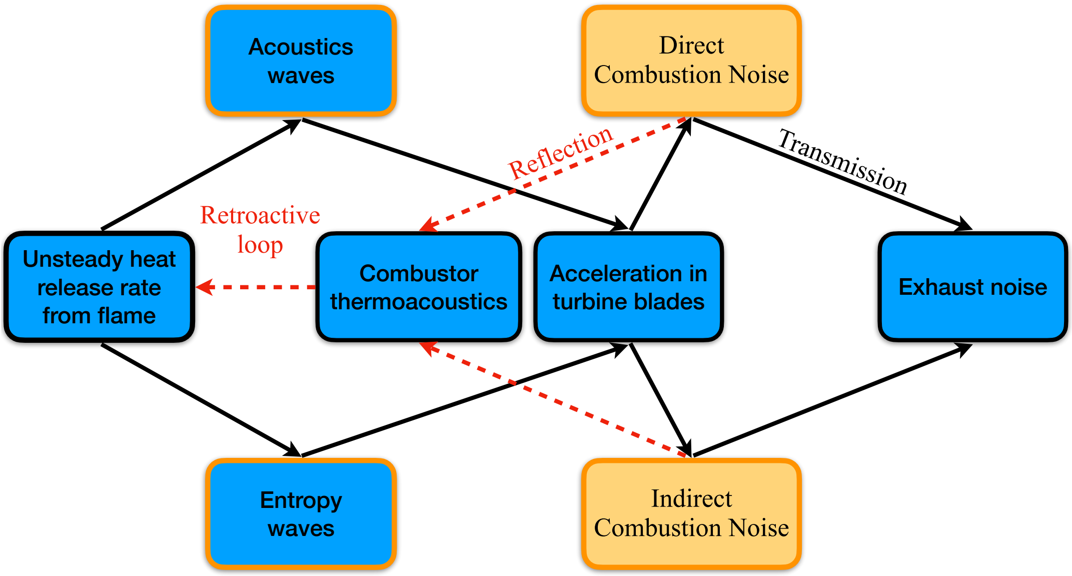

Figure 1.45. Combustion noise mechanisms, from Férand PhD thesis [154]

To study the contribution of the composition noise to the overall indirect noise, the model problem is evaluated by considering a nozzle at the outlet of the combustion chamber as depicted in Fig. 1.46. Moreover, the flow is assumed quasi-one dimensional (small variations of nozzle cross-section $A(x)$), chemically frozen, and isentropic. Under these assumptions, the non-reacting multi-species flow behavior can be described by the linearized conservative Euler equations. In the following $(\bar{\cdot})$ and $(\hat{\cdot})$ denote time average and fluctuating variables, respectively. Subscript i denote the i^{th} species.

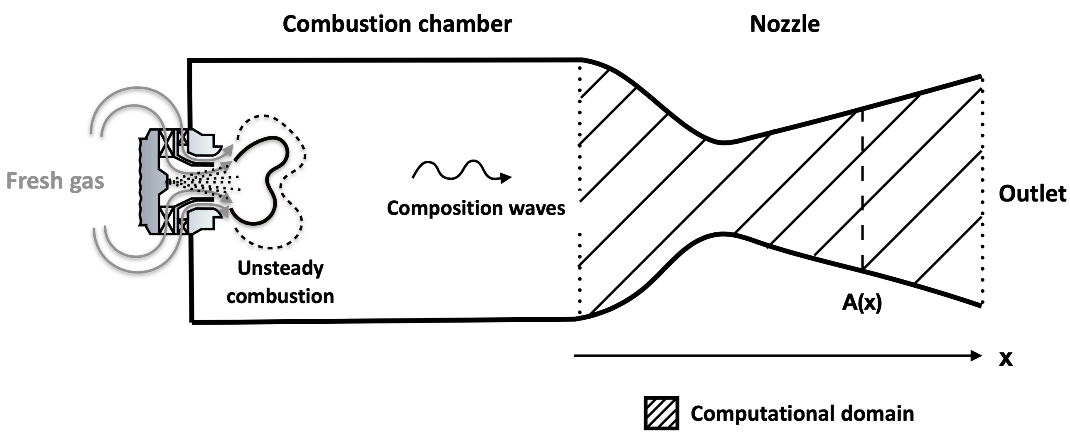

Figure 1.46. Composition noise model problem test case

In order to properly evaluate the composition noise, the idea of the model is to decouple the entropy s contribution from the species mass fraction Y_i. To do so, the specific entropy fluctuation $\hat{s}$ equation is linearized as follows:

(1.40)
$$\hat{s} = \underbrace{\sum_{i=1}^{N} \frac{\overline{C_{p,i}}}{\overline{C_p}} \bar{Y}_i \hat{s}_i}_{(1)} + \underbrace{\frac{1}{\bar{C_p}} \sum_{i=1}^{N} \left(\bar{s}_i - r_i \ln(\bar{X}_i)\right) \hat{Y}_i}_{(2)}$$

where C_p is the constant specific heat capacity, $r = \mathcal{R}_u/W$ (with $\mathcal{R}_u$ the universal gas constant and W the mean molar mass) and $X_i = Y_i W/W_i$ is the molar fraction of the i^{th} species. N is the number of species considered in the mixture.

To close the linearized Euler equations, the linearized perfect gas law $\bar{\gamma}\hat{p} = \hat{\rho} + \hat{r} + \hat{T}$ and the linearized Gibb's energy equation are considered:

(1.41)
$$\frac{\mathrm{D}}{\mathrm{D}t}\left((1-\bar{\gamma})\hat{p} + \hat{T} + \log(2 + (\bar{\gamma}-1)\bar{M}^2)\frac{\hat{\gamma}}{\bar{\gamma}(\bar{\gamma}-1)}\right) = 0$$

where $M = u/c$ is the Mach number, u the axial velocity, c the sound celerity, T the static temperature, p the static pressure and γ the heat-capacity ratio.

Finally, the model problem is described by the following system of linearized multicomponent gas equations, with $\hat{s}_n$ the term (1) in Eq. 1.40:

$$\begin{cases} \dfrac{\mathrm{D}}{\mathrm{D}t}\left[\hat{p} - \hat{s}_n\right] + \bar{u}\dfrac{\partial \hat{u}}{\partial x} = 0 & (1.42a) \\[2ex] \dfrac{\mathrm{D}}{\mathrm{D}t}\hat{u} + \dfrac{\bar{c}^2}{\bar{u}}\dfrac{\partial \hat{p}}{\partial x} + \left(2\hat{u} - (\bar{\gamma}-1)\hat{p} - \hat{s}_n - \Lambda\hat{Z}\right)\dfrac{\partial \bar{u}}{\partial x} = 0 & (1.42b) \\[2ex] \dfrac{\mathrm{D}}{\mathrm{D}t}\left(\hat{s}_n + \log(2 + (\bar{\gamma}-1)\bar{M}^2)(\Lambda - \chi)\hat{Z}\right) = 0 & (1.42c) \\[2ex] \dfrac{\mathrm{D}}{\mathrm{D}t}\hat{Z} = 0 & (1.42d) \end{cases}$$

where

$$\Lambda = \sum_{i=1}^{N} \frac{W}{W_i}\frac{\mathrm{d}Y_i}{\mathrm{d}Z}\ , \quad \chi = \sum_{i=1}^{N} \frac{\bar{C}_{p,i}}{\bar{C}_p}\frac{\mathrm{d}Y_i}{\mathrm{d}Z} \quad \text{and} \quad \frac{\mathrm{D}}{\mathrm{D}t} = \frac{\partial}{\partial t} + \bar{u}\frac{\partial}{\partial x}$$

with Z the mixture-fraction space introduced by Williams [168].

In order to describe the wave propagations through an isentropic nozzle, this system (1.42) is recast into characteristic equations, using acoustics ($w^+ = \hat{p} + \bar{M}\hat{u}$, $w^- = \hat{p} - \bar{M}\hat{u}$), entropy

($w_h^s = \hat{s}_n$) and composition ($w^z = \hat{Z}$) wave variables[15]:

$$
\begin{cases}
\left[\dfrac{\partial}{\partial t} + (\bar{u}+\bar{c})\dfrac{\partial}{\partial x}\right] w^+ = \left\{\dfrac{\eta^+ - \zeta\alpha^-}{\bar{M}} w^+ - \dfrac{\eta^+ - \zeta\alpha^+}{\bar{M}} w^- + \zeta w_h^s + \zeta\mu^+ w^z\right\} \bar{u}\dfrac{\mathrm{d}\bar{M}}{\mathrm{d}x} & (1.43a) \\[2ex]
\left[\dfrac{\partial}{\partial t} + (\bar{u}-\bar{c})\dfrac{\partial}{\partial x}\right] w^- = \left\{\dfrac{\zeta\alpha^- - \eta^-}{\bar{M}} w^+ + \dfrac{\eta^- - \zeta\alpha^+}{\bar{M}} w^- - \zeta w_h^s - \zeta\mu^- w^z\right\} \bar{u}\dfrac{\mathrm{d}\bar{M}}{\mathrm{d}x} & (1.43b) \\[2ex]
\left[\dfrac{\partial}{\partial t} + \bar{u}\dfrac{\partial}{\partial x}\right] w_h^s = -\left\{(\Lambda - \chi)\zeta(\gamma - 1)\bar{M} w^z\right\} \bar{u}\dfrac{\mathrm{d}\bar{M}}{\mathrm{d}x} & (1.43c) \\[2ex]
\left[\dfrac{\partial}{\partial t} + \bar{u}\dfrac{\partial}{\partial x}\right] w^z = 0 & (1.43d)
\end{cases}
$$

where

$$\eta^\pm = \frac{1}{2}\left(1 \pm \frac{1}{\bar{M}}\right), \quad \alpha^\pm = 1 \pm \frac{(\bar{\gamma}-1)}{2}\bar{M}, \quad \zeta = \left(1 + \frac{\bar{\gamma}-1}{2}\bar{M}^2\right)^{-1},$$

and $\quad \mu^\pm = \Lambda \pm (\Lambda - \chi)(\bar{\gamma} - 1)\bar{M}$

From the system of equations 1.43 it can be first observed that the waves are coupled through the mean flow gradient $\mathrm{d}\bar{M}/\mathrm{d}x$. Two indirect noise mechanisms can be identified first: an entropy-to-acoustic and a composition-to-acoustic couplings. In addition, the acceleration of the composition fluctuations represents an additional entropy noise source via a composition-to-entropy coupling. Moreover, the model from literature [167] is extended with the existence of coupling between composition w^z and entropy w_h^s waves. All these mechanisms are one-way couplings.

ϕ'	Y'_{O_2}	Y'_{H_2O}	Y'_{CO}	Y'_{CO_2}	Y'_{N_2}
∓ 0.1	± 0.0112	∓ 0.004	$\mp 2 \times 10^{-4}$	∓ 0.0094	± 0.0024

Table 1.4: Composition fluctuation amplitudes

Analytical solutions of system 1.43 can be found using the compact assumption (see Marble & Candel [17]) or computed using the Magnus expansion for non-compact frequencies as performed by Duran & Moreau [169]. In the following, these two analytical solutions are used to validate the model with the ***AVBP*** simulations of the Goh & Morgans inviscid nozzle [170]. Burnt gas fluctuations from an air-kerosene mixture at an equivalence ratio $\phi = 0.7$ are injected.

[15] Acoustic waves w^+ and w^- propagate at $\bar{u}+\bar{c}$ and $\bar{u}-\bar{c}$, respectively, whereas entropic w_h^s and composition w^z waves propagate at $\bar{u}$

The inlet Mach number is $M = 0.48$ with a total temperature and pressure of $T = 1966$ K and $P = 1.17$ bar, respectively. Moreover, in order to properly inject composition waves into the nozzle inlet, an extension of the boundary conditions developed in chapter 4 is proposed (detailed in the second paper of chapter 6 [65]). The composition fluctuations amplitude injected for each species is given in table 1.4. A subsonic and choked flow regimes are considered in the simulations whose Mach number and pressure profiles are described in Fig. 1.47. In each case, the quasi-one dimensional flow assumption is verified.

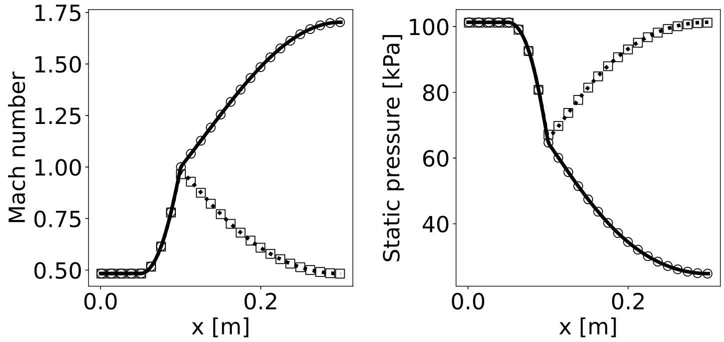

Figure 1.47. Nozzle profile (a) Mach number (b) static pressure for subsonic flow: 1D-model (······), AVBP (□) and choked flow: 1D-model (——), AVBP (○)

The composition-to-acoustic transfer functions for both simulations are shown in Fig. 1.48. It can be observed that in both cases, the analytical solution from the non-compact method is in agreement with the results from the simulations with less than 6% of error. In the subsonic case the compact analytical solution is equal to zero (Fig. 1.48 (a) & (b)), whereas in the choked case (Fig. 1.48 (c) & (d)), it converges with other results in low frequency only. These results validate the model (Eq. 1.43). Furthermore, using a parametric study, it is shown in Gentil *et al.* [65] that the contribution of the composition noise in a choked flow and lean combustion does not exceed 10% of the entropy noise whereas it decreases to 4.4% in a subsonic regime.

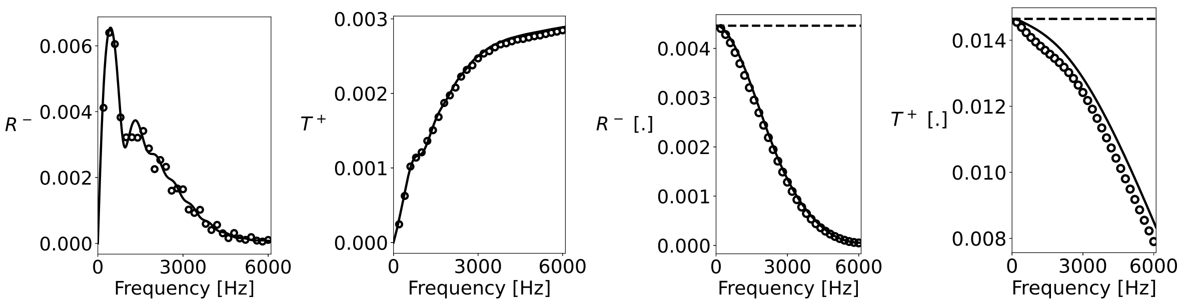

(a) Subsonic Reflection **(b)** Subsonic Transmission **(c)** Choked Reflection **(d)** Choked Transmission

Figure 1.48. Acoustic transfer functions $Non - Compact$ (——), $Compact$ (- - -), $AVBP$ (○)

This second activity on the combustion noise is realized in partnership with the University of Sherbrooke and IMFT. This work constitutes the continuation of the M. Férand Ph.D. thesis [154] and presents many challenges for future aircraft noise certification. Indeed, not only the contribution of combustion noise will increase with the UHBR architectures but it could also be amplified by the use of fuel like hydrogen [171][16].

1.7 Conclusion and Perspectives

The research project presented in this manuscript has four main components devoted to Large-Eddy Simulation of acoustics in a High-Performance Computing context: (1) numerical methods; (2) CFD meshing; (3) boundary conditions; and (4) aerodynamic noise prediction & analysis.

When dealing with Computational AeroAcoustics simulations, high-order numerical methods are the first key point to address. Traditional continuous methods such as the finite volume method have been used for industrial design for over two decades. Further improvements of the parallel scalability needed to reduce the CPU time of acoustic simulation predictions require new numerical formulations. Discontinuous approaches, like the Spectral Differences technique, discussed in chapter 2, are promising. Simplex cell elements are suitable for more complex geometries. However, research efforts in this domain must continue in order to improve robustness and overcome the CFL constraint. In particular, ongoing studies must determine whether this method is suitable for performing accurate aeroacoustic simulations. Work is also underway on shock-capturing and reactive flow simulation capabilities of Spectral Differences. On a separate path, alongside traditional Navier-Stokes based-solvers, the emergence and development of the Lattice Boltzmann Method (LBM) is also very promising. Indeed, LBM is characterized by reduced mesh generation and CPU costs, in addition to its intrinsic low dissipation properties. Cerfacs CFD team has been involved in the development of this method for ten years in collaboration with the M2P2 laboratory in order to eliminate the technological bottlenecks that prevent its use for high-speed compressible flows. Although both of these methods are beginning to show some maturity to predict airframe & turbulent noise such as landing gear or jet noise, many weaknesses must be addressed regarding turbomachinery acoustics. In particular, both Spectral Differences and Lattice Boltzmann methods suffer from meshing problems: the former require to generate high-quality unstructured high-order meshes, and the latter is not body-fitted.

Mesh generation is the second contribution of this work. Chapter 3 provides a method for automatically defining a mesh that accurately captures the physics of complex flow geometries. Numerous studies are ongoing in order to transfer this technology to the industry and extend

[16] In a turbulent hydrogen flame, broadband noise radiating at higher frequencies was observed than in a hydrocarbon-fueled flame

this method to dynamic mesh adaptation. This issue requires many skills in physics, algorithms, computational sciences & code coupling, under the constraint of low CPU cost. The natural capacity of the Spectral Differences method to deal with mesh refinement in both space h and polynomial degree p offers many perspectives in this domain. However, this may involve a projection step of the mesh to fit the original geometry as well as load balancing to preserve the high computational performance. On the contrary, the Lattice Boltzmann method does not suffer from the mesh generation process as it consists of a cartesian grid with an octree approach to define refinement areas. The first downside of this method is that the global calculation cost is multiplied by a factor of 16 for each new refinement area. In light of the resolution needed to capture the acoustics of tip leakage flows presented in the last chapter, this problem must be solved in order to achieve a reasonable turnaround CPU time. Moreover, the second issue to address with the Lattice Boltzmann method is near-wall modeling. Indeed, due to the non-body fitted mesh, some difficulties can be encountered regarding the resolution of the turbulence of wall-bounded flows, which is well-known to drive most of the aeroacoustics phenomena.

Modeling boundary conditions is critical for Computational AeroAcoustics using Large-Eddy Simulations. Research in this area has been ongoing since the 1970s, but the problem is still unsolved due to the closure issue inherent in the non-linearity of the Navier–Stokes equations. The modeling efforts described in chapter 4 have improved some of the non-reflecting inlet boundary conditions and turbulent boundary layer computational cost issues. However, these achievements must be pursued and three tasks seem to have priority. Due to the difficulty of separating the turbulence into acoustic and non-acoustic components, the output boundary conditions always pose reflection problems, especially for confined flows, such as in combustion chambers. The second issue to investigate is the wall modeling with strong flow separation, as encountered in rocket nozzle flows or on high lift devices on aircraft wings. Finally, turbulence tripping is certainly one of the most important points to address in order to develop a systematic, user-independent Computational AeroAcoustics methodology useful for industrial design. Furthermore, when dealing with Spectral Differences or Lattice Boltzmann methods, these issues represent other challenges. For Spectral Differences methods on simplex cells, the definition of non-reflecting or wall model boundary conditions is not resolved. Indeed, as the Solution Points are not collocated on the mesh, finding the boundary-normal direction is tricky. The same conclusion can be draw for the Lattice Boltzmann method: as the equation resolution is done on the particle distribution functions and not on the hydrodynamic Eulerian macroscopic variables, most of the existing boundary conditions are not well-posed.

The last contribution of this work is devoted to the study of jet, fan, and combustion noise. First, the work described in chapter 5 allowed to study the jet noise radiated by realistic nozzle flow geometries using Large-Eddy Simulation, considering subsonic and supersonic regimes. It should be noted that few studies consider the coaxial jet in the literature and that efforts must continue to improve our understanding of these flows and their radiated acoustics, especially considering the integration of the engine on an aircraft, i.e. with the presence of the pylon and wing. Due to the computational cost of converging acoustic data on such industrial configurations, this will likely be done using the Lattice Boltzmann method, but much effort is still needed to develop and validate this approach. However, the realization of complete aircraft engine noise simulations integrating at least jet noise, fan noise and especially core noise will certainly take place via a coupling of different codes at first. Indeed, although simulations including the combustion chamber, the compressor, and turbine are now feasible, it seems more cost-effective at this time to simulate the internal hydrodynamics and acoustics of UHBR and CROR engine components independently and use the outputs as boundary conditions for the jet noise simulation. The analysis and modeling described in chapter 6 go in this direction and a collaborative effort must be sustained to achieve this.

In the continuity of the present study, these key points must be addressed in the coming years to develop the methodology necessary for a complete numerical certification of aircraft noise. It seems that this goal will be reached before completely understanding the physical phenomena involved. This represents the next challenge to reach to design radiated noise control devices using CFD.

In this regard, the use of Artificial Intelligence (AI) should be considered. Indeed, recent progress in physics-informed machine learning [172, 173] could lead to improved physical and numerical models. As a prospect, new collaborative efforts have been initiated in this direction

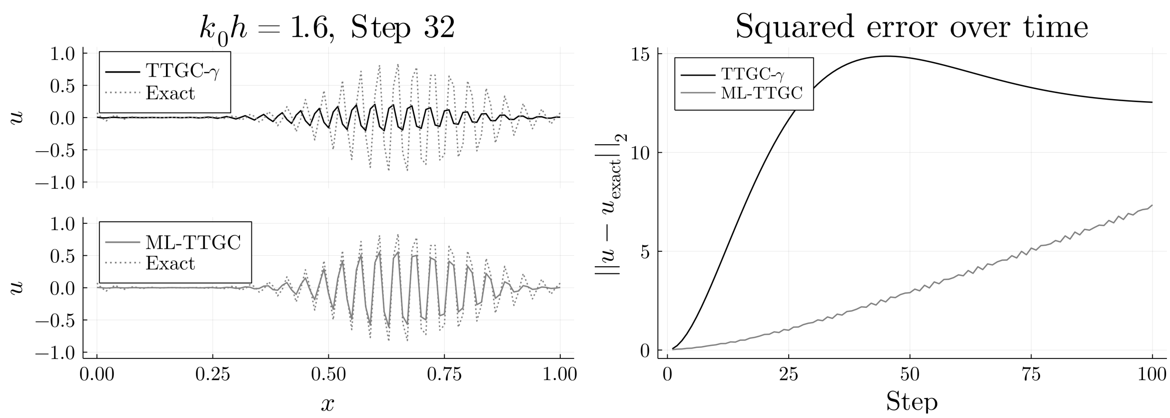

(a) Wavepacket convection after 32 iterations

(b) L2 norm of the error evolution

Figure 1.49. High frequency wavepacket convection over a regular mesh for TTGC-γ scheme vs ML-TTGC scheme, from Drozda *et al.* [174]

to design optimized numerical schemes [174, 175]. During the current PhD of L. Drozda, a Graph Neural Network (GNN) has been used to improve the stability and dissipation of the Taylor-Galerkin C (TTGC)-γ scheme [176]. Indeed, in the original TTGC scheme, an optimal global value γ is fixed to control the dissipation at high wavenumbers. However, this choice in a single value for γ requires an additional artificial dissipation to stabilize the scheme on discontinuities like shocks [177]. To circumvent the problem, the idea was to used a GNN model to tune locally the parameter γ. The resulting optimized dissipation of the Machine Learned TTGC (ML-TTGC) is illustrated in Fig. 1.49 considering a wavepacket advection (k_0 is the wavenumber and h the mesh spacing). These results are very encouraging with a reduction of 40% in dissipation compared to the original TTGC scheme after 100 time steps.

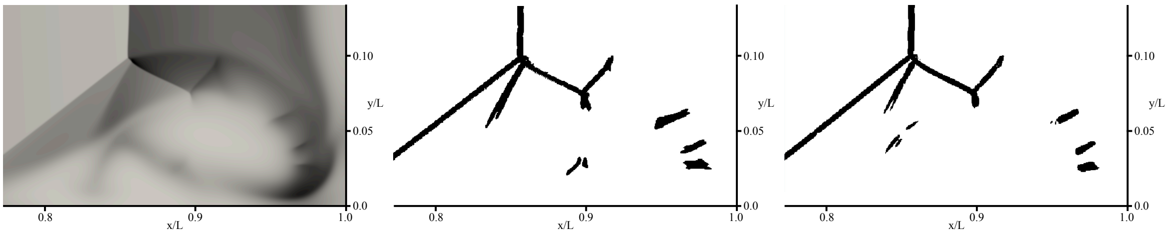

(a) Density $1.2 \leq \rho/\rho_0 \leq 120$ **(b)** Pressure-based shock sensor **(c)** Neural Network shock sensor

Figure 1.50. Reflected shock-boundary layer interaction in a shock tube for Reynolds number $Re = 1000$ at a dimensionless time $t = 0.4$. The solid black lines in Fig. (b) and (c) indicate the regions where shocks are detected. Internship of N. Cazard

One other interesting recent application of using Deep Learning models to aid fluid mechanics simulations has been to provide a general and accurate shock detection method for CFD. This data-informed shock-capturing method was explored during the internship of N. Cazard on a reflected shock-boundary layer interaction in a shock tube for Reynolds number $Re = 1000$, illustrated in Fig. 1.50 (the flow field configuration can be found in Daru & Tenau [178]). The density field after the reflection of the initial shock on the right wall at $x/L = 1$ is shown in Fig. 1.50 (a), where the shock pattern exhibits a lambda shape followed by a separation region. The shock-detection procedure proposed by Bogey *et al.* [179] is compared with those given by a GNN in Fig. 1.50 (b) and (c), respectively. The prediction seems at first sight very good, but some differences remain in the separation region. Nevertheless, it remains rather difficult to judge only visually the quality of the shock prediction in an objective way. The next step would be to couple the shock detection GNN model with a CFD solver as AVBP to quantify the efficiency of the approach, as performed by Lapeyre *et al.* [180] for a premixed turbulent combustion model. Machine learning for CFD is a research topic of growing interest and work in this area will be continued to improve numerical methods and physical models of CFD solvers.

Finally, the last research perspectives of this work concern aerospace applications and high-speed compressible flows. Since 2018, research efforts have been conducted in collaboration with CNES and ArianeGroup on predicting the flow separation and resulting side loads in rocket nozzles. Jet flow separation is a phenomenon observed during the ignition and extinction of rocket engines. As a first step, the mesh generation methodology presented in Chapter 3 has been applied and validated on an academic Truncated Ideal Contour (TIC) nozzle [57]. In particular, it has been shown that the Free-Shock Separation (FSS) regime that characterizes the over-expanded flow physics in a TIC nozzle was correctly predicted.

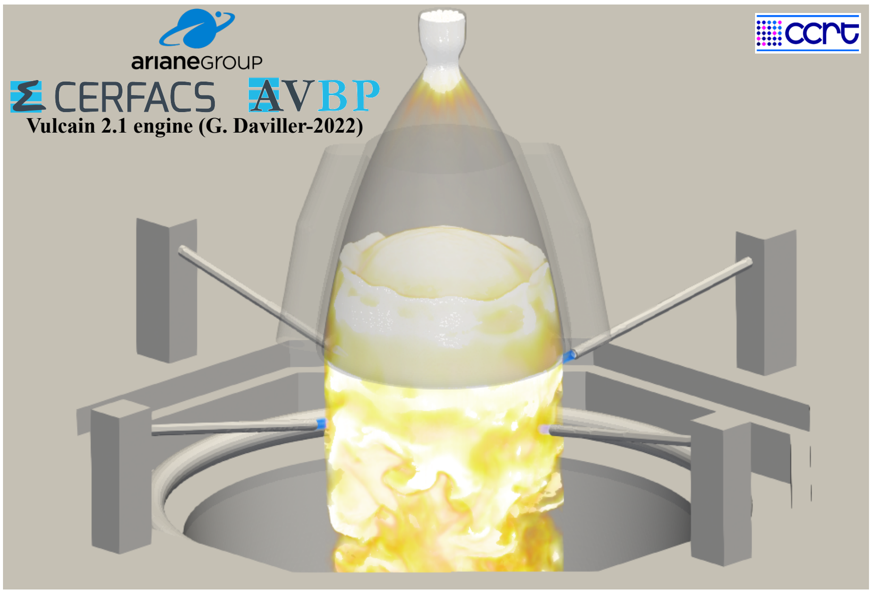

Figure 1.51. Temperature isosurface during the full-scale *Vulcain®2.1* engine ignition sequence, from Daviller *et al.* [181]

To study this phenomenon under realistic conditions, recent works done during the Grand Challenge CCRT 2022 have allowed the simulation of the ignition sequence of the full-scale *Vulcain®2.1* engine [181]. A view of the flow field during the mass flow rates increase phase is shown using a temperature isosurface in Fig. 1.51. In particular, the non-axisymmetric separation line from the Restricted Shock Separation (RSS) along the wall of the nozzle divergent is visible. This study has demonstrated the feasibility of this type of simulation and allows us to consider further research not only on side loads generation but also on numerical methods and physical models.

Chapter 2

High order numerical method

The article presented in this chapter is part of Adèle Veilleux's PhD thesis. This thesis was funded by Cerfacs and Onera from 2017 to 2021. The objective was to extend the Spectral Difference (SD) method on unstructured hybrid grids. Using Raviart-Thomas elements, the SD method (SDRT) was first extended up to sixth-order of accuracy on triangles. Then the SDRT method was shown to be stable on tetrahedra up to third-order using Fourier stability analysis, presented in the following. All details can also be found in the thesis manuscript of A. Veilleux [75].

A. Veilleux, G. Puigt, H. Deniau, and G. Daviller. Stable spectral difference approach using raviart-thomas elements for 3D computations on tetrahedral grids. *Journal of Scientific Computing*, 91(7), 2022. https://doi.org/10.1007/s10915-022-01790-2

Stable Spectral Difference Approach Using Raviart-Thomas Elements for 3D Computations on Tetrahedral Grids

Adèle Veilleux[1,2] · Guillaume Puigt[1] · Hugues Deniau[1] · Guillaume Daviller[2]

Received: 21 May 2021 / Revised: 7 December 2021 / Accepted: 25 January 2022 /
Published online: 21 February 2022

Abstract
In this paper, the Spectral Difference approach using Raviart-Thomas elements (SDRT) is formulated for the first time on tetrahedral grids. To determine stable formulations, a Fourier analysis is conducted for different SDRT implementations, i.e. different interior flux points locations. This stability analysis demonstrates that using interior flux points located at the Shunn-Ham quadrature rule points leads to linearly stable SDRT schemes up to the third order. For higher orders of accuracy, a significant impact of the position of flux points located on faces is shown. The Fourier analysis is then extended to the coupled time-space discretization and stability limits are determined. Additionally, a comparison between the number of interior FP required for the SDRT scheme and the Flux Reconstruction method is proposed and shows that the two approaches always differ on the tetrahedron. Unsteady validation test cases include a convergence study using the Euler equations and the simulation of the Taylor-Green vortex.

Keywords High-order · Spectral difference · Raviart-Thomas · Tetrahedra

1 Introduction

Numerical schemes using piecewise continuous polynomials approximation are an efficient way to obtain high-order accuracy on unstructured grids. Their interest comes from the

Adèle Veilleux
Adele.Veilleux@onera.fr

Guillaume Puigt
Guillaume.Puigt@onera.fr

Hugues Deniau
Hugues.Deniau@onera.fr

Guillaume Daviller
Guillaume.Daviller@cerfacs.fr

1 ONERA/DMPE, Université de Toulouse, 31055 Toulouse, France

2 Centre Européen de Recherche et de Formation Avancée en Calcul Scientifique (CERFACS), 42 avenue Gaspard Coriolis, 31057 Toulouse Cedex 01, France

possibility to handle a high-order representation of the unknowns using polynomials and a compact stencil, which allows to achieve a good parallel efficiency. By nature, the solution is sought under the form of a polynomial defined locally, in each mesh cell. Since continuity is not required at cell interfaces, a Riemann solver is introduced to define the flux from two different extrapolated quantities. In the case of the most popular high-order discontinuous method called the Discontinuous Galerkin (DG) approach, the full system of equations is built using the weak formulation, as in the standard finite element method. For a solution approximated as a polynomial of degree p defined on a given basis, test functions are also polynomials of degree p and quadrature rules are necessary to compute either volume or surface integrals at the appropriate order of accuracy. Depending on the definition of the solution approximation, different DG implementations are possible. On one hand, the DG method is said nodal if the solution approximation is defined by an interpolation from solution values at dedicated points (such as Lagrange interpolation). On the other hand, if the solution approximation is expressed as a linear combination over a basis, the DG method is modal, since coefficients from the linear combination are simply modes of the solution.

An advantage of standard DG methods (either nodal or modal) is their ability to deal with unstructured mesh. The formulation naturally accounts for simplex cells (tetrahedron in 3D), which are the standard elements for (automatic) mesh generation on complex geometry. The literature on the Discontinuous Galerkin method on simplex cells is very rich ([1–6] for example). However, using the integral formulation leads to a heavy computational cost to obtain a high-order of accuracy since high-order surface and volume integral evaluations using quadrature rules are required.

The main objective of the present paper is to draw attention to more recent classes of numerical methods using piecewise polynomials based on the strong form of equations for tetrahedral grids. Alternative methods explicitly compute two polynomials, one for the solution and one for the flux. For consistency, the flux divergence must lie in the same polynomial space as the solution. Today, there are essentially two different methods based on the strong form.

The first method is called the Correction Procedure for Reconstruction (CPR) or the Flux Reconstruction (FR) approach. Following the pioneering work of Huynh [7], the solution and the flux approximations are first defined with the same polynomial degree from a set of points called solution points. This leads to a flux polynomial inconsistent with the solution since its divergence loses one degree. In addition, the flux is defined from the solution and therefore not continuous at cell interfaces. To remedy both problems, a correction polynomial is introduced. This correction polynomial is defined from the flux at the cell interfaces at a degree equal to the one of the solution plus one. Several FR reconstructions can be built depending on the definition of the correction polynomial, associated with different properties and capabilities. Several studies investigate the FR implementation on tetrahedral cells. The class of Vincent-Castonguay-Jameson-Huynh (VCJH) [8] schemes were first extended to tetrahedral elements by Williams and Jameson [9]. The effect of the solution point location was studied in [10, 11] to determine their effect on the stability and the accuracy of FR schemes on tetrahedral grids. Both works indicate that the best choice in terms of stability and accuracy is to locate the solution points following the Shunn-Ham quadrature rule [12]. The FR method was then used to simulate turbulent flows on tetrahedral meshes by Bull and Jameson [13].

The second approach is called the Spectral Difference method. Initiated by Kopriva [14] as the staggered-grid Chebyshev multi-domain method for structured grids, it was then introduced for triangular elements together with the naming Spectral Difference (SD) [15]. The standard formulation was found unstable on triangles for an order of accuracy strictly greater than two by Van Abeele [16]. Researchers essentially focused attention on unstructured quadrilateral and hexahedral grids, following a tensorial formulation from the 1D stable discretization. An alternative formulation called the Spectral Difference method using the Raviart-Thomas space (SDRT) was introduced for Euler equations in [17] on triangles and proven to be linearly stable up to the fourth-order under a Fourier stability analysis originally initiated by May and Schöberl [18]. The SDRT method was then formulated to simulate 2D viscous flows on unstructured hybrid grids up to the fourth-order by Li *et al.* [19] and used for the simulation of vortex-induced vibrations using a sliding-mesh method on hybrid grids by Qiu *et al.* [20]. Finally, the method was extended to higher orders of accuracy in [21] for triangular and 2D hybrid grids. To the author's knowledge, the literature on the Spectral Difference is dedicated to quadrilateral, triangular and hexahedral cells.

In this context, the present paper introduces the first linearly stable formulation of the Spectral Difference method on 3D simplex cells. The paper is organized as follows. In Sect. 2, the SDRT scheme is presented on tetrahedral cells. The linear stability of the SDRT method based on interior FP located at known quadrature rules points is studied using Fourier analysis in Sect. 3. Stable formulations are determined up to the third-order of accuracy. The influence of flux points located on faces for $p = 3$ is highlighted. The Fourier analysis is then extended to the coupled time-space discretization. Unsteady validation test cases are presented in Sect. 4 and include a convergence study using the Euler equations and the simulation of the Taylor-Green vortex.

2 Spectral Difference Scheme on Tetrahedral Grids

2.1 Reference Domain

Let us consider the following 3D scalar conservation law under its differential form:

$$\frac{\partial u(\mathbf{x}, t)}{\partial t} + \nabla \cdot \mathbf{f}(u) = 0, \quad \text{in } \Omega \times [0, t_f], \tag{1}$$

where u is the state variable, $\mathbf{f} = (f, g, h)$ is the flux vector where f, g and h are flux densities in the x, y and z directions respectively and ∇ is the differential operator in the physical domain $\mathbf{x} = (x, y, z)$. The computational domain Ω is discretized into N non-overlapping tetrahedral cells and the i-th element is denoted Ω_i:

$$\Omega = \bigcup_{i=1}^{N} \Omega_i. \tag{2}$$

For implementation simplicity, Eq. (1) is solved in the reference domain. Each cell Ω_i of the domain Ω is transformed into a reference tetrahedron $\mathcal{T}_e := \{(\xi, \eta, \zeta) : 0 \leq \xi, \eta, \zeta \leq 1, \xi + \eta + \zeta \leq 1\}$. The transformation can be written as:

$$\begin{pmatrix} x \\ y \\ z \end{pmatrix} = \sum_{i=1}^{N_p} M_i(\xi, \eta, \zeta) \begin{pmatrix} x_i \\ y_i \\ z_i \end{pmatrix}, \tag{3}$$

where (x_i, y_i, z_i) are the Cartesian coordinates of the N_p vertices of the cells and $M_i(\xi, \eta, \zeta)$ are the shape functions. The Jacobian matrix of the transformation given by Eq. (3) from the physical (x, y, z) to the reference domain (ξ, η, ζ) takes the following form:

$$J = \frac{\partial(x, y, z)}{\partial(\xi, \eta, \zeta)} = \begin{bmatrix} x_\xi & x_\eta & x_\zeta \\ y_\xi & y_\eta & y_\zeta \\ z_\xi & z_\eta & z_\zeta \end{bmatrix}. \tag{4}$$

For a non-singular transformation, the inverse transformation is related to the Jacobian matrix according to:

$$\frac{\partial(\xi, \eta, \zeta)}{\partial(x, y, z)} = \begin{bmatrix} \xi_x & \xi_y & \xi_z \\ \eta_x & \eta_y & \eta_z \\ \zeta_x & \zeta_y & \zeta_z \end{bmatrix} = J^{-1}. \tag{5}$$

In the reference domain, Eq. (1) becomes:

$$\frac{\partial \hat{u}(\boldsymbol{\xi}, t)}{\partial t} + \hat{\nabla} \cdot \hat{\mathbf{f}} = 0, \tag{6}$$

where $\hat{\nabla}$ is the differential operator in the reference domain, $\boldsymbol{\xi} = (\xi, \eta, \zeta)$ are the coordinates in the reference domain and $\hat{u}, \hat{\mathbf{f}}$ are the solution and the flux in the reference domain defined by:

$$\hat{u} = |J|u, \tag{7}$$

and

$$\hat{\mathbf{f}} = |J|J^{-1}\mathbf{f}. \tag{8}$$

2.2 SDRT Scheme on Tetrahedra

The SDRT scheme introduced in [17, 22] for triangles is here extended to 3D simplex cells, i.e. tetrahedra.

2.2.1 Solution Polynomial

The solution $\hat{u}$ is approximated on the reference tetrahedron $\mathcal{T}_e$ by a polynomial of degree p, $\hat{u}_h(\boldsymbol{\xi}) \in \mathbb{P}_p$, through a set of distinct Solution Points (SP) $\boldsymbol{\xi}_j$, $j \in [\![1, N_{SP}]\!]$ where

$$N_{SP} = \frac{(p+1)(p+2)(p+3)}{6}, \tag{9}$$

and

$$\mathbb{P}_p = \text{span}\{\xi^i \eta^j \zeta^k, 0 \le i, 0 \le j, 0 \le k \text{ and } i + j + k \le p\}. \tag{10}$$

The polynomial $\hat{u}_h(\boldsymbol{\xi})$ is expanded using a modal representation:

$$\hat{u}_h(\boldsymbol{\xi}) = \sum_{m=1}^{N_{SP}} \bar{u}_m \, \Phi_m(\boldsymbol{\xi}), \tag{11}$$

where $\Phi_m(\boldsymbol{\xi}) \in \mathbb{P}_p$ is a complete polynomial basis and $\bar{u}_m$ are the modal basis coefficients. Coefficients $\bar{u}_m$ are determined by performing a collocation projection at the points $\boldsymbol{\xi}_j$:

$$\hat{u}_h(\boldsymbol{\xi}_j) = \hat{u}_j = \sum_{m=1}^{N_{SP}} \bar{u}_m \, \Phi_m(\boldsymbol{\xi}_j), \tag{12}$$

$$\bar{u}_m = \sum_{m=1}^{N_{SP}} \hat{u}_j \, \left(\Phi_m(\boldsymbol{\xi}_j)\right)^{-1}. \tag{13}$$

The basis Φ is chosen as the orthonormal Proriol-Koornwinder-Dubiner (PKD) [23–25] basis, given on the tetrahedron for a polynomial approximation of degree p as:

$$\begin{aligned}\Phi_{i,j,k} &= \sqrt{(i+1/2)(i+j+1)(i+j+k+3/2)}\; P_i^{0,0}(\xi)\\ &\left(\frac{1-\eta}{2}\right)^i P_j^{2i+1,0}(\eta)\left(\frac{1-\zeta}{2}\right)^{i+j} P_k^{2(i+j+1),0}(\zeta),\\ &i+j+k \le p,\end{aligned} \tag{14}$$

where $P_n^{\alpha,\beta}$ are the corresponding n-th order Jacobi polynomials on the interval $[-1, 1]$ which, under the Jacobi weight $(1-x)^\alpha(1+x)^\beta$ are orthogonal polynomials. For simplicity, the subscript (i, j, k) can be replaced by the single index m, $m \in [\![1, N_{SP}]\!]$ with any arbitrary bijection $m \equiv m(i, j, k)$. The polynomial approximation $\hat{u}_h$ of the solution $\hat{u}$ is thus defined in the reference space by:

$$\hat{u}_h(\boldsymbol{\xi}) = \sum_{m=1}^{N_{SP}} \hat{u}_j\, \left(\Phi_m(\boldsymbol{\xi}_j)\right)^{-1}\, \Phi_m(\boldsymbol{\xi}). \tag{15}$$

2.2.2 Solution Computation at Flux Points

To compute the flux values at flux points (FP), we first have to determine the solution values at those points. With the polynomial distribution given by Eq. (15), the solution at the FP (denoted $\boldsymbol{\xi}_k$) can be computed as:

$$\hat{u}_h(\boldsymbol{\xi}_k) = \sum_{m=1}^{N_{SP}} \hat{u}_j\, \left(\Phi_m(\boldsymbol{\xi}_j)\right)^{-1}\, \Phi_m(\boldsymbol{\xi}_k) = \sum_{m=1}^{N_{SP}} \hat{u}_j\, (\mathcal{V}_{j,m})^{-1}\, \Phi_m(\boldsymbol{\xi}_k), \tag{16}$$

where $\mathcal{V}$ is the generalized Vandermonde matrix. Numerically, the extrapolation step is represented by the transfer matrix $\mathbf{T}_{kj} = \left[(\mathcal{V}_{j,m})^{-1}\, \Phi_m(\boldsymbol{\xi}_k)\right]$.

2.2.3 Definition of the Flux Polynomial from the Set of Fluxes at Flux Points

The flux function in the reference domain is approximated by $\hat{\mathbf{f}}_h$ in the Raviart-Thomas (RT) space (see Appendix A for details) as:

$$\hat{\mathbf{f}}_h(\boldsymbol{\xi}) = \sum_{k=1}^{N_{FP}} \hat{f}_k \boldsymbol{\psi}_k(\boldsymbol{\xi}), \tag{17}$$

where N_{FP} is the number of degrees of freedom needed to represent a vector-valued function in the RT_p space:

$$N_{FP} = \frac{1}{2}(p+1)(p+2)(p+4), \tag{18}$$

and $\boldsymbol{\psi}_k$ are interpolation functions which form a basis in the RT space with the property:

$$\boldsymbol{\psi}_j(\boldsymbol{\xi}_k) \cdot \hat{\mathbf{n}}_k = \delta_{jk}, \tag{19}$$

where δ is the Kronecker symbol and $\hat{\mathbf{n}}_k$ are the unit normal vectors defined at FP. As for the SDRT formulation on triangles, for interior FP, one physical point is associated with d degrees of freedom, where d is the dimension, through the definition of unit vectors in different directions. In 3D, the unit vectors for interior FPs are $\hat{\mathbf{n}} = (1, 0, 0)^\top$, $\hat{\mathbf{n}} = (0, 1, 0)^\top$ and $\hat{\mathbf{n}} = (0, 0, 1)^\top$ in the reference element.

Scalar flux values f_k at FP on which the polynomial approximation given by Eq. (17) relies on are determined in the same manner as for 2D simplex cells. For a first-order partial differential equation, they are given as:

$$\hat{f}_k = \begin{cases} \hat{\mathbf{f}}_k \cdot \hat{\mathbf{n}}_k = |J| J^{-1} \mathbf{f}_k(u_h(\boldsymbol{\xi}_k)) \cdot \hat{\mathbf{n}}_k, & \boldsymbol{\xi}_k \in \mathcal{T}_e \setminus \partial\mathcal{T}_e, \\ \left(\hat{\mathbf{f}}_k \cdot \hat{\mathbf{n}}_k\right)^* = \left(\mathbf{f}_k \cdot |J| (J^{-1})^\top \hat{\mathbf{n}}_k\right)^*, & \boldsymbol{\xi}_k \in \partial\mathcal{T}_e. \end{cases} \tag{20}$$

where $\left(\hat{\mathbf{f}}_k \cdot \hat{\mathbf{n}}_k\right)^*$ is the standard numerical flux in the reference element and $u_h(\boldsymbol{\xi}_k) = \frac{1}{|J|}\hat{u}_h(\boldsymbol{\xi}_k)$ is the approximated solution in the physical domain.

2.2.4 Differentiation of the Flux Polynomial in the Set of Solution Points

Once the flux vector is approximated on the reference element by Eq. (17), it can be differentiated at SP:

$$\begin{aligned} \hat{\nabla} \cdot \hat{\mathbf{f}}(u) &= \left(\hat{\nabla} \cdot \hat{\mathbf{f}}_h\right)(\boldsymbol{\xi}_j) \\ &= \sum_{k=1}^{N_{FP}} \hat{f}_k \left(\hat{\nabla} \cdot \boldsymbol{\psi}_k\right)(\boldsymbol{\xi}_j). \end{aligned} \tag{21}$$

Numerically, the differentiation step is represented by the differentiation matrix $\mathbf{D}_{jk} = \left[\left(\hat{\nabla} \cdot \boldsymbol{\psi}_k\right)(\boldsymbol{\xi}_j)\right]$. The term $\left(\hat{\nabla} \cdot \boldsymbol{\psi}_k\right)(\boldsymbol{\xi}_j)$ in Eq. (21) is fully defined through the determination of the vector-valued interpolation basis functions $\boldsymbol{\psi}_k$ and their derivatives detailed in [21].

The final form of the SDRT scheme can be written for each degree of freedom of the solution function in each cell i as:

$$\frac{d\hat{u}_j^{(i)}}{dt} + \sum_{k=1}^{N_{FP}} \hat{f}_k^{(i)} \left(\hat{\nabla} \cdot \boldsymbol{\psi}_k\right)(\boldsymbol{\xi}_j) = 0, \quad j \in [\![1, N_{SP}]\!], \quad i \in [\![1, N]\!]. \tag{22}$$

and the solution can be time-integrated using any standard time integration scheme (Runge-Kutta scheme for instance).

3 Linear Stability Analysis of the SDRT Formulation

The SDRT formulation on tetrahedral elements was introduced but the position of the flux points is still an open question. In this section, the position of the flux points is described and the stability of the formulation is justified by a Fourier analysis.

3.1 Choice of Solution Points and Flux Points Location

The location of SP and FP needs to be chosen for the reference tetrahedron. The number of SP and FP are respectively given by:

$$N_{SP} = \frac{1}{6}(p+1)(p+2)(p+3), \tag{23}$$

$$N_{FP} = \frac{1}{2}(p+1)(p+2)(p+4). \tag{24}$$

Table 1 Number of SP and physical interior FP for SDRT scheme on tetrahedral elements

p	N_{SP}	N_{pi}
1	4	1
2	10	4
3	20	10
4	35	20
5	56	35
6	84	56

Remark In this article, the FP location is constrained so that there are no points located at vertices and on edges of the tetrahedron. Actually, if such points were used, FP could be shared by more than two cells and a multi-dimensional Riemann solver should be used. If the interface FP are located on the face (and not on edges), such a configuration will never appear.

Applying this requirement, the number of FP located on each face is equal to $(p+1)(p+2)/2$, which corresponds to the number of SP on a triangle. By choosing their location to be the same as the SP on a triangle, we ensure that a tetrahedral and a prismatic element will share the same FP on faces, avoiding the need to apply mortar techniques. For $p \in [\![1, 2]\!]$, the face FP are thus located following the Williams-Shunn-Jameson quadrature rule [26]. The number of interior FP is then given by:

$$N_i = \frac{1}{2} p(p+1)(p+2). \tag{25}$$

Since each physical FP is counted as three separated DoF, the number of interior physical FP for which the position has to be settled is $N_{pi} = \frac{1}{6} p(p+1)(p+2)$. The number of SP and physical interior FP is summarized in Table 1. It can be noted that the number of physical interior FP for a SDRT$_p$ scheme corresponds to the number of SP for a SDRT$_{p-1}$ scheme.

To set the SP and physical interior FP locations on tetrahedral elements, quadrature rules available in the literature are studied. To be suitable for the SDRT implementation, the quadrature rules should not have points located on corner, edge or face. Among the possible quadratures, three quadrature rules are found to lead to the appropriate number of points for each degree p while fulfilling this requirement: the Newton-Cotes Open (NCO) [27], the Vioreanu-Rokhlin [28] and the Shunn-Ham [12] quadrature rules. Since those quadrature rules are suitable for each degree p, they can be used for both the SP and the physical interior FP by choosing the adequate quadrature order. Other quadrature rules can lead to the proper number of points for a given degree p and will be given below. The SP are chosen to be located at the Shunn-Ham quadrature points. For the physical interior FP:

- For $p = 1$, all the studied quadrature rules led to the same physical interior point located at $(x, y, z) = (0.25, 0.25, 0.25)$ in the reference domain.
- For $p = 2$, it is noted that several quadrature rules lead to the very same set of points (Keast [29], Vioreanu-Rokhlin [28], Shunn-Ham [12], Witherden-Vincent [30], Yu [31], Hammer-Marlowe-Stroud [32], Liu-Vinokur [33]). This set of point will be referred here as the Shunn-Ham quadrature rule. Three other quadrature rules containing four points will be studied: the Jaśkowiec-Sukumar [34], the Xiao-Gimbutas [35] and the NCO [27].
- For $p > 2$, the studied quadrature rules are Shunn-Ham, Vioreanu-Rokhlin and NCO, which contain the appropriate number of points for each p.

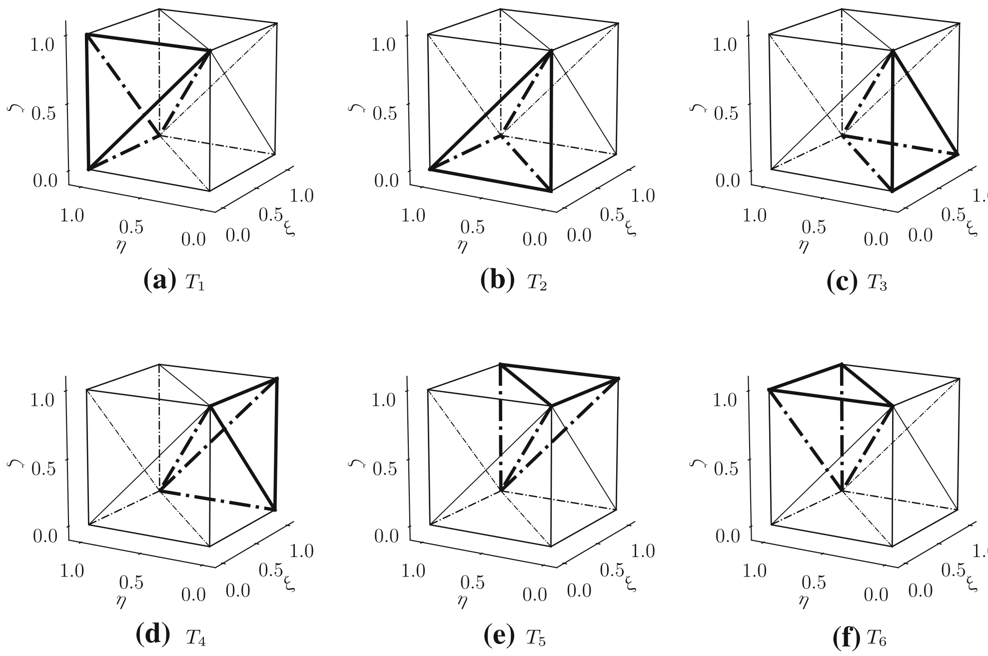

(a) T_1 **(b)** T_2 **(c)** T_3

(d) T_4 **(e)** T_5 **(f)** T_6

Fig. 1 Computational domain for the Fourier stability analysis on tetrahedral elements

3.2 Matrix Form

We consider the 3D linear advection equation:

$$\frac{\partial u(\mathbf{x}, t)}{\partial t} + \nabla \cdot \mathbf{f} = 0, \quad \text{in } \Omega \times [0, t_f] \tag{26}$$

within a domain $\Omega = [0, L]^3$ with periodic boundary conditions, where u is a conserved scalar quantity and $\mathbf{f} = \mathbf{c} \cdot u$ is the flux. The velocity vector is $\mathbf{c} = (\sin\theta_2 \cos\theta_1, \sin\theta_2 \sin\theta_1, \cos\theta_2)^\top$ where $(\theta_1, \theta_2) \in [0, \pi/4]$. The domain Ω is meshed as a Cartesian mesh composed of $N_x \times N_y \times N_z$ hexahedral elements of size $\Delta x \times \Delta y \times \Delta z$, with $\Delta x = \Delta y = \Delta z$. Each hexahedral cell is then divided into tetrahedron. A hexahedron can be decomposed into a minimum of five tetrahedral elements, but to ensure the periodicity, six tetrahedrons are required. The six tetrahedrons of the hexahedral cell (i_1, i_2, i_3) are denoted $T^{i_1,i_2,i_3,1}$, $T^{i_1,i_2,i_3,2}$, $T^{i_1,i_2,i_3,3}$, $T^{i_1,i_2,i_3,4}$, $T^{i_1,i_2,i_3,5}$, $T^{i_1,i_2,i_3,6}$ and are represented in Fig. 1.

Defining:

$$\hat{\mathbf{U}}_j^{i_1,i_2,i_3} = [\hat{\mathbf{U}}_j^{i_1,i_2,i_3,1}, \hat{\mathbf{U}}_j^{i_1,i_2,i_3,2}, \hat{\mathbf{U}}_j^{i_1,i_2,i_3,3}, \hat{\mathbf{U}}_j^{i_1,i_2,i_3,4}, \hat{\mathbf{U}}_j^{i_1,i_2,i_3,5}, \hat{\mathbf{U}}_j^{i_1,i_2,i_3,6}]^\top, \tag{27}$$

as the vector collecting the solution in the reference domain on the six tetrahedrons for each SP $j \in [\![1, N_{SP}]\!]$ on cell (i_1, i_2, i_3), the SDRT spatial discretization using an upwind flux on this mesh takes the form:

$$
\begin{aligned}
\frac{d\mathbf{U}_j^{i_1,i_2,i_3}}{dt} = -\frac{||\mathbf{c}||}{\Delta x}\Big[& \mathbf{M}^{0,0,0}\,\hat{\mathbf{U}}_j^{i_1,i_2,i_3} + \mathbf{M}^{-1,0,0}\,\hat{\mathbf{U}}_j^{i_1-1,i_2,i_3} \\
& + \mathbf{M}^{+1,0,0}\,\hat{\mathbf{U}}_j^{i_1+1,i_2,i_3} \\
& + \mathbf{M}^{0,-1,0}\,\hat{\mathbf{U}}_j^{i_1,i_2-1,i_3} \\
& + \mathbf{M}^{0,+1,0}\,\hat{\mathbf{U}}_j^{i_1,i_2+1,i_3} \\
& + \mathbf{M}^{0,0,-1}\,\hat{\mathbf{U}}_j^{i_1,i_2,i_3-1} \\
& + \mathbf{M}^{0,0,+1}\,\hat{\mathbf{U}}_j^{i_1,i_2,i_3+1}\Big].
\end{aligned}
\tag{28}
$$

In Eq. (28), $\mathbf{M}^{0,0,0}$, $\mathbf{M}^{-1,0,0}$, $\mathbf{M}^{+1,0,0}$, $\mathbf{M}^{0,-1,0}$, $\mathbf{M}^{0,+1,0}$, $\mathbf{M}^{0,0,-1}$ and $\mathbf{M}^{0,0,+1}$ are matrices of size $[6N_{SP}, 6N_{SP}]$ containing the three steps of the spatial discretization (extrapolation, flux computation and differentiation), which depend on the advection angles as well as on the SP and FP locations. The exact formulation of those matrices is given in Appendix B.

3.3 Fourier Stability Analysis

To perform the Fourier stability analysis on tetrahedral elements, the discretized numerical solution is assumed under the form of a planar harmonic wave:

$$
\hat{\mathbf{U}}^{i_1,i_2,i_3} = \tilde{\mathbf{U}} \exp\Big(I\mathbf{k}\,(i_1\mathbf{x} + i_2\mathbf{y} + i_3\mathbf{z})\Big), \tag{29}
$$

where

$$
(\mathbf{x}, \mathbf{y}, \mathbf{z}) = \left(\begin{pmatrix} \Delta x \\ 0 \\ 0 \end{pmatrix}, \begin{pmatrix} 0 \\ \Delta x \\ 0 \end{pmatrix}, \begin{pmatrix} 0 \\ 0 \\ \Delta x \end{pmatrix} \right) \tag{30}
$$

are the vectors defining the mesh, $\tilde{\mathbf{U}}$ is a complex vector of dimension $6N_{SP}$, independent of i_1, i_2 and i_3, and

$$
\mathbf{k} = k \begin{pmatrix} \cos\vartheta_1 \sin\vartheta_2 \\ \sin\vartheta_1 \sin\vartheta_2 \\ \cos\vartheta_2 \end{pmatrix}, \tag{31}
$$

k being the wave number of the harmonic wave and $(\vartheta_1, \vartheta_2)$ its orientation angles. Using non-dimensional quantities, Eq. (29) becomes:

$$
\hat{\mathbf{U}}^{i_1,i_2,i_3} = \tilde{\mathbf{U}} \exp\Big(I\kappa\,(i_1 \cos\vartheta_1 \sin\vartheta_2 + i_2 \sin\vartheta_1 \sin\vartheta_2 + i_3 \cos\vartheta_2)\Big), \tag{32}
$$

$\kappa = k\Delta x$ being the grid frequency. Injecting Eq. (32) into Eq. (28), one gets:

$$
\begin{aligned}
\frac{d\tilde{\mathbf{U}}}{dt} = -\frac{||\mathbf{c}||}{\Delta x}\Big[\mathbf{M}^{0,0,0} & + \mathbf{M}^{-1,0,0} \exp(-I\kappa \cos\vartheta_1 \sin\vartheta_2) \\
& + \mathbf{M}^{+1,0,0} \exp(I\kappa \cos\vartheta_1 \sin\vartheta_2) \\
& + \mathbf{M}^{0,-1,0} \exp(-I\kappa \sin\vartheta_1 \sin\vartheta_2) \\
& + \mathbf{M}^{0,+1,0} \exp(I\kappa \sin\vartheta_1 \sin\vartheta_2) \\
& + \mathbf{M}^{0,0,-1} \exp(-I\kappa \cos\vartheta_2) \\
& + \mathbf{M}^{0,0,+1} \exp(I\kappa \cos\vartheta_2)\Big]\,\tilde{\mathbf{U}}
\end{aligned}
$$

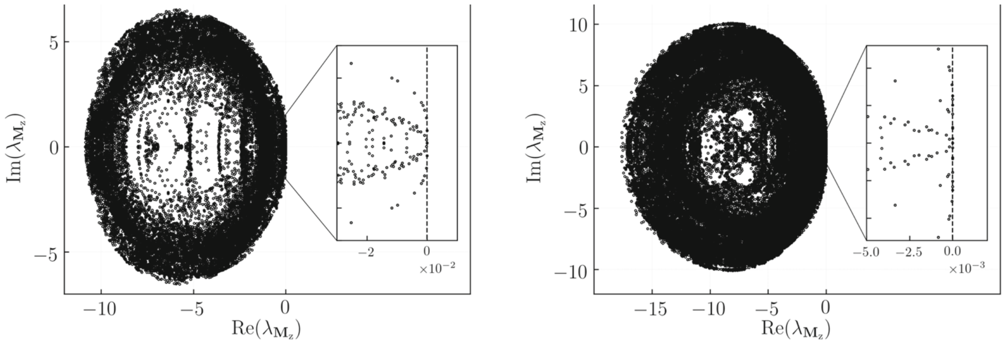

(a) SDRT_1 **(b)** SDRT_2, Shunn-Ham rule

Fig. 2 Spectrum of matrix $\mathbf{M}_z$ for stable SDRT schemes on tetrahedral elements, $(\theta_1, \theta_2) \in (0, \pi/8, \pi/4)^2$

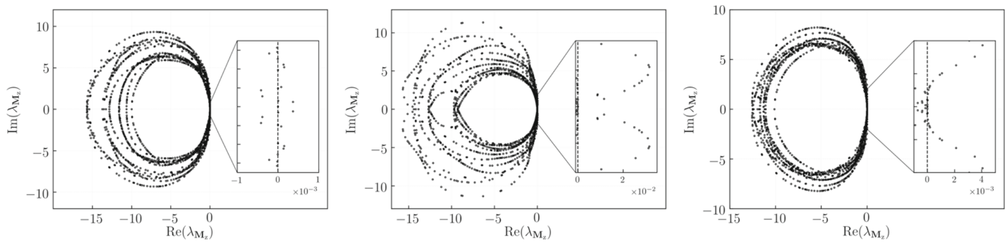

(a) Jaśkowiec-Sukumar rule **(b)** Xiao-Gimbutas rule **(c)** NCO rule

Fig. 3 Spectrum of matrix $\mathbf{M}_z$ for unstable SDRT_2 schemes on tetrahedral elements, $(\theta_1, \theta_2) = (0, 0)$

$$= \frac{||\mathbf{c}||}{\Delta x} \mathbf{M}_z \tilde{\mathbf{U}}. \tag{33}$$

Using the eigenvalue analysis, the SDRT spatial discretization is stable under a Fourier stability analysis if the real part of all eigenvalues of the matrix $\mathbf{M}_z$ are non-positive, i.e. if $\mathrm{Re}(\lambda_{\mathbf{M}_z}) \leq 0$. The complete spectrum of the SDRT spatial operator $\lambda_{\mathbf{M}_z}$ is obtained by computing the eigenvalues of $\mathbf{M}_z$ over the grid frequency $\kappa \in [-\pi, \pi]$ considering $(\vartheta_1, \vartheta_2) \in [0, 2\pi]$. For $p = 1$, the spectrum of $\mathbf{M}_z$ is plotted in Fig. 2a for $(\theta_1, \theta_2) \in (0, \pi/8, \pi/4)^2$. A closer view on the spectrum allows to see the non-positivity of $\mathrm{Re}(\lambda_{\mathbf{M}_z})$ and to establish the stability of the spatial discretization.

For $p = 2$, there are 4 interior physical FP. In Fig. 2b, the spectrum of the SDRT_2 discretization using the Shunn-Ham rule for interior FP is plotted for $(\theta_1, \theta_2) \in (0, \pi/8, \pi/4)^2$. A closer view on the spectrum allows to see the non-positivity of $\mathrm{Re}(\lambda_{\mathbf{M}_z})$, indicating a stable SDRT scheme.

In Fig. 3, the spectrum is plotted for the particular case $(\theta_1, \theta_2) = (0, 0)$ for the three other quadrature rules: the Jaśkowiec-Sukumar (Fig. 3a), the Xiao-Gimbutas (Fig. 3b) and the NCO (Fig. 3c). The SDRT scheme using those three quadrature rules is found unstable with $\max(\mathrm{Re}(\lambda_{\mathbf{M}_z})) \sim 3 \cdot 10^{-4}$ for Jaśkowiec-Sukumar, $\max(\mathrm{Re}(\lambda_{\mathbf{M}_z})) \sim 3 \cdot 10^{-2}$ for Xiao-Gimbutas and $\max(\mathrm{Re}(\lambda_{\mathbf{M}_z})) \sim 4 \cdot 10^{-3}$ for NCO. Using the NCO instead of the Shunn-Ham rule for the SP location did not influence the stability.

For $p > 2$, the SDRT stability has been studied using the position of physical interior FP as Shunn-Ham, NCO and Vioreanu-Rokhlin quadrature rules while using the Williams-Shunn-Jameson quadrature rule points as the face FP. None of these rules have been able to

Table 2 Impact of the FP located on faces: values of $\max(\mathrm{Re}(\lambda_{\mathbf{M}_z}))$ for SDRT$_3$, $(\theta_1, \theta_2, \vartheta_1, \vartheta_2) = (0, 0, 0, 0)$

Interior FP	Face FP		
	WSJ [26]	VR [28]	OPT
Shunn-Ham [12]	78.41	156.04	70.53
VR [28]	79.17	153.82	72.59
NCO [27]	68.74	110.68	95.92

lead to stable formulations, with a $\max(\mathrm{Re}(\lambda_{\mathbf{M}_z}))$ of $\sim$ 80, 400 and 5000 for $p = 3, 4$ and 5 (respectively).

The SDRT scheme on tetrahedral elements is demonstrated as linearly stable under a Fourier analysis up to the third-order of accuracy, provided that the interior FP location is defined according to the Shunn-Ham quadrature rule.

3.4 Influence of Flux Points Located on Faces

It has been mentioned in the previous section that using different SP locations (either the NCO or the Shunn-Ham rule) did not influence the stability. Actually, it led to the exact same value of $\max\left(\mathrm{Re}(\lambda_{\mathbf{M}_z})\right)$. This result extends the statement that the SP location has no impact on the stability to tetrahedra. However, the influence of FP located on faces has not been studied yet. To do so, the SP location is fixed at the Shunn-Ham rule [12] whereas different locations of interior FP and FP located on faces are studied.

For $p = 3$, there are 10 FP located on each face (denoted Face FP). Several location are studied: the 10-points quadrature rules on a triangle from Williams-Shunn-Jameson (WSJ) [26] and Vioreanu-Rokhlin (VR) [28]) and the set of 10-points determined using the optimization process in [21], denoted OPT. For interior FP, the three quadrature rules on a tetrahedron introduced in Sect. 3.3 are considered: the Shunn-Ham [12], the Vioreanu-Rokhlin (VR) [28] and the Newton-Cotes Open (NCO) [27] quadrature rules.

Table 2 shows values of $\max(\mathrm{Re}(\lambda_{\mathbf{M}_z}))$ for all the possible combinations of FP locations. They were obtained using $(\theta_1, \theta_2, \vartheta_1, \vartheta_2) = (0, 0, 0, 0)$ and $\kappa \in [0, \pi]$, $\Delta\kappa = \pi/32$. From this table, the impact of the position of the FP located on faces is clearly highlighted. The impact of the Face FP is even more important than the impact of interior FP: the interval of values obtained by changing the Face FP location is larger than by changing the interior FP location.

3.5 Fourier Analysis of the Coupled Time-Space Discretization

To investigate the linear stability of the coupled time-space discretization, the semi-discretized form needs to be integrated in time. A general m-stage Runge-Kutta (RK) method for a differential equation can be written as in [36]:

$$u^{(n+1)} = u^n + \sum_{j=1}^{m} \gamma_j \, \Delta t^j \, \frac{\partial^j u^n}{\partial t^j}. \tag{34}$$

In this paper, the time-integration scheme used is the RKo6s, which is part of the low storage RK schemes optimized to ensure low dissipation and low dispersion properties given by Bogey and Bailly in [36].

Table 3 CFL stability limits ν for SDRT schemes on tetrahedra coupled with the RKo6s temporal schemes

(θ_1, θ_2)	$(0, 0)$	$(\pi/8, \pi/8)$	$(\pi/4, \pi/4)$	$[0, 2\pi]^2$
SDRT_1	0.458	0.394	0.382	0.380
SDRT_2	0.275	0.243	0.235	0.235

The semi-discretized matrix form containing the planar harmonic wave given by Eq. (33) integrated in time using Eq. (34) is:

$$\begin{aligned} \tilde{\mathbf{U}}^{(n+1)} &= \left(\mathbf{I} + \sum_{j=1}^{m} \gamma_j \nu^j \mathbf{M}_z^j \right) \tilde{\mathbf{U}}^{(n)} \\ \Leftrightarrow \tilde{\mathbf{U}}^{(n+1)} &= \mathbf{G}\tilde{\mathbf{U}}^{(n)}. \end{aligned} \tag{35}$$

where ν is the CFL number defined by:

$$\nu = \frac{||\mathbf{c}||\Delta t}{\Delta x}. \tag{36}$$

The stability condition on the coupled time-space discretization is thus obtained by requiring that the amplitude of any harmonic does not grow in time, i.e.:

$$|\mathbf{G}| = \left| \frac{\tilde{\mathbf{U}}^{(n+1)}}{\tilde{\mathbf{U}}^{(n)}} \right| \leq 1. \tag{37}$$

In other words, to ensure a stable discretization, the spectral radius of the matrix $\mathbf{G}$, denoted $\rho_{\mathbf{G}}$ should be lower than 1, meaning that all the eigenvalues $\lambda_{\mathbf{G}}$ should be in the unit circle of the complex plane. The transfer matrix $\mathbf{G}$ between time steps n and $n+1$ is the amplification factor (or the Fourier symbol) of the full discretization.

The Fourier analysis of the coupled time-space discretization is conducted on tetrahedral elements for SDRT_1 and SDRT_2. The interior FP locations are in both cases taken as following the Shunn-Ham quadrature rule. Additionally to the SP and FP locations, the matrix $\mathbf{M}_z$ depends on the advection velocity defined by (θ_1, θ_2), the grid frequency κ and the harmonic wave orientation angles $(\vartheta_1, \vartheta_2)$. These parameters are taken as:

- $\theta_1 \in [0, 2\pi]$, $\Delta\theta_1 = \pi/8$,
- $\theta_2 \in [0, 2\pi]$, $\Delta\theta_2 = \pi/8$,
- $\kappa \in [0, \pi]$, $\Delta\kappa = \pi/8$,
- $\vartheta_1 \in [0, 2\pi]$, $\Delta\vartheta_1 = \pi/8$,
- $\vartheta_2 \in [0, 2\pi]$, $\Delta\vartheta_2 = \pi/8$.

The CFL stability limits are given for those parameters in Table 3. To the authors' knowledge, there is no consensus on the definition on an equivalent CFL number for high-order discontinuous methods on simplex cells. The classical CFL definition given by Eq. (36) is thus preferred here.

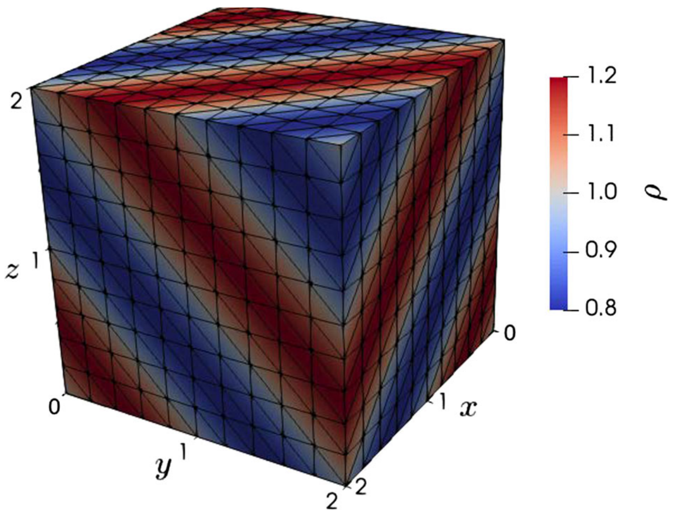

Fig. 4 Initial density condition on a $10 \times 10 \times 10$ regular tetrahedral grid using $p = 2$

4 Numerical Experiments

4.1 Euler Equations

We consider the three-dimensional Euler equations:

$$\frac{\partial \mathbf{u}}{\partial t} + \frac{\partial \mathbf{f}}{\partial x} + \frac{\partial \mathbf{g}}{\partial y} + \frac{\partial \mathbf{h}}{\partial z} = 0, \quad \text{in } \Omega \times [0, t_f], \tag{38}$$

where $\mathbf{u}$, $\mathbf{f}$, $\mathbf{g}$ and $\mathbf{h}$ are given by:

$$\mathbf{u} = \begin{pmatrix} \rho \\ \rho U \\ \rho V \\ \rho W \\ E \end{pmatrix}, \quad \mathbf{f} = \begin{pmatrix} \rho U \\ \rho U^2 + P \\ \rho U V \\ \rho U W \\ U(E+P) \end{pmatrix}, \quad \mathbf{g} = \begin{pmatrix} \rho V \\ \rho V U \\ \rho V^2 + P \\ \rho V W \\ V(E+P) \end{pmatrix}, \quad \mathbf{h} = \begin{pmatrix} \rho W \\ \rho W U \\ \rho W V \\ \rho W^2 + P \\ W(E+P) \end{pmatrix}. \tag{39}$$

In Eq. (39), ρ is the density, U (respectively V, W) is the velocity component in the x (respectively y, z) direction, E is the total energy and P is the pressure determined from the following equation of state:

$$P = (\gamma - 1)\left(E - \frac{1}{2}\rho(U^2 + V^2 + W^2)\right), \tag{40}$$

where the constant ratio of specific heats γ is equal to 1.4 for air.

To validate the SDRT scheme implementation on tetrahedral elements, a 3D period Euler test case from [37, 38] is considered. The 3D Euler equations are solved on a cubic computational domain $\Omega = [0, L]^3$ where $L = 2\,\text{m}$ with periodic boundary conditions. The initial solution is:

$$\rho = 1 + 0.2\sin(\pi(x + y + z)), \quad (U, V, W, P) = (1, 1, 1, 1). \tag{41}$$

The density initial condition is displayed on Fig. 4 for a regular $10 \times 10 \times 10$ tetrahedral grid using $p = 2$.

Table 4 L_2 error and order of accuracy values for regular and irregular tetrahedral grids

p	Regular mesh			Irregular mesh		
	DoF number	L_2 error	Order of accuracy	DoF number	L_2 error	Order of accuracy
1	3000	2.183E-02	–	2132	7.713E-02	–
	24000	5.754E-03	1.92	11792	2.988E-02	1.66
	81000	2.582E-03	1.98	36460	1.437E-02	1.95
	192000	1.458E-03	1.99	82164	8.349E-03	2.00
	375000	9.345E-04	1.99	151448	5.448E-03	2.09
2	7500	1.366E-03	–	5330	2.156E-02	–
	60000	1.508E-04	3.18	29480	3.277E-03	3.30
	202500	4.343E-05	3.07	91150	9.946E-04	3.17
	480000	1.813E-05	3.04	205410	4.148E-04	3.23
	937500	9.233E-06	3.02	378620	2.173E-04	3.17

The solution is advanced in time using the RKo6s temporal scheme and the simulation is carried out until $t_f = 1$ s. The time step is chosen sufficiently small so that the error from the time discretization is negligible compared to the spatial discretization error by setting the CFL number to 10^{-2}. The analytical solution of the density at any time t [38] is:

$$\rho_a = 1 + 0.2\sin(\pi(x + y + z - t(U + V + W))), \tag{42}$$

whereas velocity and pressure remain constant in time.

The convergence study was conducted on two types of grids (regular and irregular). Each mesh is refined several times and the order of accuracy is verified by computing the density L_2 error using the 84 points quadrature rule from [26]. Table 4 shows the L_2 errors and orders of accuracy for the two different types of grids (regular and irregular). For both second- and third-order schemes, a $p + 1$ order of accuracy is recovered.

4.2 Taylor-Green Vortex

To validate the implementation of the SDRT method for the Navier-Stokes equations using tetrahedral grids, the Direct Numerical Simulation of the Taylor-Green Vortex (TGV) at $\mathrm{Re} = \rho_\infty U_\infty L/\mu_{d\infty} = 1600$ is considered. The TGV test case was proposed in the International Workshop on High-Order CFD Methods [39] to test the accuracy and performance of high-order methods. A three-dimensional periodic and transitional flow is considered and defined by:

$$U = U_\infty \sin\left(\frac{x}{L}\right)\cos\left(\frac{y}{L}\right)\cos\left(\frac{z}{L}\right), \tag{43}$$

$$V = -U_\infty \cos\left(\frac{x}{L}\right)\sin\left(\frac{y}{L}\right)\cos\left(\frac{z}{L}\right), \tag{44}$$

$$W = 0, \tag{45}$$

$$P = P_\infty + \frac{\rho_\infty U_\infty^2}{16}\left(\cos\left(\frac{2x}{L}\right) + \cos\left(\frac{2y}{L}\right)\right)\left(\cos\left(\frac{2z}{L}\right) + 2\right). \tag{46}$$

The flow is governed by the 3D compressible Navier-Stokes equations with constant physical properties and at low Mach number so that the obtained solutions are close to incompressible solutions. The test case conditions are summed up in Table 5.

Table 5 Flow conditions for the TGV test case

Variable	Notation	Value	Unit
Reynolds number	Re	1600	–
Temperature	T_∞	300	K
Dynamic viscosity	$\mu_{d\infty}$	$1.846 \cdot 10^{-5}$	kg/m/s
Mach number	M_∞	0.1	–
Gas constant	R_{gas}	287.058	J/kg/K
Density	ρ_∞	$8.506 \cdot 10^{-4}$	kg/m^3
Pressure	P_∞	73.254	Pa
Ratio of specific heat	γ	1.4	–
Prandtl number	Pr	0.71	–
Reference length	L	1.0	m

Table 6 Computational conditions for the TGV test case

Scheme	Mesh	Number of Elements	DOF Number	Δt (sec)
$SDRT_1$	M_1	663,552	2,654,208	$7.5 \cdot 10^{-5}$
	M_2	1,572,864	6,291,456	$5.5 \cdot 10^{-5}$
	M_3	3,072,000	12,288,000	$4.5 \cdot 10^{-5}$
$SDRT_2$	M_1	663,552	6,635,520	$4.5 \cdot 10^{-5}$
	M_2	1,572,864	15,728,640	$3.5 \cdot 10^{-5}$
	M_3	3,072,000	30,720,000	$3.0 \cdot 10^{-5}$

The computational domain is a cube defined by $\Omega = [-\pi L, \pi L]^3$ and periodic boundary conditions are imposed in the three directions. The SDRT implementation for interior FP is based on the Shunn-Ham quadrature rule. Diffusive flux are computed following the very same procedure given for triangular cells in [19, 21] using a centered formulation [40]. Solutions are time-integrated using the RKo6s temporal scheme and the time step Δt is imposed. Roe's Riemann solver is used to compute flux at cell interfaces. Computations are carried out on 600 processors. Three different regular grids (M_1, M_2 and M_3) are considered. Their number of elements and associated time steps are given in Table 6.

The physical duration of the computation is based on the characteristic convective time $t_c = L/U_\infty$ and is set to $t_f = 20t_c$. The kinetic energy dissipation rate ε is computed for $t \in [0, t_f]$ and compared to a reference incompressible flow solution obtained using a dealiased pseudo-spectral code (developed at Université Catholique de Louvain, UCL) on a 512^3 mesh and provided by the International Workshop on High-Order CFD Methods [39]. The reference data is denoted 'Spectral-512^3'. To compute the kinetic energy dissipation rate, one first needs to compute the kinetic energy E_k, defined by:

$$E_k(t) = \int_\Omega \frac{1}{2}\rho(U^2 + V^2 + W^2)\mathrm{d}\Omega. \tag{47}$$

The kinetic energy is computed at each time t as:

$$E_k(t) = \sum_{i=1}^{N}\sum_{j=1}^{N_q} \omega_j |J^{(i,j)}| E_k^{(i)}(\boldsymbol{\xi}_j), \tag{48}$$

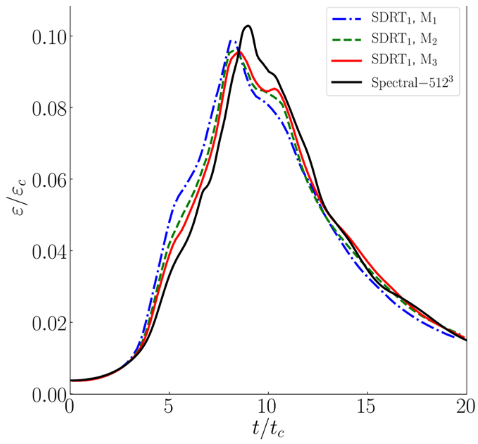

(a) SDRT$_1$

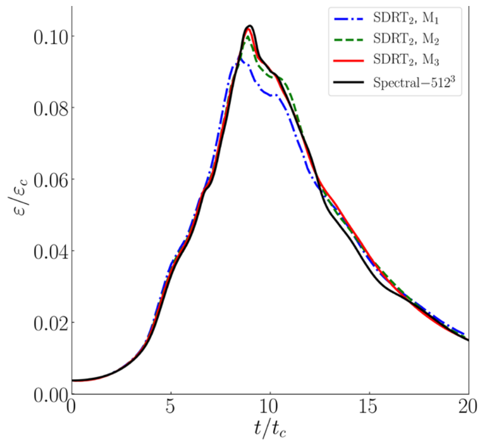

(b) SDRT$_2$

Fig. 5 Dimensionless kinetic energy dissipation rate obtained with second and third-order SDRT schemes compared to reference data

where $|J^{(i,j)}|$ is the Jacobian determinant at the j-th integration point of the i-th cell and N_q is the number of quadrature points. The quadrature points are located at $\boldsymbol{\xi}_j$ and associated with the weight ω_j. The integration is performed using the 84 points quadrature rule from [26]. The kinetic energy dissipation rate is defined by:

$$\varepsilon(t) = -\frac{\mathrm{d}E_k}{\mathrm{d}t}(t), \tag{49}$$

and is computed using a first-order upwind scheme. The kinetic energy dissipation rate is rendered dimensionless by $\varepsilon_c = E_k(t=0)/t_c$. Results obtained with the second and third-order SDRT schemes are compared with reference data in Fig. 5. Using the second-order SDRT scheme (Fig. 5a), the dimensionless kinetic energy dissipation rate $\varepsilon/\varepsilon_c$ evolution is first quite accurate ($t/t_c \in [0, 3]$) but grows too fast from $t/t_c > 3$ for all grid resolutions. The maximal peak value is underestimated (of 4% for M$_1$ and 7% for M$_2$ and M$_3$) and shifted (of 8% for M$_1$ and M$_2$ and 5% for M$_3$). However, results get closer to the reference data as the number of DOF increases. Using the second-order SDRT scheme leads to better results (Fig. 5b). For $t/t_c \in [0, 9]$, results obtained using the M$_1$ mesh slightly overestimate $\varepsilon/\varepsilon_c$ whereas results on M$_2$ and M$_3$ grids show an excellent agreement with the reference data. The improvement of the solution accuracy when the number of DOF increases can be clearly seen at $t/t_c = 9$. Compared to the reference data, the peak value is particularly well predicted on the M$_3$ mesh (underestimation of 0.7%). For $t/t_c \in [12, 17]$, $\varepsilon/\varepsilon_c$ is a little overestimated but the final value at $t/t_c = 20$ matches the reference.

5 Conclusion

Tetrahedrons are the reference elements for automatic mesh generation on complex geometries and they are widely used in the case of mesh adaptation. Accounting for tetrahedral cells is today essential for a numerical scheme to be usable on unstructured grids.

When using the weak formulation associated with the Discontinuous Galerkin formulation, stability is ensured. When one studies formulations based on the strong form of the equations, stability was demonstrated for tetrahedral cells considering the Flux Reconstruction (FR) or the Correction Procedure for Reconstruction (CPR). In this context, the present paper introduces a new formulation usable on tetrahedrons, following the Spectral Difference method. The idea is to define the flux vector in the Raviart-Thomas space, rather than the flux components in the Lagrange space. Such a procedure changes essentially the definition of the flux polynomial approximation: the procedure is vector-based and not component-based. A simple analysis of the number of interior flux points shows that the proposed scheme and the Flux Reconstruction method will always differ.

The key point remains the position of the flux points since this position significantly influences the scheme stability. It was demonstrated in the paper that using Shunn-Ham quadrature rule points as interior flux points and Williams-Shunn-Jameson quadrature rule points as face flux points leads to a stable formulation for polynomial degrees of $p = 1$ and $p = 2$, leading to an order of accuracy of 2 and 3.

For $p > 2$, several quadrature rule sets of points were tested as interior flux points while keeping the Williams-Shunn-Jameson points as face flux points but none of them lead to a stable formulation. Such a result does not mean that a stable formulation does not exist but states the fact that additional research is required. In particular, the influence of the flux points located on faces was highlighted in this paper and their location should be taken into account to determine stable formulations. Changing their location will not imply the use of mortar techniques between a tetrahedral and a prismatic element as long as the solution points location of a triangle is chosen to be the same as the flux points on a tetrahedral face. Since the solution points do not influence the stability, this requirement can easily be fulfilled.

Finally, the procedure was validated for Euler and Navier-Stokes equations on academic cases. Future efforts concern an extensive validation on more complex configurations up to the third-order of accuracy and research of stable formulations for $p > 2$.

Acknowledgements Dr. Guillaume Puigt is partially supported by LMA2S (Laboratoire de Mathématiques Appliquées à l'Aéronautique et au Spatial), the Applied Mathematics Lab of ONERA.

Funding. The authors did not receive support from any organization for the submitted work.

Availability of data and material. The datasets generated during and/or analyzed during the current study are available from the corresponding author on reasonable request.

Declarations

Conflicts of interests. The authors have no conflicts of interest to declare that are relevant to the content of this article.

Appendix A. Definition of the Raviart-Thomas (*RT*) Space

The Raviart-Thomas (RT) finite element spaces were originally introduced by Raviart and Thomas [41] to approximate the Sobolev space H(div) defined by:

$$\mathrm{H(div)} = \{u \in \left(L^2(K)\right)^d, \ \ \nabla \cdot u \in L^2(K)\}, \tag{A.1}$$

where d is the dimension, K is a bounded open subset of $\mathbb{R}^d$ with a Lipshitz continuous boundary, $L^2(K)$ is the Hilbert space of square-integrable function defined on K. The extension to the three-dimensional case considering K as a tetrahedron or a cube was proposed by Nedelec [42]. The space RT_p spanned by the Raviart-Thomas basis functions of degree

p is the smallest polynomial space such that the divergence maps RT_p onto $\mathbb{P}_p$, the space of piecewise polynomials of degree $\leq p$. Considering the reference tetrahedron $\mathcal{T}_e$, the RT space of order p is defined in 3D by:

$$RT_p = (\mathbb{P}_p)^3 + \begin{pmatrix} x \\ y \\ z \end{pmatrix} \bar{\mathbb{P}}_p, \tag{A.2}$$

where $\mathbb{P}_p$ is the space of polynomials of degree at most p:

$$\mathbb{P}_p(x, y, z) = span\{x^i y^j z^k,\ i, j, k \geq 0, i + j + k \leq p\}, \tag{A.3}$$

$\bar{\mathbb{P}}_p$ is the space of polynomials of degree p:

$$\bar{\mathbb{P}}_p(x, y, z) = span\{x^i y^j z^k,\ i, j, k \geq 0, i + j + k = p\}, \tag{A.4}$$

and $(\mathbb{P}_p)^3 = (\mathbb{P}_p, \mathbb{P}_p, \mathbb{P}_p)^\top$ is the three dimensional vector space for which each component is a polynomial of degree at most p. The dimension of each space is dim $\mathbb{P}_p = \frac{(p+1)(p+2)(p+3)}{6}$, dim $\mathbb{P}_p^3 = \frac{(p+1)(p+2)(p+3)}{2}$, dim $\bar{\mathbb{P}}_p = \frac{(p+1)(p+2)}{2}$ and thus dim $RT_p = \frac{(p+1)(p+2)(p+4)}{2}$. We denote $\boldsymbol{\phi}_n$, $n \in [\![1, N_{FP}]\!]$ the monomials which form a basis in the RT_p space where

$$N_{FP} = \frac{(p+1)(p+2)(p+4)}{2}. \tag{A.5}$$

Determination of $\boldsymbol{\phi}_n$ for RT_1, $N_{FP} = 15$

$$\boldsymbol{\phi} = \{\phi_1, \cdots, \phi_{15}\} = \left\{ \begin{pmatrix} 1 \\ 0 \\ 0 \end{pmatrix}, \begin{pmatrix} x \\ 0 \\ 0 \end{pmatrix}, \begin{pmatrix} y \\ 0 \\ 0 \end{pmatrix}, \begin{pmatrix} z \\ 0 \\ 0 \end{pmatrix}, \begin{pmatrix} 0 \\ 1 \\ 0 \end{pmatrix}, \begin{pmatrix} 0 \\ x \\ 0 \end{pmatrix}, \begin{pmatrix} 0 \\ y \\ 0 \end{pmatrix}, \begin{pmatrix} 0 \\ z \\ 0 \end{pmatrix}, \begin{pmatrix} 0 \\ 0 \\ 1 \end{pmatrix}, \begin{pmatrix} 0 \\ 0 \\ x \end{pmatrix}, \begin{pmatrix} 0 \\ 0 \\ y \end{pmatrix}, \begin{pmatrix} 0 \\ 0 \\ z \end{pmatrix}, \begin{pmatrix} x^2 \\ xy \\ xz \end{pmatrix}, \begin{pmatrix} yx \\ y^2 \\ yz \end{pmatrix}, \begin{pmatrix} zx \\ zy \\ z^2 \end{pmatrix} \right\}. \tag{A.6}$$

Appendix B. Matrices Formulation for the Fourier Analysis

The matrices $\mathbf{M}^{0,0,0}$, $\mathbf{M}^{-1,0,0}$, $\mathbf{M}^{+1,0,0}$, $\mathbf{M}^{0,-1,0}$, $\mathbf{M}^{0,+1,0}$, $\mathbf{M}^{0,0,-1}$ and $\mathbf{M}^{0,0,+1}$ involved in the SDRT spatial discretization for the Fourier analysis on tetrahedral elements (Eq. (28)) are detailed in this appendix. Those matrices are given as:

$$\mathbf{M}^{0,0,0} = \begin{bmatrix} \mathbf{D}_{jk} & \cdots & O_{N_{SP},N_{FP}} \\ \vdots & \ddots & \vdots \\ O_{N_{SP},N_{FP}} & \cdots & \mathbf{D}_{jk} \end{bmatrix} \mathbf{C}^{0,0,0} \begin{bmatrix} \mathbf{T}_{kj} & \cdots & O_{N_{FP},N_{SP}} \\ \vdots & \ddots & \vdots \\ O_{N_{FP},N_{SP}} & \cdots & \mathbf{T}_{kj} \end{bmatrix}, \tag{B.1}$$

where $O_{m,n}$ is the zero matrix of size $m \times n$. The same goes for $\mathbf{M}^{-1,0,0}$, $\mathbf{M}^{+1,0,0}$, $\mathbf{M}^{0,-1,0}$, $\mathbf{M}^{0,+1,0}$, $\mathbf{M}^{0,0,-1}$ and $\mathbf{M}^{0,0,+1}$, associated respectively to the velocity matrices $\mathbf{C}^{-1,0,0}$, $\mathbf{C}^{+1,0,0}$, $\mathbf{C}^{0,-1,0}$, $\mathbf{C}^{0,+1,0}$, $\mathbf{C}^{0,0,-1}$ and $\mathbf{C}^{0,0,+1}$. The transfer matrix is given by Eq. (16):

$$\mathbf{T}_{kj} = \sum_{m=1}^{N_{SP}^{tet}} \left(\Phi_m(\boldsymbol{\xi}_j)\right)^{-1} \Phi_m(\boldsymbol{\xi}_k), \tag{B.2}$$

and the differentiation matrix by Eq. (21):

$$\mathbf{D}_{jk} = \sum_{n=1}^{N_{FP}^{tet}} \left(\boldsymbol{\phi}_n(\boldsymbol{\xi}_k) \cdot \hat{\mathbf{n}}_k\right)^{-1} \ \hat{\nabla} \cdot \boldsymbol{\phi}_n(\boldsymbol{\xi}_j). \tag{B.3}$$

The velocity matrices are given as:

$$\mathbf{C}^{0,0,0} = \begin{bmatrix} \mathbf{C}^L & \mathbf{C}^{T_1,T_2} & O_{N_{FP},N_{FP}} & O_{N_{FP},N_{FP}} & O_{N_{FP},N_{FP}} & \mathbf{C}^{T_1,T_6} \\ \mathbf{C}^{T_2,T_1} & \mathbf{C}^L & \mathbf{C}^{T_2,T_3} & O_{N_{FP},N_{FP}} & O_{N_{FP},N_{FP}} & O_{N_{FP},N_{FP}} \\ O_{N_{FP},N_{FP}} & \mathbf{C}^{T_3,T_2} & \mathbf{C}^L & \mathbf{C}^{T_3,T_4} & O_{N_{FP},N_{FP}} & O_{N_{FP},N_{FP}} \\ O_{N_{FP},N_{FP}} & O_{N_{FP},N_{FP}} & \mathbf{C}^{T_4,T_3} & \mathbf{C}^L & \mathbf{C}^{T_4,T_5} & O_{N_{FP},N_{FP}} \\ O_{N_{FP},N_{FP}} & O_{N_{FP},N_{FP}} & O_{N_{FP},N_{FP}} & \mathbf{C}^{T_5,T_4} & \mathbf{C}^L & \mathbf{C}^{T_5,T_6} \\ \mathbf{C}^{T_6,T_1} & O_{N_{FP},N_{FP}} & O_{N_{FP},N_{FP}} & O_{N_{FP},N_{FP}} & \mathbf{C}^{T_6,T_5} & \mathbf{C}^L \end{bmatrix}, \tag{B.4}$$

$$\mathbf{C}^{-1,0,0} = \begin{bmatrix} O_{N_{FP},N_{FP}} & O_{N_{FP},N_{FP}} & O_{N_{FP},N_{FP}} & O_{N_{FP},N_{FP}} & \mathbf{C}^{T_1,T_5} & O_{N_{FP},N_{FP}} \\ O_{N_{FP},N_{FP}} & O_{N_{FP},N_{FP}} & O_{N_{FP},N_{FP}} & \mathbf{C}^{T_2,T_4} & O_{N_{FP},N_{FP}} & O_{N_{FP},N_{FP}} \\ \multicolumn{6}{c}{\left[O_{4N_{FP},6N_{FP}}\right]} \end{bmatrix}, \tag{B.5}$$

$$\mathbf{C}^{+1,0,0} = \begin{bmatrix} \multicolumn{6}{c}{\left[O_{3N_{FP},6N_{FP}}\right]} \\ O_{N_{FP},N_{FP}} & \mathbf{C}^{T_4,T_2} & O_{N_{FP},N_{FP}} & O_{N_{FP},N_{FP}} & O_{N_{FP},N_{FP}} & O_{N_{FP},N_{FP}} \\ \mathbf{C}^{T_5,T_1} & O_{N_{FP},N_{FP}} & O_{N_{FP},N_{FP}} & O_{N_{FP},N_{FP}} & O_{N_{FP},N_{FP}} & O_{N_{FP},N_{FP}} \\ \multicolumn{6}{c}{\left[O_{N_{FP},6N_{FP}}\right]} \end{bmatrix}, \tag{B.6}$$

$$\mathbf{C}^{0,-1,0} = \begin{bmatrix} \multicolumn{6}{c}{\left[O_{2N_{FP},6N_{FP}}\right]} \\ \mathbf{C}^{T_3,T_1} & O_{N_{FP},N_{FP}} & O_{N_{FP},N_{FP}} & O_{N_{FP},N_{FP}} & O_{N_{FP},N_{FP}} & O_{N_{FP},N_{FP}} \\ O_{N_{FP},N_{FP}} & O_{N_{FP},N_{FP}} & O_{N_{FP},N_{FP}} & O_{N_{FP},N_{FP}} & O_{N_{FP},N_{FP}} & \mathbf{C}^{T_4,T_6} \\ \multicolumn{6}{c}{\left[O_{2N_{FP},6N_{FP}}\right]} \end{bmatrix}, \tag{B.7}$$

$$\mathbf{C}^{0,+1,0} = \begin{bmatrix} O_{N_{FP},N_{FP}} & O_{N_{FP},N_{FP}} & \mathbf{C}^{T_1,T_3} & O_{N_{FP},N_{FP}} & O_{N_{FP},N_{FP}} & O_{N_{FP},N_{FP}} \\ \multicolumn{6}{c}{\left[O_{4N_{FP},6N_{FP}}\right]} \\ O_{N_{FP},N_{FP}} & O_{N_{FP},N_{FP}} & O_{N_{FP},N_{FP}} & \mathbf{C}^{T_6,T_4} & O_{N_{FP},N_{FP}} & O_{N_{FP},N_{FP}} \end{bmatrix}, \tag{B.8}$$

$$\mathbf{C}^{0,0,-1} = \begin{bmatrix} \multicolumn{6}{c}{\left[O_{N_{FP},6N_{FP}}\right]} \\ O_{N_{FP},N_{FP}} & O_{N_{FP},N_{FP}} & O_{N_{FP},N_{FP}} & O_{N_{FP},N_{FP}} & O_{N_{FP},N_{FP}} & \mathbf{C}^{T_2,T_6} \\ O_{N_{FP},N_{FP}} & O_{N_{FP},N_{FP}} & O_{N_{FP},N_{FP}} & O_{N_{FP},N_{FP}} & \mathbf{C}^{T_3,T_5} & O_{N_{FP},N_{FP}} \\ \multicolumn{6}{c}{\left[O_{3N_{FP},6N_{FP}}\right]} \end{bmatrix}, \tag{B.9}$$

$$\mathbf{C}^{0,0,+1} = \begin{bmatrix} \multicolumn{6}{c}{\left[O_{4N_{FP},6N_{FP}}\right]} \\ O_{N_{FP},N_{FP}} & O_{N_{FP},N_{FP}} & \mathbf{C}^{T_5,T_3} & O_{N_{FP},N_{FP}} & O_{N_{FP},N_{FP}} & O_{N_{FP},N_{FP}} \\ O_{N_{FP},N_{FP}} & \mathbf{C}^{T_6,T_2} & O_{N_{FP},N_{FP}} & O_{N_{FP},N_{FP}} & O_{N_{FP},N_{FP}} & O_{N_{FP},N_{FP}} \end{bmatrix}, \tag{B.10}$$

where $\mathbf{C}^L$ is defined by:

$$\mathbf{C}^L = \begin{bmatrix} \begin{bmatrix} (\mathbf{c}\cdot\mathbf{n})\,\frac{1+\mathrm{sign}(\mathbf{c}\cdot\mathbf{n})}{2} & \cdots & 0 \\ \vdots & \ddots & \vdots \\ 0 & \cdots & (\mathbf{c}\cdot\mathbf{n})\,\frac{1+\mathrm{sign}(\mathbf{c}\cdot\mathbf{n})}{2} \end{bmatrix}_{4N_f,4N_f} & O_{4N_f,N_i} \\ O_{N_i,4N_f} & \begin{bmatrix} |J|J^{-1}(\mathbf{c}\cdot\hat{\mathbf{n}}) & \cdots & 0 \\ \vdots & \ddots & \vdots \\ 0 & \cdots & |J|J^{-1}(\mathbf{c}\cdot\hat{\mathbf{n}}) \end{bmatrix}_{N_i,N_i} \end{bmatrix}. \tag{B.11}$$

The matrix $\mathbf{C}^{T_i,T_j}$ links the FP between the triangular faces of T_i and T_j. Its expression will depend on the local connectivity, i.e. the number and the orientation of the two faces in their respective element. The face number gives the local FP numbering whereas the orientation (how the two faces are facing each other) gives the FP order. An example of its determination is provided below for two arbitrary tetrahedral elements.

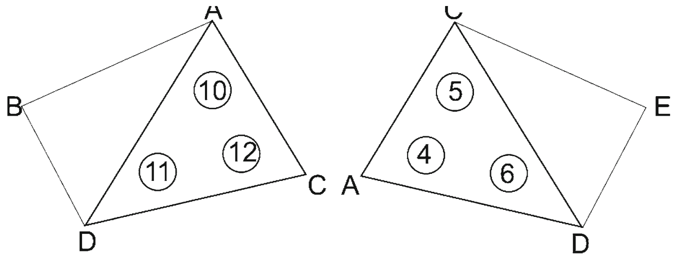

Fig. 6 Illustration of the orientation determination: T_1 (on the left) and T_2 (on the right)

Determination of the Matrix $\mathbf{C}^{\mathbf{T_i},\mathbf{T_j}}$ —Example for $\mathbf{p} = \mathbf{1}$ Let us consider two tetrahedron T_1 and T_2 defined by their four nodes:

$$T_1 : \quad N_1, N_2, N_3, N_4 = A, B, C, D, \tag{B.12}$$

$$T_2 : \quad N_1, N_2, N_3, N_4 = A, C, E, D. \tag{B.13}$$

Following the CGNS notations, their faces are defined by:

- T_1, Face 1: A, C, B,
- T_1, Face 2: A, B, D,
- T_1, Face 3: B, C, D,
- T_1, Face 4: C, A, D,

- T_2, Face 1: A, E, C,
- T_2, Face 2: A, C, D,
- T_2, Face 3: C, E, D,
- T_2, Face 4: E, A, D.

They are sharing a face corresponding to Face 4 in T_1 and Face 2 in T_2. In the case of $p = 1$, this indicates that the FP numbers on (T_1, Face 4) are [10, 12] whereas the FP number (Face 2, T_2) are [4, 6]. Then, the orientation between the faces needs to be determined to know in which order the FP are facing each other. For two arbitrary faces A and B defined respectively by nodes (A_1, A_2, A_3) and (B_1, B_2, B_3), three cases are possible:

- $A_1 = B_3, A_2 = B_2, A_3 = B_1$,
- $A_1 = B_2, A_2 = B_1, A_3 = B_3$,
- $A_1 = B_1, A_2 = B_3, A_3 = B_2$.

Our example is illustrated in Fig. 6 and corresponds to the second case.

In this example, the matrix $\mathbf{C}^{T_1,T_2}$ will take the following expression:

$$\mathbf{C}^{T_1,T_2} = (\mathbf{c}\cdot\mathbf{n}) \left[\begin{array}{c} O_{3N_f,N_{FP}} \\ \left[O_{N_f,N_f} \begin{bmatrix} 0 & \frac{1+\text{sign}(\mathbf{c}\cdot\mathbf{n})}{2} & 0 \\ 0 & 0 & \frac{1+\text{sign}(\mathbf{c}\cdot\mathbf{n})}{2} \\ \frac{1+\text{sign}(\mathbf{c}\cdot\mathbf{n})}{2} & 0 & 0 \end{bmatrix} O_{N_f,2*N_f+N_i} \right] \\ O_{N_i,N_{FP}} \end{array} \right]. \tag{B.14}$$

References

1. Hesthaven, J.S., Teng, C.H.: Stable spectral methods on tetrahedral elements. SIAM J. Sci. Comput. **21**(6), 2352–2380 (2000). https://doi.org/10.1137/S1064827598343723
2. Hesthaven, J., Warburton, T.: Nodal high-order methods on unstructured grids: I. time-domain solution of Maxwell's equations. J. Comput. Phys. **181**(1), 186–221 (2002). https://doi.org/10.1006/jcph.2002.7118
3. Bettess, P., Laghrouche, O., Perrey-Debain, E., Hesthaven, J.S., Warburton, T.: High-order nodal discontinuous Galerkin methods for the Maxwell eigenvalue problem, Philosophical Transactions of the Royal

Society of London. Ser. A Math. Phys. Eng. Sci. **362**(1816), 493–524 (2004). https://doi.org/10.1098/rsta.2003.1332
4. Hesthaven, J.S., Warburton, T.: Nodal Discontinuous Galerkin Methods. Springer, New York (2008). https://doi.org/10.1007/978-0-387-72067-8
5. Dosopoulos, S., Zhao, B., Lee, J.-F.: Non-conformal and parallel discontinuous galerkin time domain method for Maxwell's equations: EM analysis of IC packages. J. Comput. Phys. **238**, 48–70 (2013). https://doi.org/10.1016/j.jcp.2012.11.048
6. Chan, J., Wang, Z., Modave, A., Remacle, J., Warburton, T.: GPU-accelerated discontinuous Galerkin methods on hybrid meshes. J. Comput. Phys. **318**, 142–168 (2016). https://doi.org/10.1016/j.jcp.2016.04.003
7. Huynh, H.T.: A Flux Reconstruction Approach to High-Order Schemes Including Discontinuous Galerkin Methods, In: 18th AIAA Computational Fluid Dynamics Conference, (2007). https://doi.org/10.2514/6.2007-4079
8. Vincent, P.E., Castonguay, P., Jameson, A.: A new class of high-order energy stable flux reconstruction schemes. J. Sci. Comput. **47**(1), 50–72 (2011). https://doi.org/10.1007/s10915-010-9420-z
9. Williams, D.M., Jameson, A.: Energy stable flux reconstruction schemes for advection-diffusion problems on Tetrahedra. J. Sci. Comput. **59**(3), 721–759 (2014). https://doi.org/10.1007/s10915-013-9780-2
10. Williams, D.M., Jameson, A.: Nodal points and the nonlinear stability of high-order methods for unsteady flow problems on tetrahedral meshes. In 21st AIAA Computational Fluid Dynamics Conference. American Institute of Aeronautics and Astronautics, June (2013)
11. Witherden, F.D., Park, J.S., Vincent, P.E.: An analysis of solution point coordinates for flux reconstruction schemes on tetrahedral elements. J. Sci. Comput. **69**, 905–920 (2016). https://doi.org/10.1007/s10915-016-0204-y
12. Shunn, L., Ham, F.: Symmetric quadrature rules for tetrahedra based on a cubic close-packed lattice arrangement. J. Comput. Appl. Math. **236**(17), 4348–4364 (2012). https://doi.org/10.1016/j.cam.2012.03.032
13. Bull, J.R., Jameson, A.: Simulation of the Taylor-Green vortex using high-order flux reconstruction schemes. AIAA J. **53**(9), 2750–2761 (2015). https://doi.org/10.2514/1.J053766
14. Kopriva, D.A.: A Conservative Staggered-Grid Chebyshev multidomain method for compressible flows. ii. a semi-structured method. J. Comput. Phys. **128**(2), 475–488 (1996). https://doi.org/10.1006/jcph.1996.0225
15. Liu, Y., Vinokur, M., Wang, Z.J.: Spectral difference method for unstructured grids i: basic formulation. J. Comput. Phys. **216**(2), 780–801 (2006). https://doi.org/10.1016/j.jcp.2006.01.024
16. Van den Abeele, K., Lacor, C., Wang, Z.J.: On the stability and accuracy of the spectral difference method. J. Sci. Comput. **37**(2), 162–188 (2008). https://doi.org/10.1007/s10915-008-9201-0
17. Balan, A., May, G., Schöberl, J.: A stable high-order Spectral Difference method for hyperbolic conservation laws on triangular elements. J. Comput. Phys. **231**(5), 2359–2375 (2012). https://doi.org/10.1016/j.jcp.2011.11.041
18. May, G., Schöberl, J.: Analysis of a Spectral Difference Scheme with Flux Interpolation on Raviart-Thomas Elements, Tech. rep., Aachen Institute for Advanced Study in Computational Engineering Science (2010)
19. Li, M., Qiu, Z., Liang, C., Sprague, M., Xu, M., Garris, C.A.: A new high-order spectral difference method for simulating viscous flows on unstructured grids with mixed-element meshes. Comput. Fluids **184**, 187–198 (2019). https://doi.org/10.1016/j.compfluid.2019.03.010
20. Qiu, Z., Zhang, B., Liang, C., Xu, M.: A high-order solver for simulating vortex-induced vibrations using sliding-mesh spectral difference method and hybrid grids. Int. J. Numer. Methods Fluids **90**, 171–194 (2019). https://doi.org/10.1002/fld.4717
21. Veilleux, A., Puigt, G., Deniau, H., Daviller, G.: A stable Spectral Difference approach for computations with triangular and hybrid grids up to the 6^{th} order of accuracy. J. Comput. Phys. **449**, 110774 (2022). https://doi.org/10.1016/j.jcp.2021.110774
22. Balan, A., May, G., Schöberl, J.: A Stable and Spectral Difference and Method for Triangles, In: 49th AIAA Aerospace Sciences Meeting including the New Horizons Forum and Aerospace Exposition, (2011). https://doi.org/10.2514/6.2011-47
23. Proriol, J.: Sur une famille de polynômes à deux variables orthogonaux dans un triangle. Sci. Paris **257**, 2459–2461 (1957)
24. Koornwinder, T.: Two-variable analogues of the classical orthogonal polynomials, In: R. Askey (Eds), Theory and Applications of Special Functions, San Diego, (1975)
25. Dubiner, M.: Spectral methods on triangles and other domains. J. Sci. Comput. **6**(4), 345–390 (1991). https://doi.org/10.1007/BF01060030

26. Williams, D., Shunn, L., Jameson, A.: Symmetric quadrature rules for simplexes based on sphere close packed lattice arrangements. J. Comput. Appl. Math. **266**, 18–38 (2014). https://doi.org/10.1016/j.cam.2014.01.007
27. Silvester, P.: Symmetric quadrature formulae for simplexes. Math. Comput. **24**, 95–100 (1970). https://doi.org/10.1090/S0025-5718-1970-0258283-6
28. Vioreanu, B., Rokhlin, V.: Spectra of multiplication operators as a numerical tool. SIAM J. Sci. Comput. **36**, 267–288 (2014). https://doi.org/10.1137/110860082
29. Keast, P.: Moderate degree tetrahedral quadrature formulas. Comput. Methods Appl. Mech. Eng. **55**(3), 339–348 (1986). https://doi.org/10.1016/0045-7825(86)90059-9
30. Witherden, F., Vincent, P.: On the identification of symmetric quadrature rules for finite element methods. Comput. Math. Appl. **69**, 1232–1241 (2015). https://doi.org/10.1016/j.camwa.2015.03.017
31. Jinyun, Y.: Symmetyric Gaussian quadrature formulae for tetrahedronal regions. Comp. Methods Appl. Mech. Eng. **43**, 349–353 (1984). https://doi.org/10.1016/0045-7825(84)90072-0
32. Hammer, P., Marlowe, O., Stroud, A.: Numerical integration over simplexes and cones. Math. Tables Other Aids Comput. **10**(55), 130–137 (1956). https://doi.org/10.1090/S0025-5718-1956-0086389-6
33. Liu, Y., Vinokur, M.: Exact integrations of polynomials and symmetric quadrature formulas over arbitrary polyhedral grids. J. Comput. Phys. **140**, 122–147 (1998). https://doi.org/10.1006/jcph.1998.5884
34. Jaśkowiec, J., Sukumar, N.: High-order cubature rules for tetrahedra. Numer. Methods Eng. **121**(11), 2418–2436 (2020). https://doi.org/10.1002/nme.6313
35. Xiao, H., Gimbutas, Z.: A numerical algorithm for the construction of efficient quadrature rules in two and higher dimensions. Comput. Math. Appl. **59**(2), 663–676 (2010). https://doi.org/10.1016/j.camwa.2009.10.027
36. Bogey, C., Bailly, C.: A family of low dispersive and low dissipative explicit schemes for flow and noise computations. J. Comput. Phys. **194**, 194–214 (2004). https://doi.org/10.1016/j.jcp.2003.09.003
37. Jiang, G.-S., Shu, C.-W.: Efficient implementation of weighted ENO schemes. J. Comput. Phys. **126**(1), 202–228 (1996). https://doi.org/10.1006/jcph.1996.0130
38. Pazner, W., Persson, P.-O.: Approximate tensor-product preconditioners for very high order discontinuous Galerkin methods. J. Comput. Phys. **354**, 344–369 (2018). https://doi.org/10.1016/j.jcp.2017.10.030
39. https://how5.cenaero.be/. [link]. URL https://how5.cenaero.be/
40. Sun, Y., Wang, Z.J., Liu, Y.: High-order multidomain spectral difference method for the Navier–Stokes equations on unstructured hexahedral grids. Commun. Comput. Phys. **2**(2), 310–333 (2007)
41. Raviart, P., Thomas, J.: A mixed finite element method for 2nd order elliptic problem, In: Lecture Notes in Mathematics 606, p. 292–315 (1977)
42. Nedelec, J.: Mixed finite elements in R3. Numerische Mathematik **35**, 315–341 (1980)

CHAPTER 3

Meshing technique

The work presented in the following paper is a part of Maxence Brebion PhD thesis that took place at IMFT from 2015 to 2017. It was funding by the European Research Council INTECOCIS. The objective was the study of thermoacoustics instabilities in order to take into account acoustic dissipation and to develop Reduce Order Model for combustion instabilities. In this chapter, an adaptive mesh refinement strategy is developped to capture with accuracy mean and acoustic pressure losses. To do so, a joint experimental and numerical LES based study was performed.

G. Daviller, M. Brebion, P. Xavier, G. Staffelbach, J.-D. Müller, and T. Poinsot. A mesh adaptation strategy to predict pressure losses in les of swirled flows. *Flow, Turbulence and Combustion*, 99:93-118, 2017. https://doi.org/10.1007/s10494-017-9808-z

A Mesh Adaptation Strategy to Predict Pressure Losses in LES of Swirled Flows

Guillaume Daviller[1] · Maxence Brebion[2] · Pradip Xavier[2] · Gabriel Staffelbach[1] · Jens-Dominik Müller[3] · Thierry Poinsot[2]

Received: 23 June 2016 / Accepted: 16 March 2017

Abstract Large-Eddy Simulation (LES) has become a potent tool to investigate instabilities in swirl flows even for complex, industrial geometries. However, the accurate prediction of pressure losses on these complex flows remains difficult. The paper identifies localised near-wall resolution issues as an important factor to improve accuracy and proposes a solution with an adaptive mesh h-refinement strategy relying on the tetrahedral fully automatic MMG3D library of Dapogny et al. (J. Comput. Phys. **262**, 358-378, 2014) using a novel sensor based on the dissipation of kinetic energy. Using a joint experimental and numerical LES study, the methodology is first validated on a simple diaphragm flow before to be applied on a swirler with two counter-rotating passages. The results demonstrate that the new sensor and adaptation approach can effectively produce the desired local mesh refinement to match the target losses, measured experimentally. Results shows that the accuracy of pressure losses prediction is mainly controlled by the mesh quality and density in the swirler passages. The refinement also improves the computed velocity and turbulence profiles at the swirler outlet, compared to PIV results. The significant improvement of results confirms that the sensor is able to identify the relevant physics of turbulent flows that is essential for the overall accuracy of LES. Finally, in the appendix, an additional comparison of the sensor fields on tetrahedral and hexahedral meshes demonstrates that the methodology is broadly applicable to all mesh types.

Keywords LES · Swirl injector · Pressure losses · Adaptive mesh refinement

✉ Guillaume Daviller
guillaume.daviller@cerfacs.fr

1 CERFACS, 42 Avenue Gaspard Coriolis, 31057 Toulouse Cedex 01, France

2 IMFT, Allée du Professeur Camille Soula, 31400 Toulouse, France

3 School of Engineering and Materials Science, Queen Mary University of London, E1 4NS, London UK

1 Introduction

The design of swirl injectors used in combustion chambers is often based on multiple passages and relies on complex geometrical shapes. The swirler controls a large part of the chamber performances: flame stabilisation, mixing between fuel and air, flame stability, ignition capabilities, etc. [1] and its optimisation is a crucial part of an engine design. Large-Eddy Simulation (LES) has become a reference method for the simulation of swirling flows in the last ten years [2–4]. Nevertheless, the prediction of pressure losses in swirl burners using LES remains a challenge for most industrial solvers: errors on pressure losses in swirled systems computed with LES can be surprisingly high as discussed below.

LES have been applied with tremendous success to swirled injectors used in combustion chambers for both non-reacting [5, 6] and reacting flows [4, 7–9]. Velocity profiles at various positions downstream of the swirled injectors usually match experimental velocity profiles very well, with and without reaction. What is seldom studied, however, is the capability of the LES solvers to predict pressure losses through these systems. These losses are a first order parameter in the design of swirled injectors: excessive pressure losses directly impact the engine efficiency so that predicting them accurately is as important as predicting velocity profiles. Unfortunately, recent studies show that while most LES capture velocity profiles accurately downstream of the swirler, they fail to predict pressure losses through the swirler itself with precision, usually overestimating them by 20 to 50%. Pressure losses in a swirling system are mainly induced by sudden expansion within the swirler passages, where strong flow directional perturbations occur [10]. Of course, increasing the total number of points inside the swirler helps to improve the accuracy of the prediction of pressure losses, but refining uniformly in the swirler is not affordable. Only few studies have addressed prediction of losses in combustors with complex geometry [10, 11], whereas the sensitivity of LE,S to mesh quality is a well-known issue for non-reacting flows [12] as well as for reacting flows [3, 13].

Three different approaches are commonly used in Adaptive Mesh Refinement (AMR) strategies in CFD: r-refinement methods where cells of a given mesh are redistributed, p-refinement methods where the order of discretisation is locally increased and h-refinement approaches where cells are subdivided isotropically or anisotropically [14]. In this latter case, a new mesh with a modified density distribution is generated [15, 16]. Whereas r- and p-refinement are most useful for dynamic mesh refinement as they do not change the mesh topology, h-refinement and remeshing are very appropriate for static mesh adaptation as they allow to add cells. While h-refinement is the most costly approach, it is the only one which can produce a high-quality mesh that is independent of the initial mesh. AMR methods have been developed for Reynolds Average Navier-Stokes (RANS) methods for a long time [17, 18] but they remain a challenge in LES: being able to generate LES meshes on the basis of well-established metrics instead of relying on the intuition of the LES user is probably the overarching question for future LES.

The objective of the present study focuses on this problem for one specific case: non-reacting flows in swirlers. Uniform mesh refinement is not an affordable option, so that adaptive mesh refinement appears as an appropriate tool. In turn, a local mesh refinement approach based on h-refinement requires a sensor which robustly flags all areas relevant to pressure loss inside the swirler, but does not use valuable mesh resources in irrelevant areas. The present work proposes an adaptive h-refinement method to increase the accuracy of the prediction of pressure losses while keeping the total number of mesh points to a minimum.

The approach employs remeshing which is driven by a sensor based on mean flow data. The sensor considers as Quantity of Interest (QOI) the dissipation of kinetic energy.

This QOI is averaged during the simulation and provided as field function to the MMG3D library [19] which carries out the remeshing operations. A new solution is then computed on the refined mesh, and the process is repeated once or twice during a full simulation. This is sufficient to reach an accuracy of a few percent on pressure losses while preserving or improving the quality of all velocity profiles and retaining an appropriate number of cells.

This paper is organised as follows: Section 2 shows why the kinetic energy dissipation is the right mesh metric to predict pressure losses and presents the mesh adaptation procedure where the LES solver is coupled to the tetrahedral mesh refinement code MMG3D. The remeshing methodology is then validated on the canonical case of a simple orifice-plate in Section 3. Section 4 presents first the experimental configuration and the flow parameters for the swirl fuel injector. LES and PIV results are then compared and analyzed. Additionally, as the choice between hexahedral and tetrahedral meshes in LES and CFD is a general CFD topic, a LES on an unstructured fully hexahedral grid for the same swirl burner is shown in the Appendix, highlighting the universality of the adaptation criteria in this paper.

2 Mesh Metric for the Prediction of Pressure Losses

As underlined by Mitran [20], the criterion governing grid refinement in CFD should represent the physics of the problem. Due to the unsteady chaotic nature of turbulence, knowing where to refine the mesh in an LES is a complicated question which may depend on the objectives of the simulation: the best mesh to predict far field noise sources is probably not the best mesh to capture pressure losses. Metrics for CFD have been proposed for RANS meshes for a long time [15, 21] and are still studied today [22, 23]. Metrics for LES or DNS have also been derived recently. This can be done either as a dynamic approach, i.e. performed at run time, so that the mesh is adapted to the instantaneous solution (see [24–26]), but can also be done statically, i.e. performed using mean flow characteristics once or twice during the whole simulation [11], as proposed here.

The first step to build a proper QOI adapted to the accurate prediction of pressure losses in swirlers is to identify which physical mechanisms generate these losses. This can be obtained by considering conservation equations for kinetic energy $E_c = (1/2)\rho u_i u_i$ and for entropy s. The instantaneous equation for kinetic energy E_c can be written in incompressible flows as:

$$\underbrace{\frac{\partial E_c}{\partial t}}_{1} + \underbrace{\frac{\partial}{\partial x_j}\left(u_j\left(E_c + P\right)\right)}_{2} = \underbrace{\frac{\partial\left(\tau_{ij} u_i\right)}{\partial x_j}}_{3} + \underbrace{\tau_{ij}\frac{\partial u_i}{\partial x_j}}_{4} \tag{1}$$

where terms (1), (2), (3) and (4) correspond respectively to the temporal variation of the kinetic energy, the mechanical energy flux, the viscous diffusion and the viscous dissipation. The instantaneous entropy equation expressed with the same notations is:

$$\frac{\partial \rho s}{\partial t} + \frac{\partial \rho u_j s}{\partial x_j} = \frac{1}{T}\left(\tau_{ij}\frac{\partial u_i}{\partial x_j} + \frac{\partial}{\partial x_j}\left(\lambda \frac{\partial T}{\partial x_j}\right)\right) \tag{2}$$

Equations 1 and 2 reveal the importance of the viscous dissipation Φ:

$$\Phi = \tau_{ij}\frac{\partial u_i}{\partial x_j} = \frac{\mu}{2}\left(\frac{\partial u_i}{\partial x_j} + \frac{\partial u_j}{\partial x_i}\right)^2 \tag{3}$$

This term is present in the entropy equation and measures the losses due to fluid friction irreversibilities [27–29]. Of course, this is not a surprising result and the dissipation Φ plays a major role in all turbulence theories where it controls the dissipation to the small scales. The aerodynamic community [27, 29–32] and the applied mathematicians [33, 34], have also been using entropy as a quality indicator for a long time. The dissipation Φ also appears in the kinetic energy equation and rewriting this equation to introduce the total pressure $P_t = P + E_c$ shows that the dissipation Φ is the quantity which controls the dissipation of total pressure and therefore pressure losses:

$$\frac{\partial E_c}{\partial t} + \frac{\partial}{\partial x_j}\left(u_j P_t\right) = \frac{\partial\left(\tau_{ij} u_i\right)}{\partial x_j} + \Phi \tag{4}$$

For a steady flow, the integration of Eq. 4 over the whole computational domain of volume Δ bounded by a surface Σ, with the Ostrogradsky's theorem gives:

$$\int_\Sigma P_t u_i n_i d\sigma = \int_\Delta \frac{\partial\left(\tau_{ij} u_i\right)}{\partial x_j} dV + \int_\Delta \Phi dV \tag{5}$$

Finally, for a case with non-moving walls, the first right-hand side term of Eq. 6, which corresponds to the power of external viscous forces, cancels. The pressure losses are then directly expressed by the integral of the volumetric dissipation rate:

$$Q_v \Delta P_t = \int_\Delta \Phi dV \tag{6}$$

where Q_V is the volume flow rate and ΔP_t is the pressure loss between inlet and outlet sections. Equation 6 confirms that errors on pressure losses ΔP_t in a simulation are due to the fact that the total dissipation $\int_\Delta \Phi dV$ is not computed with sufficient accuracy. The fact that the dissipation field Φ controls the irreversible losses in the entropy equation as well as the pressure losses in the kinetic energy equations suggests that a proper QOI to use in a metric aiming at adapting meshes to improve pressure losses prediction is the field of Φ: this is the QOI chosen in this paper.

An additional complexity introduced by LES is that the equations used in LES are not Eq. 1. Some differences must be accounted for to construct the QOI to use in an LES:

- Many LES use compressible formulations where additional phenomena (dilatation dissipation for example [35]) contribute to losses. To first order however, it is reasonable to accept, especially for low speed flows, that Φ is the simplest quantity to use for mesh adaptation even if the flow is compressible.
- In the present mesh adaptation strategy, Eq. 1 will be averaged over time to produce a steady field. Therefore the proper QOI is not the instantaneous field Φ but its time averaged field $\overline{\Phi}$.
- Finally, LES does not resolve all spatial scales: the LES field corresponds to a filtered velocity $\tilde{u}_i$ and not the local velocity u_i [36, 37]. The filtering operation introduced by LES leads to an expression for dissipation which contains two parts: the first one is produced by the fluctuations resolved on the LES grid and can be written $\phi = \mu\left(\frac{\partial \tilde{u}_i}{\partial x_j} + \frac{\partial \tilde{u}_j}{\partial x_i}\right)^2$. The second contribution to dissipation corresponds to the unresolved part and can be written $\varphi = \mu_t\left(\frac{\partial \tilde{u}_i}{\partial x_j} + \frac{\partial \tilde{u}_j}{\partial x_i}\right)^2$ where μ_t is the local turbulent

viscosity. Therefore a proper expression for the QOI is the time averaged of the sum of these two contributions: $\overline{\tilde{\Phi}} = \overline{\phi + \varphi}$:

$$\overline{\tilde{\Phi}} = \overline{(\mu + \mu_t)\left(\frac{\partial \tilde{u}_i}{\partial x_j} + \frac{\partial \tilde{u}_j}{\partial x_i}\right)^2} \tag{7}$$

This is the QOI used in the following sections. It is expected to provide a metric leading to mesh refinement in zones where $\overline{\tilde{\Phi}}$ will be large so that the precision of pressure losses, which are controlled by this field, will improve. Interestingly, results show that the prediction of the velocity fields is also more accurate and suggest that this metric improves the quality of all results and not just of pressure losses.

In practice, the implementation of the metric in the LES code AVBP is performed as follows (Fig. 1). From the time-averaged dissipation field $\overline{\tilde{\Phi}}$, a dimensionless variable $\Phi^\star$ is first defined as:

$$\Phi^\star = \left[1 - \left(\frac{\overline{\tilde{\Phi}} - \overline{\tilde{\Phi}}_{\text{min}}}{\overline{\tilde{\Phi}}_{\text{max}} - \overline{\tilde{\Phi}}_{\text{min}}}\right)\right]^\alpha, \quad \Phi^\star \in [0:1] \tag{8}$$

where the parameter α in Eq. 8 scales the value of $\Phi^\star$ in order to ensure continuous variation of QOI and to obtain smoother stretching of the cells size in the new mesh. The values $\overline{\tilde{\Phi}}_{\text{min}}$ and $\overline{\tilde{\Phi}}_{\text{max}}$ correspond to the minimum and maximum of the time-averaged dissipation field

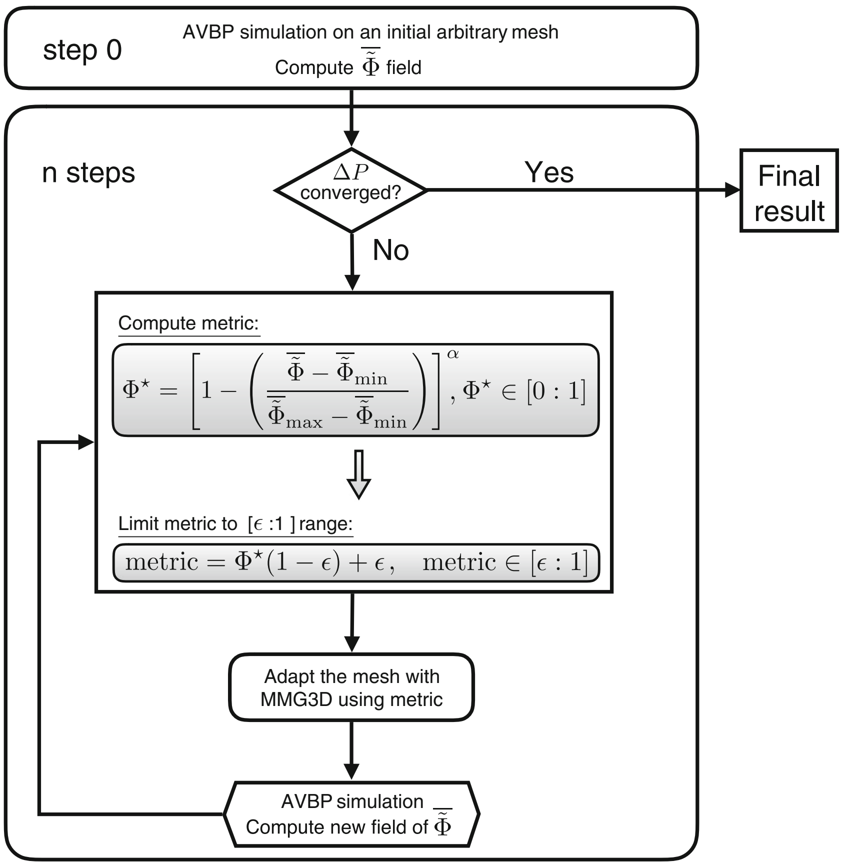

Fig. 1 Mesh adaptation procedure

$\tilde{\Phi}$ measured in the whole computational domain, respectively. Then the maximum factor to divide the volume of the tetrahedral cells is imposed by the variable ϵ in the metric:

$$\text{metric} = \Phi^{\star}(1-\epsilon)+\epsilon \tag{9}$$

Typical range of values used for these two terms in this study are $0.3 \le \epsilon \le 0.7$ and $30 \le \alpha \le 100$. The value of ϵ fixes the maximum refinement: no cell with a volume Δ is allowed to be reduced to less than $\epsilon\Delta$. The value of α controls the dilatation of the cells allowed on the mesh. The MMG3D library [19] then interpolates the mesh size to use from the prescribed metric on the current mesh. Finally, the MMG3D library is used to generate an entirely new mesh. The mesh refinement strategy is shown on Fig. 1. No restriction on the number of tetrahedra is specified but a minimal cell volume is fixed. This parameter is simply defined using the maximum of the metric and the minimal cell volume of the mesh before adaptation. The AVBP code uses a compressible formulation with explicit time-stepping and is hence subject to a CFL condition based on the fastest acoustic wave. To maintain an appropriate time-step Δt, the local mesh size must not be too small. Only isotropic subdivisions of the tetrahedra are considered to preserve the mesh quality [38]. While anisotropic remeshing can be very appropriate in producing high-aspect ratio cells aligned with strong gradients in steady flow [16], the present computations are unsteady and the extreme element angles found in anisotropic tetrahedral meshes would adversely affect accuracy. All simulations in Sections 3 and 4 are performed using the compressible cell-vertex Navier-Stokes solver AVBP [39, 40]. The third-order scheme TTGC [41] is used on a fully tetrahedral mesh. In order to remove spurious numerical oscillations, an artificial viscosity operator of 2nd and 4th order is also applied according to a local sensor [41]. At the inlet and outlet boundaries, the classical Local One-Dimensional Inviscid (LODI) Navier-Stokes Characteristic Boundary Conditions (NSCBC) are used [42]. These boundaries conditions are derived from the time-dependent boundary conditions proposed by Thompson [43] and are non-reflective, based on the work of Rudy & Strikwerda [44]. An eddy-viscosity approach is considered for the SubGrid-Scale (SGS) stress, based on the SIGMA model [45]. The choice of SIGMA is motivated by its low computational cost and its good results compared to the Dynamic Smagorinsky model and experiments [46–48]. The SIGMA model is computed from the singular values of the local velocity gradient tensor. No-slip adiabatic conditions are applied at all walls.

3 Validation on a Canonical Test Case: Pressure Losses through a Diaphragm

The AVBP-MMG3D strategy is first validated for the canonical test case of an orifice plate in a straight duct (Fig. 2). The evaluation of the pressure losses through a diaphragm is a usual task in the industry to measure flow rates. Due to the simplicity of the geometry, many pressure loss correlations derived from experiment are available in the literature [49, 50]. In order to compare LES and experimental data, a series of experimental measurement were performed on a diaphragm to make sure that pressure losses were evaluated correctly.

The geometry of the sharp-edged orifice is defined by a single circular hole of diameter $d = 18$ mm and thickness $t = 2$ m, centered in a pipe with an inner diameter of $D = 81$ mm. The air stream is controlled with a Brooks mass flow controller for a range of mass flow rates $0.43\,\mathrm{g\cdot s^{-1}} \le \dot{m} \le 3.55\,\mathrm{g\cdot s^{-1}}$. Flow rates are measured with an uncertainty of 1%. The flow is then guided in a 590 mm long tube upstream of the orifice. The latter expands in a tube having a length of 360 mm which is opened to the atmosphere. Total pressure loss

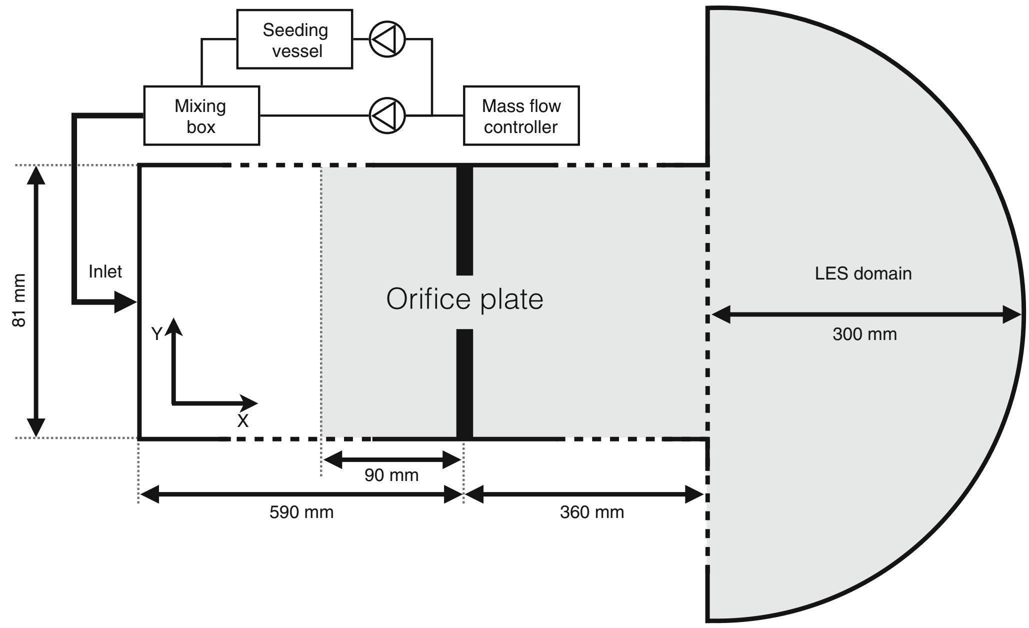

Fig. 2 Schematic view of the experimental setup of the diaphragm. The shaded area correspond to the LES domain

through the orifice is measured with an electronic micro-manometer, and with an uncertainty smaller than 0.25%. The experimental pressure drop curve measured with this device is displayed on Fig. 3. The Idel'Cik correlation [49] for orifice plate and Reynolds number $Re < 10^5$ is in agreement with the LES results.

The mesh refinement procedure is tested first for a mass flow rate of $\dot{m} = 3.55\,\mathrm{g \cdot s^{-1}}$ where the pipe flow upstream of the orifice-plate is characterised by a bulk velocity $U_b = 0.55\,\mathrm{m \cdot s^{-1}}$ and a Reynolds number $Re_D = U_b D/\nu = 3000$. The ambient pressure and temperature of the experiment are $P = 101150\,\mathrm{Pa}$ and $T = 292\,\mathrm{K}$. The computational domain is shown on Fig. 2. The inlet plenum is truncated at $x = -90\,\mathrm{mm}$ in the LES. A semi-hemisphere, defined by a radius of ($r = 0.3\,\mathrm{m}$) is added at the duct outlet in order

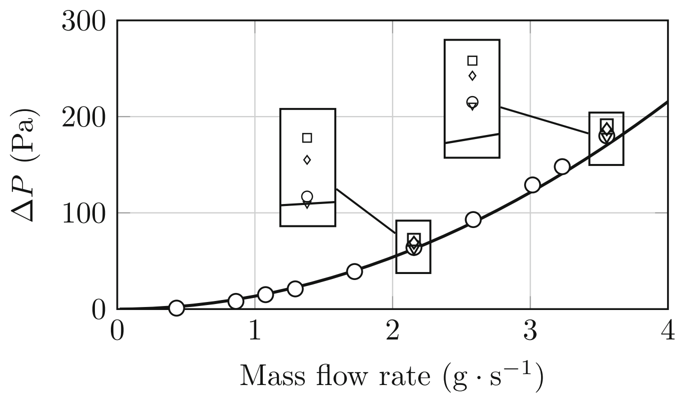

Fig. 3 Experimental pressure loss evolution across the orifice plate for different mass flow rates. Comparison of the measured values (○) with the Idel'Cik model [49] (——) and the LES results for the coarse (□), AD 1 (◇) and AD 2 (▽) meshes

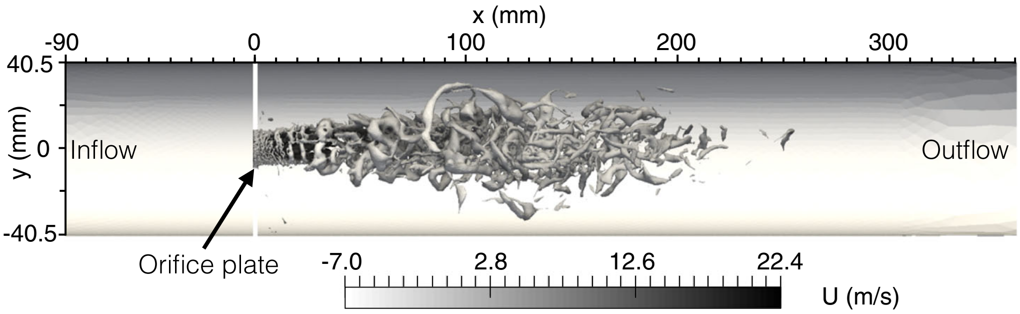

Fig. 4 LES of the orifice-plate at $\dot{m} = 3.55\,\mathrm{g \cdot s^{-1}}$. The instantaneous flow is represent using Q-criterion $Q = 1.62(U_j/D_j)^2$ colored by axial velocity, on mesh AD 2

to mimic the atmosphere in the experiment and dissipate free-jet flow fluctuations. Downstream of the orifice-plate, centered at $x = 0$ mm (the upstream inlet edge is at $x = -1$ mm), a jet-plume flow develops as expected. This is shown using Q-criterion (as defined by Hunt et al. [51]) on Fig. 4.

In this test case, the target pressure loss is obtained in two adaptation steps and three LES. Table 1 summarises the parameters and the cost. From an initial coarse mesh (Fig. 5), a first adapted mesh "AD 1" is obtained. The central picture in Fig. 5 shows that the mesh refinement follows the distribution of viscous dissipation $\overline{\tilde{\Phi}}$ obtained on the coarse mesh. This first refinement step leads to an overestimation of the pressure drop compared to the experiment of only 3.8% while it was 6.1% on the coarse mesh. Finally, an acceptable discretisation is obtained in the second step and the mesh "AD 2". The error on the predicted losses is less than 1%. Figure 6 shows radial profiles of the mean and r.m.s. axial velocity across the orifice at the leading edge ($x = -1$ mm), the center ($x = 0$ mm) and the trailing edge ($x = 1$ mm), respectively. Only the last mesh "AD 2", allows the apparition of the "vena-contracta" effect, with a flow separation zone across the diaphragm. Indeed, no reverse flow appears downstream the leading edge of the diaphragm at $x = 0$ mm and $x = 1$ mm with the coarse and AD 1 mesh.

Moreover, a remarkable change is observed for the mean kinetic energy dissipation field between mesh AD 1 and AD 2 on Fig. 5. The solution on mesh AD 1 would suggest that a persistent shear layer has been captured well at the orifice and is then swept downstream. AD 2 refinement leads to a mesh which is refined much more close, to the orifice plate:

Table 1 Summary of the mesh adaptation LES on the orifice-plate at $\dot{m} = 3.55\,\mathrm{g \cdot s^{-1}}$

	Coarse	AD 1	AD 2
α	—	100	50
ϵ	—	0.3	0.4
T_{init} (s)	1.5	0.3	0.3
T_{stat} (s)	0.5	0.5	0.5
time step ($\times 10^{-6}$ s)	1.4	0.41	0.13
number of cells ($\times 10^{6}$)	0.71	1.55	2.75
number of CPU hours	3h06	5h30	19h
number of cores	256	720	1152
ΔP error	6.1%	3.8%	−0.5%

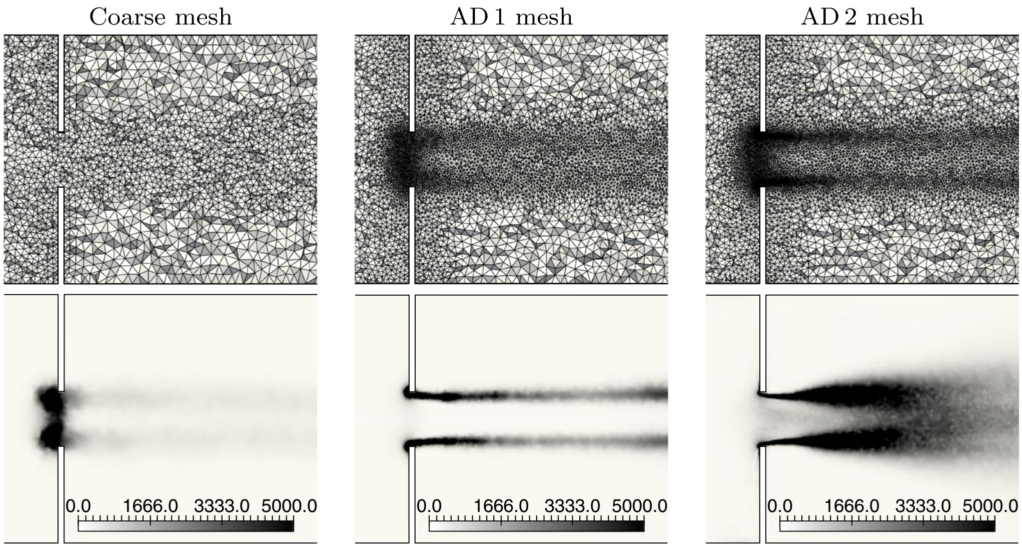

Fig. 5 Orifice-plate test case at $\dot{m} = 3.55\,\mathrm{g}\cdot\mathrm{s}^{-1}$: zoom on the mesh on the orifice for each LES (*top images*) and mean kinetic energy dissipation $\overline{\tilde{\Phi}}$ (*bottom images*) in $\mathrm{W}\cdot\mathrm{m}^{-3}$

this allows the growth of Kelvin-Helmholtz instabilities and a rapid transition to a fully developed turbulent jet-plume. This is in agreement with the spectral power density obtained from the axial velocity signal recorded at $x = 2d$ and $r = 0.5d$ for the three meshes (Fig. 7). Only the axial velocity spectrum of mesh AD 2 is fully broadband and exhibit a typical $k = -5/3$ slope over one decade. Mesh AD 1 allows the development of instabilities, characterised by a narrow band with a maximum for $f = 700$ Hz, but no inertial zone is found in the spectrum. The result for the coarse mesh suggests that the flow remains fully laminar.

The adaptation approach was repeated at a mass flow rate of $\dot{m} = 2.15\,\mathrm{g}\cdot\mathrm{s}^{-1}$ to further check its validity (cf. Fig. 3). The experimental target is also reached in two mesh refinement steps with a final error of 1.6%.

4 Pressure Losses in a Swirled Injector

4.1 Description of the swirler

A schematic view of the radial swirl injector used for this study is shown in Fig. 8. The air entering the swirler is divided into two passages: the primary flow passes through the inner region of the passages with eight tangential vanes. The secondary flow passes through the outer passages with the same number of vanes but with counter-rotating swirl direction. No fuel is injected for these tests: in order to replace the fuel injection system, a plug is inserted in the primary flow along the centerline of the swirler producing a recess of 14 mm with respect to the exit plane.

4.2 Experimental set-up

The flow is guided in a 590 mm plenum (Fig. 8) before reaching the swirl injection system with an exit diameter of $D = 0.018$ m which blows into the atmosphere. PIV measurements

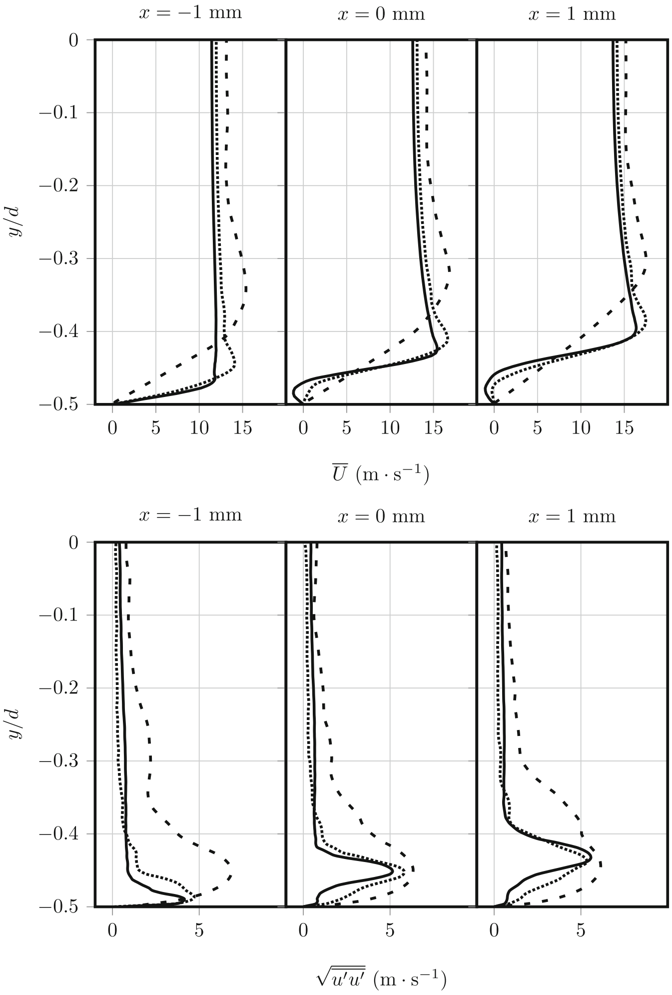

Fig. 6 Orifice-plate test case at $\dot{m} = 3.55\,\mathrm{g \cdot s^{-1}}$: Up, radial distribution of axial mean velocity across the orifice. Down, radial distribution of r.m.s. axial velocity. Coarse mesh (- - - -); mesh AD 1 (.........) and mesh AD 2 (——)

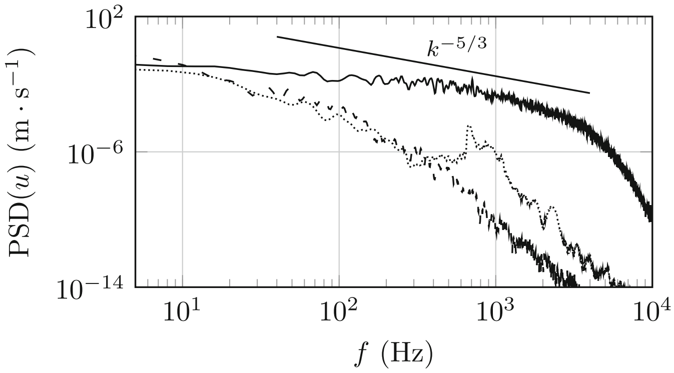

Fig. 7 Orifice-plate test case at $\dot{m} = 3.55\,\mathrm{g \cdot s^{-1}}$: power spectral density of the axial velocity in the jet-plume shear layer at $x = 2d$ and $r = 0.5d$. Coarse mesh (- - - -); mesh AD 1 (.........) and mesh AD 2 (——)

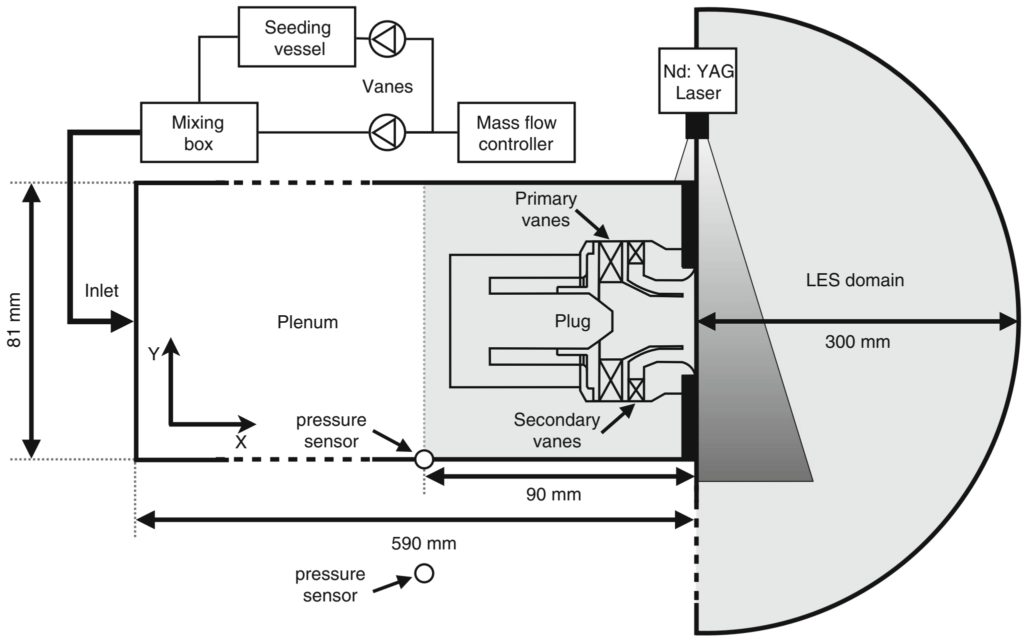

Fig. 8 Schematic view of the experimental setup, swirler device and LES domain. The longitudinal (xOy) PIV plane is highlighted. The shaded area corresponds to the LES domain

of the velocity field have been performed downstream of the injector, along a longitudinal (xOr) plane (Fig. 8). A double cavity Nd:YAG laser (Quantel Big Sky) operating at 532 nm fires two laser beams, with a delay varying between 4 μs and 11 μs according to the operating conditions. The beam is expanded through a set of fused silica lenses (spherical and diverging). Because of the important out-of-plane velocity component, the laser sheet was intentionally thickened to approximately 1 mm. Olive oil particles (typical size of $1-2\,\mu$m) were seeded through the various flow injections systems (by means of venturi seeders). Mie scattering is collected on a 4 Hz PCO-Sensicam, operating with a resolution of 1280 $\times$ 600 pixels for the longitudinal plane. A f/16 182 mm telecentric lens (TC4M64, Opto-engineering) is used to reduce parallax displacements occurring with classical lenses. PIV images are processed with a cross-correlation multi-pass algorithm (Davis 8.2.3),

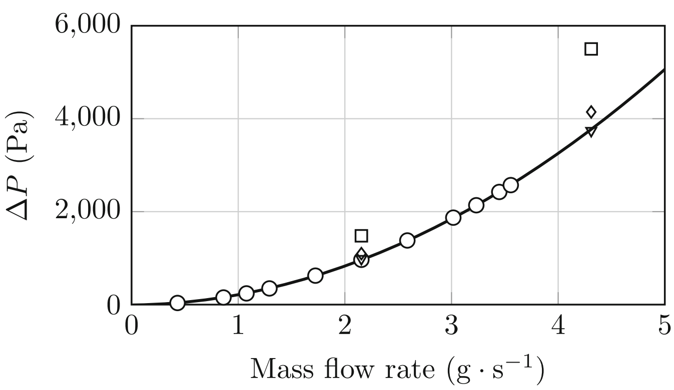

Fig. 9 Pressure loss evolution through the swirler: experimental data (○), fit function (——), LES results for the coarse (□), AD 1 (◇) and AD 2 (▽) meshes

resulting in a final window of $16 \times 16\,\mathrm{px}^2$ and a 50% overlap. 1320 images are collected over a region of $20 \times 32\,\mathrm{mm}^2$ with a vector resolution of 0.4 mm. The pressure loss through the swirler is measured with the differential pressure sensor used for the orifice-plate test case (see Section 3). The two pressure sensors are located on the wall (flush mounted) of the plenum and in the atmosphere, respectively, at 90 mm from the swirler exit (Fig. 8).

4.3 Flow parameters

The pressure losses of the swirled injector system are measured over a range of mass flow rates $0.43\,\mathrm{g}\cdot\mathrm{s}^{-1} \leq \dot{m} \leq 3.55\,\mathrm{g}\cdot\mathrm{s}^{-1}$ (Fig. 9). PIV measurements are performed at three mass flow rates $\dot{m} = 2.15,\ 3.22,\ 4.29\,\mathrm{g}\cdot\mathrm{s}^{-1}$ with an ambient temperature and pressure of $T = 298\,\mathrm{K}$ and $P = 101150\,\mathrm{Pa}$, respectively. First, LES are performed at $\dot{m} = 4.29\,\mathrm{g}\cdot\mathrm{s}^{-1}$. The bulk velocity at the nozzle exit for this case is defined as $U_b = \dot{m}/(\rho A) = 13.9\,\mathrm{m}\cdot\mathrm{s}^{-1}$. The theoretical swirl number is $S = 0.76$ (estimated from the definition given by Merkle [52]) and a Reynolds number based on the bulk velocity and the swirler exit diameter is $Re = U_b D/\mu \sim 14 \times 10^3$. The inlet plenum is truncated to $x = -90\,\mathrm{mm}$ in the LES. The experimental mean axial velocity profile at this position is measured using hot-wire anemometry data (Fig. 10). A fit function is then used as inlet boundary condition in the LES. Downstream of the swirler exit, the LES domain is bounded by a semi-hemisphere with a radius $r = 0.3\,\mathrm{m}$.

4.4 Pressure losses

Figure 11 shows the time evolution of the instantaneous pressure loss measured in the LES, for one reference case where the flow rate is $4.29\,\mathrm{g}\cdot\mathrm{s}^{-1}$. The pressure loss evolves during the coarse mesh computation until its average becomes steady with the value overestimated by 46%, compared to the experiment. As observed by many LES users in recent years [10, 11], the pressure losses error obtained on a first arbitrary mesh can be very large and the 46% error measured here is not acceptable. The application of the refinement method corrects this problem: pressure losses change abruptly when the mesh is refined for the first time to AD 1 and a second one to AD 2. The error on the pressure losses drops to 10% for AD 1 and finally to less than 1% for AD 2. To investigate mesh convergence, an additional adaptation step AD 3 was performed. The pressure losses predicted on this mesh are again in agreement

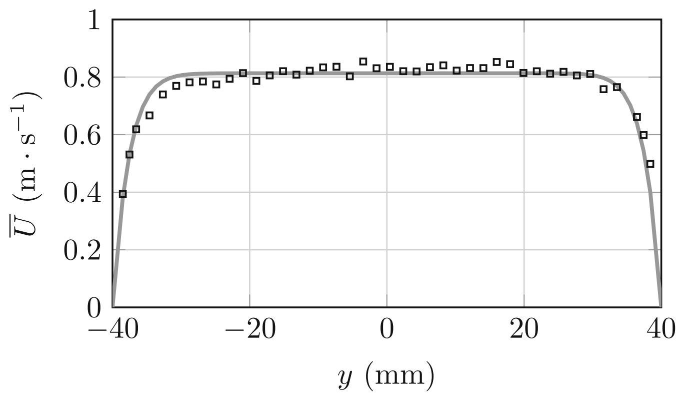

Fig. 10 $\dot{m} = 4.29\,\mathrm{g}\cdot\mathrm{s}^{-1}$ case: mean axial velocity profile inside the plenum at $x = -90\,\mathrm{mm}$ from hot-wire measurement (□), fit function (——) used as inlet condition in the LES

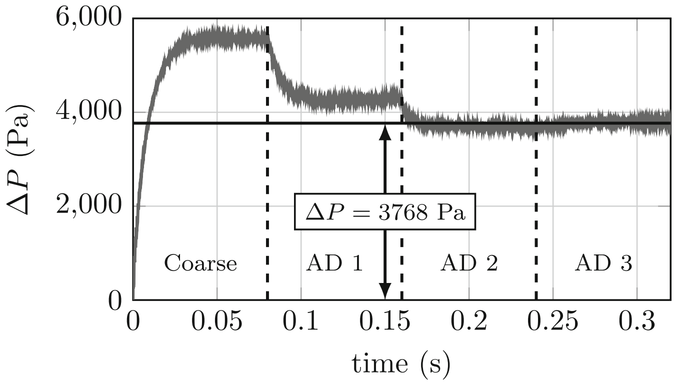

Fig. 11 $\dot{m} = 4.29\,\mathrm{g \cdot s^{-1}}$ case: Evolution of the pressure loss computed with LES as a function of time and comparison with the target experimental value (*straight solid line*). The pressure signal is recorded in the upstream plenum at the wall ($x = -50$ mm and $r = 40.5$ mm). The mesh is refined by the AVBP-MMG3D three times during the whole procedure

with the experiment (less than 1% of error). These results and the values for the parameters α and ϵ, used to build the mesh refinement metric (cf. Fig. 1) are summarised in Table 3.

In addition, in order to assess the numerical uncertainty on the pressure losses prediction, the Grid Convergence Index (GCI) is also computed using the procedure described by Celik et al. [53]. The GCI is defined as:

$$\mathrm{GCI} = \frac{1.25 e_a}{r^p - 1} \tag{10}$$

where the approximate relative error e_a between two meshes is defined using pressure losses ΔP as key variable and the grid refinement factor r is defined using the number of cells h of each mesh. The apparent order p is computed using a fixed point algorithm as suggested in [53]. The discretisation uncertainty on ΔP for mesh AD 1, AD 2 and AD 3 are 7.8%, 1% and 0.05% which corresponds to ± 327.2 Pa, ± 40.4 Pa and ± 2.1 Pa, respectively.

An important parameter of the LES is the evaluation of the flow characteristic time $\tau_F = D/U_b = 1.3$ ms. The simulation time based on this value need to be chosen sufficiently long for the flow to reach steady state as well as the averaged time needed to gather samples in the LES.[1] Figure 11 shows that the flow adapts to all changes of mesh within 30 τ_F. All statistics used in the rest of the paper were gathered over a period of 40 ms corresponding to 30 flow-through times.

The four meshes (coarse, AD 1, AD 2 and AD 3) are displayed in Fig. 12. As expected, mesh refinement is performed in regions where the total mean dissipation $\overline{\tilde{\Phi}}$ is large, allowing to resolve the field of $\overline{\tilde{\Phi}}$ with precision, thereby increasing the precision of the pressure loss evaluation. The convergence of the process can be clearly observed: meshes and results on AD 2 and AD 3 are almost similar.

The automatic refinement procedure AVBP+MMG3D was also applied to an other flow rate at $\dot{m} = 2.15\,\mathrm{g \cdot s^{-1}}$. Fig. 9 displays the values of the experimental pressure loss vs

[1] In the experiment, all measurements were performed over 110 mm, corresponding to very long times compared to τ_F.

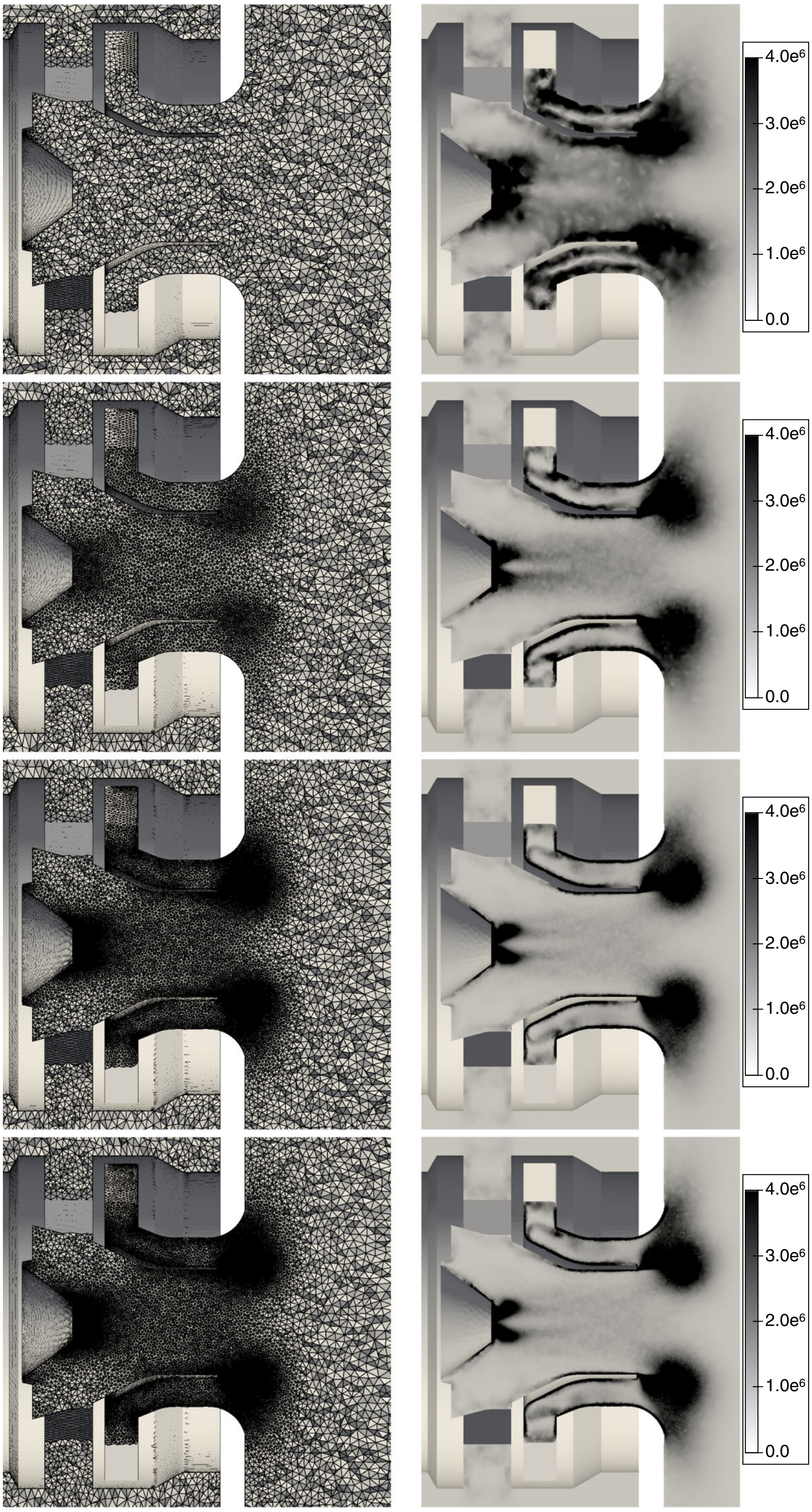

Fig. 12 $\dot{m} = 4.29\,\mathrm{g \cdot s^{-1}}$ case: meshes (*left*) and fields of $\overline{\widetilde{\Phi}}$ in $\mathrm{W \cdot m^{-3}}$ (*right*) for the coarse, AD 1, AD 2 and AD 3 meshes in the central plane of the swirler, from *top* to *bottom*, respectively

Table 2 Error on the experimental mass flow rates recover from PIV result

Target mass flow rates ($g \cdot s^{-1}$)	PIV mass flow rates ($g \cdot s^{-1}$)	error (%)
4.29	3.99	7.0
3.22	2.95	8.4
2.15	2.04	5.1

flow rate compared to the values obtained by the LES for each refinement step. All values of pressure losses correspond to the average pressure loss measured over at least 30 flow-through times (Fig. 11 shows that this time is sufficient for the pressure loss to converge). The procedure appears to be robust for all cases tested here: the refinement procedure leads systematically to small errors compared to the experiment. Note that the procedure is unmodified for all cases: this is a fully automatic method determining a sufficiently resolved mesh in terms of pressure losses, independent of the LES user.

Moreover, in most cases, two refinement steps are sufficient to reach the target so that the simulation costs remain comparable to a normal simulation where the user would try

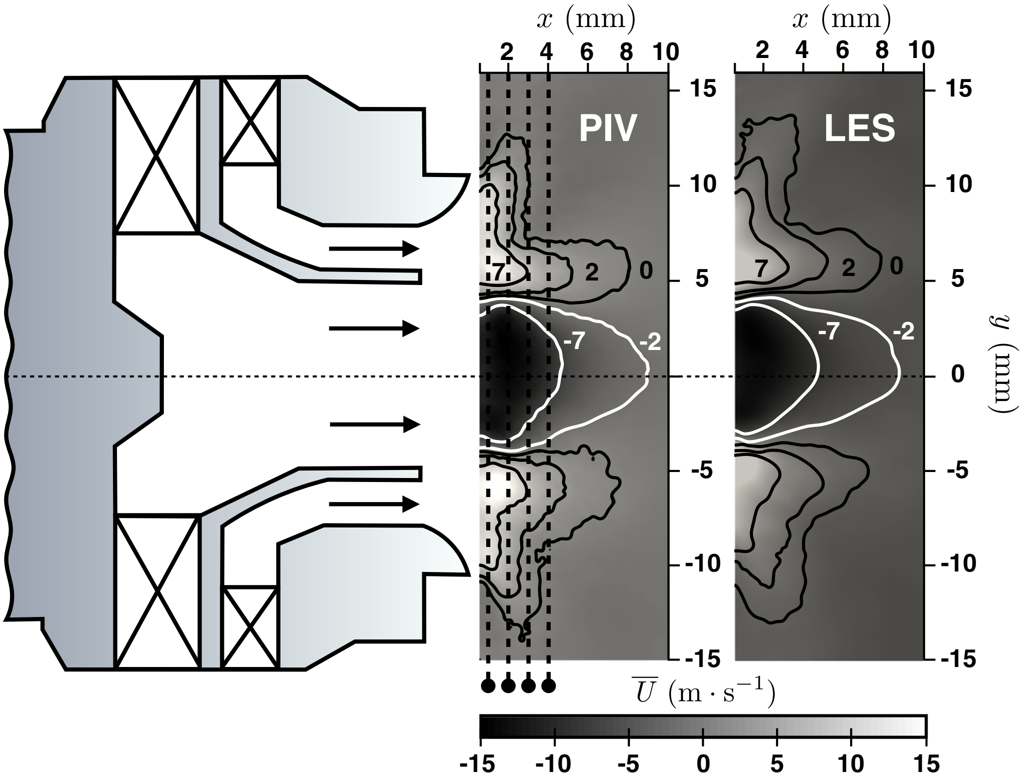

Fig. 13 Comparison of the mean axial velocity from PIV measurement (*center*) and LES on AD 2 mesh (*right*) for the $\dot{m} = 4.29\,\mathrm{g \cdot s^{-1}}$ case. A schematic representation of the swirl injector is depicted on the *left*. White lines denotes negative mean velocity contours at -7 and $-2\,\mathrm{m \cdot s^{-1}}$. Positive and zero mean velocity contours of 7, 2 and $0\,\mathrm{m \cdot s^{-1}}$ are shown with *black line*. *Dashed-lines* identify the position of the measurement cross-sections downstream of the exit plane at $x = 1, 2, 3, 4$ mm

to refine the grid using intuition. Obviously, it is also much cheaper than a brute-force strategy where the whole mesh would be refined homogeneously: here, the homogeneous mesh having the same refinement everywhere as mesh AD 2 has in the swirler region would require 1.4 billion points. The next section shows that the mesh refinement procedure allows also to better predict the velocity field in the chamber itself.

4.5 Velocity fields

The previous section has shown that the AVBP+MMG3D tool was able to produce an acceptable mesh for the pressure loss because it allowed a proper resolution of the time-averaged dissipation field. It is to be expected that with a correct resolution of the mixing phenomena, not only pressure losses but also velocity fields will be predicted more accurately.

To assess this aspect, PIV measurements were performed in the experimental setup (Section 4.2) for the $\dot{m} = 4.29\,\mathrm{g \cdot s^{-1}}$ case and compared to the LES velocity fields on the coarse, AD 1 and AD 2 meshes (AD 3 gave results which are very similar to AD 2). The accuracy of the PIV data was carefully checked by investigating the effects of the measurement windows. Results (Table 2) exhibit less than 9% of error on the mass flow rates recover from PIV compared to the target imposed by the mass flow controller at the plenum inlet in the experiement. Figure 13 compares the mean axial velocity field from PIV and LES (on the AD 2 mesh) in the vicinity of the swirl injector. Results are in excellent agreement. Indeed, in both cases, a strong flow reversal due to vortex breakdown dominates downstream of the exhaust of the primary swirler, which is as expected for flows with a swirl number $S > 0.6$. This very compact reverse flow zone is associated with high turbulence levels [54].

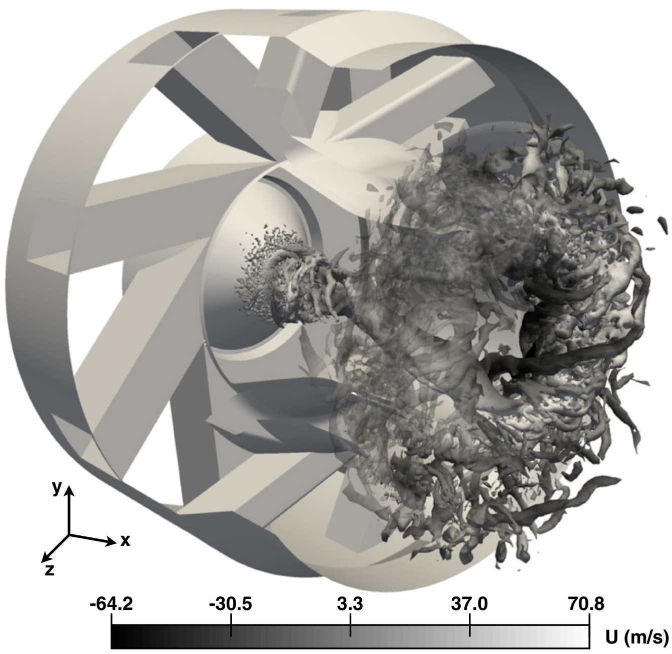

Fig. 14 LES of the swirler on AD 2 mesh: Q-criterion $Q = 1.67 \times 10^4 (U_b/D)^2$ colored by axial velocity for the $\dot{m} = 4.29\,\mathrm{g \cdot s^{-1}}$ swirler case

Even if the mean PIV data reveal a smooth averaged field, a visualisation of the instantaneous structures obtained by LES for the same regime (Fig. 14) shows that the flow is highly turbulent with multiple structures developing in the breakdown zone.

Figure 15 shows that the precision of the LES, in terms of velocity fields, also increases with mesh refinement levels defined by the AVBP+MMG3D procedure. This is particularly obvious on the mean axial velocity profile at $x = 1$ mm for -5 mm $\leq y \leq 5$ mm. Nevertheless, the differences between simulation and PIV results in the shear regions may be explained by a limitation of the PIV spatial resolution [55, 56]. The LES results for the radial profiles of axial velocity on the AD 2 and AD 3 meshes gives similar fields, again confirming grid convergence for the adaptation for this feature. The swirl number is computed from these mean values at $x = 2$ mm using the method given in [57]. The experimental swirl number is $S_{PIV} = 0.77$, which is very close to the theoretical values $S = 0.76$. The simulated swirl number for the mesh coarse, AD 1, AD 2 and AD 3 are $S_{LES} = 0.62, 0.88, 0.79$ and 0.75, respectively. This means that the swirl motion, which drives the characteristics of

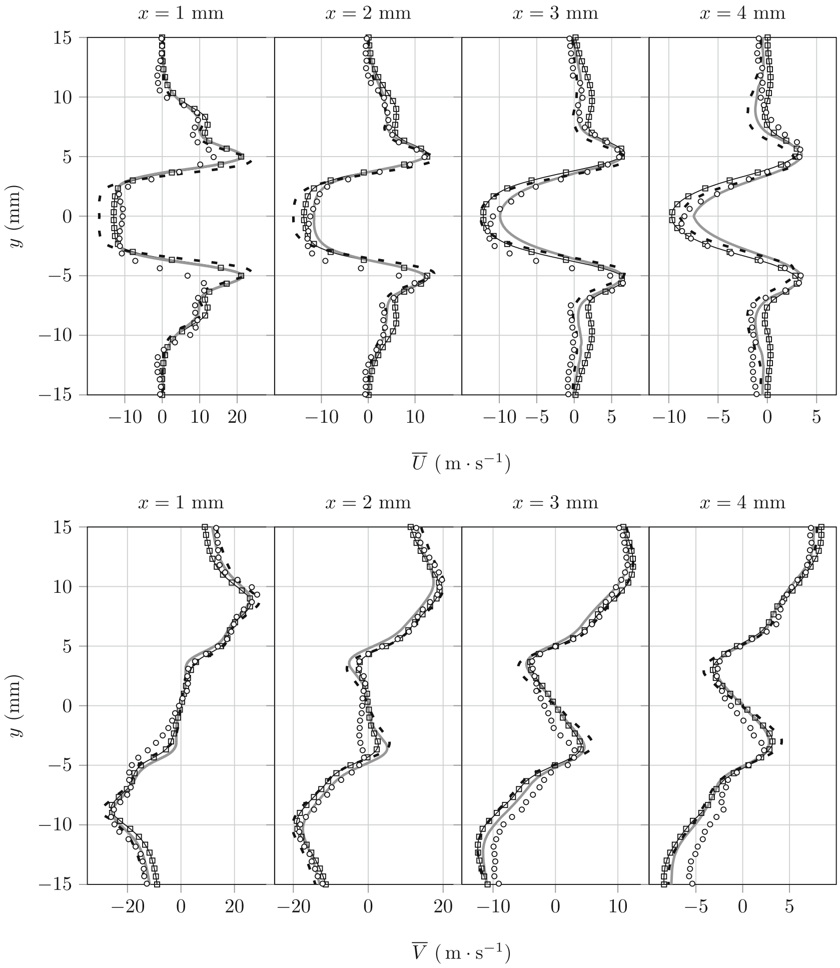

Fig. 15 $\dot{m} = 4.29\,\mathrm{g \cdot s^{-1}}$ case: comparison of the radial distribution of mean axial (*top*) and tangential (*bottom*) velocity at four axial locations (from *left* to *right* $x = 1, 2, 3, 4$ mm). Coarse mesh (- - -); mesh AD 1 (—□—); mesh AD 2 (——) and experiments PIV (○)

Table 3 Summary of the mesh adaptation LES on the swirler

	Coarse	AD 1	AD 2	AD 3
α	—	30	30	30
ϵ	—	0.3	0.3	0.7
T_{init} (s)	0.04	0.04	0.04	0.04
T_{stat} (s)	0.04	0.04	0.04	0.04
time step ($\times 10^{-7}$ s)	1.0	1.0	0.35	0.23
number of cells ($\times 10^{6}$)	1.4	3.1	10.8	14.7
number of CPU hours	6h22	11h44	20h20	33h40
number of cores	240	240	1140	1728
ΔP error	46%	10%	−0.7%	0.8%
error on swirl number S at $x = 2$ mm	18.5%	15.5%	4.3%	1.0%
$error_{L^2}(\sqrt{\overline{u'u'}})$ at $x = 3$ mm	11.2%	16.1%	5.8%	5.1%
$error_{L^2}(\sqrt{\overline{v'v'}})$ at $x = 3$ mm	11.1%	8.2%	4.6%	4.3%
GCI	—	7.8%	1%	0.05%

this type of flow [58], is correctly reproduced by the LES (see error in Table 3) and better predict with this mesh refinement strategy. A similar conclusion can be drawn for the radial profiles of turbulence intensities given in Fig. 16. The predictability of these quantities is clearly improved by refining the mesh (at $x = 3$ mm and $x = 4$ mm for example). More quantitatively, the relative error in the L^2 norm is computed on these profiles at $x = 3$ mm. This error is defined by:

$$error_{L^2}(f)\,(\%) = \sqrt{\frac{\int_{y_1}^{y_2} (f_{exp}(y) - f_{LES}(y))^2 dy}{\int_{y_1}^{y_2} (f_{exp}(y))^2 dy}} \tag{11}$$

where $y_1 = 0$ mm and $y_2 = 15$ mm are the lower and upper limits of the integral. Results are resumed in Table 3 and show that L^2 norm error is clearly reduced by mesh adaptation. This confirms that capturing the flow features that govern pressure losses through the swirler passages is sufficient for a good prediction of velocity fields further downstream in the chamber. This is not an obvious result: most mechanisms controlling pressure losses occur within the swirler passages where separation on the vanes change the effective sections and directly affect pressure losses. On the other hand, velocity and temperature profiles in the chamber downstream of the swirler are expected to be controlled by the local resolution in the chamber itself and not in the swirler. It is interesting to observe that an improved resolution within the swirler also increases the quality of the velocity profile far downstream of the swirler passages. This suggests that the mesh refinement metric for the pressure losses based on the kinetic energy dissipation provides most if not all of the refinement information needed to predict the flow with accuracy.

4.6 Evaluation of costs

The previous sections have shown that the AVBP+MMG3D procedure provides accurate predictions of pressure losses as well as of velocity and turbulence profiles. A natural

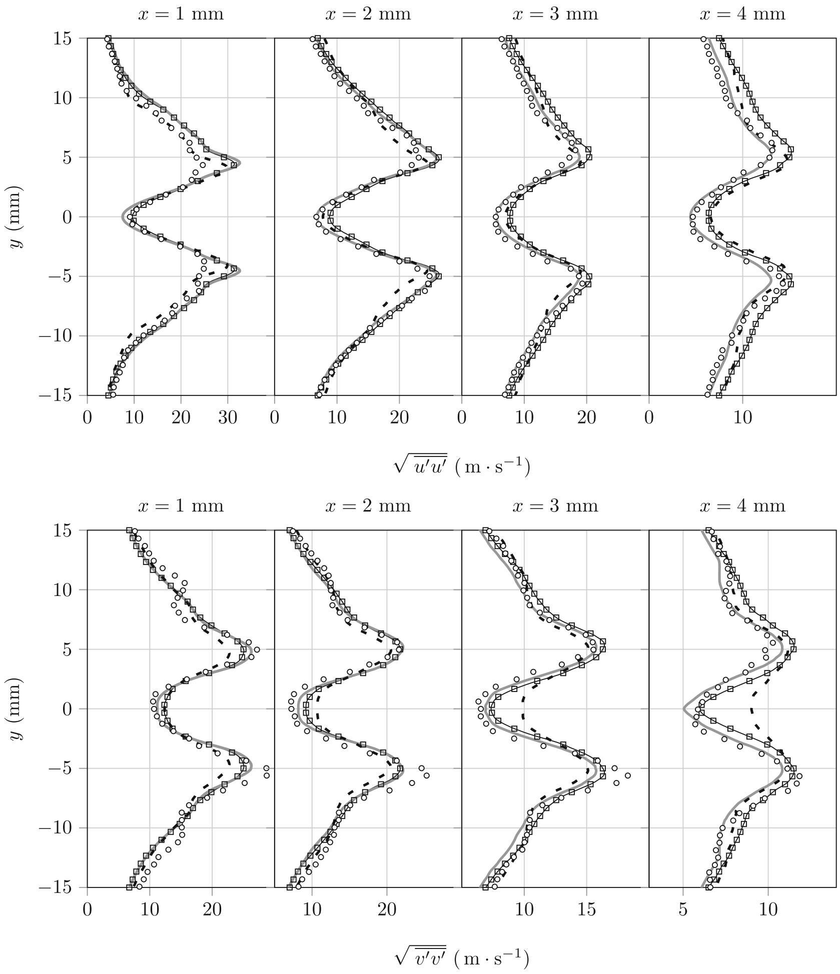

Fig. 16 $\dot{m} = 4.29\,\mathrm{g \cdot s^{-1}}$ case: comparison of the radial distribution of turbulence intensities in axial (*top*) and tangential (*bottom*) direction at four axial locations (from *left* to *right* $x = 1, 2, 3, 4$ mm). Coarse mesh (- - -); mesh AD 1 (—◻—); mesh AD 2 (——) and experiments PIV (○)

question is to determine the cost of this procedure: going from a coarse mesh to refined meshes increases the number of nodes and therefore the overall cost of the simulation. Table 3 summarises the number of cells and the CPU cost (number of hours to compute one flow-through time)[2] on all grids used for the $\dot{m} = 4.29\,\mathrm{g \cdot s^{-1}}$ case. Obviously the cost per flow through time increases when the mesh is refined. The increase is not proportional to the number of cells as the total time needed on each grid to achieve statistical convergence decreases because the initial flow is interpolated from the converged-average state on the previous mesh and hence is close to its own converged-average state. As a result, the cost

[2] All CPU costs are given on a single processor. Most runs were performed on 500 to 1000 processors but the parallel efficiency is almost unity for these cases so that the total CPU cost is a good measure of the mesh efficiency.

of the refined mesh cases remains affordable to improve the capture of physical phenomena relevant to pressure losses.

Another relevant question is whether the proposed AVBP+MMG3D refinement algorithm is more efficient than a purely intuitive mesh refinement method, as typically performed manually by the user based on strong gradients in pressure or velocities. Looking at the various meshes created by the AVBP+MMG3D method (Fig. 12) shows that the method adds points in places which are not obvious to guess: they correspond to regions where $\overline{\tilde{\Phi}}$ is large and these regions, and their extent, do not correlate with easily identified flow-features. For example, not all shear layers are refined to the same extent, but only those that are highly relevant for pressure losses. As a result, an important aspect of the present refinement procedure is to offer a systematic and robust, user-independent method to optimise meshes for swirler computations. It is acknowledged that while certain users who have very good knowledge of a particular configuration may obtain a similarly efficient refinement based on their specific experience, a systematic computation methodology as AVBP+MMG3D allows to retain this efficiency for a large variety of flows.

5 Conclusion

A mesh refinement algorithm has been proposed that improves the prediction of pressure losses in Large Eddy Simulations of turbulent flow in swirlers at reasonable computational cost. The method is based on an existing compressible LES code (AVBP) and mesh refinement program (MMG3D). Mesh refinement is done only a few times (1 to 3) during a complete simulation and it uses only mean flow information. It is performed outside the LES solver and needs no intrusive modification of the solver itself. The metric that defines the local mesh size is the time-averaged value of the kinetic energy dissipation $\overline{\tilde{\Phi}}$. When this field is sufficiently well resolved, both pressure losses and velocity fields are correctly predicted.

The method is validated on two cases: (1) the flow through a diaphragm and (2) the flow through a swirl fuel injector used for helicopter engines. However, the method is not specific to these flows but may be applied to other flows. Results confirm its power in these two cases and suggest that it can be used for other LES solvers where it would bring a systematic, user-independent method to define meshes for LES tools.

Acknowledgements The research leading to these results has received funding from the European Research Council under the European Union's Seventh Framework Program (FP/2007-2013) / ERC Grant Agreement ERC-AdG 319067-INTECOCIS. This work was granted access to the HPC resources of CINES under the allocation 2016-[x20162b7036] made by GENCI. The authors acknowledge the support of C. Dobrzynski and A. Froehly from INRIA Bordeaux for the support on the MMG3D library. The support of SAFRAN HELICOPTER ENGINES (C. Berat, N. Savary) is also gratefully acknowledged.

Appendix: Comparison between hexahedral and tetrahedral meshes

This paper focused on automatic mesh adaptation for swirled flows using tetrahedral meshes. However, the methodology and the refinement sensor are not limited to any

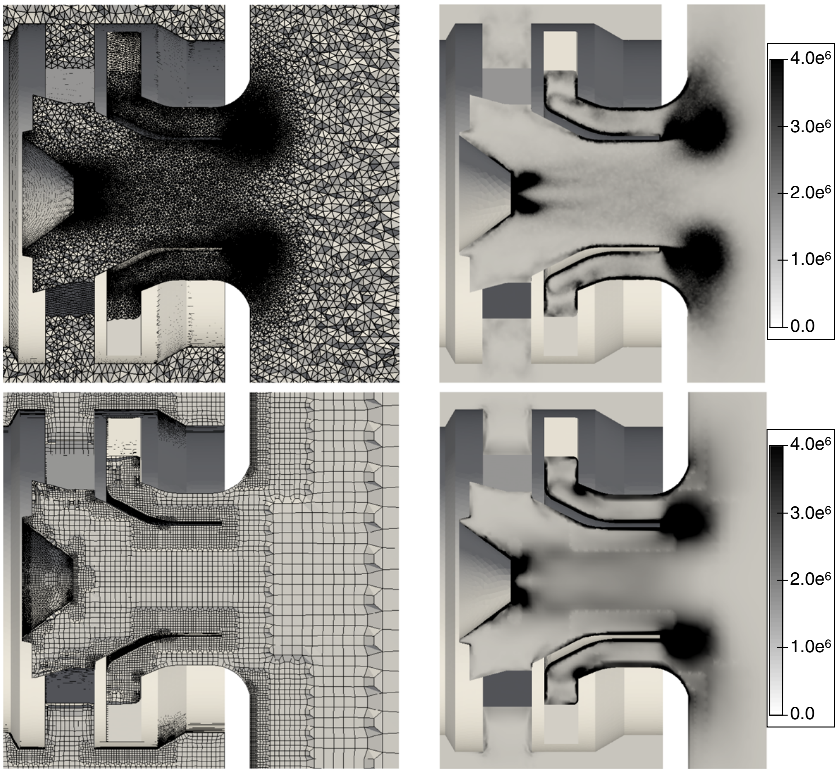

Fig. 17 $\dot{m} = 4.29\,\mathrm{g \cdot s^{-1}}$ case: meshes (*left*) and fields of $\overline{\tilde{\Phi}}$ in $\mathrm{W \cdot m^{-3}}$ (*right*) for the tetrahedral AD 2 (*up*) and hexahedral H 2 (*bottom*) meshes

particular mesh element type. This appendix compares the LES results obtained with the same solver (AVBP) on the tetrahedral AD 2 mesh and on an unstructured fully hexahedral mesh H 2 (Fig. 17). The smallest element size of the hexahedral H 2 mesh is equivalent to that of the AD 2 mesh, and hence the explicit time-step is also equivalent, see Table 4. All

Table 4 Summary of the results between hexahedral H 2 and tetrahedral AD 2 meshes

	Tetrahedral AD 2	Hexahedral H 2
time step ($\times 10^{-7}$ s)	0.35	0.33
number of cells ($\times 10^{6}$)	10.8	6.8
number of CPU hours	20h20	20h48
ΔP error	−0.7%	7.8%
error on swirl number S at $x = 2$ mm	4.3%	25.0%

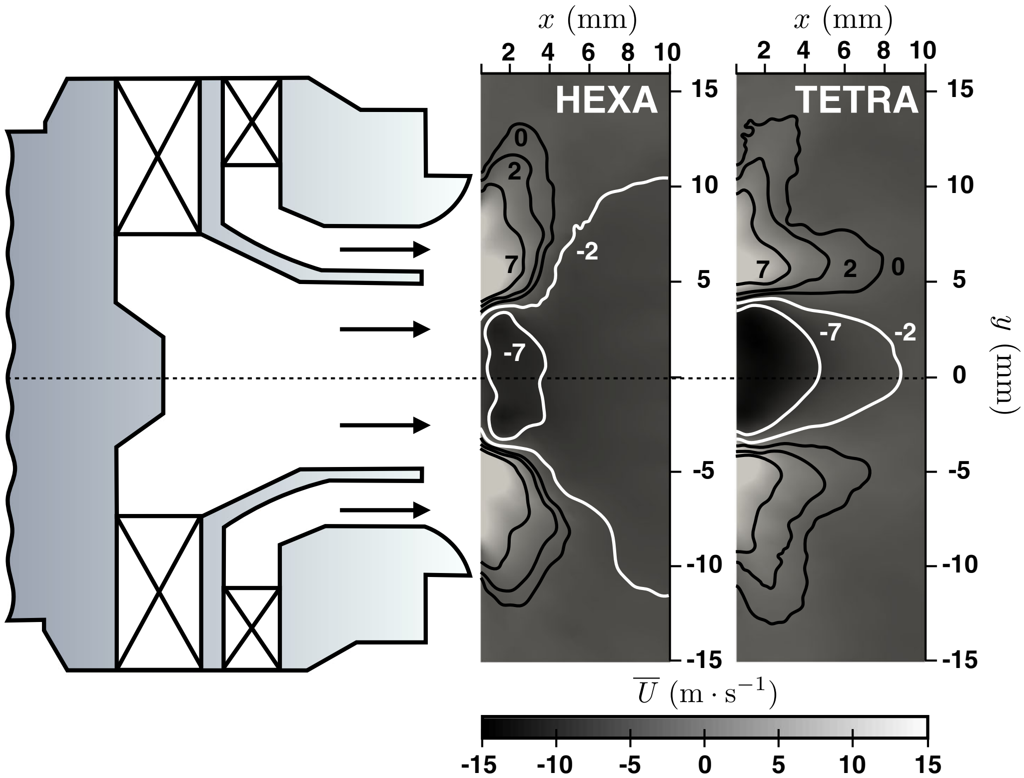

Fig. 18 Comparison of the mean axial velocity from LES on hexahedral H 2 mesh (*center*) and AD 2 tetrahedral mesh (*right*) for the $\dot{m} = 4.29\,\mathrm{g \cdot s^{-1}}$ case. A schematic representation of the swirl injector is depicted on the *left*. White lines denotes negative mean velocity contours at -7 and $-2\,\mathrm{m \cdot s^{-1}}$. Positive and zero mean velocity contours of 7, 2 and $0\,\mathrm{m \cdot s^{-1}}$ are shown with *black line*

other numerical parameters for the H 2 LES are chosen identical to the ones for AD 2 which are discussed in Section 2.

As shown on Fig. 17, result on the total mean dissipation field $\overline{\tilde{\Phi}}$ on the hexahedral mesh is very close to one obtained on the AD 2 mesh although some differences are naturally visible. In particular, the boundary layers has been well captured despite some differences on the plug tip and on the mixing zone downstream the primary nozzle. Fig. 18 shows a comparison of the mean axial velocity fields downstream of the swirler exit. Results are similar close to the nozzle exit ($x < 3\,\mathrm{mm}$) with some discrepancies downstream ($x > 4\,\mathrm{mm}$).

More quantitatively, Figs. 19 and 20 show the first and second order moment statistics at four axial locations (from left to right $x = 1, 2, 3, 4\,\mathrm{mm}$, see Fig. 13). For the mean axial and tangential velocity profiles (Fig. 19) at $x = 1\,\mathrm{mm}$ and $x = 2$ mm, results are very similar between H 2 and AD 2 meshes. The discrepancies observed downstream at $x = 3$ mm and $x = 4$ mm for the hexahedral H 2 mesh are due to the local mesh coarsening imposed by the hexahedral mesher to avoid hanging nodes (see

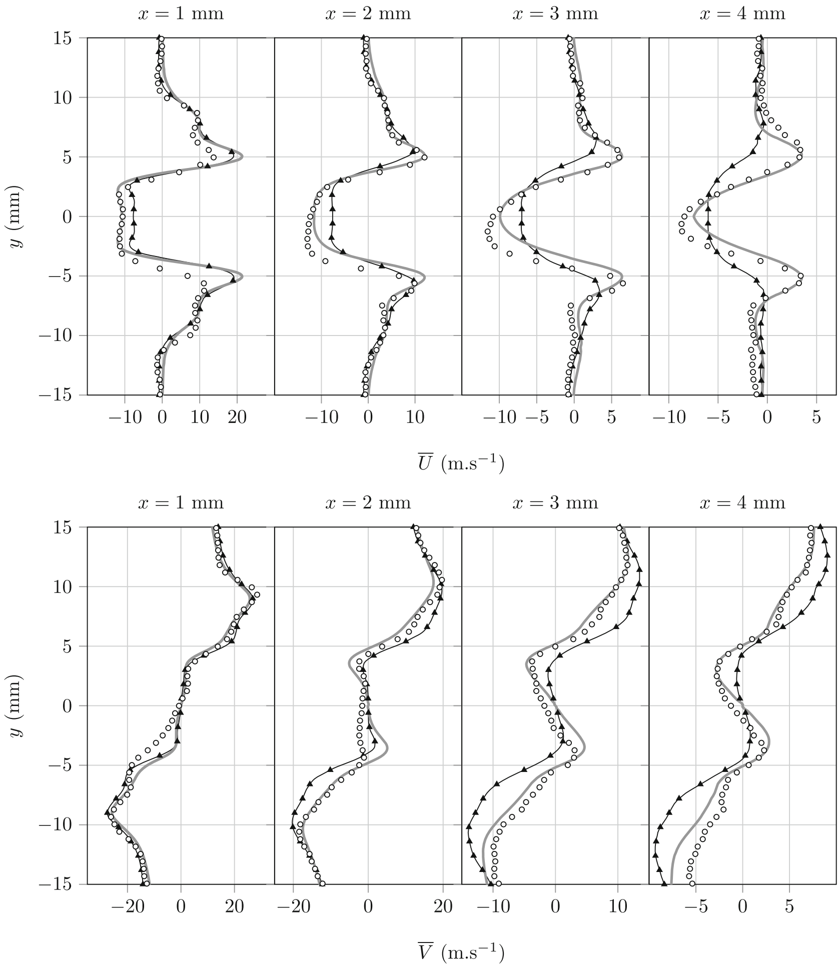

Fig. 19 $\dot{m} = 4.29\,\mathrm{g\cdot s^{-1}}$ case: comparison of the radial distribution of mean axial (*top*) and tangential (*bottom*) velocity at four axial locations (from *left* to *right* $x = 1, 2, 3, 4$ mm). Hexahedral H 2 mesh (—▲—); mesh AD 2 (——) and experiments PIV (○)

Fig. 17 left column bottom). The same observations can be made regarding the radial distribution of turbulence intensities in axial (top) and tangential (bottom) direction on Fig. 20.

The swirl number obtained at $x = 2$ mm is 0.57. This is a 25% error compared to the theoretical value and higher than the one obtained with the tetrahedral meshes. Comparison of the results between hexahedral and AD 2 tetrahedral meshes is given in Table 4.

Finally, the QOI (the time averaged total mean dissipation field) in the right column of Fig. 17 clearly indicate the same regions that need to be refined to improve pressure loss predictions. Provided an automatic re-mesher is available, the same methodology can therefore be applied regardless of the mesh element type.

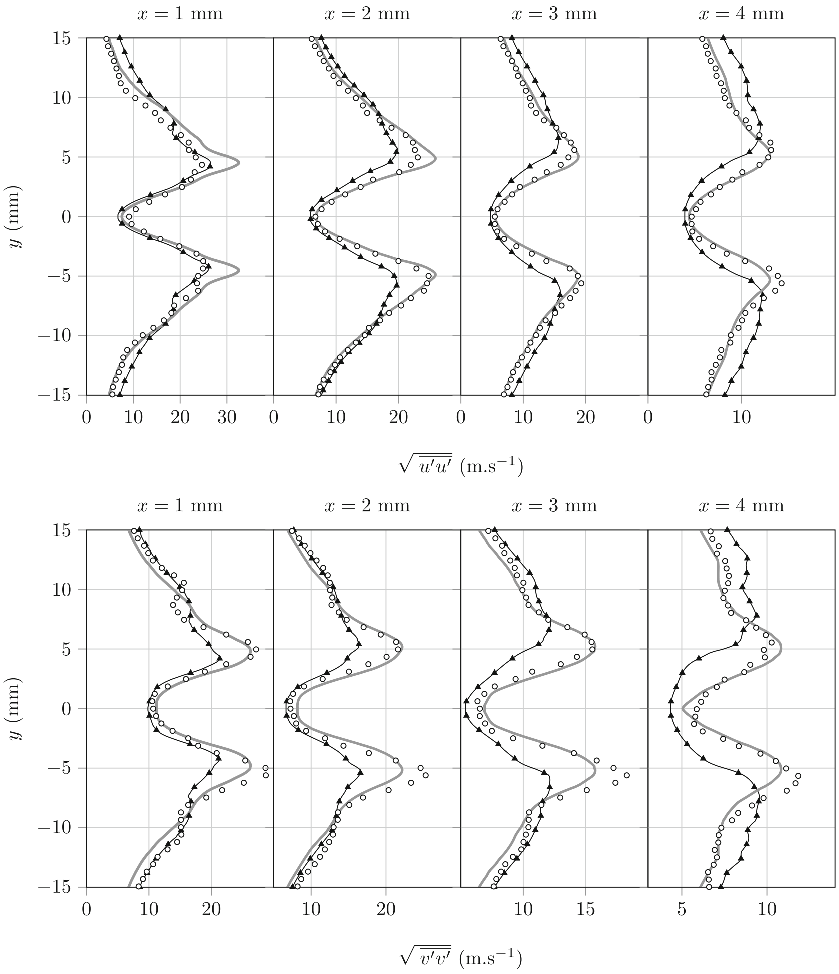

Fig. 20 $\dot{m} = 4.29\,\mathrm{g}\cdot\mathrm{s}^{-1}$ case: comparison of the radial distribution of turbulence intensities in axial (*top*) and tangential (*bottom*) direction at four axial locations (from left to right $x = 1, 2, 3, 4$ mm). Hexahedral H 2 mesh (—▲—); mesh AD 2 (——) and experiments PIV (○)

References

1. Syred, N.: A review of oscillation mechanisms and the role of the precessing vortex core (PVC) in swirl combustion systems. Prog. Energy Combust. **32**(2), 93–161 (2006)
2. Huang, Y., Sung, H.G., Hsieh, S.Y., Yang, V.: Large-eddy simulation of combustion dynamics of lean-premixed swirl-stabilized combustor. J. Prop. Power **19**(5), 782–794 (2003)
3. Moureau, V., Domingo, P., Vervisch, L.: From large-eddy simulation to direct numerical simulation of a lean premixed swirl flame: Filtered laminar flame-pdf modeling. Combust. Flame **158**(7), 1340–1357 (2011)
4. Roux, S., Lartigue, G., Poinsot, T., Meier, U., Bérat, C.: Studies of mean and unsteady flow in a swirled combustor using experiments, acoustic analysis and large eddy simulations. Combust. Flame **141**, 40–54 (2005)
5. Apte, S.V., Mahesh, K., Moin, P., Oefelein, J.C.: Large-eddy simulation of swirling particle-laden flows in a coaxial-jet combustor. Int. J. Multiphase Flow **29**(8), 1311–1331 (2003)
6. Falese, M., Gicquel, L.Y., Poinsot, T.: LES of bifurcation and hysteresis in confined annular swirling flows. Comput. Fluids **89**, 167–178 (2014)
7. Sankaran, V., Menon, S.: LES of spray combustion in swirling flows. J. Turb. **3**, 011 (2002)

8. Huang, Y., Yang, V.: Dynamics and stability of lean-premixed swirl-stabilized combustion. Prog. Energy Comb. Sci. **35**(4), 293–364 (2009)
9. Gicquel, L.Y.M., Staffelbach, G., Poinsot, T.: Large eddy simulations of gaseous flames in gas turbine combustion chambers. Prog. Energy Comb. Sci. **38**(6), 782–817 (2012)
10. Barré, D., Kraushaar, M., Staffelbach, G., Moureau, V., Gicquel, L.Y.M.: Compressible and low Mach number LES of a swirl experimental burner. CR – Mec **341**, 277–287 (2013)
11. Falese, M.: A Study of the Effects of Bifurcations in Swirling Flows Using Large Eddy Simulation and Mesh Adaptation. Ph.D. thesis, Université de Toulouse (2013)
12. Choi, H., Moin, P.: Grid-point requirements for large eddy simulation: Chapman's estimates revisited. Phys. Fluids **24**(011), 702–5 (2012)
13. Boudier, G., Gicquel, L.Y.M., Poinsot, T., Bissières, D., Bérat, C.: Effect of mesh resolution on Large Eddy Simulation of reacting flows in complex geometry combustors. Combust. Flame **155**(1-2), 196–214 (2008)
14. Hertel, C., Fröhlich, J.: Error Reduction in LES via Adaptive Moving Grids. In: Qual. Reliab. Large-Eddy Simulations I, vol. 16, pp. 309–318 (2011)
15. Frey, P.J., Alauzet, F.: Anisotropic mesh adaptation for CFD computations. Comput. Methods Appl. Mech. Eng. **194**(48), 5068–5082 (2005)
16. Loseille, A., Dervieux, A., Alauzet, F.: Fully anisotropic goal-oriented mesh adaptation for 3D steady Euler equations. J. Comput. Phys. **229**(8), 2866–2897 (2010)
17. Rai, M.M., Anderson, D.: The Use of Adaptive Grids in Conjunction with Shock-Capturing Methods. In: 11th AIAA Fluid Dynamics Conference, AIAA 81–1012 (1981)
18. Berger, M.J., Oliger, J.: Adaptive mesh refinement for hyperbolic partial differential equations. J. Comput. Phys. **53**(3), 484–512 (1984)
19. Dapogny, C., Dobrzynski, C., Frey, P.: Three-dimensional adaptive domain remeshing, implicit domain meshing, and applications to free and moving boundary problems. J. Comput. Phys. **262**, 358–378 (2014)
20. Mitran, S.M.: A Comparison of Adaptive Mesh Refinment Approaches for Large-Eddy Simulation. In: 3rd AFOSR International Conference on DNS/LES (2001)
21. Lohner, R., Baum, J.D.: Adaptive h-refinement on 3D unstructured grids for transient problems. Int. J. Numer. Meth. Fluids **14**(12), 1407–1419 (1992)
22. Majewski, J., Rokicki, J.: Anisotropic Mesh Adaptation in the Presence of Complex Boundaries. In: ADIGMA - a Eur. Initiat. Dev. Adapt. Higher-Order Var. Methods Aerosp. Appl., pp. 441–453 (2010)
23. Majewski, J., SzaTys, P., Rokicki, J.: Anisotropic Adaptation for Simulation of High-Reynolds Number Flows Past Complex 3D Geometries. In: Kroll, N., Hirsch, C., Bassi, F., Johnston, C., Hillewaert, K. (eds.) IDIHOM Ind. High-Order Methods - A Top-Down Approach, Notes on Numerical Fluid Mechanics and Multidisciplinary Design, vol. 128, pp. 101–124 (2015)
24. Lombardini, M., Deiterding, R.: Three-Dimensional Parallel Adaptive Mesh Refinement Simulations of Shock-Driven Turbulent Mixing in Plane and Converging Geometries. In: 21st International Conference on Parallel Computational Fluid Dynamics (2009)
25. Zhang, B., Wang, T., Gu, C.G., Dai, Z.Y.: An adaptive control strategy for proper mesh distribution in large eddy simulation. J. Hydrodyn. Ser. B **22**(6), 865–870 (2010)
26. Benard, P., Balarac, G., Moureau, V., Dobrzynski, C., Lartigue, G., D'Angelo, Y.: Mesh adaptation for Large-Eddy Simulations in complex geometries. Int. J. Numer. Meth. Fluids **81**(12), 719–740 (2015)
27. Bejan, A.: Entropy generation minimization: The new thermodynamics of finite-size devices and finite-time processes. J. Applied Phy **79**(3), 1191–1218 (1996)
28. Kock, F., Herwig, H.: Entropy production calculation for turbulent shear flows and their implementation in CFD codes. Int. J. Heat Fluid Flow **26**(4), 672–680 (2005)
29. McEligot, D.M., Walsh, E.J., Laurien, E., Spalart, P.R.: Entropy generation in the viscous parts of turbulent boundary layers. J. of Fluids Eng. **130**(6), 1–12 (2008)
30. Prigogine, I.: Time, structure, and fluctuations. Science **201**(4358), 777–785 (1978)
31. Horne, W.C., Karamcheti, K.: Extrema principles of entropy production and energy dissipation in fluid mechanics. Tech. Rep NASA-TM-100992 (1988)
32. Denton, J.D.: Loss mechanisms in turbomachines. J. Turbomach **115**, 621–656 (1993)
33. Lax, P.: Hyperbolic systems of conservation laws II. Comm. Pure Appl. Math **10**(4), 537–566 (1957)
34. Osher, S., Chakravarthy, S.: High resolution schemes and the entropy condition. SIAM J. Num. Anal **21**(5), 955–984 (1984)
35. Zeman, O.: Dilatation dissipation: the concept and application in modeling compressible mixing layers. Phys. Fluids **2**, 178–188 (1990)
36. Sagaut, P.: Large eddy simulation for incompressible flows Springer-Science (1998)
37. Piomelli, U.: Large-eddy simulation: achievements and challenges. Prog. Aero. Sci. **35**(4), 335–362 (1999)

38. Biswas, R., Strawn, R.C.: Tetrahedral and hexahedral mesh adaptation for CFD problems. App. Num. Math **26**, 135–151 (1998)
39. Schønfeld, T., Rudgyard, M.: Steady and unsteady flow simulations using the hybrid flow solver avbp. AIAA J **37**(11), 1378–1385 (1999)
40. Selle, L., Lartigue, G., Poinsot, T., Koch, R., Schildmacher, K.U., Krebs, W., Prade, B., Kaufmann, P., Veynante, D.: Compressible large eddy simulation of turbulent combustion in complex geometry on unstructured meshes. Combust. Flame **137**(4), 489–505 (2004)
41. Colin, O., Rudgyard, M.: Development of high-order Taylor-Galerkin schemes for unsteady calculation. J. Comput. Phys. **162**(2), 338–371 (2000)
42. Poinsot, T., Lele, S.K.: Boundary conditions for direct simulations of compressible viscous flows. J. Comput. Phys. **101**(1), 104–129 (1992)
43. Thompson, K.W.: Time dependent boundary conditions for hyperbolic systems. J. Comput. Phys. **68**(1), 1–24 (1987)
44. Rudy, D., Strikwerda, J.: A non-reflecting outflow boundary condition for subsonic navier-stokes calculations. J. Comp. Phy. **36**, 55–70 (1980)
45. Nicoud, F., Baya Toda, H., Cabrit, O., Bose, S., Lee, J.: Using singular values to build a subgrid-scale model for large eddy simulations. Phys. Fluids 23 (2011)
46. Baya Toda, H., Cabrit, O., Balarac, G., Bose, S., Lee, J., Choi, H., Nicoud, F.: A Subgrid-Scale Model Based on Singular Values for LES in Complex Geometries. In: Proceedings Summer Progr., pp. 193–202. Center for Turbulence Research (2010)
47. Baya Toda, H., Cabrit, O., Truffin, K., Gilles, B., Nicoud, F., Applications, E., Energy, T., Techniques, A.: A Dynamic Procedure for Advanced Subgrid-Scale Models and Wall-Bounded Flows. In: Seventh Int. Symp. Turbul. Shear Flow Phenom (2011)
48. Rieth, M., Proch, F., Stein, O.T., Pettit, M.W.A., Kempf, A.M.: Comparison of the Sigma and Smagorinsky LES models for grid generated turbulence and a channel flow. Comput. Fluids **99**, 172–181 (2014)
49. Idel'Cik, I.: Memento des pertes de charge Eyrolles (1969)
50. White, F.: Fluid Mechanics McGraw-Hill series in mechanical engineering (2011)
51. Hunt, J., Wray, A., Moin, P.: Eddies, Stream, and Convergence Zones in Turbulent Flows. In: Proceedings of the Summer Program, pp. 193–208. Center for Turbulence Research (1988)
52. Merkle, K.: Einfluss Gleich- Und GegensinNiger Drehrichtung Der Verbrennungsluftströme Auf Die Stabilisierung Turbulenter Doppeldrall-Diffusionsflammen. Ph.D. thesis, Universität Fridericiana Karlsruhe (2006)
53. Celik, I.B., Ghia, U., Roache, P.J., Freitas, C.J.: Procedure for estimation and reporting of uncertainty due to discretization in CFD applications. J. Fluids Eng. 130(7) (2008)
54. Lilley, D.G.: Swirl flows in combustion: a review. AIAA J **15**(8), 1063–1078 (1977)
55. Midgley, K., Spencer, A., McGuirk, J.J.: Unsteady flow structures in radial swirler fed fuel injectors. J. Eng. Gas Turbines Power **127**(4), 755–764 (2005)
56. Westerweel, J.: On velocity gradients in PIV interrogation. Exp. Fluids **44**(5), 831–842 (2008)
57. Palies, P., Durox, D., Schuller, T., Candel, S.: The combined dynamics of swirler and turbulent premixed swirling flames. Combust. Flame **157**(9), 1698–1717 (2010)
58. Gupta, A.K., Lilly, D.G., Syred, N.: Swirl flows abacus (1984)

CHAPTER 4

Boundary conditions

This chapter resume part of the PhD thesis of G. Oztarlik done at IMFT as part of the European Research Council INTECOCIS and S. Le Bras carried out at Cerfacs in collaboration with Airbus.

4.1 Compressible non-reflecting boundary conditions

The study presented in this paper is devoted to the extension of the inlet Navier-Stokes characteristics boundary conditions in order to inject both acoustics and turbulence without reflection of spurious waves. This work was carried out in the framework of the PhD thesis of G. Oztarlik at IMFT defended in 2020. It was motivated by the study of the combustions instabilities of swirled premixed methane-air flames with hydrogen. In the following, limitations of the classical inlet subsonic NSCBC formulation is improved as well as simulations convergence.

G. Daviller, G. Oztarlik, and T. Poinsot. A generalized non-reflecting inlet boundary condition for steady and forced compressible flows with injection of vortical and acoustic waves. *Computers & Fluids*, 190:503 – 513, 2019. https://doi.org/10.1016/j.compfluid.2019.06.027

A generalized non-reflecting inlet boundary condition for steady and forced compressible flows with injection of vortical and acoustic waves

G. Daviller[a,*], G. Oztarlik[b], and T. Poinsot[b]

[a]CERFACS, 31100 Toulouse, France, daviller@cerfacs.fr
[b]IMF Toulouse, INP de Toulouse and CNRS.

Abstract

This paper describes a new boundary condition for subsonic inlets in compressible flow solvers. The method uses characteristic analysis based on wave decomposition and the paper discusses how to specify the amplitude of incoming waves to inject simultaneously three-dimensional turbulence and one-dimensional acoustic waves while still being non-reflecting for outgoing acoustic waves. The non-reflecting property is ensured by using developments proposed by Polifke *et al* [1, 2]. They are combined with a novel formulation to inject turbulence and acoustic waves simultaneously at an inlet. The paper discusses the compromise which must be sought by the boundary condition formulation between conflicting objectives: respecting target unsteady inlet velocities (for turbulence and acoustics), avoiding a drift of the mean inlet velocities and ensuring non-reflecting performances for waves reaching the inlet from the computational domain. This well-known limit of classical formulations is improved by the new approach which ensures that the mean inlet velocities do not drift, that the unsteady components of velocity (turbulence and acoustics) are correctly introduced into the domain and that the inlet remains non-reflecting. These properties are crucial for forced unsteady flows but the same formulation is also useful for unforced cases where it allows to reach convergence faster. The method is presented by focusing on the expression of the ingoing waves and comparing it with the classical NSCBC approach [3]. Four tests are then described: (1) the injection of acoustic waves through a non reflecting inlet, (2) the compressible flow establishment in a nozzle, (3) the simultaneous injection of turbulence and ingoing acoustic waves into a duct terminated by a reflecting outlet and (4) a turbulent, acoustically forced Bunsen-type premixed flame.

Keywords: Characteristic boundary conditions, Non reflecting boundary conditions, Turbulence injection, Acoustic forcing

*Corresponding author
Email address: `daviller@cerfacs.fr` (G. Daviller)

1. Introduction

Specifying boundary conditions for compressible flow simulations is still a major issue in many fields such as astrophysics [4, 5], aerodynamics and aeroacoustics [6, 7, 8, 9, 10, 11] or combustion instabilities and noise [12, 13, 14, 15, 2, 16]. The present paper focuses on a limited part of this problem: the specification of inlet boundary conditions in subsonic compressible flows. Its objective is to construct a boundary condition which should satisfy three properties:

- P1 - Provide a well-posed formulation for the Navier-Stokes equations as well as perfectly non-reflecting inlet properties
- P2 - Allow to inject plane acoustic waves
- P3 - Allow to inject three-dimensional turbulence

It is important to satisfy P1, P2 and P3 simultaneously: the capability to inject ingoing acoustic waves and turbulence at the same time on an inlet patch while letting outgoing acoustic waves cross the boundary without reflection is crucial in many configurations. For example, the determination of the transfer function of turbulent flames [17, 15], the prediction of combustion noise in gas turbines [18, 19, 20] or the evaluation of the acoustic transfer matrix of singular elements in turbulent flows [21, 22, 23, 24] require to introduce harmonic acoustic forcing and turbulence on the same inlet boundary while letting acoustic waves propagate from the computational domain to the outside without reflection (Fig. 1). Similarly, studies of combustion noise in gas turbines [20, 25, 26] require to perform simulations of the noise produced by a jet forced simultaneously by turbulence and by acoustic waves generated in the combustion chamber.

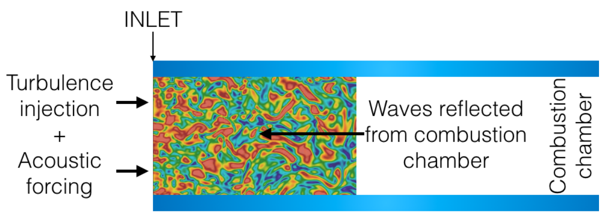

Figure 1: An example where turbulence and acoustic waves must be introduced through the inlet of a compressible simulation while acoustic waves reflected from the computational domain must propagate without reflection through the same surface: the computation of the Flame Transfer Function of a turbulent flame [15].

This paper uses characteristic boundary conditions [4, 27, 3] which have become the standard approach in most compressible solvers [28, 29, 30, 11]. These methods use characteristic analysis to decompose the Navier-Stokes equations at the boundary and identify waves going into the domain and waves leaving the domain. Wave amplitudes can be expressed as spatial derivatives of the primitive variables. The amplitudes of waves leaving the domain depend only on the flow within the computational domain: they can be computed using one-sided derivatives of the resolved field inside this domain. Inversely, the amplitudes of the waves entering the computational domain can not be obtained by differentiating the field in the domain because this would lead to an ill-posed problem: they must be imposed using information given by the boundary conditions. Figure 2 shows that, for a subsonic inlet, only the outgoing acoustic wave $\mathcal{L}_1$ (see section 2 for wave definitions) is leaving the computational domain at speed $u - c$ where u is the local convection velocity and c the local sound speed. All other waves (the acoustic wave $\mathcal{L}_5$ at speed $u + c$, the entropy wave $\mathcal{L}_2$ at speed u and the two transverse waves $\mathcal{L}_3$ and $\mathcal{L}_4$ at speed u) are entering the domain and must be specified using the boundary conditions. This paper focuses on the determination of these incoming wave amplitudes.

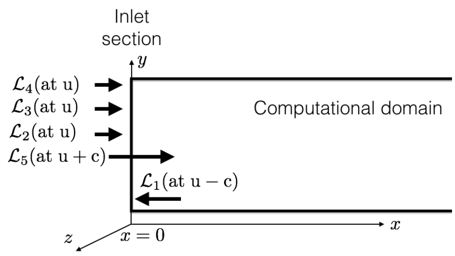

Figure 2: Characteristic waves at a subsonic inlet (inlet at $x = 0$).

Section 2 recalls the basis of the NSCBC technique applied to an inlet. The specification of the incoming waves is presented in Section 3 and a novel inlet condition able to satisfy properties P1 to P3 is discussed (called NRI-NSCBC for Non Reflecting Inlet NSCBC). Before performing any simulation, a simple theoretical approach is used to predict the reflection coefficient of the standard NSCBC formulation and of the new NRI-NSCBC condition for the injection of acoustic waves in one dimension (Section 4). These results are validated using a one-dimensional simulation of a forced duct in Section 5. The impact of the NRI-NSCBC formulation is then illustrated through three examples[1]:

- Section 6 shows that, for an unforced multi-dimensional flow (a nozzle case), using the NRI-NSCBC condition allows to eliminate acoustic waves and to converge much faster to steady state, a crucial property for compressible flow solvers which often remain limited by small time steps and long computation times before convergence.
- Section 7 presents an example of simultaneous acoustic forcing and turbulence injection in a three-dimensional channel and shows that the NRI-NSCBC is able to satisfy Properties 1 to 3 simultaneously.
- Finally Section 8 proposes a DNS of a premixed turbulent flame which is

[1] Note that the present paper focuses on inlet boundary conditions: readers are referred to [2, 31, 32] which discuss similar methods for outlets.

forced acoustically using both boundary conditions formulations.

2. Characteristic inlet boundary condition for subsonic flows

Consider a subsonic inlet (Fig. 2) where the boundary plane is the $(y,\ z)$ plane. The velocity components to impose at this inlet are (u^t, v^t, w^t). These components can be steady or change with time when turbulence and/or acoustic waves are injected through the inlet. Note that these fields are "target" values: they correspond to the injected velocity signals which must be imposed at the inlet, not necessarily to the values (u, v, w) which will be actually reached during the computation because outgoing reflected waves (coming from the computational domain) also change the velocity and pressure field on the inlet patch (Fig. 1).

The Navier-Stokes equations at the inlet can be recast in terms of waves propagating in the x direction, leaving the other two directions unchanged:

$$\frac{\partial \rho}{\partial t} + d_1 + \frac{\partial}{\partial y}(\rho v) + \frac{\partial}{\partial z}(\rho w) = 0 \tag{1}$$

$$\frac{\partial(\rho E)}{\partial t} + \frac{1}{2}\left(u^2 + v^2 + w^2\right) d_1 + \frac{d_2}{\gamma - 1} + \rho u d_3 + \rho v d_4 + \rho w d_5$$
$$+ \frac{\partial}{\partial y}[v(\rho e_s + p)] + \frac{\partial}{\partial z}[w(\rho e_s + p)] = \nabla(\lambda \nabla T) + \nabla(u.\tau) \tag{2}$$

$$\frac{\partial(\rho u)}{\partial t} + u d_1 + \rho d_3 + \frac{\partial}{\partial y}(\rho v u) + \frac{\partial}{\partial z}(\rho w u) = \frac{\partial \tau_{1j}}{\partial x_j} \tag{3}$$

$$\frac{\partial(\rho v)}{\partial t} + v d_1 + \rho d_4 + \frac{\partial}{\partial y}(\rho v v) + \frac{\partial}{\partial z}(\rho w v) + \frac{\partial p}{\partial y} = \frac{\partial \tau_{2j}}{\partial x_j} \tag{4}$$

$$\frac{\partial(\rho w)}{\partial t} + w d_1 + \rho d_5 + \frac{\partial}{\partial y}(\rho v w) + \frac{\partial}{\partial z}(\rho w w) + \frac{\partial p}{\partial z} = \frac{\partial \tau_{3j}}{\partial x_j} \tag{5}$$

where τ is the viscous stress tensor. e_s and E are the sensible and total energies respectively:

$$e_s = \int_{To}^{T} C_v dT \ \text{ and } \ E = e_s + \frac{1}{2}(u^2 + v^2 + w^2) \tag{6}$$

The system of equations (1) to (5) contains derivatives normal to the x boundary (d_1 to d_5), derivatives parallel to the x boundary (called "transverse terms"), and viscous terms. The vector $\mathbf{d}$ is given by characteristic analysis:

$$\mathbf{d} = \begin{pmatrix} d_1 \\ d_2 \\ d_3 \\ d_4 \\ d_5 \end{pmatrix} = \begin{pmatrix} \frac{1}{c^2}\left[\mathcal{L}_2 + \frac{1}{2}\left(\mathcal{L}_5 + \mathcal{L}_1\right)\right] \\ \frac{1}{2}\left(\mathcal{L}_5 + \mathcal{L}_1\right) \\ \frac{1}{2\rho c}\left(\mathcal{L}_5 - \mathcal{L}_1\right) \\ \mathcal{L}_3 \\ \mathcal{L}_4 \end{pmatrix} = \begin{pmatrix} \frac{\partial(\rho u)}{\partial x} \\ \rho c^2 \frac{\partial u}{\partial x} + u\frac{\partial p}{\partial x} \\ u\frac{\partial u}{\partial x} + \frac{1}{\rho}\frac{\partial p}{\partial x} \\ u\frac{\partial v}{\partial x} \\ u\frac{\partial w}{\partial x} \end{pmatrix} \quad (7)$$

where c is the local speed of sound given by $c^2 = \gamma p/\rho$ and the $\mathcal{L}_i$'s are the amplitudes of characteristic waves propagating at the characteristic velocities $u-c$, u and $u+c$:

$$\mathcal{L}_1 = (u-c)\left(\frac{\partial p}{\partial x} - \rho c\frac{\partial u}{\partial x}\right) \quad (8)$$

$$\mathcal{L}_2 = u\left(c^2\frac{\partial \rho}{\partial x} - \frac{\partial p}{\partial x}\right) \quad (9)$$

$$\mathcal{L}_3 = u\frac{\partial v}{\partial x} \quad \text{and} \quad \mathcal{L}_4 = u\frac{\partial w}{\partial x} \quad (10)$$

$$\mathcal{L}_5 = (u+c)\left(\frac{\partial p}{\partial x} + \rho c\frac{\partial u}{\partial x}\right) \quad (11)$$

3. Specification of incoming waves

For a subsonic three-dimensional inlet, the problem is well posed if four conditions are imposed [33, 3]. In NSCBC, this means that the four incoming waves $\mathcal{L}_2, \mathcal{L}_3, \mathcal{L}_4$ and $\mathcal{L}_5$ must be imposed. The outgoing wave $\mathcal{L}_1$ does not depend on the boundary conditions and can be computed using one-sided derivatives of the field inside the computational domain. Therefore, the solution can be advanced in time on the inlet, using the system of equations (1) to (5) for boundary values if an evaluation for $\mathcal{L}_2$ to $\mathcal{L}_5$ can be found. The principle of NSCBC is to evaluate these wave amplitudes as if the flow was locally one-dimensional and inviscid (LODI). LODI equations provide an estimation of the wave amplitudes $\mathcal{L}_i$ which is usually chosen so that the physical boundary condition is satisfied. Usual LODI equations are:

$$\frac{\partial \rho}{\partial t} + \frac{1}{c^2}\left(-\mathcal{L}_2 + \frac{1}{2}(\mathcal{L}_5 + \mathcal{L}_1)\right) = 0 \quad (12)$$

$$\frac{\partial u}{\partial t} + \frac{1}{2\rho c}(\mathcal{L}_5 - \mathcal{L}_1) = 0 \quad (13)$$

$$\frac{\partial v}{\partial t} + \mathcal{L}_3 = 0 \quad (14)$$

$$\frac{\partial w}{\partial t} + \mathcal{L}_4 = 0 \qquad (15)$$

$$\frac{\partial p}{\partial t} + \frac{1}{2}(\mathcal{L}_5 + \mathcal{L}_1) = 0 \qquad (16)$$

The difficult question and the differentiating factor between characteristic methods is the specification of the ingoing wave amplitudes $\mathcal{L}_2, \mathcal{L}_3, \mathcal{L}_4$ and $\mathcal{L}_5$ as a function of the chosen inlet conditions. For example, for a constant velocity inlet, the LODI equation (13) would suggest that the incoming acoustic wave amplitude $\mathcal{L}_5$ should be equal to the outgoing wave $\mathcal{L}_1$ but this approach is often too simple for unsteady cases[2]. For the sake of simplicity, the presentation is limited now to an isentropic inlet where the entropy wave $\mathcal{L}_2$ is set to zero. Using Eq. 13 to 15, the LODI expression for such an isentropic inlet is to write the incoming waves as:

$$\mathcal{L}_5 = -2\rho c \frac{\partial u^t}{\partial t},\ \mathcal{L}_3 = -\frac{\partial v^t}{\partial t} \text{ and } \mathcal{L}_4 = -\frac{\partial w^t}{\partial t} \qquad (17)$$

which allows to inject an unsteady signal of components (u^t, v^t, w^t). Unfortunately, Eq. 17 does not work in practice for three reasons:

1. For a steady inlet ($u^t = v^t = w^t =$ constant), this condition is perfectly reflecting as the ingoing waves $\mathcal{L}_3$, $\mathcal{L}_4$ and $\mathcal{L}_5$ are all exactly zero: the solver knows that the inlet velocity is constant but it has no information on the values of the target velocities so that, in multidimensional configurations, the mean inlet velocities usually drift because of transverse and viscous terms present in the system of equations (1) to (5). This is usually corrected by adding a linear relaxation term to the target values u^t, v^t and w^t as proposed initially by Rudy and Strikwerda [33, 35]. For the normal velocity u, the ingoing acoustic wave $\mathcal{L}_5$ becomes:

$$\mathcal{L}_5 = \rho c \left(-2\frac{\partial u^t}{\partial t} + 2K(u - u^t) \right) \qquad (18)$$

while the two transverse waves are written:

$$\mathcal{L}_3 = -\frac{\partial v^t}{\partial t} + 2K(v - v^t) \text{ and } \mathcal{L}_4 = -\frac{\partial w^t}{\partial t} + 2K(w - w^t) \qquad (19)$$

Terms such as $(u - u^t)$ are called "relaxation" terms [33, 35]. They do not have a theoretical basis[3]: they offer the simplest linear correction form which can be added to the NSCBC theory to avoid a drift of mean values as it forces the instantaneous velocity u to go to its target value u^t

[2]One aspect of this problem which is not discussed here is the need to also incorporate transverse terms in the ingoing wave expressions [11, 30, 34]. At an inlet, these terms play a limited role and they will be omitted throughout the present paper.

[3]A temptative explanation for this expression was actually proposed recently by Pirozzoli and Colonius [10], leading to a similar expression.

with a relaxation time $1/K$. Independently of its exact form, this term in Eq. (18) is sufficient to avoid drifting mean inlet speed values when K is "sufficiently" large but it also deteriorates the non-reflecting character of the inlet as will be shown later. Transverse waves ($\mathcal{L}_3$ and $\mathcal{L}_4$) raise no difficulty as they are not associated to any axial acoustic wave and will not be discussed any more in the rest of the paper.

2. An interesting issue in the correction term $(u - u^t)$ of Eq. 18 is how to choose the "target" value u^t. A simple choice would be $u^t = \bar{u} + u^t_+$ where $\bar{u}$ is the target mean velocity and u^t_+ is the target unsteady velocity (either acoustic or vortical) imposed on the inlet patch. A better choice was proposed in [1, 2] who pointed out that outgoing acoustic waves (inducing velocity fluctuations which will be called u_-) may also reach the inlet when they propagate from the computational domain to the inlet and should be accounted for in u^t. Fortunately, these outgoing waves can be evaluated in the limit of plane, low-frequency waves using the outgoing wave amplitude $\mathcal{L}_1$ which is readily available in all NSCBC methods. Therefore, the proper way to account for u_- is to add it to the target velocity to have $u^t = \bar{u} + u^t_+ + u_-$.
A last issue linked to Eq. (17) is the choice of the relaxation coefficient K (units: s^{-1}). The proper scaling for K is the reduced factor $\sigma = KL/c$ where L and c are a characteristic length and a typical sound speed of the domain respectively [33, 35]. Choosing an adequate value for K is a critical issue in many cases. Very large values of σ can lead to an unstable solution (Fig. 3). Low values provide non-reflecting characteristics but allow the mean solution to drift from its target mean value $\bar{u}$ because of viscous and transverse terms affecting the solution in the system of equations (1) to (5). There usually is a range of σ values which provide both non drifting and quasi non-reflecting properties. Rudy and Strikwerda suggest that this occurs near $\sigma = 0.25$ but in practice, wide ranges of σ have to be tested by NSCBC users, leading to inefficient trial and error procedures. In some cases, large values of K are used, leading to inlets where the velocity is totally fixed but the boundary is fully reflecting.
3. Another and more surprising problem was pointed out by Prosser [36] and confirmed by Guezennec and Poinsot [37]. In the classical NSCBC approach, to inject a perturbation u^t, the incoming wave is expressed as:

$$\mathcal{L}_5 = -2\rho c \frac{\partial u^t}{\partial t} \tag{20}$$

This is a correct formulation to inject acoustic waves but Prosser [36] used a low Mach number expansion of the Navier-Stokes equations to show that the proper expression to inject vortical perturbations was different and that the factor 2 had to be suppressed to have:

$$\mathcal{L}_5 = -\rho c \frac{\partial u^t}{\partial t} \tag{21}$$

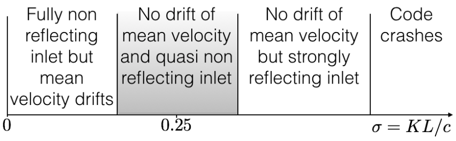

Figure 3: Typical behavior of the solution for the classical NSCBC inlet condition (Eq. (18)) as a function of the reduced relaxation coefficient $\sigma = KL/c$. L is a typical domain length of the domain and c the sound speed. The shaded area is the desired operational zone.

> The fact that the factor 2 of Eq. 20 used for acoustic wave injection must be removed for vorticity injection in Eq. 21 was confirmed by the analysis of Polifke et al [1] and tests [37] show that indeed, Eq. 21 is the proper wave expression to inject vortical perturbations (isolated vortices or fully developed turbulence) but raise a simple question: which expression (Eq. 20 or 21) should be used in practice? The present paper shows that they actually must be added as discussed below.

These recent results suggest a generalized formulation for inlet boundary conditions which is the basis for the NRI-NSCBC condition described here. In this formulation, ingoing perturbations are split into two separate components which are added to the incoming wave amplitude: the vortical fluctuation, corresponding to a signal u_v^t and the acoustic fluctuation corresponding to a signal u_a^t. Each component is handled individually and the incoming wave is written as follows:

$$\frac{\mathcal{L}_5}{\rho c} = \underbrace{-2\frac{\partial u_a^t}{\partial t} - \frac{\partial u_v^t}{\partial t}}_{I} + \underbrace{2K[u - (\bar{u} + u_a^t + u_v^t + u_-)]}_{II} \tag{22}$$

where part I of expression 22 combines a term $2\partial u_a^t/\partial t$ to introduce acoustic waves and another one $\partial u_v^t/\partial t$ to inject turbulence, each of them with the correct factor (2 for acoustics and 1 for turbulence). Part II of expression 22 is the relaxation term. It is introduced to avoid drift and is not proposed by the characteristic theory. It includes u_a^t and u_v^t but also u_- as suggested by Polifke et al [1]. This formulation allows to use exact terms for $2\partial u_a^t/\partial t$ and $\partial u_v^t/\partial t$ (satisfying properties P2 and P3 introduced in Sec. 1) while providing an expression for the relaxation term which should be zero as long as non acoustic terms remain small at the inlet (satisfying property P1). This should allow to use large relaxation factors K avoiding the drift of mean values while still being non reflecting for all normal acoustic waves: the relaxation term in Eq. 22 becomes non zero only when viscous and transverse terms become non negligible on the inlet. For all other cases, the relaxation term (II) is zero and Eq. 22 reduces to the exact NSCBC approach for $\mathcal{L}_5$: $\mathcal{L}_5 = -2\rho c\frac{\partial u_a^t}{\partial t} - \rho c\frac{\partial u_v^t}{\partial t}$.

In the expression of the incoming wave $\mathcal{L}_5$ (Eq. 22), the acoustic velocity u_- associated to the reflected wave reaching the inlet from the computation domain must be evaluated. In the case of an outlet, Polifke et al [1, 38] used a method called CBF (characteristics based filter) to obtain a plane averaged value for the

BOUNDARY CONDITION	TRANSVERSE WAVES $\mathcal{L}_3$ and $\mathcal{L}_4$	AXIAL WAVE $\mathcal{L}_5$
NSCBC	$\mathcal{L}_3 = -\frac{\partial v^t}{\partial t}$ and $\mathcal{L}_4 = -\frac{\partial w^t}{\partial t}$	$\frac{\mathcal{L}_5}{\rho c} = -2\frac{\partial u_a^t}{\partial t} - 2\frac{\partial u_v^t}{\partial t}$ $+2K[u - (\bar{u} + u_a^t + u_v^t)]$
NRI-NSCBC	$\mathcal{L}_3 = -\frac{\partial v^t}{\partial t}$ and $\mathcal{L}_4 = -\frac{\partial w^t}{\partial t}$	$\frac{\mathcal{L}_5}{\rho c} = -2\frac{\partial u_a^t}{\partial t} - \frac{\partial u_v^t}{\partial t}$ $-2K[u - (\bar{u} + u_a^t + u_v^t + u_-)]$

Table 1: Comparison of the classical NSCBC and the NRI-NSCBC conditions. $\bar{u}$ is the mean target velocity, u_a^t is the target acoustic fluctuation, u_v^t is the target vortical fluctuation and u_- is the reflected velocity fluctuation reaching the inlet from the computational domain.

outgoing wave amplitude. This requires introducing a series of planes near the oulet of the computational domain where the outgoing wave can be evaluated. CBF is precise but can be difficult or impossible to implement in cases where the domain outlet has a complex shape or typically at an inlet as studied in the present work. Here an alternative technique is used where u_- is evaluated locally at each point of the inlet patch from the time integral of the acoustic wave amplitude $\mathcal{L}_1$ which is available in NSCBC:

$$u_- = \frac{1}{2\rho c} \int_0^t \mathcal{L}_1 dt \tag{23}$$

Expression 23 for u_- avoids using the PWM approach [1] and can be used in any code using NSCBC boundary conditions[4].

The following sections compare the new NRI-NSCBC formulation to the classical NSCBC conditions [3, 12]. Table 1 summarizes the wave expressions which will be used for both boundary conditions.

4. Theoretical analysis of reflection coefficients in one dimension

A first method to analyze the differences between the standard NSCBC and the NRI-NSCBC conditions is to consider a simple case (Fig. 4) such as the inlet of a configuration where waves can be assumed to be one-dimensional. No vortical perturbation is introduced: $u_v^t = 0$. The inlet patch has a constant mean velocity $\bar{u}$ and is submitted to an acoustic harmonic forcing at pulsation ω with a target amplitude u_a^t. A reflected wave inducing an acoustic perturbation u_- associated to a wave amplitude $\mathcal{L}_1$ also reaches the inlet so that the exact

[4]In practice, for certain cases, Eq. 23 must be high-pass filtered to remove any continuous component.

velocity fluctuation at the inlet should be $u_a^t + u_-$. At this point u_- could be any signal: the only assumption is that u_- is a reflection due to the acoustic forcing and that it is therefore a harmonic signal at pulsation ω too.

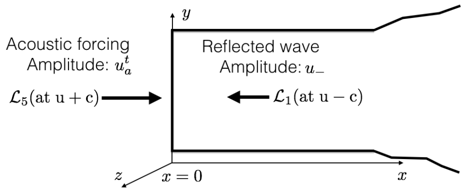

Figure 4: Characteristic waves at a subsonic inlet (inlet at $x = 0$). The acoustic forcing induces a velocity fluctuation u_a^t. A longitudinal acoustic wave (amplitude u_-) is reaching the inlet from the computation domain.

This case allows to derive analytically, what the inlet velocity will be in a code using the boundary conditions of Table 1. To obtain this result, the two ingoing wave formulations of Table 1 are gathered in a single notation for this case with acoustic forcing only and no turbulence injection ($u_v^t = 0$):

$$\frac{\mathcal{L}_5}{\rho c} = -2\frac{\partial u_a^t}{\partial t} + 2K[u - (\bar{u} + u_a^t + \alpha u_-)] \tag{24}$$

When $\alpha = 0$, the standard NSCBC condition is obtained while $\alpha = 1$ yields the NRI-NSCBC condition. The reflected wave (amplitude $\mathcal{L}_1$) creates an acoustic velocity u_- which reaches the inlet and interacts with the inlet boundary condition. In general, u_- is never zero: reflected waves are found at the inlet of most compressible computations.

Assuming that all quantities fluctuate at pulsation ω and expressing all variables as $f(t) = Re[\hat{f}\exp(-i\omega t)]$, it is possible to combine Eq. 24 and 13 to obtain the velocity fluctuations $u' = u - \bar{u}$ at the inlet. To do this, $\mathcal{L}_1$ is obtained from u_- using:

$$\frac{\partial u_-}{\partial t} = \frac{1}{2\rho c}\mathcal{L}_1 \text{ so that } \hat{\mathcal{L}}_1 = -2i\omega\rho c\hat{u}_- \tag{25}$$

Eq. 13 can then be used to obtain the inlet velocity fluctuations $\hat{u}'$ using Eq. 24 for $\mathcal{L}_5$ and Eq. 25 for $\mathcal{L}_1$:

$$\frac{\partial u}{\partial t} = -\frac{1}{2\rho c}(\mathcal{L}_5 - \mathcal{L}_1) \tag{26}$$

which leads to:

$$\hat{u}' = \hat{u}_a^t + \frac{K\alpha - i\omega}{K - i\omega}\hat{u}_- \tag{27}$$

Eq. 27 conveys two messages:

- In general, the inlet velocity fluctuation $\hat{u}'$ is not equal to the acoustic forcing amplitude imposed on the boundary $\hat{u}_a^t$. For both boundary conditions ($\alpha = 0$ or 1), the only cases where $\hat{u}'$ is equal to $\hat{u}_a^t$ corresponds to situations where no outgoing wave reaches the inlet ($\hat{u}_- = 0$).

- The exact solution is that the inlet velocity should be the sum of the acoustic contributions coming from left and right: $\hat{u}' = \hat{u}_a^t + \hat{u}_-$. When $\alpha = 1$ (NRI-NSCBC condition), Eq. 27 shows that this property is always satisfied. For the standard NSCBC condition ($\alpha = 0$), the conclusion is opposite: the inlet velocity $\hat{u}'$ is never equal to its theoretical value except in rare cases where $K = 0$ or $\hat{u}_- = 0$.

Knowing $\hat{u}'$, it is also possible to express the inlet wave $\mathcal{L}_5$:

$$\hat{\mathcal{L}}_5 = \hat{\mathcal{L}}_5^t + R_1 \hat{\mathcal{L}}_1 \text{ with } R_1 = \frac{K(1-\alpha)}{K - i\omega} \tag{28}$$

where $\hat{\mathcal{L}}_5^t = 2i\omega\rho c \hat{u}_a^t$ is the target forcing wave and R_1 can be viewed as the reflection coefficient of the boundary condition: it measures how much of a left going wave $\mathcal{L}_1$ reflects into the ingoing acoustic wave $\mathcal{L}_5$. When $\alpha = 1$ (NRI-NSCBC), R_1 is exactly zero: the inlet is truly non reflecting and the injected wave $\hat{\mathcal{L}}_5$ contains only the imposed wave $\hat{\mathcal{L}}_5^t$. For the standard NSCBC condition ($\alpha = 0$), R_1 is never zero: the inlet is reflecting and any outgoing wave reaching it will be reflected back into the domain, making the inlet effectively more and more reflecting as K is increased. Note that, in this case, the reflection coefficient R_1 in Eq. 28 matches the expression obtained for the reflection coefficient by Selle et al [31], Polifke et al [1] and Pirozzoli and Colonius [10].

5. A one-dimensional duct with inlet acoustic forcing

The two boundary conditions of Table 1 are tested first on a one-dimensional duct of length L (Fig. 5) forced acoustically at its inlet ($x = 0$) and terminated by a fixed pressure outlet ($p' = 0$ at $x = L$). This is a direct application of the results of Section 4 where u_- will be specified: the inlet forcing is harmonic and corresponds to a velocity fluctuation $\hat{u}_a^t$. The outlet is fully reflecting so that ingoing waves will reflect at $x = L$ into outgoing waves (u_-) and interact with the inlet condition at $x = 0$. For all test cases presented in this section and the following ones, the fourth-order TTGC scheme (on regular meshes [39]) is used in the AVBP solver [40, 41]. Time advancement is fully explicit and a CFL number of 0.7 is used for all runs.

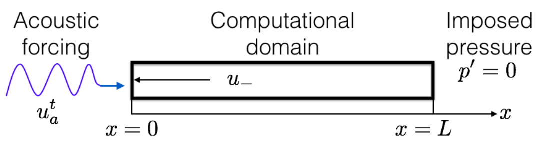

Figure 5: Tests of inlet boundary conditions for a one-dimensional duct forced by a harmonic wave at the inlet and terminated by a pressure node at $x = L$.

Since the outlet reflection coefficient is -1 (to ensure $p' = 0$), the ratio between $\mathcal{L}_1$ and $\mathcal{L}_5$ is known ($\mathcal{L}_1/\mathcal{L}_5 = -\exp(2ikL)$ where $k = \omega/c$ is the wave number). Therefore the ratio I between the wave amplitude which the boundary condition should impose ($\mathcal{L}_5^t$) and the wave which will actually be imposed ($\mathcal{L}_5$) by Eq. 24 can also be expressed as:

$$I = \frac{\hat{\mathcal{L}}_5}{\hat{\mathcal{L}}_5^t} = \frac{1}{1 + R_1 \exp(2ikL)} \tag{29}$$

I is a quality index of the boundary condition. When it is equal to unity, the boundary condition is perfect, the injected wave is the one imposed by the user and the inlet velocity is $u = \bar{u} + u_a^t + u_-$ which is the exact solution. Any non unity I value indicates that the relaxation term in Eq. 24 is perturbing the inlet boundary condition and making it partially reflecting. Obviously for the NRI-NSCBC condition where $\alpha = 1$ and $R_1 = 0$, I is equal to unity for all K values while it is not for the standard NSCBC approach. To check this result, one-dimensional simulations of the configuration of Fig. 5 were performed for $\sigma = 0$, 2 and 5 at three forcing frequencies (100, 200 and 500 Hz). The results obtained in terms of the index I as a function of the reduced relaxation coefficient σ are displayed in Fig. 6. The simulations match exactly the analytical result of Eq. 29. They confirm that for the NSCBC standard formulation, I can reach large values, very different from unity (more than 20 for $\sigma = 5$), indicating that this method is much less accurate than the new NRI-NSCBC condition which offers a unity I index for all values of the relaxation coefficient σ.

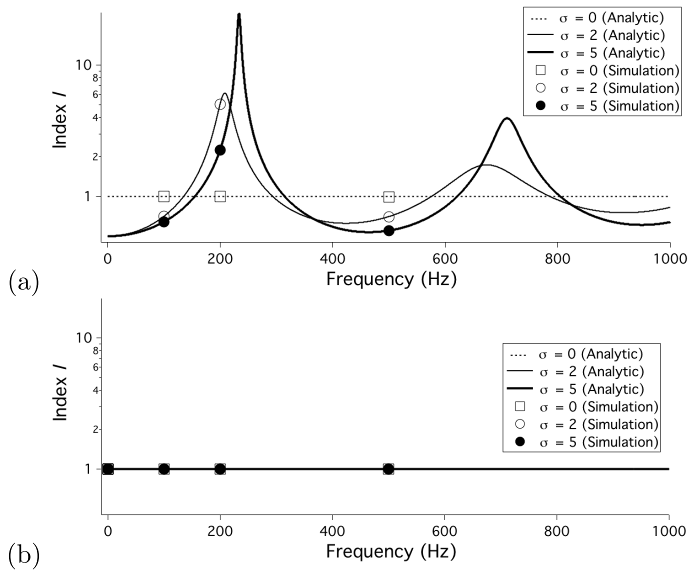

Figure 6: Comparison of the quality index I (Eq. 29) in log scale, for the pulsated duct of Fig. 5: analytical result (Eq. 29) vs compressible simulations. (a) standard NSCBC method, (b) new NRI-NSCBC method. Lines: analytical solutions; symbols: simulations.

6. Faster convergence for unforced compressible flows

The capabilities of the NRI-NSCBC can be illustrated in a second test, to demonstrate that it allows faster convergence in multi-dimensional, compressible, unforced flows because acoustic waves are perfectly evacuated through the boundaries while avoiding a drift of mean values, thanks to a large value of the inlet relaxation coefficient K. For an unforced flow ($u_a^t = u_v^t = 0$), the inlet wave of Eq. 22 becomes:

$$\mathcal{L}_5 = 2K\rho c[u - \bar{u}] \text{ for NSCBC} \tag{30}$$

and

$$\mathcal{L}_5 = 2K\rho c[u - (\bar{u} + u_-)] \text{ for NRI} - \text{NSCBC} \tag{31}$$

The test case is a subsonic nozzle (Fig. 7) where the inlet Mach number is 0.014, corresponding to an inlet velocity of 5 m/s. The outlet condition is $p' = 0$. The initial condition corresponds to a zero velocity field and constant pressure and temperature everywhere in the domain, including on the inlet patch. As soon as the simulation begins, the inlet boundary condition starts acting on the inlet variables. The objective of the test is to measure physical times required to reach steady state and to check whether acoustic modes of the configuration are triggered.

Figure 7: Geometry of nozzle used for convergence tests to steady state. The domain length is $L = 0.6$m. The sound speed is $c = 345$ m/s.

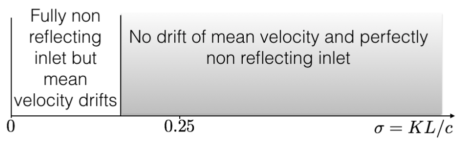

Figure 8: Typical behavior of the solution for the new NRI-NSCBC inlet condition as a function of the reduced relaxation coefficient $\sigma = KL/c$. L is a typical domain length and c the sound speed. The shaded area is the desired operational zone.

This flow is a good prototype of many compressible simulations. The initial conditions (zero velocity everywhere) combined with the inlet condition (which ramps rapidly to its target value) can generate strong perturbations and acoustic waves: with the standard NSCBC conditions (Fig. 3), low values of K lead to mean values which do not converge to the target values or drift away from them.

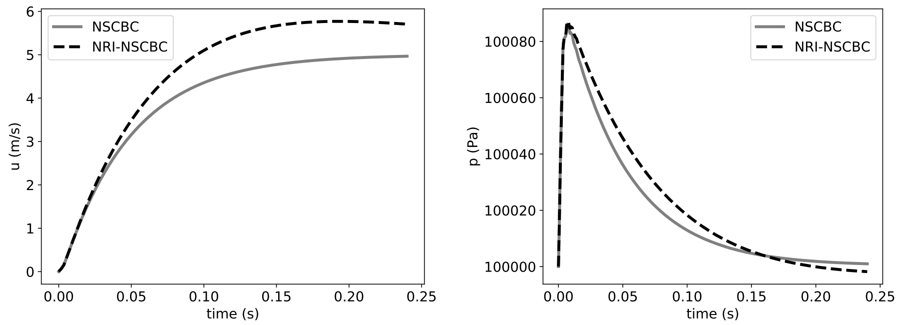

Figure 9: Inlet velocity (left) and pressure (right) time evolutions for $\sigma = KL/c = 0.017$. NSCBC: solid line. NRI-NSCBC: dashed line.

On the other hand, large values of K avoid drifting mean values but induce reflections and undamped acoustic waves which delay convergence. With NRI-NSCBC, this problem disappears: it is possible to use large values of K and still be non reflecting so that convergence is reached very fast. Fig. 8 summarizes this observation and can be compared to Fig. 3.

Figure 9 displays a typical time evolution of inlet velocity and pressure for a reduced relaxation coefficient $\sigma = KL/c = 0.017$. Since this coefficient is small, the inlet velocity (Fig. 9, left) increases slowly and no acoustic waves are triggered. However, convergence is reached after a long time for both methods (NSCBC in solid line and NRI-NSCBC in dashed line).

To increase the convergence speed, the natural solution is to increase the inlet relaxation factor: Figure 10 shows the solutions for a reduced relaxation coefficient $\sigma = KL/c = 17$. The inlet velocity rapidly reaches its target (5 m/s) but acoustic oscillations are triggered using the classical NSCBC method (solid line) because acoustic waves are trapped within the domain: pressure and velocity oscillate at 150 Hz which is the frequency of the first mode of the setup

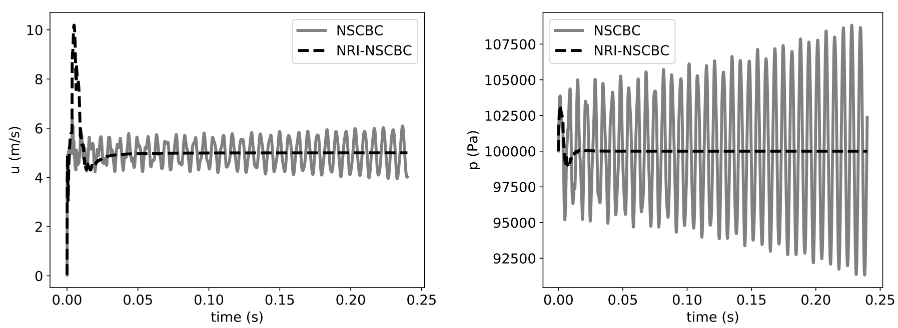

Figure 10: Inlet velocity (left) and pressure (right) time evolutions for $\sigma = KL/c = 17$. NSCBC: solid line. NRI-NSCBC: dashed line.

with $u' = 0$ at the inlet and $p' = 0$ at the outlet. Inversely, the NRI-NSCBC method gives a solution (dashed line) which is stabilized after one acoustic time.

Increasing the relaxation coefficient even more (as often done by NSCBC users when they observe an oscillating inlet velocity) does stabilize the inlet velocity (Fig. 11, left) but makes the inlet even more reflecting, leading to pressure inlet excursions which actually grow in time (Fig. 11, right) and a boundary condition which is ill posed and will eventually lead to full divergence. NRI-NSCBC, as expected, is only weakly affected by the increase of σ and leads to a stable solution rapidly. This simple example reveals another interesting feature of the NRI-NSCBC condition, which provides fast convergence to steady state, using large relaxation coefficients, a useful property in all compressible solvers.

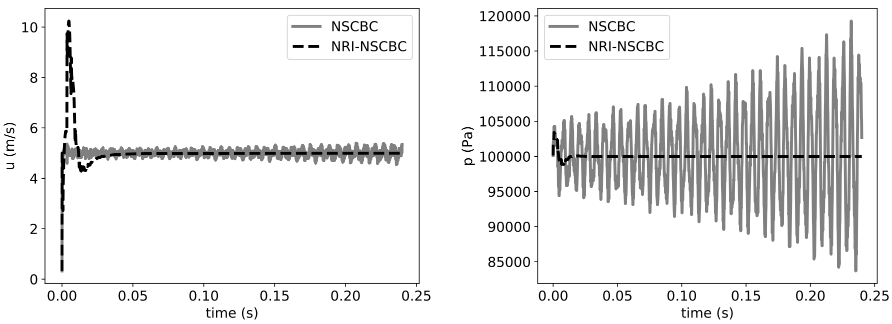

Figure 11: Inlet velocity (left) and pressure (right) time evolutions for $\sigma = KL/c = 170$. NSCBC: solid line. NRI-NSCBC: dashed line.

7. Simultaneous injection of turbulence and acoustic waves through a non-reflecting inlet

This test case corresponds to a situation where an inlet ($x = 0$ in Fig. 12) is used to inject both turbulence and an harmonic acoustic wave into a square section channel. The domain is a three-dimensional parallelepipedic box where the outlet is fully reflecting (imposed pressure: $p' = 0$ at $x = L$). Therefore, the inlet is submitted to three waves:

- vorticity waves associated to the turbulence injection u_v^t,
- an ingoing acoustic wave associated to the acoustic forcing u_a^t,
- an outgoing acoustic wave reflected from the outlet and propagating back to the inlet u_-.

The mesh is a pure hexahedra grid with $392 \times 98 \times 98$ points corresponding to a domain size of $L = 4 \times 1 \times 1$ mm. The mean inlet velocity is homogeneous in the $x = 0$ plane: $U = 100$ m/s. Periodicity conditions are applied in the y

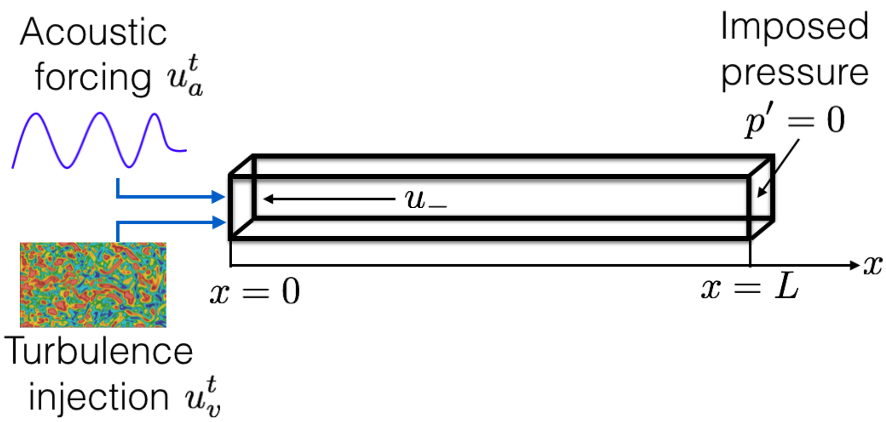

Figure 12: Simultaneous injection of three-dimensional turbulence (velocity amplitude u_v^t) and one-dimensional acoustic forcing (velocity amplitude u_a^t) at the inlet of a domain with reflecting outlet ($p' = 0$).

and z planes. Very large values of the relaxation coefficient K are used in both NSCBC and NRI-NSCBC: $K = 2.10^6 s^{-1}$ corresponding to a reduced coefficient $\sigma = KL/c = 23$. The inlet is submitted to two simultaneous outside excitations:

1. Three-dimensional turbulence: the RMS velocity of the injected field is $u_t = 5$ m/s and the most energetic wavelength is 0.5 mm. The turbulence spectrum has a Passot Pouquet expression [42].
2. One-dimensional planar acoustic wave: the acoustic forcing is a longitudinal wave introduced at the domain inlet, at $f = 260$ kHz with a peak amplitude of $u_a = 2$ m/s.

Note that the ratio between the two excitations levels can be fixed arbitrarily and is configuration dependent. It is defined here by the ratio of the excitation velocities $u_t/u_a = 2.5$.

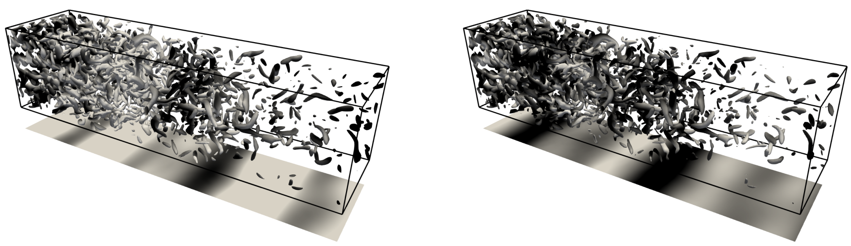

Figure 13: Simultaneous injection of isotropic homogeneous turbulence and acoustic wave. Isosurface of Q criterion $Q = 2.5(U/L)^2$ colored by the axial velocity ($95 \leq u(m/s) \leq 105$) and fluctuating pressure in the range $-1.2e-2 \leq p/p_\infty - 1 \leq 1.2e-2$ in one plane. Left: NSCBC, right: NRI-NSCBC.

Figure 13 displays fields of Q-criterion [43] for the standard NSCBC (left) and the NRI-NSCBC approaches (right), showing a usual decaying turbulent field. The same figure displays a pressure field in one plane, revealing that the axial plane acoustic forcing can be identified on the pressure signal. These qualitative results require more analysis to see the influence of the boundary condition. Figure 14 shows the FFTs of pressure (left) and velocity (right) at $x = 0.2$ mm. As expected for a case where $u_t/u_a = 2.5$, the acoustic forcing induces a discrete tone at $f_a = 260$ kHz, which is observed on both pressure and velocity.

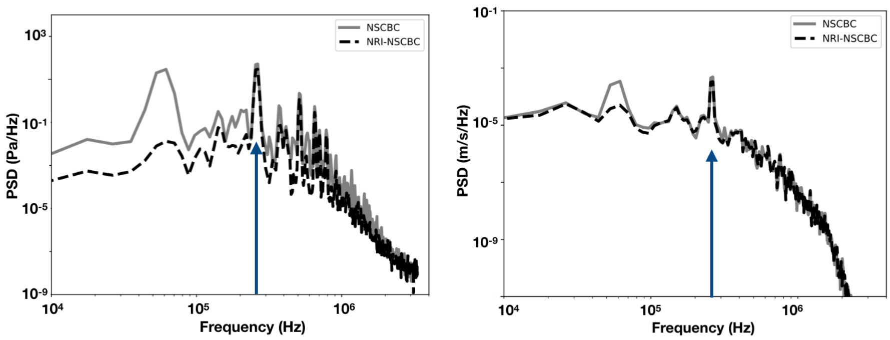

Figure 14: Simultaneous injection of isotropic homogeneous turbulence and acoustic wave. Spectra of pressure (left) and velocity (right) at $x = 0.002$ m, $y = z = 0.005$ m. Solid line: NSCBC, dashed line: NRI-NSCBC. The arrows indicate the frequency ($f_a = 260$ kHz) at which the acoustic wave is introduced.

The two velocity spectra of Fig. 14 are close but the pressure spectra differ: it is interesting to compare the pressure field obtained in the LES with the analytical solution corresponding to a forced inlet at frequency f and an outlet condition $p' = 0$. In a laminar flow (in the absence of turbulence injection), taking into account the correction due to non-zero Mach number, this solution is:

$$p'(x,t) = \rho c u_a \left(e^{-ik^+x} - e^{-i(k^+L+k^-(L-x))} \right) e^{i\omega t} \tag{32}$$

and

$$u'(x,t) = u_a \left(e^{-ik^+x} + e^{-i(k^+L+k^-(L-x))} \right) e^{i\omega t} \tag{33}$$

where $k^+ = \omega/(c+u)$, $k^- = \omega/(c-u)$ and $\omega = 2\pi f$. The variance of pressure $\overline{p'^2}$ can be obtained by $\overline{p'^2} = p_a p_a^*/2$, with p_a^* the conjugate complex of p_a. Figure 15 shows variations of $\sqrt{\overline{p'^2}}$ along the duct axis for both boundary conditions and compares it to the analytical solution of Eq. 32. The NRI-NSCBC captures perfectly the analytical solution showing that for these conditions ($u_t/u_a = 2.5$), the unsteady pressure field is only weakly affected by the turbulence injection and that the boundary condition does not alter this property. On the other hand, similarly to the case of acoustic forcing in a laminar flow (Section 5), the classical NSCBC formulation modifies the acoustic field structure and fails to capture the analytic solution.

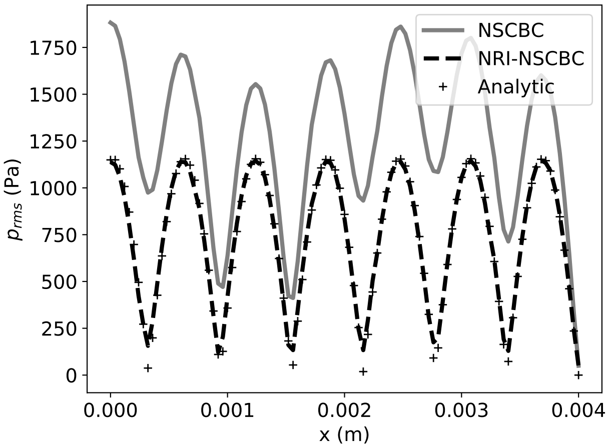

Figure 15: Pressure perturbation structure along duct axis: field of $\sqrt{(p'^2)}$ vs x. Solid line: NSCBC, dashed line: NRI-NSCBC, symbols: analytical solution.

8. A turbulent, acoustically forced premixed flame

The last example is a direct numerical simulation (DNS) of a stoichiometric, premixed turbulent flame stabilized in a slot-burner configuration. The inlet is forced by turbulence and by an harmonic acoustic wave introduced simultaneously, a usual situation for example to study Flame Transfer Functions in thermoacoustics.

The DNS is performed with the explicit, compressible solver (AVBP) for the 3D Navier-Stokes equations with simplified thermochemistry on unstructured meshes [40, 44]. A Taylor–Galerkin finite element scheme called TTGC [39] of third-order in space and time is used. The outlet boundary condition is handled using an imposed pressure, NSCBC approach [3] with transverse terms corrections [34]. The inlet is treated either with the standard NSCBC formulation or with the new NRI-NSCBC approach. Other boundaries are treated as periodic.

Methane/air chemistry at 1 bar is modeled using a global 2-step scheme fitted to reproduce the flame propagation properties such as the flame speed, the burned gas temperature and the flame thickness [45]. This simplified chemistry description is sufficient to study the dynamics of premixed turbulent flames. Fresh gases are stoichiometric: the laminar flame speed is $S_L^0 = 40.5$ cm/s. The flame thicknesses are $\delta_L^0 = 0.34$ mm (based on the maximum temperature gradient) and $\delta_L^1 = 0.7$ mm (based on the distance between reduced temperatures of 0.01 and 0.99). The mesh is a homogeneous hexahedra grid with a constant element size $\Delta x = 0.1$ mm, ensuring 7 to 9 points in the preheat zone and 4 to 5 in the reaction zone. With this resolution, the temperature and heat release profiles given by the DNS code match perfectly the results given by a specialized one-dimensional flame code (Cantera) for a laminar premixed flame. The domain size is 512 cells ($5,12$ cm) in the x direction and 256 cells ($2,56$ cm)

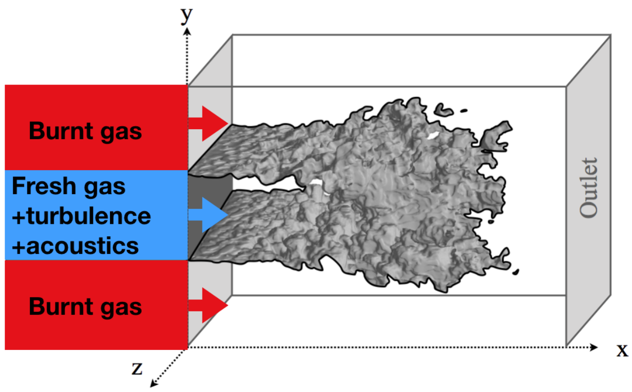

Figure 16: Physical domain used for the DNS. At the inlet, a double hyperbolic tangent profile is used to inject fresh gases in a sheet ≈ 8 mm high, surrounded by a coflow of burnt gases. Top-bottom (along y) and left-right (along z) boundaries are periodic. The isosurface is a typical view of $T = 1600$ K.

in the y and z ones, for a total of 33.55 million cells (Fig. 16). The fresh gas injection channel has a height $h = 8$ mm ($h/\delta_L^0 \approx 25$).

The inlet is set with a double hyperbolic tangent profile in the y direction, with a central flow of stoichiometric fresh gases surrounded by a coflow of burnt gases at low injection velocity. Inlet temperatures are 300 and 2256 K in the fresh and burnt gases, respectively. The temperature and composition of the burnt gas coflow corresponds to the products of an adiabatic combustion of the fresh gases. Inlet velocities are $u_{in} = 10$ m/s and $u_{coflow} = 0.1$ m/s. The width of the shear layer, as defined by Pope [46], is $\delta_m = 0.34$ mm, corresponding to a Reynolds number of $Re_m \approx 200$. Turbulence is injected in the fresh gases only. The RMS velocity of the incoming flow is 1 m/s and the integral length scale is $l_F = 2$ mm. The spectrum of the inject turbulence corresponds to a Passot-Pouquet form [42]. Acoustic forcing is introduced at the inlet on the fresh gas stream. The forcing frequency is $f_a = 1$ kHz and the forcing amplitude is 2 m/s.

A series of 4 snapshots showing the flame response to turbulent and acoustic forcing is displayed in Fig. 17. Mushroom-shaped flame structures are created at 1 Khz as expected for acoustically forced flames [47]. These structures are separated spatially by $u_{in}/f_a = 1$ cm and interact with the injected turbulence.

The two DNS of Fig. 17, obtained by NRI-NSCBC and NSCBC, are obviously different but it is difficult to say which one is the best. A more quantitative result can be obtained by looking at the pressure spectra at the domain inlet in Fig. 18. The spectra observed for NRI-NSCBC corresponds to the expected result: a discrete peak at the acoustic forcing frequency f_a superimposed on broadband turbulent noise. On the other hand, for NSCBC, three additional high-level peaks also appear: they are due to the excitation by the flame of the eigenmodes of the computational domain. It is possible to verify that these modes are indeed acoustic modes by using an Helmholtz solver [48] taking into

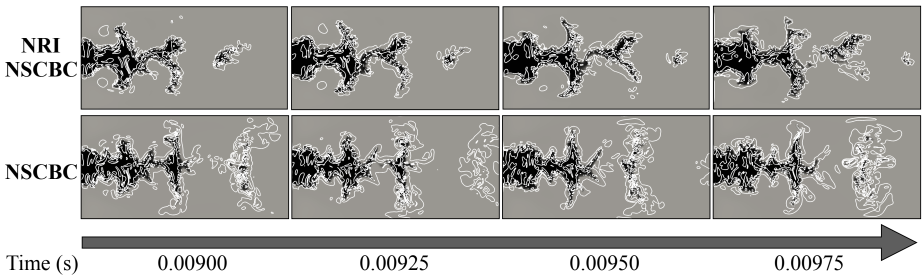

Figure 17: Flame response at four instants of the acoustic forcing period ($f_a = 1$ kHz). Temperature field and isolevels of vorticity.

account the mean temperature distribution in the domain and the boundary conditions (imposed inlet velocity and imposed outlet pressure). The frequencies predicted for the first three acoustic modes given by the Helmholtz solver are marked by arrows in Fig. 18. The three modes which are excited when NSCBC is used are the longitudinal 1/4, 3/4 and 5/4 wave modes. Their frequencies, computed with the Helmholtz solver, match the frequencies observed in the LES with a 5 percent accuracy. These modes interact with the flame response at the acoustic forcing frequency ($f_a = 1$ kHz) and make the NSCBC run difficult to interpret: measuring the flame response at $f_a = 1$ kHz would be impossible for the NSCBC run because this response is polluted by the three acoustic eigenmodes forced by the boundary conditions. Clearly, NSCBC fails to inject acoustic forcing and turbulence without exciting the cavity modes of the computational domain while NRI-NSCBC succeeds in this task.

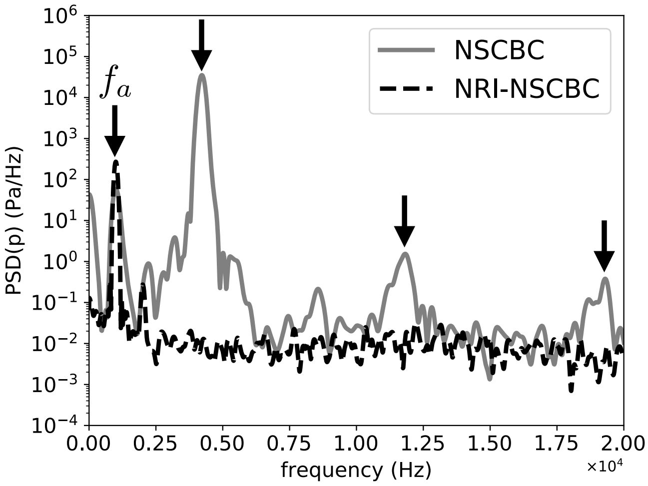

Figure 18: Pressure spectra for NSCBC (solid line) and NRI-NSCBC (dotted line) at the domain inlet. The f_a arrow corresponds to the acoustic forcing at 1 kHz. The three other arrows are the first three longitudinal eigenmodes of the computational box at 4350, 12500 and 19500 Hz. The spectral resolution is 70 Hz.

9. Conclusions

This paper has described a new boundary condition for subsonic inlet, based on a combination of the formalism proposed by Polifke and coworkers [1, 2] to account for outgoing acoustic waves and an extension of the method of Guezennec et al [37] to introduce both turbulence and acoustic waves simultaneously. The approach can be summarized in the expression of the ingoing wave:

$$\frac{\mathcal{L}_5}{\rho c} = -2\frac{\partial u_a^t}{\partial t} - \frac{\partial u_v^t}{\partial t} + 2K[u - (\bar{u} + u_a^t + u_v^t + u_-)] \tag{34}$$

where u_a^t is the velocity of the injected acoustic wave, u_v^t is the axial velocity of the turbulent signal, $\bar{u}$ is the mean target velocity, K is a relaxation coefficient and u_- is the velocity of the outgoing wave which is estimated locally using the outgoing wave amplitude $\mathcal{L}_1$:

$$u_- = \frac{1}{2\rho c}\int_0^t \mathcal{L}_1 dt \tag{35}$$

Analysis and tests show that this NRI-NSCBC condition performs better than standard NSCBC approaches: it allows to use very large values for the relaxation coefficient K and to obtain non-drifting mean values and non reflective capabilities simultaneously. Tests were performed for one-dimensional acoustic forcing in a duct, for flow establishment in a compressible nozzle, for simultaneous injection of acoustic waves and turbulence in a three-dimensional channel terminated by a fixed pressure outlet and finally for a turbulent premixed flame forced acoustically. For all cases, NRI-NSCBC captured the expected solution accurately suggesting that this could become a standard approach in compressible codes.

10. Acknowledgments

We thank Dr L. Selle (IMF Toulouse, CNRS) for helpful discussions and the CERFACS CFD team staff for their scientific and technical support about the CFD code AVBP. The contribution of V. Bouillin to the development of NRI-NSCBC is gratefully acknowledged.

References

[1] W. Polifke, C. Wall, P. Moin, Partially reflecting and non-reflecting boundary conditions for simulation of compressible viscous flow, J. Comput. Phys. 213 (1) (2006) 437–449. doi:10.1016/j.jcp.2005.08.016.

[2] P. Tudisco, R. Ranjan, S. Menon, S. Jaensch, W. Polifke, Application of the Time-Domain Impedance Boundary Condition to Large-Eddy Simulation of Combustion Instability in a Shear-Coaxial High Pressure Combustor, Flow, Turb. and Combustion 177 (2017) 1–23. doi:10.1007/s10494-017-9804-3.

[3] T. Poinsot, S. Lele, Boundary conditions for direct simulations of compressible viscous flows, J. Comput. Phys. 101 (1) (1992) 104–129. doi:10.1016/0021-9991(92)90046-2.

[4] K. W. Thompson, Time dependent boundary conditions for hyperbolic systems ii, J. Comput. Phys. 89 (1990) 439–461. doi:10.1016/0021-9991(90)90152-Q.

[5] R. Grappin, J. Léorat, A. Buttighoffer, Alfvén wave propagation in the high solar corona, Astron. and Astrophys. 362 (2000) 342–358.

[6] J. B. Freund, Proposed inflow/outlow boundary cndition for direct computation of aerodynamic sound, AIAA J. 35 (1997) 740–742. doi:10.2514/2.167.

[7] T. Colonius, Numerically nonreflecting boundary and interface conditions for compressible flow and aeroacoustic computations, AIAA J. 35 (7) (1997) 1126–1133. doi:10.2514/2.235.

[8] T. Colonius, S. K. Lele, Computational aeroacoustics: progress on nonlinear problems of sound generation, Prog. Aerospace Sci. 40 (6) (2004) 345–416. doi:10.1016/j.paerosci.2004.09.001.

[9] C. Bogey, C. Bailly, Effects of inflow conditions and forcing on subsonic jet flows and noise, AIAA J. 43 (5) (2005) 1000–1007. doi:10.2514/1.7465.

[10] S. Pirozzoli, T. Colonius, Generalized characteristic relaxation boundary conditions for unsteady compressible flow simulations, J. Comput. Phys. 248 (C) (2013) 109–126. doi:10.1016/j.jcp.2013.04.021.

[11] G. Lodato, P. Domingo, V. L., Three-dimensional boundary conditions for direct and large-eddy simulation of compressible viscous flow, J. Comput. Phys. 227 (10) (2008) 5105–5143. doi:10.1016/j.jcp.2008.01.038.

[12] T. Poinsot, D. Veynante, Theoretical and Numerical Combustion, Third Edition (www.cerfacs.fr/elearning), 2011.

[13] E. Albin, Y. D'Angelo, L. Vervisch, Using staggered grids with characteristic boundary conditions when solving compressible reactive Navier–Stokes equations, Int. J. Numer. Meth. Fluids 68 (5) (2011) 546–563.

[14] A. Coussement, O. Gicquel, J. Caudal, B. Fiorina, G. Degrez, Three-dimensional boundary conditions for numerical simulations of reactive compressible flows with complex thermochemistry, J. Comput. Phys. 231 (17) (2012) 5571–5611. doi:10.1016/j.jcp.2012.03.017.

[15] T. Poinsot, Prediction and control of combustion instabilities in real engines (Invited Hottel lecture), Proc. Combust. Inst. (2017) 1–28.doi:10.1016/j.proci.2016.05.007.

[16] J. M. Lourier, M. Stöhr, B. Noll, S. Werner, A. Fiolitakis, Scale Adaptive Simulation of a thermoacoustic instability in a partially premixed lean swirl combustor, Comb. Flame 183 (2017) 1–15. doi:10.1016/j.combustflame.2017.02.024.

[17] H. J. Krediet, C. H. Beck, W. Krebs, S. Schimek, C. O. Paschereit, J. B. W. Kok, Identification of the flame describing function of a premixed swirl flame from les, Combust. Sci. Technol. 184 (7-8) (2012) 888–900. doi:10.1080/00102202.2012.663981.

[18] I. Duran, S. Moreau, T. Poinsot, Analytical and numerical study of combustion noise through a subsonic nozzle, AIAA J. 51 (1) (2013) 42–52. doi:10.2514/1.J051528.

[19] A. P. Dowling, Y. Mahmoudi, Combustion noise, Proc. Combust. Inst. 35 (1) (2015) 65 – 100. doi:10.1016/j.proci.2014.08.016.

[20] M. Ihme, Combustion and Engine-Core Noise, Ann. Rev. Fluid Mech. 49 (2016) 1–35. doi:10.1146/annurev-fluid-122414-034542.

[21] M. Abom, A note on the experimental determination of acoustical two-port matrices, J. Sound Vib. 155 (1) (1991) 185–188. doi:10.1016/0022-460X(92)90655-H.

[22] W. Polifke, A. Poncet, C. O. Paschereit, K. Doebbeling, Reconstruction of acoustic transfer matrices by instationnary computational fluid dynamics, J. Sound Vib. 245 (3) (2001) 483–510. doi:10.1006/jsvi.2001.3594.

[23] J. Tournadre, K. Förner, W. Polifke, P. Martínez-Lera, W. Desmet, Determination of Acoustic Impedance for Helmholtz Resonators Through Incompressible Unsteady Flow Simulations, AIAA J. (2016) 1–9doi:10.2514/1.J055337.

[24] F. Ni, M. Miguel-Brebion, F. Nicoud, T. Poinsot, Accounting for acoustic damping in a helmholtz solver, AIAA J. 55 (4) (2017) 1205–1220. doi:10.2514/1.J055248.

[25] L. Magri, J. O'Brien, M. Ihme, Compositional inhomogeneities as a source of indirect combustion noise, J. Fluid Mech. 799 (2016) R4–1. doi:10.1017/jfm.2016.397.

[26] T. Livebardon, S. Moreau, L. Gicquel, T. Poinsot, E. Bouty, Combining LES of combustion chamber and an actuator disk theory to predict combustion noise in a helicopter engine, Comb. Flame 165 (2016) 272–287. doi:10.1016/j.combustflame.2015.12.012.

[27] K. W. Thompson, Time dependent boundary conditions for hyperbolic systems, J. Comput. Phys. 68 (1987) 1–24. doi:10.1016/0021-9991(87)90041-6.

[28] M. Giles, Non-reflecting boundary conditions for euler equation calculations, AIAA J. 28 (12) (1990) 2050–2058. doi:10.2514/3.10521.

[29] C. Yoo, Y. Wang, A. Trouvé, H. Im, Characteristic boundary conditions for direct simulations of turbulent counterflow flames, Combust. Theor. Model. 9 (2005) 617–646. doi:10.1080/13647830500307378.

[30] C. Yoo, H. Im, Characteristic boundary conditions for simulations of compressible reacting flows with multi-dimensional, viscous, and reaction effects, Combust. Theor. Model. 11 (2007) 259–286. doi:10.1080/13647830600898995.

[31] L. Selle, F. Nicoud, T. Poinsot, The actual impedance of non-reflecting boundary conditions: implications for the computation of resonators, AIAA J. 42 (5) (2004) 958–964. doi:10.2514/1.1883.

[32] P. Tudisco, R. Ranjan, S. Menon, S. Jaensch, W. Polifke, Simulation of transverse combustion instability in a multi-injector combustor using the time -domain impedance boundary conditions, Flow, Turb. and Combustion 101 (2018) 55–76. doi:10.1007/s10494-017-9885-z.

[33] D. H. Rudy, J. C. Strikwerda, A non-reflecting outflow boundary condition for subsonic Navier Stokes calculations, J. Comput. Phys. 36 (1980) 55–70. doi:10.1016/0021-9991(80)90174-6.

[34] V. Granet, O. Vermorel, T. Leonard, L. Gicquel, , T. Poinsot, Comparison of nonreflecting outlet boundary conditions for compressible solvers on unstructured grids, AIAA J. 48 (10) (2010) 2348–2364. doi:10.2514/1.43729.

[35] D. H. Rudy, J. C. Strikwerda, Boundary conditions for subsonic compressible Navier Stokes calculations, Comput. Fluids 9 (1981) 327–338. doi:10.1016/0045-7930(81)90005-0.

[36] R. Prosser, Improved boundary conditions for the direct numerical simulation of turbulent subsonic flows i: Inviscid flows, J. Comput. Phys. 207 (2005) 736–768. doi:10.1016/j.jcp.2005.01.027.

[37] N. Guezennec, T. Poinsot, Acoustically nonreflecting and reflecting boundary conditions for vorticity injection in compressible solvers, AIAA J. 47 (2009) 1709–1722. doi:10.2514/1.41749.

[38] J. Kopitz, E. Brocker, W. Polifke, Characteristics-based filter for identification of acoustic waves in numerical simulation of turbulent compressible flow, in: 12th Int'l Congress on Sound and Vibration (ICSV 12), no. IIAV. 00004, Lisbon, Portugal, 2005.

[39] O. Colin, M. Rudgyard, Development of high-order taylor-galerkin schemes for unsteady calculations, J. Comput. Phys. 162 (2) (2000) 338–371. doi:10.1006/jcph.2000.6538.

[40] T. Schønfeld, M. Rudgyard, Steady and unsteady flows simulations using the hybrid flow solver avbp, AIAA J. 37 (11) (1999) 1378–1385. doi:10.2514/2.636.

[41] N. Gourdain, L. Gicquel, M. Montagnac, O. Vermorel, M. Gazaix, G. Staffelbach, M. Garcia, J. Boussuge, T. Poinsot, High performance parallel computing of flows in complex geometries: I. methods, Comput. Sci. Disc. 2 (1) (2009) 015003.

[42] T. Passot, A. Pouquet, Numerical simulation of compressible homogeneous flows in the turbulent regime, J. Fluid Mech. 181 (1987) 441–466. doi:10.1017/S0022112087002167.

[43] J. Jeong, F. Hussain, On the identification of a vortex, J. Fluid Mech. 285 (1995) 69–94. doi:10.1017/S0022112095000462.

[44] L. Selle, G. Lartigue, T. Poinsot, R. Koch, K.-U. Schildmacher, W. Krebs, B. Prade, P. Kaufmann, D. Veynante, Compressible large-eddy simulation of turbulent combustion in complex geometry on unstructured meshes, Comb. Flame 137 (4) (2004) 489–505. doi:10.1016/j.combustflame.2004.03.008.

[45] B. Franzelli, E. Riber, L. Y. Gicquel, T. Poinsot, Large eddy simulation of combustion instabilities in a lean partially premixed swirled flame, Comb. Flame 159 (2) (2012) 621 – 637. doi:10.1016/j.combustflame.2011.08.004.

[46] S. B. Pope, Turbulent flows, Cambridge University Press, 2000. doi:10.1017/CBO9780511840531.

[47] T. Poinsot, A. Trouvé, D. Veynante, S. Candel, E. Esposito, Vortex driven acoustically coupled combustion instabilities, J. Fluid Mech. 177 (1987) 265–292. doi:10.1017/S0022112087000958.

[48] F. Nicoud, L. Benoit, C. Sensiau, T. Poinsot, Acoustic modes in combustors with complex impedances and multidimensional active flames, AIAA J. 45 (2007) 426–441. doi:10.2514/1.24933.

4.2 Wall modelling

The needs for high-order numerical method to predict jet noise has motivated S. Le Bras PhD thesis. This work, defended in 2016, was co-directed in collaboration with LMFA and funded by Airbus. In the paper thereafter, analytical wall model is combined with a high-order scheme for modeling the near-wall region of adiabatic and isothermal boundary layers. The model is validated on turbulent channel flows.

S. Le Bras, H. Deniau, C. Bogey, and G. Daviller. Development of compressible large-eddy simulations combining high-order schemes and wall modeling. *AIAA Journal*, 55(4):1152– 1163, 2017. https://doi.org/10.2514/1.J055107

Development of Compressible Large-Eddy Simulations Combining High-Order Schemes and Wall Modeling

S. Le Bras*
Centre Européen de Recherche et de Formation Avancée en Calcul Scientifique, 31057 Toulouse, France
H. Deniau†
ONERA — The French Aerospace Lab, 31000 Toulouse, France
C. Bogey‡
École Centrale de Lyon, 69134 Ecully, France
and
G. Daviller§
Centre Européen de Recherche et de Formation Avancée en Calcul Scientifique, 31057 Toulouse, France

DOI: 10.2514/1.J055107

Compressible large-eddy simulations combining high-order methods with a wall model have been developed in order to compute wall-bounded flows at high Reynolds numbers. The high-order methods consist of low-dissipation and low-dispersion implicit finite volume schemes for spatial discretization on structured grids. In the first part, the procedure used to apply these schemes in near-wall regions is presented. It is based on a ghost cell reconstruction. Its validity is assessed by performing the large-eddy simulation of a turbulent channel flow at a friction Reynolds number of $Re_\tau = 395$. In the second part, to consider flows at higher Reynolds numbers, a large-eddy simulation approach using a wall model is proposed. The coupling between the wall model and the high-order schemes is described. The performance of the approach is evaluated by simulating a turbulent channel flow at $Re_\tau = 2000$ using meshes with grid spacings of $\Delta x^+ = 100$, 200, and 300 in the streamwise direction and $\Delta^+ = 50$, 100, and 150 in the wall-normal and spanwise directions (in wall units). The effects of the choice of the point used for data exchange between the wall model and the large-eddy simulation algorithm, as well as of the positions of the ghost cells used for the coupling, are examined by performing additional computations in which these parameters vary. The results are in agreement with direct numerical simulation data. In particular, the turbulent intensities obtained in the logarithmic region of the boundary layers of the channel flow are successfully predicted.

I. Introduction

IN COMPUTATIONAL aeroacoustics, the direct calculation of the acoustic field from the Navier–Stokes equations requires accurate numerical methods to capture noise sources in turbulent flows and to propagate sound waves. Among various approaches available in the literature [1], the large-eddy simulation (LES) using high-order low-dissipation and low-dispersion schemes is an attractive way. In the LES approach, the large structures of the flows are computed, whereas the effects of the smallest turbulent scales are taken into account by a subgrid-scale model. Using high-order implicit schemes for spatial discretization offers the advantage of resolving the flow over a wide range of length scales using a reduced number of grid points. However, for wall-bounded flows at high Reynolds numbers (typically for $Re_L \geq 10^6$, where Re_L is the Reynolds number based on an integral flow scale L), the LES requires very fine grids to capture the small but dynamically important turbulent structures developing in the near-wall regions. These constraints on the grid resolution lead to computational costs that increase [2] with the Reynolds number as $Re_L^{13/7}$. In addition, according to the estimations of Piomelli and Balaras [3], to ensure the resolution of a boundary layer at $Re_L = 10^6$, around 99% of the grid points should be contained in the inner region of the boundary layer located between the wall and a distance corresponding to 20% of the boundary-layer thickness δ. Consequently, the LES of flows in the presence of walls with realistic geometries is out of reach using current numerical resources.

To perform LESs of wall-bounded flows at high Reynolds numbers, one solution consists of using a wall model in the near-wall regions instead of resolving the boundary layers. Wall modeling aims to reproduce the variations of the mean flow in the inner part of boundary layers by imposing approximate boundary conditions close to the walls. In that way, the LES can be performed on coarse grids that do not resolve the near-wall fluctuations. Consequently, the computational grid size is drastically reduced with respect to wall-resolved LESs. Wall modeling for the LES appeared in the 1970s in Deardorff's (1970) [4] and Schumann's (1975) [5] works, and it still knows great success among the scientific community [6]. In recent years, wall models have been applied to different flow configurations and implemented using several numerical approaches. In particular, the quality of LESs combining wall models and high-order methods has been examined by many authors. For instance, very promising results have been obtained using finite difference approaches [7] and spectral difference methods [8].

In this study, a compressible wall model [9] is combined with sixth-order finite volume compact schemes for spatial discretization in order to perform LESs of wall-bounded flows at high Reynolds numbers. The LES approach is based on the use of a selective filter as a subgrid-scale model. The present paper is organized as follows. In the first part, a procedure is proposed to apply the compact schemes near the walls. The procedure is validated for a turbulent channel flow at a low Reynolds number, with boundary-layer resolution at the wall.

Presented as Paper 2015-3135 at the 21st AIAA/CEAS Aeroacoustics Conference, Dallas, TX, 22–26 June 2015; received 9 February 2016; revision received 8 September 2016; accepted for publication 16 December 2016; published online 16 March 2017.

*lebras@cerfacs.fr (Corresponding Author).
†ONERA Research Scientist.
‡CNRS Research Scientist, Laboratoire de Mécanique des Fluides et d'Acoustique, UMR CNRS 5509; also Université de Lyon.
§Senior Researcher.

In the second part, to deal with flows at higher Reynolds numbers, the combination of the wall model with the high-order schemes is presented. The influence of the parameters used for wall modeling is investigated. In particular, the choice of the point where data are exchanged between the LES solver and the wall model is discussed. In addition, the importance of the positions of the ghost cells used to apply the selective filter near the wall is studied. The validity of the approach is finally examined for a turbulent channel flow with different spatial resolutions.

II. Wall-Resolved Simulations

A. Numerical Approach

1. Governing Equations

In the present work, the fully compressible three-dimensional Navier–Stokes equations are solved. In Cartesian coordinates, they can be written as follows:

$$\frac{\partial \boldsymbol{U}}{\partial t}+\frac{\partial \boldsymbol{E}_c}{\partial x}+\frac{\partial \boldsymbol{F}_c}{\partial y}+\frac{\partial \boldsymbol{G}_c}{\partial z}-\frac{\partial \boldsymbol{E}_d}{\partial x}-\frac{\partial \boldsymbol{F}_d}{\partial y}-\frac{\partial \boldsymbol{G}_d}{\partial z}=0 \qquad (1)$$

where $\boldsymbol{U}=(\rho,\rho u,\rho v,\rho w,\rho e)^t$ is the variable vector; $(u,\ v,\ w)$ are the velocity components; ρ is the density; ρe represents the total energy; $\boldsymbol{E}_c$, $\boldsymbol{F}_c$, and $\boldsymbol{G}_c$ are the convective fluxes; and $\boldsymbol{E}_d$, $\boldsymbol{F}_d$, and $\boldsymbol{G}_d$ are the diffusive fluxes. The total energy ρe for a perfect gas is defined by

$$\rho e=\frac{p}{\gamma-1}+\frac{1}{2}\rho(u^2+v^2+w^2) \qquad (2)$$

where γ is the specific heat ratio, and p is the static pressure. The convective fluxes are given by

$$\begin{cases}\boldsymbol{E}_c=(\rho u,\rho u^2+p,\rho uv,\rho uw,(\rho e+p)u)^t\\ \boldsymbol{F}_c=(\rho v,\rho uv,\rho v^2+p,\rho vw,(\rho e+p)v)^t\\ \boldsymbol{G}_c=(\rho w,\rho uw,\rho vw,\rho w^2+p,(\rho e+p)w)^t\end{cases} \qquad (3)$$

and the diffusive fluxes are given by

$$\begin{cases}\boldsymbol{E}_d=(0,\tau_{11},\tau_{12},\tau_{13},\tau_{11}u+\tau_{12}v+\tau_{13}w+\Phi_1)^t\\ \boldsymbol{F}_d=(0,\tau_{21},\tau_{22},\tau_{23},\tau_{21}u+\tau_{22}v+\tau_{23}w+\Phi_2)^t\\ \boldsymbol{G}_d=(0,\tau_{31},\tau_{32},\tau_{33},\tau_{31}u+\tau_{32}v+\tau_{33}w+\Phi_3)^t\end{cases} \qquad (4)$$

where $\tau_{i,j}$ is the viscous stress tensor, and $\boldsymbol{\Phi}=(\Phi_1,\Phi_2,\Phi_3)^t$ is the heat flux vector. The viscous stress tensor $\tau_{i,j}$ is defined by $\tau_{i,j}=2\mu S_{i,j}$, where μ is the dynamic molecular viscosity and $S_{i,j}$ is the deformation stress tensor:

$$S_{i,j}=\frac{1}{2}\left(\frac{\partial u_i}{\partial x_j}+\frac{\partial u_j}{\partial x_i}-\frac{2}{3}\frac{\partial u_k}{\partial x_k}\delta_{i,j}\right) \qquad (5)$$

The heat flux vector $\boldsymbol{\Phi}$ is computed using Fourier's law, yielding $\boldsymbol{\Phi}=-\lambda\nabla T$, where ∇T is the temperature gradient, $\lambda=C_p\mu/Pr$ is the thermal conductivity, C_p is the specific heat at constant pressure, and Pr is the Prandtl number.

2. Finite Volume Approach and High-Order Numerical Schemes

The computations are performed using the elsA software [10], which is a finite volume multiblock structured solver. Direct numerical simulations (DNSs) or large-eddy simulations can be carried out. In a finite volume approach, the computational domain is partitioned into nonoverlapping control volumes $\Omega_{i,j,k}$, where i, j, and k are the volume indices. For clarity, the finite volume method is presented for the linear convection equation:

$$\frac{\partial \boldsymbol{U}}{\partial t}+\nabla\cdot\boldsymbol{f}(\boldsymbol{U})=0 \qquad (6)$$

where $\boldsymbol{f}$ is a linear vectorial function of the variable vector $\boldsymbol{U}$. Equation (6) is integrated on the elementary volumes $\Omega_{i,j,k}$ using the divergence theorem:

$$\frac{\mathrm{d}}{\mathrm{d}t}\int_{\Omega_{i,j,k}}\boldsymbol{U}\,\mathrm{d}V+\int_{\partial\Omega_{i,j,k}}\boldsymbol{f}(\boldsymbol{U})\cdot\boldsymbol{n}\,\mathrm{d}S=0 \qquad (7)$$

where $\partial\Omega_{i,j,k}$ represents the faces of $\Omega_{i,j,k}$, and $\boldsymbol{n}$ is the outgoing unitary normal of $\Omega_{i,j,k}$. Supposing that $\Omega_{i,j,k}$ is an hexahedron and using the linearity of $\boldsymbol{f}$, Eq. (7) is equivalent to the relation:

$$\frac{\mathrm{d}}{\mathrm{d}t}\int_{\Omega_{i,j,k}}\boldsymbol{U}\,\mathrm{d}V+\boldsymbol{f}\left(\int_{\partial\Omega_{i,j,k}}\boldsymbol{U}\,\mathrm{d}S\right)\cdot\boldsymbol{n}=0 \qquad (8)$$

Therefore, in a finite volume method, the computation of the derivatives of the convective fluxes corresponds to the calculation of the fluxes from the averaged value of $\boldsymbol{U}$ at the cell interfaces. To approximate the interface-averaged value of $\boldsymbol{U}$, an interpolation is performed using the primitive variables $\boldsymbol{W}=(u,v,w,p,T)$. In the following, the averaged value of $\boldsymbol{W}$ at the interface of the volume $\Omega_{i,j,k}$ is defined by the following:

$$\tilde{\boldsymbol{W}}=\frac{1}{|\partial\Omega_{i,j,k}|}\int_{\partial\Omega_{i,j,k}}\boldsymbol{W}\,\mathrm{d}S \qquad (9)$$

and the averaged value of $\boldsymbol{W}$ in the volume $\Omega_{i,j,k}$ is defined by the following:

$$\bar{\boldsymbol{W}}=\frac{1}{|\Omega_{i,j,k}|}\int_{\Omega_{i,j,k}}\boldsymbol{W}\,\mathrm{d}V \qquad (10)$$

To obtain a high-order calculation of the convective fluxes derivatives, a high-order interpolation is performed to compute the values $\tilde{\boldsymbol{W}}$. Considering the one-dimensional computational domain of Fig. 1, the interpolated vector $\tilde{\boldsymbol{W}}$ at the interface $i+1/2$ is obtained by solving the implicit relation:

$$\alpha_{i+1/2}\tilde{\boldsymbol{W}}_{i-1/2}+\tilde{\boldsymbol{W}}_{i+1/2}+\beta_{i+1/2}\tilde{\boldsymbol{W}}_{i+3/2}=\sum_{l=-1}^{2}a_l\bar{\boldsymbol{W}}_{i+l} \qquad (11)$$

where $\alpha_{i+1/2}$, $\beta_{i+1/2}$, and a_l are the interpolation coefficients that are determined using a fifth-order Taylor series. The determination of these coefficients is described in detail in [11]. For a uniform Cartesian mesh, Fosso et al. [11] demonstrated that the formulation given by Eq. (11) is equivalent to Lele's sixth-order implicit compact finite difference scheme [12].

As the numerical scheme [Eq. (11)] is centered, the stability of the computations is ensured using a sixth-order selective compact filter originally introduced by Lele [12] and used by Visbal and Gaitonde [13]. The filter is applied to the flow variables at the end of each iteration to remove grid-to-grid oscillations. This filter also plays the role of an implicit subgrid-scale model for LES, relaxing turbulent energy at high frequencies [14–16]. The filtering operator applies to cell-averaged values, and it allows the filtered values denoted $\hat{\boldsymbol{W}}$ to be estimated from the unfiltered cell-averaged quantities $\bar{\boldsymbol{W}}$ in the following way:

$$\alpha_f\hat{\boldsymbol{W}}_{i-1}+\hat{\boldsymbol{W}}_i+\alpha_f\hat{\boldsymbol{W}}_{i+1}=\sum_{l=-3}^{3}\beta_l\bar{\boldsymbol{W}}_{i+l} \qquad (12)$$

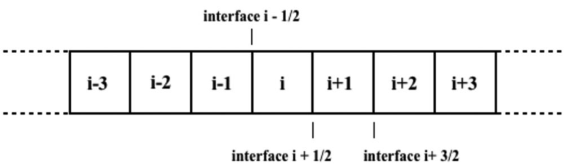

Fig. 1 Representation of a one-dimensional computational domain.

where α_f is a constant equal to 0.47, and β_l are the filter coefficients [13]. These coefficients are determined by using Taylor series and imposing that the filter transfer function is equal to zero for normalized wave number $k\Delta = \pi$, as described in [13].

The diffusive fluxes in Eq. (4) are computed using a second-order method [17]. In this method, the gradient of the primitive variables $\nabla \boldsymbol{W}$ is evaluated at the cell interfaces to compute the deformation stress $S_{i,j}$ and the heat flux vector $\boldsymbol{\Phi}$. Time discretization is performed using a low-storage six-stage Runge–Kutta algorithm [18]. Radiation boundary conditions and Navier–Stokes characteristic boundary conditions are implemented [19]. A full description of the numerical algorithm is available in the work of Fosso et al. [20].

3. Boundary Condition for Simulation with Boundary-Layer Resolution at the Wall

Close to the walls, the high-order schemes [Eqs. (11) and (12)] cannot be applied because of the reduced number of points available. More precisely, the variable vector at interfaces $1/2$ and $3/2$, represented by triangles in Fig. 2, cannot be computed using the four-point stencil spatial scheme [Eq. (11)]. In the same way, the selective filter cannot be applied at the points symbolized by squares. Therefore, a specific discretization must be proposed close to the boundaries. Such near-wall discretizations have been studied for finite difference schemes [21,22]. However, to the best of our knowledge, no formulation is available for a finite volume approach. Therefore, a new boundary discretization is presented here.

a. Spatial Scheme. For a wall, the boundary conditions depend on the nature of the wall and on the flow variables. The velocity satisfies a Dirichlet condition at the wall, leading to a nil velocity. The pressure follows a Neumann condition, yielding a zero wall-normal pressure gradient. The temperature satisfies a Neumann condition in the case of an adiabatic wall but a Dirichlet condition for an isothermal wall.

In this study, the implicit centered scheme on four points [Eq. (11)] is applied down to the wall. For this purpose, the computational domain is extended using ghost cells, as illustrated in Fig. 3a. In particular, a ghost interface $\boldsymbol{I}_{-1/2}$ (depicted by the dashed line) and two ghost cells (numbered P_0 and P_{-1}) are introduced. They are positioned symmetrically with respect to the wall, the locations of the points P_1 and P_2, and the interface $\boldsymbol{I}_{3/2}$.

The primitive variables (u, v, w, p, T) are reconstructed in the ghost cells to prescribe an adiabatic or an isothermal condition at the wall. More precisely, to impose a nil velocity at the wall, the velocity components are considered as odd functions along the wall-normal direction. They are computed from the values of the velocity at the points P_1 and P_2 and at the interface $3/2$, yielding the following relations:

$$\begin{cases} \bar{u}_i = -\bar{u}_{1-i} \\ \bar{v}_i = -\bar{v}_{1-i} \\ \bar{w}_i = -\bar{w}_{1-i} \end{cases} \quad \text{for } i = 0, -1, \text{ and } -1/2 \tag{13}$$

In the case of an isothermal wall, the values at the ghost points for the temperature are defined in order to specify the wall temperature T_w:

$$\bar{T}_i = 2T_w - \bar{T}_{1-i} \quad \text{for } i = 0, -1, \text{ and } -1/2 \tag{14}$$

Finally, the temperature for an adiabatic wall and the pressure are characterized by a zero gradient in the wall-normal direction. A simple way to impose this condition is to consider the temperature and the pressure as even functions with respect to the wall-normal direction. Therefore, the temperature in the ghost cells is defined by

$$\bar{T}_i = \bar{T}_{1-i} \quad \text{for } i = 0, -1, \text{ and } -1/2 \tag{15}$$

and the pressure is defined by

$$\bar{p}_i = \bar{p}_{1-i} \quad \text{for } i = 0, -1, \text{ and } -1/2 \tag{16}$$

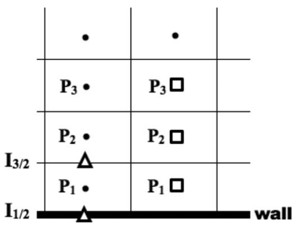

Fig. 2 Representation of interfaces (triangles (Δ)) and points (squares (□)) for which the spatial scheme and selective filter cannot be applied.

b. Selective Filtering. The implicit centered filter on seven points [Eq. (12)] is applied down to the wall. Therefore, a third ghost cell is used, as illustrated in Fig. 3b where the additional cell is denoted by P_{-2}. A technique, similar to that previously developed for the spatial scheme, is employed to specify the flow variables in this cell, using point P_3.

In addition, to apply the implicit filter [Eq. (12)] at point P_1, filtered values at point P_0 are specified from the filtered quantities at point P_1. For instance, the velocity components are defined as follows:

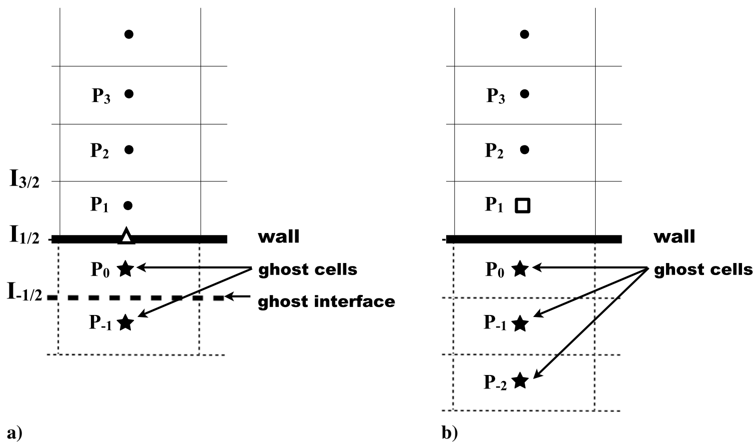

Fig. 3 Spatial discretization for a wall-resolved LES: a) for the spatial scheme [11], and b) for the selective filter [13].

$$\begin{cases} \hat{u}_0 = -\hat{u}_1 \\ \hat{v}_0 = -\hat{v}_1 \\ \hat{w}_0 = -\hat{w}_1 \end{cases} \tag{17}$$

The performance of the numerical algorithm is now evaluated for a turbulent channel flow.

B. Turbulent Channel Flow

1. Parameters

A three-dimensional turbulent channel flow is computed by LES using the wall discretization described previously. The flow is characterized by a Mach number of $M = U_b/c = 0.2$ and a friction Reynolds number of $Re_\tau = u_\tau h/\nu_w \simeq 395$, where c is the sound speed, u_τ is the friction velocity at the wall, h is the channel half-height, ν_w is the kinematic molecular viscosity at the wall, and U_b is the bulk velocity defined from the streamwise velocity u and the density ρ as follows:

$$U_b = \frac{\int_0^h \bar{\bar{\rho}}(y)\bar{\bar{u}}(y)\,\mathrm{d}y}{\int_0^h \bar{\bar{\rho}}(y)\,\mathrm{d}y} = \frac{(1/h)\int_0^h \bar{\bar{\rho}}(y)\bar{\bar{u}}(y)\,\mathrm{d}y}{\rho_b} \tag{18}$$

where ρ_b is the bulk density, and $\bar{\bar{\cdot}}$ represents a statistical mean in the homogeneous flow directions x and z. In the following, the streamwise, the wall-normal, and the spanwise spatial coordinates are denoted by x, y, and z.

Channel flows at $Re_\tau = 395$ have also been simulated by Abe et al. [23,24] and Moser et al. [25], using direct numerical simulation. In this study, the channel lengths are equal to $L_x = 2\pi h$, $L_y = 2h$, and $L_z = \pi h$, as in the DNS of Abe et al. [23]. At the top and the bottom channel walls, adiabatic conditions are imposed. Periodic conditions are applied in the streamwise and spanwise directions. To compensate the effects of the viscous dissipation, and thus impose the mass flow rate $\rho_b U_b$ in the channel, a source term S_x in the form of a pressure gradient is introduced in the streamwise momentum equation [26]. The source term is defined by the following:

$$S_x = \frac{\tau_{w_{\mathrm{ref}}}}{h} + \rho_b U_b - \frac{1}{V}\iiint_\Omega \rho u \,\mathrm{d}V \tag{19}$$

where ρ and u are instantaneous LES data, Ω is the computational domain, V represents its volume, and $\tau_{w_{\mathrm{ref}}}$ is the value of the wall shear stress of the DNS of Abe et al. [23]. A resultant term uS_x is also added in the energy equation.

2. Grid Definition

The grid parameters in the present LES including the numbers of mesh points n_x, n_y, and n_z in each direction, as well as the streamwise, normal, and spanwise grid spacings Δx^+, Δy^+, and Δz^+ in wall units, are given in Table 1. At the wall, the grid spacing Δy_w^+ is equal to one in order to capture the small structures developing in the near-wall regions. From the wall, the mesh is stretched in the y direction to reach $\Delta y_{\max}^+ = 8$ at the center of the channel in order to reduce computational cost. The stretching rate remains lower than 4% to avoid the generation of spurious numerical waves. In the streamwise and the spanwise directions, the grid spacings are uniform, and they are equal to $\Delta x^+ = 15$ and $\Delta z^+ = 10$. For comparison, the grid parameters used in the DNS of Abe et al. [23] and Moser et al. [25] are also provided in Table 1. The DNS grids are finer than the LES mesh, particularly in the wall-normal direction where the mesh spacing Δy_w^+ is close to 0.2; whereas $\Delta y_w^+ = 1$ in the LES.

Table 1 Grid parameters to simulate a turbulent channel flow at $Re_\tau = 395$

Simulation	$n_x \times n_y \times n_z$	Δx^+	Δz^+	Δy_w^+	$\Delta y_{\max}^+$
LES	$161 \times 181 \times 241$	15	5	1	8
DNS [23]	$256 \times 192 \times 256$	10	5	0.2	9.6
DNS [25]	$256 \times 193 \times 192$	10	6.5	0.15	6.5

3. Initial Conditions

At initial time $t = 0$, the streamwise velocity u in the channel is given by the analytical turbulent profile:

$$u(y) = \frac{8}{7}U_b\left(\frac{y}{h}\right)^{1/2} \tag{20}$$

and the velocity components in directions y and z are equal to zero. Initially, the static pressure p_0 and the static temperature T_0 are uniform, with $p_0 = 10^5$ Pa and $T_0 = 273$ K. The transition toward turbulence is accelerated by adding perturbations in the form of spanwise vortices to the initial velocity profile [27]. The time step Δt for the simulation is chosen so that the Courant–Friedrichs–Lewy number is $\mathrm{CFL} = c\Delta t/\Delta y_w \simeq 0.7$ to ensure the stability of time integration. The transient period of the simulation lasts during the nondimensional time $t^* = tU_b/h = 102$, which is equivalent to 15 flow periods through the channel. The statistics are then collected during a time period of $t^*_{\mathrm{stat}} \simeq 100$. The results are averaged in time and in space in the homogeneous directions x and z, and they are compared with the DNS data [23,24].

4. Results

The mean and rms values of the streamwise velocity $u^+ = \langle u \rangle / u_\tau$ and $u'^+ = \langle u'u' \rangle^{1/2}/u_\tau$ obtained in the LES are represented by the dashed lines in Fig. 4, where $\langle \cdot \rangle$ corresponds to a statistical mean in time and space in the homogeneous flow directions. The results are displayed in wall units as a function of the radial distance y^+, and they are compared with the DNS data of Abe et al. [24]. A good agreement between the LES and DNS profiles is found for both mean and rms quantities. This suggests that the present numerical algorithm, based on the application of a selective filter as a subgrid-scale model for LES, can be used to simulate turbulent wall-bounded flows at low Reynolds numbers. Note that the influence of the spatial resolution of the channel on the LES results is discussed in the Appendix.

III. Simulations Using a Wall Model

A. Numerical Approach

1. Description of the Wall Model

When flows at high Reynolds numbers are considered, a wall modeling must be introduced. The wall model [9] used here relies on Reichardt's [28] and Kader's [29] analytical laws. The first one allows the mean velocity U to be estimated as a function of the height y above the wall. In wall units, one gets

$$u^+ = \frac{U}{\sqrt{\tau_w/\rho_w}} = \frac{1}{\kappa}\ln(1+\kappa y^+) + \left(B - \frac{1}{\kappa}\ln\kappa\right)\left(1 - \exp\left(-\frac{y^+}{11}\right) - \frac{y^+}{11}\exp(-0.33y^+)\right) \tag{21}$$

where $y^+ = \rho_w u_\tau y/\mu_w$, μ_w is the dynamic molecular viscosity at the wall, κ is the von Kármán constant equal to 0.41, and B is a constant equal to 5.25. The Kader law approximates the variations of the temperature T as, in wall units,

$$T^+ = -\frac{(T - T_w)\rho_w C_p u_\tau}{\Phi_w} = Pr y^+ \exp(\Gamma) + \left(2.12\ln(1+y^+) + (3.85Pr^{1/3} - 1.3)^2 + 2.12\ln Pr\right)\exp\left(\frac{1}{\Gamma}\right) \tag{22}$$

where

$$\Gamma = -(10^{-2}(Pry^+)^4)/(1 + 5Pr^3y^+)$$

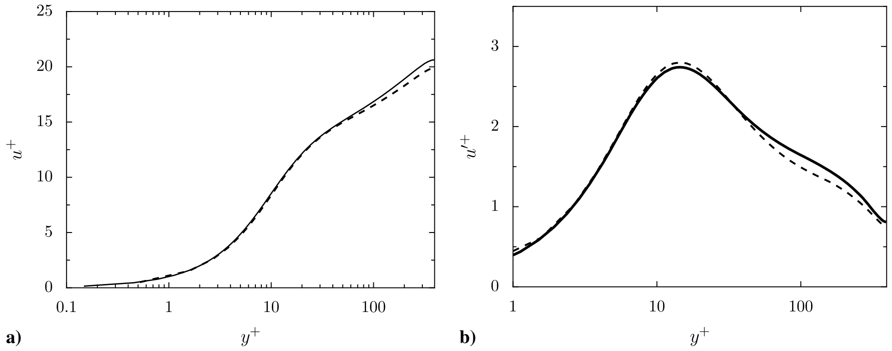

Fig. 4 Streamwise velocity profiles in the channel: a) mean, and b) rms. Dashed lines denote LES, and solid lines denote DNS of [24].

In addition, in the boundary layer, the pressure variations are assumed to be negligible in the wall-normal direction, yielding

$$\frac{\partial p}{\partial y} = 0 \tag{23}$$

Equations (21) and (22) are valid for incompressible flows, assuming weak pressure gradients in the streamwise direction. The validity of these wall laws can be extended to compressible flows thanks to van Driest's transformation [30].

When a wall model is used to compute a wall-bounded flow, the inner part of the boundary layer close to the wall is simulated without resolving the turbulent structures developing in this region. As a consequence, a coarse mesh can be used near the wall and the computational cost is considerably reduced compared to a wall-resolved simulation. In our finite volume approach, the wall model is involved in the computation of the variable vector $\boldsymbol{W}$ and its gradient $\nabla \boldsymbol{W}$ at the wall. Indeed, the value of $\nabla \boldsymbol{W}$ at the wall cannot be obtained in the same way as for a wall-resolved LES. In particular, the velocity and the temperature gradients at the wall are not correctly predicted by the numerical schemes. Consequently, the wall model allows the velocity and the temperature gradients to be estimated at each temporal iteration. In practice, the model gives estimations of the wall shear stress $\tau_w = \mu_w \partial U/\partial y|_{y=0}$ and of the wall heat flux $\Phi_w = -\lambda \partial T/\partial y|_{y=0}$, as illustrated in Fig. 5.

2. Estimation of Velocity and Temperature Gradients at the Wall

To obtain the values of τ_w and Φ_w from Reichardt's [28] and Kader's [29] laws, the values of the velocity U and the temperature T that appear in Eqs. (21) and (22) need to be determined. For that, a computational point M located at a distance y_M from the wall is chosen. This point M is named the matching point [7]. Represented in Fig. 5, it is the center of one of the cells located along the wall-normal direction. It must be located in the inner part of the boundary layer such that the conditions of application of the wall laws are satisfied. The choice of the position of the matching point will be discussed in Sec. III.A.4. To compute the values of U and T, the instantaneous LES variables at point M are collected. They are denoted $\boldsymbol{u}_{\text{LES}}$ and T_{LES} in Fig. 5. The scalar velocity value U is obtained by writing the velocity vector $\boldsymbol{u}_{\text{LES}}$ in the local coordinate frame defined by the flow direction $\boldsymbol{m}$, the wall-normal direction $\boldsymbol{n}$, and the vector $\boldsymbol{m} \wedge \boldsymbol{n}$. The components of $\boldsymbol{u}_{\text{LES}}$ in this frame are denoted u_m, u_n, and $u_{m\wedge n}$; and the velocity U is given by the relation $U = \sqrt{u_m^2 + u_{m\wedge n}^2}$. The temperature T is equal to T_{LES}. To determine the values of τ_w and Φ_w from relations (21) and (22), it is also necessary to estimate the values of the temperature T_w, the dynamic viscosity μ_w, and the density at the wall ρ_w. These quantities are computed differently, depending on the isothermal or the adiabatic nature of the wall.

a. Isothermal Wall. In the case of an isothermal wall, the temperature at the wall T_w is known. Therefore, the dynamic viscosity at the wall μ_w is computed from Sutherland's law for the temperature T_w. Then, the wall density ρ_w is obtained using the perfect gas equation, yielding $\rho_w = p_{\text{LES}}/(RT_w)$, where p_{LES} is the value of the pressure from the LES field at point M and R is the perfect gas constant. From the quantities T_w, μ_w, ρ_w, U, and T, the wall laws can now be used to estimate the velocity and the temperature gradients at the wall. The friction velocity u_τ is estimated from Reichardt's law [28] using a Newton algorithm. The wall shear stress $\tau_w = \rho_w u_\tau^2$ is then computed. As for the wall heat flux Φ_w, it is obtained from Kader's law [29] and $T = T_{\text{LES}}$.

b. Adiabatic Wall. In the case of an adiabatic wall, the value of Φ_w is equal to zero, leading to $T_w = T_{\text{LES}}$. The wall shear stress τ_w is then computed in the same way as for an isothermal wall.

3. Implementation with High-Order Numerical Schemes

As for the wall-resolved LES approach, the high-order schemes [Eqs. (11) and (12)] cannot be applied down to the wall. Consequently, in this study, for the LES with wall modeling, new spatial discretizations for the spatial scheme [Eq. (11)] and the selective filter [Eq. (12)] have been proposed in the near-wall regions. More precisely, the velocity components u, v, and w; the pressure p; and the temperature T at the cells and interfaces represented by symbols in Fig. 2 are computed differently from the interior points. The wall model is involved in this procedure.

a. Spatial Scheme. The wall discretization depends on the variables and the adiabatic or the isothermal nature of the wall. A first discretization is proposed for the variables satisfying a Dirichlet

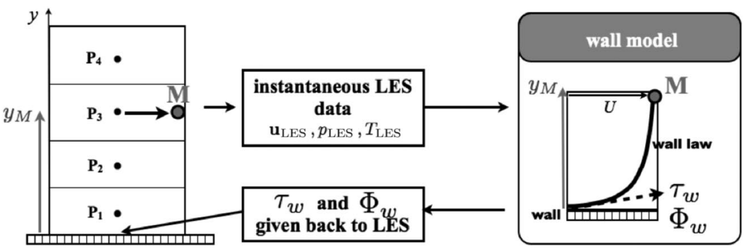

Fig. 5 Wall model application. The values of τ_w and Φ_w are computed by the model using instantaneous LES data at matching point M.

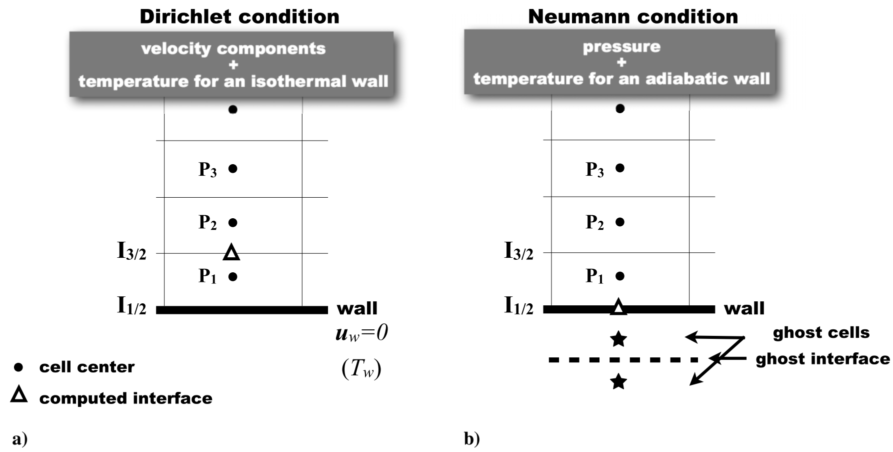

Fig. 6 Spatial discretization close to the wall for the spatial scheme [11] in the case of a wall-modeled LES: a) Dirichlet condition, and b) Neumann condition at the wall.

condition, such as the velocity components and the temperature for an isothermal wall. A second discretization is used for the variables verifying a Neumann condition such as the pressure and the temperature in the case of an adiabatic wall. For clarity, the discretizations corresponding to the Dirichlet and the Neumann conditions are presented for the velocity and the pressure, respectively.

For a Dirichlet condition, the no-slip condition $\boldsymbol{u}_w = \boldsymbol{0}$ is imposed at the wall, as illustrated in Fig. 6a. The velocity vector $\tilde{\boldsymbol{u}}_{3/2}$, at the interface between points P_1 and P_2, is computed using a second-order centered scheme:

$$\tilde{\boldsymbol{u}}_{3/2} = \alpha''_{3/2}\bar{\boldsymbol{u}}_1 + \beta''_{3/2}\bar{\boldsymbol{u}}_2 \tag{24}$$

where $\alpha''_{3/2}$ and $\beta''_{3/2}$ are the interpolation coefficients, determined using the second-order Taylor series.

In the case of a Neumann condition, the spatial discretization is similar to the one used in the wall-resolved LES approach and described in Sec. II.3. To apply the four-point implicit centered scheme [Eq. (11)] down to the wall, two ghost cells and a ghost interface are introduced, as represented in Fig. 6b. The values of the pressure in these cells are computed to impose $\partial p/\partial y|_{y=0} = 0$ using relation (16).

b. Selective Filtering. The selective filter is applied down to the wall, using three rows of ghost cells. The definition of the ghost cells depends on the Neumann or the Dirichlet conditions satisfied by the flow variables at the wall.

For a Neumann condition, three ghost cells are introduced beyond the wall. They are represented in Fig. 7b and reconstructed in the same way as for the spatial scheme [11].

For the variables satisfying a Dirichlet condition at the wall, such as the velocity, three new cells are added between the wall and the point P_1. These cells allow us to apply the filter down point P_1. They are symbolized by stars in Fig. 7a. The methodology used to define the velocity in these cells is now presented. In the following, these cells correspond to points P_0, P_{-1}, and P_{-2}. Their positions from the wall are defined by $y_i = h_1/d_i$, where h_1 is the height of the point P_1; i is the index of point P_i; and d_0, d_1, and d_2 are constants chosen such as $d_0 < d_{-1} < d_{-2}$. The importance of the ghost cell locations, determined by the values of d_i, is discussed in Sec. III.B.2. To specify the velocity in these additional cells, the wall model is used. The wall shear stress τ_w is determined from Reichardt's law [28] and the LES data collected at the matching point M, as described in the previous section. Once the value of τ_w obtained, the Reichardt law provides a relation for the mean velocity U as a function of the wall distance y, as plotted in Fig. 7a. This wall law profile is then used to compute the mean velocity U_i for $i = 0$, -1, and -2. A similar reconstruction allows the temperature to be specified using Kader's law [29]. The velocity vectors in the ghost cells are then computed from the values of U_i. They are assumed to be colinear with the velocity $\boldsymbol{u}_1$ at point P_1:

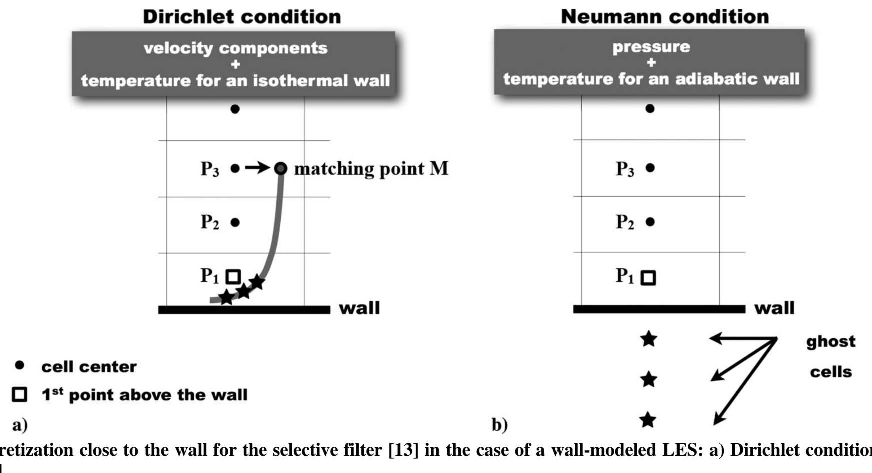

Fig. 7 Spatial discretization close to the wall for the selective filter [13] in the case of a wall-modeled LES: a) Dirichlet condition, and b) Neumann condition at the wall.

$$\boldsymbol{u}_i = U_i \frac{\boldsymbol{u}_1}{\|\boldsymbol{u}_1\|} \tag{25}$$

Finally, in order to apply the implicit centered filter [Eq. (12)] at point P_1, the filtered velocity $\hat{\boldsymbol{u}}_0$ at point P_0 is needed. The filter is assumed to have no effect on the velocity field at point P_0, leading to the approximation $\hat{\boldsymbol{u}}_0 = \bar{\boldsymbol{u}}_0$.

4. Influence of the Matching Point Location

The matching point M, represented in Figs. 5 and 7a, plays a considerable role in the wall-modeled LES approach, as it provides the LES data used to estimate the values of τ_w and Φ_w. Therefore, the influence of its position must be examined. Usually [9], this point corresponds to first computational point P_1 above the wall. However, recent works [7,31] demonstrated that selecting a matching point located further from the wall improves results. Two reasons for that can be raised. First, the smallest structures captured by a mesh are necessarily under-resolved near the mesh cutoff scale. Because these small structures have a major influence on the development of the flow in the near-wall region, the LES flowfield is not accurately computed at the first points above the wall. Second, as presented previously, the high-order discretization must generally be adapted when approaching the wall, which may produce numerical errors in this region. The influence of the choice of the matching point location on the LES results will be investigated in the following section, where the performance of the numerical approach with wall modeling is examined for a turbulent channel flow.

B. Turbulent Channel Flows

1. Parameters

The LES approach with wall modeling is used to compute the turbulent channel flow at a Mach number of $M = 0.2$ and a friction Reynolds number of $Re_\tau \simeq 2000$, which was also considered by Hoyas and Jiménez [32] using DNS. The channel lengths are equal to $L_x = 2\pi h$, $L_y = 2h$, and $L_z = \pi h$, as in the LES of the previous section for the channel flow at $Re_\tau = 395$. Periodic conditions are implemented in directions x and z. At the walls, adiabatic or isothermal boundary conditions are specified. The mass flow rate $\rho_b U_b$ in the channel is imposed using the source term S_x defined in Eq. (19) and its resultant term uS_x. In the case of an isothermal wall, the wall temperature T_w is imposed and an additional source term Q_x is introduced [26] in the energy equation to prescribe the bulk temperature T_b. The temperature T_b is obtained from the averaged values of ρ, u, and T in the homogeneous directions x and z using the following relation:

$$T_b = \frac{\int_0^h \bar{\bar{\rho}}(y)\bar{\bar{u}}(y)\bar{\bar{T}}(y)\,\mathrm{d}y}{\int_0^h \bar{\bar{\rho}}(y)\bar{\bar{u}}(y)\,\mathrm{d}y} \tag{26}$$

and the source term Q_x is defined by

$$Q_x = -\frac{\Phi_{w_{\mathrm{ref}}}}{h} + T_b - \frac{1/V \iint_\Omega \rho u T\,\mathrm{d}V}{1/V \iint_\Omega \rho u\,\mathrm{d}V} \tag{27}$$

where ρ, u, and T are instantaneous LES data; and $\Phi_{w_{\mathrm{ref}}}$ is a wall heat flux estimated from the empirical correlation of Sleicher and Rouse [33] in order to impose a temperature gradient at the wall corresponding to $T_b/T_w = 1.1$.

At initial time $t = 0$, the streamwise velocity u in the channel is identical to that of the LES of the turbulent channel flow at $Re_\tau = 395$. The velocity components in directions y and z are equal to zero. The static pressure and temperature are equal to $p_0 = 10^5$ Pa and $T_0 = 293$ K. The time step is chosen such that $\mathrm{CFL} = c\Delta t/\Delta y \simeq 0.7$. The simulation transient period lasts during the nondimensional time $t^* = tU_b/h = 200$, corresponding to 30 flow periods through the channel. Then, the statistics are sampled over 30 flow periods. The results are averaged in time and in space, and they are compared with the results of the DNS of Hoyas and Jiménez [32]. In the case of isothermal walls, the temperature profile is compared with the profile given by the analytical law of Kader [29].

2. Results for Adiabatic Walls

a. Choice of the Matching Point Location. The influence of the matching point on the LES results is evaluated by performing four simulations using matching points located at different positions y_M^+ from the wall. These positions are those of cell centers P_1, P_2, P_3, or P_4. The mesh used for the computations is designed to satisfy the grid constraints for LES with wall modeling proposed by Bocquet et al. [9]. In particular, the grid cells are chosen to capture the large turbulent structures of the outer region of the boundary layers. These structures, elongated in the streamwise direction, are found for $y^+ > 100$. Therefore, the grid spacing of the mesh in the wall-normal direction is equal to 100 in wall units. In the streamwise and spanwise directions, the mesh spacings in wall units are, respectively, equal to 200 and 100. In that way, matching points P_1, P_2, P_3, and P_4 are, respectively, located at $y_M^+ = 50$, 150, 250, and 350 in wall units. In the computation, the ghost cell positions are arbitrarily chosen using $d_0 = 1.3$, $d_{-1} = 1.5$, and $d_{-2} = 2$, according to the notations introduced in Sec. III.A.3.

The profiles obtained for the mean and rms streamwise velocities and for the Reynolds shear stresses $- < uv' > /u_\tau$ are displayed in Fig. 8. They are plotted in wall units as a function of the wall distance y^+, and they are compared with DNS profiles [32]. The matching points are indicated by symbols. They are all located on the DNS mean velocity profile in Fig. 8a, which supports that the numerical algorithm with wall modeling is correctly implemented. For the LES performed with the matching point P_1 closest to the wall, the mean and rms profiles present discrepancies with respect to the DNS profiles. In particular, the amplitude of the mean velocity and those of the Reynolds stresses are underpredicted over all the channel half-height. On the contrary, the use of matching point P_2 leads to an overprediction of the mean velocity u^+ in the logarithmic region with respect to the DNS results. However, turbulent levels in better agreement with the DNS data are obtained as compared to the LES

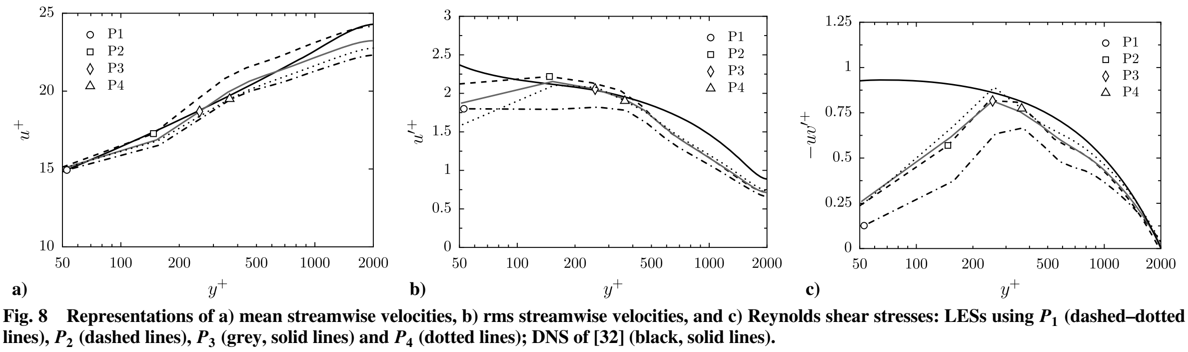

Fig. 8 Representations of a) mean streamwise velocities, b) rms streamwise velocities, and c) Reynolds shear stresses: LESs using P_1 (dashed–dotted lines), P_2 (dashed lines), P_3 (grey, solid lines) and P_4 (dotted lines); DNS of [32] (black, solid lines).

results determined using P_1. Finally, the best match with the DNS data for both the mean and rms profiles is observed for the LES using matching points P_3 and P_4. These results demonstrate the importance of choosing a matching point located far from the wall, for $y^+ > 150$, to predict the turbulent intensities in the channel with a good accuracy. Therefore, in the following, point P_3 is selected as the matching point in the computations.

b. Influence of the Position of the Ghost Cells. In Sec. III.A.3, ghost cells have been introduced for LES with wall modeling in order to apply the selective filter towards the wall. The influence of the position of these cells on the LES results is evaluated by performing four simulations (G1, G2, G3, and G4) using different ghost cell locations. The ghost cell configuration for each LES is illustrated in Fig. 9. In LES G1, the ghost cells are regularly distributed between the wall and point P_1. In LESs G2, G3, and G4, these cells are located between $y = 0.5y_{P_1}$ and point P_1. More precisely, for LES G2, the ghost cells are located at $0.5y_{P_1}$, $2y_{P_1}/3$, and $5y_{P_1}/6$. In LES G3, the ghost cell positions are arbitrarily chosen as $0.5y_{P_1}$, $2y_{P_1}/3$, and $y_{P_1}/1.3$. This configuration was used in the previous section dealing with the effects of the matching point location. Finally, in LES G4, the ghost cells are positioned at $y = 0.5y_{P_1}$, $5y_{P_1}/8$, and $0.75y_{P_1}$. The mesh used in the four LESs is identical to that in the study reported previously. Moreover, the matching point is point P_3.

The mean velocity profiles u^+ obtained in LESs G1, G2, G3, and G4, as well as in the DNS of Hoyas and Jiménez [32], are depicted in wall units in Fig. 10a as a function of the wall distance. The four LES profiles are superimposed, which suggests that the choice of the ghost cell positions, between the wall and point P_1, has a weak influence on the mean velocity in the channel. They are also in good agreement with the DNS profile, except in the wake region where the velocity is slightly underestimated.

The fluctuating velocity profiles u'^+ and Reynolds stresses $-uv'^+$ from the LES and from the DNS of Hoyas and Jiménez [32] are displayed in Figs. 10b and 10c in wall units. The LES profiles have similar shapes. Compared to the DNS data, the turbulence intensities from the LES are lower. The highest turbulent levels are observed in LESs G3 and G4. The best agreement with the DNS results is obtained in LES G3.

These results demonstrate that the choice of the ghost cell positions does not considerably affect the LES results. In the following, the ghost cell positions defined for the LES G3 are used.

c. Study of the Grid Sensitivity. The influence of the spatial resolution is investigated by performing wall-modeled LES (WMLES) on meshes with different grid spacings. The mesh parameters, including the numbers of points n_x, n_y, and n_z in each direction; the grid spacings Δ^+, and the matching point location $y^+_{P_3}$ (in wall units), as well as the grid spacing $\Delta x/h$ normalized by the channel half-height, are provided in Table 2. In all directions, the grid spacing is uniform. To examine the influence of the mesh spacing in directions x, y, and z, three groups of meshes named grid$x$, grid$y$ and grid$z$ are considered. For grid$x$300, grid$x$200, and grid$x$100, the mesh spacings Δz^+ and Δy^+ are equal to 100; whereas Δx^+ reduces from 300 to 100. In grid$y$150, grid$y$100, and grid$y$50, $\Delta x^+ = 200$ and $\Delta z^+ = 100$ are imposed; whereas Δy^+ decreases from 150 down to 50. Finally, in grid$z$150, grid$z$100, and grid$z$50, $\Delta x^+ = 200$; $\Delta y^+ = 100$; and $\Delta z^+ = 150$, 100, and 50 are specified. Note that the position of the matching point is $y^+_{P_3} = 250$ in all the LESs using grid$x$ and grid$z$ meshes, but it varies from $y^+_{P_3} = 125$ to $y^+_{P_3} = 375$ using grid$y$ meshes.

For comparison, the characteristics of the mesh in the DNS of Hoyas and Jiménez [32], as well as those of the grids used to perform wall-modeled LES in the literature [9,34–36], are reported in Table 2. Compared to the DNS mesh, grid$x$200 is 25 times coarser in directions x and z, and it is 330 times coarser in direction y at the wall. Furthermore, note that the grid parameters chosen in this study are close to those used in the wall-modeled LES of the literature.

In the following, the influence of the mesh resolution is examined by representing the profiles of the mean streamwise velocity u^+, the rms streamwise velocity u'^+, and the Reynolds shear stresses $-uv'^+$ as functions of the wall distance y^+ in wall units. The maching points (MP) are indicated by symbols in the figures. The LES profiles are compared with the profiles given by the DNS of Hoyas and Jiménez [32].

Regarding the influence of the mesh resolution in the wall-normal direction, the results obtained in simulation grid$y$ are displayed in Fig. 11. The mean velocity profiles differ in the logarithmic region, whereas they have similar shapes for $y^+ > 1000$. A better agreement

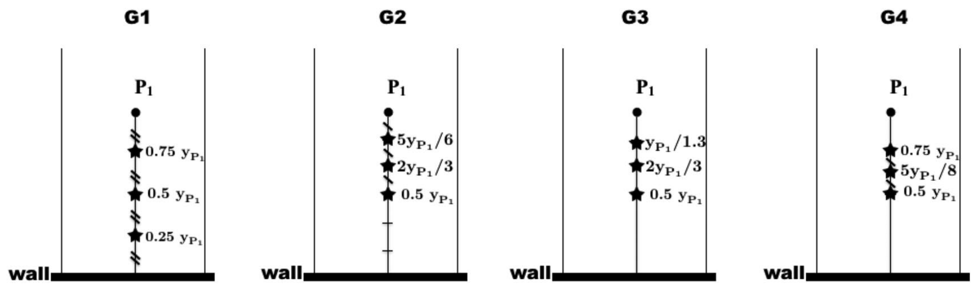

Fig. 9 Representation of the ghost cell positions (⋆) in the wall-normal direction for LESs G1, G2, G3, and G4.

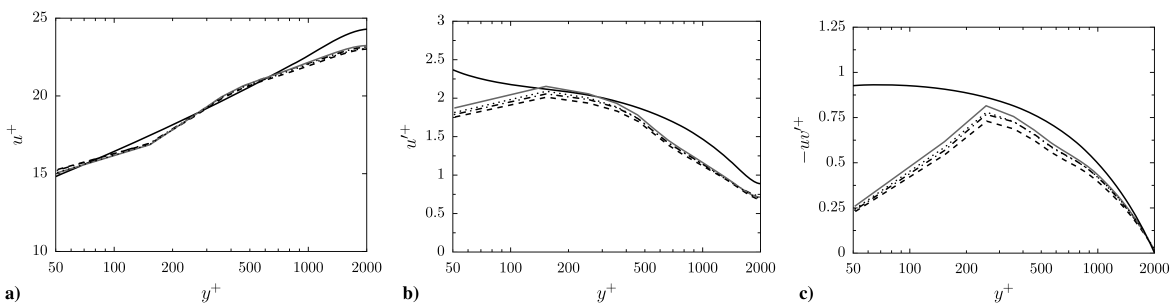

Fig. 10 Representations of a) mean streamwise velocities, b) rms streamwise velocities, and c) Reynolds shear stresses: LESs G1 (dashed–dotted lines), G2 (dashed lines), G3 (grey, solid lines), and G4 (dotted lines); DNS of [32] (black, solid lines).

Table 2 Grid parameters

Simulation	$n_x \times n_y \times n_z$	Δx^+	Δz^+	Δy_w^+	$\Delta y_{\max}^+$	Matching point $y_{P_3}^+$	$\Delta x/h$
WMLES grid$x$300	$43 \times 41 \times 65$	300	100	100	100	250	0.15
WMLES grid$x$200	$65 \times 41 \times 65$	200	100	100	100	250	0.10
WMLES grid$x$100	$127 \times 41 \times 65$	100	100	100	100	250	0.05
WMLES grid$y$150	$65 \times 27 \times 65$	200	100	150	150	375	0.10
WMLES grid$y$100	$65 \times 41 \times 65$	200	100	100	100	250	0.10
WMLES grid$y$50	$65 \times 81 \times 65$	200	100	50	50	125	0.10
WMLES grid$z$150	$65 \times 41 \times 43$	200	150	100	100	250	0.10
WMLES grid$z$100	$65 \times 41 \times 65$	200	100	100	100	250	0.10
WMLES grid$z$50	$65 \times 41 \times 127$	200	50	100	100	250	0.10
DNS of Hoyas and Jiménez [32]	$1536 \times 633 \times 1536$	8.2	4.1	0.3	8.9	— —	0.004
WMLES of Bodart and Larsson [34]	— —	200	40	125	125	300	0.10
WMLES of Bocquet et al. [9]	— —	260	160	100	100	50	0.13
WMLES of Lee et al. [35]	— —	200	135	125	125	312	0.10
WMLES of Park and Moin [36]	— —	200	125	40	40	200	0.10

with the DNS is obtained using grid$y$150 and grid$y$100 than using grid$y$50, suggesting that coarse cells must be used in the wall-normal direction. In the same way, in Fig. 11b, the rms profile from the LES using grid$y$50 presents discrepancies with the DNS result on the channel half-height with a peak at $y^+ = 75$. On the contrary, using grid$y$100 and grid$y$150, the turbulent intensities are better predicted. In particular, the matching points are located on the DNS profiles in these cases. In Fig. 11c, the LES Reynolds stresses are lower when compared to the DNS result. For $y^+ > 500$, the highest turbulent levels are obtained using grid$y$150, supporting the idea to choose $\Delta y^+ > 100$, as is generally found in the literature [9,34,35].

Regarding the influence of the mesh resolution in the spanwise direction, the profiles obtained using grid$z$150, grid$z$100, and grid$z$50 are represented in Fig. 12. The mean and rms velocity profiles are superimposed. In particular, the mean velocity is correctly estimated in the logarithmic region, but its value is underpredicted compared to the DNS profile in the wake area. The turbulent intensities u'^+ are well predicted near the matching point for $y^+ \simeq 250$, and they are underestimated for $y^+ > 500$. The Reynolds stresses profiles obtained using grid$z$150 and grid$z$100 are very similar, whereas that from the LES using grid$z$50 provides higher turbulent levels, which are in better agreement with the DNS profile for $y^+ \geq 250$.

Regarding the influence of the mesh resolution in the streamwise direction, the profiles obtained in the LES with $100 \leq \Delta x^+ \leq 300$ are plotted in Fig. 13. They are very close to those represented in Fig. 12. They are superimposed over all the channel half-height, indicating grid convergence in direction x. According to these results, $\Delta x^+ = 300$ is sufficient for wall-modeled LES, although $\Delta x^+ \leq 260$ is generally chosen in the literature [9,34,35].

3. *Results for Isothermal Walls*

For simulations with isothermal walls as described in Sec. III.B.1, unfortunately, no corresponding DNS data are available. To bypass this issue, the results of the DNS of Hoyas and Jiménez [32] for the channel flow at $Re_\tau = 2000$ with adiabatic walls are used. Indeed, the flow has a low Mach number and the temperature gradient at the wall is sufficiently weak to consider the temperature as a passive scalar. The flow regime is considered as quasi incompressible in this case.

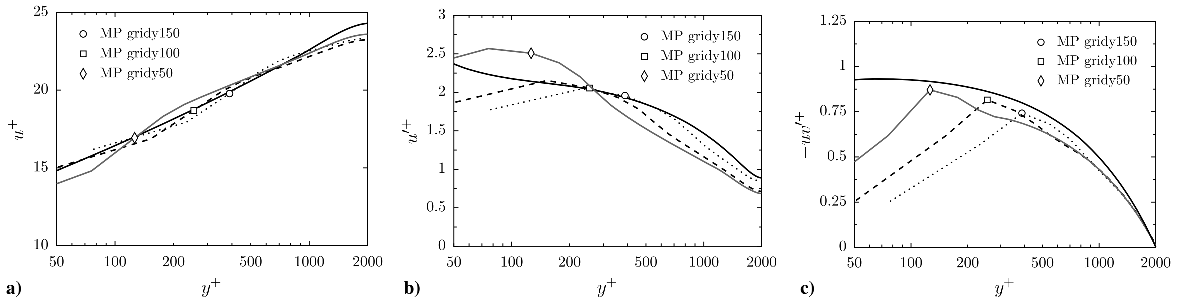

Fig. 11 Representations of a) mean streamwise velocities, b) rms streamwise velocities, and c) Reynolds shear stresses: LESs using grid$y$150 (dotted lines), grid$y$100 (dashed lines), and grid$y$50 (grey, solid lines); DNS of [32] (black, solid lines).

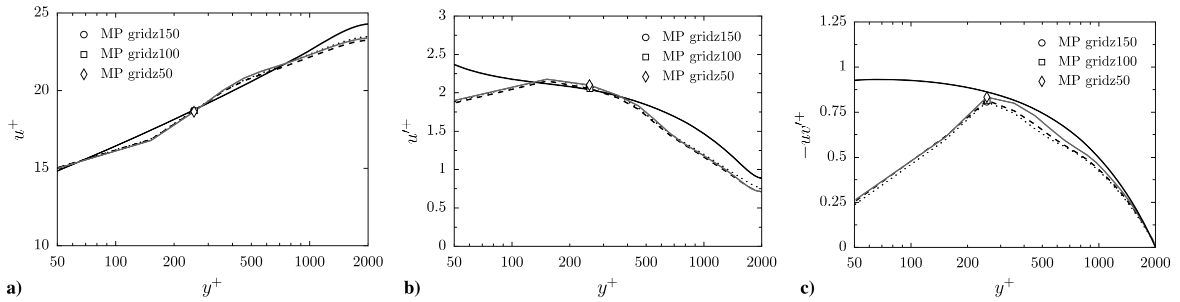

Fig. 12 Representations of a) mean streamwise velocities, b) rms streamwise velocities, and c) Reynolds shear stresses: LESs using grid$z$150 (dotted lines), grid$z$100 (dashed lines), and grid$z$50 (grey, solid lines); DNS of [32] (black, solid lines).

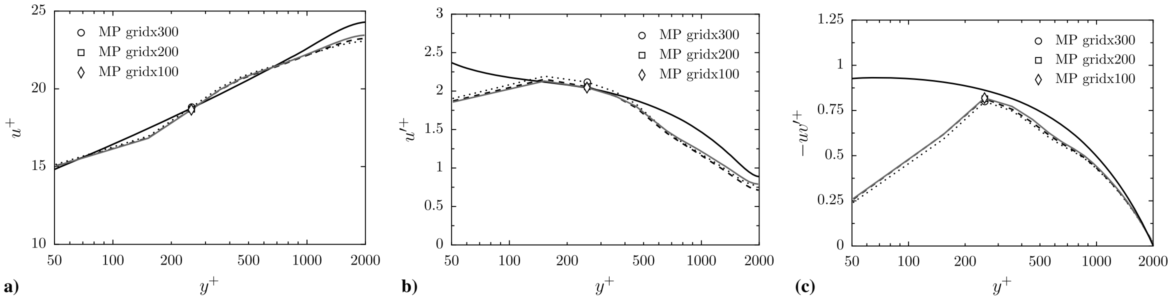

Fig. 13 Representations of a) mean streamwise velocities, b) rms streamwise velocities, and c) Reynolds shear stresses: LESs using grid*x*300 (dotted lines), grid*x*200 (dashed lines), and grid*x*100 (grey, solid lines); DNS of [32] (black, solid lines).

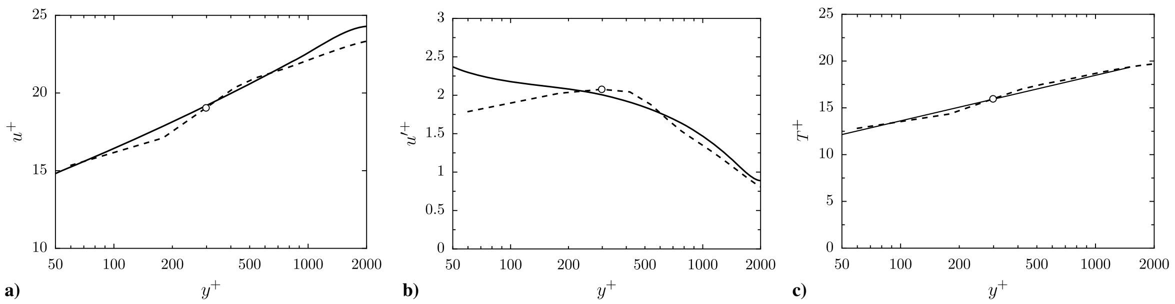

Fig. 14 Representations of a) mean and b) rms streamwise velocities: LES (dashed lines), and DNS of [32] (solid lines); and c) mean temperature: LES (dashed line) and Kader's law [29] (solid lines).

For brevity, only the results obtained using grid$x$200 are presented. The mean velocity u^+ and the rms component u'^+ are depicted in Figs. 14a and 14b, in wall units, as functions of the wall distance. They are compared with the DNS results of Hoyas and Jiménez [32]. The LES results are close to those given by the simulations with adiabatic walls in the previous section. The mean velocities obtained in the LES and in the DNS are in good agreement in the logarithmic zone, whereas small discrepancies are reported in the wake region for $y^+ > 1000$. The matching point represented by a circle in Fig. 14a is located on the DNS velocity profile. In Fig. 14b, the LES profile is close to the DNS profile for wall distances greater than the matching point position: that is, for $y_M^+ > 250$.

The evolution of the mean temperature along the wall distance y^+ is displayed in wall units in Fig. 14c. The profile estimated by Kader's law [29] is also represented for comparison. It is obtained from the wall law given by relation (22) using the values of the wall shear stress τ_w and the wall heat flux Φ_w, respectively, computed from the empirical coefficients of Petukhov [37] and Sleicher and Rouse [33]. The LES profile is in very good agreement with Kader's law [29].

These results suggest the capability of the present numerical algorithm to correctly estimate thermal effects with wall-modeled LES.

IV. Conclusions

In this paper, a numerical procedure is presented to perform a LES of wall-bounded flows using high-order implicit numerical schemes. The spatial discretization in the LES approach is carried out using a sixth-order compact scheme in conjunction with a sixth-order selective filter. A ghost cell reconstruction is proposed to apply these schemes in the near-wall regions. This approach is validated by computing a turbulent channel flow at a Reynolds number of $Re_\tau = 395$. In this case, the results agree very well with DNS data, which demonstrate that the LES algorithm, based on the use of a selective filter as a subgrid-scale model, can be applied to compute wall-bounded turbulent flows. For flows at high Reynolds numbers, a wall model is coupled with the high-order schemes to carry out LESs at an acceptable computational cost. In particular, a ghost cell reconstruction from the wall law velocity and temperature profiles is performed in order to apply the selective filter down to the wall. In addition, a matching point, for data exchange between the wall model and the LES algorithm, has to be chosen. The performance of the wall-modeled LES approach is examined for a turbulent channel flow at $Re_\tau = 2000$. The choice of the matching point is found to have a considerable influence on the LES results. Selecting a matching point far from the wall (typically for $y^+ > 150$) provides turbulent intensities in fairly good agreement with the DNS results of the literature, whereas the turbulent levels are underpredicted when the matching point is the first point above the wall. On the contrary, the choice of the ghost cell positions does not significantly affect the results. Moreover, a study of the grid sensitivity demonstrates that meshes with grid spacings of $\Delta x^+ = 300$, $\Delta y^+ = 100$, and $\Delta z^+ = 50$ are sufficiently refined to correctly predict the mean velocity and the turbulent intensities in the channel. Finally, the results obtained in the simulation performed for isothermal walls demonstrate the ability of wall-modeled LES to estimate thermal effects. Reliable results are thus expected when using the wall modeling approach in order to simulate more complex flow configurations, such as the development of a turbulent jet flow in the vicinity of the nozzle.

Appendix: Grid Sensitivity in Wall-Resolved Simulations

In Sec. II.B, a turbulent channel flow at $Re_\tau = 395$ has been simulated to evaluate the performance of the numerical algorithm. The influence of the spatial resolution of the channel on the LES

Table A1 Grid parameters to simulate a turbulent channel flow at $Re_\tau = 395$

LES	$n_x \times n_y \times n_z$	Δx^+	Δz^+	Δy_w^+	$\Delta y_{\max}^+$
Mesh M1	$101 \times 181 \times 121$	25	10	1	8
Mesh M2	$161 \times 181 \times 121$	15	10	1	8
Mesh M3	$161 \times 181 \times 241$	15	5	1	8

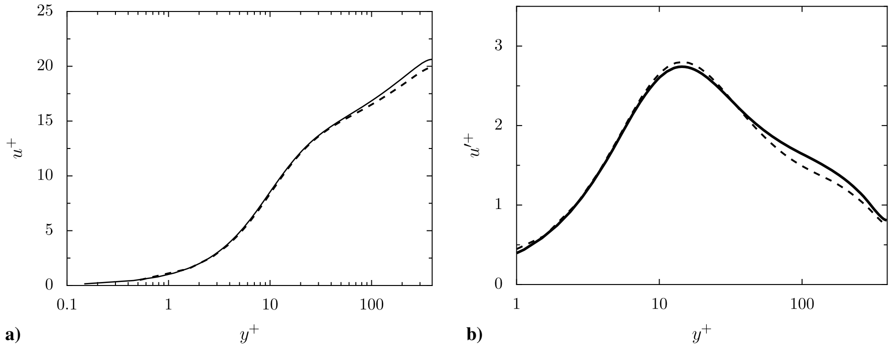

Fig. A1 Representations of a) mean and b) rms streamwise velocity profiles: LESs using mesh M1 (dashed–dotted lines), M2 (dotted lines), M3 (dashed lines); and DNS of [24] (solid lines).

results is now examined by performing three simulations using different meshes: M1, M2, and M3. The grid parameters (namely, the numbers of mesh points n_x, n_y, and n_z in each direction) as well as the streamwise, normal, and spanwise grid spacings (Δx^+, Δy^+, and Δz^+) in wall units are given in Table A1. The LES using mesh M2 corresponds to the simulation presented in Sec. II.B.

In wall-normal direction y, meshes M1, M2, and M3 are identical. In particular, at the wall, the grid spacing Δy_w^+ is equal to one. Further from the wall, the mesh is stretched in the y direction to obtain $\Delta y_{\max}^+ = 8$ at the center of the channel. In the streamwise and the spanwise directions, the grid spacings are uniform. They are equal to $\Delta x^+ = 25$ and $\Delta z^+ = 10$ in mesh M1, $\Delta x^+ = 15$ and $\Delta z^+ = 10$ in mesh M2, and $\Delta x^+ = 15$ and $\Delta z^+ = 5$ in mesh M3. The initial conditions and the procedure used to compute the statistical results are identical for the three computations. They are reported in Sec. II.B.3.

The mean longitudinal velocity profiles u^+ are displayed in wall units in Fig. A1a as a function of the wall distance y^+. For the three LESs, the agreement with the DNS is satisfactory in the inner region of the boundary layer for $y^+ \leq 20$. For values of $y^+ > 20$, discrepancies are observed between the profile of the LES using grid M1 and the DNS profile. For higher mesh resolution, differences between the LES and the DNS results are reduced. In particular, the LES performed with grid M3 provides a good agreement with the DNS.

The rms profiles for the streamwise velocity component u'^+, obtained in the three LESs and in the DNS of Abe et al. [24], are represented in Fig. A1b in wall units. In the LES using mesh M1, the amplitude of the peak is overestimated compared to the DNS results. The LES using refined grids M2 and M3 provide rms velocity profiles in better agreement with the DNS profile. In this case, the intensity of the rms peak is correctly estimated using the finest mesh, M3. These results demonstrate that the successive grid refinements in directions x and z allow the differences between the LES and the DNS to be reduced. In addition, using grid M3, one can note that increasing the grid resolution in direction z significantly improves the agreement with the DNS for both rms and mean velocity profiles.

Acknowledgments

This study is financially supported by Airbus. The postprocessing was performed using Antares.

References

[1] Colonius, T., and Lele, S. K., "Computational Aeroacoustics: Progress on Nonlinear Problems of Sound Generation," *Progress in Aerospace Sciences*, Vol. 40, No. 6, 2004, pp. 345–416. doi:10.1016/j.paerosci.2004.09.001

[2] Choi, H., and Moin, P., "Grid-Point Requirements for Large Eddy Simulation: Chapman's Estimates Revisited," *Center for Turbulence Research Annual Research Briefs*, Stanford Univ. Stanford, CA, 2011, pp. 31–36.

[3] Piomelli, U., and Balaras, E., "Wall-Layer Models for Large-Eddy-Simulations," *Annual Review of Fluid Mechanics*, Vol. 34, No. 1, 2002, pp. 349–374. doi:10.1146/annurev.fluid.34.082901.144919

[4] Deardorff, J. W., "A Numerical Study of Three-Dimensional Turbulent Channel Flow at Large Reynolds Numbers," *Journal of Fluid Mechanics*, Vol. 41, No. 2, 1970, pp. 453–480. doi:10.1017/S0022112070000691

[5] Schumann, U., "Subgrid Scale Model for Finite Difference Simulations of Turbulent Flows in Plane Channels and Annuli," *Journal of Computational Physics*, Vol. 18, No. 4, 1975, pp. 376–404. doi:10.1016/0021-9991(75)90093-5

[6] Slotnick, J., Khodadoust, A., Alonso, J., Darmofal, D., Gropp, W., Lurie, E., and Mavriplis, D., "CFD Vision 2030 Study: A Path to Revolutionary Computational Aerosciences," NASA CR-2014-218178, 2014.

[7] Kawai, S., and Larsson, J., "Wall-Modeling in Large Eddy Simulation: Length Scales, Grid Resolution, and Accuracy," *Physics of Fluids*, Vol. 24, No. 1, 2012, Paper 015105. doi:10.1063/1.3678331

[8] Lodato, G., Castonguay, P., and Jameson, A., "Structural Wall-Modeled LES Using a High-Order Spectral Difference Scheme for Unstructured Meshes," *Flow, Turbulence and Combustion*, Vol. 92, Nos. 1–2, 2014, pp. 579–606. doi:10.1007/s10494-013-9523-3

[9] Bocquet, S., Sagaut, P., and Jouhaud, J., "A Compressible Wall Model for Large-Eddy Simulation with Application to Prediction of Aerothermal Quantities," *Physics of Fluids*, Vol. 24, No. 6, 2012, Paper 065103. doi:10.1063/1.4729614

[10] Cambier, L., Heib, S., and Plot, S., "The Onera Elsa CFD Software: Input from Research and Feedback from Industry," *Mechanics and Industry*, Vol. 14, No. 3, 2013, pp. 159–174. doi:10.1051/meca/2013056

[11] Fosso, A., Deniau, H., Sicot, F., and Sagaut, P., "Curvilinear Finite Volume Scheme Using High Order Compact Intepolation," *Journal of Computational Physics*, Vol. 229, No. 13, 2010, pp. 5090–5122. doi:10.1016/j.jcp.2010.03.027

[12] Lele, S. K., "Compact Finite Difference Schemes with Spectral-Like Resolution," *Journal of Computational Physics*, Vol. 103, No. 1, 1992, pp. 16–42. doi:10.1016/0021-9991(92)90324-R

[13] Visbal, M. R., and Gaitonde, D. V., "On the Use of Higher-Order Finite-Difference Schemes on Curvilinear and Deforming Meshes," *Journal of Computational Physics*, Vol. 181, No. 1, 2002, pp. 155–185. doi:10.1006/jcph.2002.7117

[14] Bogey, C., and Bailly, C., "Computation of a High Reynolds Number Jet and Its Radiated Noise Using Large Eddy Simulation Based on Explicit Filtering," *Computers and Fluids*, Vol. 35, No. 10, 2006, pp. 1344–1358. doi:10.1016/j.compfluid.2005.04.008

[15] Fauconnier, D., Bogey, C., and Dick, E., "On the Performance of Relaxation Filtering for Large-Eddy Simulation," *Journal of Turbulence*, Vol. 14, No. 1, 2013, pp. 22–49. doi:10.1080/14685248.2012.740567

[16] Kremer, F., and Bogey, C., "Large-Eddy Simulation of Turbulent Channel Flow Using Relaxation Filtering: Resolution Requirement and Reynolds Number Effects," *Computers and Fluids*, Vol. 116, Aug. 2015,

pp. 17–28.
doi:10.1016/j.compfluid.2015.03.026

[17] Lazareff, M., Vuillot, A. M., and Cambier, L., "elsA Theoretical Manual," Ver. 2.1, Reference /ELSA/STB-97020, Property of ONERA, 2010.

[18] Bogey, C., and Bailly, C., "A Family of Low Dispersive and Low Dissipative Explicit Schemes for Flow and Noise Computations," *Journal of Computational Physics*, Vol. 194, No. 1, 2004, pp. 194–214.
doi:10.1016/j.jcp.2003.09.003

[19] Fosso, A., Deniau, H., Lamarque, N., and Poinsot, T., "Comparison of Outflow Boundary Conditions for Subsonic Aeroacoustic Simulations," *International Journal for Numerical Methods in Fluids*, Vol. 68, No. 10, 2012, pp. 1207–1233.
doi:10.1002/fld.v68.10

[20] Fosso Pouangué, A., Sanjosé, M., Moreau, S., Daviller, G., and Deniau, H., "Subsonic Jet Noise Simulations Using Both Structured and Unstructured Grids," *AIAA Journal*, Vol. 53, No. 1, 2015, pp. 55–69.
doi:10.2514/1.J052380

[21] Carpenter, M. H., Gottlieb, D., and Abarbanel, S., "Time-Stable Boundary Conditions for Finite-Difference Schemes Solving Hyperbolic Systems: Methodology and Application to High-Order Compact Schemes," *Journal of Computational Physics*, Vol. 111, No. 2, 1994, pp. 220–236.
doi:10.1006/jcph.1994.1057

[22] Sengupta, T. K., Ganeriwal, G., and De, S., "Analysis of Central and Upwind Compact Schemes," *Journal of Computational Physics*, Vol. 192, No. 2, 2003, pp. 677–694.
doi:10.1016/j.jcp.2003.07.015

[23] Abe, H., Kawamura, H., and Matsuo, Y., "Direct Numerical Simulation of a Fully Developed Turbulent Channel Flow with Respect to the Reynolds Number Dependence," *Journal of Fluids Engineering*, Vol. 123, No. 2, 2001, pp. 382–393.
doi:10.1115/1.1366680

[24] Abe, H., Kawamura, H., and Choi, H., "Very Large-Scale Structures and Their Effects on the Wall Shear-Stress Fluctuations in a Turbulent Channel Flow up to $Re_\tau = 60$," *Journal of Fluids Engineering*, Vol. 126, No. 5, 2004, pp. 835–843.
doi:10.1115/1.1789528

[25] Moser, R. D., Kim, J., and Mansour, N. N., "Direct Numerical Simulation of Turbulent Channel Flow up to $Re_\tau = 560$," *Physics of Fluids*, Vol. 11, No. 4, 1999, pp. 943–945.
doi:10.1063/1.869966

[26] Cabrit, O., "Direct Simulations for Wall Modeling of Multicomponent Reacting Compressible Turbulent Flows," *Physics of Fluids*, Vol. 21, No. 5, 2009, Paper 055108.
doi:10.1063/1.3123528

[27] Kremer, F., "Étude Numérique D'Écoulements de Paroi Compressibles: Méthodes D'Intégration Temporelle Semi-Implicites et Application du Canal Plan Turbulent," Ph.D. Thesis, École Centrale de Lyon, Lyon, France, 2012.

[28] Reichardt, H., "The Fundamentals of Turbulent Heat Transfer," *Archiv fuer die Gesamte Waermetechnik, (West Germany)*, Vol. 6, Nos. 6/7, 1951, pp. 129–143.

[29] Kader, B. A., "Temperature and Concentration Profiles in Fully Turbulent Boundary Layers," *International Journal of Heat and Mass Transfer*, Vol. 24, No. 9, 1981, pp. 1541–1544.
doi:10.1016/0017-9310(81)90220-9

[30] van Driest, E. R., "Turbulent Boundary Layer in Compressible Fluids," *Journal of the Aeronautical Sciences*, Vol. 18, No. 3, 1951, pp. 145–160.
doi:10.2514/8.1895

[31] Aikens, K. M., Dhamankar, N. S., Martha, C. S., Yingchong, S., Blaisdell, G. A., Lyrintzis, A. S., and Li, Z., "Equilibrium Wall Model for Large Eddy Simulations of Jets for Aeroacoustics," *AIAA SciTech, 52nd Aerospace Sciences Meeting*, AIAA Paper 2014-0180, 2014.

[32] Hoyas, S., and Jiménez, J., "Scaling of the Velocity Fluctuations in Turbulent Channels up to $Re_\tau = 2003$," *Physics of Fluids*, Vol. 18, No. 1, 2006, Paper 011702.
doi:10.1063/1.2162185

[33] Sleicher, C. A., and Rouse, M. W., "A Convenient Correlation for Heat Transfer to Constant and Variable Property Fluids in Turbulent Pipe Flow," *International Journal of Heat and Mass Transfer*, Vol. 18, No. 5, 1975, pp. 677–683.
doi:10.1016/0017-9310(75)90279-3

[34] Bodart, J., and Larsson, J., "Wall-Modeled Large Eddy Simulation in Complex Geometries with Application to High-Lift Devices," Center for Turbulence Research, Annual Research Briefs, Stanford Univ., Stanford, CA, 2011, pp. 37–48.

[35] Lee, J., Cho, M., and Choi, H., "Large Eddy Simulations of Turbulent Channel and Boundary Layer Flows at High Reynolds Number with Mean Wall Shear Stress Boundary Conditions," *Physics of Fluids*, Vol. 25, No. 11, 2013, Paper 110808.

[36] Park, G. I., and Moin, P., "An Improved Dynamic Non-Equilibrium Wall-Model for Large Eddy Simulation," *Physics of Fluids*, Vol. 26, No. 1, 2014, Paper 015108.
doi:10.1063/1.4861069

[37] Petukhov, B. S., "Heat Transfer and Friction in Turbulent Pipe Flow with Variable Physical Properties," *Advances in Heat Transfer*, Vol. 6, 1970, pp. 503–564.
doi:10.1016/S0065-2717(08)70153-9

M. R. Visbal
Associate Editor

Chapter 5

Jet noise source mechanisms

In this chapter, two papers dealing with jet noise are included. The first is from Romain Biolchini (Cifre Safran/Cerfacs/LMFA) PhD thesis and the second is part of the work of Carlos Pérez Arroyo (FP7 Marie Curie Action).

5.1 Subsonic jet flow

During the PhD thesis of Romain Biolchini, defended in 2017, temperature effects on jet noise was aborded. The following paper presents this work considering a realistic subsonic dual stream jet.

R. Biolchini, G. Daviller, C. Bailly, and G. Bodard. Temperature effects on the noise source mechanisms in a realistic subsonic dual-stream jet. *Computers & Fluids*, 213, 2020. https://doi.org/10.1016/j.compfluid.2020.104720

Temperature effects on the noise source mechanisms in a realistic subsonic dual-stream jet

Romain Biolchini [a,c], Guillaume Daviller [a,*], Christophe Bailly [b], Guillaume Bodard [c]

[a] CERFACS, 31100 Toulouse, France
[b] LMFA, Ecole Centrale de Lyon, 69134, France
[c] Safran Aircraft Engines, Aerodynamics and Acoustics Department, 77550 Moissy-Cramayel, France

ARTICLE INFO

Article history:
Received 10 February 2020
Revised 24 July 2020
Accepted 14 August 2020
Available online 19 September 2020

Keywords:
Dual-stream jet noise
Large-eddy simulation
Temperature effects

ABSTRACT

A detailed numerical investigation of temperature effects on both aerodynamics and acoustics of a dual-stream jet including a central plug is carried out. The geometry is representative of a realistic turbofan with a high by-pass-ratio (BPR) close to 9. Two take-off high-subsonic operating points are investigated numerically by compressible large-eddy simulation. For these two selected points, the secondary stream is exactly the same in terms of static temperature and velocity. Both jets have also the same primary velocity. The only difference lies in the static temperature of the primary jet. There is a ratio of two between the two jets considered in this study, namely $T_j = 400$ K and $T_j = 800$ K. More precisely, the primary jet temperature is reduced while keeping the acoustic Mach number constant, leading to an increase of the primary jet Mach number from $M_j = 0.65$ in the heated case to $M_j = 0.89$ in the cold case. Some experimental data are available for the hot jet while the cold jet is introduced for academic reasons. The heated jet compares reasonably well with the experimental data, taking into account the complexity of the geometry. Temperature effects have a limited impact on aerodynamic development and acoustic radiation. The influence of the core flow is found to be weak due to the high BPR considered and the radiated acoustic is mainly driven by the secondary flow. Further investigations are carried out in order to highlight the differences between the two cases. The acoustic production area are identified by the way of axial velocity skewness coefficient maps. Finally, a decrease of the primary stream temperature leads to the development of trapped acoustic waves inside the jet core. An increase of the overall sound spectrum level about 5 dB is thus observed in the upstream direction for the cold jet, in agreement with the vortex sheet theory.

1. Introduction

Noise pollution produced by commercial aircraft is a major environmental challenge in the next few years. Despite the mechanical reduction of noise induced by the architecture evolution of turbofan engines, with the increase of the fan diameter and the by-pass ratio, the propulsive jet remains a major component to the total noise during the take-off phase. As a consequence, research efforts on jet mixing noise are being pursued through experimental investigations and numerical studies. The latter have a privileged role, in particular compressible large-eddy simulation (LES), to directly obtain the turbulent flow and the radiated acoustic field in a large physical domain [1–4]. An increasingly clear picture of the role played by different turbulent flow regions for acoustic radiation has emerged over time, at least for isolated subsonic jets. The importance of initial conditions for convective shear flows has also been pointed out [5], in connection with the value of the Reynolds number in numerical simulations.

The noise radiated by dual-stream jets has also been investigated. Numerically, a direct noise computation of a coplanar coaxial hot jet has been performed by Bogey et al. [6]. Increasing the complexity of the geometries, Viswanathan et al. [7] have studied the flow field and noise from dual beveled nozzles. The influence of numerical parameters on the noise radiated by a dual-stream jets of a short cowl nozzle has been investigated by Andersson et al. [8] using a block-structured finite-volume approach. Unstructured meshes [9] are, however, most often used to tackle such complex configurations. The numerical simulation of convective coaxial turbulent flows with the presence of multiple velocity and temperature gradients, requires the use of high-order numeri-

* Corresponding author.
E-mail address: guillaume.daviller@cerfacs.fr (G. Daviller).

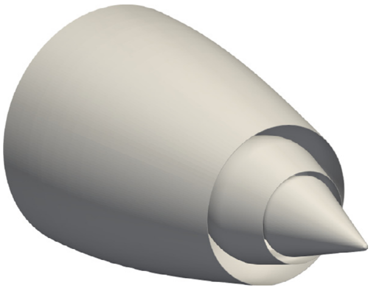

Fig. 1. Geometry of the baseline EXEJET nozzle [16].

cal solvers and suitable turbulence models [10,11]. A good overview of best practices for jet aeroacoustics can be found in the work by Brès et al. [12], see also references herein.

Only a few experimental [13,14] studies deal with more realistic configurations. The EXEJET experimental project [15] was conducted in order to document the noise radiated by a realistic jet having a bypass ratio of 9, including flight effects, the presence of a plug nozzle and also possible installation effects. The baseline nozzle geometry is shown in Fig. 1. The turbulent flow and noise database [16] is representative of new airliners operating at take-off conditions, and was generated to support the validation of advanced numerical tools. In the present study, one operating point selected from the EXEJET database is simulated, corresponding to a take-off condition without flight effects. The primary stream is characterized by a high speed subsonic stream and a static temperature $T_j = 800$ K. In addition, a second point, not present in the database, is also computed with the same nominal parameters except the static temperature of the primary stream, $T_j = 400$ K. The aim of the present work is to complement the EXEJET experimental project with a numerical investigation based on LES. The objective is to have a thorough knowledge of the flow and noise radiated by coaxial jets exhausting from a plug nozzle, with a focus on temperature effects induced by the primary hot stream.

Temperature effects on jet noise still remain a tricky problem in aeroacoustics, even for an isolated single jet. Pioneering experimental studies [17,18] have shown the emergence of an additional noise component related to entropy fluctuations, as predicted by Lighthill's analogy [19]. There is however no general agreement regarding extra sources associated with entropy fluctuations. Indeed, related measurements have recently been completed by Viswanathan [20] and Bridges & Wernet [21], by avoiding two pitfalls. First, the heating system itself can introduce a spurious noise component in such experiments. Second, increasing the temperature for a given geometry decreases the Reynolds number value of the jet. As observed experimentally by Zaman [22] and numerically by Bogey et al. [23], a too low Reynolds number value ($Re_j < 10^5$) will not allow a turbulent state of the boundary layer at the nozzle exit. These difficulties can be partly overcomed by numerical simulations, and the reader can refer to the study by Bogey & Marsden [24] for a deeper discussion regarding the separation of temperature effects with respect to Reynolds number effects. Furthermore, Towne et al. [25] have shown that an acoustic resonance could appear in the potential core for particular velocity and temperature exhaust conditions, whose characteristics can be predicted by a vortex-sheet model.

Fisher et al. [26] have developed a semi-empirical model based on dimensional laws for a coaxial jet. The radiated noise is basically obtained by the quadripolar contribution of the cold secondary flow and the dipolar contribution of the hot primary stream, that is noise induced by velocity fluctuations and temperature fluctuations respectively. More recently, Viswanathan [27] has performed a parametric study on temperature effects in dual-stream jets. For fixed Nozzle Pressure Ratio in both primary (NPR=2.1) and secondary (NPR=1.6) jets, the author has observed that the increase of primary jet's temperature leads to a uniform increase of sound pressure level (SPL) for all angles of observation. A cold subsonic secondary stream at fixed Mach number $M = 0.85$ and a slightly supersonic primary stream with different exit velocities (depending on the temperature ratio) were considered. As a consequence, it is difficult to link the increase of the SPL to the temperature ratio of the primary jet only.

In the present work, two large-eddy simulations based on the realistic turbofan jet nozzle, displayed in Fig. 1, are performed in order to investigate the noise radiated by a dual-stream jet in the presence of temperature effects. The two operating points and the nozzle design are first described. The numerical methodology, the mesh construction and the inflow boundary conditions are provided in a next section. The aerodynamic behaviour of both jets is then analyzed and compared to available experimental data, with a specific investigation on temperature fluctuations. The acoustic far field is extrapolated from a control surface and the radiated sound field is studied in a subsequent section. Numerical predictions are again validated with available measurements. The last section is devoted to the identification of a strong acoustic resonance taking place in the primary stream, leading to acoustic tones observed in the far field [28,29]. The model developed by Towne et al. [25] is applied with success to predict this behaviour as a function of the temperature ratio between the two streams. Concluding remarks are finally drawn.

2. Geometry and flow parameters

The dual-stream nozzle considered in this study includes a central plug, as shown in Fig. 1, and corresponds to the baseline configuration in Huber et al. [15] for a nominal bypass ratio of 9. In order to investigate temperature effects, two subsonic operating points at take-off conditions without flight effects have been retained. The first dual-stream jet, denoted T800, has a hot primary stream and corresponds to a point documented in the database [15]. The second, denoted T400, has been defined for academic purposes with a cold primary stream, but has no experimental counterpart. The primary exhaust velocity of both jets are the same, and only the temperature of the primary stream differs. However, whereas the acoustic Mach number is keep constant for the two case, a temperature decrease at constant exhaust velocity leads to an increase of the jet Mach number. The jet properties of the secondary stream are identical. To validate the LES simulation of the jet T800, the following measurements extracted from the EXEJET database can be used: first, the mean flow field from Particles Image Velocimetry (PIV) data without flight effects; second, five-hole probe measurements coupled with thermocouples at the nozzle exhaust with flight effects; and third, sound pressure levels in the far field at $r = 40D^s_{\mathrm{ef}}$ for polar angle between 30° and 140°, again without flight effect. For the second set of measurements, it is assumed that the primary and secondary streams at the nozzle exit are not affected by flight effects.The effective diameter of the secondary stream D^s_{ef} is defined as the difference between the secondary stream diameter and the primary stream nacelle diameter at the secondary jet exit plane, that is $D^s_{ef} = \sqrt{D_j^{s2} - D_p^2(x = x^s_{ep})}$, where x^p_{ep} and x^s_{ep} are the axial coordinate of the primary and secondary flow exhaust planes. The primary effective aerodynamic diameter is defined as $D^p_{ef} = \sqrt{D_j^{p2} - D^2_{plug}(x = x^p_{ep})}$. The notations are also displayed in Fig. 2 (b), along with the computational domain at the nozzle exhaust. Details about acoustic measurements can be found in [15], whereas methodologies about PIV and five-hole probe measurements are presented in David et al. [16].

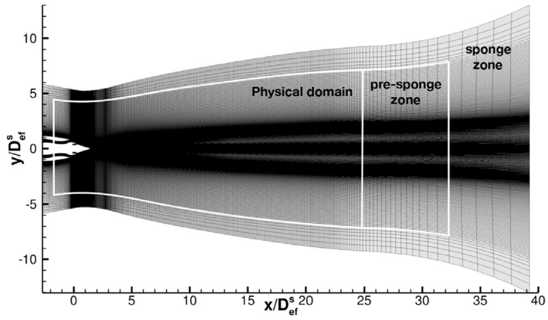

(a)

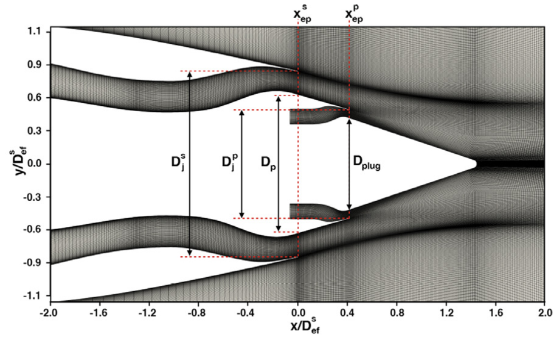

(b)

Fig. 2. Mesh of the computational domain containing the jet axis, only every second point is shown: (a) whole computational domain (b) zoom around the nozzle exit.

Table 1
Flow properties of the two jets T800 & T400 [15].

	primary stream				secondary stream			
jet	M^p	M_j^p	T_j^p (K)	Re_D^p	M^s	M_j^s	T_j^s (K)	Re_D^s
T800	1.07	0.65	776	5.5×10^5	0.84	0.82	286	3.8×10^6
T400	1.07	0.89	405	1.7×10^6	0.84	0.82	286	3.8×10^6

The flow properties of both jets are summarized in Table 1. Both jet flows are characterized by an acoustic Mach number of $M^p = U_j^p/c_0 = 1.07$ for the primary stream and $M^s = U_j^s/c_0 = 0.84$ for the secondary stream, where U_j denotes the primary exhaust velocity and c_0 the ambient speed of sound. The superscripts $.^p$, and $.^s$ are respectively associated with the primary and secondary streams. In addition, M_j stands for the Mach number of the jet and T_j for the exhaust static temperature.

The T800 case is characterized by a temperature ratio of $T_j^p/T_j^s = 2.7$ and a diameter-based Reynolds number of the primary jet $Re^p = U_j^p D^p/\nu_j = 5.5 \times 10^5$. In the T400 case the temperature ratio is 1.4 and the Reynolds number is $Re^p = 1.7 \times 10^6$. The Reynolds number of the secondary stream is $Re^s = U_j^s D^s/\nu_j = 3.8 \times 10^6$ for both cases. The two jet parameters have been chosen to preserve a primary stream Reynolds number value for the hot case greater than the threshold around 4×10^5, for which Reynolds number effects can interfere with temperature effects [20].

3. Numerical methods

3.1. Flow solver

The present numerical simulations have been performed with the *elsA* solver [30]. The compressible Navier-Stokes equations are solved on structured body-fitted grids using a finite volume formulation. Optimized finite-difference schemes developed for computational aeroacoustics are implemented. The temporal discretization is performed by a six-step Runge-Kutta scheme, developed by Bogey et al. [31]. In the two simulations, the same time step Δt is chosen to satisfy the Courant-Friedrichs-Lewy criterion CFL = 0.9 for both jets. A sixth-order compact scheme adapted by Fosso et al. [32] is used for the spatial discretization, combined with a sixth order compact filter proposed by Visbal & Gaitonde [33]. This filter also acts as an explicit subgrid scale model. As a consequence, small scales discretized by less than four points perwavelength are removed without affecting the larger scales of the turbulent flow [34].

The boundary conditions used for the Reynolds-averaged Navier-Stokes (RANS) simulations are imposed as follows. At the inlet of each duct, an in-going subsonic condition prescribes the total pressure P_t, the total temperature T_t is then used to get the target Mach number (see 1). The ambient pressure is imposed on the side and downstream limits. To ensure stability and a faster convergence of the simulations, a low co-flow ($u/U_j^p = .05$) is imposed on the free stream inflow around the nozzle. Finally adiabatic no-slip wall conditions are applied to the nozzle surface. In LES, a three dimensional formulation of acoustic radiation conditions [35] based on Tam and Dong conditions [36] is imposed on the side and downstream boundaries of the computational domain. Moreover, a sponge zone is added when the convective flow leaves the physical domain. In this zone, the grid is stretched by a ratio of 10% in order to dissipate the most energetic turbulent structures. This numerical procedure is however not sufficient, and some spurious waves can still be generated. A second-order filter combined with a cooling term [37] are also applied in the sponge zone. This outflow condition has shown the best results in the ***elsA*** software [38]. The inflow conditions of both streams are prescribed using the radiative boundary condition of Tam and Webb [39]. As for outflow boundary conditions, a sponge zone where a cooling term is applied to the conservative field to preserve exhaust conditions is used in the LES stages [40]. The turbulent state of the incoming flow is mimicked by the addition of a vortex ring tripping. The aim of such procedure is not to reach a fully developed turbulent boundary layer, which is overly demanding in CPU cost, but to mimic this stage. All the detail of the procedure is explain in Bogey et al. [41]. The vortex center is added in the nozzle boundary layer, at $r_{vr} = r_{wall}(x_{vr}) - \delta_0(x_{vr})$ where r_{vr} and x_{vr} are respectively the radius and the axial coordinate of the vortex ring center, $r_{wall}(x_{vr})$ the radius of the wall at x_{vr} and $\delta_0(x_{vr})$ the boundary layer thickness at x_{vr}. In the primary stream $x_{vr} = -0.018D_j^s$ and $\delta_0(x_{vr}) = 0.003D_j^s$, while in the secondary flow $x_{vr} = -0.9D_j^s$ and $\delta_0(x_{vr}) = 0.017D_j^s$. In the LES, a wall law based on Reichardt's analytical expression [42] is applied to all the walls. More details on the implementation of this numerical procedure in a high-order workflow can be found in Le Bras et al. [11].

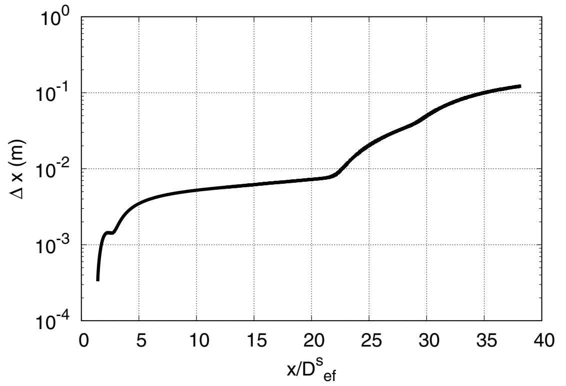

(a)

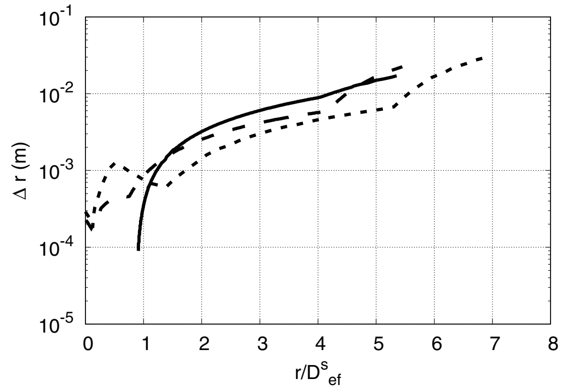

(b)

Fig. 3. Mesh distribution along: (a) the centerline and (b) radial lines at $x = 0.65D^s_{ef}$ (——), $3.3D^s_{ef}$ (– – –) and $10D^s_{ef}$ (……).

3.2. Mesh construction

A view of the computational domain is shown in Fig. 2 (a). The total length of the domain is approximately $39D^s_{ef}$ in the axial direction and $11D^s_{ef}$ in the radial direction at $x = 0$. The dimensions of the physical domain are approximately $25D^s_{ef}$ in the axial direction and $8D^s_{ef}$ in the radial direction at $x = 0$. The origin of the coordinate system is placed on the jet axis and in the secondary stream exit plane. The outer shape of the computational domain follows the jet flow expansion in the physical domain and the mesh stretching in the sponge zone as explained below.

The mesh is constructed with the aim to ensure a cut off frequency f_c of 7500 Hz for acoustic waves in the physical domain on the largest grid cell, which corresponds to the Strouhal cut-off number $\mathrm{St} = f \times D^s_{ef}/U^s_j = 4$. The second limit is the mesh size at the wall, which is constructed to obtain a distance in wall unit of $y^+ = yu_\tau/\nu = 40$ with u_τ the friction velocity. The expansion ratio is maintained under 4% in the physical domain to avoid the production of spurious noise. In the nozzle, the grid size in the axial direction is constant and chosen as $\Delta x = 3\Delta r_{wall}$ to ensure a good discretization of turbulence. The total mesh size is about 256×10^6 cells with $N_x = 1200$, $N_r = 600$ and an azimuthal discretization $N_\theta = 256$. This leads to an azimuthal grid size of $\Delta\theta^p = 8\Delta r_{wall}$ and $\Delta\theta^s = 15\Delta r_{wall}$ on the primary jet leap and on the secondary jet leap, respectively. The grid spacing at the secondary nozzle exhaust in the axial and azimuthal direction in wall unit are $x^+ = 180$ and $\theta^+ = 680$, respectively. The same mesh is used for the two operating points.

In Fig. 2 (b) refinement zones are also clearly visible close to the nozzle exit planes and in the shear layers. The mesh distribution on the centerline and on radial lines for three axial positions $0.65D^s_{ef}$, $3.3D^s_{ef}$ and $10D^s_{ef}$ are plotted in Fig. 3 (a) and (b) respectively. As shown in Fig. 3 (a), the smallest axial discretization is located just after the plug tip with $\Delta_x = 3 \times 10^{-4}$ m. Then, the mesh is stretched in the axial direction until $x = 5D^s_{ef}$, which corresponds to the merging point of the two streams. After this position, the axial distribution increases to reach the maximal mesh size $\Delta_x = 8 \times 10^{-3}$ m at $x = 22D^s_{ef}$. In the axial direction, a pre-sponge layer is added before the sponge zone in order to obtain a smoother transition between the physical zone and the sponge zone.

3.3. Simulation stages

In order to prescribe the initial conditions at the boundaries with accuracy, a two stage RANS-LES calculation is applied. This methodology has been developed by Shur et al. [43–45]. First, the boundary conditions are computed by a RANS simulation with a Spalart-Allmaras turbulence model [46]. For this kind of simulation a dedicated RANS mesh is used, which is wall-resolved in the entire nozzle to obtain an accurate description of the boundary layers. This mesh is composed by a total of 13×10^6 cells. The computation reaches a converged state when the residuals are reduced by three orders of magnitude using the Roe third-order spatial scheme.

The RANS solutions at the secondary stream exit $x = 0$ are compared with the five-hole probe from T800 experiment (with flight effects, see Section 2) in Fig. 4, for the radial profile of the mean axial velocity (a) and the temperature (b). Keeping in mind that the conditions for T800 and T400 are identical for the secondary stream, consistent results are obtained and compare well with experiment [15]. The differences observed for $y > 0.5D^s_j$ are due to the flight effect in the experiment, not taken into account in the simulations. As a consequence, a boundary layer is present on the external part of the nacelle in the experiment. The non-zero flow around the nacelle is induced by the small coflow added in the simulation, see Section 3.1, and also by entrainment.

Fig. 5 (a) and (b) show respectively the axial velocity and temperature radial profiles at the primary stream exit $x = 0.25D^s_j$. Velocity profiles of the primary stream are identical for both cases (as defined in Table 1) and are in agreement with experimental data ($y < 0.3D^s_j$). Regarding the differences on the velocity profile for $y > 0.3D^s_j$, they are again due to the flight effect which is not take into account here. The radial temperature profile in the primary jet is also in agreement with experiment for the case T800 and divided by two for the case T400.

In Figs. 4 and 5, the radial profiles obtained by LES at the same localization are also plotted. It can be observed that the inflow boundary conditions used in both LES allow to retrieve the exhaust velocity profiles of both streams.

An additional step is performed between the RANS simulation and the high-order LES. It consists of the computation of a transitional flow with Roe third-order scheme on a coarser grid. This coarse grid has only one point over two in each direction which divides by eight the total number of cells compare to the full mesh. Including the transient time needed to obtain an instantaneous solution from a stationary one, this procedure led to a saving of 30% of CPU time during the transition step between a classical computation and the LES low-order methodology. The last step of the process is finally to compute the flow with the high-order algorithm and on the full resolved mesh. The low order solution is first

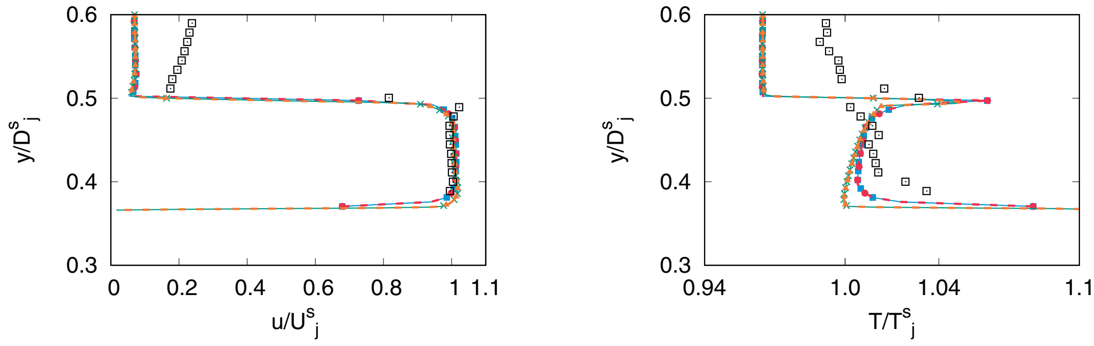

(a) (b)

Fig. 4. Radial profile at the nozzle exit of the secondary flow $x = 0$: (a) axial velocity and (b) static temperature. RANS : —●— T800 ; —■— T400; LES : —▲— T800; —×— T400 and ⊡ Experiment [16].

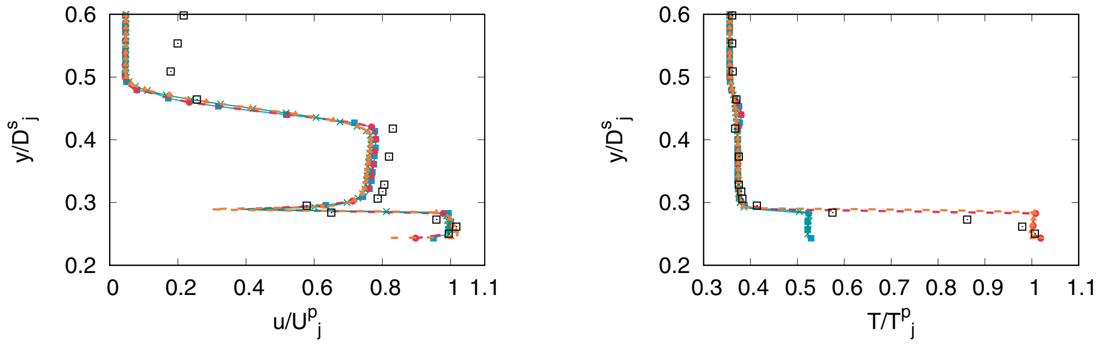

(a) (b)

Fig. 5. Radial profile at the nozzle exit of the primary flow $x = 0.25D^s_j$: (a) axial velocity and (b) static temperature. RANS : —●— T800 ; —■— T400; LES : —▲— T800; —×— T400 and ⊡ Experiment [16].

Table 2
Simulation times of the three step for both cases T800 & T400.

	Iterations	$\Delta t(s)$	$T(ms)$	$T \times U^p_j/D^p_j$	f_{min} (Hz)	St_{min}	CPU time / simulation (kh)
(1) RANS	310×10^3	-	-	-	-	-	4
(2) LES	300×10^3	1×10^{-7}	30	90	-	-	35
(3) LES	950×10^3	3×10^{-8}	30	90	350	0.2	1 160

evacuated from the computational domain before starting the flow statistics record. During this stage, the time step is $\Delta t = 3 \times 10^{-8}$s and the total simulated time is $T = 32.5$ms. Assuming that a temporal event is resolved if the total time contains 10 times its periods, the minimal frequency associated with the simulation time is $f_{min} = 350$Hz or $St_{min} = f \times D^s_{ef}/U^s_j = 0.2$. All computation times are summarized in Table 2.

4. Analysis of aerodynamic fields

An instantaneous snapshot of the T800 jet flow field in the physical LES domain, identified from the vorticity norm $|\Omega| = \sqrt{\omega_x^2 + \omega_y^2 + \omega_z^2}$ is shown in Fig 6. The acoustic radiation is also depicted with a map of the fluctuating pressure. The vorticity field exhibits large structures after $x = 5D^s_{ef}$ and smaller one close to the nozzle exit and the central plug. No spurious wave is identifiable in the acoustic field. The jet noise directivity is characterized with low frequency waves traveling downstream and higher frequency waves propagating perpendicular to the nozzle. Differences are too

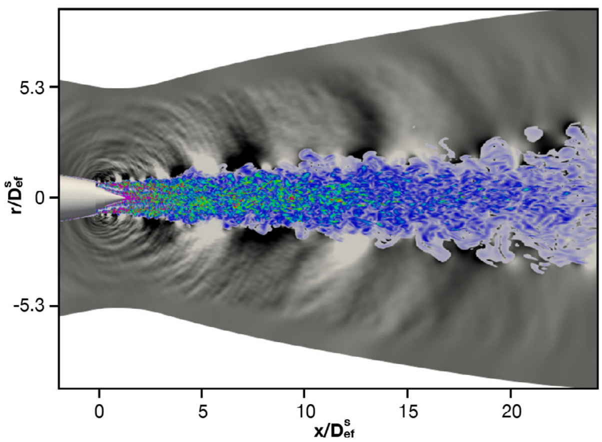

Fig. 6. T800 case: Instantaneous vorticity field $4 \times 10^2 \leq |\Omega|(s^{-1}) \leq 3 \times 10^6$ superimposed on the fluctuating pressure field $-200 \leq p'(\text{Pa}) \leq 200$ in the physical domain of the simulation.

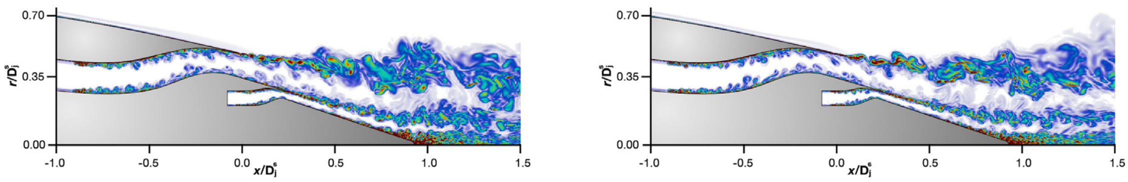

(a) T800 (b) T400

Fig. 7. Longitudinal plane of the instantaneous vorticity modulus $5 \times 10^2 \leq |\Omega|(s^{-1}) \leq 3 \times 10^6$ in the vicinity of the nozzle exit.

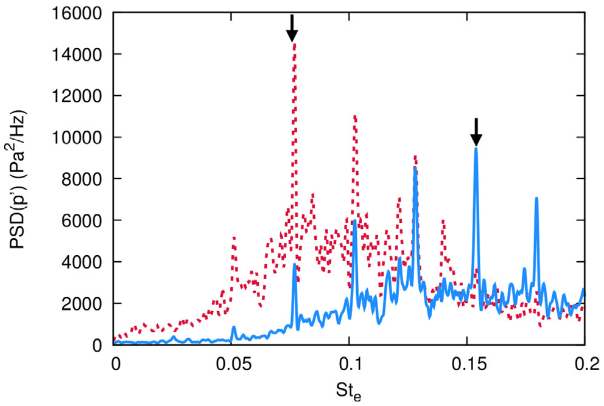

Fig. 8. T800 case: PSD of pressure fluctuations at $r = 0.44D_j^s$ for axial positions : —— $x = 0.2D_j^s$ and – – – $x = 0.3D_j^s$. Arrows mark the frequencies $St_0 = 0.154$ and $St_0/2 = 0.076$.

minor to perform a visual comparison with the T400 jet, which has the same secondary stream.

4.1. Vorticity field in the vicinity of the nozzle exit

A longitudinal plane of the vorticity modulus close to the nozzle exit is presented in Fig 7 for both jets T400 (a) and T800 (b). The jet flow development looks very similar and no significant difference appears due to temperature effects. Turbulence in both boundary layers and the jet flow seem to be fully developed. Small and large turbulent structures can be seen as expected in flow with such high Reynolds number. The turbulent activity in the area downstream the plug tip is high. The boundary layer tripping is applied at $x = -0.9D_j^s$ in the secondary stream and at $x = 0$ for the primary stream. Resulting perturbations are thus convected by the mean flow up to the nozzle exit. Nevertheless, a vortex shedding phenomenon occur downstream the nozzle lip of the secondary stream. This phenomenon is difficult to identify for high Reynolds number flow and has a real impact on radiated noise as shown by Bogey [47].

In order to characterize the vortex shedding, pressure spectra are computed along the secondary flow shear layer ($r = 0.44D_j^s$) in the T800 case. The power spectral density (PSD) of the pressure for axial positions $x = 0.2D_j^s$ and $0.3D_j^s$ are plotted in Fig. 8. The Strouhal number $St_e = f \times e/U_j^s$ is based on the secondary nozzle lip thickness e and the secondary stream exhaust velocity U_j^s. At $x = 0.2D_j^s$ (solid line), the PSD is dominated by a peak frequency at $St_0 = 0.154$. This frequency peak is the fundamental frequency St_0 of the von Kármán vortex street based on the secondary nozzle lip thickness e. In the same spectrum, subharmonic frequencies are also visible due to non-linearity effects [6]. Downstream, at $x = 0.3D_j^s$ (dashed line), the subharmonic peak at $St_e = 0.076$ is predominant. This frequency is close to $St_0/2$, and is directly associated with vortex pairings occurring in the external shear layer. This event can be also seen in Fig. 7 Despite the inner boundary layer tripping, the limited azimuthal discretization leads to highly anisotropic cells at the secondary stream exit, and avoid the development of a fully turbulent flow. The same result is observed in the T400 jet.

4.2. Comparisons of the velocity field with PIV for the T800 case

Comparisons are performed in Fig. 9 for the mean axial velocity radial profile from PIV planes at $x = 2D_{ef}^s$, $10D_{ef}^s$, and $14D_{ef}^s$. For each position, the jet growth rate is slightly overestimated. Nevertheless, at $x = 2D_{ef}^s$, the thickness of the primary stream is in agreement with experiment whereas only the secondary stream thickness is overestimated. Moreover the axial velocity amplitude for the secondary stream is slightly underestimated compared to the PIV measurements. This difference tends to disappear for downstream positions.

Overall, comparisons between LES and experiment for the mean axial velocity are in good agreement. These differences could be explained by different factors but mostly due to the mesh discretization. Indeed, as mentioned before, the large mesh size in the azimuthal direction leads to a vortex pairing phenomenon. This means that too strong coherent vortices exist downstream the nozzle exit of the secondary stream in the shear layer, regarding this high Reynolds number flow type. As observed previously by Bodony [48], organized turbulent structures could lead to an increased rate of the velocity decay induced by approximations in the LES modeling.

4.3. Jet flow aerodynamic downstream the nozzle

In Fig. 7, the jet flow is fully attached to the nozzle wall for both cases. This observation based on instantaneous vorticity modulus field is confirmed with streamlines of the mean velocity field shown in Fig. 10. In particular, the boundary layer on the central plug remains also fully attached. The numerical ingredients (wall law, tripping) used in these simulations, combined with the mesh discretization, allows to obtain a realistic flow field with a turbulent boundary layer and no flow separation, as expected and observed in experiments in such configurations [49]. On the contrary, as underlined by Brès et al. [50], laminar nozzle boundary layers could lead to an unrealistic flow separation and spurious noise prediction.

Fig. 11 shows the radial profiles of the mean axial velocity, which look very similar for both cases. Indeed, as the exhaust velocity of the primary jet is kept constant in the two simulations, temperature effects on the aerodynamics for this non-potential jet flow are limited. Moreover, the velocity defect in the plug wake is weak and disappears rapidly. Indeed, at $x = 1D_j^s$ the velocity defect is about 35% whereas at $x = 2D_j^s$ it is about 4%. However, some differences are observed on the radial profiles of the axial velocity fluctuations plotted in Fig. 12. In particular, the intensity of the turbulence is higher in the shear layer for the T800 case in the

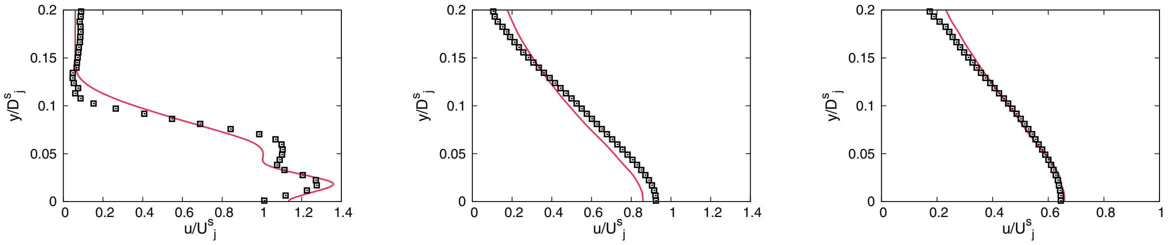

(a) (b) (c)

Fig. 9. T800 case: mean axial velocity along a radial profile at : (a) $x = 2D^s_{ef}$, (b) $x = 10D^s_{ef}$ and (c) $x = 14D^s_{ef}$. —— LES and ⊡ Experiment [16].

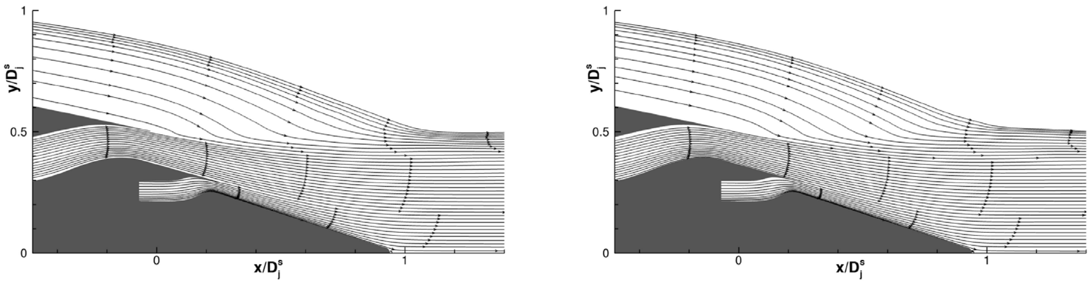

(a) T800 (b) T400

Fig. 10. Streamlines in the vicinity of the dual-stream nozzle.

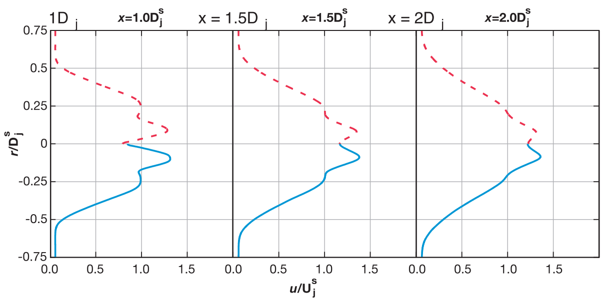

Fig. 11. Mean axial velocity profile in the plug wake. — — T800; —— T400.

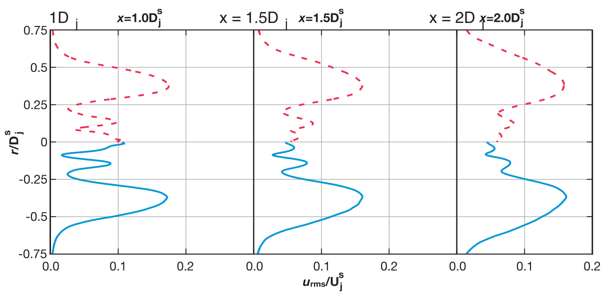

Fig. 12. Axial velocity fluctuations profile in the plug wake. — — T800 (top); —— T400 (bottom).

primary stream, i.e. for $-0.2 \le r/D^s_j \le 0.2$. That suggests that the turbulent coherent structures contain more energy due to temperature increase. The same behavior is observable in a hot single stream jet as shown in numerical [51] and experimental studies [52].

For an axial spacing ξ and a temporal separation τ, the two-point space-time correlation of the fluctuating axial velocity u' is

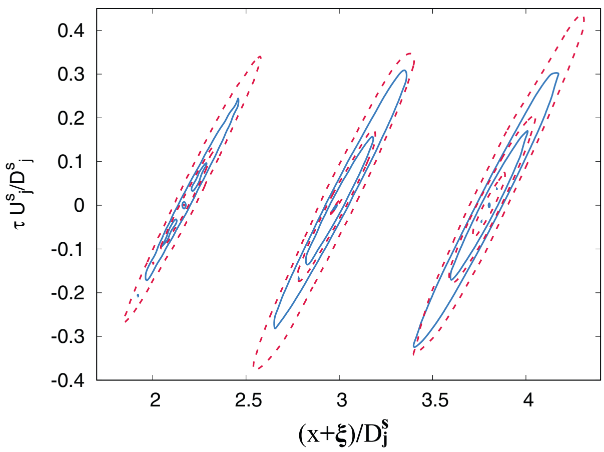

Fig. 13. Two-point space-time correlations of the axial velocity along the jet axis $R_{uu} \in [0.5, 0.75, 1.0]$ for $x = 2.16D^s_j$, $x = 2.96D^s_j$ and $x = 3.80D^s_j$. — — T800; —— T400.

defined as

$$R_{uu}(x, \xi, \tau) = \frac{\langle u'(x,t)u'(x+\xi, t+\tau)\rangle}{\sqrt{\langle u'^2(x)\rangle}\sqrt{\langle u'^2(x+\xi)\rangle}}, \quad (1)$$

where x and t are the spatial position on the jet axis and the time where the two-point correlation is evaluated, respectively. Two-points space-time correlations based on axial fluctuating velocity on the jet centerline are plotted in Fig. 13. The spatial separation is $\Delta\xi = 4 \times 10^{-2} D^s_j$ and the time step is $\Delta\tau = 1.8 \times 10^{-2} U^s_j D^s_j$.

From Fig. 13, it can be observed that turbulent scales are larger in space and longer in time for the T800 case and for axial positions $x/D^s_j \le 4$, which confirms observations made from Fig. 12. In the simulation of T800 case, an increase of temperature leads to an increase of turbulence coherence. These observations were also

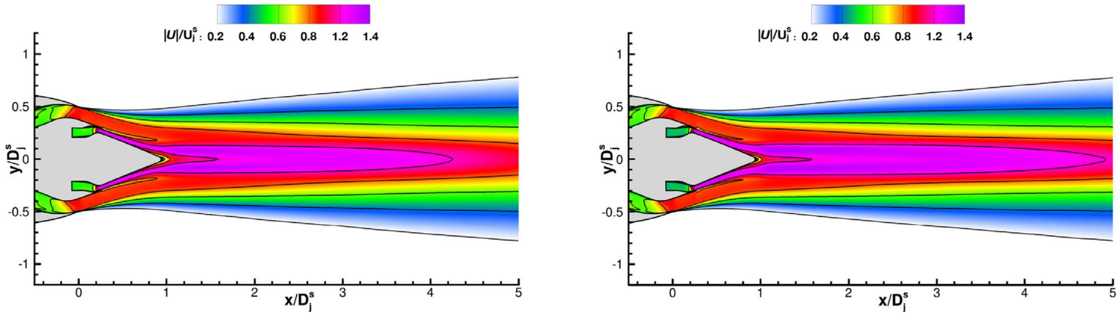

(a) T800 (b) T400

Fig. 14. Longitudinal axial plane of the mean axial velocity for (a) T800 and (b) T400.

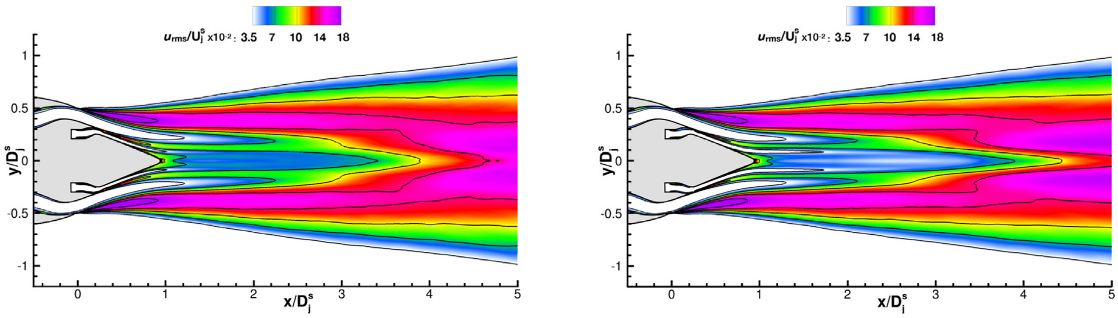

(a) T800 (b) T400

Fig. 15. Longitudinal axial plane of the axial velocity fluctuations for (a) T800 and (b) T400.

done by Bridges [53] on a hot single stream jet. However, temperature effects do not modify the convection velocity on the jet axis.

4.4. Temperature effects on the mean axial velocity and turbulence

In order to investigate temperature effects, the mean axial velocity map of the two configurations T800 and T400 are respectively presented in Fig. 14 (a) and (b). The plug does not allow the development of a classical potential flow, as encountered for a single jet. A jet core length can still be defined such as $u(x_c) = 0.95 \times \max(u(r=0))$ where x_c is the jet core length. Following this definition, the jet core length is $x_c = 4D_j^s$ for the case T800 and $x_c = 4.54D_j^s$ for the case T400.

As for a single jet [54], a temperature increase leads to a shorter jet core length caused by an increase of the turbulent intensity in the primary stream, as shown in Fig. 12 and Fig. 15. Except this difference, the two flows are quite similar regarding the mean axial velocity. Same conclusions can be drawn regarding the fluctuating velocity in Fig. 15. This result can be explained by the high by-pass ratio of the present dual-stream geometry. Temperature effects on the global mean flow and turbulence are restricted to the primary stream and no significant differences are noticed after the mixing of the two stream for $x/D_j^s \geq 5$.

4.5. Skewness of velocity and temperature

Bogey [51] has shown that a negative skewness of aerodynamic values, such as the axial velocity, is a good indicator of low frequency acoustic production in a single free jet. The location of the skewness peak is consistent with the correlation peak between velocity fluctuations on the central axis and the acoustic pressure in the near field. In order to identify a possible region of acoustic production in this dual-stream jet, a two dimensional mapping of the axial velocity skewness $u_{skew} = \overline{u'u'u'}/\overline{u'u'}^{3/2}$ is plotted in Fig. 16 (a) for the T800 jet and (b) for the T400. The skewness fields are plotted for $r \leqslant 0.2D_j^s$, that is in the region where intermittency is expected to be significant. Two zones can be distinguished, the growing shear layers associated with entrainment and mixing, and the coalescence of these shear layers at the end of the potential cone. Isolines of the axial velocity standard deviation are also superimposed to facilitate interpretation.

In both cases, the maximum amplitude of the skewness factor is approximately $u_{\text{skew}} = -2$ and observed around the end of the jet core. In addition, for the case T400, this maximum is also located in the shear layer in the transition region before the end of the jet core. This result indicates that the mixing between the two streams in the T400 case leads to more intermittent events and could be responsible for the low frequency acoustic radiation.

5. Acoustic fields

The acoustic radiation is calculated from the integral formulation of the Ffowcs-Williams and Hawkings (FWH) analogy [55]. The input surface for the FWH processing is positioned around the jet aerodynamic structures, represented by vorticity modulus isosurfaces in Fig. 17 The surface starts at $x_i = -2D_{ef}^s$ with a radius $r(x_i) = 1.3D_{ef}^s$ and finishes at $x_f = 30D_{ef}^s$ with a radius $r(x_f) = 4.7D_{ef}^s$. The axial length of the surface is thus $L = 32D_{ef}^s$, which corresponds to a minimal Strouhal of St = 0.05. The cut off frequency based on the mesh size is about St = 6. The FWH formulation is applied with a closed surface. An open surface leads to an increase in the low-frequency acoustic level, as demonstrated by Shur et al. [44] and by Mendez et al. [56]. No correction is however applied to the FWH formulation in this study. Density fluctuations [44] induced by the hot primary stream and leaving the control volume are indeed weak, thanks to the mixing induced by the coaxial jets.

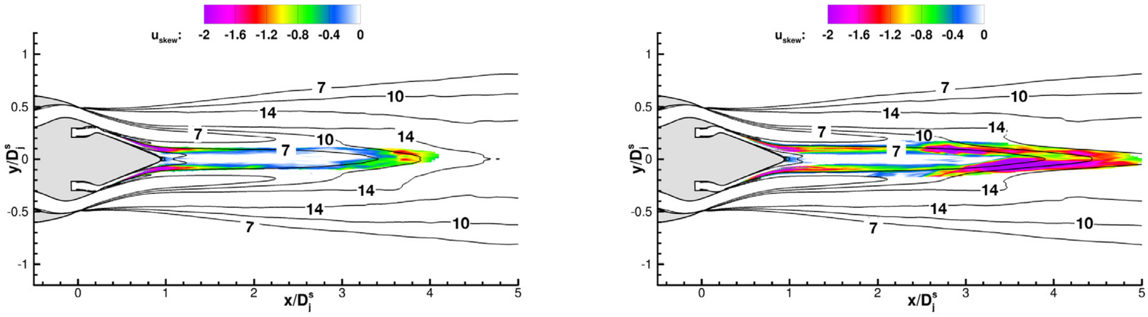

(a) T800 (b) T400

Fig. 16. Two dimensional mapping of the axial velocity skewness coefficient for (a) T800 et (b) T400. Iso-lines indicate level of the axial velocity standard deviation.

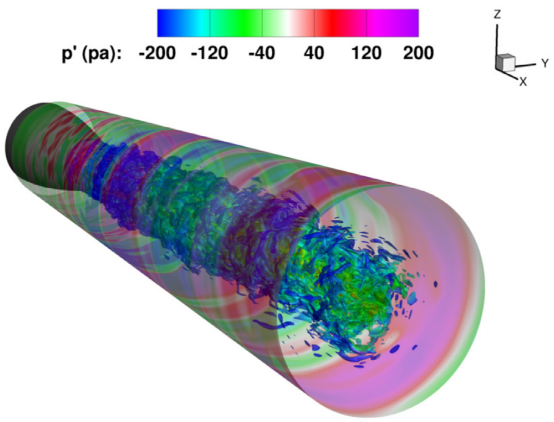

Fig. 17. Vorticity modulus isosurfaces colored by the axial velocity enclosed by the conical surface used for acoustic propagation via the Ffowcs-Williams et Hawkings (FWH) analogy, colored by pressure fluctuations.

Acoustic perturbations are propagated to the far-field and recorded by 2400 microphones positioned at $r = 6$m from $\theta = 20^\circ$ to 140°. For each polar angle position, 20 microphones are placed in the azimuthal direction in an uniform way. First, an acoustic validation is proposed based on the case T800 and then the temperature influence is analyzed. In the following, all acoustic results are normalized to a radial distance $r = 1$ m, from the primary nozzle exit plane $x = 0$, in assuming that acoustic sound pressure levels decrease as a function of $1/r$. In the following, all acoustic spectra are plotted as a function of the Strouhal number defined by $\mathrm{St} = f \times D^s_{ef}/U^s_j$.

5.1. T800 Configuration

Sound pressure level at $\theta = 30^\circ$ and 90° are plotted respectively in Fig. 18 (a) and (b). For an observer at 30°, the LES results are in agreement with the experimental data for $\mathrm{St} \geq 0.3$. However, in the vicinity of $\mathrm{St} = 0.2$ the noise level is under-estimated by about 7dB. This may be attributed to the lack of mesh discretization close to the secondary exhaust. Bogey [57] pointed out the importance of the mesh refinement in order to form, develop and transport large coherent structures. Theses structures play a key role in the flow development and in the sound generation specially at low frequencies. As a consequence, the underestimation of SPL at $\mathrm{St} = 0.2$ is here a signature of these structures in the region between the secondary jet exhaust and the jet core. For Strouhal number $\mathrm{St} > 2$, the noise level is slightly higher with a difference less than 1dB. At 90°, the noise emitted is highly related to the turbulence level close to the exit plane of the secondary stream. As seen in Section 4, a vortex pairing is present in the shear layer, which affects the noise generated perpendicular to the main flow direction. These observations have already been formulated by Bogey et al. [47]. For $\mathrm{St} > 1.5$, the LES predictions are 1 to 2 dB higher than the noise level from experimental measurements. The spectrum also shows some tonal components at $4 \leq \mathrm{St} \leq 6$. They have

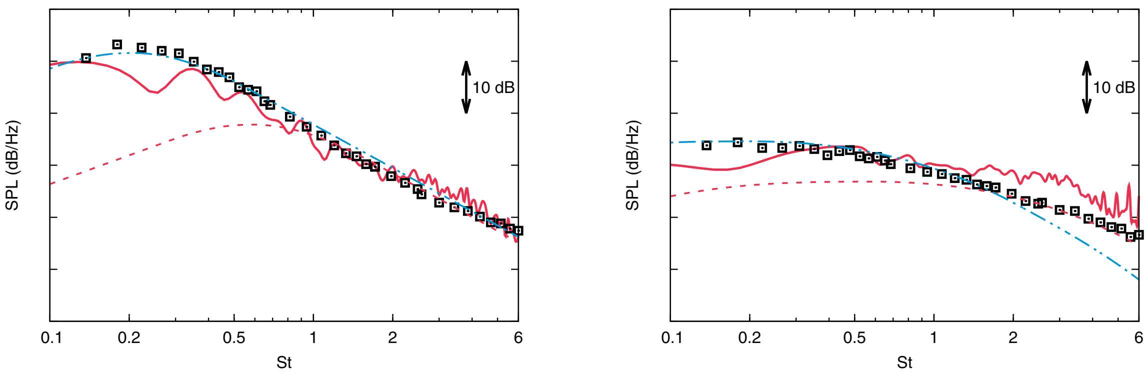

(a) (b)

Fig. 18. T800 case: acoustic spectra in far-field normalized to an observer distance of $r = 1m$ at θ : (a) 30° and (b) 90°. Two sources spectra from Tam [58] by using effective diameters and velocity exhaust of the primary and secondary streams : (a) Large scale similarity et (b) Fine scale similarity. —— LES and ⊡ Experiment. Tam spectra : — · — secondary stream ; — — — primary stream.

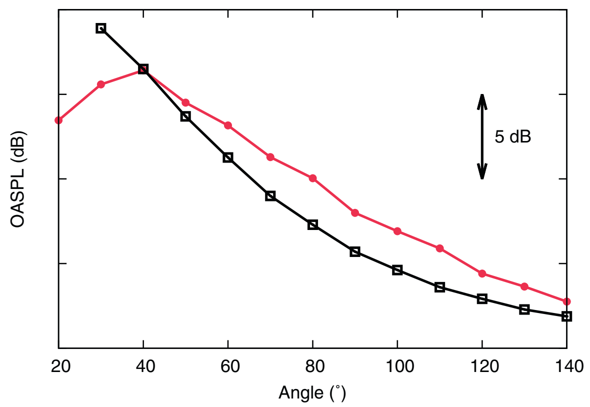

Fig. 19. T800 case: overall sound pressure level integrated on frequency between $0.2 \le \mathrm{St} \le 6$. —●— LES and —⊡— Experiment.

no physical meaning and are maybe caused by numerical spurious noise. However, for frequencies between $0.3 \le \mathrm{St} \le 1.5$, LES provides good acoustic results.

A simple identification of the acoustic contributions of each stream is proposed by the mean of Tam's empirical spectra [58]. Tam defined two kind of template, one for the acoustic radiation of coherent structures used at $\theta = 30^\circ$ and one for the acoustic radiation of fine scales used at $\theta = 90^\circ$. The spectral peak is first defined at $\mathrm{St} = 0.2$ for both kind of acoustic radiation. For the primary stream, the empirical law is calculated with the exit static temperature T_j^p and exit velocity U_j^p and the Strouhal is defined by $\mathrm{St}^p = f \times D_{ef}^p / U_j^p$. The same methodology is applied to determine the acoustic radiation of the secondary stream. The spectrum level are adapted individually according to the jet operating conditions and directivity angle [59]. At 30°, the noise radiated in the far-field is clearly dominated by the noise component from the large coherent structures of the secondary stream. At 90°, where acoustic perturbations are caused by fine scale structures of the flow, the noise from the secondary stream dominates the low-frequencies up to the crossing frequency $\mathrm{St} = 1.5$. The primary stream contribution represents the major part of the noise radiated for $\mathrm{St} \ge 1.5$.

In Fig. 19, the OASPL from LES and experimental data, obtained by integration of spectra between frequency range $0.2 \le \mathrm{St} \le 6$, are plotted for angles between 20° and 140°. For low angles $\theta < 40^\circ$, an underestimation of the noise level by approximately 2dB in the LES is observed. Against all expectations, for angles higher than 40°, the estimated noise level is slightly overestimated by less than 2dB. This additional noise is mostly due to high frequency spurious noise. The presence of the co-flow ($u/U_j^p = .05$) should indeed lead to a slight underestimation of the OASPL. Computation methodology applied for the T800 case gives good acoustic estimations. Moreover, this computation has been performed without the possibility to validate sensitive aerodynamic values for noise generation, like shear layer thickness and the level of turbulence intensity due to the lack of exploitable experimental data.

As already mentioned before, the grid resolution in the azimuthal direction is the limiting parameter of the present simulation. For realistic geometries, the strategy based on a structured

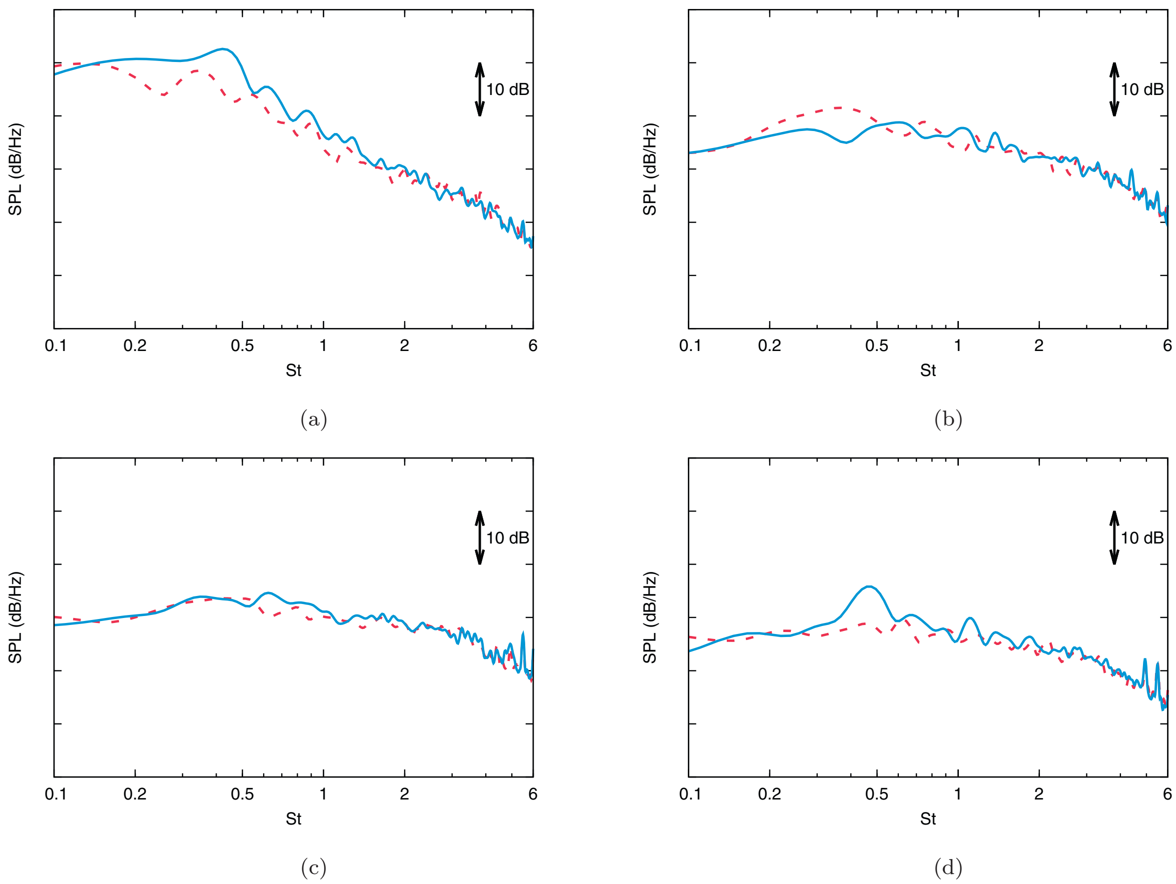

Fig. 20. Acoustic spectra in far-field normalized to an observer distance of $r = 1m$ for θ : (a) 30°, (b) 60°, (c) 90° and (d) 130°. – – – T800 and —— T400.

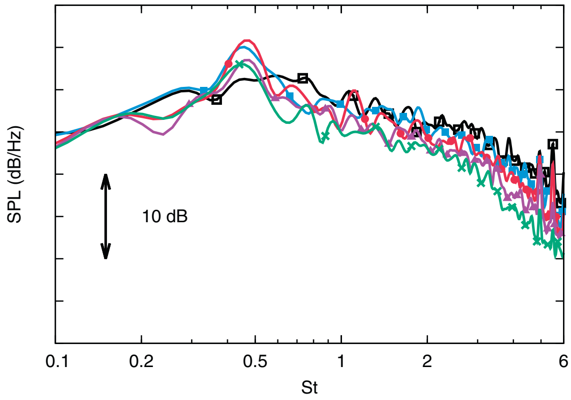

Fig. 21. Acoustic spectra in far-field related to $r = 1m$ for the case T400 for an angle θ between 110° and 150°. —□— : $\theta = 110°$; —■— : $\theta = 120°$; —●— : $\theta = 130°$; —▲— : $\theta = 140°$; —×— : $\theta = 150°$.

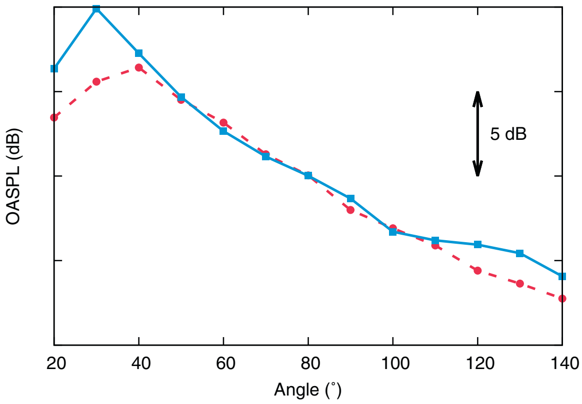

Fig. 22. OASPL integrated over $0.2 \leq \mathrm{St} \leq 6$ for cases T800 and T400. — ● — T800 and —■— T400.

meshing approach is probably reached here, at least for the present solver.

5.2. Temperature effects on far-field noise

Comparisons between the T800 and T400 jets are shown in Fig. 20 for polar angles 30°, 60°, 90° and 130°. For $\theta = 30°$ (Fig. 20 (a)), the low frequency noise level $\mathrm{St} \leq 1.5$ is higher for the T400 jet. This result is in agreement with the velocity skewness fields (Fig. 16), an indicator of turbulence intermittency. For higher frequencies $\mathrm{St} > 1.5$, the modification of the primary stream temperature has no impact on the acoustic radiation, in contrast to what is observed for a single jet [60]. At 60° (Fig. 20 (b)), noise level is 4dB higher close to $\mathrm{St} = 0.35$ for the T800 case whereas for higher frequencies, no difference can be observed between the two configurations. For an angle of 90° (Fig. 20 (c)), there is no difference for all the frequency range. At this angle, the major part of the acoustic radiation is due to the secondary stream. However, an extra bump about 8dB is clearly visible at 130° and $\mathrm{St} = 0.46$ for T400 case (Fig. 20 (d)) and will be discussed in the next section. The acoustic radiation of this unknown component starts to be visible for an angle close to 120° until 150° with a maximum for $\theta = 130°$ as plotted in Fig. 21.

The OASPL integrated for frequency between $0.2 \leq \mathrm{St} \leq 6$ are plotted in Fig. 22 for the two jets. For angles between 50° and 110°, the acoustic noise level is not influenced by the temperature of the primary stream with less than 1 dB difference. However, for angles outside of these bounds, the jet T400 is louder than the jet T800 with a difference up to 4 dB. Indeed, in a dual-streams configuration, temperature effect in the primary stream has a limited influence on noise generation compared to a single stream configuration. As shown in Fig. 18 (a) and (b), most of the acoustic radiation is caused by the secondary stream, which has a mass flow rate 10 times higher than the primary stream. Higher acoustic levels for small angles is linked to the higher intermittent behaviour of the case T400 but nothing can explain the difference for the upstream acoustic radiation ($\theta > 110°$). The last part of this work is devoted to finding the physical mechanism of this acoustic radiation.

6. Acoustic trapped waves in the jet core

6.1. Description of the phenomenon

Some recent works [28,29] have shown that a subsonic single jet could produce tonal noise in the near field for axial positions corresponding to the nozzle exit plane. Moreover, these tones are sensitive to jet exhaust conditions. Towne et al. [25] have demonstrated that tonal components are produced by acoustic trapped waves in the potential core. Their study is based on the numerical database of Brés et al. [61], which is a single stream isothermal jet at $M_\mathrm{j} = 0.9$.

A way to reveal the presence of this kind of waves in the potential core is to perform a frequency-wavenumber decomposition of the pressure signal on the jet centerline. A regular line array (226 probes) is thus considered on the jet axis with axial spacing increments of $\Delta x = 0.045D_\mathrm{j}^\mathrm{s}$ between $x = 0.94D_\mathrm{j}^\mathrm{s}$ and $x = 11.12D_\mathrm{j}^\mathrm{s}$. The diagrams obtained with this procedure are displayed in Fig. 23 (a) for T800 and (b) for T400. Three lines are also plotted (Fig. 23 (b)), representing the wave celerity in agreement with the dispersion relation $k = \omega/c$, where ω is the frequency, k is the wave number and c the wave celerity. Three celerities are chosen, one is the convection velocity $u_c = 0.7U_\mathrm{j}^\mathrm{p}$ (solid line), second the free upstream acoustic wave $-c_0$ (dashed-dotted line) and then the upstream acoustic wave slowed down by the jet flow $u_c - c_0$ (dashed line).

Moreover, the cylindrical soft duct model proposed by Towne et al. [25] is also plotted on the diagram (dotted line). This model provides the dispersion relation between wave number modes and frequencies for an azimuthal mode m as

$$k_d^\pm = \frac{-\omega M \pm \sqrt{T_r}\sqrt{\omega^2 - 4(T_r - M^2)\beta_m^2}}{T_r - M^2} \tag{2}$$

where $\omega = 2\pi \mathrm{St} M$ is the normalized frequency, $T_r = T_\mathrm{j}/T_0$ is the temperature ratio, M is the acoustic Mach number with $M_\mathrm{j} = M/\sqrt{T_r}$, and $\beta_m = i\gamma_i/2$ is the first root of the Bessel function J_m, with $\gamma_i = \sqrt{k^2 - (\omega - Mk)^2/T}$. For the first azimuthal mode of the T400 case, the values are $T_r = 1.4$, $M = 1$ and $\beta_0 = 2.4048$. Only the first azimuthal mode is here considered. In the two jets, the most energetic band corresponds to the well known Kelvin-Helmholtz instability waves (Fig. 23) and the group velocity is close to $0.7U_\mathrm{j}^\mathrm{p}$. For the jet T800, upstream waves are not detected, whereas for the T400 case a band of energy with a negative phase velocity is observed. The group velocity is bounded by $-c_0$ and $u_c - c_0$. For this wave packet, the energy is concentrated around the Strouhal value of $\mathrm{St} = 0.46$. Two important observations can thus be made: first, the single round jet vortex sheet model given by Towne et al. [25] provides a good estimation of the frequency modes of the trapped waves in a complex dual-stream configuration. Secondly, trapped waves phenomenon can occur in non-potential jet flows.

Towne et al. [25] have also explored the sensitivity for the presence of trapped waves to the operating conditions. In their work, a necessary condition to find trapped waves is to detect two saddle

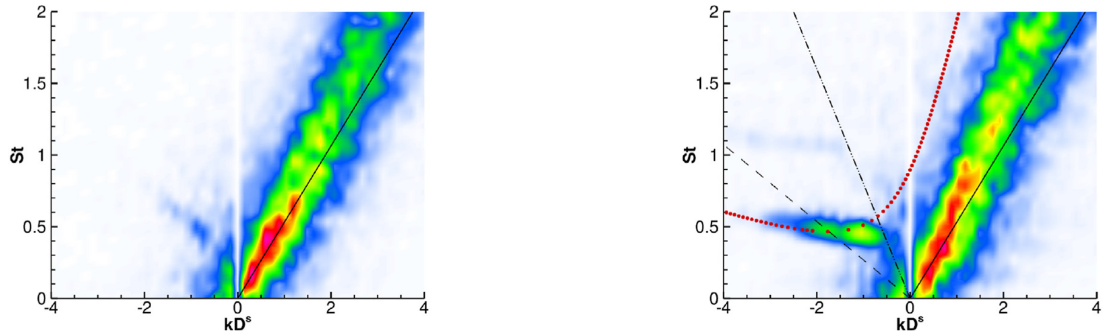

(a) T800 (b) T400

Fig. 23. Frequency-wavenumber diagram from probes on jet axis: (a) T800 and (b) T400. The lines represent waves with constant group and phase velocity with dispersion relation $k = \omega/c$, where c is the wave celerity, ω is the frequency and k is the wave number: —— $u_c = 0.7U_j^p$; — . . $-c_0$; — — — $u_c - c_0$ and ● cylindrical soft duct model from Towne et al. [25].

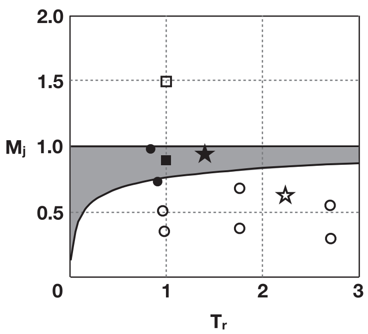

Fig. 24. Diagram $(M_j, T_r = T_j/T_0)$. Gray area represents exhaust conditions where acoustic resonance can occur according to Towne et al. [25]. Closed symbols are jets where trapped waves have been observed. Open symbols are jets where trapped waves have not been observed. ■ numerical jets ; • experimental jets; ☆ T800 et ★ T400.

points by the vortex sheet model for a given couple (M_j, $T_r = T_j/T_0$). Fig. 24 summarizes this condition for the first azimuthal and radial mode. The grey area corresponds to the couple of (M_j, T_r) where trapped waves could be observed. This area is delimited by $M_j = 1$ for which the saddle point asymptotically vanishes. Single jets with different operating conditions provided by Towne et al. [25] are also added to this diagram. As expected, if the primary stream operating conditions are considered, the jet T800 is out of the gray area whereas the case T400 is in. This diagram confirms the previous observations. In a dual-stream jet, the couple (M_j, $T_r = T_j^p/T_0$) of the primary stream has to be considered to determine the presence of trapped waves in the jet core.

In order to determine the axial position of the generation of trapped waves inside the dual-stream jet core, snapshots of the filtered fluctuating pressure field at $St = 0.46$ over one period T are plotted in Fig. 25 (a) to (h). To filter the fluctuating pressure, a two-dimensional discrete Fourier transform is performed to obtain the pressure field in the frequency domain. The number of snapshots allow a frequency resolution of $St = 0.03$ between two modes. The mode at $St = 0.46$ is then extracted and transformed back in the temporal domain using an inverse transform. Two waves called k^- and k^+ are identified by an arrow on each snapshot. Initially, the wave k^- is defined at $x = 1.6D_j^s$ and the wave k^+ at $x = 2.2D_j^s$ in Fig. 25 (a). Following the time advancement, from $t = 0$ up to $t = 7T/8$, the wave k^- clearly travels upstream with an amplitude modulation, whereas the wave k^+ is going downstream. Two waves k^+ and k^- are clearly produced in the vicinity of $x = 2D_j^s$. This occurs before the end of the length core jet as observed by Towne et al. [25], and is called the wave turning point. The spatio-temporal correlation of the filtered pressure signal on the jet axis is plotted in Fig. 26 (a) for an axial position $x = 1.3D_j^s$ and (b) for $x = 3.0D_j^s$, respectively upstream and downstream the wave turning point. These correlation maps enabled a more quantitative identification of the production area of the waves k^- and k^+. For the wave k^-, the correlation path is high for $1 \leq x/D_j^s \leq 1.8$ (Fig. 26 (a)). As expected, the convection velocity is negative and its amplitude is lower than the downstream wave about $c_{k^-} = u_c - c_j$ where u_c is the convection velocity. For the wave k^+ in Fig. 26 (a), the correlation coefficient is close to 1 between $x = 1.8D_j^s$ up to $x = 3.8D_j^s$. On the contrary, its convection velocity is positive. As a conclusion from these two maps, the trapped wave turning point emerges near $x = 1.8D_j^s$.

6.2. Impact on noise

As seen in Fig. 20 (d), the trapped wave has a strong influence on jet noise radiated in the far-field whereas Towne et al. [25] have detected these tones only in the near-field of a single stream jet. The fact that this phenomenon propagates in the far-field can be explained principally by the presence of the central plug in the geometry. In order to characterize the modal structure of the radiated noise, an azimuthal decomposition of the acoustic near-field of the T400 case is shown in Fig. 27 for the modes $m = 0$ (a) and $m = 1$ (b). Only the two first modes are shown, because they contain more than 90% of the total acoustic energy. The azimuthal decomposition is based on a azimuthal array of 20 microphones defined in the physical domain at $r = 2.5D_s^j$ for $-1 \leq x/D_j^s \leq 16$ with an axial spacing increment $\Delta x = 0.045D_j^s$.

For the mode $m = 0$, a peak is clearly visible for $x/D_j^s \leq 0$ at $St = 0.46$. Nevertheless, the noise level is lower than those observed downstream the jet core ($x/D_j^s \geq 10$). On the contrary, no conclusion can be made regarding the mode $m = 1$ (Fig. 27 (b)), as no energy peak appears on the SPL map. For downstream positions, the noise level is related to the flow behavior rather than acoustic resonance in the core jet. To confirm this hypothesis, the filtered acoustic and aerodynamic pressure field at frequency $St = 0.46$ shown in Fig. 28 is analyzed.

The aerodynamic pressure is plotted from -1000 to 1000 Pa and the acoustic one from -20 to 20 Pa to handle with the large dynamic range. Acoustic waves propagating in all directions are clearly visible. In order to characterize the origin of these waves, the coherence function C_{pp} between a probe close to the plug and two microphones at $r = 2.5D_j^s$, one upstream at $x/D_j^s = -0.5$ and

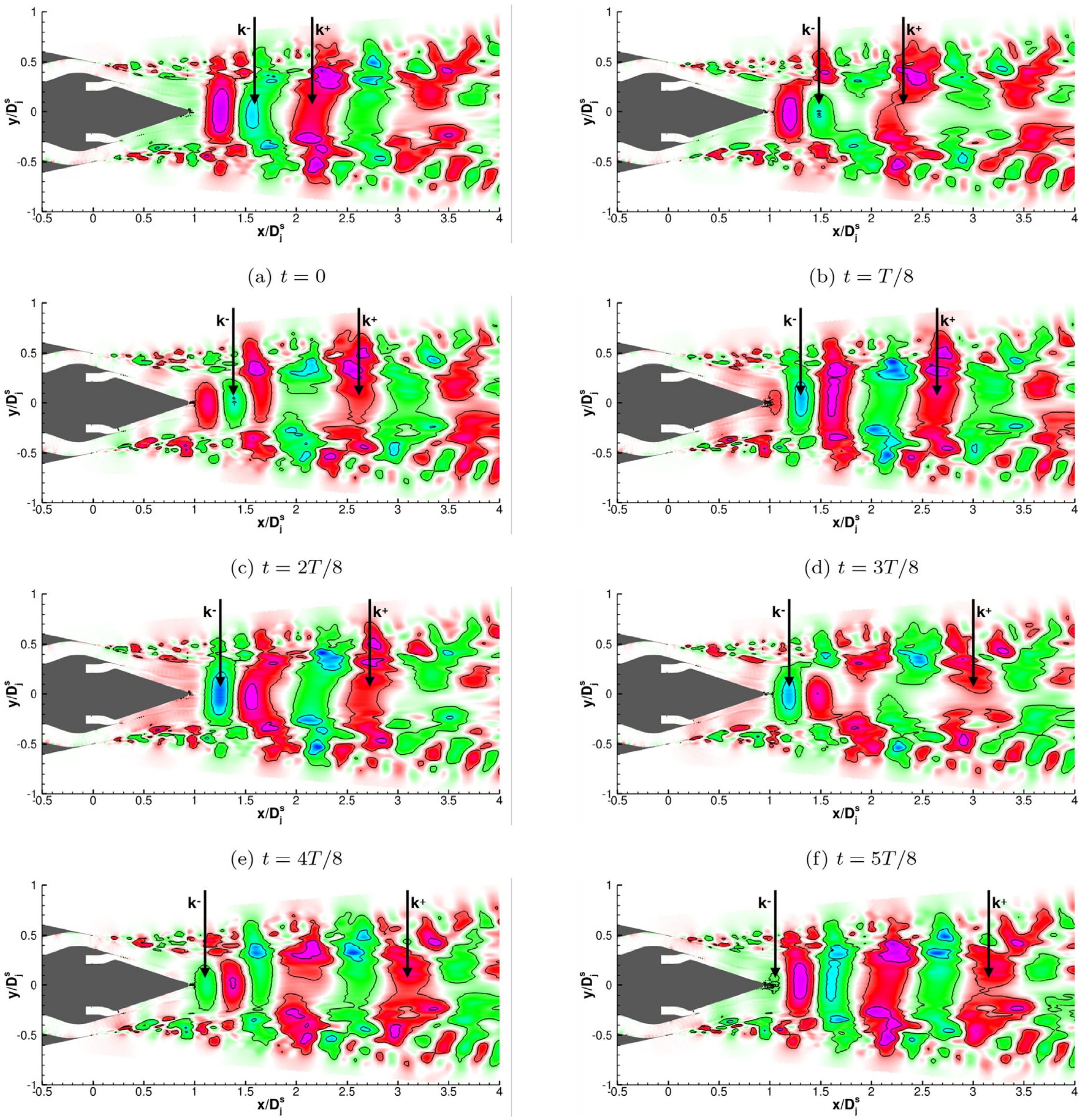

(a) $t = 0$ (b) $t = T/8$

(c) $t = 2T/8$ (d) $t = 3T/8$

(e) $t = 4T/8$ (f) $t = 5T/8$

(g) $t = 6T/8$ (h) $t = 7T/8$

Fig. 25. T400 case: Instantaneous snapshots of the filtered pressure at St = 0.46 over a period T.

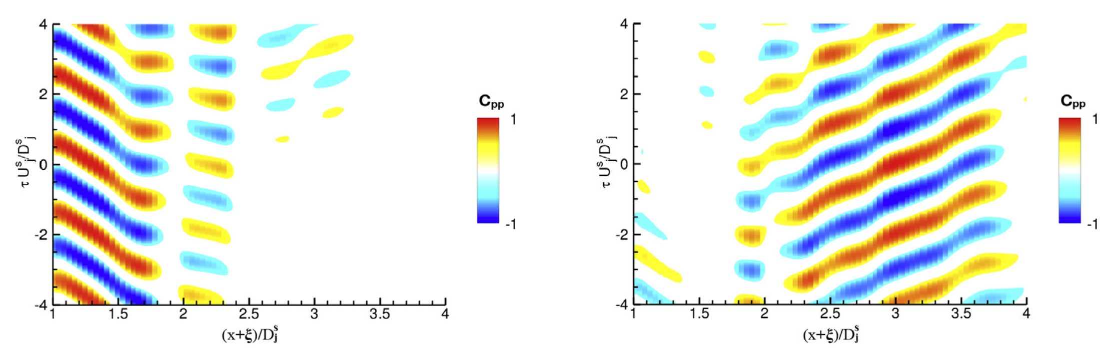

(a) (b)

Fig. 26. T400 case: Spatio-temporal correlation maps from the filtered pressure at St = 0.46 on the jet axis for an initial position : (a) $x = 1.3D_j^s$ and (b) $x = 3.0D_j^s$.

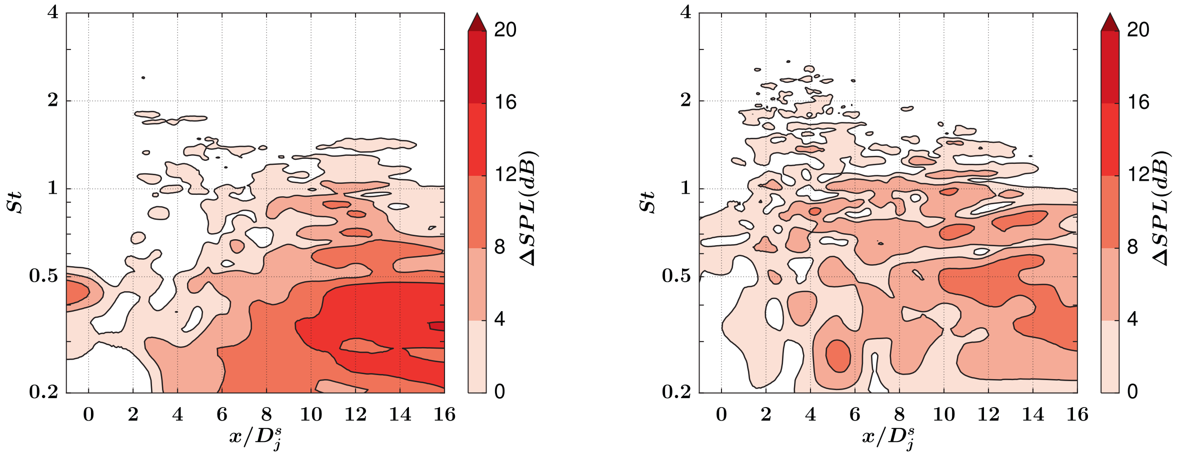

(a) (b)

Fig. 27. T400 case: SPL for a microphone located at $r = 2.5D_s^j$ (a) azimuthal mode 0 and (b) azimuthal mode 1.

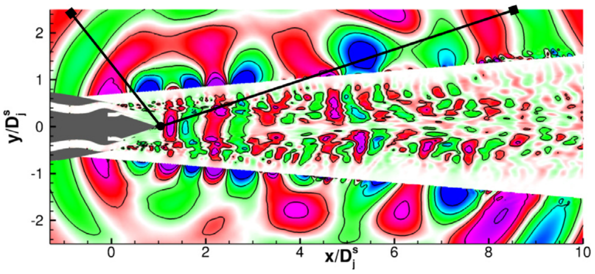

Fig. 28. T400 case: Instantaneous snapshots of the filtered pressure at $\mathrm{St} = 0.46$. Dynamic range inside the flow comes from -1000 to $1000Pa$ and from -20 to $20Pa$ outside the flow. The two microphones chosen for the coherence function are indicated by squares and the probe inside the jet core by the point at the plug tip.

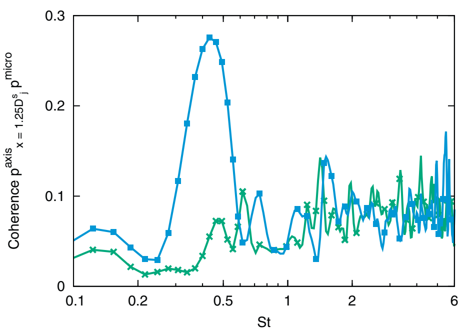

Fig. 29. T400 case: Coherence function (C_{pp}) between pressure for probes at $x = 1.25D_j^s$ and acoustic pressure at two positions : —■— $r = 2.5D_j^s$ et $x = -0.9D_j^s$ ($\theta = 130°$) ; —×— $r = 2.5D_j^s$ and $x = 9D_j^s$ ($\theta = 30°$).

another one downstream at $x/D_j^s = 9$, are plotted in Fig. 29. The probe and two microphones are respectively indicated by the circle and the two square in Fig. 28.

For the upstream microphone, the coherence function shows a peak at $\mathrm{St} = 0.46$ with $C_{pp} = 0.28$. The upstream acoustic radiation is thus correlated with the acoustic wave trapped in the core jet. On the other hand, for the downstream microphone, the coherence function does not display a clear peak for any frequencies. This result indicates that no link can be established between the acoustics radiated for aft angles and the events that occur in the vicinity of the plug tip. On the contrary, the acoustic wave and the noise peak observed in the near- and far-field for high angles are clearly related to the interaction of the trapped wave k^- with the central plug.

7. Conclusion

The influence of temperature effects on complex dual-stream jets including a central plug has been carried out in this study. The results have been obtained by high-fidelity LES, based on sixth-order numerical schemes. The algorithm is combined with an explicit filtering to drain the energy cascade at the cut-off wavenumber while leaving the resolved scales unaffected by this filtering.

Numerical results have been generally found in agreement with the corresponding experiments of the EXEJET program. The primary stream temperature is observed to have a small influence on the aerodynamic development of the dual-stream jet from the nozzle. In fact, no significant influence of the well-known bi-polar source induced by the temperature fluctuations occurs in a realistic configuration. Indeed, the aerodynamic jet behavior is mostly driven by the secondary stream in a high by-pass-ratio nozzle. As a consequence, the convection velocity is not significantly affected with the temperature increase. On the contrary, the jet core length is reduced when the primary stream is heated, as for a single jet, in agreement with changes also observed on the axial velocity fluctuations.

An additional acoustic source is also found in the cold case for upstream angles at $\mathrm{St} = 0.46$. This study highlights the existence of trapped wave in non-potential jet flow. It is shown that this acoustic source is caused by trapped waves in the jet core interacting with the central plug. Moreover, a good estimation of the frequency modes of these waves is provided by a vortex sheet model developed for single jets [25]. Finally, in a complex dual-stream configuration, the couple (M_j, T_j) of the primary stream has to be considered to determine the presence of trapped waves in the jet core. The consideration of an installed configuration with a dual stream jet in the vicinity of a wing could amplified this phenomena.

Declaration of Competing Interest

The authors declare that they have no known competing financial interests or personal relationships that could have appeared to influence the work reported in this paper.

CRediT authorship contribution statement

Romain Biolchini: Writing - original draft, Writing - review & editing, Investigation, Formal analysis, Conceptualization, Methodology, Software, Visualization. **Guillaume Daviller:** Writing - original draft, Writing - review & editing, Investigation, Formal analysis, Visualization, Supervision. **Christophe Bailly:** Writing - original draft, Writing - review & editing, Investigation, Formal analysis, Supervision. **Guillaume Bodard:** Writing - review & editing, Resources.

Acknowledgements

This work was granted access to the HPC resources of CINES under the allocation 2017-[x20172a6074] made by GENCI. The authors acknowledge the support of Airbus Operation SAS, Safran Aircraft Engines and Onera partners for the provision of the EXEJET database.

References

[1] Bogey C, Bailly C, Juvé D. Noise investigation of a high subsonic, moderate reynolds number jet using a compressible large eddy simulation. Theor Comput Fluid Dyn 2003;16(4):273–97. doi:10.1007/s00162-002-0079-4.
[2] Shur ML, Spalart PR, Strelets MK, Travin AK. Towards the prediction of noise from jet engines. Int J Heat Fluid Flow 2003;24(4):551–61. doi:10.1016/S0142-727X(03)00049-3.
[3] Andersson N, Eriksson L-E, Davidson L. Large-eddy simulation of subsonic turbulent jets and their radiated sound. AIAA J 2005;43(9):1899–912. doi:10.2514/1.13278.
[4] Bodony D, Lele SK. Current status of jet noise predictions using large-Eddy simulation. AIAA J 2008;46(2):364–80. doi:10.2514/1.24475.
[5] Bogey C, Marsden O. Simulations of initially highly disturbed jets with experiment-Like exit boundary layers. AIAA J 2016;54(4):1299–312. doi:10.2514/1.J054426.
[6] Bogey C, Barré S, Juvé D, Bailly C. Simulation of a hot coaxial jet: direct noise prediction and flow-acoustics correlations. Phys Fluids 2009;21(3):1–14. doi:10.1063/1.3081561.
[7] Viswanathan K, Shur M, Spalart P, Strelets M. Flow and noise predictions for single and dual-Stream beveled nozzles. AIAA J 2008;46(3):601–26. doi:10.2514/1.27299.
[8] Andersson N, Eriksson L-E, Davidson L. LES prediction of flow and acoustic field of a coaxial jet. In: 11th AIAA/CEAS Aeroacoustics Conference, no. AIAA 2005–2884; 2005. p. 1–26. doi:10.2514/6.2005-2884.
[9] Eastwood S, Xia H, Tucker P. Large-eddy simulation of complex geometry jets. J Propul Power 2012;28(2):235–45. doi:10.2514/1.B34322.
[10] Mockett C, Haase W, Schwamborn D. Go4Hybrid: grey area mitigation for hybrid RANS-LES methods: results of the 7th framework research project go4hybrid, funded by the european union, 2013–2015, 134. Springer; 2017. doi:10.1007/978-3-319-52995-0.
[11] Le Bras S, Deniau H, Bogey C, Daviller G. Development of compressible large-Eddy simulations combining high-Order schemes and wall modeling. AIAA J 2017;55(4):1–12. doi:10.2514/1.J055107.
[12] Brès GA, Ham FE, Nichols JW, Lele SK. Unstructured large-eddy simulations of supersonic jets. AIAA J 2017;55(4):551–61. doi:10.2514/1.J055084.
[13] Murakami E, Papamoschou D. Mean flow development in dual-stream compressible jets. AIAA J 2002;40(6):1131–8. doi:10.2514/2.1762.
[14] Tinney C, Jordan P. The near pressure field of co-axial subsonic jets. J Fluid Mech 2008;611(1):175–204. doi:10.1017/S0022112008001833.
[15] Huber J, Drochon G, Bonnaud C, Pintado-Peno A, Cléro F, Bodard G. Large-scale jet noise testing, reduction and methods validation "EXEJET": 1. Project overview and focus on installation. In: 20th AIAA/CEAS aeroacoustics conference, no. AIAA 2014–3032; 2014. p. 1–17. doi:10.2514/6.2014-3032.
[16] David F, Jourdan JM, Cléro F, Koenig M, Huber J. Large-scale jet noise testing, reduction and methods validation "EXEJET": 4 - Flows characterization with PIV in the CEPRA19 anechoic wind tunnel of Onera. In: 20th AIAA/CEAS Aeroacoustics Conference, no. AIAA 2014–3035; 2014. p. 1–11. doi:10.2514/6.2014-3035.
[17] Fisher M, Lush P, Harper Bourne M. Jet noise. J Sound Vib 1973;28(3):563–85. doi:10.1016/S0022-460X(73)80040-9.
[18] Tanna H. An experimental study of jet noise part i: turbulent mixing noise. J Sound Vib 1977;50(3):405–28. doi:10.1016/0022-460X(77)90493-X.
[19] Lilley G. The radiated noise from isotropic turbulence with applications to the theory of jet noise. J Sound Vib 1996;190(3):463–76. doi:10.1006/jsvi.1996.0074.
[20] Viswanathan K. Aeroacoustics of hot jets. J Fluid Mech 2004;51(1):39–82. doi:10.1017/S0022112004000151.
[21] Bridges J, Wernet M. Establishing Consensus Turbulence Statistics for Hot Subsonic Jets. In: 16th AIAA/CEAS Aeroacoustics Conference, no. AIAA 2010–3751; 2010. p. 1–41. doi:10.2514/6.2010-3751.
[22] Zaman KBMQ. Far-field noise of a subsonic jet under controlled excitation. J Fluid Mech 1985;152:83–111. doi:10.1017/S0022112085000581.
[23] Bogey C, Bailly C. Large eddy simulations of transitional round jets: influence of the reynolds number on flow development and energy dissipation. Phys Fluid 2006;18(6):1–15. doi:10.1063/1.2204060.
[24] Bogey C, Marsden O. Numerical investigation of temperature effects on properties of subsonic turbulent jets. In: 19th AIAA/CEAS Aeroacoustics Conference, no. AIAA 2013–2140; 2013. p. 1–19. doi:10.2514/6.2013-2140.
[25] Towne A, Cavalieri A, Jordan P, Colonius T, Schmidt O, Jaunet V, et al. Acoustic resonance in the potential core of subsonic jets. J Fluid Mech 2017;825(1):1113–52. doi:10.1017/jfm.2017.346.
[26] Fisher MJ, Preston GA, Mead CJ. A modelling of the noise from simple coaxial jets, part II: with heated primary flow. J Sound Vib 1998;209(3):405–17. doi:10.1006/jsvi.1997.1217.
[27] Viswanathan K. Parametric study of noise from dual-stream nozzles. J Fluid Mech 2004;521(1):35–68. doi:10.1017/S0022112004000813.
[28] Suzuki T, Colonius T. Instability waves in a subsonic round jet detected using a near-field phased microphone array. J Fluid Mech 2006;565(1):197–226. doi:10.1017/S0022112006001613.
[29] Sinha A. Development of reduced-order models and strategies for feedback control of high-speed axisymmetric jets. The Ohio State University; 2011. Ph.D. thesis.
[30] Cambier L, Heib S, Plot S. The onera elsa CFD software: input from research and feedback from industry. Mech Ind 2013;14(3):159–74. doi:10.1051/meca/2013056.
[31] Bogey C, Bailly C. A family of low dispersive and low dissipative explicit schemes for flow and noise computations. J Comput Phys 2004;194(1):194–214. doi:10.1016/j.jcp.2003.09.003.
[32] Fosso Pouangue A, Deniau H, Sicot F, Sagaut P. Curvilinear finite-volume schemes using high-order compact interpolation. J Comput Phys 2010;229(13):5090–122. doi:10.1016/j.jcp.2010.03.027.
[33] Visbal M, Gaitonde D. Very high-Order spatially implicit schemes for computational acoustics on curvilinear meshes. J Comput Acoust 2001;9(4):1259–86. doi:10.1142/S0218396X01000541.
[34] Bogey C, Bailly C. Decrease of the effective reynolds number with eddy-Viscosity subgrid modeling. AIAA J 2005;43(2):437–9. doi:10.2514/1.10665.
[35] Bogey C, Bailly C. Three-dimensional non-reflective boundary conditions for acoustics simulations: far field formulation and validation test cases. Acta Acustica united Acustica 2002;88(1):463–71.
[36] Tam C, Dong Z. Radiation and outflow boundary conditions for direct computation of acoustics and flow disturbances in a nonuniform mean flow. J Comput Acoust 1996;4(2):175–201. doi:10.1142/S0218396X96000040.
[37] Bodony D. Analysis of sponge zones for computational fluid mechanics. J Comput Phys 2006;212(2):681–702. doi:10.1016/j.jcp.2005.07.014.
[38] Fosso Pouangue A, Deniau H, Lamarque N, Poinsot T. Comparison of outflow boundary conditions for subsonic aeroacoustic simulations. Int J Numer Methods Fluids 2012;68(10):1207–33. doi:10.1002/fld.2597.
[39] Tam C, Webb J. Dispersion-Relation-Preserving finite difference schemes for computational acoustics. J Comput Phys 1993;107(2):262–81. doi:10.1006/jcph.1993.1142.
[40] Fosso Pouangue A, Deniau H, Lamarque N. A sixth-order compact finite-volume scheme for aeroacoustics: application to a large eddy simulation of a jet. In: V European Conference on Computational Fluid Dynamics; 2010. p. 1–15.
[41] Bogey C, Bailly C. Effects of inflow conditions and forcing on subsonic jet flows and noise. AIAA J 2005;43(5):1000–7. doi:10.2514/1.7465.
[42] Reichardt H. The principles of turbulent heat transfer. Tech. Rep.; 1957.
[43] Shur M, Spalart P, Strelets M. Noise prediction for increasingly complex jets. part II: applications. Int J Aeroacoust 2005;4(3):247–66. doi:10.1260/1475472054771385.
[44] Shur M, Spalart P, Strelets M. Noise prediction for increasingly complex jets. part i: methods and tests. Int J Aeroacoust 2005;4(3):213–45. doi:10.1260/1475472054771376.
[45] Shur M, Spalart P, Strelets M, Garbaruk A. Further steps in LES-based noise prediction for complex jets. In: 44th AIAA Aerospace Sciences Meeting and Exhibit, no. AIAA 2006-485; 2006. p. 1–26. doi:10.2514/6.2006-485.
[46] Spalart P, Allmaras S. A one-equation turbulence model for aerodynamic flows. La Recherche Aerospatiale 1994;1(1):5–21. doi:10.2514/6.1992-439.
[47] Bogey C, Marsden O, Bailly C. Large-eddy simulation of the flow and acoustic fields of a reynolds number 10e5 subsonic jet with tripped exit boundary layers. Phys Fluids 2011;23(3):1–20. doi:10.1063/1.3555634.
[48] Bodony D, Lele SK. Jet noise prediction of cold and hot subsonic jets using large-eddy simulation. In: 10th AIAA/CEAS Aeroacoustics Conference, no. AIAA 2004–3022; 2004. p. 1–17. doi:10.2514/6.2004-3022.
[49] Doty HBS, Michael J, Kinzie KW. Turbulence measurements of separate-flow nozzles with pylon interaction using particle image velocimetry. AIAA J 2017;45(6):1281–9. doi:10.2514/1.20420.
[50] Brès G, Ham FE, Nichols JW, Lele SK. Nozzle wall modeling in unstructured large eddy simulations for hot supersonic jet predictions. In: 19th AIAA/CEAS aeroacoustics Conf., no. AIAA 2013–2142; 2013. p. 1–19. doi:10.2514/6.2013-2142.
[51] Bogey C. A study of the effects of temperature on velocity and density fluctuations in high-subsonic jets. In: 52nd Aerospace sciences meeting, no. AIAA 2014-0524; 2014. p. 1–15. doi:10.2514/6.2014-0524.
[52] Panda J. Experimental investigation of turbulent density fluctuations and noise generation from heated jets. J Fluid Mech 2007;591(1):73–96. doi:10.1017/S0022112007007173.

[53] Bridges J. Effect of heat on space-time correlations in jets. In: 12th AIAA/CEAS aeroacoustics conference, no. AIAA 2006–2534; 2006. p. 1–16. doi:10.2514/6.2006-2534.
[54] Lau J. Effects of exit mach number and temperature on mean-flow and turbulence characteristics in round jets. J Fluid Mech 1981;105(1):193–218. doi:10.1017/S0022112081003170.
[55] Casalino D. An advanced time approach for acoustic analogy predictions. J Sound Vib 2003;261(4):583–612. doi:10.1016/S0022-460X(02)00986-0.
[56] Mendez S, Shoeybi M, Lele SK, Moin P. On the use of the Ffowcs Williams-Hawkings equation to predict far-field jet noise from large-eddy simulations. Int J Aeroacoust 2013;12(1–2):1–20. doi:10.1260/1475-472X.12.1-2.1.
[57] Bogey C. Grid sensitivity of flow field and noise of high-Reynolds-number jets computed by large-eddy simulation. Int J Aeroacoust 2018;17(4–5):399–424. doi:10.1177/1475472X18778287.
[58] Tam C, Golebiowski M, Seiner J. On the two components of turbulent mixing noise from supersonic jets. In: 2nd AIAA/CEAS aeroacoustics conference, no. AIAA 96–1716; 1996. p. 1–17. doi:10.2514/6.1996-1716.
[59] Viswanathan K. Analysis of the two similarity components of turbulent mixing noise. AIAA J 2002;40(9):1735–44. doi:10.2514/2.1878.
[60] Biolchini R, Bailly C, Boussuge J-F, Fernando R. Numerical study on the relation between hydrodynamic fluctuations and noise in hot jets at high Reynolds number. In: 22nd AIAA/CEAS aeroacoustics conference, no. AIAA 2016–3048; 2016. p. 1–15. doi:10.2514/6.2016-3048.
[61] Brès G, Jordan P, Colonius T, Le Rallic M, Jaunet V, Lele SK. Large eddy simulation of a mach 0.9 turbulent jet. Center Turbul Res Proc Summer Program 2014 2014;1(1):221–30.

5.2 Supersonic jet flow

The PhD thesis of Carlos Pérez Arroyo was defended in 2016. His work was devoted on the study of the BroadBand Shock-Associated Noise using Large-Eddy Simulations. In the article presented below, the signature of supersonic jet noise is investigated using a wavelet analysis.

C. Pérez Arroyo, G. Daviller, G. Puigt, C. Airiau, and S. Moreau. Identification of temporal and spatial signatures of broadband shock-associated noise. *Shock Waves*, 29:117 − 134, 2018. https://doi.org/10.1007/s00193-018-0806-4

Identification of temporal and spatial signatures of broadband shock-associated noise

C. Pérez Arroyo[1] · G. Daviller[2] · G. Puigt[3] · C. Airiau[4] · S. Moreau[1]

Received: 4 September 2017 / Revised: 19 December 2017 / Accepted: 15 January 2018

Abstract Broadband shock-associated noise (BBSAN) is a particular high-frequency noise that is generated in imperfectly expanded jets. BBSAN results from the interaction of turbulent structures and the series of expansion and compression waves which appears downstream of the convergent nozzle exit of moderately under-expanded jets. This paper focuses on the impact of the pressure waves generated by BBSAN from a large eddy simulation of a non-screeching supersonic round jet in the near-field. The flow is under-expanded and is characterized by a high Reynolds number $\mathrm{Re_j} = 1.25 \times 10^6$ and a transonic Mach number $M_\mathrm{j} = 1.15$. It is shown that BBSAN propagates upstream outside the jet and enters the supersonic region leaving a characteristic pattern in the physical plane. This pattern, also called signature, travels upstream through the shock-cell system with a group velocity between the acoustic speed $U_\mathrm{c} - a_\infty$ and the sound speed a_∞ in the frequency–wavenumber domain (U_c is the convective jet velocity). To investigate these characteristic patterns, the pressure signals in the jet and the near-field are decomposed into waves traveling downstream (p^+) and waves traveling upstream (p^-). A novel study based on a wavelet technique is finally applied on such signals in order to extract the BBSAN signatures generated by the most energetic events of the supersonic jet.

Keywords LES · Identification · Shock cells · Jet noise · Wavelet analysis

1 Introduction

Supersonic jet noise has been studied since the discovery of screech phenomenon by Powell [1] in the 1950s. Utilizing Schlieren-based flow visualization, he identified sound waves that were propagating upstream. This noise, called screech, was explained as a feedback loop between the vortical structures convected downstream from the nozzle lip and the noise generated from the interaction with the shock cells that appear due to the mismatch in pressure at the exit of the nozzle. Supersonic jet noise is mainly composed of three components: screech tonal noise, broadband shock-associated noise (BBSAN), and turbulent mixing noise. The BBSAN was studied theoretically by Harper-Bourne and Fisher [2]. Their model was able to predict the pressure spectrum for different pressure ratios and angles of observation modeling shock cells by single-point acoustic sources. Tam and Tanna [3] investigated the BBSAN experimentally, concluding that it was generated by the same process as the screech tones, i.e., the weak but coherent interaction between large-scale turbulent structures convected downstream and the quasi-periodic shock-cell system. The origin of BBSAN was located by Norum and Seiner [4] in the downstream weaker shock cells as opposed to the screech phenomenon that is generated where the shock cells have a higher intensity and oscillation, usually located between the second and fourth shock-cell positions [5]. The shock-cell noise generation mechanism was extensively studied by Tam in the

Communicated by D. Zeidan and H. D. Ng.

G. Daviller
guillaume.daviller@cerfacs.fr

1 Department of Mechanical Engineering, Sherbrooke University, Sherbrooke, QC J1K 2R1, Canada

2 CERFACS, 42 Avenue Gaspard Coriolis, 31057 Toulouse, France

3 ONERA, 2 Avenue Edouard Belin, 31000 Toulouse, France

4 IMFT, CNRS, Université de Toulouse, Allée du Professeur Camille Soula, 31400 Toulouse, France

1980s when he developed the stochastic model theory [6]. The model is based on the assumption that the large vortical structures can be modeled by a superposition of several intrinsic instability waves of the mean jet flow and that the nearly periodic shock-cell system can be decomposed into time-independent waveguide modes. The broadband shock-cell noise is therefore the superposition of the spectra generated by the unsteady disturbances that appear from the interaction between the instability waves and each of the waveguide modes. Finally, turbulent mixing noise of axisymmetric jets was analyzed by Tam et al. [7] who evidenced the existence of two universal similarity spectra, one for the noise generated by large turbulent structures and the other for fine-scale turbulence. Exhaustive reviews on supersonic jet noise were done by Raman [8] and Tam [9].

A new approach to the physical phenomenon of supersonic jet noise was introduced by Manning and Lele [10] with the increase in computing power at the end of the twentieth century. In performing a direct Navier–Stokes simulation (DNS), a two-dimensional weak shock impinging upon a shear layer was presented as the simplification of the shock-cell system of an imperfectly expanded jet. The shock is subjected to large fluctuations produced by the passage of the instability wave vortices. These fluctuations are coupled with the generation of a sharp compression of the acoustic wave that occurs when the shock travels upstream after the passage of the vortex, i.e., in the saddle-point of its oscillation cycle where the local vorticity becomes the weakest. At this point, the shock leaks through the shear layer as shock-cell noise. The shock-leakage phenomenon was further investigated by Suzuki and Lele [11] using the geometrical acoustic theory. The mechanism was numerically demonstrated by solving the time-dependent Eikonal equation on DNS data. Shock-leakage theory was further confirmed in the large eddy simulation (LES) of a planar jet by Berland et al. [12] who observed the shock waves responsible for the leak of the screech tonal noise through the saddle-points.

Several authors investigated the noise generated by supersonic jets using LES. In particular, Schulze and Sesterhenn [13], Schulze et al. [14], and Berland et al. [12] simulated a three-dimensional supersonic under-expanded planar jet. Mendez et al. [15] studied supersonic perfectly expanded axisymmetric jets at $M_\mathrm{j} = 1.4$ and Bodony et al. [16] examined supersonic under-expanded and perfectly expanded jets at $M_\mathrm{j} = 1.95$. The same jet was considered by Lo et al. [17], obtaining good agreement with numerical results from Bodony et al. [16]. The noise emitted from supersonic under-expanded rectangular nozzles at $M_\mathrm{j} = 1.4$ and the effect of chevrons were studied by Nichols et al. [18, 19] on the same configuration. Furthermore, temperature effects have been correctly captured by Brès et al. [20] for an over-expanded supersonic jet at $M_\mathrm{j} = 1.35$.

Many numerical studies of imperfectly expanded jets focus mostly on aerodynamic statistics and far-field noise spectra. The use of a wavelet decomposition represents an efficient alternative to a Fourier transform in order to perform a deep analysis of both hydrodynamic and acoustic near-field components. The wavelet transform originated in the 1980s with Morlet [21] and is nowadays one of the most popular time–frequency transforms, originating from the seminal work done by Farge in the 1990s [22]. The regular wavelet transform decomposes a one-dimensional signal into a two-dimensional representation of the signal. For a temporal signal, the wavelet transform represents the signal in time and scale. Wavelet-based techniques are able to detect intermittent events that are not periodic in time. The use of wavelet transforms in jet aerodynamics and acoustics is quite limited, and it has been centered on experimental long time signals. Camussi and Guj [23, 24] and Grassucci et al. [25] used wavelet techniques in order to identify the intermittent, but coherent, structures that are convected through the shear layer of subsonic experimental jets and airfoils responsible for subsonic mixing noise. Similarly, Camussi et al. [26] used a wavelet-based conditional analysis of unsteady flow and sound signals to highlight the role of intermittent perturbations both in the sound generation and the unsteady field of an aerofoil tip leakage flow experiment. Grizzi and Camussi [27] used a wavelet approach to study the near-field pressure fluctuations of a subsonic jet. Moreover, the filtering capabilities of the wavelet transform have been exploited by Crawley and Samimy [28] and Mancinelli et al. [29] to filter the hydrodynamic and acoustic components in the near-field of a subsonic jet. In addition, Cavalieri et al. [30] used a continuous wavelet transform in the temporal direction to identify intermittent acoustic events in the far-field radiated by a subsonic jet from an LES. Finally, Walker et al. [31] demonstrated with a wavelet study that multiple acoustic modes produced by the jet coexist for a screeching supersonic jet.

The present work investigates the near-field BBSAN source mechanisms in a supersonic under-expanded jet at $M_\mathrm{j} = 1.15$. The main analysis of the LES results is performed with a wavelet-based procedure and focuses on shock-cell noise. This post-processing technique gives a conditional-averaged time signature representing the most probable shape of the most energetic events in the jet flow responsible for BBSAN. The paper is structured as follows: First, the wavelet-based technique is introduced in Sect. 2. Section 3 presents the configuration for both jet parameters and numerical approach. The identification of temporal and spatial signatures of the BBSAN of the simulated jet is detailed in Sect. 4. The analysis is carried out first by identifying particular patterns in the frequency–wavenumber domain. Then, a wavelet-based procedure is used in order to study the signatures in time and space of the events responsible for the detected patterns. Additionally, validation results are presented in the Appendix to demonstrate the ability of the present LES to reproduce experimental data of an under-expanded turbulent jet.

2 Wavelet-based signature identification procedure

The wavelet-based technique applied in this work follows the works of Camussi et al. [26]. It was also implemented by Gefen et al. [32] in order to extract the signature through a conditional average of the most characteristic events of the flow. The continuous wavelet transform $w(s, \tau)$ of the signal of interest $q(t)$ can be expressed as

$$w(s, \tau) = \frac{1}{\sqrt{|s|}} \int_{-\infty}^{+\infty} q(t) \psi^* \left(\frac{t - \tau}{s} \right) \mathrm{d}t, \tag{1}$$

where τ is the translation parameter, s is the dilatation or scale parameter, and $\psi^* \left(\frac{t-\tau}{s}\right)$ is the complex conjugate of the daughter wavelet $\psi \left(\frac{t-\tau}{s}\right)$ obtained by the translation and dilatation of the so-called mother wavelet $\psi_0(t)$. Mathematically, the wavelet transform is a convolution of a temporal signal with a dilated function with different scales of dilatation. Each scale represents a different window size in the windowed Fourier transform. In this work, the non-orthogonal continuous wavelet transform was carried out using the first derivative of a Gaussian function (DOG) as mother wavelet. The DOG function is also known as Marr or Mexican Hat function and it is defined as

$$\psi_0(\eta) = \frac{\mathrm{d}^m}{\mathrm{d}\eta^m} \mathrm{e}^{-\eta^2/2}, \tag{2}$$

where $m = 2$. The reference scale s (with units of time for a temporal signal) can be expressed in terms of frequency $f(s)$ or Strouhal number $\mathrm{St}(s)$. To avoid confusion, the equivalent frequency is denoted as a function of s which implies that the frequency (and similarly, the Strouhal number) is a function of the scale s. For the DOG mother wavelet, they are related as

$$f(s) = \frac{\sqrt{m + \frac{1}{2}}}{2\pi s}. \tag{3}$$

The mother wavelet DOG was chosen among others (such as Paul and Morlet) as it allows for a better temporal discretization of peaks or discontinuities. This temporal accuracy is necessary due to the short-time signal obtained in general from simulations. Moreover, the low discretization in scale that offers the DOG mother wavelet implies that the signatures obtained are an average of different events from similar scales. This allows to study broadband

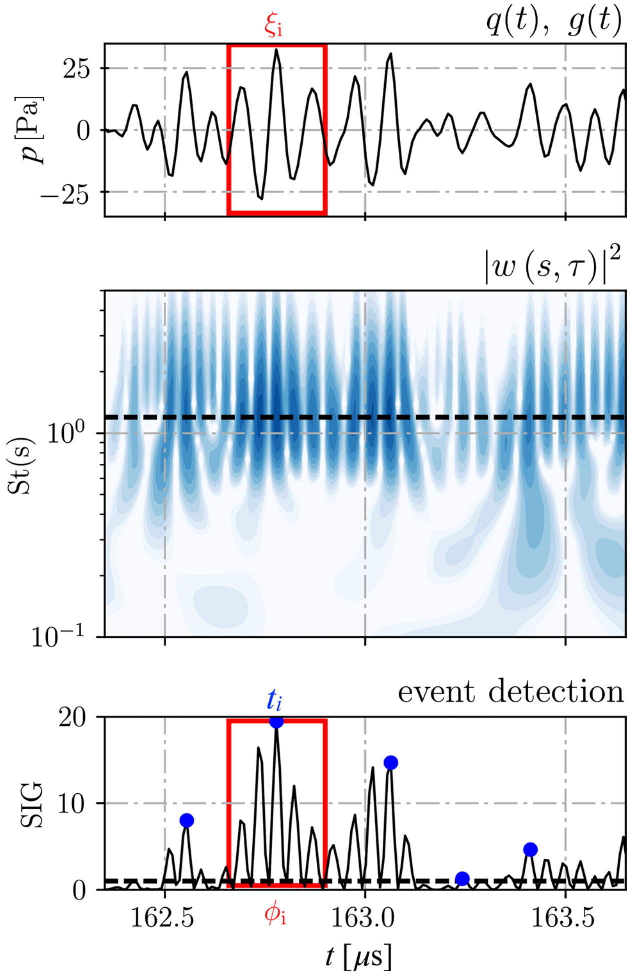

Fig. 1 Wavelet transform procedure: (top) initial pressure signal $q(t)$, (center) resulting wavelet power and scale of interest in dashed line, (bottom) filtered detected events at times t_i

phenomena and to increase the convergence of the signature because more events are being detected.

Figure 1 shows an example of the wavelet transform of a pressure signal with the mother wavelet DOG. This initial pressure signal (Fig. 1, top) is recorded at 120° from the jet axis in the far-field of the supersonic jet introduced in Sect. 3.1 (see also Appendix). In Fig. 1 bottom, the event detection method compares the local wavelet power $|w(s, \tau)|^2$ (Fig. 1, center) with a defined background spectrum energy at all scales as

$$\mathrm{SIG}(s, \tau) = \frac{|w(s, \tau)|^2}{\sigma P_k \chi_2^2}, \tag{4}$$

where σ is the variance of the signal $q(t)$, P_k is the normalized Fourier power spectrum of the background noise and χ_2^2 is the value of the Chi-squared distribution at a defined percentile value. In this work, a white noise and the value of the Chi-squared distribution at 95% are chosen. The reader is

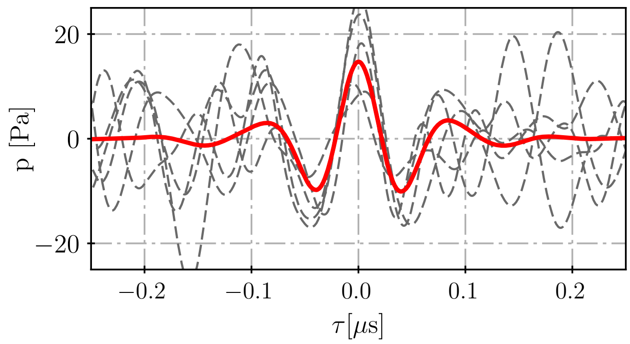

Fig. 2 Example of conditional averaging (auto-conditioning) from the example shown in Fig. 1. —— signature. - - - windows ξ_i before averaging

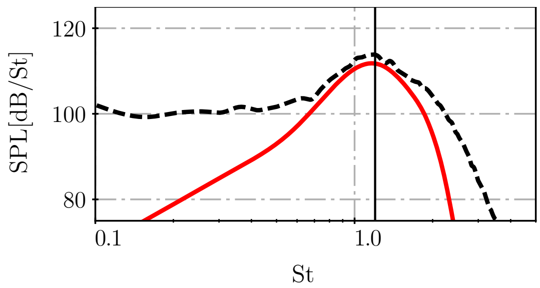

Fig. 3 Far-field sound pressure level: - - - from the original pressure signal shown in Fig. 1 and —— from the signature shown in Fig. 2. The vertical line depicts the scale selected for the event detection procedure

referred to the work of Torrence and Compo [33] for further details. Once the events have been selected and well localized in the time domain (t_i in Fig. 1, bottom), a conditional average can be performed at scales of interest. It is called auto-conditioning if the original signal $q(t)$ is used or cross-conditioning if a different variable or signal is employed. At each instant t_i corresponding to a peak of energy (event), it is possible to extract a window of fixed time-length t_W from the target signal $g(t)$. The conditional average $\{q; g\}$ can be calculated from the average of this set of windows as

$$\{q; g\} = \frac{1}{N}\sum_{i=1}^{N} g(\xi_i), \tag{5}$$

where ξ_i is the interval surrounding each peak (Fig. 1, top). $\xi_i \in \left[\tilde{t}_i - \frac{t_W}{2}, \tilde{t}_i + \frac{t_W}{2}\right]$ and N is the number of events used for the conditional average. N can be lower than the total number of events detected. Indeed, a filtering window ϕ_i centered at t_i can be used to discard events based on characteristic lengths of the problem as illustrated in Fig. 1 (bottom). The averaged signal is known as the signature representing the most probable shape of the most energetic events. An example of the averaged signature is shown in Fig. 2.

As the signature obtained is a function of time, its spectrum can be computed as shown in Fig. 3. The spectrum of the signature recovers the energy of the original signal at the Strouhal number where the events were detected. Moreover, the cross-conditioning can be applied to a full two- or three-dimensional field in order to obtain the influence of the event on the complete flow.

One of the limitations of this procedure is the fact that two different types of events that have the same or a similar scale cannot be easily identified. The event detection procedure of this study is based on the energy of the signal for different scales. In acoustics, if two independent events radiate noise at similar scales and with a similar energy content, the event detection procedure will not be able to discriminate between them. Having the knowledge of the physics and the case that is being studied can be used to pre-process the signal before applying the wavelet-based procedure.

Table 1 Physical parameters of the under-expanded jet

D (mm)	M_j	NPR	P_t (Pa)	T_t (K)
38	1.15	2.27	2.225×10^5	303.15

3 Configuration

3.1 Jet definition

The case of study is an under-expanded single jet at Mach number M_j of 1.15 with a nozzle to pressure ratio (NPR) of 2.27. The jet is established from a round convergent nozzle with an exit diameter $D = 38$ mm [34]. The lip of the nozzle at the exit has a thickness of 0.5 mm. The Reynolds number based on the exit diameter and perfectly expanded conditions noted with the subscript $(\bullet)_j$ is

$$\mathrm{Re}_j = \frac{\rho_j U_j D}{\mu_j} = 1.25 \times 10^6, \tag{6}$$

where the density is $\rho_j = 1.42$ kg/m^3, the axial velocity is $U_j = 356.96$ m/s and the dynamic viscosity is $\mu_j = 1.54 \times 10^{-5}$ kg/m/s. The ambient conditions used for this case are $P_{ref} = 9.8 \times 10^4$ Pa and $T_{ref} = 288.15$ K. The total pressure is $P_t = 2.225 \times 10^5$ Pa, and the total temperature is $T_t = 303.15$ K. The main conditions are summarized in Table 1.

3.2 Numerical formulation

The full compressible three-dimensional Navier–Stokes equations are solved using the finite volume multi-block structured solver ***elsA*** (Onera's software [35]). The spatial scheme is based on the implicit compact finite difference scheme of sixth order of Lele [36], extended to finite volumes by Fosso-Pouangué et al. [37]. The above scheme is stabilized by the compact filter of Visbal and Gaitonde [38] of sixth order that is also used as an implicit subgrid-scale model for the present LES. This scheme is able to capture perturbation waves when they are discretized by at least six points per wavelength. Time integration is performed by a six-step second-order Runge–Kutta dispersion–relation-preserving scheme of Bogey and Bailly [39].

3.3 Simulation parameters and procedure

In order to obtain inflow conditions as close as possible to the experiment at the nozzle exit, a coupled nozzle/jet-plume three-dimensional Reynolds average Navier–Stokes (RANS) computation is first performed using the Spalart–Allmaras turbulence model [40]. The LES is then initialized from the RANS solution, as in [41,42], keeping the conservative variables at the exit plane of the nozzle (the internal part of the nozzle is not included in the simulation). In the LES, the flow field is initialized over 120 dimensionless convective times ($T_c = ta_\infty/D$), with the sound velocity at ambient conditions being $a_\infty = 340.29$ m/s. The flow statistics are then collected over $T_c = 140$ convective times, with a non-dimensional time step $(\Delta t a_\infty)/D = 4 \times 10^{-4}$.

The computational domain is depicted in Fig. 4. Non-reflective boundary conditions of Tam and Dong [43] extended to three dimensions by Bogey and Bailly [44] are used at the lateral boundaries. Downstream, the outflow boundary condition is based on the characteristic formulation of Poinsot and Lele [45]. Additionally, sponge layers are set around the physical domain (marked out by the red line in Fig. 4) to attenuate exiting vorticity waves. No inflow forcing is applied as the interior of the nozzle is not modeled, but as it is shown in the Appendix, the turbulence levels reach experimental values [46] within the first diameter. Last, no-slip adiabatic wall conditions are defined at all external wall boundaries of the nozzle. Moreover, a small external co-flow of 0.5 m/s is added to help with the convergence of the

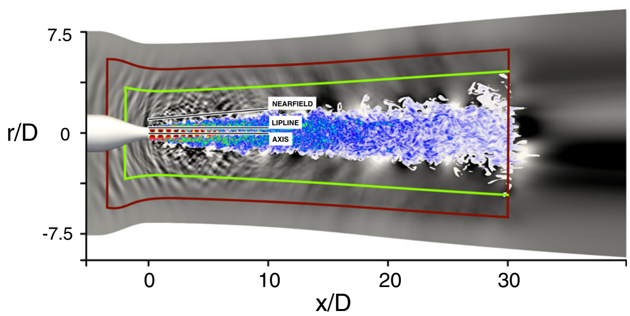

Fig. 4 LES of the under-expanded jet: vorticity modulus (in color, $|\Omega| \in [1.8, 320.0] \times 10^4$ s^{-1}) and acoustic radiated pressure fluctuations (in gray, $p' \in [-500, 500]$ Pa). Red line physical domain limit. Green line FW–H surface position

simulation. The propagation of pressure fluctuations into the far-field is done by means of a Ffowcs Williams and Hawkings [47] (FW–H) acoustic analogy with the formulation 1A of Farassat [48]. The solution is saved at the sampling frequency f_s of 112 kHz on the FW–H surface (identified by the green line in Fig. 4) located at r/D= 3.5 at the nozzle exit and following a topological grid expanding radially with the jet.

This simulation was run without any shock-capturing methodology. Indeed, as the jet is moderately under-expanded, the NPR is relatively low. In addition, since the interior of the nozzle was not included in the LES, no strong shock occurs at the nozzle exit [49]. As a consequence, the formed shock cells are weak and diffused (reflection from a Prandtl–Meyer expansion fan [50]) with Mach numbers lower than 1.4 (see Appendix).

3.4 Mesh definition

The LES mesh contains 75×10^6 cells with about ($1052 \times 270 \times 256$) cells in axial, radial, and azimuthal directions respectively. In order to avoid the singularity at the jet axis, the mesh combines Cartesian and polar grid blocks, also known as butterfly (or O–H) topology [42,51]. The lip of the nozzle and initial momentum thickness at the nozzle exit are discretized using 8 and 15 cells respectively. In the physical region of the domain (Fig. 4), the maximum expansion ratio between adjacent cells in the mesh is not greater than 4%. At the nozzle exit ($x/D = 0$), the mesh has an aspect ratio of 2.5. This ensures an appropriate definition of the first expansion fan of the shock-cell system. The axial mesh size along the axis line is shown in Fig. 5a. The axial mesh size at the nozzle exit is $\Delta x/D = 0.003$ and stretches at a rate of 3% up to one jet diameter (point A) where it reaches a value of $\Delta x/D = 0.017$. Then, the mesh consists in a uniform discretization up to five diameters (point B) and slowly varies up to a mesh size $\Delta x/D = 0.063$ able to capture a maximum Strouhal number St $= fD/U_j$ about 2 at the end of the physical domain (point C). In the sponge layer, the mesh has a stretching ratio of 10%. The radial mesh size at different axial sections is shown in Fig. 5b. On the axis ($r/D = 0$), the radial mesh size is mainly constant, reaching a value of $\Delta r/D = 0.007$ at the nozzle exit. Then, it is refined with a constant rate of 2.5% for all axial positions. At the nozzle exit, the mesh achieves its minimum size at the lip-line with a value of $\Delta r/D = 0.001$. The mesh is then coarsened up to the sponge layer at a rate between 3.5 and 4% assuring a Strouhal number of about 2 on the FW–H surface.

4 Characterization of BBSAN

The jet flow field represented by the vorticity modulus and the acoustic radiated (pressure fluctuation) are shown in Fig. 4.

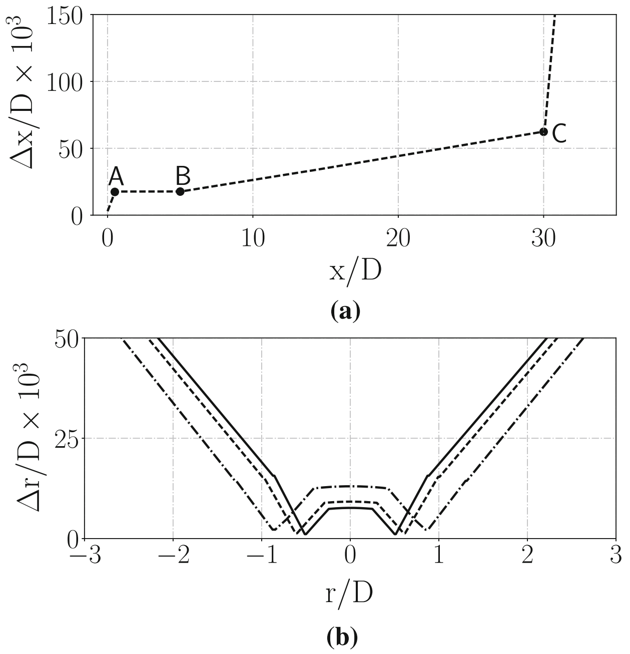

Fig. 5 Mesh size **a** along the axis of the jet and **b** along gridlines perpendicular to the jet axis at $x/D = 0$ (solid), $x/D = 5$ (dashed), $x/D = 10$ (dash-dotted)

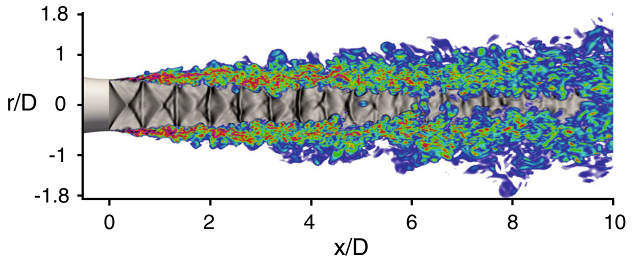

Fig. 6 LES of under-expanded jet: magnitude of density gradient (numerical Schlieren, in gray) and vorticity modulus (in color $|\Omega| \in [1.8, 320.0] \times 10^4\ \mathrm{s}^{-1}$)

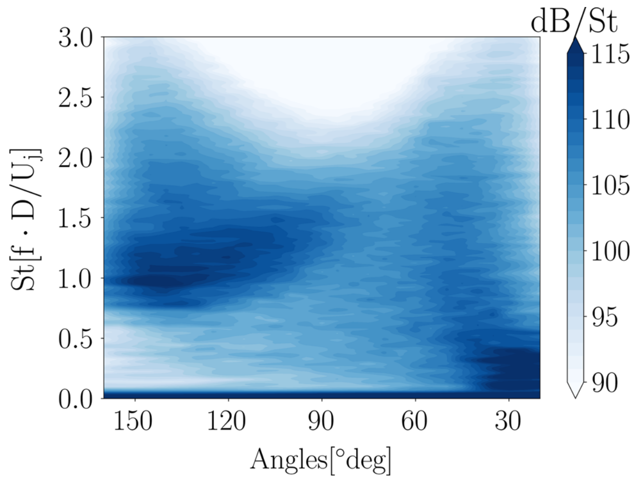

Fig. 7 Far-field directivity of sound pressure level at $r/D = 53$ from the nozzle exit with respect to the jet direction

The two main jet noise components, i.e., the mixing noise traveling downstream and the BBSAN traveling upstream, are clearly visible. In order to have a better description of the jet flow field, an instantaneous view of the train of shock cells interacting with turbulence is shown in Fig. 6 using numerical Schlieren and vorticity magnitude. The periodic structure of the shock cells originating from the imposed overpressure at the nozzle exit is well observed.

The sound pressure level (SPL) directivity of the jet noise predicted in the far-field using FW–H analogy is shown in Fig. 7 for different angles at a radial distance $r/D = 53$ from the nozzle exit with respect to the jet direction. The reference pressure used to compute the SPL is 2×10^{-5} Pa. The mixing noise can be clearly found dominant at angles lower than 60° and Strouhal numbers in the range $0 < \mathrm{St} < 0.5$. Shock-cell noise is well captured for high angles $\theta \geq 90°$ and high frequencies $\mathrm{St} > 0.6$. Moreover, the noise spectrum exhibits a Doppler shift [52] with an increase in the central frequency of BBSAN when moving toward lower angles. This explains why BBSAN is mostly dissipated in the downstream direction in higher frequencies due to a lower mesh discretization.

In order to characterize the BBSAN in the current LES, three sets of lines and azimuthal arrays of numerical probes with an equi-distribution every $\Delta x/D = 0.01$ are analyzed (see Fig. 4). The first data set is located on the jet centerline (noted as AXIS). The second data set is located at the jet lipline (noted as LIPLINE), and the third data set is located in the near-field (noted as NEARFIELD). The latter line has a radial position relative to the exit plane of the nozzle $x/D = 0$ of $r/D = 1$, with an expansion angle of 5° with respect to the jet axis. Both LIPLINE and NEARFIELD data sets are arranged in an equally distributed azimuthal array of four probes ($\Delta\theta = 90°$) that lay on the xy-plane and xz-plane. All data were collected at the same sampling rate as the FW–H surface of 112 kHz.

4.1 Shock-cell noise pattern

The shock-cell pressure pattern is first studied in the Fourier domain in order to obtain some general insights about the under-expanded jet dynamics and about shock-cell noise. The two-dimensional spectral characteristics are first analyzed on the xy-plane in Fig. 8 for $\mathrm{St} = 0.3, 0.6$, and 0.9. The power spectral density (PSD) of pressure is performed on each point of the plane and azimuthally averaged. Results show that at $\mathrm{St} = 0.3$, a maximum is reached near the jet axis at $6 < x/D < 8$ (end of the potential core). Moreover, the PSD map follows the jet expansion downstream (identified by the dashed line). This is expected at this low Strouhal number as it is characteristic of the mixing noise from tur-

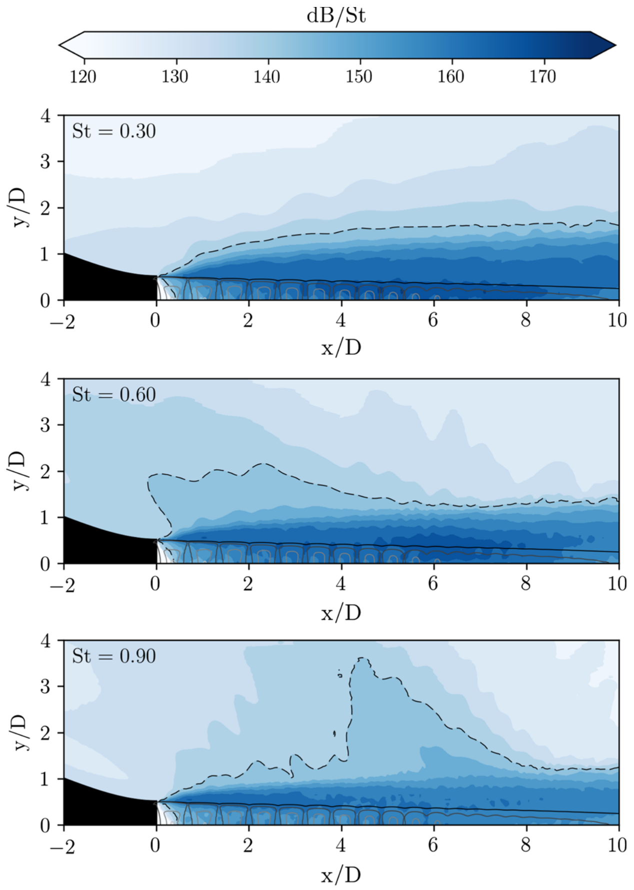

Fig. 8 Average PSD maps of pressure at Strouhal numbers St $=$ 0.3, 0.6, 0.9, from top to bottom, respectively. The dashed line depicts the contour at 140 dB/St. The black solid lines represent the sonic line

bulent structures that propagate downstream in correlation with Fig. 7. At St $= 0.6$, the contour at 140 dB/St shows that the spectral energy extends more in the upstream angles with respect to the jet axis. Similarly, at St $= 0.9$, the PSD of pressure in the near-field is stretched out above the last shock cells near the jet potential core with a lower angle (highlighted by the dashed line). These two frequencies (St $= 0.6, 0.9$) are related to shock-cell noise in the far-field in Fig. 7 and seem to come from different regions in the jet. The different origin centers of shock-cell noise can be explained noting that the central frequency of BBSAN is inversely proportional to the spacing of the shock cells [9] and that the shock-cell spacing decreases as the jet develops.

Furthermore, the PSD of pressure for the data sets AXIS and NEARFIELD can be used to represent the PSD along the x-coordinate. The PSD on AXIS is displayed in Fig. 9a. It illustrates the distribution of energy over the shock-cell system. The vertical patterns correspond to each axial position where the maximum compression of the shock cells is achieved. Horizontal patterns are detected at about St $=$ 0.3, 0.6, and 0.9. The maximum of energy spectrum is found at the location $x/D = 5$ that is used as a reference point in the next section. In order to highlight the acoustic pattern of the shock cell in the near-field, the pressure data NEARFIELD is filtered using an acoustic–hydrodynamic filtering procedure [53,54]. Figure 9b shows the PSD in NEARFIELD of the acoustic component of pressure, which has the banana-shaped pattern of shock-cell noise as found in the literature [55] which resembles the BBSAN pattern obtained in the far-field (Fig. 7). This pattern appears due to the Doppler effect of shock-cell noise shown in Fig. 8. However, the tonal peaks shown in Fig. 9a are mostly dissipated and hidden by the BBSAN peak (the peak at St $= 0.6$ can be seen for $x/D < 3$).

Moreover, additional details can be obtained from the spectral results if the signal in the region within the shock cells ($0 < x/D < 10$, see Fig. 6) is transformed into the frequency–wavenumber domain. The transformation on AXIS is shown in Fig. 10a and on the LIPLINE in Fig. 10b. Both locations illustrate that the excited waves previously found at St $=$ 0.3, 0.6, and 0.9 are in fact mainly in the negative part of the axial wavenumber and travel at a group velocity between $U_{\mathrm{c}} - a_\infty$ and a_∞ where U_{c} is equal to U_{j} at the axis and $U_{\mathrm{c}} = 0.67U_{\mathrm{j}}$ at the lip-line. This indicates that both the axis and the lip-line are capturing a pressure wave traveling upstream even when the flow is fully supersonic on the axis. This can be explained taking into account the upstream directivity of shock-cell noise and it is further developed in the following.

The shock-cell noise generated from the interaction between the vortices of the shear layer and the shock cells is not only convected outside the jet at the ambient speed of sound but also convected inside the supersonic region of the jet at a mean axial velocity of $U_{\mathrm{j}} - a_\infty$ as sketched in Fig. 11. The wave is deformed in the axial direction due to the supersonic velocity of the jet displacing it downstream locally. However, due to the fact that the origin of the wave in the shear layer is moving upstream at the speed of sound a_∞, it creates an oblique front wave that is recorded by an axial array of probes to travel upstream at the same speed a_∞. This phenomenon is clearly illustrated by the interaction of a spatially developing supersonic mixing-layer with a compression wave separating a supersonic stream as in [56].

4.2 Shock-cell noise signature

The decomposition in frequency–wavenumber domain (Sect. 4.1) allows the signal to be filtered into waves that travel upstream and waves that travel downstream (p^- and p^+ signals respectively). The pressure signal of the different arrays is reconstructed using only the second and fourth quadrants (p^- signal) and the first and third quadrants (p^+ signal) from Fig. 10.

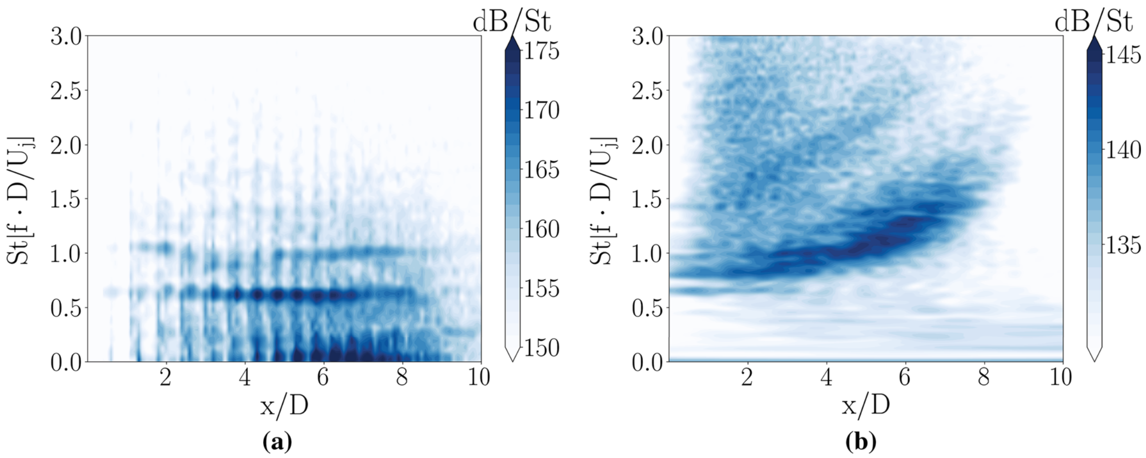

Fig. 9 Frequency–space PSD maps of pressure along the axial direction for the data set **a** AXIS and **b** NEARFIELD

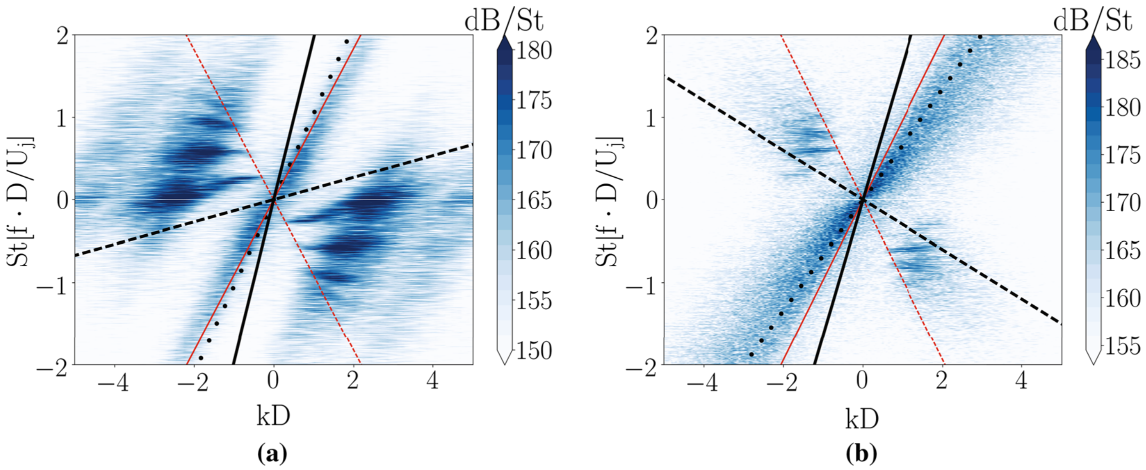

Fig. 10 Frequency–wavenumber pressure energy distribution maps along the axial direction for the data set **a** AXIS and **b** LIPLINE. The dotted line depicts the mean convective velocity U_c. The thin red lines represent the acoustic speeds $+a_\infty$ (solid) and $-a_\infty$ (dashed). The thick lines represent $U_c + a_\infty$ (solid) and $U_c - a_\infty$ (dashed)

The decomposition into two signals p^- and p^+ is performed for each of the data sets. Due to the fact that shock-cell noise is mainly radiated upstream, the event identification procedure provides similar results on the near-field line array when it is applied to a hydrodynamic–acoustic filtered pressure signal (as in Fig. 9b) or to the above-mentioned p^- and p^+ reconstructed signals [57]. For conciseness, in the NEARFIELD, only the results from the signals p^- and p^+ are shown. Moreover, the event identification procedure is also performed on the axial velocity u (reference signal) on both AXIS and LIPLINE. For all data sets, the signatures are obtained using the axial velocity fluctuations u and the initial pressure fluctuations p without any filtering as target signals of the conditional average. Additionally, the spectra computed from the signatures are compared against the spectra from the full target signals at four locations of interest noted as: P0 on AXIS ($x/D = 5$), P1 on LIPLINE ($x/D = 5$ and $r/D = 0.5$), P2 in NEARFIELD ($x/D = 4.5$ and $r/D = 1.4$), and P3 in NEARFIELD ($x/D = 0$ and $r/D = 1$). P0 represents the position with the highest PSD in the shock cells (see Fig. 10a). P1 is a point in the shear layer where the interaction between vortical structures and the shock cells is the highest. P2 illustrates a point in the near-field where both low frequency mixing noise and shock-cell noise are present and P3 depicts a point where the acoustic component is mainly constituted by shock-cell noise and the hydrodynamic perturbations are low.

4.2.1 Signature of the front wave traveling upstream

Shock-cell noise is generated from the interaction between shock cells and the vortical structures convected through the shear layer. For this reason, the signature of the front wave traveling upstream depicted in Fig. 11 is first stud-

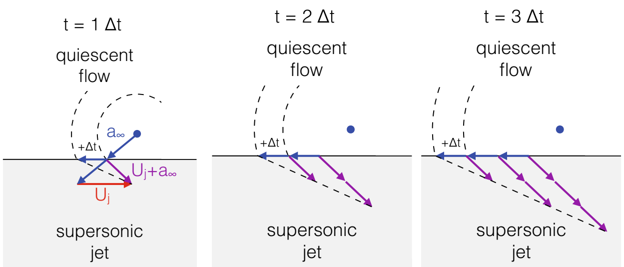

Fig. 11 Evolution of a front wave traveling upstream inside a supersonic jet

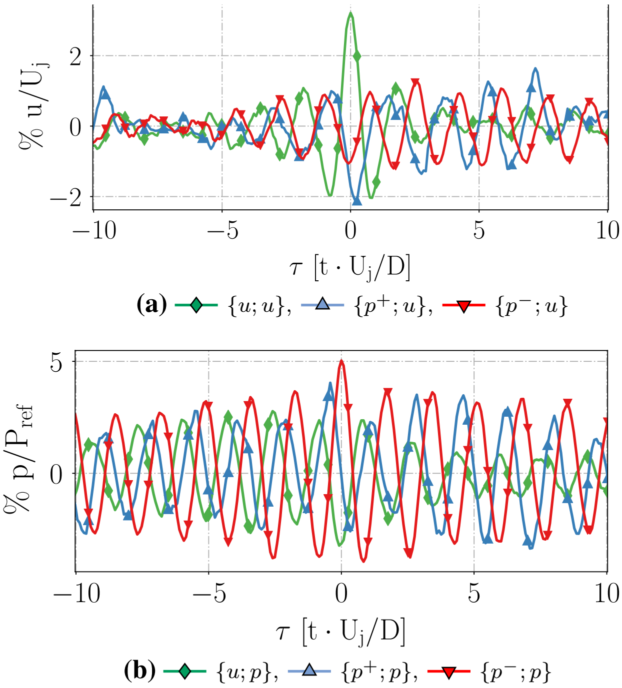

Fig. 12 Signature at P0 (AXIS) of **a** u and **b** p variables

ied at P0 where the shock cells have maximum amplitude, at a reference scale of $\mathrm{St}(s) = 0.6$, which is the Strouhal number for which the higher energy content is identified on the axis as shown in Fig. 9a for the pressure PSD. In order to investigate pressure–velocity correlations responsible for the PSD peaks, cross-conditionings with a combination of axial velocity and pressure signals are computed. Following the notation from Sect. 2, the auto- and cross-conditionings between u, p^+, and p^- signals (as reference signal) and u and p signals (as target, or plotting signals) are shown in Fig. 12. All signatures presented in this section and in the following sections are obtained through the averaging of several temporal windows of size $10D/U_\mathrm{j}$ centered in time at the most energetic events of the reference scale with a filtering window of size $2.5D/U_\mathrm{j}$. At this location, a total of 50, 21, and 91 events were used for the conditional averaging for u, p^+, and p^- signals, respectively.

On the one hand, Fig. 12a shows that the signature $\{u; u\}$ is centered at $\tau = 0$ with a maximum. Moreover, both p^+ and p^- events detect a signature with origin ($\tau = 0$) on a minimum (absolute for p^+ and local for p^- signals) and its wavepacket shape is shifted into positive times. As u is the plotted variable, the pressure events detected at $\tau = 0$ perceive a velocity fluctuation delayed in time which means that pressure events are followed in time by velocity events. On the other hand, Fig. 12b shows how the signature $\{u; p\}$ is, first, centered on the minimum of the signature and second, shifted into negative times. In this case, because the variable that is plotted is p, the signature computed with u events is advanced in time with respect to $\tau = 0$ where the events are centered. This confirms that the signature $\{u; p\}$ is preceding in time the events related to u. Moreover, the maximum values of the signatures $\{p^+; p\}$ and $\{p^-; p\}$ are mostly centered at $\tau = 0$ and do not show any significant bias in time.

The signatures shown in Fig. 12 represent the most probable shape of the characteristic events detected at P0 ($x/D = 5$) plotted at the same location P0. In order to study the evolution of the signatures (and thus of the events) along the axis of the jet and through the shock cells, a different axial location for the target signal can be used maintaining in time the same averaging windows used at P0. This cross-conditioning along the axis is shown in Fig. 13. As the signatures at the different axial positions are a function of time, only the central values of the signatures at time $\tau = 0$ are plotted. In addition, as it is depicted in Fig. 12, the maximum and minimum of the signature may not lay at $\tau = 0$. For this reason, the extrema are searched over the averaging temporal window at each axial position and outlined as the envelopes of the temporal signature in dashed lines in Fig. 13.

The signature $\{u; u\}$ of the event detected in Fig. 13a grows axially. Most of the envelope peaks are localized on the compression peaks of the shock cells (vertical dashed line). The compression peaks are computed from the average flow and are illustrated in Fig. 6 by the vertical lines inside the diamond cells. The maximum peak of the signature is observed at $x/D = 5$, where shock cells start breaking down. Some other peaks are found farther downstream possibly due to a poor averaging because of a low number of events detected. Moreover, the signature obtained for the target signal p (Fig. 13b) shows that the pressure related to these events is contained in the potential core and decays after $x/D = 6$ to a small value at $x/D = 10$, even when the envelope for u is maximum. As it can be seen from these figures, the values of u and p are shifted in phase by 180° meaning that a positive amplitude in u correlates with a negative amplitude in p. Similarly, the signatures $\{p^-; p\}$ are illustrated in Fig. 13c. The cross-conditioning presents as well a maximum around $x/D = 5$ (as in Fig. 13b) and the amplitudes of the signatures exhibit

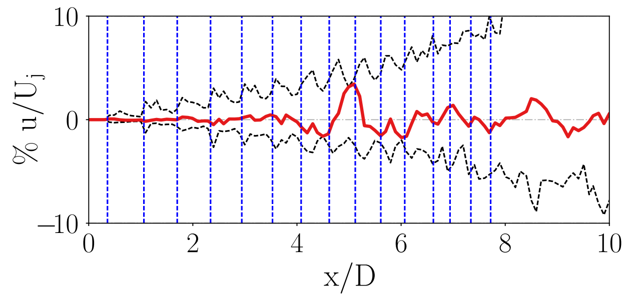

(a) $\{u; u\}$

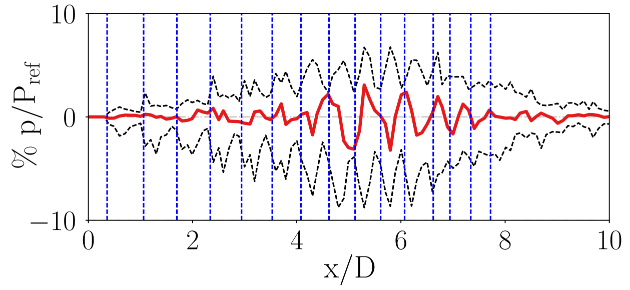

(b) $\{u; p\}$

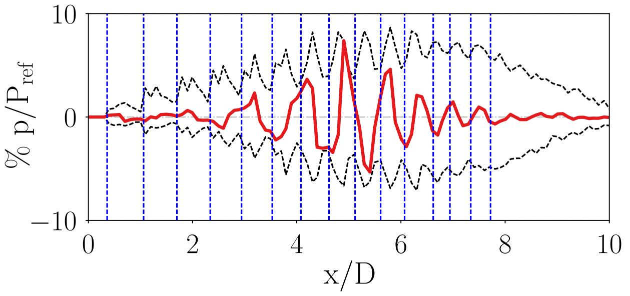

(c) $\{p^{-}; p\}$

Fig. 13 Cross-conditioning at AXIS ($x/D = 5$) of axial velocity and pressure variables using different localization variables. The dashed black line represents the envelope of the signature for all axial positions. The vertical dashed blue lines represent the peak of the expansion region of each shock cell

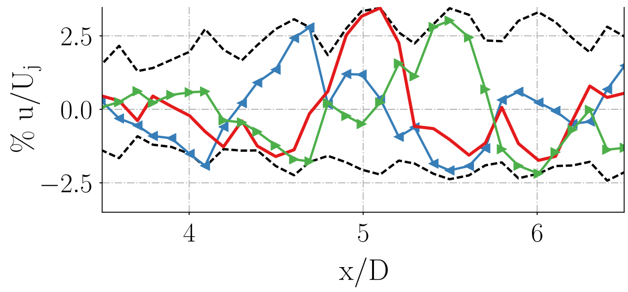

(a) $\{u; u\}$

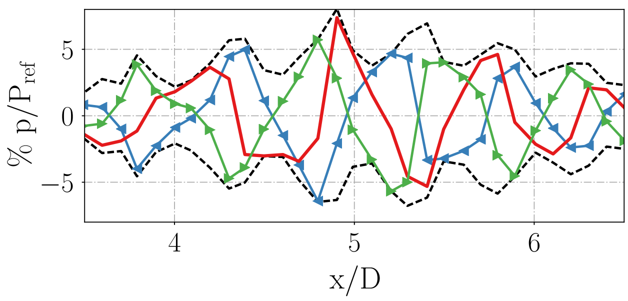

(b) $\{p^{-}; p\}$

Fig. 14 Cross-conditioning at AXIS ($x/D = 5$) of **a** axial velocity u and **b** pressure p at different times. The left blue triangles (◁) represent the signature at $\tau = -0.42D/U_{\mathrm{j}}$, the solid red line (——) at $\tau = 0$ and the right green triangles (▷) at $\tau = +0.42D/U_{\mathrm{j}}$. The dashed line represents the envelope of the signature for all shifted times

a bias for positive values as opposed to the signature $\{u;\ p\}$ shown in Fig. 13b.

Furthermore, signatures are illustrated at $\tau \in \{-0.42D/U_{\mathrm{j}}, 0, +0.42D/U_{\mathrm{j}}\}$ for all axial locations in Fig. 14 in order to give some insights into the axial direction to which the events are traveling. Figure 14a shows that the signature $\{u;\ u\}$ moves downstream with an average speed close to the jet exit velocity U_{j}. The average speed of the signature is computed simply by measuring the spatial displacement of the main peak over the time shift. In a similar fashion, the signature $\{p^{-};\ p\}$ moves upstream as shown in Fig. 14b with an average speed comparable to the ambient acoustic speed. This signature corresponds to the shock-cell noise that enters the jet as explained in Sect. 4.1 as it is the only signal that travels upstream.

In order to have a better physical description of the evolution of these events in the jet flow, a spatial cross-conditioning can be applied as well over a two-dimensional field [26]. Because the amplitude of the hydrodynamic pressure inside the jet differs by several orders of magnitude with respect to the acoustic component propagating outside, the results are made dimensionless by the local standard deviation σ in order to discriminate the event influence. A signature is considered here to be relevant and converged if the modulus normalized by the standard deviation is greater than 1 and if there are enough windows to average out other turbulence scales. This means that the normalized amplitudes are close to zero outside of the region of influence of the signature. Figure 15a shows the signature $\{u;\ u\}$ of the cross-conditioning obtained in the xy-plane where the reference events are detected at P0. The two-dimensional signature $\{u;\ u\}$ illustrates localized events inside the potential core. The two-dimensional signature $\{p^{-};\ p\}$ is depicted in Fig. 15b, c. This signature presents a pattern inside the potential core and another outside with opposite amplitudes that extend up to $r/D = 1$. As it was presented in Fig. 11, the pressure waves are convected upstream inside the potential core. Because they are being convected diagonally, the positive region of the external pressure wave lies on top of the negative pressure wave which gives this distinctive checkerboard pattern. The diago-

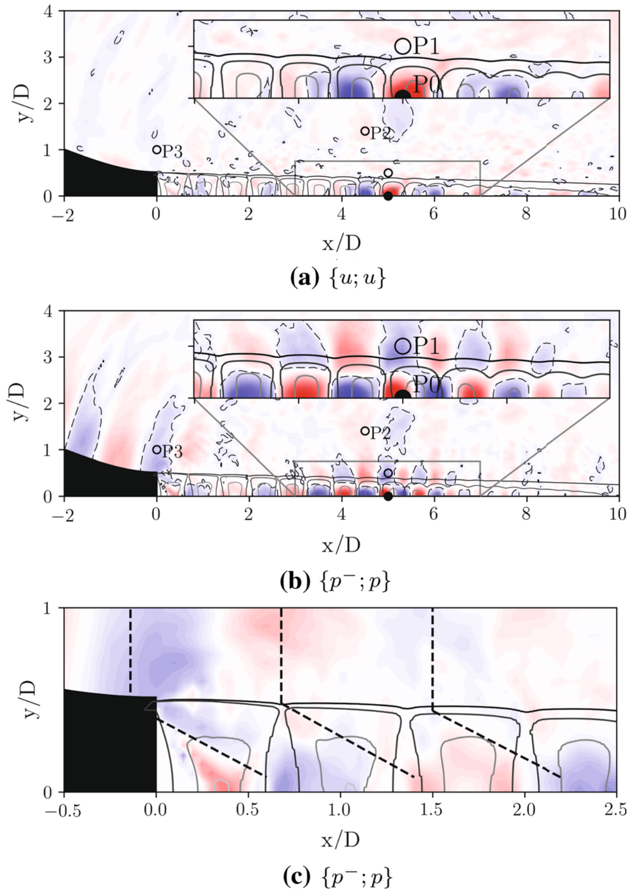

Fig. 15 Normalized two-dimensional cross-conditioning maps of **a** $\{u; u\}$ and **b** $\{p^-; p\}$. The results are normalized by the local standard deviation and are plotted between $+1$ (red contours) and -1 (blue contours). The dashed contours depict the negative regions. The black solid lines represent the Mach number contours $M > 1$. Figure (**c**) is a detail of (**b**) at the nozzle exit where the waves that enter the potential core are depicted by dashed lines

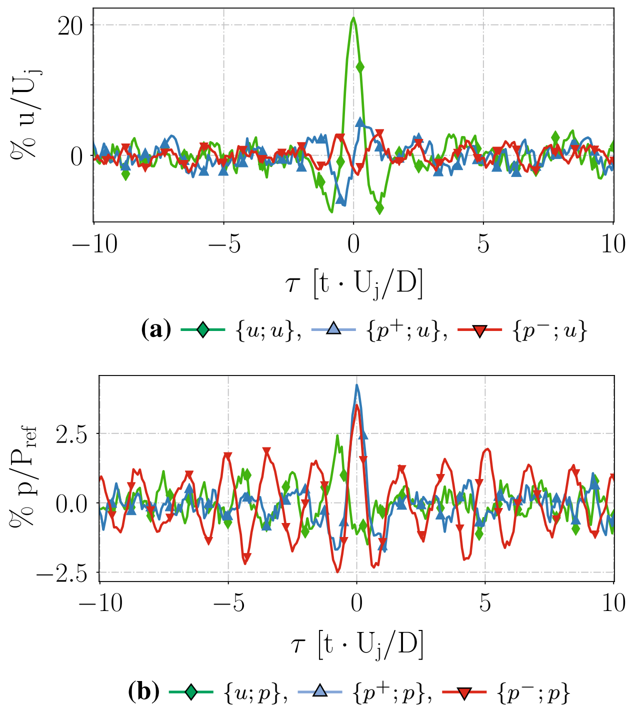

Fig. 16 Signature at P1 (LIPLINE) of **a** u and **b** p variables

nal pattern is emphasized with dashed lines in Fig. 15c close to the nozzle exit.

4.2.2 Signature of the shock/shear layer interaction

Turbulent vortical structures are generated and convected at the convection speed U_c downstream in the shear layer. These structures interact with the shock cells not only generating shock-cell noise at the tips of the shocks but also distorting the shock cells due to pressure variations [58]. The shock/shear layer interaction responsible for the generation of BBSAN is studied in this section by analyzing the signatures of the characteristic events in the shear layer at P1 (LIPLINE). The events at P1 are detected at the same reference scale of $\mathrm{St}(s) = 0.6$ as performed at AXIS. At this location, a total of 81, 99, and 250 events were used for the conditional averaging of u, p^+, and p^- events, respectively. For this data set, the two-dimensional cross-conditioning is averaged over the xy-plane and xz-plane. Moreover, as the events detected at $r/D = 0.5$ and $x/D = 5$ lay on four different azimuthal positions, each of them is treated independently before doing the average. This means that the times at which the events are detected may differ for the four azimuthal positions. Because of the averaging of the signatures over the four planes, information related to azimuthal modes is lost in the process [59,60]. Nonetheless, using the same scale implies that the identified events correspond to the same characteristic frequency $\mathrm{St}(s)$. For the same reason, events related to an axisymmetric mode should have similar detection times.

The signatures computed with events from u, p^+, and p^- signals are shown in Fig. 16a, b for u and p variables. Figure 16a displays the signatures computed for u centered at $\tau = 0$ with a positive peak from events detected with u (in phase) and a negative peak from events related to p^- (opposite phase). Otherwise, the signature $\{p^+; u\}$ lies in between a minimum and a maximum. This is characteristic of turbulent structures convected downstream in the shear layer. Moreover, no major time bias is discerned from these results. As P1 is located in the shear layer, the signature $\{u; u\}$ shows an order of magnitude higher than the signatures $\{p^+; u\}$ and $\{p^-; u\}$ signals computed from pressure events. The signatures of pressure depicted in Fig. 16b shows that both events detected with p^+ and p^- produce a signature with a maximum at $\tau = 0$ and a minimum for u with a slight negative time bias as in Fig. 12b.

The two-dimensional signatures $\{u;\, u\}$ and $\{u;\, p\}$, are displayed in Fig. 17a, b. Similarly to the results on the axis illustrated in Fig. 15a at P0, the signature $\{u;\, u\}$ shows a structure centered at point P1 where the events are detected. This pattern is contained in a small region which extends about 1.8 D axially and $D/2$ radially. It is in fact contained in the shear layer and does not enter the potential core (nor the supersonic region). On the other hand, the signature obtained for the variable p shown in Fig. 17b presents structures that are extended radially through the shear layer and continue in the near-field region ($r/D > 1.5$ at $x/D = 5$). Moreover, similarly to what was shown in Fig. 16a for the p^+ events, the pressure p at P1 (computed from u events) lies in between a maximum and a minimum in the axial direction. These results suggest that p^+ and u events give similar information but shifted in time as it was found on the axis. Furthermore, both signatures do not show any relevant patterns with values above ± 1 inside the potential core. This could indicate that the events that are captured by u do not influence the shock-cell region (depicted by the solid black contours).

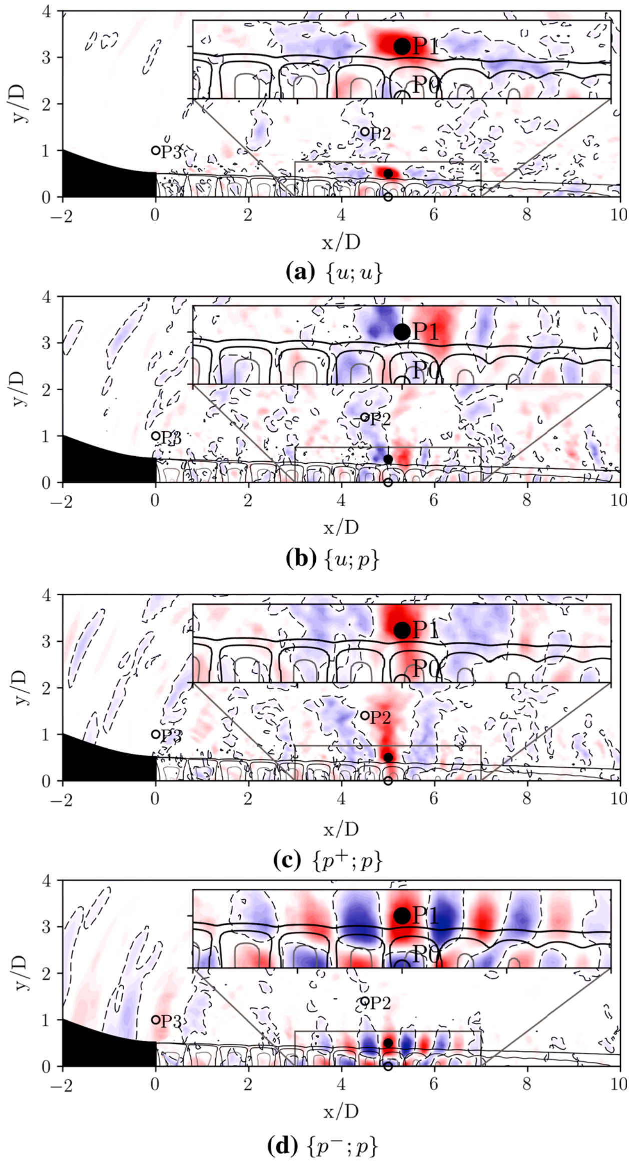

(a) $\{u; u\}$
(b) $\{u; p\}$
(c) $\{p^+; p\}$
(d) $\{p^-; p\}$

Fig. 17 Normalized two-dimensional cross-conditioning maps of **a** $\{u;\, u\}$, **b** $\{u;\, p\}$, **c** $\{p^+;\, p\}$, and **d** $\{p^-;\, p\}$, where the reference signal is located at P1. The results are normalized by the local standard deviation and are plotted between $+\,1$ (red contours) and $-\,1$ (blue contours). The dashed contours depict the negative regions. The black solid lines represent the Mach number contours $M > 1$

The two-dimensional signature $\{p^+;\, p\}$ is shown in Fig. 17c. The pressure signature exhibits vertical patterns that extend from the axis to up $y/D = 2$ in the near-field region. This signature identifies the influence of the pressure in the near-field of the vortical structures convected downstream through the shear layer. Lastly, the two-dimensional signature $\{p^-;\, p\}$ shown in Fig. 17d presents the same checkerboard pattern as shown in Fig. 15b for the events detected at P0. This implies that both locations detect the same event. Nevertheless, contrary to the results on AXIS, the maximum of the pattern is not located at the position where the events are detected (P0 on AXIS and P1 on LIPLINE), but they are located near the sonic line (noted with the black solid line) which suggests that the pressure perturbation is generated at this location as it is expected from shock-leakage phenomena [11].

4.2.3 Near-field signature of BBSAN

Once shock-cell noise is generated by the interaction of vortical structures and the shock cells, it travels through the shear layer and reaches the near-field region. In the following, the signatures are studied at P2 computed only from pressure events (p^+ and p^- signals) as velocity fluctuations give the same information. The signature is computed at two different Strouhal numbers $\mathrm{St}(s) = 0.2$ and $\mathrm{St}(s) = 1.03$ for p^+ and p^- events, respectively, which symbolizes the hydrodynamic and acoustic (BBSAN) fluctuations. At this location, a total of 104 and 257 events have been detected and used for p^+ and p^-, respectively, for the conditional averaging.

The one-dimensional temporal signals are shown in Fig. 18a, b plotting, respectively, u and p variables. The signatures $\{p^+;\, u\}$ and $\{p^+;\, p\}$ are centered at $\tau = 0$ with a positive peak, even though they are plotting with different variables. At this location, hydrodynamic fluctuations are equivalent in terms of velocity and pressure fluctuations, with similar amplitudes and shapes. On the other hand, the signatures $\{p^-;\, u\}$ and $\{p^-;\, p\}$ are in opposite phase presenting a positive peak at $\tau = 0$ for $\{p^-;\, p\}$ and a negative one for $\{p^-;\, u\}$. Moreover, due to the fact that two scales are used to identify the events p^+ and p^-, their signatures exhibit a different temporal period. Nonetheless, the signature of pressure highlights how the central peaks of the signature for the

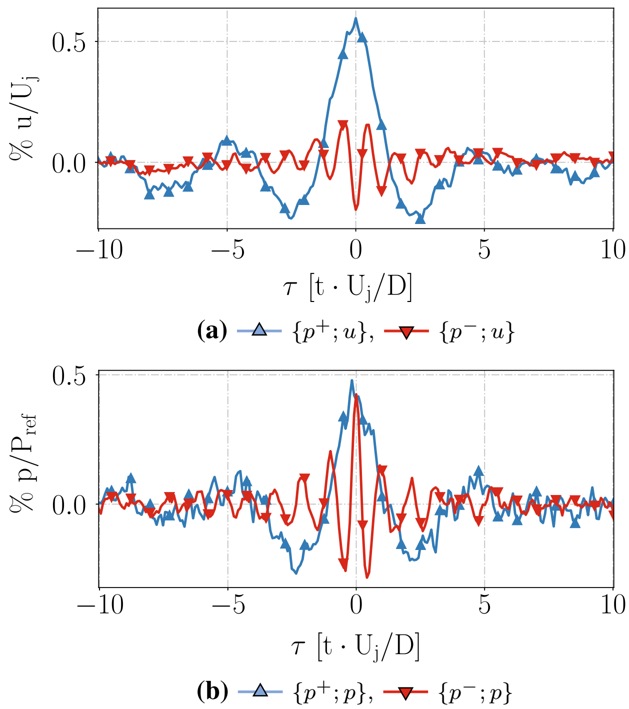

Fig. 18 Signature at P2 (NEARFIELD) of **a** u and **b** p variables

p^- events are modulated by the signature of the p^+ events (Fig. 18b). This illustrates again how shock-cell noise (p^-) is generated from the interaction of the large-scale vortical structures (p^+) and shock cells.

The two-dimensional cross-conditioning shown in Fig. 19 allows to highlight clearly the two components of noise radiated in the near-field by a supersonic under-expanded jet. Indeed, the signature obtained outside the jet shear layer, for u in Fig. 19a and p in Fig. 19b, is characteristic of downstream propagating pressure waves, i.e., mixing noise. It presents a spatial length-scale $\lambda \approx 3D$ greater than the one found at P1 (LIPLINE). In fact, if a convection speed $U_c \approx 0.67U_j$ is taken, the characteristic frequency computed $f = U_c/\lambda$ is in the order of the characteristic scale $\mathrm{St}(s) = 0.2$. A reason is that the scale s (with units of time and equivalent to $\mathrm{St}(s) = 0.6$) used to detect events at P1 is a smaller one, which corresponds to a higher $\mathrm{St}(s)$ [see (3)]. Nonetheless, the signature of shock-cell noise is detected as well over the nozzle at P3. Furthermore, in the jet shear layer, the signature disappears when plotting u. Due to the fact that the two-dimensional signature is made dimensionless by the local standard deviation, the patterns that are visible outside the shear layer for u are an artifact that comes from the velocity variations linked to the pressure variable. Indeed, as it was shown in Fig. 16a, the signature $\{u; u\}$ in the shear layer computed is an order of magnitude higher than the signature $\{p^+; u\}$. This indicates that the actual signature is masked under these more energetic events, which, in this case, are not correlated in time in the shear layer.

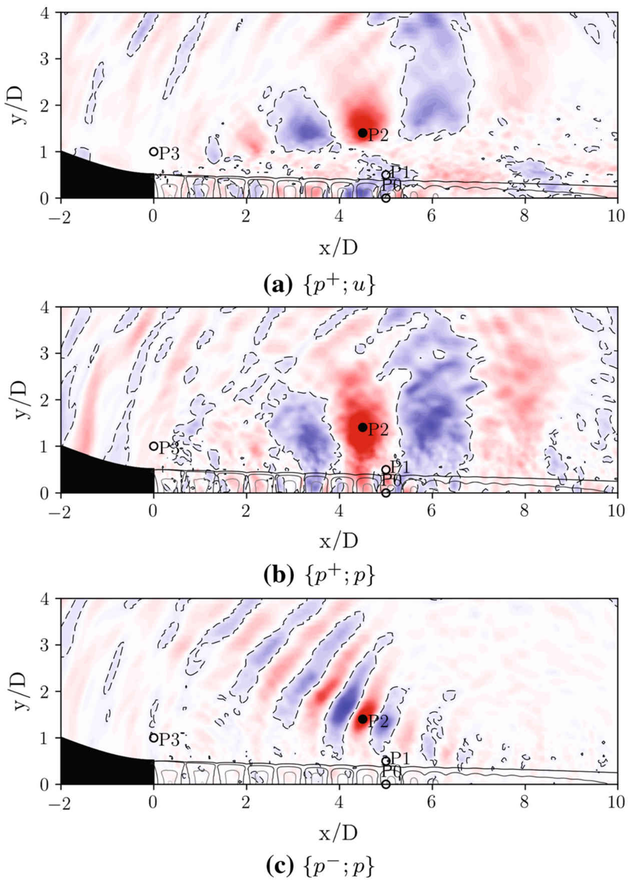

Fig. 19 Normalized two-dimensional cross-conditioning maps of **a** $\{p^+; u\}$, **b** $\{p^+; p\}$, and **c** $\{p^-; p\}$, where the reference signal is located at P2. The results are normalized by the local standard deviation and are plotted between + 1 (red contours) and − 1 (blue contours). The dashed contours depict the negative regions. The black solid lines represent the Mach number contours $M > 1$

Last, the two-dimensional cross-conditioning $\{p^-; p\}$ (Fig. 19c) clearly identifies the signature of pressure perturbations coming from the shock cell/jet shear layer interaction region (near $x/D = 8$) and propagating upstream at an average angle of 140°.

4.3 Frequency response of the signatures

The two-dimensional signatures shown in Sect. 4.2 represent a filtered field regarding the turbulence, the mixing noise, or the shock-cell noise. They give an instantaneous qualitative idea of the spatial distribution of the signatures for events detected at $\tau = 0$. As the signatures are defined between $-12D/U_j < \tau < 12D/U_j$, it allows a spectral analysis to be performed (as in Fig. 3). Figure 20 shows the PSD spectra of the signatures $\{p^-; p\}$ and $\{p^+; p\}$ at locations P0, P1, P2, and P3.

At P0 on the jet axis (Fig. 20a), P1 in the jet shear layer (Fig. 20b), and P3 in the near-field (Fig. 20d), the peak at

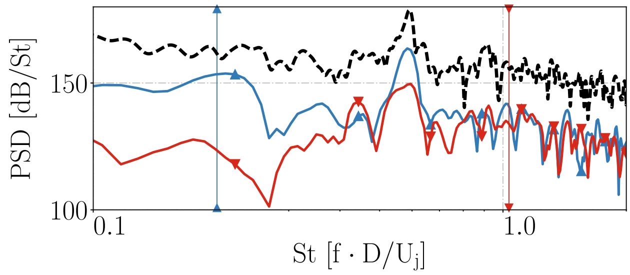

(a) P0

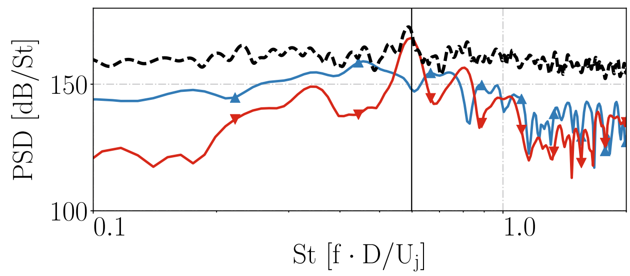

(b) P1

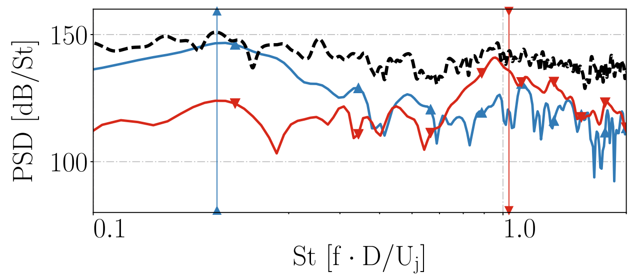

(c) P2

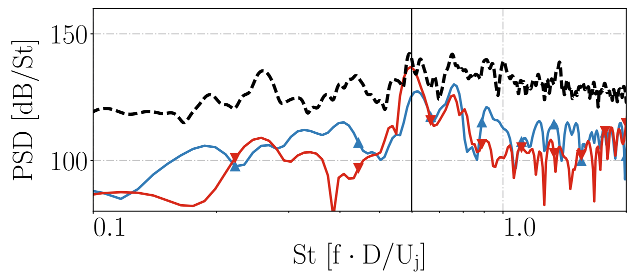

(d) P3

Fig. 20 PSD spectra of the cross-conditioning of pressure at **a** P0, **b** P1, **c** P2, and **d** P3 computed with events detected at P1 (**b** and **d**) and P2 (**a** and **c**). - - - corresponds to the PSD of the actual pressure p signal at the corresponding location, —▼— is the PSD of $\{p^-; p\}$, —△— is the PSD of $\{p^+; p\}$ and the vertical lines depict the reference scales at St = 0.2, 0.6, 1.03 used in Sect. 4.2 to detect the events

St = 0.6 in Fig. 9 is well retrieved by $\{p^-; p\}$. This clearly identifies a shock-cell noise component. However, this is not the case for signature $\{p^+; p\}$ computed from the pressure propagating downstream which instead shows a broadband peak at St = 0.44 at locations P1 (Fig. 20a). In fact, for St < 0.6, the contribution of the $\{p^+; p\}$ spectra is higher than the ones for $\{p^-; p\}$. This shows that this region is dominated by events propagating downstream with a range of frequencies typical of mixing noise. At P3, both $\{p^+; p\}$ and $\{p^-; p\}$ capture similar spectra with peaks at St = 0.6 and St = 0.8. These results demonstrate that the events detected at P1 are able to reproduce a part of the spectra at P3, which mainly comes from shock-cell noise. This confirms that the wavelet-based procedure is able to detect this phenomenon even in a highly turbulent flow region such as the shear layer at the P1 location.

This result is clearly highlighted in Fig. 20c. At P2, the main difference between the signatures from p^+ and p^- events is found. The vortical structures traveling downstream detected by p^+ perfectly capture the low frequency peak amplitude at St = 0.2 (Fig. 19b), which corresponds to the hydrodynamic component of the pressure. Moreover, the acoustic component (represented by pressure waves traveling upstream, see also Fig. 19c) is fully recovered by p^- events matching the shock-cell noise signature with the BBSAN peak in the vicinity of St = 1.03, which is in agreement with the spectra of the unfiltered pressure p, and the acoustic component shown in Fig. 9b.

5 Conclusion

This paper is dedicated to the near-field analysis of a non-screeching supersonic under-expanded jet. The study focuses on the impact of the pressure waves generated by Broadband shock-associated noise (BBSAN). The analysis is performed on a numerical database generated using large eddy simulation (LES).

The power spectral density of pressure on the jet axis depicts several tones at St = 0.3, 0.6, and 0.9 that present peaks at the compression regions of the shock cells and the absolute maximum at $x/D = 5$. If the PSD is represented in the frequency–wavenumber domain, the different waves are seen to travel at a group velocity that lies between the acoustic speed $U_c - a_\infty$ and the sound speed a_∞ in the negative region of the axial wavenumber. This region represents the part of the signal that is traveling upstream. A characteristic pattern is identified from the PSD on the axis (supersonic with shock cells) and on the jet lip-line (mainly subsonic). This wave that seems to travel upstream is an artifact of shock-cell noise that actually travels upstream through the subsonic shear layer and enters the supersonic region leaving this distinct pattern. This shows that shock-cell noise acts as a moving source that travels upstream and enters the potential core. As a result, an oblique front wave traveling upstream is generated and identified using an axial array of probes. In order to study the influence of this wave traveling upstream, the pressure signal was decomposed into waves traveling upstream and downstream (p^- and p^+ signals respectively) and used as reference signals.

A wavelet-based post-processing technique was then performed on these reference signals and the axial velocity u on the axis, the lip-line, and the near-field. The wavelet analysis is used in this work to extract a temporal signature representative of the most energetic events generated from the BBSAN at the scales of interest. The results in the shock-cell region show that the pressure events precede the events in u which travel at the speed U_{j}. Moreover, the signatures of u grow in amplitude with the axial direction. On the other hand, the pressure signatures are caught in the potential core showing a global maximum at $x/D = 5$ and peaks at the compression regions of the shock cells. The two-dimensional cross-conditioning shows that both p^{-} events from the axis and from the shear layer (lip-line) highlight a checkerboard pattern in the range $3 < x/D < 7$ and $r/D < 1$ that travels upstream. This pattern appears because the BBSAN enters the potential core as a diagonal front wave as illustrated close to the nozzle exit. Moreover, the two-dimensional signature obtained from p^{+} in the near-field is not well defined in the shear layer when plotting the axial velocity u but shows a continuous pattern for the pressure p because the shear layer contains u events an order of magnitude higher than in the rest.

The influence of the vortical structures (represented by p^{+}) responsible for the generation of shock-cell noise is depicted by the PSD of the pressure signatures at four locations of interest: the shock-cell region (P0), the shear layer (P1), and the near-field (P2 and P3). The PSD shows that the lower frequencies St < 0.6 are dominated by the vortical structures at all locations. Moreover, events detected in the highly noisy region of the shear layer are able to reproduce part of the spectra over the nozzle, which mainly comes from shock-cell noise. When the events are detected in the near-field with different reference scales, the procedure described in the paper is able to easily separate the hydrodynamic from the acoustic fluctuations and recover the broadband shock-cell noise.

To conclude, the wavelet-based methodology developed to analyze temporal signatures in subsonic jets has been applied to supersonic jets. Two-dimensional field analysis from LES was performed. This analysis allowed the influence of different events on the field to be identified. Characteristic patterns that travel upstream were identified and analyzed. The extension of this methodology to a three-dimensional field can be easily foreseen. This should allow for the decomposition of the signal into azimuthal modes that will be used to perform the wavelet-based procedure in order to obtain a three-dimensional signature of the different modes.

Acknowledgements The authors are thankful to L. Gefen from Università Degli Study di Roma, UniRomaTre for his help with the wavelet post-processing. This work was granted access to the HPC resources of CINES under the allocation 2016-[x20162a6074] made by GENCI. Moreover, It was supported by the Marie Curie Initial Training Networks (ITN) AeroTraNet 2 of the European Community's Seventh Framework Programme (FP7) under Contract No. PITN-GA-2012-317142.

Appendix: Validation of the simulation against experimental results

This appendix presents a comparison between the numerical results obtained from the large eddy simulation of the non-screeching under-expanded supersonic single jet and the experimental results from LMFA [46] and VKI [61].

Jet aerodynamics

The averaged Mach number profile on the axis for the LES and the experimental results are shown in Fig. 21. The LES shows good agreement for shock-cell spacing in the first three shock cells. However, further downstream, there is a shift between the experimental and the numerical Mach number profiles. Nonetheless, the shock-cell spacing is only reduced by about 5%. Even though the amplitudes are higher than in the experimental results, they follow the same decay and they capture the end of the potential core at the same position.

The turbulence levels of the velocity components on the lip-line are shown in Fig. 22. As no turbulence injection is used in the LES, the initial turbulence levels at $x/D = 0$ are equal to zero. However, they reach the same levels of rms as in the experiments after one radius. The overshoot observed within the first two diameters can be explained by a rapid transition to turbulence. Due to this, the amplitude decays about 20% relative to the experiments at $x/D = 10$. Nonetheless, the rms values are high enough to be considered as turbulent flow as it can be deduced by the vorticity contours in Fig. 6.

The turbulence length-scale L_{uu} computed from the auto-correlations R_{uu} along the lip-line is illustrated in Fig. 23. The integration of R_{uu} is calculated up to the value 0.1. The length-scale obtained has the same growth rate, but shifted 1.5 diameters in the axial direction. This displacement is

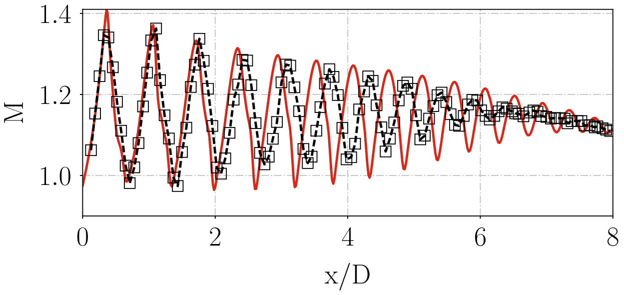

Fig. 21 Mach number profile at AXIS. LMFA experiment [46] (notched nozzle), LES

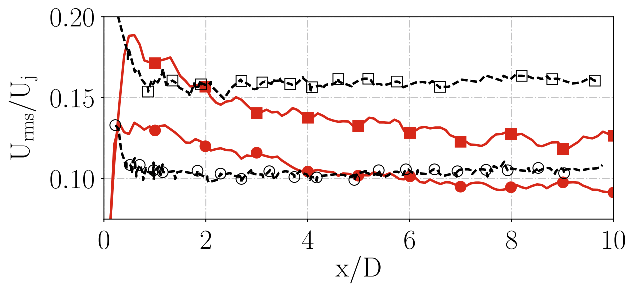

Fig. 22 Turbulence levels of the axial (U_{rms}) and radial (V_{rms}) component of velocity at LIPLINE ($r/D = 0.5$). U_{rms} -⊟- and V_{rms} -⊖- from LMFA experiment [46]. U_{rms} -■- and V_{rms} -●- from LES

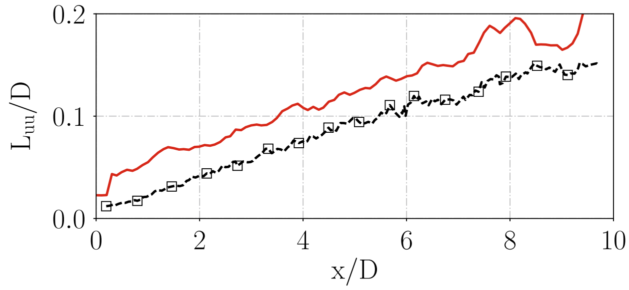

Fig. 23 Axial turbulence length-scale at LIPLINE($r/D = 0.5$). -⊟- LMFA experiment [46], —— LES

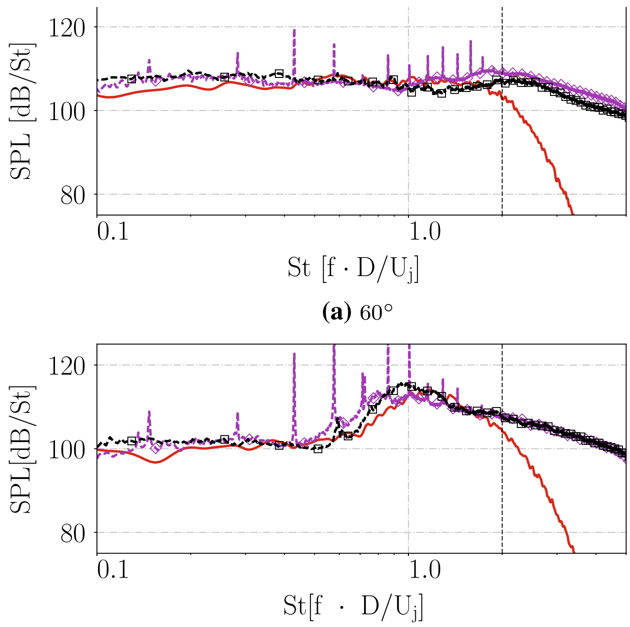

(a) 60°

(b) 120°

Fig. 24 Far-field sound pressure level at $r/D = 53$ from the nozzle exit at **a** 60° and **b** 120° with respect to the jet direction. The vertical dashed line represents the cut-off St for the LES. -⊟- LMFA experiment [46], -◇- experiment VKI [61], and —— LES

probably due to the inlet steady profiles at the exit of the nozzle, where the laminar vortex pairing triggering transition to turbulence occurs in a more abrupt fashion as seen in Fig. 22.

Far-field acoustics

The sound pressure level (SPL) in the far-field at $r/D = 53$ from the nozzle exit plane is compared against experimental results from LMFA [46] (notched nozzle) and VKI [61]. The pressure fluctuations from the LES were propagated to the far-field using the Ffowcs Williams and Hawking's analogy [48] and averaged over 20 azimuthal probes in order to artificially increase the convective time of the signal. The comparisons are shown in Fig. 24 for two different angles computed from the jet direction.

At 60° (Fig. 24a), the LES pressure spectra are dissipated by the cut-off Strouhal number of the mesh above St ≈ 2. Good agreement is obtained with the experimental results between $0.5 < \mathrm{St} < 2$. Below $\mathrm{St} = 0.5$, the amplitude differs because of the lack of convergence of the large structures and the differences in turbulence values and length-scales.

The BBSAN peak from the LES captured at 120° (Fig. 24b) has the correct amplitude (up to St ≈ 2), but it is shifted in frequency with respect to the experimental SPL due to the fact that the shock-cell length captured is 5% smaller than the experimental one. The screech is not captured in the numerical simulations. The initial conditions used for this LES and the fact that the interior of the nozzle is not modeled [12, 14, 62, 63] are probably the key reasons for not obtaining screech because the feedback loop cannot take place in the development of the boundary layer inside the nozzle.

Overall, the acoustic results show good agreement with experiments without screech, despite the slight differences in turbulence levels and turbulence length-scales. This shows that the phenomenon generating shock-cell noise is well represented in the simulation and can be studied without discussing the impact of screech on the flow. Moreover, from [46], it can be seen that the acoustic and aerodynamic results for the case at $M_j = 1.15$ are the ones the least impacted by screech.

References

1. Powell, A.: On the mechanism of choked jet noise. Proc. Phys. Soc. Lond. Sect. B **66**(12), 1039 (1953). doi:10.1088/0370-1301/66/12/306
2. Harper-Bourne, M., Fisher, M.J.: The noise from shock waves in supersonic jets. In: Advisory Group for Aerospace Research and Development. AGARD-CP-131 (1973)
3. Tam, C.K.W., Tanna, H.K.: Shock associated noise of supersonic jets from convergent–divergent nozzles. J. Sound Vib. **81**(3), 337–358 (1982). doi:10.1016/0022-460X(82)90244-9

4. Norum, T.D., Seiner, J.M.: Broadband shock noise from supersonic jets. AIAA J. **20**(1), 68–73 (1982). doi:10.2514/3.51048
5. Krothapalli, A., Hsia, Y., Baganoff, D., Karamcheti, K.: The role of screech tones in mixing of an underexpanded rectangular jet. J. Sound Vib. **106**(1), 119–143 (1986). doi:10.1016/S0022-460X(86)80177-8
6. Tam, C.K.W.: Stochastic model theory of broadband shock associated noise from supersonic jets. J. Sound Vib. **116**(2), 265–302 (1987). doi:10.1016/S0022-460X(87)81303-2
7. Tam, C.K.W., Golebiowski, M., Seiner, J.M.: On the two components of turbulent mixing noise from supersonic jets. In: 2nd AIAA/CEAS Aeroacoustics Conference, 6–8 May, State College, Pennsylvania, AIAA Paper 1996-1716 (1996). doi:10.2514/6.1996-1716
8. Raman, G.: Supersonic jet screech: half-century from Powell to the present. J. Sound Vib. **225**(3), 543–571 (1999). doi:10.1006/jsvi.1999.2181
9. Tam, C.K.W.: Supersonic jet noise. Annu. Rev. Fluid Mech. **27**(1), 17–43 (1995). doi:10.1146/annurev.fl.27.010195.000313
10. Manning, T.A., Lele, S.K.: A numerical investigation of sound generation in supersonic jet screech. DTIC document, Standford University (1999)
11. Suzuki, T., Lele, S.K.: Shock leakage through an unsteady vortex-laden mixing layer: application to jet screech. J. Fluid Mech. **490**, 139–167 (2003). doi:10.1017/S0022112003005214
12. Berland, J., Bogey, C., Bailly, C.: Large eddy simulation of screech tone generation in a planar underexpanded jet. In: 12th AIAA/CEAS Aeroacoustics Conference (27th AIAA Aeroacoustics Conference), 8–10 May, Cambridge, Massachusetts, AIAA Paper 2006-2496 (2006). doi:10.2514/6.2006-2496
13. Schulze, J., Sesterhenn, J.: Numerical simulation of supersonic jet-noise. Proc. Appl. Math. Mech. **8**(1), 10703–10704 (2008). doi:10.1002/pamm.200810703
14. Schulze, J., Sesterhenn, J., Schmid, P., Bogey, C., de Cacqueray, N., Berland, J., Bailly, C.: Numerical simulation of supersonic jet noise. In: Brun, C., Juvé, D., Manhart, M., Munz, C.-D. (eds.) Numerical Simulation of Turbulent Flows and Noise Generation, pp. 29–46. Springer, Berlin (2009). doi:10.1007/978-3-540-89956-3_2
15. Mendez, S., Shoeybi, M., Sharma, A., Ham, F.E., Lele, S.K., Moin, P.: Large-eddy simulations of perfectly-expanded supersonic jets: quality assessment and validation. In: 48th AIAA Aerospace Sciences Meeting Including the New Horizons Forum and Aerospace Exposition, 4–7 January 2010, Orlando, Florida, AIAA Paper 2010-271 (2010). doi:10.2514/6.2010-271
16. Bodony, D.J., Ryu, J., Lele, S.K.: Investigating broadband shock-associated noise of axisymmetric jets using large-eddy simulation. In: 12th AIAA/CEAS Aeroacoustics Conference, 8–10 May, Cambridge, Massachusetts, AIAA Paper 2006-2495 (2006). doi:10.2514/6.2006-2495
17. Lo, S.C., Aikens, K., Blaisdell, G., Lyrintzis, A.: Numerical investigation of 3-D supersonic jet flows using large-eddy simulation. Int. J. Aeroacoust. **11**(7–8), 783–812 (2012). doi:10.1260/1475-472X.11.7-8.783
18. Nichols, J.W., Ham, F.E., Lele, S.K., Moin, P.: Prediction of supersonic jet noise from complex nozzles. In: Annual Research Briefs 2011, pp. 3–14. Center for Turbulence Research (2011)
19. Nichols, J., Ham, F., Lele, S., Bridges, J.: Aeroacoustics of a supersonic rectangular jet: experiments and LES predictions. In: 50th AIAA Aerospace Sciences Meeting Including the New Horizons Forum and Aerospace Exposition, 9–12 January, Nashville, Tennessee, AIAA Paper 2012-0678 (2012). doi:10.2514/6.2012-678
20. Brès, G.A., Ham, F.E., Nichols, J.W., Lele, S.K.: Unstructured large-eddy simulations of supersonic jets. AIAA J. **55**(4), 1164–1184 (2017). doi:10.2514/1.J055084
21. Morlet, J.: Sampling theory and wave-propagation. In: Chen, C.H. (ed.) Issues in Acoustic Signal–Image Processing and Recognition, pp. 233–261. Springer, Berlin (1983). doi:10.1007/978-3-642-82002-1_12
22. Farge, M.: Wavelet transforms and their applications to turbulence. Annu. Rev. Fluid Mech. **24**(1), 395–458 (1992). doi:10.1146/annurev.fl.24.010192.002143
23. Camussi, R., Guj, G.: Orthonormal wavelet decomposition of turbulent flows: intermittency and coherent structures. J. Fluid Mech. **348**, 177–199 (1997)
24. Camussi, R., Guj, G.: Experimental analysis of intermittent coherent structures in the near field of a high Re turbulent jet flow. Phys. Fluids **11**(2), 423–431 (1999). doi:10.1063/1.869859
25. Grassucci, D., Camussi, R., Jordan, P., Grizzi, S.: Intermittency of the near pressure field induced by a compressible coaxial jet. Exp. Fluids **56**(2), 1–13 (2015). doi:10.1007/s00348-014-1883-5
26. Camussi, R., Grilliat, J., Caputi-Gennaro, G., Jacob, M.C.: Experimental study of a tip leakage flow: wavelet analysis of pressure fluctuations. J. Fluid Mech. **660**, 87–113 (2010). doi:10.1017/S0022112010002570
27. Grizzi, S., Camussi, R.: Wavelet analysis of near-field pressure fluctuations generated by a subsonic jet. J. Fluid Mech. **698**, 93–124 (2012). doi:10.1017/jfm.2012.64
28. Crawley, M., Samimy, M.: Decomposition of the near-field pressure in an excited subsonic jet. In: 20th AIAA/CEAS Aeroacoustics Conference, 16–20 June, Atlanta, Georgia, AIAA Paper 2014-2342 (2014). doi:10.2514/6.2014-2342
29. Mancinelli, M., Pagliaroli, T., Di Marco, A., Camussi, R., Castelain, T.: Wavelet decomposition of hydrodynamic and acoustic pressures in the near field of the jet. J. Fluid Mech. **813**, 716–749 (2017). doi:10.1017/jfm.2016.869
30. Cavalieri, A., Daviller, G., Comte, P., Jordan, P., Tadmor, G., Gervais, Y.: Using large eddy simulation to explore sound-source mechanisms in jets. J. Sound Vib. **330**(17), 4098–4113 (2011). doi:10.1016/j.jsv.2011.04.018
31. Walker, S.H., Gordeyev, S.V., Thomas, F.O.: A wavelet transform analysis applied to unsteady aspects of supersonic jet screech resonance. Exp. Fluids **22**(3), 229–238 (1997). doi:10.1007/s003480050041
32. Gefen, L., Pérez Arroyo, C., Camussi, R., Puigt, G., Airiau, C.: Broadband shock-cell noise signature identification using a wavelet-based method. In: 22nd AIAA/CEAS Aeroacoustics Conference, 30 May–1 June, Lyon, AIAA Paper 2016-2732 (2016). doi:10.2514/6.2016-2732
33. Torrence, C., Compo, G.P.: A practical guide to wavelet analysis. Bull. Am. Meteorol. Soc. **79**(1), 61–78 (1998). doi:10.1175/1520-0477(1998)079<0061:APGTWA>2.0.CO;2
34. André, B., Castelain, T., Bailly, C.: Broadband shock-associated noise in screeching and non-screeching underexpanded supersonic jets. AIAA J. **51**(3), 665–673 (2013). doi:10.2514/1.J052058
35. Cambier, L., Heib, S., Plot, S.: The Onera *elsA* CFD software: input from research and feedback from industry. Mech. Ind. **14**(03), 159–174 (2013). doi:10.1051/meca/2013056
36. Lele, S.K.: Compact finite difference schemes with spectral-like resolution. J. Comput. Phys. **103**, 16–42 (1992). doi:10.1016/0021-9991(92)90324-R
37. Fosso-Pouangué, A., Deniau, H., Sicot, F., Sagaut, P.: Curvilinear finite volume schemes using high order compact interpolation. J. Comput. Phys. **229**(13), 5090–5122 (2010). doi:10.1016/j.jcp.2010.03.027
38. Visbal, M.R., Gaitonde, D.V.: On the use of higher-order finite-difference schemes on curvilinear and deforming meshes. J. Comput. Phys. **181**, 155–185 (2002). doi:10.1006/jcph.2002.7117
39. Bogey, C., Bailly, C.: A family of low dispersive and low dissipative explicit schemes for flow and noise computations. J. Comput. Phys. **194**(1), 194–214 (2004). doi:10.1016/j.jcp.2003.09.003

40. Spalart, P.R., Allmaras, S.: A one-equation turbulence model for aerodynamic flows. In: 30th Aerospace Sciences Meeting and Exhibit, 6–9 January, Reno, Nevada, AIAA Paper 1992-0439 (1992). doi:10.2514/6.1992-439
41. Shur, M.L., Spalart, P.R., Strelets, M.K.: Noise prediction for increasingly complex jets. Part I: Methods and tests. Int. J. Aeroacoust. **4**(3&4), 213–246 (2005). doi:10.1260/1475472054771376
42. Shur, M.L., Spalart, P.R., Strelets, M.K., Garbaruk, A.V.: Further steps in LES-based noise prediction for complex jets. In: 44th AIAA Aerospace Sciences Meeting and Exhibit, 9–12 January, Reno, Nevada, AIAA Paper 2006-485 (2006). doi:10.2514/6.2006-485
43. Tam, C.K.W., Dong, Z.: Radiation and outflow boundary conditions for direct computation of acoustic and flow disturbances in a nonuniform mean flow. J. Comput. Phys. **4**(02), 175–201 (1996). doi:10.1142/S0218396X96000040
44. Bogey, C., Bailly, C.: Three-dimensional non-reflective boundary conditions for acoustic simulations: far field formulation and validation test cases. Acta Acoust. **88**(4), 463–471 (2002)
45. Poinsot, T.J., Lele, S.K.: Boundary conditions for direct simulations of compressible viscous flows. J. Comput. Phys. **101**, 104–129 (1992). doi:10.1016/0021-9991(92)90046-2
46. André, B.: Etude expérimentale de l'effet du vol sur le bruit de choc de jets supersoniques sous-détendus. PhD Thesis, L'École Centrale de Lyon (2012)
47. Ffowcs Williams, J.E., Hawkings, D.L.: Sound generation by turbulence and surfaces in arbitrary motion. Philos. Trans. R. Soc. Lond. **264**(1151), 321–342 (1969). doi:10.1098/rsta.1969.0031
48. Farassat, F.: Derivation of formulations 1 and 1A of Farassat. Technical Memorandum 2007-214853, NASA (2007)
49. Tam, C.K.W.: Broadband shock-associated noise of moderately imperfectly expanded supersonic jets. J. Sound Vib. **140**(1), 55–71 (1990). doi:10.1016/0022-460X(90)90906-G
50. Lui, C.C.M.: A numerical investigation of shock-associated noise. PhD Thesis, Stanford University (2003)
51. Andersson, N., Eriksson, L.E., Davidson, L.: A study of Mach 0.75 jets and their radiated sound using large-eddy simulation. In: 10th AIAA/CEAS Aeroacoustics Conference, May 10–12, Manchester, AIAA Paper 2004-3024 (2004). doi:10.2514/6.2004-3024
52. Tam, C.K.W.: Broadband shock associated noise from supersonic jets measured by a ground observer. AIAA J. **30**(10), 2395–2401 (1992). doi:10.2514/3.11239
53. Pérez Arroyo, C., Daviller, G., Puigt, G., Airiau, C.: Hydrodynamic–acoustic filtering of a supersonic under-expanded jet. In: Grigoriadis, D., Geurts, B., Kuerten, H., Fröhlich, J., Armenio, V. (eds.) Direct and Large-Eddy Simulation X, pp. 79–84. Springer, Cham (2018). doi:10.1007/978-3-319-63212-4_9
54. Tinney, C.E., Jordan, P.: The near pressure field of co-axial subsonic jets. J. Fluid Mech. **611**, 175–204 (2008). doi:10.1017/S0022112008001833
55. Savarese, A., Jordan, P., Girard, S., Royer, A., Fourment, C., Collin, E., Gervais, Y., Porta, M.: Experimental study of shock-cell noise in underexpanded supersonic jets. In: 19th AIAA/CEAS Aeroacoustics Conference, Aeroacoustics Conferences, 27–29 May, Berlin, AIAA Paper 2013-2080 (2013). doi:10.2514/6.2013-2080
56. Daviller, G., Lehnasch, G., Jordan, P.: Numerical investigation of the influence of upstream conditions on properties of shock noise in shock/mixing layer interaction. In: International Symposium of Turbulence and Shear Flow Phenomena, vol. 1 (2013)
57. Pérez Arroyo, C.: Large eddy simulations of a dual-stream jet with shockcells and noise emission analysis. PhD Thesis, CERFACS and Institut National Polytechnique de Toulouse (2016)
58. Suda, H., Manning, T.A., Kaji, S.: Transition of oscillation modes of rectangular supersonic jet in screech. In: 15th AIAA Aeroacoustics Conference, 25–27 October, Long Beach, California, AIAA Paper 1993-4323 (1993). doi:10.2514/6.1993-4323
59. André, B., Castelain, T., Bailly, C.: Experimental study of flight effects on screech in underexpanded jets. Phys. Fluids **23**(12), 1–14 (2011). doi:10.1063/1.3671735
60. Ray, P.K., Lele, S.K.: Sound generated by instability wave/shock-cell interaction in supersonic jets. J. Fluid Mech. **587**, 173–215 (2007). doi:10.1017/S0022112007007306
61. Guariglia, D.: Shock-cell noise investigation on a subsonic/supersonic coaxial jet. PhD Thesis, von Karman Institute for Fluid Dynamics and Università Degli Study di Roma, La Sapienza (2017)
62. Singh, A., Chatterjee, A.: Numerical prediction of supersonic jet screech frequency. Shock Waves **17**(4), 263–272 (2007). doi:10.1007/s00193-007-0110-1
63. Shur, M.L., Spalart, P.R., Strelets, M.K.: Noise prediction for underexpanded jets in static and flight conditions. AIAA J. **49**(9), 2000–2017 (2011). doi:10.2514/1.J050776

CHAPTER 6

New research activities

This chapter presents two news research areas on turbomachinery noise. In the first paper, published durind the PhD thesis of David Lamidel (Cifre/Cerfacs/LMFA), fan noise is investigated using Large-Eddy Simulation. The second activity is dedicated to indirect combustion noise sources and is part of Yann Gentil's PhD thesis realized in collaboration with University of Sherbrooke and Safran. This work is funded by the CleanSky Project CIRRUS.

6.1 Turbomachinery aeroacoustics

The PhD of David Lamidel, defended in 2022, aimed to investigate the aerodynamic noise sources of the tip flow in fan stage of turbofan engines. The paper hereafter presents the methodology implemented to be able to study tip leakage vortex noise.

D. Lamidel, G. Daviller, M. Roger, and H. Posson. Numerical prediction of the aerodynamics and acoustics of a tip leakage flow using large-eddy simulation. *International Journal of Turbomachinery Propulsion and Power*, 27(6), 2021. https://doi.org/10.3390/ijtpp6030027

Numerical Prediction of the Aerodynamics and Acoustics of a Tip Leakage Flow Using Large-Eddy Simulation †

David Lamidel [1,2,3,*], Guillaume Daviller [2], Michel Roger [1] and Hélène Posson [3]

[1] Ecole Centrale de Lyon, Universite de Lyon, CNRS, Universite Claude Bernard Lyon 1, INSA Lyon, LMFA, UMR 5509, 69130 Ecully, France; michel.roger@ec-lyon.fr
[2] CFD Team, CERFACS, 31057 Toulouse, France; daviller@cerfacs.fr
[3] Safran Aircraft Engines, 77550 Moissy Cramayel, France; helene.de-laborderie@safrangroup.com
* Correspondence: david.lamidel@ec-lyon.fr
† This paper is an extended version of our paper published in the Proceedings of the 14th European Turbomachinery Conference, Gdansk, Poland, 12–16 April 2021.

Abstract: A Large-Eddy Simulation of the tip leakage flow of a single airfoil is carried out. The configuration consists of a non-rotating, isolated airfoil between two horizontal plates with a gap of 10 mm between the tip of the airfoil and the lower plate. The Mach number of the incoming flow is 0.2, and the Reynolds number based on the chord is 9.3×10^5. The objective of the present study is to investigate the best way to compute both the aerodynamics and acoustics of the tip leakage flow. In particular, the importance of the inflow conditions on the prediction of the tip leakage vortex and the airfoil loading is underlined. On the other hand, the complex structure of the tip leakage vortex and its convection along the airfoil was recovered due to the use of a mesh adaptation based on the dissipation of the kinetic energy. Finally, the ability of the wall law to model the flow in the tip leakage flow region was proven in terms of wall pressure fluctuations and acoustics in the far-field.

Keywords: large-eddy simulation; fan noise; tip leakage flow; tip clearance noise

Citation: Lamidel, D.; Daviller, G.; Roger, M.; Posson H. Numerical Prediction of the Aerodynamics and Acoustics of a Tip Leakage Flow using Large-Eddy Simulation. *Int. J. Turbomach. Propuls. Power* **2021**, *6*, 27. https://doi.org/10.3390/ijtpp6030027

Academic Editor: Raúl Vázquez Díaz

Received: 1 June 2021
Accepted: 6 July 2021
Published: 13 July 2021

1. Introduction

Due to strong environmental constraints regarding the noise emitted by aircraft, the bypass ratio of modern turbofan engines has tended to increase. This ratio is associated with a reduction of the fan rotation speed, the exhaust jet speed, and possibly the nacelle length. When looking at the noise sources of an engine at the approach regime, the fan stage is one of the major contributors. In this context, the understanding and prediction of secondary noise sources, such as the tip clearance noise in the fan stage, is required.

In the fan stage of turbofan engines, a gap between the tip of fan blades and the casing wall is present. As a consequence, a highly three-dimensional unsteady secondary flow develops. The tip leakage flow goes from the pressure side to the suction side of the blade. When the tip leakage flow leaves the gap, it interacts with the primary flow and rolls up to form the tip leakage vortex. The aerodynamic phenomena are mainly controlled by the blade tip loading, gap height, blade tip thickness, stagger angle, and Reynolds and Mach numbers. The consequences of a too strong gap are a drop in the aerodynamic fan performance and an increase in radiated far field noise [1].

This increase of the radiated noise from axial fans was first observed experimentally when the height of the gap increased [2]. Then, source mechanisms responsible for tip clearance noise generation were investigated. First, Kameier and Neise [3] identified a component of the tip clearance noise called the rotating instability. This mechanism consists of coherent vortical structures coming from the tip clearance that interact with the fan blades, causing periodic fluctuations of the blade loading, and thus inducing tonal noise in the far field. Yet, as these vortices have a range of tangential velocities, broadband humps are observed instead of sharp tonal peaks. This mechanism appears at off-design conditions, close to the rotating stall, and the structure of the tip clearance flow region is completely changed. Secondly, Fukano et al. [4] studied the tip clearance self noise. The periodic velocity fluctuations generated by the wandering of the tip leakage vortex produce tonal noise. Simultaneously, a broadband noise due to the enhancement of stochastic velocity fluctuations in the blade passage is generated. Previous observations were more detailed in the experiment of Jacob et al. [5]. Indeed, the authors described the vortical structures generated by the tip leakage flow and observed that they were scattered as sound by the edges of the tip trailing-edge corner, acting as dipole sources. Moreover, they described the jet-like leakage flow as another component of the tip clearance noise with the characteristic of a quadrupole noise source.

Various numerical studies were performed to investigate the tip clearance noise. An Unsteady Reynolds-Averaged Navier-Stokes (URANS) simulation of a rotor was achieved by März et al. [6] to confirm the experimentally-observed phenomena of rotating instability and to interrogate the physical mechanism behind it. Then, Zhu et al. [7] used unsteady aeroacoustic predictions with the Lattice Boltzmann Method (LBM) to shed more light on this noise generation mechanism. Moreover, Boudet et al. [8] achieved a Zonal Large-Eddy Simulation (ZLES) of a fan rotor where the region of interest at the tip was simulated with full Large Eddy Simulation (LES), and the hub and midspan regions were simulated with Reynolds-Averaged Navier–Stokes (RANS). This allowed them to identify a tip leakage vortex that was wandering and producing tonal noise. An isolated fixed airfoil with a gap designed to study the tip clearance noise self noise is considered in this paper. ZLES [9], LES [10], and LBM [11] approaches were achieved on this configuration.

The isolated non-rotating airfoil is mounted in an open-jet wind-tunnel facility. This experimental environment is tough to reproduce numerically due to the strong interaction between the jet and the airfoil. Indeed, when testing a lifting airfoil, the main stream is deflected by the equivalent lateral momentum injection, which reduces the effective angle of attack. The flow around an airfoil when installed in a free-jet wind tunnel significantly deviates from that of the same airfoil placed in a uniform stream. A solution to compute the airfoil in an uniform flow is to modify the angle of attack to retrieve the proper airfoil loading. Although the integrated lift can be adjusted in this way, the precise distribution of pressure coefficient is not perfectly recovered. As proposed by Moreau et al. [12], one way is to impose a more realistic inlet boundary condition from a precursor RANS calculation. The other way is to account for the full experiment set-up.

The objective of the present study is to investigate the best way to compute both the aerodynamics and acoustics of the tip leakage flow in order to transfer the methodology to real turbomachinery configurations. To do so, we simulated the same experimental set-up using two different computational domains, including modelling the inflow conditions, with a predictive LES approach. The use of a wall model, synthetic-turbulence injection and adaptive mesh refinement are also considered.

The paper starts with a description of the experimental set-up. Then, the numerical set for each configuration is detailed in the second section. In the third section, LES results for the two different computational domain approaches are compared and discussed. Next, the effect of mesh refinement on the prediction of the tip leakage vortex is shown. Finally, the ability of the wall law to model the boundary layer in the gap region is analysed, as well as its impact on the acoustic radiation. Concluding remarks and perspectives are also given in the last section.

2. Experimental Set-Up

The numerical study is based on the isolated non-rotating airfoil experiment conducted by Jacob et al. [13]. Indeed, the advantage is that the tip clearance noise contribution to the far field noise is more easily isolated than in a rotating turbomachinery configuration. A sketch of the experimental set-up is shown in Figure 1. A fixed single airfoil is mounted between two flat plates with a tunable gap between the lower plate and the airfoil tip. Air is coming from a rectangular nozzle. To ensure a uniform flow, the isolated airfoil is placed into the potential core of the rectangular freejet.

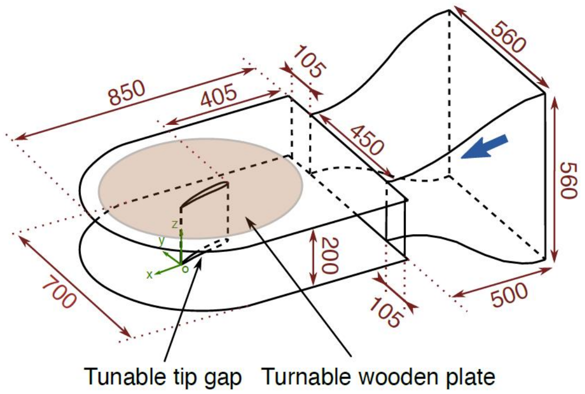

Figure 1. Sketch of the experimental set-up from Jacob et al. [13]. Dimensions are in millimeters.

The airfoil is a NACA 5510 of chord c = 200 mm. The geometrical angle of attack is $\beta = 16.5^{\circ}$. The gap height is s = 10 mm. The mean flow velocity at the exit nozzle is $U_0 = 70$ m/s, corresponding to a Mach number Ma = 0.20 and a Reynolds number based on the chord $Re = U_0.c/\nu = 9.3 \times 10^5$. One chord upstream of the airfoil, the boundary layer thickness on the plate is 6.2 mm. The experiment was carried out under ambient pressure p_a = 97,700 Pa and ambient temperature T_a = 290 K.

The coordinate system $(O, \vec{x}, \vec{y}, \vec{z})$ used in this study is depicted in Figure 1. The origin, defined at the trailing edge-tip corner, is more appropriate to study the tip leakage vortex. The $\vec{x}$ axis is in the streamwise direction. The $\vec{y}$ axis is in the cross-stream direction, from pressure side to suction side. The $\vec{z}$ axis is in the spanwise direction, from the lower to the upper plate.

3. Numerical Settings

The simulations performed in this study are based on the LES methodology developed at CERFACS [14,15]. LES are performed using ***AVBP***, an explicit, unstructured, massively parallel solver [16] which solves the compressible Navier–Stokes equations. The package ***pyhip*** [17] to handle unstructured computational grids and their associated datasets is used in combination with the ***antares*** [18] pre-postprocessing library. In this paper, each LES is performed using the same following set-up. The convective fluxes are computed using the Two-Step Taylor-Galerkin C (TTGC) finite element scheme [19]. This scheme is third-order accurate in time and space. The viscous fluxes are computed using the 2Δ diffusion operator from Colin [20]. Finally, the closure of the LES equations is done using the SIGMA subgrid scale model from Nicoud et al. [21]. Regarding the boundary condition, each simulation shares the wall modelling approach and the outlet boundary modelling: a wall law [22] is applied on each wall, and a characteristic boundary condition (NSCBC) based on static pressure is applied at outlet [23]. The inlet boundary conditions are detailed below.

In order to define the best approach to correctly predict the airfoil flow-field, tip-leakage vortex, and associated acoustics, we chose to compare the full experimental set-up, including the convergent of the open-jet (see Figure 1) with a case where the inlet condition is imposed from a RANS simulation that included a convergent. The computational domains and the boundary conditions are summed up in Figure 2a. The simulation, including the convergent, is referred to as 'LES CONV'. In this case, the total pressure and temperature are imposed at the inlet of the convergent using a dedicated NSCBC [24]. On either side of the nozzle, a colinear flow of 1% of the jet velocity U_0 (0.7 m/s) is imposed. No synthetic turbulence is injected in this case at inlet.

In the second LES (referred to as 'LES NO CONV'), in order to save CPU time, the inlet is placed one chord upstream the airfoil leading edge (the blue line in Figure 2a). The mean velocity field and static temperature are specified from a RANS computation [25]. A fully non-reflecting inlet boundary condition is used to inject three-dimensional turbulence while still being non-reflecting for outgoing acoustic waves [26]. The injected synthetic turbulence that is required to trigger the mixing layers is based on Kraichan's method [27]. The turbulence spectrum has a Passot-Pouquet expression [28]. The Root-Mean-Square (RMS) velocity of the injected turbulent field is the one from the RANS simulation, and its most energetic turbulent length scale L_e is 6.3 mm. The latter is computed using a property of the Passot-Pouquet spectrum (L_e=$\sqrt{2\pi}L_t$) and the measured integral length scale L_t (2.5 mm).

In each case, the edge size of the mesh around the airfoil is unchanged as depicted with close-ups in Figure 2b. The mesh sizes at the wall of the lower plate and the airfoil are $\Delta x^+ = \Delta y^+ = \Delta z^+ < 100$ in wall units. 20 elements are used to discretise the gap. The total number of tetrahedrons of is 229×10^6 for the case without convergent, whereas it is 252×10^6 with it. The fixed time-step is 3.5×10^{-5} c/U_0 corresponding to a CFL number of 0.82. In each case, a computational time of $T_{ini} = 7c/U_0$ is required to leave the transient state. The convergence is monitored with pressure probes in the incoming flow, in the tip leakage vortex and on the airfoil. A total of 4096 processors during 70 h were used to acquire statistics over $T_{sim} = 14c/U_0$. For the same simulated time, the computational cost is increased by 20% when adding the convergent. All calculations were performed on the Joliot–Curie supercomputer in production in CEA's Very Large Computing Centre (TGCC).

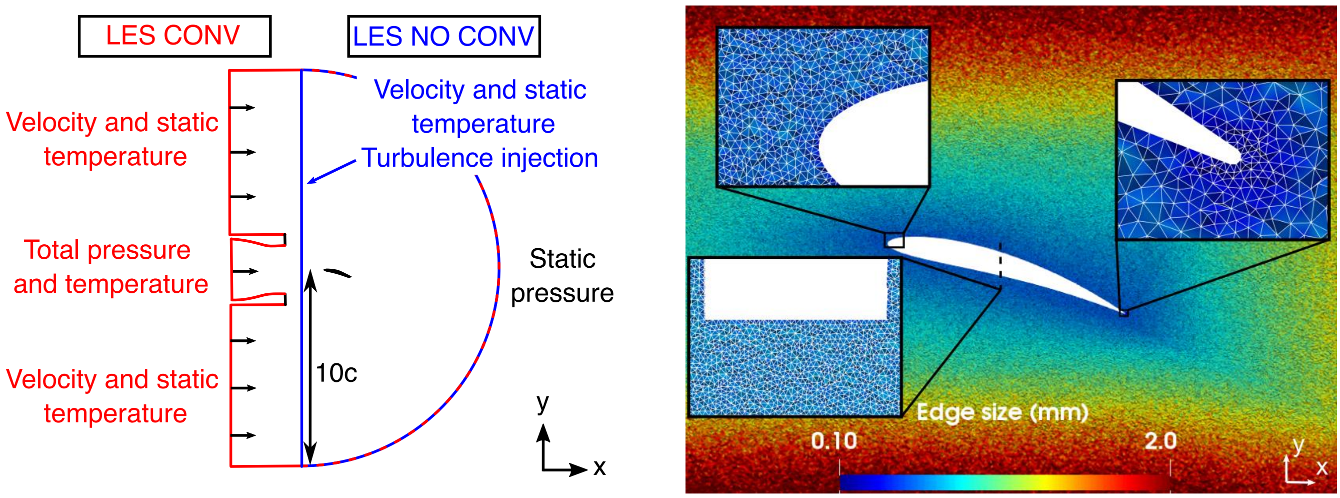

(**a**) (**b**)

Figure 2. (**a**) Sketch of the computational domains and the boundary conditions. (**b**) Edge size of the mesh around the airfoil at z/c = 0.1 and close-ups at the airfoil leading and trailing edges and in the gap.

Table 1 summarizes the simulation parameters as well as the simulation time and cost. In the following, probe data were sampled at 0.01 ms leading to a LES cut-off frequency of 50 kHz. Welch's method was used to compute Power Spectral Density (PSD) using 10 Hanning windows with an overlap of 50%. Instantaneous quantities on the airfoil surfaces are dumped every 0.025 ms leading to a cut-off frequency of 20 kHz.

Table 1. Simulation parameters, time and cost of the two computational domain approaches.

	LES NO CONV	LES CONV
Mesh size	229×10^6	252×10^6
Wall resolution $\Delta x^+ = \Delta y^+ = \Delta z^+$	100	100
Wall model	yes	yes
Convective scheme	TTGC	TTGC
Subgrid scale model	SIGMA	SIGMA
Δt c/U_0	3.5×10^{-5}	3.5×10^{-5}
T_{sim} c/U_0	14	14
CPU time	70 h	84 h

4. Effects of Inflow Conditions

4.1. Instantaneous Flow

In order to have a global view of the flow field in the zone of interest, Figure 3 shows instantaneous iso-surfaces of Q criterion (Q = 3.0×10^2 $(U_0/c)^2$) coloured by the velocity magnitude in the tip leakage flow region for the LES CONV case. As the instantaneous flow looks very similar in the LES NO CONV case, it is not shown here. The airfoil is seen from the suction side. Three vortices are identified. The tip separation vortex in the gap is generated by the separation of the tip leakage flow from the airfoil tip. The tip leakage vortex developing from the airfoil leading edge is the major one. Next to it, an induced vortex is generated by the important circulation of the tip leakage vortex. The last two vortices are contra-rotating to each other.

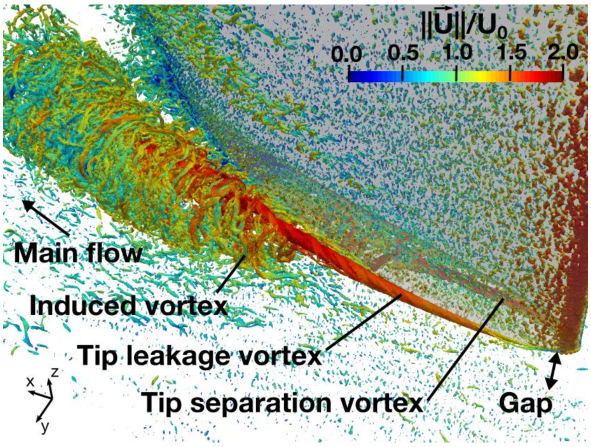

Figure 3. LES instantaneous iso-surfaces of Q criterion (Q = 3.0×10^2 $(U_0/c)^2$) coloured by the velocity magnitude in the tip leakage flow region.

Figure 4 shows the instantaneous vorticity and dilatation fields in both cases at $z/c = 0.1$. Large differences are observed between the two approaches. First, in the vorticity field, while the tip leakage vortex ($x/c > -0.5$, $0 < y/c < 0.5$) and the airfoil wake are similar between the two cases, the mixing layers starting from $y/c = -1.0$ and 1.3 are different. Indeed, considering the full experimental setup with the convergent seems to lead to a more natural growth of the jet mixing layers (Figure 4a) than with the 'LES NO CONV' case in Figure 4b.

Secondly, when considering the acoustic field represented by the dilation field, the case without the nozzle is polluted by a strong numerical spurious noise coming from the inlet. The two sources seem to be located on the jet mixing layers and generated by the interaction of the injected turbulence and the non-constant inflow condition imposed (mean and turbulent velocity fields from RANS).

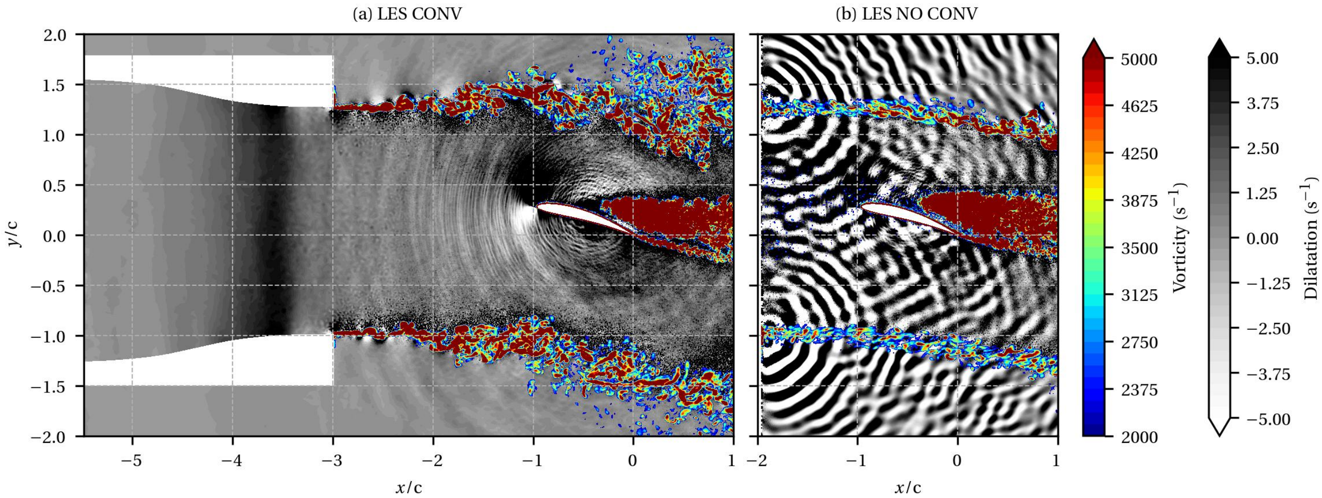

Figure 4. Instantaneous vorticity and dilatation fields with (**a**) and without (**b**) the convergent at $z/c = 0.1$.

4.2. Mean Flow

The mean velocity magnitude is presented in Figure 5. The two mixing layers developed from the convergent exit section of LES CONV (Figure 5a) and from the inlet of LES NO CONV (Figure 5b) are observed as well as their deviation. Indeed, when the rectangular jet reaches the airfoil leading edge at $x/c = -1$, it is deflected about 8° by the circulation generated by the airfoil. Lobes of velocity around the airfoil interact with the mixing layers at $x/c = -0.5$, $y/c = \pm 1$ in both cases.

However, the mixing layer development and tip leakage vortex signature differ. Indeed, as mentioned before, the mixing layers exhibit a larger growth with the add of the convergent (Figure 5a), whereas their thickness in the LES NO CONV case (Figure 5b) seems to remain constant. Regarding the tip leakage vortex flow region, a deficit of velocity magnitude is observed at $y/c = 0.25$, from $x/c = 0$ in both cases. This corresponds to the trajectory of the tip leakage vortex. Whereas the structure of the tip leakage vortex looks similar with and without the convergent, the deficit of velocity magnitude is amplified without the convergent.

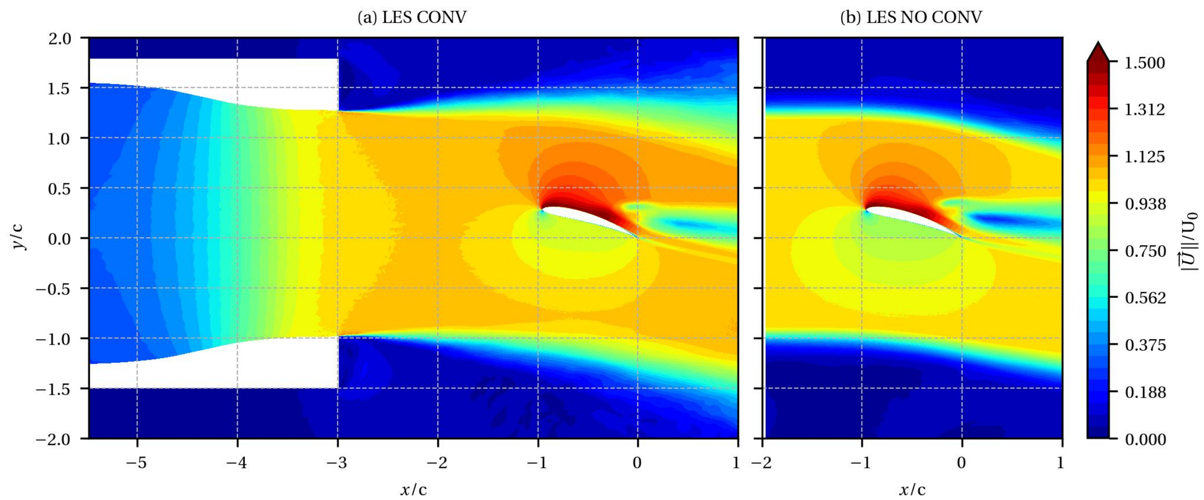

Figure 5. Mean velocity magnitude fields with (**a**) and without (**b**) the convergent at $z/c = 0.1$.

The pressure coefficients on the airfoil presented in Figure 6 are similar in both cases to the measured ones (in circles) at midspan (Figure 6a) and at the tip (Figure 6b). The LES without the convergent is a blue solid line, whereas the LES with the convergent is in red. The following definition of pressure coefficient is used:

$$C_p = \frac{p - p_0}{0.5\rho_0 U_0^2} \quad (1)$$

At midspan (Figure 6a), the LES without the convergent globally matches the experiment. The operating point of the simulation is then validated. A slight deviation is observed on the suction side, close to the leading edge (upper line for $x/(\text{c.cos}(\beta)) < -0.8$). The prediction in this region is improved by adding the convergent, while the rest of the airfoil surface exhibits the same level of pressure between the two cases.

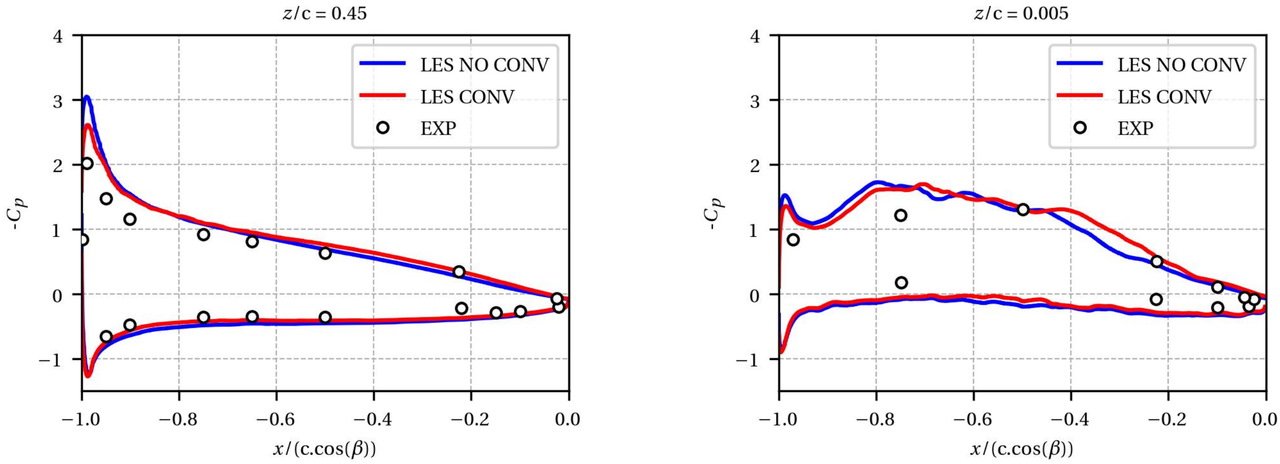

(**a**) (**b**)

Figure 6. Mean pressure coefficients on the airfoil at midspan, $z/c = 0.45$ (**a**) and at the tip, $z/c = 0.005$ (**b**).

At the tip (Figure 6b), the measured airfoil loading is globally reduced compared to the one at midspan. Indeed, the tip leakage flow from the pressure side to the suction side partially balances the pressure difference. Again, the two computed cases are able to properly predict the pressure distribution at tip which is a key point of validation. Indeed, the airfoil tip loading is one of the main parameters that control the tip leakage flow. For $-0.5 < x/(\text{c.cos}(\beta)) < -0.2$ on the suction side, a difference in the level of pressure was observed between the two LES. Unfortunately, no measurement was performed in this area. Further explanations will be given to understand the difference.

5. Tip Leakage Vortex Trajectory

Figure 7 shows the streamwise U, horizontal V and vertical W mean velocity components of the tip leakage vortex at the airfoil trailing edge ($x/c = 0.01$), from top to bottom, respectively. LES with and without the convergent are compared with 3D Particle Image Velocimetry (PIV) performed by Jacob et al. [13]. Since the tip leakage vortex is roughly aligned with the x axis, the considered plane is almost perpendicular to the trajectory of the tip leakage vortex. The flow is viewed from downstream. The velocity components are normalised by the reference mean velocity U_0. The airfoil trailing edge is plotted in a black solid line at $y/c = 0$. The white rectangle ($0.0 < y/c < 0.1$) in Figure 7d,g defines the airfoil projected surface as seen from the camera; however, it has no physical meaning in terms of velocity since the signal in this region is disrupted by light reflections [13].

When looking at the mean axial velocity component U of the tip leakage vortex from the PIV data (Figure 7a), two distinct regions are identified. First, a strong acceleration region with a maximum of $1.4U_0$ is measured at $y/c = 0.22$ and $z/c = 0.04$. This position corresponds to the centre of the tip leakage vortex. Secondly, a low velocity region surrounding the zone of acceleration extends from the plate until $z/c = 0.15$. The latter is generated by the detachment of the plate boundary layer by the tip leakage flow.

In both cases, LES predicts a topology that is different from the experiment but tends to recover the two regions. We observed that the LES with convergent captures better the acceleration, meaning that the incoming flow is more realistic. Nevertheless, the velocity magnitudes are lower than the measured ones. Indeed, in the LES NO CONV, the longitudinal velocity component at the centre of the tip leakage vortex is underestimated by 50% compared with experiment. When adding the convergent, the difference is about 21%. This underprediction is attributed to the mesh resolution and will be discussed later.

Looking at the PIV measurements in Figure 7d,g, a region of positive V is observed for $z/c < 0.05$, whereas a region of negative V is shown for $z/c > 0.05$. For the vertical mean component W, two regions are also identified: positive W for $y/c > 0.2$ and negative W for $y/c < 0.2$. This clearly shows the roll up of the tip leakage vortex. The same kind of flow topology is noticeable around $y/c = 0.35$ but with a smaller spatial extension and opposite signs compared to the tip leakage vortex. This flow topology indicates an induced vortex. In addition, for the horizontal component V, the extension of the region in red in the gap ($z/c < 0$) brings out the tip leakage flow that feeds the vortex.

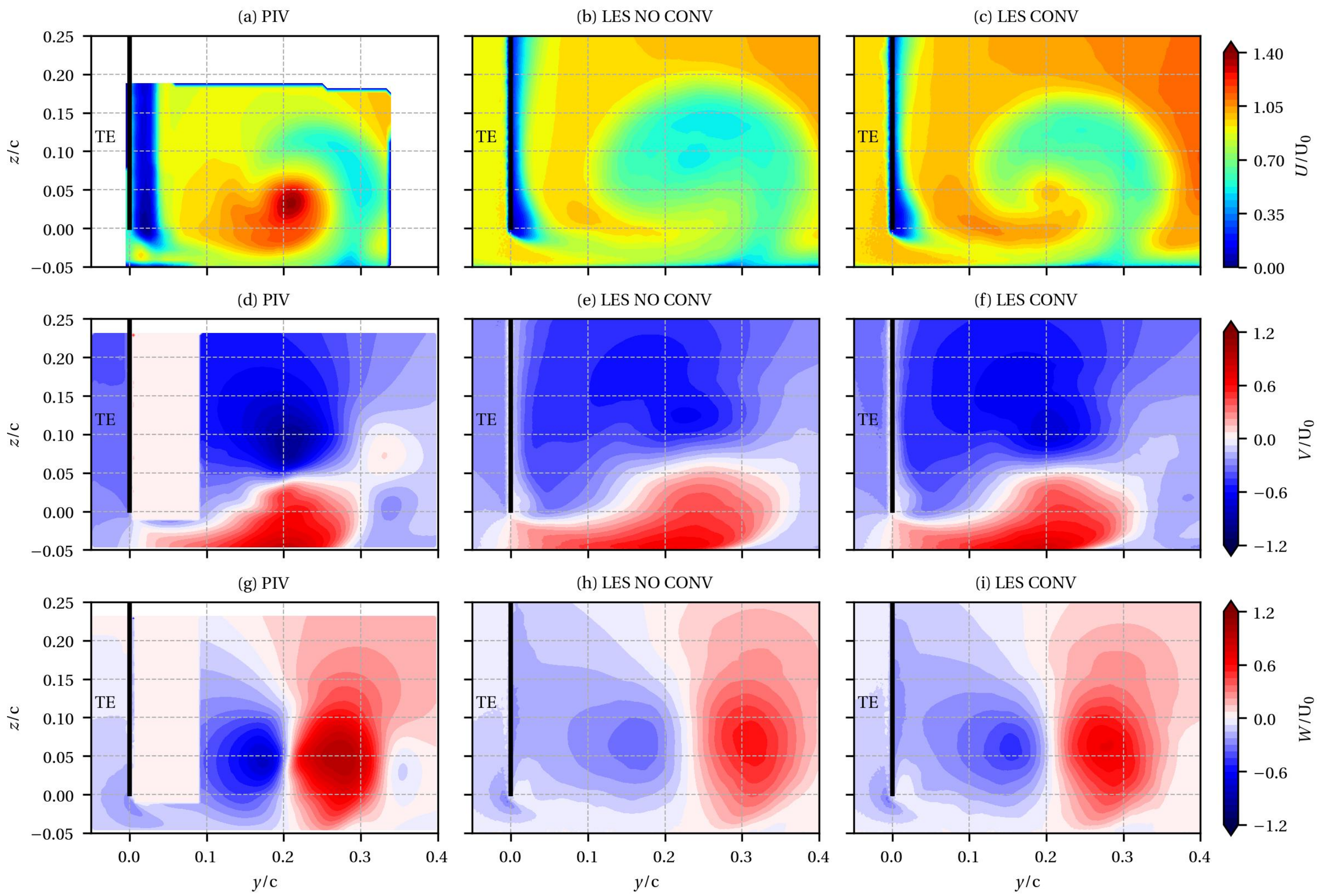

Figure 7. Streamwise U, horizontal V, and vertical W mean velocity components of the tip leakage vortex at the airfoil trailing edge ($x/c = 0.01$).

The LES without the convergent, in Figure 7e,h, correctly reproduces the topology of the tip leakage flow region but diffusion is noted. Indeed, a lower velocity magnitude is observed, and the tip leakage vortex is much more spatially spread out compared to the PIV. This is even more pronounced for the vertical component W. The LES with convergent in Figure 7f,i also reproduces the topology of the tip leakage vortex with an improvement on the position of the vortex. On the PIV data, the y position of the tip leakage vortex, which is identified by the sudden change of sign on W, is $y/c = 0.2$. While the LES without the convergent predicts the vortex at $y/c = 0.23$, adding the convergent allows obtaining the correct y position of the vortex. A slight improvement is also observed on the z position.

In order to quantify more precisely the tip leakage vortex trajectory, a vortex identification method developed by Graftieux et al. [29] was applied. This method is based on the function Γ_1 derived from the velocity field. This function is able to characterise the locations of the large-scale vortex centres, by considering only the topology of the velocity field and not its magnitude.

The function Γ_1 is defined as

$$\Gamma_1(P) = \frac{1}{S} \int_{M \in S} \frac{(\mathbf{PM} \wedge \mathbf{U_M}) \cdot \mathbf{n}}{\parallel \mathbf{PM} \parallel \cdot \parallel \mathbf{U_M} \parallel} dS \tag{2}$$

where S is a surface surrounding P, M lies in S, and $\mathbf{n}$ is the unit vector normal to S. $\mathbf{U_M}$ is the velocity vector at M, and $\mathbf{PM}$ is the distance vector between P and M. Γ_1 is dimensionless and $\Gamma_1 \in [-1, 1]$. Γ_1 may be interpreted as the normalized angular momentum of the velocity field. The sign of Γ_1 defines the rotation sign of the vortex. $\Gamma_1 > 1$ is for clockwise rotation, whereas $\Gamma_1 < 1$ is for counterclockwise rotation. The centre of the vortex is defined as the maximum of $\mid \Gamma_1 \mid$ with a pragmatic threshold value at 0.9 for validity. The integration over the surface S plays the role of a spatial filter.

Using the previous algorithm at different spatial positions in the streamwise direction on yOz planes allowed us to identify the vortex centre. The resulting trajectory projected on planes xOy (Figure 8a) and xOz (Figure 8b) is displayed in Figure 8 for the experiment and each LES. The airfoil is in grey. We observed that, if the correct inflow conditions were taken into account, as in the LES CONV, the experimental trajectory was well retrieved.

As explained by Storer et al. [30], the vortices at tip have an influence on the pressure on the airfoil surface. The modification of the trajectory of the tip leakage vortex observed in Figure 8 explains the difference on the pressure coefficient in Figure 6b. With the convergent, the tip leakage vortex is closer to the airfoil, as shown in Figure 8a. Therefore, the pressure on the airfoil surface is lower compared to the case without the convergent.

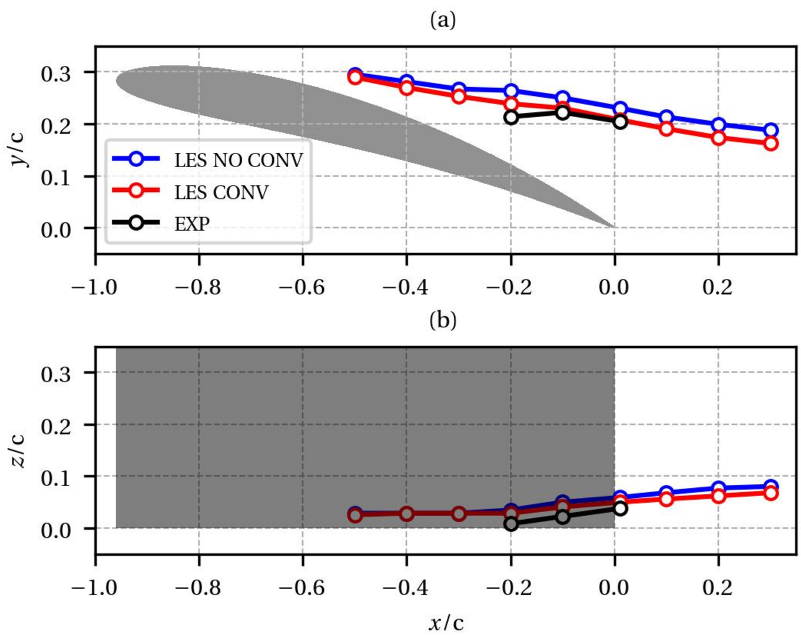

Figure 8. Projected mean trajectory of the tip leakage vortex on planes xOy (**a**) and xOz (**b**).

6. Tip Leakage Vortex Convection

In the previous section, the mean trajectory of the tip leakage vortex was improved in the LES with the convergent (Figure 8). However, the longitudinal velocity acceleration of the tip leakage vortex, that is to say the convection of the vortex, remains an issue (Figure 7).

To improve the prediction of the LES, a mesh adaptation based on the dissipation of the kinetic energy was performed. Following the approach sets up by Daviller et al. [31], a static h-refinement strategy was used to refine precisely the tip leakage vortex region. From the previous LES CONV simulation, the time-average dissipation field $\overline{\tilde{\Phi}}$ is used to build a metric. The quantity of interest $\overline{\tilde{\Phi}}$ is defined as:

$$\overline{\tilde{\Phi}} = \overline{(\mu + \mu_t)\left(\frac{\partial \tilde{u}_i}{\partial x_j} + \frac{\partial \tilde{u}_j}{\partial x_i}\right)^2} \tag{3}$$

with μ as the kinematic viscosity and μ_t as the local turbulent viscosity computed by the LES subgrid scale model. The operators $\tilde{\cdot}$ and $\bar{\cdot}$ represent the LES filtered variables and the time-average, respectively. A normalization is first performed with the minimum and maximum values of $\overline{\tilde{\Phi}}$:

$$\Phi^* = \left[1 - \left(\frac{\overline{\tilde{\Phi}} - \overline{\tilde{\Phi}}_{\text{min}}}{\overline{\tilde{\Phi}}_{\text{max}} - \overline{\tilde{\Phi}}_{\text{min}}}\right)\right]^{\alpha} \tag{4}$$

Then, the metric range is defined using the ϵ parameter:

$$\text{metric} = \Phi^*(1 - \epsilon) + \epsilon \tag{5}$$

Using the ***pyhip*** [17] tool, 38×10^6 tetrahedrons are added to the initial mesh, and the minimal edge size is divided by a factor of 1.12. The magnification factor is set to $\alpha = 100$, and the minimum of the metric field to $\epsilon = 0.7$. The spatial extension of the adaptation is limited to $z_{max}/c = 0.5$ spanwise and to $x_{max}/c = 1.25$ streamwise.

The adapted mesh at $z/c = 0.1$ is shown in Figure 9. The mesh was refined in the zones of interest, that is to say the tip leakage vortex, the wake, and around the airfoil surface. For the same simulated time, the computational cost was increased by 25%. The edge size of the mesh before and after adaptation at the airfoil trailing edge is, respectively, presented in Figure 10a,b.

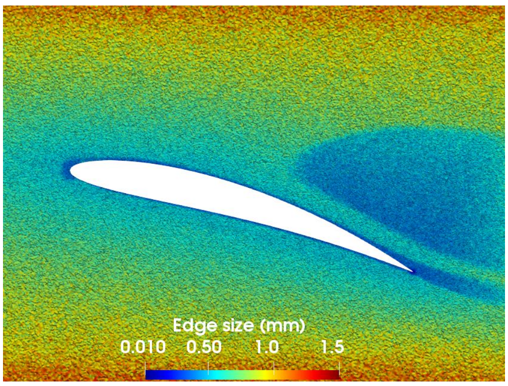

Figure 9. Adapted mesh at $z/c = 0.1$.

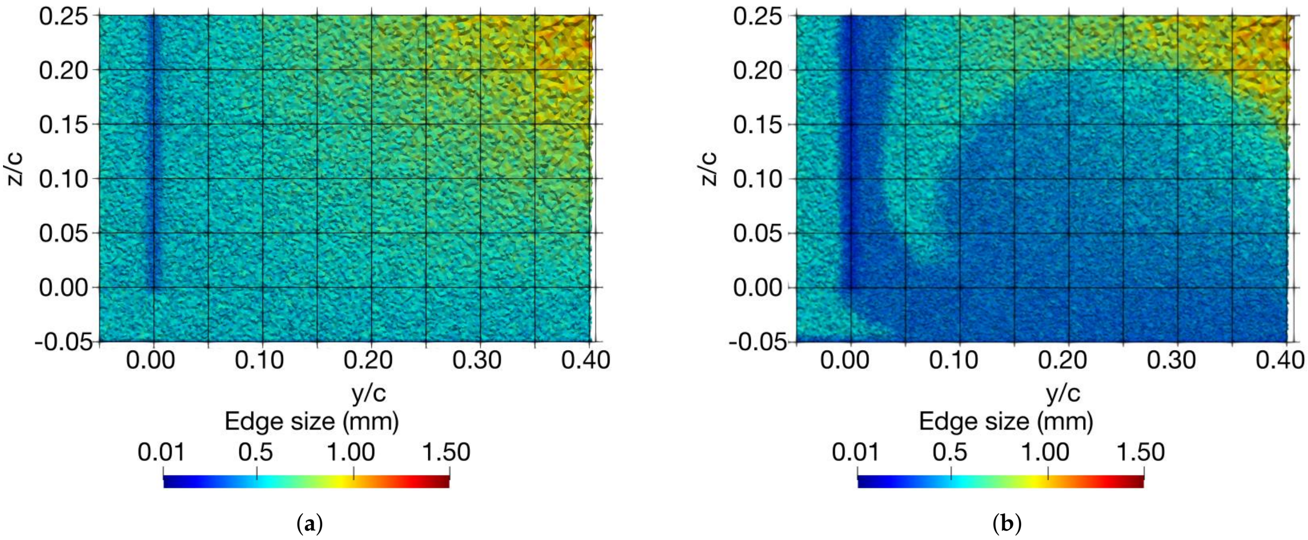

Figure 10. Mesh cuts at the airfoil leading edge at $x/c = 0.01$ before (**a**) and after (**b**) adaptation.

Figure 11 compares the mean axial velocity U between PIV, LES CONV, and LES ADAPT of the tip leakage vortex at the airfoil trailing edge ($x/c = 0.01$). With the proper mesh refinement, LES ADAPT is able to better retrieve the topology measured by the PIV. Indeed, the two velocity regions and even the position of the maximum of U are captured with less than 15% of the error as PIV.

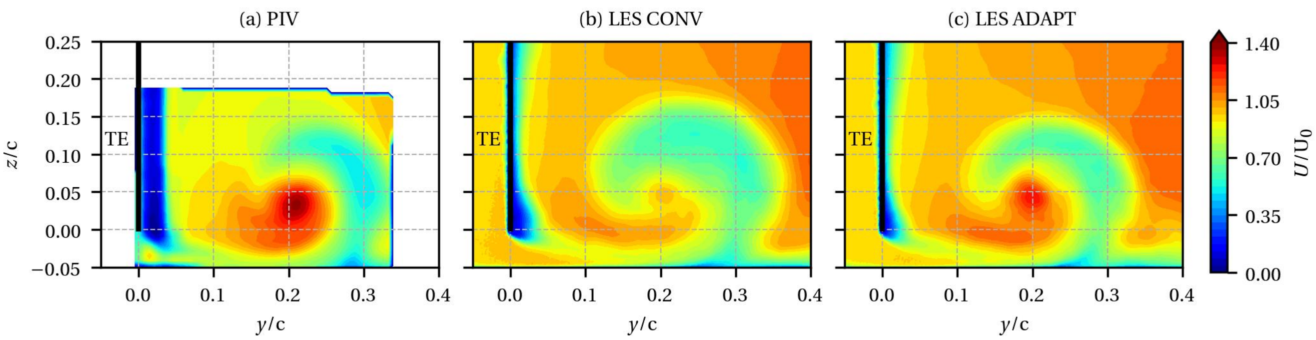

Figure 11. Longitudinal velocity component U of the tip leakage vortex at the airfoil trailing edge ($x/c = 0.01$).

To deepen the analysis, 1D velocity profiles are plotted at $z/c = 0.05$ in Figure 12. Using the mesh adaptation, the predicted velocity profile is clearly improved. Indeed, whereas the deficit of velocity caused by the airfoil wake is retrieved by both LES around $y/c = 0$ with the correct amplitude, some discrepancies are observed in the tip leakage vortex zone, which extends from $y/c = 0.17$ to 0.35. Indeed, the LES with mesh adaptation in green is able to recover the amplitude of the maximum U at $y/c = 0.2$. Mesh adaptation allows to recover the complex structure of the tip leakage vortex and especially the acceleration of the longitudinal velocity component.

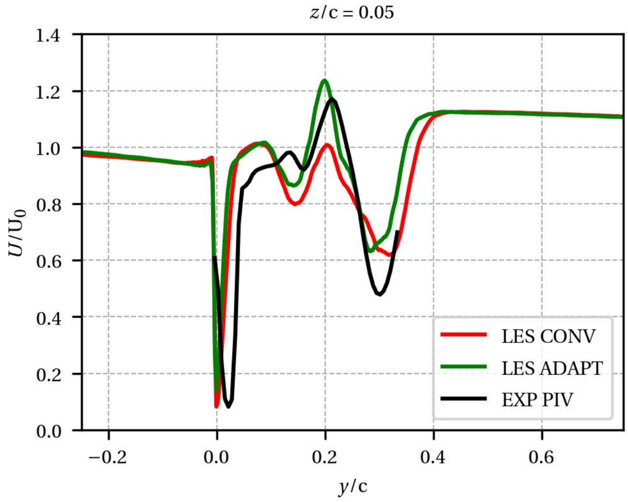

Figure 12. Mean velocity profile of U at $x/c = 0.01$ and $z/c = 0.05$.

7. Spectral Signature of the Tip Leakage Flow

Regarding the high Reynolds number that characterises the flow in a real turbomachinery configuration, a wall law is required for the computational cost issue. Therefore, the capability of the wall law to predict the aerodynamics and acoustics of the tip leakage flow of the isolated airfoil is studied in this section. The wall-modelled LES performed in this paper is compared to two previous wall-resolved LES from Boudet et al. [9] and Koch et al. [10]. These two LES are achieved at an angle of attack of 15°, whereas the current LES is at 16.5°. Figure 6 shows that the wall law is able to reproduce the mean pressure distribution on the airfoil surface, especially in the tip region.

Figure 13 presents the PSD of the wall pressure fluctuations on the airfoil surface. For clarity, only results from LES ADAPT are shown. Two positions at 77.5% of chord were considered. Probe 21 (Figure 13a) is located on the airfoil suction side, 1.5-mm away from the tip, whereas probe B (Figure 13b) is on the airfoil tip, on the camber line. Since wall pressure spectra of the LES from Koch et al. are not available at 77.5%, the spectra at 75% are used in Figure 13. The three LES are compared to the measurements extracted from Jacob et al. [5]. The experimental cut-off frequency was 22 kHz; however, data were only available until 10 kHz.

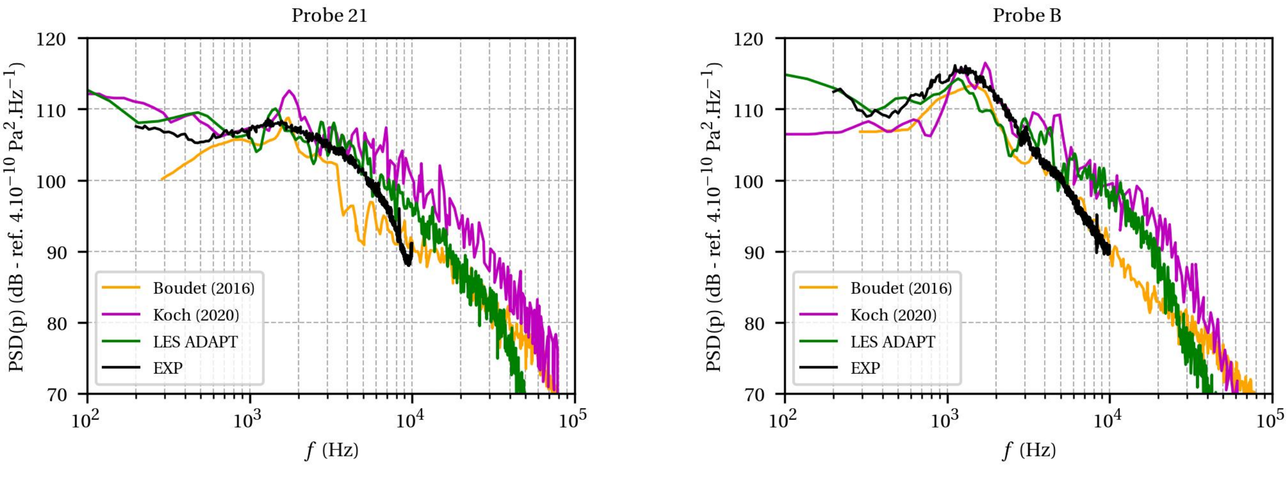

Figure 13. PSD of the wall pressure on the airfoil suction side (**a**) and on the airfoil tip (**b**) at 77.5% of the chord.

For probe 21, the LES exhibits a good agreement with the experiment regarding both shape and level. The spectrum is even in better agreement than the two wall-resolved cases. The LES from Koch et al. (magenta) that was also performed with ***AVBP*** exhibits the same shape than the current LES with a shift in frequency.

On probe B, the hump around 1.3 kHz characterises the pressure fluctuations induced by the detachment of the tip leakage flow on the airfoil pressure side-tip corner. A broadband hump is observed instead of a tonal peak because of the intermittency of the phenomenon [32]. The LES is able to well retrieve the hump at 1.3 kHz. For frequencies higher than 6 kHz, a slight overprediction is observed from the experiment. The LES from Koch et al. is again showing the same trend. The ZLES from Boudet et al. remarkably predicted the wall pressure fluctuations even at high frequencies. Figure 13 shows the capacity of the wall law to predict the wall pressure fluctuations on the airfoil surface in the tip region.

Figure 14 presents the PSD of the acoustic pressure in the far-field. The microphone was placed 2-m away from the airfoil suction side, forming an angle of 90° with the airfoil chord. The acoustic propagation in the far-field was ensured using the solid Ffowcs–Williams and Hawkings' analogy (FWH). This means that only the dipole sources are taken into account to estimate the sound; the aforementioned quadrupoles associated with the tip-gap jet are ignored. The python library ***antares*** [18] is used following the advanced time formulation of Casalino [33].

The microphone recorded the noise emitted by the airfoil in no-gap (grey) and 10-mm-gap (black) configurations. It allowed us to identify a frequency range of the tip clearance noise from 0.7 to 7 kHz. The wall-resolved LES in orange and magenta are able to retrieve the noise level in this range. The wall-modelled LES in green is able to predict the noise level on an even wider range of frequencies. Whereas the acoustic spectra from the two wall-resolved LES drop for frequencies higher than 7 kHz, the LES presented in this paper manages to predict the proper noise level.

It may be explained by the size of the LES domain. Indeed, Boudet et al. performed a ZLES with a LES zone reduced to the tip region and Koch et al. achieved a LES on a modified geometry with a reduced span. In both cases, the pressure fluctuations on the airfoil surface are not computed over the full span. This comparison demonstrates also the capacity of the wall law to model the tip leakage flow for the purpose of acoustic prediction.

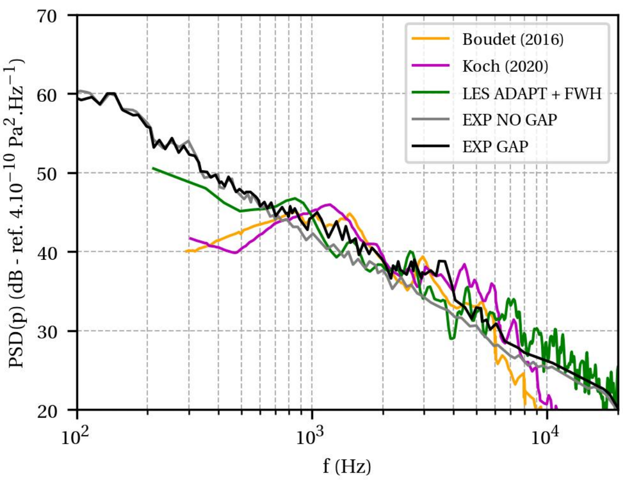

Figure 14. PSD of acoustic pressure 2-m away from the airfoil suction side, forming an angle of 90° with the airfoil chord.

8. Conclusions

With the aim of improving existing prediction models or to model new noise sources features of the tip clearance noise, a LES of an isolated airfoil with a gap was performed. Two computational domains with the same experimental set-up were considered, including modelling the inflow conditions. We observed that the LES with a modelling of the inflow conditions (i.e., without the convergent of the open-jet wind-tunnel facility) allows to obtain correct results in terms of airfoil loading and mean tip leakage vortex. However, some deviations were observed when compared to the measurements. In particular, the mean axial velocity of the tip leakage vortex was underestimated, and its mean trajectory was farther away from the airfoil. On the other hand, taking into account the full experimental set-up in the computational domain allowed us to correct these differences and better match the experiment. This improvement is explained by a more realistic development of the jet, which has a non-negligible interaction with the flow around the airfoil.

Moreover, we demonstrated that the use of a mesh adaptation was necessary in order to recover the complex structure of the tip leakage vortex and especially the acceleration of the longitudinal velocity component. Finally, the present wall-modelled LES methodology allowed us to accurately predict the wall pressure fluctuations on the airfoil surface and the acoustic spectrum in the far-field. In particular, the frequency range of the tip clearance noise was correctly captured.

Resorting to the LES is essential for the intended future acoustic applications, such as Ultra-High Bypass Ratio turbofan engine, the details of which are beyond the scope of the present paper. Indeed, explicit wall-pressure statistics requiring the simulation of the turbulence are generally used as input data in the sound prediction models. The wall-modelled LES strategy developed in this paper was designed to address this issue on more realistic rotating configurations.

Author Contributions: Conceptualization, D.L., G.D., M.R. and H.P.; methodology, D.L.; software, D.L. and G.D.; validation, D.L.; formal analysis, D.L.; investigation, D.L.; resources, D.L.; data curation, D.L.; writing—original draft preparation, D.L. and G.D.; writing—review and editing, D.L. and G.D.; visualization, D.L.; supervision, G.D., M.R. and H.P.; project administration, D.L., G.D., M.R. and H.P.; funding acquisition, H.P. All authors have read and agreed to the published version of the manuscript.

Funding: This research was co-funded by Safran Aircraft Engines and ANRT through the CIFRE PhD thesis n° 2018/1057.

Data Availability Statement: Not applicable.

Acknowledgments: This work was performed within the framework of the LABEX CeLyA (ANR-10-LABX-0060) of Université de Lyon, within the program "Investissements d'Avenir" (ANR-16-IDEX-0005) operated by the French National Research Agency (ANR). The authors are grateful for the experimental data provided by Emmanuel Jondeau and Marc Jacob from the Laboratoire de Mécanique des Fluides et d'Acoustique de l'Ecole Centrale de Lyon. This work was granted access to the HPC resources of TGCC under the allocation A0082A06074 made by GENCI. The authors also acknowledge Laurent Gicquel, Florent Duchaine, Jérôme Dombard and Nicolas Odier from *CERFACS* for their precious advice.

Conflicts of Interest: The authors declare no conflict of interest.

Abbreviations

β	Angle of attack (°)
Γ_1	Vortex identification function
$\bar{\Phi}$	Time-average dissipation
C_p	Pressure coefficient
f	Frequency (Hz)
p	Static pressure (Pa)
T	Static temperature (K)
U, V, W	Mean velocity components (m·s^{-1})
c	Chord (m)
Ma	Mach number (-)
Q	Q criterion (s^{-2})
Re	Reynolds number (-)
s	Gap height (m)

Acronyms

CFL	Courant–Friedrichs–Lewy
LBM	Lattice Boltzmann Method
LES	Large Eddy Simulation
PIV	Particle Image Velocimetry
PSD	Power Spectral Density
RANS	Reynolds-Averaged Navier-Stokes
RMS	Root-Mean-Square
URANS	Unsteady Reynolds-Averaged Navier-Stokes
ZLES	Zonal Large-Eddy Simulation

References

1. Lakshminarayana, B. *Fluid Dynamics and Heat Transfer of Turbomachinery*; John Wiley & Sons Inc.: Hoboken, NJ, USA, 1996; pp. 339–354.
2. Longhouse, R.E. Control of tip-vortex noise of axial flow fans by rotating shrouds. *J. Sound Vib.* **1978**, *58*, 201–214. [CrossRef]
3. Kameier, F.; Neise, W. Experimental Study of Tip Clearance Losses and Noise in Axial Turbomachines and their Reduction. *J. Turbomach.* **1997**, *119*, 460–471. [CrossRef]
4. Fukano, T.; Jang, C.M. Tip clearance noise of axial flow fans operating at design and off-design condition. *J. Sound Vib.* **2004**, *275*, 1027–1050. [CrossRef]
5. Jacob, M.C.; Grilliat, J.; Camussi, R.; Gennaro, G.C. Aeroacoustic Investigation of a Single Airfoil Tip Leakage Flow. *Int. J. Aeroacoustics* **2010**, *9*, 253–272. [CrossRef]
6. März, J.; Hah, C.; Neise, W. An Experimental and Numerical Investigation into the Mechanisms of Rotating Instability. *J. Turbomach.* **2002**, *124*, 367. [CrossRef]
7. Zhu, T.; Lallier-Daniels, D.; Sanjosé, M.; Moreau, S.; Carolus, T. Rotating coherent flow structures as a source for narrowband tip clearance noise from axial fans. *J. Sound Vib.* **2018**, *417*, 198–215. [CrossRef]
8. Boudet, J.; Cahuzac, A.; Kausche, P.; Jacob, M.C. Zonal large-eddy simulation of a fan tip-clearance flow, with evidence of vortex wandering. *J. Turbomach.* **2015**, *137*, 061001. [CrossRef]
9. Boudet, J.; Caro, J.; Li, B.; Jondeau, E.; Jacob, M.C. Zonal large-eddy simulation of a tip leakage flow. *Int. J. Aeroacoustics* **2016**, *15*, 646–661. [CrossRef]
10. Koch, R.; Sanjose, M.; Moreau, S. Large-eddy simulation of a single airfoil tip-leakage flow. In Proceedings of the AIAA Aviation 2020 Forum, Virtual Event, 15–19 June 2020; p. 2514.
11. Mann, A.; Kim, M.S.; Wu, J.; Perot, F.; Grilliat, J.; Jacob, M.C.; Colman, M. Airfoil Tip Leakage Aeroacoustics Predictions using a Lattice Boltzmann Based Method. In Proceedings of the 22nd AIAA/CEAS Aeroacoustics Conference, Lyon, France, 30 May–1 June 2016.
12. Moreau, S.; Henner, M.; Iaccarino, G.; Wang, M.; Roger, M. Analysis of flow conditions in freejet experiments for studying airfoil self-noise. *AIAA J.* **2003**, *41*, 1895–1905. [CrossRef]
13. Jacob, M.C.; Jondeau, E.; Li, B. Time-resolved PIV measurements of a tip leakage flow. *Int. J. Aeroacoustics* **2016**, *15*, 662–685. [CrossRef]
14. Gourdain, N.; Gicquel, L.; Montagnac, M.; Vermorel, O.; Gazaix, M.; Staffelbach, G.; Garcia, M.; Boussuge, J.; Poinsot, T. High performance parallel computing of flows in complex geometries: I. methods. *Comput. Sci. Discov.* **2009**, *2*, 015003. [CrossRef]
15. Gourdain, N.; Gicquel, L.; Staffelbach, G.; Vermorel, O.; Duchaine, F.; Boussuge, J.F.; Poinsot, T. High performance parallel computing of flows in complex geometries—Part 2: Applications. *Comput. Sci. Discov.* **2009**, *2*, 015004. [CrossRef]
16. Schønfeld, T.; Rudgyard, M. Steady and unsteady flow simulations using the hybrid flow solver AVBP. *AIAA J.* **1999**, *37*, 1378–1385. [CrossRef]
17. Hip Development Team. *Pyhip*; Version 0.3.2; CERFACS: Toulouse, France, 2021.
18. Antares Development Team. *Antares*; Version 1.17.0; CERFACS: Toulouse, France, 2021.
19. Colin, O.; Rudgyard, M. Development of high-order Taylor–Galerkin schemes for LES. *J. Comput. Phys.* **2000**, *162*, 338–371. [CrossRef]
20. Colin, O. *A Finite Element Operator for Diffusion Terms in AVBP*; Technical Report; Institut Français du Pétrole: Rueil-Malmaison, France, 2003.
21. Nicoud, F.; Toda, H.B.; Cabrit, O.; Bose, S.; Lee, J. Using singular values to build a subgrid-scale model for large eddy simulations. *Phys. Fluids* **2011**, *23*, 085106. [CrossRef]
22. Schmitt, P.; Poinsot, T.; Schuermans, B.; Geigle, K. Large-eddy simulation and experimental study of heat transfer, nitric oxide emissions and combustion instability in a swirled turbulent high-pressure burner. *J. Fluid Mech.* **2007**, *570*, 17–46. [CrossRef]
23. Poinsot, T.; Lele, S. Boundary conditions for direct simulations of compressible viscous flows. *J. Comput. Phys.* **1992**, *101*, 104–129. [CrossRef]
24. Odier, N.; Sanjosé, M.; Gicquel, L.; Poinsot, T.; Moreau, S.; Duchaine, F. A characteristic inlet boundary condition for compressible, turbulent, multispecies turbomachinery flows. *Comput. Fluids* **2018**, *178*, 41–55. [CrossRef]

25. Lamidel, D.; Daviller, G.; Roger, M.; Posson, H. Numerical investigation of the tip leakage vortex of an isolated plate/airfoil T-junction with gap. In Proceedings of the 14th European Conference on Turbomachinery Fluid Dynamics & Thermodynamics—ETC14, Gdansk, Poland, 12–16 April 2021.
26. Daviller, G.; Oztarlik, G.; Poinsot, T. A generalized non-reflecting inlet boundary condition for steady and forced compressible flows with injection of vortical and acoustic waves. *Comput. Fluids* **2019**, *190*, 503–513. [CrossRef]
27. Kraichnan, R.H. Diffusion by a random velocity field. *Phys. Fluids* **1970**, *13*, 22–31. [CrossRef]
28. Passot, T.; Pouquet, A. Numerical simulation of compressible homogeneous flows in the turbulent regime. *J. Fluid Mech.* **1987**, *181*, 441–466. [CrossRef]
29. Graftieaux, L.; Michard, M.; Grosjean, N. Combining PIV, POD and vortex identification algorithms for the study of unsteady turbulent swirling flows. *Meas. Sci. Technol.* **2001**, *12*, 1422. [CrossRef]
30. Storer, J.A.; Cumpsty, N.A. Tip Leakage in Axial Compressors. *J. Turbomach.* **1991**, *113*, 252. [CrossRef]
31. Daviller, G.; Brebion, M.; Xavier, P.; Staffelbach, G.; Müller, J.M.; Poinsot, T. A Mesh Adaptation Strategy to Predict Pressure Losses in LES of Swirled Flows. *Flow Turbul. Combust.* **2017**, *99*, 93–118. [CrossRef]
32. Boudet, J.; Jacob, M.C.; Caro, J.; Jondeau, E.; Li, B. Wavelet Analysis of a Blade Tip-Leakage Flow. *AIAA J.* **2018**, *56*, 3332–3336. [CrossRef]
33. Casalino, D. An advanced time approach for acoustic analogy predictions. *J. Sound Vib.* **2003**, *261*, 583–612. [CrossRef]

6.2 Combustion Noise

The objective of Yann Gentil's PhD thesis, started in 2020, is to predict the combustion noise through the turbine stages using analytical models. The recent work included in the following article presents a new model to account for the compositional noise mechanism.

Y. Gentil, G. Daviller, S. Moreau, N. C. W. Treleaven, and T. Poinsot. Theoretical analysis and numerical validation of the mechanisms controlling composition noise. Submitted in *Journal of Fluid Mechanics*, 2022.

Theoretical analysis and numerical validation of the mechanisms controlling composition noise

Y. Gentil[1] †, G. Daviller[1], S. Moreau[2], N. C. W. Treleaven [1], and T. Poinsot[1,3]

[1]CERFACS, 42 Avenue Gaspard Coriolis, 31057 Toulouse, France

[2]Department of Mechanical Engineering, University of Sherbrooke, Sherbrooke, J1K2R1, QC, Canada

[3]Institut de Mécanique des Fluides de Toulouse, 31400 Toulouse, France

(Received 26/04/2022; revised 23/11/2022; accepted xx)

Indirect combustion noise is created when entropy waves, vorticity or composition waves cross turbine stages and can be a significant contributor to turboengine noise. Composition noise is caused by waves of chemical composition entering the turbine stage. Its importance and definition are revisited here: a new decomposition of the entropy between temperature and mixture composition contributions is proposed, which provides an independent set of variables to describe an ideal, non-reacting gas mixture. This decomposition provides a proper definition of the entropy wave in the context of heterogeneous species mixture flow. When considering quasi one-dimensional flow in nozzles, the resulting linearized Euler equations yield a system of equations similar to previous models ignoring the gas mixture composition and show a remarkable one-way coupling between composition waves and both acoustic and entropy waves. Two solutions of the linearized Euler equations system are investigated in this paper: the first analytical model relies on the compact assumption and the second one is an exact solution based on the Magnus-expansion method. Composition noise is shown to be caused by the acceleration/deceleration of fluctuations of species mass fractions fluctuations. This new theory is validated by comparing the model predictions with direct numerical simulation of nozzle flows in which composition fluctuations are pulsed. An extension of the Navier-Stokes characteristics boundary conditions to account for the properly defined entropy wave is provided as well as original non-reflecting boundary conditions for pulsing composition waves. For an air-kerosene mixture in a choked nozzle representative of actual take-off conditions in a turboengine, composition transfer functions are accessed with high-fidelity simulations and compared with the two analytical models. Within the framework of the literature (Magri (2017)), similar test case is reproduced with high-fidelity simulation. Composition transfer functions from simulations are found to agree with the two analytical models of the present study. Finally, a parametric study based on an air-kerosene mixture and an ideal framework shows that composition noise can reach a maximum of 10% of entropy noise for lean combustion and choked nozzle meanwhile for rich combustion, composition noise and entropy noise shows comparable levels.

Key words: Combustion Noise, Acoustics, Reacting Flows, Gas Dynamics

† Email address for correspondence: gentil@cerfacs.fr

1. Introduction

Combustion noise was initially studied in the framework of combustion instabilities in rocket engines by the pioneering work of Tsien (1952). Marble & Candel (1977) then explained the mechanisms responsible for combustion noise by introducing the notion of wave propagation through nozzles. In principle, the noise created within the combustion chamber and successively transmitted through each stage of the turbine is responsible for what is called combustion noise, but it is not the only mechanism. Indeed, this mechanism, commonly referred to as *direct noise*, is often overcome by a second mechanism, called *indirect noise*, where other non-acoustic waves produced within the combustion chamber cross the turbine stages and generate additional noise. Indirect noise can be decomposed into three contributions. Historically, the main indirect combustion noise component was entropy noise (Marble & Candel 1977; Bake *et al.* 2009; Morgans & Duran 2016). A second well identified component comes from the acceleration of vorticity waves (Ullrich *et al.* 2015). It has been demonstrated recently that the compositional inhomogeneities of a multi-component mixture also contribute to the indirect combustion noise (Magri *et al.* 2016; Ihme 2017). This latter mechanism is known as the composition noise.

To analyze direct and indirect combustion noise, it is necessary to understand the transmission mechanism of waves across turbine stages. A common simplification is to consider and investigate only the effects of flow acceleration and deceleration across the stages, replacing turbine stages by simple nozzles similarly to the idea of Marble & Candel (1977). A nozzle is characterized by the transmission and reflection coefficients, which are defined as the ratios of the generated waves to the incident one. Assuming low-frequency or compact waves, an analytical formulation can be found for these coefficients (Marble & Candel 1977; Magri *et al.* 2016).

Marble and Candel's approach (1977) only gives transmission coefficients in the low frequency limit, while experiments show that those coefficients are frequency-dependent. To correct the model, single low-frequency coefficients must be replaced by transfer functions, which are the ratios of the complex outgoing to incoming wave magnitudes given at different frequencies. Moase *et al.* (2007) developed a linear analytical model for studying transfer functions beyond the low frequency limit, assuming a piecewise-linear approximation of the velocity profile. Avoiding the velocity profile approximation, Stow *et al.* (2002) and later, Goh & Morgans (2011) proposed an effective nozzle length model. Although these two analytical models correct the phase of the transfer functions with respect to the wave frequency, they do not correct the amplitude. A complete solution of the quasi one-dimensional linearized Euler equations was then proposed by Duran & Moreau (2013) for arbitrary nozzle geometries. A strong dependence of the transfer functions with respect to frequency was demonstrated. This solution was originally developed for planar wave propagation only, and an extension to circumferential waves was then proposed by Duran & Morgans (2015). However, as these models consider isentropic flows only, they do not take into account boundary layer and local flow friction at walls, as well as flow separations that may appear in real flows through the nozzle. In order to consider the pressure losses through the nozzle for noise prediction, De Domenico *et al.* (2019) have proposed an extension of the compact model of Marble & Candel (1977) for subsonic-to-sonic flows including these dissipative mechanisms that lead to a drop in static pressure. Yeddula *et al.* (2022) also recently added the effect of mean heat transfer.

Finally, downstream of a combustion chamber at the turbine inlet, the multi-species flow is usually inhomogeneous due to several mechanisms such as turbulence, dilution or film cooling. Inhomogeneities of temperature have been investigated extensively in the past whilst assuming homogeneous composition mixture (Marble & Candel 1977; Duran & Moreau 2013). Nevertheless, the homogeneous composition mixture assumption is not always verified and composition inhomogeneities can be measured. Magri *et al.* (2016) were first to investigate the generation of noise due to these composition inhomogeneities. Whereas in uniform fluid flows, composition waves evolve independently of acoustic waves, all these waves, including the entropy wave, become coupled in accelerated/decelerated flows. Magri *et al.* (2016) and Ihme (2017) studied composition-to-acoustic transfer functions through several nozzles at compact frequencies, and highlighted the possible significant noise due to compositional inhomogeneities. To extend the results to non-compact frequencies, Magri (2017) recast the quasi-one-dimensional linearized Euler equations for multi-species flow into an invariant formulation following the methodology of Duran & Moreau (2013) and proposed a mathematical solution using an asymptotic expansion. As found for other transfer functions, a strong frequency dependence for composition-to-acoustic transfer functions is observed.

Simulating a realistic rich-quench-lean (RQL) combustor coupled with a nozzle guide vane with LES, Giusti *et al.* (2019) were able to track the formation and evolution of composition and temperature inhomogeneities and to investigate the different noise generation mechanism. While significant composition and temperature fluctuations were found at the combustor exit, indirect noise generated by temperature fluctuations was found to be larger than indirect noise generated by composition fluctuations. Nevertheless, near lean blow-out operating conditions, Shao *et al.* (2020) found comparable indirect-noise contributions between composition and temperature waves using a hybrid framework consisting of unsteady combustor LES and low-order nozzle simulation. Both indirect noise contributions were found to be shifted in phase so that cancellation of indirect noise occurs. Furthermore, the impact of different operating conditions: cruise and take-off, was then assessed by Shao & Ihme (2020) by relying on the same method (Shao *et al.* 2020). For take-off operating conditions, the level of inhomogeneities was shown to be higher than at cruise condition, resulting in higher core noise with 10 to 20 dB difference. Moreover, the authors observed that composition noise always exceeds entropy noise induced by temperature fluctuations for the studied configuration. On the contrary, the recent work of Rahmani *et al.* (2022) that considered a blob of products of a complete combustion of n-dodecane in a planar channel flow at a Reynolds number based on the bulk velocity and the channel hydraulic diameter of 13600 suggests that compositional sources are affected and dissipated more than entropy fluctuations by the flow field, resulting in a minor contribution to the observable noise produced. Finally, it should also be noted that all previous comparisons with full simulations of actual engines using the CONOCHAIN methodology (Livebardon *et al.* 2016; Férand *et al.* 2019) showed very good agreement with experiment without considering composition noise. Therefore, up to now, there is no clear consensus on the importance of composition noise, and contradictory results on its relevance have been reported so far.

The present article shows that this may be caused by the differences in definition of entropy waves, which are clarified in section 3. Indeed, current predictions of composition-to-acoustic transfer functions may be incomplete because of the wave decomposition vector previously considered (Magri *et al.* 2016; Ihme 2017; Magri 2017; Giusti *et al.* 2019; Shao *et al.* 2020; Shao & Ihme 2020). In these references, the definition of the entropy wave w^s reveals that it is varying with temperature fluctuations and also composition fluctuations. As a consequence, the common wave decomposition vector of these models, given by the two acoustic waves w^+ and w^- (traveling upstream and downstream, respectively), the entropy wave w^s and the composition wave $w^z = Z'$ which corresponds to the mixture fraction space

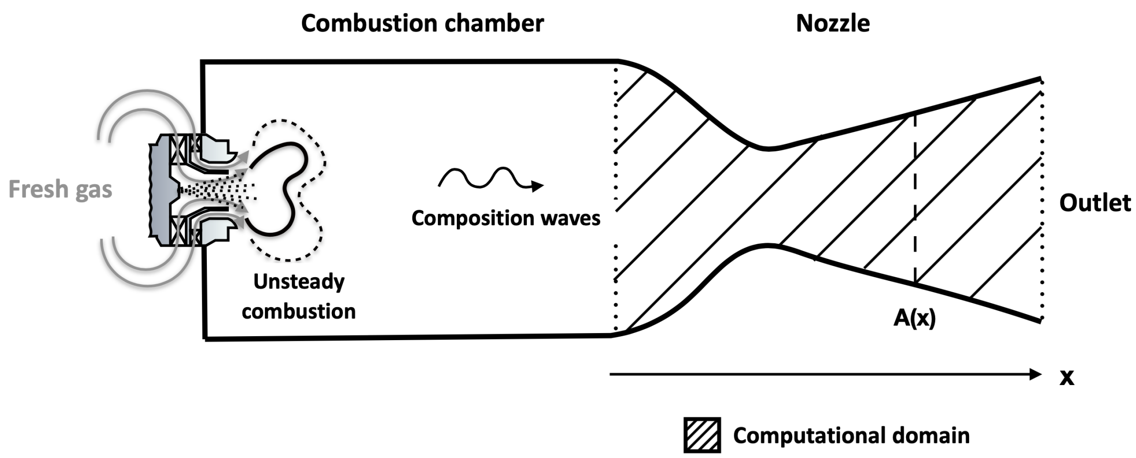

Figure 1: Sketch of the test case

fluctuation, does not form a basis of independent variables. In order to correctly predict the composition-to-acoustic transfer functions, the pulsation of composition waves and its associated entropy wave is required. To do so, a new wave decomposition basis is introduced in this work to properly separate the contributions due to temperature fluctuations and to composition fluctuations.

The aim of the present study is therefore to investigate the potential of the composition noise source mechanism to contribute significantly to the overall noise. The first section is dedicated to the modelling of the problem to predict composition fluctuations. Then, the mathematical model and its assumptions, the system linearization are described in section 3, leading to a new wave decomposition.Two analytical solutions of the system of the quasi-one dimensional linearized Euler equations are also presented as well as the definition of the composition transfer functions. In order to account for the new defined wave decomposition, an extension of the Navier-Stokes characteristic boundary conditions is provided in section 4, along with an original non-reflecting boundary condition for pulsing composition waves. In section 5, the two analytical solutions of the model are validated with two-dimensional nozzle simulations, solving the compressible Euler equations. Composition noise is evaluated for two different burning gas mixtures: kerosene-air and methane-air. On the one hand, the first case (kerosene-air) focuses on the comparison between composition transfer functions from analytical solutions and direct numerical simulations for two operating regimes: subsonic and choked flows, typical of modern turboengines (Férand *et al.* 2019). On the other hand, the second case deals with the evaluation of composition transfer functions by the model in the similar framework as the original test case studied by Magri (2017). Finally, section 6 presents a parametric study on the estimation of total noise and its contributions due to fluctuation of equivalence ratio in a compact flame unilaterally coupled to a compact nozzle.

2. Model problem

The study of composition noise mechanisms can be assessed by considering a nozzle placed at the exhaust of a combustion chamber (figure 1). The noise measured at the nozzle outlet results from the propagation and acceleration through the nozzle of the composition fluctuations generated by the unsteady combustion.

While the computational domain is restricted to the nozzle part, an estimation of the production of composition fluctuations downstream of the combustion chamber is still required. Two different mechanisms have been identified that lead to the formation of compositional inhomogeneities in combustion chambers:

• Fuel is generally injected in a liquid form within the combustion chamber. After undergoing primary atomization, secondary break-up, evaporation and passing through the unsteady swirling airflow, the fuel gas may be in-homogeneous in terms of equivalence ratio before burning in the flame front. These fluctuations of local equivalence ratio in the flame front directly leads to in-homogeneous burnt gases downstream of the flame with different adiabatic temperatures and species compositions.

• Some of the pure air leaving the compressor is drawn off and injected into the combustion chamber for another use: dilution jets and film cooling. Film cooling plays a major role downstream of the flame, decreasing the wall temperatures. On the other hand, although the dilution jets act to mix and homogenize the multi-species burnt gases downstream of the flame, hot spots of temperature may appear, survive and propagate until the first turbine stages.

For simplicity, composition fluctuations are estimated through the first mechanism: fluctuation of local equivalence ratio, noted thereafter as ϕ'. For this purpose, an ideal case of one-dimensional and compact combustion is then chosen to investigate noise generation mechanisms, omitting the second mechanism that may modify the fluctuations.

3. Composition noise mechanism through an isentropic nozzle

3.1. *Theoretical flow model*

To model the behaviour of the burnt gas mixture entering the nozzle, the conservation equations for a non-reactive flow must be considered (Bailly *et al.* 2010) and simplified under the following assumptions: the flow is assumed adiabatic and chemically frozen, i.e. no heat addition, no heat conduction and no combustion. The gas flow is calorifically perfect so that the heat capacity only depends on the mixture composition, as used in previous models (Magri *et al.* 2016). An ideal gas mixture is considered. The flow is attached and at high Reynolds number (thin boundary layers and negligible viscosity effects). It is also reversible and thus isentropic. The flow is assumed quasi-one dimensional, i.e. the nozzle cross-section $A(x)$ in figure 1 is supposed to vary slowly with the axial coordinate x and the variations of velocity only occur in this direction. Finally, conservation equations modelling the non-reacting gas mixture flow behaviour are described by the quasi-one dimensional Euler equations:

$$\frac{D\rho}{Dt} + \rho\frac{\partial u}{\partial x} = -\frac{\rho u}{A}\frac{\partial A}{\partial x}, \qquad (3.1a)$$

$$\rho\frac{Du}{Dt} + \frac{\partial p}{\partial x} = 0, \qquad (3.1b)$$

$$T\frac{Ds}{Dt} = -\sum_{i=1}^{N}\frac{\tilde{G}_i}{W_i}\frac{DY_i}{Dt}, \qquad (3.1c)$$

$$\frac{DY_i}{Dt} = 0 \qquad (3.1d)$$

where the substantial derivative is defined as $\dfrac{D}{Dt} = \dfrac{\partial}{\partial t} + u\dfrac{\partial}{\partial x}$; ρ, u, p and T are the fluid density, the axial velocity, the static pressure and the static temperature respectively; s is the specific entropy; Y_i, $\tilde{G}_i$ and W_i are the mass fractions, the partial molar Gibbs' energy and the molar mass of the i^{th} species respectively; N is the total number of species. Note

$\tilde{G}_i \equiv \mu_i$ is also the chemical potential and equations (3.1) correspond to equations (2.1) to (2.4) in Magri (2017).
This system is closed using the perfect gas law:

$$p = \rho \frac{\mathcal{R}_u}{W} T \equiv \rho\, r\, T \tag{3.2}$$

where $\mathcal{R}_u$ is the universal gas constant and W is the mean molar mass such that: $1/W = \sum_{i=1}^{N} Y_i/W_i$. In addition, the specific entropy is defined through Gibbs' equation (3.3) for multi-component gases (equation (2.5) in Magri (2017)):

$$T\mathrm{d}s = \mathrm{d}h - \frac{\mathrm{d}p}{\rho} - \sum_{i=1}^{N} \frac{\tilde{G}_i}{W_i}\mathrm{d}Y_i \equiv \mathrm{d}h - \frac{\mathrm{d}p}{\rho} - \sum_{i=1}^{N} \frac{\mu_i}{W_i}\mathrm{d}Y_i \tag{3.3}$$

where h and s are the specific enthalpy and entropy respectively.

By definition of the free enthalpy energy, the partial molar Gibbs' energy $\tilde{G}_i$ or chemical potential is given by:

$$\tilde{G}_i = \tilde{H}_i - T\tilde{S}_i \tag{3.4}$$

where $\tilde{H}_i$ and $\tilde{S}_i$ are the partial molar enthalpy and entropy respectively. For an ideal mixture of perfect gases, the partial functions such as enthalpy and heat capacity are equal to the corresponding specific functions calculated for the pure components at a given temperature T and pressure p (DeHoff 1993). The partial molar enthalpy then takes the following form:

$$\tilde{H}_i(T, p, n_1, ...n_n) = \tilde{H}_i^{id}(T, p) \tag{3.5}$$

where the exponent $-^{id}$ corresponds to the thermodynamic function of the pure component. Therefore, the specific enthalpy of the mixture h is given by adding the specific enthalpy of each species for a pure component noted h_i:

$$h = \sum_{i=1}^{N} \frac{\tilde{H}_i^{id}(T, p)}{W_i} Y_i = \sum_{i=1}^{N} h_i Y_i \tag{3.6}$$

On the contrary, the partial molar entropy $\tilde{S}_i$ and the partial molar Gibbs' energy $\tilde{G}_i$ contain additional terms:

$$\tilde{S}_i(T, p, n_1, ...n_n) = \tilde{S}_i^{id}(T, p) - \mathcal{R}_u \ln(X_i), \tag{3.7a}$$

$$\tilde{G}_i(T, p, n_1, ...n_n) = \tilde{G}_i^{id}(T, p) + \mathcal{R}_u T \ln(X_i) \tag{3.7b}$$

where X_i is the molar fraction of the i^{th} species such that: $X_i = Y_i\, W/W_i$. This is in agreement with the fact that the extensive entropy S is modified due to irreversible mixing of species by a factor ΔS given by:

$$\Delta S = -n\mathcal{R}_u \sum_{i=1}^{N} X_i \ln(X_i) \tag{3.8}$$

The specific entropy is therefore given by the following two terms:

$$s = \sum_{i=1}^{N} s_i Y_i - \sum_{i=1}^{N} r_i \ln(X_i) Y_i \tag{3.9}$$

where s_i is the specific entropy of the i^{th} pure species and $r_i = \mathcal{R}_u/W_i$. Finally, the following relationship can be obtained using equations (3.4), (3.5) and (3.7):

$$\tilde{G}_i^{id}(T, p) = \tilde{H}_i^{id}(T, p) - T\tilde{S}_i^{id}(T, p) \tag{3.10}$$

Assuming that the gas mixture is calorically perfect, the heat capacity of the i^{th} species is only mixture-dependent and the specific enthalpy of the i^{th} species is defined as:

$$h_i = \Delta h^{\circ}_{f,i} + C_{p,i}(T - T^{\circ}) \tag{3.11}$$

where $C_{p,i}$ is the constant specific heat capacity and $\Delta h^{\circ}_{f,i}$ is the standard enthalpy of formation of the i^{th} species at constant pressure, respectively.
Thus, the specific enthalpy h and the heat capacity at constant pressure of the mixture C_p are given by:

$$h = C_p(T\breve{}T^{\circ}) + \sum_{i=1}^{N} \Delta h^{\circ}_{f,i} Y_i, \tag{3.12a}$$

$$C_p = \sum_{i=1}^{N} C_{p,i} Y_i \tag{3.12b}$$

Since a mixture of ideal gases is considered, C_p and $C_{p,i}$ verify:

$$C_p = \frac{\gamma}{\gamma - 1}\frac{\mathcal{R}_u}{W} \qquad \text{and} \qquad C_{p,i} = \frac{\gamma_i}{\gamma_i - 1}\frac{\mathcal{R}_u}{W_i} \tag{3.13}$$

where γ and γ_i are the adiabatic index of the mixture and of the i^{th} species respectively.
The differentials of the heat capacity C_p and specific enthalpy h are obtained by:

$$\mathrm{d}C_p = \sum_{i=1}^{N} C_{p,i}\mathrm{d}Y_i \qquad \text{and} \qquad \mathrm{d}h = C_p\mathrm{d}T + \sum_{i=1}^{N} h_i\mathrm{d}Y_i \tag{3.14}$$

Differentiating the specific entropy in equation (3.9) gives:

$$\mathrm{d}s = \sum_{i=1}^{N} Y_i\mathrm{d}s_i + \sum_{i=1}^{N} s_i\mathrm{d}Y_i - \sum_{i=1}^{N} r_i \ln(X_i)\mathrm{d}Y_i \tag{3.15}$$

According to equation (3.15), the elemental variation of specific entropy ds is a function of the elemental variations of each species mass-fractions dY_i and of each specific entropy ds_i.
Introducing equations (3.14) and (3.15) into Gibbs' energy equation (3.3) yields:

$$C_p\mathrm{d}T = T\sum_{i=1}^{N} Y_i\mathrm{d}s_i + \frac{\mathrm{d}p}{\rho} \tag{3.16}$$

The elemental variation of specific entropy is thus obtained by dividing equation (3.16) by C_pT:

$$\frac{1}{C_p}\sum_{i=1}^{N} Y_i\mathrm{d}s_i = \frac{\mathrm{d}T}{T} - (\gamma - 1)\frac{\mathrm{d}p}{\gamma p} \tag{3.17}$$

3.2. *Linearization of the theoretical flow model*

The quasi-1D Euler equations (3.1) for the mean steady flow are given by:

$$\frac{\partial \bar{\rho}\bar{u}A}{\partial x} = 0, \quad \bar{u}\frac{\partial \bar{u}}{\partial x} + \frac{1}{\bar{\rho}}\frac{\partial \bar{p}}{\partial x} = 0, \quad \bar{u}\frac{\partial \bar{Y}_i}{\partial x} = 0, \quad \bar{u}\frac{\partial \bar{s}}{\partial x} = 0 \tag{3.18}$$

where $(\bar{\ })$ represents the steady mean flow. In addition, C_p, $C_{p,i}$ and γ are assumed to be mixture-dependent only. Since $\bar{Y}_i$ are conserved along the nozzle, $\bar{C}_p$, $\bar{C}_{p,i}$ and $\bar{\gamma}$ are thus constant.

To study the propagation of fluctuations, the quasi-1D Euler equations are linearized assuming small dimensionless fluctuations noted $(\hat{\ })$ around the steady mean flow. To do so, variables are written as:

$$\rho = \bar{\rho}(1+\hat{\rho}), \quad p = \bar{p}(1+\bar{\gamma}\hat{p}), \quad u = \bar{u}(1+\hat{u}), \quad Y_i = \bar{Y}_i + \hat{Y}_i, \tag{3.19a}$$

$$s_i = \bar{s}_i + \bar{C}_{p,i}\hat{s}_i, \quad r = \bar{r}(1+\hat{r}), \quad C_p = \bar{C}_p(1+\hat{C}_p), \quad T = \overline{T}(1+\hat{T}), \tag{3.19b}$$

$$s = \bar{s} + \bar{C}_p\hat{s}, \qquad C_{p,i} = \bar{C}_{p,i}, \qquad \gamma = \overline{\gamma} + \hat{\gamma} \tag{3.19c}$$

If equation (3.13) is linearized, the fluctuation $\hat{\gamma}$ is then given by:

$$\frac{\hat{\gamma}}{\bar{\gamma}} = (\bar{\gamma}-1)\sum_{i=1}^{N}\left(\frac{\bar{W}}{W_i} - \frac{\bar{C}_{p,i}}{\bar{C}_p}\right)\hat{Y}_i \tag{3.20}$$

Furthermore, differentiating and linearizing the perfect gas equation (3.2) lead to:

$$\bar{\gamma}\hat{p} = \hat{\rho} + \hat{r} + \hat{T} \tag{3.21}$$

Neglecting higher order terms of fluctuations and replacing the density fluctuation $\hat{\rho}$ using equation (3.21), the quasi-1D Linearized Euler equations become:

$$\frac{\mathrm{D}_0\hat{\rho}}{\mathrm{D}_0 t} + \bar{\rho}\frac{\partial\hat{u}}{\partial x} = \frac{\mathrm{D}_0}{\mathrm{D}_0 t}\left[\bar{\gamma}\hat{p} - \hat{r} - \hat{T}\right] + \bar{u}\frac{\partial\hat{u}}{\partial x} = 0, \tag{3.22a}$$

$$\frac{\mathrm{D}_0}{\mathrm{D}_0 t}\hat{u} + \frac{\bar{c}^2}{\bar{u}}\frac{\partial\hat{p}}{\partial x} + (\hat{\rho} + 2\hat{u} - \bar{\gamma}\hat{p})\frac{\partial\bar{u}}{\partial x} = \frac{\mathrm{D}_0}{\mathrm{D}_0 t}\hat{u} + \frac{\bar{c}^2}{\bar{u}}\frac{\partial\hat{p}}{\partial x} + \left(2\hat{u} - \hat{r} - \hat{T}\right)\frac{\partial\bar{u}}{\partial x} = 0, \tag{3.22b}$$

$$\frac{\mathrm{D}_0}{\mathrm{D}_0 t}\hat{s} = 0, \tag{3.22c}$$

$$\frac{\mathrm{D}_0}{\mathrm{D}_0 t}\hat{Y}_i = 0 \tag{3.22d}$$

where the substantial derivative is defined as $\dfrac{\mathrm{D}_0}{\mathrm{D}_0 t} = \dfrac{\partial}{\partial t} + \bar{u}\dfrac{\partial}{\partial x}$

In order to close this set of equations, the linearization of Gibbs' energy equation (3.17) must be done in order to link the fluctuation of entropy $\hat{s}$ with other fluctuations. However, the fluctuation decomposition vector $\left[\hat{u}, \hat{p}, \hat{T}, \hat{s}, \hat{Y}_i\right]$ does not form a basis of independent variables since the fluctuation $\hat{s}$ encompasses fluctuations of each species mass fractions $\hat{Y}_i$. To do so, the entropy fluctuation $\hat{s}$ is split into terms related to the entropy fluctuations of each species $\hat{s}_i$ and the fluctuations of each species mass fractions $\hat{Y}_i$ in the following.

The linearization of the specific entropy $\hat{s}$ given by equation (3.9) yields the following relation:

$$\hat{s} = \underbrace{\sum_{i=1}^{N}\frac{\overline{C}_{p,i}}{\overline{C}_p}\bar{Y}_i\hat{s}_i}_{(1)} + \underbrace{\frac{1}{\overline{C}_p}\sum_{i=1}^{N}\left(\bar{s}_i - r_i\ln(\bar{X}_i)\right)\hat{Y}_i}_{(2)} \tag{3.23}$$

Introducing the entropy fluctuation $\hat{s}$ (3.23) into the linearized equation (3.22c) gives:

$$\left[\frac{\partial}{\partial t} + \bar{u}\frac{\partial}{\partial x}\right]\sum_{i=1}^{N}\frac{\overline{C}_{p,i}}{\overline{C}_p}\bar{Y}_i\hat{s}_i = -\frac{\bar{u}}{\overline{C}_p}\sum_{i=1}^{N}\frac{\partial\bar{s}_i}{\partial x}\hat{Y}_i \tag{3.24}$$

Introducing equations (3.19) into Gibbs' energy equation (3.17) yields:

$$\mathrm{d}\left(\sum_{i=1}^{N}\frac{\overline{C}_{p,i}}{\overline{C}_p}\bar{Y}_i\hat{s}_i\right)+\frac{1}{\overline{C}_p}\sum_{i=1}^{N}\hat{Y}_i\mathrm{d}\bar{s}_i=\mathrm{d}\hat{T}-\frac{\hat{\gamma}}{\bar{\gamma}}\frac{\mathrm{d}\bar{p}}{\bar{\gamma}\bar{p}}+(1-\bar{\gamma})\mathrm{d}\hat{p} \tag{3.25}$$

By taking the substantial derivative in equation (3.25), it gives:

$$\frac{\mathrm{D}_0}{\mathrm{D}_0 t}\left((1-\bar{\gamma})\hat{p}+\hat{T}\right)-\frac{\hat{\gamma}}{\bar{\gamma}}\frac{\bar{u}}{\bar{\gamma}\bar{p}}\frac{\partial\bar{p}}{\partial x}=0 \tag{3.26}$$

Finally, using the mean equations (3.18) and equation (3.26) gives the linearized Gibbs' energy equation:

$$\frac{\mathrm{D}_0}{\mathrm{D}_0 t}\left((1-\bar{\gamma})\hat{p}+\hat{T}+\log(2+(\bar{\gamma}-1)\bar{M}^2)\frac{\hat{\gamma}}{\bar{\gamma}(\bar{\gamma}-1)}\right)=0 \tag{3.27}$$

where $\bar{M}=\bar{u}/\bar{c}$ is the mean Mach number. This equation corresponds to a reduced-form of the conservation equation (3.22*c*) of $\hat{s}$. Indeed, as demonstrated in appendix A, the linearization of the specific entropy of a mixture of ideal gases reads:

$$\begin{aligned}\hat{s}=\hat{s}^{\circ}+\left(\hat{r}-\hat{C}_p\right)\log\left(2+(\bar{\gamma}-1)\bar{M}^2\right)+(1-\bar{\gamma})\hat{p}+\hat{r}+\hat{T}\\ -\frac{1}{\bar{C}_p}\sum_{i=1}^{N}r_i\log\left(\bar{X}_i\right)\hat{Y}_i+Q^{\circ}\left(\hat{r}-\hat{C}_p\right)\end{aligned} \tag{3.28}$$

where Q° is an integration constant and:

$$\hat{s}^{\circ}=-\hat{C}_p\log\left(T^{\circ}\right)+\frac{\gamma-1}{\gamma}\hat{r}\log\left(p^{\circ}\right) \tag{3.29}$$

Note that the fluctuation $\hat{r}$, $\hat{C}_p$ and $\hat{s}^{\circ}$ are conserved along the considered nozzle (figure 1) since the composition fluctuations $\hat{Y}_i$ are simply propagated, and that equation (3.27) is consequently obtained when taking the substantial derivative of $\hat{s}$ according to equation (3.28). Compared to the model proposed by Magri (2017), the specific entropy fluctuation $\hat{s}$ given by equation (B 10) is quite different from equation (3.28) as further described in the appendix B. Moreover, in equation (3.28) the entropy fluctuation $\hat{s}$ is a variable depending on the species mass fractions $\hat{Y}_i$, which implies that composition fluctuations $\hat{Y}_i$ cannot exist independently of the entropy fluctuation $\hat{s}$.
When considering an homogeneous mixture flow, the following decomposition basis was used by Duran & Moreau (2013): $[\hat{p},\ \hat{u},\ \hat{s}]$ where:

$$\hat{s}=\hat{T}+(1-\bar{\gamma})\hat{p}=\hat{p}-\hat{\rho} \tag{3.30}$$

When considering an heterogeneous species mixture flow, equation (3.30) is extended with terms related to species mass fractions $\hat{Y}_i$ as given by the generalized equation (3.28). Thereafter, a proper entropy fluctuation is defined and noted $\hat{s}_n$ such that $\hat{s}_n=\hat{T}+(1-\bar{\gamma})\hat{p}\neq\hat{p}-\hat{\rho}$. Note that this new defined entropy fluctuation $\hat{s}_n$ corresponds to the left-hand term (1) of equation (3.23).

For simplicity, the dimensionless mixture fraction space fluctuation $\hat{Z}=Z'$ or similarly the equivalence ratio fluctuation $\hat{\phi}=\phi'$ are introduced in order to reduce the size of the system of equations (3.22). To do so, the species mass-fractions fluctuations $\hat{Y}_i$ can be linked to Z' or ϕ' using the first order derivation such that:

$$\hat{Y}_i = \frac{\mathrm{dY_i}}{\mathrm{dZ}}\hat{Z} \quad \text{and} \quad \frac{\mathrm{D}_0}{\mathrm{D}_0 t}\hat{Z} = 0, \tag{3.31a}$$

$$\hat{Y}_i = \frac{\mathrm{dY_i}}{\mathrm{d}\phi}\hat{\phi} \quad \text{and} \quad \frac{\mathrm{D}_0}{\mathrm{D}_0 t}\hat{\phi} = 0 \tag{3.31b}$$

3.3. *Quasi-one dimensional linearized Euler equations for non-reacting and multi-species flow*

Finally, by replacing equations (3.22*c*), (3.22*d*) with equations (3.27), (3.31*a*) respectively and introducing the dimensionless fluctuation $\hat{s}_n$ and the mixture fraction space fluctuation $\hat{Z}$, the quasi-one dimensional linearized Euler Equations for non-reacting and multi-species flow can be written as follows:

$$\frac{\mathrm{D}_0}{\mathrm{D}_0 t}\left[\hat{p} - \hat{s}_n\right] + \bar{u}\frac{\partial \hat{u}}{\partial x} = 0, \tag{3.32a}$$

$$\frac{\mathrm{D}_0}{\mathrm{D}_0 t}\hat{u} + \frac{\bar{c}^2}{\bar{u}}\frac{\partial \hat{p}}{\partial x} + \left(2\hat{u} - (\bar{\gamma}-1)\hat{p} - \hat{s}_n - \Lambda\hat{Z}\right)\frac{\partial \bar{u}}{\partial x} = 0, \tag{3.32b}$$

$$\frac{\mathrm{D}_0}{\mathrm{D}_0 t}\left(\hat{s}_n + \log(2 + (\bar{\gamma}-1)\bar{M}^2)(\Lambda - \chi)\hat{Z}\right) = 0, \tag{3.32c}$$

$$\frac{\mathrm{D}_0}{\mathrm{D}_0 t}\hat{Z} = 0 \tag{3.32d}$$

where

$$\Lambda = \sum_{i=1}^{N}\frac{W}{W_i}\frac{\mathrm{dY_i}}{\mathrm{dZ}} \quad \text{and} \quad \chi = \sum_{i=1}^{N}\frac{\bar{C}_{p,i}}{\bar{C}_p}\frac{\mathrm{dY_i}}{\mathrm{dZ}} \tag{3.33a}$$

According to (3.32), the independent fluctuation decomposition basis is characterized by the following basis: $\left[\hat{u}, \hat{p}, \hat{s}_n, \hat{Z}\right]$. When the species gas mixture verifies the following relationship: $\dfrac{\bar{W}}{W_i} = \dfrac{\bar{C}_{p,i}}{\bar{C}_p}$, $\hat{\gamma} = 0$ and the system (3.32) yields a particular case and simplified model, which is described in appendix C.

When the mean velocity is constant (homogeneous flow), i.e. $\mathrm{d}\bar{u}/dx = 0$, four decoupled equations called the characteristic equations are obtained for a multi-species flow:

$$\left[\frac{\partial}{\partial t} + (\bar{u}+\bar{c})\frac{\partial}{\partial x}\right] w^+ = 0, \tag{3.34a}$$

$$\left[\frac{\partial}{\partial t} + (\bar{u}-\bar{c})\frac{\partial}{\partial x}\right] w^- = 0, \tag{3.34b}$$

$$\left[\frac{\partial}{\partial t} + \bar{u}\frac{\partial}{\partial x}\right] w_h^s = 0, \tag{3.34c}$$

$$\left[\frac{\partial}{\partial t} + \bar{u}\frac{\partial}{\partial x}\right] w^z = 0 \tag{3.34d}$$

with

$$w^+ = \hat{p} + \bar{M}\hat{u}, \qquad w^- = \hat{p} - \bar{M}\hat{u}, \qquad w_h^s = \hat{s}_n, \qquad w^z = \hat{Z} \tag{3.35}$$

The variables w^+, w^-, w_h^s and w^z are called *waves* and propagate at the convection speed: $\bar{u}+\bar{c}$, $\bar{u}-\bar{c}$, $\bar{u}$ and $\bar{u}$ respectively. These definitions are consistent with that of Duran & Moreau (2013) when assuming homogeneous mixture flow, i.e $\hat{Z} = 0$. When the mean flow velocity is not constant, i.e. $\mathrm{d}\bar{u}/\mathrm{d}x \neq 0$, the four waves are coupled through the mean flow gradient:

$$\left[\frac{\partial}{\partial t} + (\bar{u}+\bar{c})\frac{\partial}{\partial x}\right] w^+ = \left\{\frac{\eta^+ - \zeta\alpha^-}{\bar{M}} w^+ - \frac{\eta^+ - \zeta\alpha^+}{\bar{M}} w^- + \zeta w_h^s + \zeta\Gamma^- w^z\right\} \bar{u}\frac{\mathrm{d}\bar{M}}{\mathrm{d}x} \tag{3.36a}$$

$$\left[\frac{\partial}{\partial t} + (\bar{u}-\bar{c})\frac{\partial}{\partial x}\right] w^- = \left\{\frac{\zeta\alpha^- - \eta^-}{\bar{M}} w^+ + \frac{\eta^- - \zeta\alpha^+}{\bar{M}} w^- - \zeta w_h^s - \zeta\Gamma^+ w^z\right\} \bar{u}\frac{\mathrm{d}\bar{M}}{\mathrm{d}x} \tag{3.36b}$$

$$\left[\frac{\partial}{\partial t} + \bar{u}\frac{\partial}{\partial x}\right] w_h^s = -\left\{(\Lambda-\chi)\zeta(\bar{\gamma}-1)\bar{M}w^z\right\} \bar{u}\frac{\mathrm{d}\bar{M}}{\mathrm{d}x} \tag{3.36c}$$

$$\left[\frac{\partial}{\partial t} + \bar{u}\frac{\partial}{\partial x}\right] w^z = 0 \tag{3.36d}$$

where

$$\eta^\pm = \frac{1}{2}\left(1 \pm \frac{1}{\bar{M}}\right), \qquad \alpha^\pm = 1 \pm \frac{(\bar{\gamma}-1)}{2}\bar{M}, \qquad \zeta = \left(1 + \frac{\bar{\gamma}-1}{2}\bar{M}^2\right)^{-1}$$
$$\text{and} \quad \Gamma^\pm = \Lambda \pm (\Lambda-\chi)(\bar{\gamma}-1)\bar{M}$$

Equations (3.36) describe the wave (i.e fluctuation) propagation through an isentropic and non-reacting flow in a nozzle. Two mechanisms responsible for indirect noise generation are identified through the non-zero mean flow gradient term $d\bar{M}/dx$: a one-way coupling between the entropy wave w_h^s and the acoustics waves (w^+, w^-) and a one-way coupling between the composition wave w^z and both acoustic and entropy waves (w^+, w^-, w_h^s). The first coupling mechanism involving the entropy wave w_h^s has been extensively investigated when assuming homogeneous mixture flows by Cumpsty & Marble (1977); Goh & Morgans (2011); Duran & Moreau (2013). In the context of heterogeneous species mixture flow, similar noise generation mechanism is found. For the second mechanism, noise generation is produced by the acceleration/deceleration of the composition wave w^z, or equivalently the composition fluctuations $\hat{Y}_i$, which has been investigated by Magri *et al.* (2016); Ihme (2017); Shao *et al.* (2020). Furthermore, a new one-way coupling between composition and entropy waves is found here according to the system of equations (3.36), which extends the former model (Magri 2017).

3.4. *Composition transfer functions*

To investigate the propagation of composition waves w^z through the nozzle, incident waves are pulsed in the system of equations (3.36) and transfer functions are determined as the ratio between the nozzle outgoing waves to the incident pulsed waves. Thereafter, two analytical solutions are investigated: the first solution is known as the compact solution firstly investigated by Marble & Candel (1977) and the second solution is an exact solution of the system of equations based on the Magnus-expansion method (Blanes *et al.* (2009)).

3.4.1. *Compact solution*

A first solution of the system of equations (3.36) is to resort to the compact nozzle assumption, which assumes that the wavelengths of the incident perturbation are large compared to the nozzle length. Consequently, waves propagate quasi-steadily through the nozzle and the nozzle is modelled as a planar interface where upstream fluctuations can be related to downstream fluctuations using simple jump conditions. Four conservation equations can be written: the mass-flow rate $\dot{m}$, the specific total enthalpy h_t, the specific entropy s and the species mass fractions Y_i or the mixture fraction space Z. Note that the subscripts 0 and 1 correspond to nozzle inlet and outlet values respectively. Linearizing these conservation equations gives:

$$\left(\frac{\dot{m}'}{\bar{\dot{m}}}\right)_0 = \left(\frac{\dot{m}'}{\bar{\dot{m}}}\right)_1, \tag{3.38a}$$

$$\left(\frac{h_t'}{\bar{h}_t}\right)_0 = \left(\frac{h_t'}{\bar{h}_t}\right)_1, \tag{3.38b}$$

$$\left(\frac{s'}{\bar{C}_p}\right)_0 = \left(\frac{s'}{\bar{C}_p}\right)_1, \tag{3.38c}$$

$$(Z')_0 = (Z')_1 \tag{3.38d}$$

To obtain the transfer functions, these four fluctuations are then expressed in the decomposition wave basis: $\left[w^+, w^-, w_h^s, w^z\right]$:

$$I_A = \left(\frac{\dot{m}'}{\bar{\dot{m}}}\right) = \eta^+ w^+ + \eta^- w^- - w_h^s - \Lambda w^z, \tag{3.39a}$$

$$I_B = \left(\frac{h_t'}{\bar{h}_t}\right) = \zeta\beta^+ w^+ + \zeta\beta^- w^- + \zeta w_h^s + \zeta\chi w^z, \tag{3.39b}$$

$$I_C = \left(\frac{s'}{\bar{C}_p}\right) = w_h^s + \log(2 + (\bar{\gamma} - 1)\bar{M}^2)(\Lambda - \chi)w^z + (\Lambda + \Upsilon)w^z, \tag{3.39c}$$

$$I_D = (Z') = w^z \tag{3.39d}$$

where:

$$\beta^\pm = \frac{(\bar{\gamma} - 1)}{2}(1 \pm \bar{M}), \tag{3.40a}$$

$$\Upsilon = -\chi \log(T^\circ) + \frac{\bar{\gamma} - 1}{\bar{\gamma}}\Lambda \log(p^\circ) - \frac{1}{\bar{C}_p}\sum_{i=1}^{N} r_i \log(\bar{X}_i)\frac{\mathrm{dY_i}}{\mathrm{dZ}} + Q^\circ(\Lambda - \chi) \tag{3.40b}$$

Since w^z, Λ and Υ are conserved along the nozzle, the invariants I_A and I_C are simplified to the followings:

$$I_A^* = \eta^+ w^+ + \eta^- w^- - w_h^s, \tag{3.41a}$$

$$I_C^* = w_h^s + \log(2 + (\bar{\gamma} - 1)\bar{M}^2)(\Lambda - \chi)w^z \tag{3.41b}$$

Note that these four fluctuations are conserved through the nozzle and yield four invariants of the flow under the compact assumptions: I_A^*, I_B, I_C^* and I_D. Finally, to express the analytical composition transfer functions, boundary conditions need to be accounted for depending on the nature of the flow.

In the case of subsonic flow within the nozzle, three waves are entering at the nozzle inlet, $w_0^+, w_{h,0}^s$ and w_0^z, and one wave is leaving: w_0^-. At the nozzle outlet, three waves are leaving the nozzle, $w_1^+, w_{h,1}^s$ and w_1^z, while one wave is entering the nozzle: w_1^-. To

$R^- = \dfrac{w_0^-}{w_0^z}$	$R_s\chi - \dfrac{2M_0}{M_0-1}(\Lambda-\chi)\log\left(\dfrac{\zeta_1}{\zeta_0}\right)\left[\dfrac{-\dfrac{M_0}{\zeta_1}+\dfrac{1}{(\gamma-1)\zeta_0}}{(M_0+M_1)\left(1+\dfrac{\gamma-1}{2}M_0M_1\right)}+1\right]$	
$T^+ = \dfrac{w_1^+}{w_0^z}$	$T_s\chi - \dfrac{2M_1}{1+M_1}(\Lambda-\chi)\log\left(\dfrac{\zeta_1}{\zeta_0}\right)\dfrac{-\dfrac{M_0}{\zeta_1}+\dfrac{1}{(\gamma-1)\zeta_0}}{(M_0+M_1)\left(1+\dfrac{\gamma-1}{2}M_0M_1\right)}$	
$T^s = \dfrac{w_{h,1}^s}{w_0^z}$	$(\Lambda-\chi)\log\left(\dfrac{\zeta_1}{\zeta_0}\right)$	

Table 1: Composition transfer functions

$R_s^- = \dfrac{w_0^-}{w_{h,0}^s}$	$-\dfrac{M_1-M_0}{1-M_0}\dfrac{M_0}{1+\dfrac{\gamma-1}{2}M_0M_1}$
$T_s^+ = \dfrac{w_1^+}{w_{h,0}^s}$	$\dfrac{M_1-M_0}{1+M_1}\dfrac{M_1}{1+\dfrac{\gamma-1}{2}M_0M_1}$

Table 2: Entropy-to-acoustics transfer functions

$$-\frac{M_0}{1+\dfrac{\gamma-1}{2}M_0}\chi - \frac{2M_0}{M_0-1}(\Lambda-\chi)\log\left(\frac{2}{(\gamma+1)}\frac{1}{\zeta_0}\right)\left[\frac{\left[-\dfrac{\gamma+1}{2}M_0+\dfrac{1}{\gamma-1}+\dfrac{M_0^2}{2}\right]}{(1+M_0)\left(1+\dfrac{\gamma-1}{2}M_0\right)}+1\right]$$

Table 3: Composition-to-acoustic reflection transfer functions $R_{z,c}^- = \dfrac{w_0^-}{w_0^z}$

express the composition transfer functions using the four equations (3.39) and (3.41), the four entering waves are imposed as follows: $w_0^+ = w_{h,0}^s = w_1^- = 0$ and $w_0^z = 1$. After some algebra, the transfer functions are summarized in table 1 where R_s and T_s corresponds to the entropy-to-acoustic transfer functions given in table 2.

When the nozzle is choked, the acoustic wave w_1^- propagates downstream through the nozzle divergent and cannot be imposed anymore. To circumvent this issue, Marble & Candel (1977) proposed an additional equation. Since the product of the reduced mass flow rate times the cross section area is constant along the nozzle, its linearization implies that the fluctuation of the reduced mass flow rate must be zero along the nozzle, which consequently imposes the fluctuation of the Mach number to be zero along the nozzle. Yet, this condition does not hold anymore when considering heterogeneous mixture flows. To obtain the composition-to-acoustic reflection transfer function in choked nozzle, the continuity of analytical transfer functions between subsonic and choked nozzle is used when $M_1 \to 1$ and the result is given in table 3. The additional equation writes:

$T_z^s = \dfrac{w_{h,1}^s}{w_0^z}$	$(\Lambda - \chi)\log\left(\dfrac{\zeta_1}{\zeta_0}\right)$
$T_z^- = \dfrac{w_1^-}{w_0^z}$	$\dfrac{1-\gamma M_1}{\gamma+1}T_z^s + \dfrac{2\eta_0^-\alpha_1^-}{\gamma+1}R_{z,c}^-(M_0) + \dfrac{2\eta_1^+\alpha_1^+}{\gamma+1}R_{z,c}^-(M_1)$
$T_z^+ = \dfrac{w_1^+}{w_0^z}$	$\dfrac{2+(\gamma+1)M_1-\gamma(\gamma-1)M_1^2}{2\alpha_1^-(\gamma+1)}T_z^s + \dfrac{\alpha_1^+}{\alpha_1^-}R_{z,c}^-(M_1)\dfrac{\dfrac{1}{\zeta_1}-\dfrac{\gamma+1}{2}M_1}{M_1(\gamma+1)} + \dfrac{\alpha_1^+}{\gamma+1}2\eta_0^- R_{z,c}^-(M_0)$

Table 4: Composition transfer functions

$$w^- = R_{z,c}^-(M)w^z + R_{s,c}^-(M)w_h^s + R_{+,c}^-(M)w^+ \tag{3.42}$$

where $R_{s,c}$ and $R_{+,c}^-$ are the reflection transfer functions obtained by Duran & Moreau (2013):

$$R_{s,c}^- = -\frac{M_0}{1+\dfrac{\gamma-1}{2}M_0} \qquad R_{+,c}^- = \frac{1-\dfrac{\gamma-1}{2}M_0}{1+\dfrac{\gamma-1}{2}M_0} \tag{3.43}$$

This equation verifies that when pulsing either only composition, entropy or acoustic waves from the nozzle inlet, the correct reflection coefficients are provided by equation (3.42) when considering choked nozzle. Furthermore, the characteristic reflection coefficients of the nozzle throat are obtained using equations (3.43) and the equation in table 3 when $M_0 \longrightarrow 1$. These coefficients are the followings:

$$R_+ = \frac{3-\gamma}{\gamma+1}, \qquad R_s = \frac{-2}{\gamma+1} \qquad \text{and} \qquad R_z = \frac{-2}{\gamma+1}(\chi + \gamma(\Lambda - \chi)) \tag{3.44}$$

Equations (3.44) are consistent with the assumption of Marble & Candel (1977) that the fluctuation of the Mach number is zero at the throat position, i.e. $M'/M = 0$ but not anywhere else. Using equations (3.39) and the additional equation (3.42), the composition transmission transfer functions are summarized in table 4. In the following, these transfer functions are termed *Compact*.

3.4.2. *Non-compact solution*

A solution of the quasi-one dimensional linearized Euler equations (3.32) in heterogeneous species mixture flow can be obtained following the methodology proposed by Duran & Moreau (2013). The equations are first re-written in dimensionless form using the dimensionless spaces and times variables, $\xi = x/L_n$ and $\tau = tf$, where L_n is the nozzle length and f is a characteristic frequency of the perturbation. In addition, the Helmholtz number $\Omega = fL_n/\bar{c}_0$ is introduced and the mean flow velocity $\bar{u}$ is made dimensionless using the inlet sound speed $\bar{c}_0$. The equations read:

$$\left[\Omega\frac{\partial}{\partial\tau}+\bar{u}\frac{\partial}{\partial\xi}\right](\hat{p}-\hat{\sigma})+\bar{u}\frac{\partial\hat{u}}{\partial\xi}=0, \tag{3.45a}$$

$$\left[\Omega\frac{\partial}{\partial\tau}+\bar{u}\frac{\partial}{\partial\xi}\right]\hat{u}+\frac{\bar{c}^2}{\bar{u}}\frac{\partial\hat{p}}{\partial\xi}+\left(2\hat{u}-(\bar{\gamma}-1)\hat{p}-\hat{\sigma}-\Lambda\hat{Z}\right)\frac{\mathrm{d}\bar{u}}{\mathrm{d}\xi}=0, \tag{3.45b}$$

$$\left[\Omega\frac{\partial}{\partial\tau}+\bar{u}\frac{\partial}{\partial\xi}\right]\left(\hat{\sigma}+\log(2+(\bar{\gamma}-1)\bar{M}^2)(\Lambda-\chi)\hat{Z}\right)=0, \tag{3.45c}$$

$$\left[\Omega\frac{\partial}{\partial\tau}+\bar{u}\frac{\partial}{\partial\xi}\right]\hat{Z}=0 \tag{3.45d}$$

To recast these equations into an invariant formulation, similar procedure as described by Duran & Moreau (2013) can be achieved and the results read:

$$\frac{\mathrm{D}_0 I_A^*}{\mathrm{D}\tau}=\frac{\bar{u}}{(\bar{\gamma}-1)\bar{M}^2}\left[\frac{\partial I_C^*}{\partial\xi}-\frac{1}{\zeta}\frac{\partial I_B}{\partial\xi}+\left(\chi-(\Lambda-\chi)\log(2+(\bar{\gamma}-1)\bar{M}^2)\right)\frac{\partial I_D}{\partial\xi}\right] \tag{3.46a}$$

$$\frac{\mathrm{D}_0 I_B}{\mathrm{D}\tau}=-\frac{(\bar{\gamma}-1)\bar{u}}{\zeta}\left(\frac{\partial I_A^*}{\partial\xi}+\frac{\partial I_C^*}{\partial\xi}-\log(2+(\bar{\gamma}-1)\bar{M}^2)(\Lambda-\chi)\frac{\partial I_D}{\partial\xi}\right) \tag{3.46b}$$

$$\frac{\mathrm{D}_0 I_C^*}{\mathrm{D}\tau}=0 \tag{3.46c}$$

$$\frac{\mathrm{D}_0 I_D}{\mathrm{D}\tau}=0 \tag{3.46d}$$

where the substantial derivative is defined as $\dfrac{\mathrm{D}_0}{\mathrm{D}_0\tau}=\Omega\dfrac{\partial}{\partial\tau}+\bar{u}\dfrac{\partial}{\partial\xi}$ Assuming the invariants to be harmonic, the system of equations can be recast into a matrix formulation as follows:

$$[\boldsymbol{E}(\xi)]\frac{\mathrm{d}}{\mathrm{d}\xi}[\boldsymbol{I}]=2\pi i\Omega\boldsymbol{I} \tag{3.47}$$

where is $\boldsymbol{I}=\left[I_A^*,I_B,I_C^*,I_D\right]$ the vector of invariants and $\boldsymbol{E}(\xi)$ is a non-constant 4×4 matrix:

$$\boldsymbol{E}=-\bar{u}\begin{bmatrix} 1 & \dfrac{1}{\zeta(\bar{\gamma}-1)\bar{M}^2} & -\dfrac{1}{(\bar{\gamma}-1)\bar{M}^2} & -\dfrac{\chi-(\Lambda-\chi)\log(2+(\bar{\gamma}-1)\bar{M}^2)}{(\bar{\gamma}-1)\bar{M}^2} \\ (\bar{\gamma}-1)\zeta & 1 & (\bar{\gamma}-1)\zeta & -(\bar{\gamma}-1)\zeta(\Lambda-\chi)\log(2+(\bar{\gamma}-1)\bar{M}^2) \\ 0 & 0 & 1 & 0 \\ 0 & 0 & 0 & 1 \end{bmatrix} \tag{3.48}$$

When the matrix $\boldsymbol{E}$ is inversible ($M\neq1$), the system of equations finally reads:

$$\frac{\mathrm{d}}{\mathrm{d}\xi}[\boldsymbol{I}]=\frac{-2\pi i\Omega}{\bar{u}(\bar{M}^2-1)}[\boldsymbol{A}(\xi)]\,\boldsymbol{I} \tag{3.49}$$

where the matrix $\boldsymbol{A}$ is given by:

$$\boldsymbol{A}=\begin{bmatrix} & & & \dfrac{\chi-\bar{\gamma}(\Lambda-\chi)\log(\nu)}{(\bar{\gamma}-1)} \\ & \boldsymbol{A}_{3,3} & & \zeta\left(-\chi+(\Lambda-\chi)\log(\nu)(1+(\bar{\gamma}-1)\bar{M}^2)\right) \\ & & & 0 \\ 0 & 0 & 0 & \bar{M}^2-1 \end{bmatrix} \tag{3.50}$$

where $\nu = 2 + (\bar{\gamma} - 1)\bar{M}^2$ and $\boldsymbol{A}_{3,3}$ corresponds to the matrix formulated by Duran & Moreau (2013):

$$\boldsymbol{A}_{3,3} = \begin{bmatrix} \bar{M}^2 & -\dfrac{1}{(\bar{\gamma}-1)\zeta} & \dfrac{\bar{\gamma}}{\bar{\gamma}-1} \\ -(\bar{\gamma}-1)\bar{M}^2\zeta & \bar{M}^2 & -\zeta\left(1 + (\bar{\gamma}-1)\bar{M}^2\right) \\ 0 & 0 & \bar{M}^2 - 1 \end{bmatrix} \tag{3.51}$$

An exact solution of the system of equations (3.49) can be computed following the resolution methodology proposed by Duran & Moreau (2013). It is based on the Magnus expansion and the resolution depends on the flow conditions as described extensively in Duran & Moreau (2013).

For a choked flow at throat, the inlet subsonic-flow perturbations are first computed up to the throat area where $M \longrightarrow 1$ imposing the correct outlet boundary condition corresponding to the throat area and no upstream forced propagating wave $w_f^- = 0$. This boundary condition is characterized by the reflection coefficients given in equations (3.44). Downstream of the throat, the upstream propagating acoustic wave w^- is given using equation (3.42) when $M \longrightarrow 1$. Finally, the supersonic-flow perturbations can then be solved until the nozzle end and the composition transfer functions are computed following the definitions given in section 3.4.1. In the following, these transfer functions are termed *Non-Compact*.

4. Extension of Navier-Stokes Characteristics Boundary Conditions to multi-species flow

According to the Navier-Stokes Characteristics Boundary Conditions methodology (NSCBC) developed in Poinsot & Lele (1992), flow variables are decomposed into one entropy wave noted $\mathcal{L}_2$, one vorticity wave noted $\mathcal{L}_3$, two acoustic waves noted $\mathcal{L}_1$ and $\mathcal{L}_4$ and i species waves noted $\mathcal{L}_i$ in a two-dimensional flow. Depending on the flow nature (subsonic or supersonic) and boundary position (inlet or outlet), some waves are either ingoing or outgoing. This decomposition is correct for homogeneous mixture flow (i.e. $Y_i' = 0$) and the definition of the entropy wave $\mathcal{L}_2 = w_h^s$ is given by equation (4.1):

$$\mathcal{L}_2 = \frac{\partial \rho}{\partial x} - \frac{1}{c^2}\frac{\partial p}{\partial x} \tag{4.1}$$

Nevertheless, equations (3.34) demonstrate that the entropy wave w_h^s is defined in multi-species boundary condition similarly to equation (4.1) with an additional term linked to composition variations:

$$\mathcal{L}_2 = \frac{\partial \rho}{\partial x} + \rho \sum_{i=1}^{N} \frac{r_i}{r}\frac{\partial Y_i}{\partial x} - \frac{1}{c^2}\frac{\partial p}{\partial x} \tag{4.2}$$

For the present nozzle, $3 + N$ variables must be specified at the subsonic inlet: the mean mass-flow rate ρu, the mean transverse velocity u_{t1}, the mean static temperature T and the mean species mass-fractions Y_i with $i \in [1, N]$ are imposed to enforce the correct nozzle operating condition. In addition, waves need to be superimposed at the nozzle inlet while ensuring non-reflection. To evaluate the wave amplitudes $\mathcal{L}_i$, the flow is assumed locally one-dimensional and inviscid (LODI) and the LODI relations are given by:

$$\frac{\partial \rho}{\partial t} + \mathcal{L}_2 - \rho \sum_i \frac{r_i}{r}\mathcal{L}_i + \frac{\rho}{2c}\left(\mathcal{L}_4 + \mathcal{L}_1\right) = 0 \tag{4.3a}$$

$$\frac{\partial u_n}{\partial t} + \frac{1}{2}\left(\mathcal{L}_4 - \mathcal{L}_1\right) = 0 \tag{4.3b}$$

$$\frac{\partial u_{t1}}{\partial t} + \mathcal{L}_3 = 0 \tag{4.3c}$$

$$\frac{\partial P}{\partial t} + \frac{\rho c}{2}\left(\mathcal{L}_4 + \mathcal{L}_1\right) = 0 \tag{4.3d}$$

$$\frac{\partial Y_i}{\partial t} + \mathcal{L}_i = 0 \tag{4.3e}$$

The LODI relations to impose target values and superimpose composition waves are detailed thereafter.

4.1. *Composition pulsing inlet boundary*

According to the theory developed in section 3, composition wave w^z, i.e. composition fluctuations Y_i', are associated with a density fluctuation only such that: $\rho'/\rho = -r'/r$ when $w^+ = w^- = w_h^s = 0$. The waves amplitudes $\mathcal{L}_j$ at the inlet are thus given by:

$$\begin{aligned}\mathcal{L}_4 = &\frac{-2}{\rho(\gamma M_n+1)}\left(u_n\frac{\partial \rho_w}{\partial t} + K_{\rho u_n}\left[(\rho u_n)^{ref} + \rho_w u_n - \rho u_n + \rho u^-(1-M_n)\right]\right)\\ &+\frac{2u_n}{T(\gamma M_n+1)}\left(T\sum_{i=1}^{N}\frac{r_i}{r}\mathcal{L}_i - K_T\left[T^{ref} - T - \frac{\gamma-1}{c}Tu^-\right]\right)\end{aligned} \tag{4.4}$$

$$\begin{aligned}\mathcal{L}_2 = &-\frac{1}{u_n}\left(u_n\frac{\partial \rho_w}{\partial t} + K_{\rho u_n}\left((\rho u_n)^{ref} + \rho_w u_n - \rho u_n + \rho u^-(1-M_n)\right)\right)\\ &+\rho\sum_{i=1}^{N}\frac{r_i}{r}\mathcal{L}_i - \frac{\rho}{2u_n}\left(M_n+1\right)\mathcal{L}_4\end{aligned} \tag{4.5}$$

$$\mathcal{L}_3 = K_{u_{t1}}\left(u_{t1}^{ref} - u_{t1}\right) \tag{4.6}$$

$$\mathcal{L}_i = \frac{\partial Y_{i,w}}{\partial t} + K_{Y_i}\left(Y_i^{ref} + Y_{i,w} - Y_i\right) \tag{4.7}$$

where u^- is computed locally at each point of the inlet boundary as time integral of the wave amplitude $\mathcal{L}_1$ such that:

$$u^- = \frac{1}{2}\int_0^t \mathcal{L}_1 \mathrm{dt} \tag{4.8}$$

and where $()^{ref}$ subscript corresponds to target values, M_n and u_n are the normal Mach number and normal velocity respectively, ($K_{\rho u_n}$,K_T, $K_{u_{t1}}$, K_{Y_i}) are the relaxation coefficients,

$\bar{T}$	$\bar{p}$	$\bar{Y}_{O_2}$	$\bar{Y}_{H_2O}$	$\bar{Y}_{CO}$	$\bar{Y}_{CO_2}$	$\bar{Y}_{N_2}$
1906 K	1 bars	0.0668	0.0584	$2e-4$	0.1424	0.7322

Table 5: Mean burnt gases

$Y_{i,w}$ are the composition fluctuations and ρ_w is the induced fluctuation such that:

$$Y_{i,w} = \sum_{k=1}^{N_f} A_i^Y \sin(2\pi f \,\mathrm{k} + 2\pi\alpha_k), \qquad \rho_w = -\rho \sum_{i=1}^{N} \frac{r_i}{r} Y_{i,w}, \qquad \alpha_k = \frac{2\pi \mathrm{k}}{N_f} \tag{4.9}$$

Similarly to the work of Leyko *et al.* (2014) and Duran & Moreau (2013) for pulsing entropy or acoustics waves, each species mass fraction fluctuation $Y_{i,w}$ is composed of N_f frequencies in order to compute transfer functions at several frequencies in a single simulation. The fundamental frequency is given by f and the values A_i^Y are the amplitudes of composition waves. Furthermore, a phase-shift α_k is also introduced to decorrelate the pulsed frequencies.

5. Composition noise through annular nozzles

To verify the previous theory, direct numerical simulations of nozzle flows are performed thereafter with superimposed composition waves. A first test case deals with the prediction of the transfer functions due to the propagation of composition fluctuations through choked and subsonic nozzles, which are produced by equivalence ratio fluctuations of a kerosene-air mixture upstream of a front flame. The second test case is performed to compare the results of the two analytical models described in section 3.4 with results from high-fidelity simulations and provided by a previous model of composition noise (Magri (2017)).

5.1. *Composition noise from kerosene-air inhomogeneity*

5.1.1. *Physical model*

As described in section 2, composition fluctuations are estimated through fluctuation of local equivalence ratio ϕ'. To do so, an air-kerosene mixture at an equivalence ratio of $\phi = 0.7$, a temperature of 300 K and a pressure of 1 bar for the fresh gases is considered. Assuming the flame front to be one-dimensional and complete combustion at constant pressure, mean burnt gases downstream of the combustion chamber are obtained using the CANTERA library Goodwin *et al.* (2021). The burnt gas characteristics are provided in table 5. Note that chemical equilibrium is computed at constant pressure and enthalpy. The reaction mechanism is the BFER two-step scheme for an equivalent modified $C_{10}H_{20}$ kerosene (available at https://www.cerfacs.fr/cantera/mechanisms/kero.php). Assuming small fluctuations of equivalence ratio around the mean equivalence ratio $\phi = 0.7$, a new chemical equilibrium is computed for each equivalence ratio. Then, composition fluctuations are deduced by differentiating the new composition mixture with the mean burnt gas conditions of reference. Those fluctuation amplitudes are summarized in table 6 for an equivalence ratio fluctuation of $\phi' = 0.1$.

These mean burnt gases (table 5) are injected in simulations considering the nozzle of Goh & Morgans (2011) and the computational domain shown in figure 2. The inlet total temperature and total pressure are 1966 K and 1.17 bars respectively, leading to an inlet

ϕ'	Y'_{O_2}	Y'_{H_2O}	Y'_{CO}	Y'_{CO_2}	Y'_{N_2}
∓ 0.1	± 0.0112	∓ 0.004	$\mp 2 \times 10^{-4}$	∓ 0.0094	± 0.0024

Table 6: Composition fluctuation amplitudes when $\phi = 0.7 \mp 0.1$

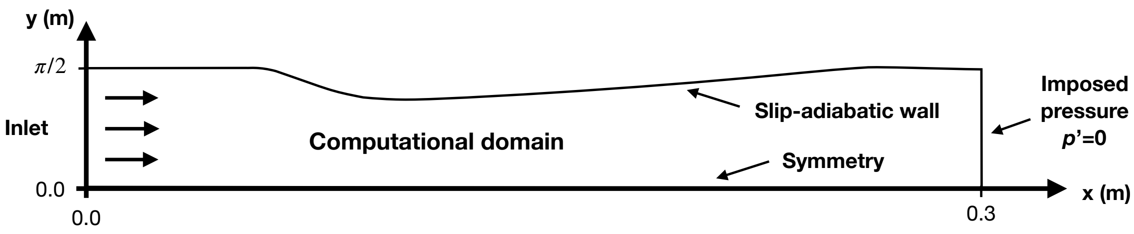

Figure 2: Axisymmetric nozzle domain (x,y) with boundary conditions

Species	O_2	H_2O	CO	CO_2	N_2
$C_{p,i}$ (J/kg/K)	1174.5	2832.4	1288.8	1365.3	1278.5

Table 7: Constant heat capacities

Mach number of $M = 0.48$. Two different regimes are simulated: subsonic and choked flows by simply modifying the outlet nozzle pressure.

Finally, note that heat capacities of each species are assumed constant to be consistent with the model in section 3 and are given in table 7.

5.1.2. *Numerical set-up*

The axisymmetric nozzle flow, sketched in figure 2, is solved with the explicit, unstructured, massively parallel solver AVBP, which can solve both compressible Navier-Stokes or Euler equations (Schønfeld & Rudgyard 1999). After performing a mesh independence study, the mesh of the computational domain shown in figure 2 is finally discretized using 17419 triangular cells, which allows capturing the pulse wave at highest frequency $f_{max} = 6000$ Hz with 68 points with the selected convection scheme. The flow is initialized for both choked and subsonic flows with the steady mean flows. Slip boundary conditions are imposed on the upper nozzle wall meanwhile having a symmetry boundary condition for the lower segment. The Navier-Stokes Characteristic Boundary Conditions (NSCBC), described in subsection 4.1 are imposed for both the inlet and the outlet boundary conditions. Composition fluctuations are pulsed at the inlet using a special treatment as described in section 4.1 with $N_f = 30$ different frequencies, $f = 200$ Hz and composition wave amplitudes given in table 6.

For the numerical parameters, the Euler equations are solved for the axisymmetric nozzle using the perfect gas equation (3.2) and the Lax-Wendroff convection scheme. The CFL number is fixed to 0.7 and the total simulation time is fixed to $T_{tot} = 0.1$s.

5.1.3. *Post-processing*

To compute the transfer functions from both simulations, the wave separation process described in section 3 is applied on the fluctuating field through the nozzle. It consists of the following computation operations:

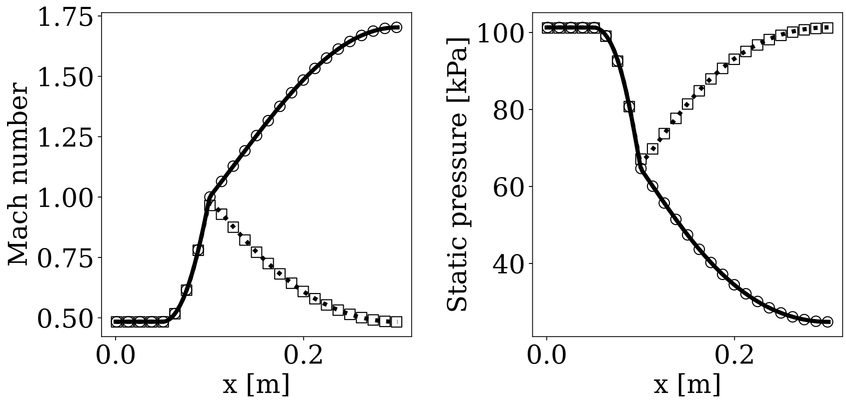

Figure 3: Cross-sectional averaged (a) Mach number and (b) static pressure profiles for both subsonic flow: 1D-model (······), AVBP (□) and choked flow: 1D-model (——), AVBP (○)

- Mean steady fields:

$$\bar{\lambda}(x,y) = \frac{1}{T}\int_{t_0}^{t_0+T} \lambda(x,y,t)dt \tag{5.1}$$

- Dimensionless fluctuation fields:

$$\lambda'(x,y,t) = \frac{\lambda(x,y,t) - \bar{\lambda}(x,y)}{\bar{\lambda}(x,y)} \tag{5.2}$$

- Wave fields using dimensionless fluctuation fields. Entropy wave w_h^s is computed as given in relation (3.35). Note that as the flow is two-dimensional, fluctuations of transverse velocity fields are allowed. Thereafter, acoustic waves w^+ and w^- are computed using the dimensionless pressure fluctuation $\hat{p}$ and the dimensionless velocity magnitude fluctuation noted $\hat{\eta} = \eta'/\bar{\eta}$ such that: $\eta = \sqrt{u^2+v^2}$ and $w^{\pm} = \hat{p} \pm \bar{M}\hat{\eta}$.
- Waves fields are then cross-sectional averaged:

$$w^{\lambda}(x,t) = \frac{1}{L_y}\int_0^{L_y} w^{\lambda}(x,y,t)dy \tag{5.3}$$

- Spectral analysis of the one-dimensional waves $w^{\lambda}(x,t)$ is then done yielding a frequency-dependent signal: $w^{\lambda}(x,f)$.

5.1.4. *Nozzle Mean flows*

To obtain the different flow regimes from similar inlet flows, the outlet static pressure is relaxed through different target values. For the choked flow, the outlet pressure is set sufficiently low such that when the flow becomes supersonic in the nozzle divergent, the boundary conditions is not anymore imposed downstream. On the contrary, the outlet static pressure is relaxed through the target value p_s^{ref} = 1 bars for obtaining the subsonic nozzle flow.

The cross-sectional averaged Mach number and static pressure profiles along the nozzle are computed in the two steady simulations and are compared in figure 3 with the analytical one-dimensional profiles. Both Mach number and static pressure profiles computed from the simulations match well with the analytical one-dimensional profiles, which confirms the quasi-one dimensional flow assumption.

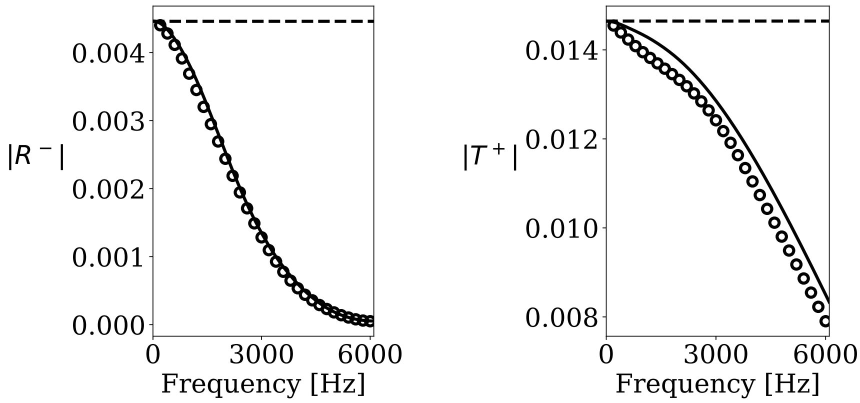

Figure 4: (a) Modulus of the reflection acoustic transfer function (b) Modulus of the transmission acoustic transfer function. *Non-Compact* (——) , AVBP (○), *Compact* (- - -)

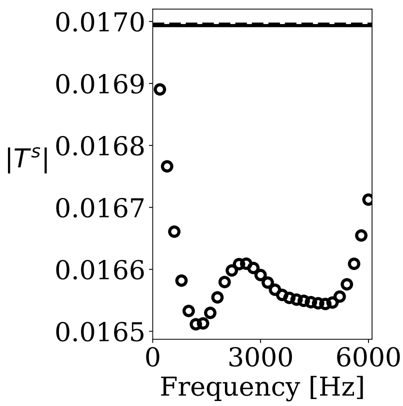

Figure 5: Modulus of the transmission composition-to-entropy transfer function. *Non-Compact* (——) , AVBP (○), *Compact* (- - -)

5.1.5. *Transfer function results : Choked nozzle*

Using the choked nozzle corresponding to the Mach number profile presented in figure 3(a), the composition-to-acoustic and composition-to-entropy transfer functions from the simulation are compared with the transfer functions computed with the *Compact* and *Non-Compact* solutions. Figure 4 shows the acoustic reflection R^- and transmission T^+ transfer functions with their frequency dependence. Both acoustic transfer functions for R^- and T^+ converge to the same result at low frequency. In figure 4(a), the modulus of the reflection transfer function R^- is retrieved by the one-dimensional solution *Non-Compact* compared to the simulation results obtained with AVBP with less than 5.3% mean relative error. Similarly, the prediction of the acoustic transmission transfer function T^+ by the *Non-Compact* solution corresponds to AVBP as observed in figure 4(b) with less than 4.4% mean relative error. The remaining difference is most likely explained by the two-dimensional nature of the present choked flow. Indeed, in figure 6, the dilatation field from the steady solution shows two-dimensional shocklets in the supersonic part of the nozzle. Furthermore, the composition-to-entropy transfer functions is presented in Figure 5. While the predictions from the *Compact* and *Non-Compact* solutions remain constant, the results computed with AVBP shows a frequency-dependency of the transfer function. Similarly to T^+, the difference for T^s can be

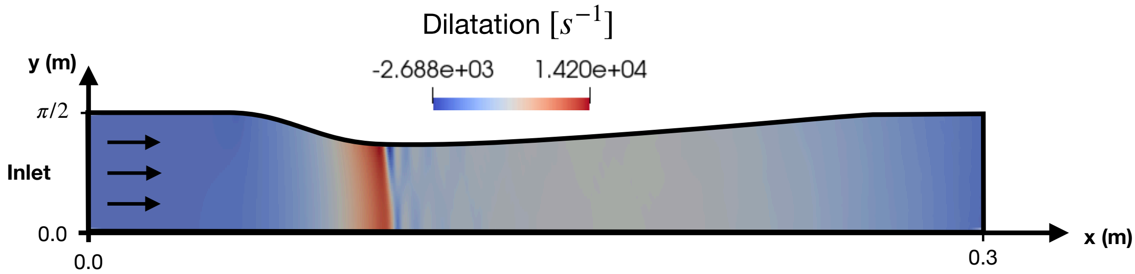

Figure 6: Shock structures within the nozzle

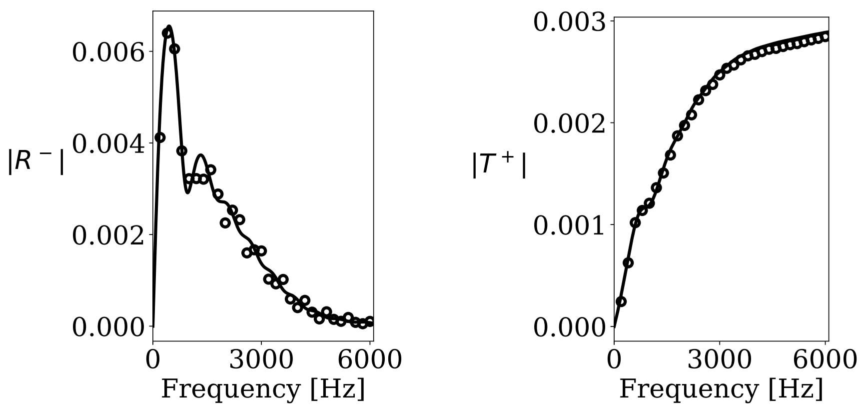

Figure 7: (a) Modulus of the reflection acoustic transfer function R^- (b) Modulus of the transmission acoustic transfer function T^+ . *Non-Compact* (——) , AVBP (○)

explained by the two-dimensional nature of the present choked flow but remains lower than 2.4% mean relative error.

In addition, the composition transfer functions are also evaluated with high-fidelity simulation in the particular case for which the species mixture flows respect the condition (C 1), as detailed in appendix C. Overall, the model is again validated with simulation results.

5.1.6. *Transfer function results : Subsonic nozzle*

After pulsing composition waves through the subsonic nozzle corresponding to the Mach number profile presented in figure 3(a), the reflection and transmission composition transfer functions computed with AVBP are compared to the *Non-Compact* solution in figure 7. Note that the *Compact* solution is not presented here since its acoustic predictions are zero for both reflection and transmission coefficients at low frequencies. Both analytical and numerical solutions also predicted a zero composition-to-entropy transfer function.

For R^- and T^+, the acoustic transfer functions frequency-dependence predicted by the one-dimensional *Non-Compact* model and the numerical results computed with AVBP are in agreement with less than 6% mean relative error.

5.2. *Composition noise from methane-air inhomogeneity*

A second test case, proposed by Magri (2017), is performed in this section. A counter-flow-diffusion-flame of methane-air is considered through a supersonic shock-free nozzle, with linear-velocity profile Marble & Candel (1977).

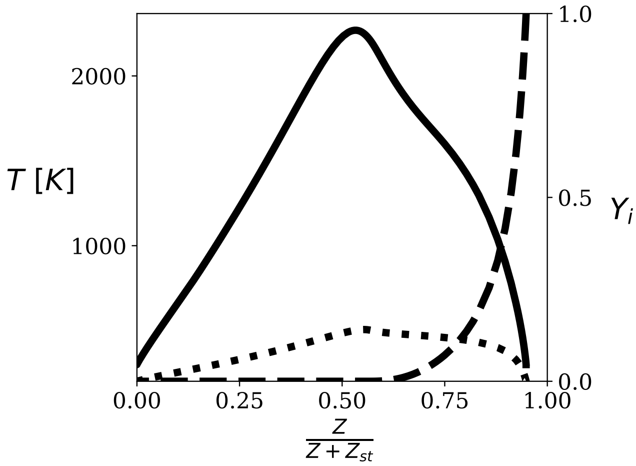

Figure 8: One-dimensional pure-methane-air counter-flow diffusion flame. Temperature (——), Mass fraction of Y_{H_2O} (⋯⋯), Mass fraction of Y_{CH_4} (- - -) profiles against the reduced mixture fraction space $Z/(Z+Z_{st})$

$\bar{T}$	$\bar{p}$	$\bar{Y}_{O_2}$	$\bar{Y}_{H_2O}$	$\bar{Y}_{CO_2}$	$\bar{Y}_{N_2}$
1306 K	1×10^5 Pa	0.173	0.064	0.037	0.726

Table 8: Mean composition and temperature of the burnt gases

Z'	Y'_{H_2O}	Y'_{CO_2}	Y'_{O_2}	Y'_{N_2}
±0.1	±0.025	±0.023	∓0.043	∓0.005

Table 9: Composition fluctuations when $\bar{Z} = 0.02 \pm 0.1$

5.2.1. *Counter-diffusion flame structure and composition fluctuations*

The one-dimensional counter-diffusion flame obtained from the conditions described in Magri (2017) is shown in figure 8. From the knowledge of this flame structure, it is then possible to estimate composition fluctuations by assuming small fluctuations of mixture fraction Z' around a mean state defined at $\bar{Z}$.

The mean burnt gas conditions entering the nozzle are taken at the mixture fraction space $\bar{Z} = 0.02$ and detailed in table 8. Thereafter, assuming small fluctuations of mixture-fraction space Z', composition fluctuations can be simply estimated using the first order derivative in Z, presented in table 9 such that:

$$Y'_k \approx \frac{\mathrm{d}Y_k}{\mathrm{d}Z} Z' \tag{5.4}$$

5.2.2. *Numerical set-up*

The nozzle cross section profile, presented in figure 9 (left), is modelled to reproduce the Mach number profile (figure 9 (right)). After performing a mesh independence study, the nozzle is discretized using 215200 triangle cells, to capture the wave up to the frequency $f = 6000$ Hz with more than 30 points.

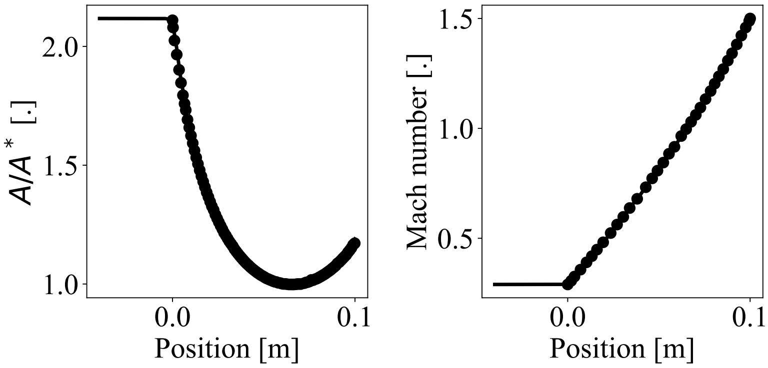

Figure 9: Non-dimensional cross section profile A/A^* (left) and Mach profile along the nozzle (right). Original profile (●) and Modelled (——)

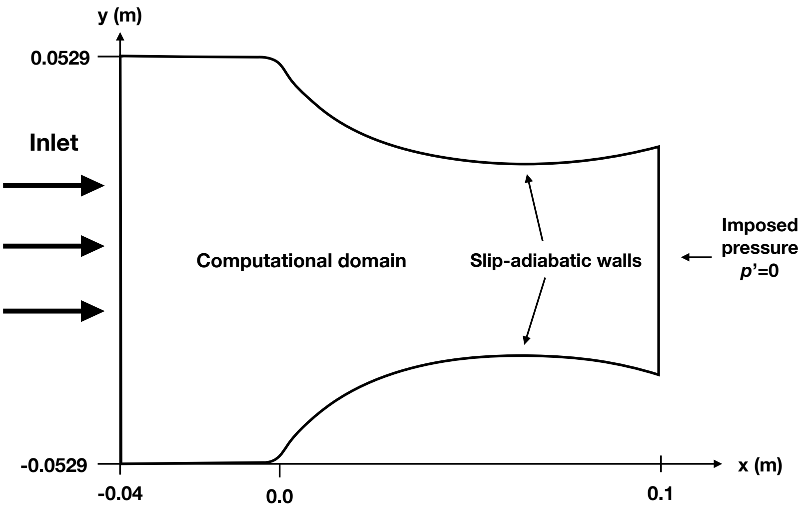

Figure 10: Nozzle computational domain and boundary conditions

Species	O_2	H_2O	CO_2	N_2
$C_{p,i}$ (J/kg/K)	1125	2505.7	1298.5	1218.4

Table 10: Constant heat capacities

Boundary conditions are presented in figure 10 with the computational domain. The mean static inlet conditions are $T = 1306$ K and $P = 1 \times 10^5$ Pa leading to an inlet total temperature of $T_t = 1323$ K and an inlet total pressure of $P_T = 105582$ Pa, respectively. For the numerical parameters, the Euler equations are solved using the perfect gas equation (3.2) and the Lax-Wendroff convection scheme. The CFL number is fixed to 0.7 and the total simulation time is fixed to $T_{tot} = 0.1$ s. To extract the transfer functions from the simulation, post-processing procedures described in subsection 5.1.3 is applied at the inlet section where $M = 0.29$ and at the section located at $x = 0.1$ m where the Mach number is $M = 1.5$ (figure 9). The constant heat capacities of the different species are given in table 10. Finally, the fluctuation frequencies are recast in Helmholtz number, noted He, using the inlet sound speed and the

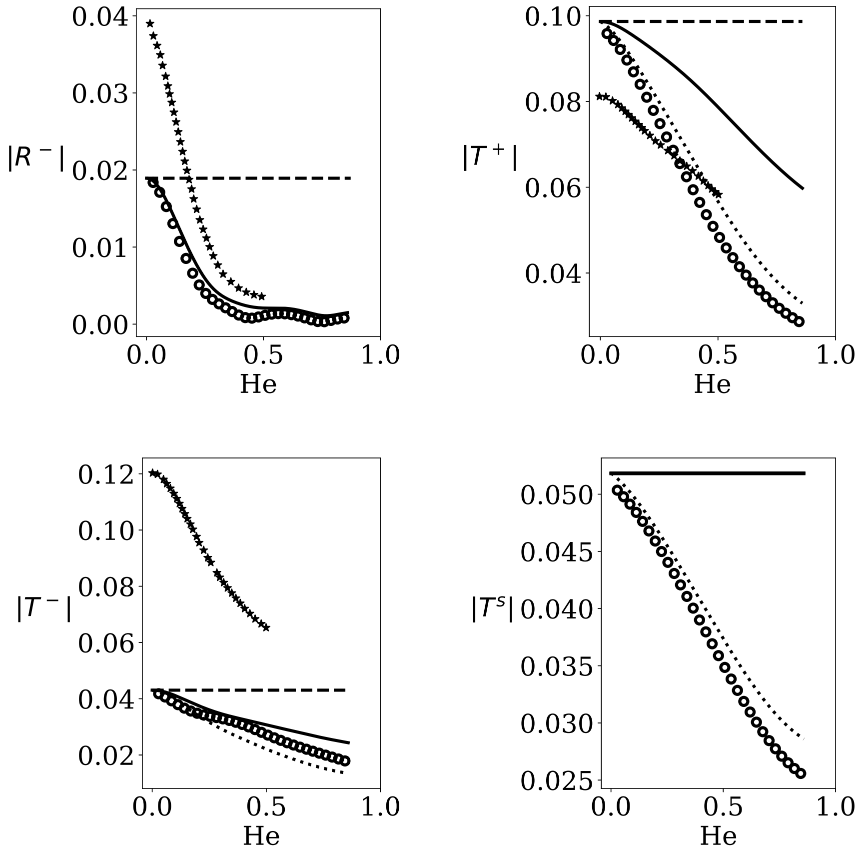

Figure 11: (Left-top) Composition-to-acoustic reflection transfer functions R^-. (Right-top) Composition-to-acoustic transmission transfer functions T^+. (Left-bottom) Composition-to-acoustic transmission transfer functions T^-. (Right-bottom) Composition-to-entropy transmission transfer functions T^s. *Non-Compact* (——), *Compact* (- - -), AVBP (○), *Magri*/κ_1 (⋆) and *Non-Compact* solution corrected with attenuation (⋯⋯)

original nozzle length, noted c_0 and L_n respectively such that:

$$He = f\frac{L_n}{c_0} \tag{5.5}$$

5.2.3. *Composition transfer functions*

Figure 11 shows the composition-to-acoustic reflection R^-, composition-to-acoustic transmission T^+, T^- and composition-to-entropy transmission T^s transfer functions with their frequency dependence. Results from the simulation are compared to the *Compact* and *Non-Compact* analytical solutions and to the results from (Magri 2017) termed *Magri*. Note that the *Magri* results are first multiplied by a factor 2 in order to be consistent with the acoustic transfer function defined in section 3.4, before being divided by a factor $\kappa_1 = 60$ in order to yield the approximate order of magnitude of the AVBP simulation results. For the acoustic transfer functions, the predictions from the analytical and numerical solutions converge at low frequencies, which is in agreement with theory (Duran & Moreau 2013). *Non-Compact* and AVBP reflection transfer function predictions R^- match well over the whole frequency range. On the contrary, a drastic and increasing gap in modulus is observed for T^+, T^-

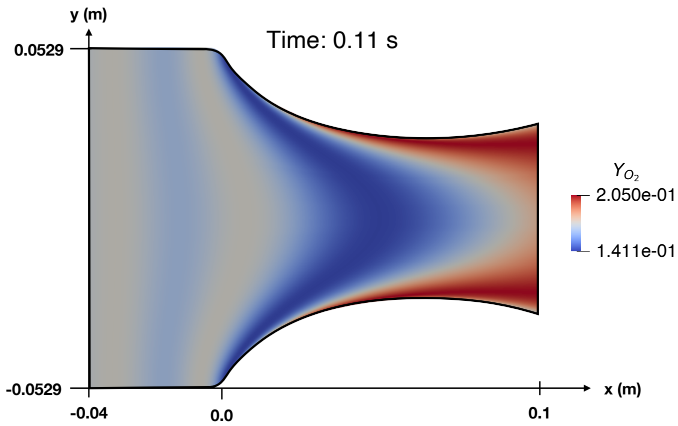

Figure 12: Instantaneous of the composition fluctuation of the mass fraction species Y_{O_2} field within the nozzle

and T^s between *Non-Compact* and AVBP results over the considered discrete perturbation frequencies. Indeed, it needs to be underlined that strong distortion of composition waves fronts occurs when propagating downstream through the nozzle as presented in figure 12, which have been not taken into account in the *Non-Compact* analytical solution.

The impact of wave distortion has been extensively investigated in the literature (Morgans *et al.* 2013; Leyko *et al.* 2014; Livebardon *et al.* 2016; Bauerheim *et al.* 2016; Giusti *et al.* 2017; Fattahi *et al.* 2017; Emmanuelli *et al.* 2020) for entropy wave, i.e. temperature fluctuation. When an entropy wave propagates though a non-uniform velocity field, its front becomes distorted during the propagation. As a consequence, when the entropy wave is cross-sectional averaged to be comparable with one-dimensional solutions, there is an overall decay in the amplitude of the entropy wave resulting in lower acoustic transfer function predictions. Similar phenomenon is impacting the composition waves as they propagate through the nozzle at the convection speed $\bar{u}$ as observed in figure 12 for the fluctuation of the species mass fractions of dioxygen noted Y'_{O_2}. In addition, the acoustic wave fronts w^+ are also distorted at the nozzle outlet $x = 0.1$ m as presented in figure 13: when the flow becomes supersonic in the nozzle divergent, high transverse velocities are observed. The convective speed of the acoustic wave given by $\bar{u} + \bar{c}$ is not the same along the cross-section. As a result, the cross-averaging operation further impacts the acoustic wave w^+, which in turn further influences the overall transmission transfer functions T^+. As a direct consequence, the transmission transfer function T^+ is impacted by both the distortion of the entropy and acoustic waves fronts.
The composition-to-composition transfer function $T^z = w_1^z/w_0^z$ between the nozzle inlet and outlet positions is computed and presented in figure 14. The composition wave is increasingly attenuated with frequency while propagating through the nozzle, as it has been observed through turbine rows for entropy wave by Livebardon *et al.* (2016); Bauerheim *et al.* (2016). Thereafter, the attenuation function T^z computed from the simulation is used to correct the one-dimensional analytical *Non-Compact* solution. It can be mentioned that 2D-axisymmetric models accounting for wave distortion exist (Emmanuelli *et al.* 2020; Yeddula *et al.* 2022) but require an extra computational cost. Correcting the *Non-Compact* transfer functions predicted with the attenuation from the simulation (figure 14) allows to better catch the frequency dependence as presented in figure 11. It also confirms that two-dimensional effects are indeed responsible for the observed discrepancies.

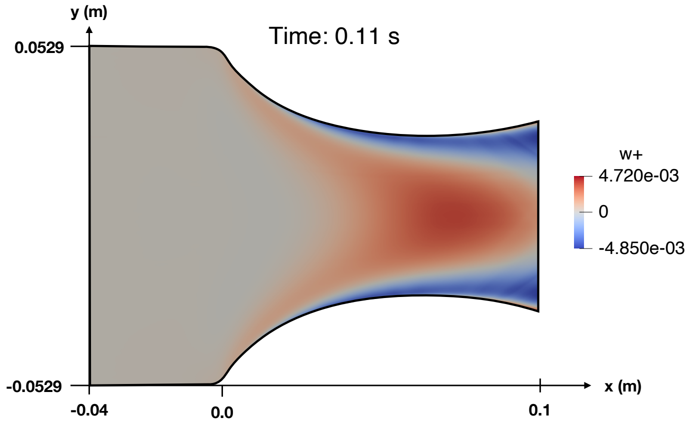

Figure 13: Instantaneous of the acoustic wave w^+ within the nozzle

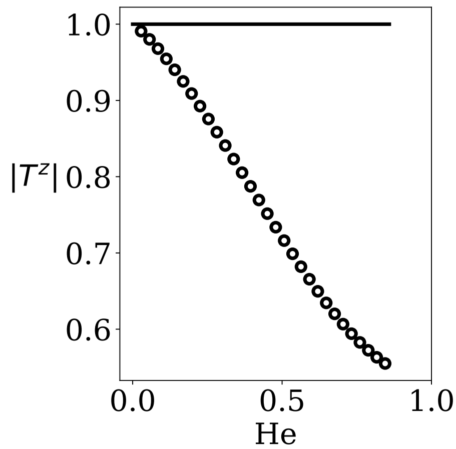

Figure 14: Attenuation transfer function of composition wave. *Non-Compact* (——), AVBP (○)

Compared to the results of Magri (2017), the acoustic transfer function results computed from the simulation are at least $\kappa_1 = 60$ times lower. This overestimation factor can be explained by two reasons. First the linearized and integrated Gibb's energy equation (B 10) of the model of the literature is missing two terms compared to equation (B 20) as further detailed in appendix B. The gap between the two models can be approximately quantified by comparing the different weighting factors of the composition fluctuations $\hat{Z}$ in these two equations (B 20) and (B 10). This already yields a factor $\kappa_2 = 13$, which significantly accentuates the impact of mixture-fraction space fluctuations $\hat{Z}$ on acoustic noise predictions. Furthermore, as emphasized in section 3, the decomposition wave vector in Magri (2017) is not a basis of independent variables since its entropy fluctuation $\hat{s}$ can be generated by composition fluctuations $\hat{Y}_i$. Consequently, the composition-to-acoustic transfer functions in Magri (2017) do not account for the overall influence of composition fluctuations since the entropy fluctuation $\hat{s}$ is forced to 0 when pulsing composition waves $\hat{Z}$. In this case, not accounting for the associated entropy wave caused by composition fluctuations finally leads to overestimate composition noise by the above approximate factor κ_1.

In addition, the composition transfer functions are also evaluated with high-fidelity simu-

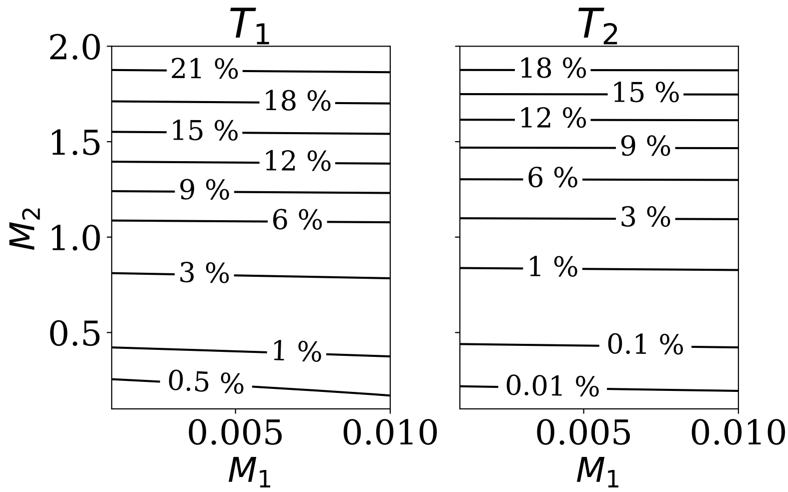

Figure 15: Ratio of T_1 (left) and T_2 (right) for lean combustion: $\phi_{ref} = 0.25$

lation in the particular case for which the species mixture flows respect the condition (C 1), as detailed in appendix C. Overall, the model is again validated whereas the results of Magri (2017) needs to be corrected by a factor $\kappa_3 \sim 73$ to get in the range of the high-fidelity simulation results.

6. Parametric study

6.1. *Comparison of acoustic generation mechanism in compact nozzles*

The different mechanisms generating acoustic are compared in the following for different compact nozzles imposing inlet M_1 and outlet M_2 Mach numbers, respectively. Two ratios are about to be computed: the ratio of composition-to-acoustic transmission transfer function to the entropy-to-acoustic transmission transfer function noted T_1 and the ratio of composition-to-acoustic transmission transfer function to the acoustic-to-acoustic transmission transfer function noted T_2. To do this comparison, a burnt gas composition of reference needs to be taken. It can be obtained using chemical equilibrium (CANTERA) from a mixture of AIR/$KERO\_LUCHE$ at $T_0 = 300$ and $P_0 = 10$ bars at two different equivalence ratio: $\phi_1 = 0.25$ and $\phi_2 = 2.1$.

The ratio T_1 and T_2 are plotted in figure 15 for a mean equivalence ratio $\phi_{ref} = 0.25$ and various inlet and outlet Mach numbers (M_1, M_2). The ratios of transfer function T_1 and T_2 seem to be independent of the inlet Mach number. It reaches up to 21% for high outlet Mach numbers M_2 and remains lower than a maximum of 6% in subsonic flows $M_2 < 1$ for both ratios.

The ratio T_1 and T_2 are given in figure 16 for a mean equivalence ratio $\phi_{ref} = 2.1$ and various inlet and outlet Mach numbers (M_1, M_2). These ratios also seem to be independent of the inlet Mach number M_1. T_1 reaches 5% for low M_2 up to 0.5% for high M_2. On the contrary, T_2 is almost zero for low M_2 and very high M_2 and reaches a maximum of 1.9% for $M_2 = 1$.

Although the different ratios can reach up to 21%, it only compares the acoustic generation potential from composition wave to the acoustic generation potential from entropy or acoustic waves. In other words, it does not imply that composition noise can reach up 21% of entropy noise since the levels of entropy, acoustic and composition fluctuations can be whatever downstream of a combustion chamber. As a consequence, the estimation of the entropy, acoustic and composition fluctuations generated downstream of a combustion

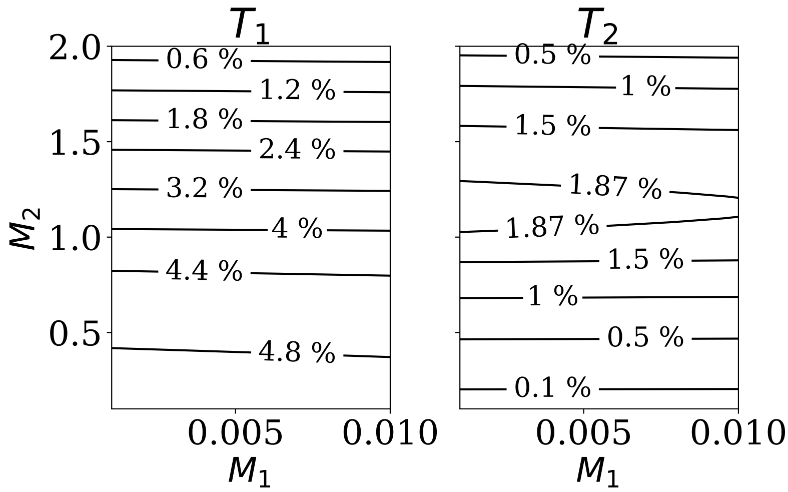

Figure 16: Ratio T_1 (left) and T_2 (right) for rich combustion: $\phi_{ref} = 2.1$

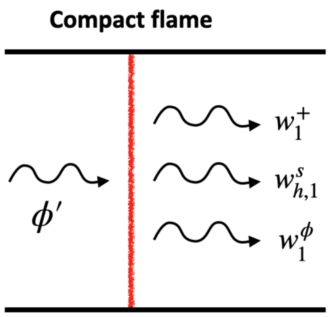

Figure 17: Compact one-dimensional flame modelling

chamber is necessary to do receivable noise comparison and interpretations. Thereafter, these fluctuations are about to be estimated in an ideal case consisting of a compact flame as presented in section 2 and further detailed here.

6.2. *Compact flame unilaterally coupled to a compact nozzle*

Considering the configuration sketched in figure 17: premixed fresh gases are on the left of the compact flame and burnt gases on the right of the compact flame front. By injecting the fresh mixture gas at the laminar flame speed s_L for different mixture characterized by an equivalence ratio ϕ, the flame is axially stabilized to an arbitrary location noted x_1. If fluctuation of equivalence ratio are pulsed upstream of the flame (i.e. ϕ'), then fluctuations of composition, acoustic and entropy are generated downstream of the flame front, i.e. composition, acoustic and entropy waves noted $w_1^+, w_{h,1}^s, w_1^\phi$.

The objectives here are two-fold: estimate the composition, acoustic and entropy waves generated by fluctuation of equivalence ratio in the compact flame and estimate the total transmitted noise and its breakdown when coupling unilaterally the mean flow and perturbations downstream of the compact flame to a compact nozzle.

To do so, different 1D-flames are computed using CANTERA from a mixture of AIR/$KERO\_LUCHE$ at $T_0 = 300$ and $P_0 = 10$ bars with different equivalence ratio from $\bar{\phi} = 0.2$ to $\bar{\phi} = 2.5$. The different burnt gas composition downstream of the flame $Y_{k,1}$, the adiabatic temperature T_1 and the velocity of the burnt gas u_1 can be obtained from the calculation results. Furthermore, for each equivalence ratio ϕ, the Mach number M_1 can be

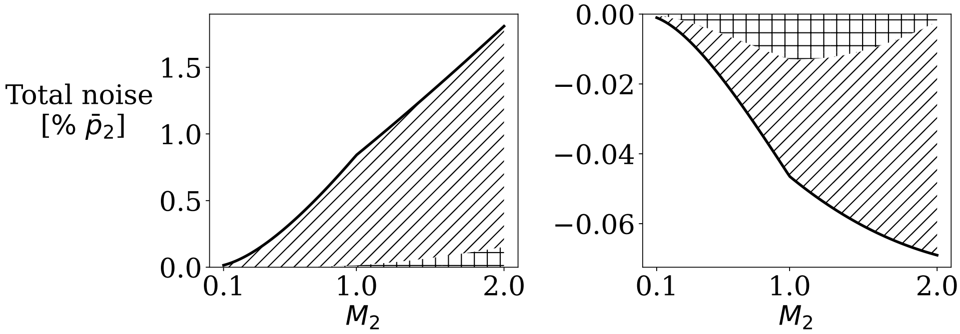

Figure 18: Total acoustic breakdown generated at the nozzle outlet for fixed inlet Mach number and two lean equivalence ratio $\phi = 0.25$ (left) and rich equivalence ratio $\phi = 2.1$ (right) in percentage of the outlet static pressure $\bar{p}_2$ for various outlet Mach numbers M_2. Entropy contribution (/), Composition contribution (+), Acoustic contribution (\) and total noise (——)

computed such that: $M_1 = u_1/\sqrt{\gamma_1 r_1 T_1}$.
In the absence of incoming waves, the acoustic wave w_1^- is zero as assumed also in the model proposed by Leyko *et al.* (2009). The outgoing entropy, composition and acoustics waves are obtained according to the wave definitions given in equation (3.35) and knowing that the combustion is performed at constant pressure, i.e $p' = 0$:

$$w_{1,h}^s = \frac{1}{T}\frac{\mathrm{dT}}{\mathrm{d}\phi}\phi', \tag{6.1a}$$

$$w_1^+ = \frac{1}{c_1}\frac{\mathrm{du}_1}{\mathrm{d}\phi}\phi', \tag{6.1b}$$

$$w_1^\phi = \phi' \tag{6.1c}$$

Then, the compact transfer functions described in section 3.4.1 are used to predict the noise generation due to these incident waves. Even if the nozzle inlet Mach number M_1 is fixed depending on $\bar{\phi}$, different nozzle regimes can be investigated by varying the outlet Mach numbers from subsonic to supersonic condition. Consequently, the overall noise can be computed downstream, compared and attributed to the different mechanism responsible for noise generation: direct or indirect. Thereafter, the scope of variable parameters are chosen to the followings: the equivalence ratio of reference ϕ_{ref} is varied from 0.2 to 2.5 and the outlet Mach number M_2 is varied from 0.1 to 2.0.

Concerning the level of equivalence ratio fluctuation downstream of the burnt gas, the order of magnitude is chosen to $\phi' = 0.01$ according to what was identified by Shao *et al.* (2020) in an unsteady 3D combustion Large-Eddy-Simulation of a rich-quench-lean combustion chamber.

6.2.1. $\phi_{ref} = (0.25, 2.1)$, $\phi' = 0.01$ *and various* M_2

The total noise and its different contributions are plotted in figure 18 against the outlet Mach number M_2 which varies from 0.1 to 2.0. According to figure 18 (left) and for a lean equivalence ratio, composition noise can reach up to 9.3% of the entropy noise contribution in the best case when $M_2 = 2.0$. Furthermore, it is observed that the fluctuation of equivalence ratio $\phi' = 0.01$ can lead to noise fluctuation of the order of 1.8% of the isentropic static pressure p_2 at the nozzle outlet.
On the contrary, according to figure 18 (right) and for a rich equivalence ratio, composition

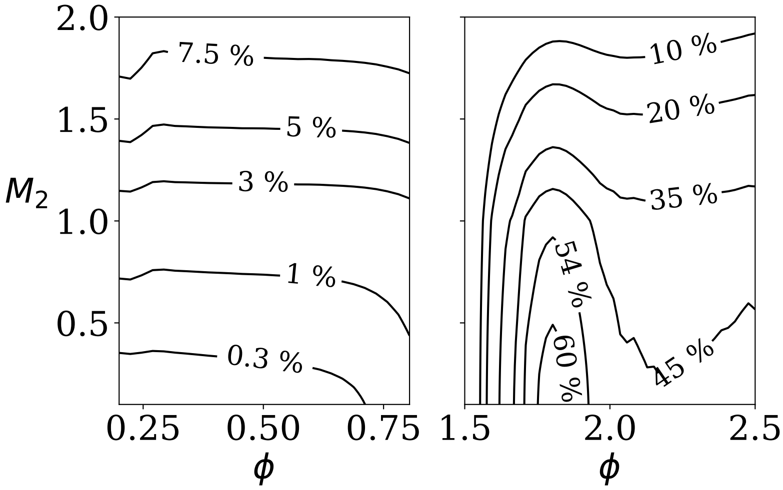

Figure 19: Ratio of composition noise to entropy noise for various outlet Mach numbers M_2 and various equivalence ratio ϕ

noise contribution is comparable in terms of amplitude to the entropy noise contribution. Nevertheless, the total noise is quite low reaching a maximum of 0.06% of p_2.

6.2.2. $\phi' = 0.01$ *and various* (ϕ, M_2)

According to figure 19 (left) and for lean equivalence ratio $\phi < 0.8$, composition noise can reach a maximum of 10% of the entropy noise when the nozzle is choked whereas it is lower than 3% for subsonic nozzle. For high equivalence ratio $\phi > 1.5$, as presented in figure 19 (right), composition noise reaches up to 62% of the entropy noise, meaning that entropy and composition noise have almost the same noise contributions although the overall noise is quite low according to figure 18.

7. Conclusions and discussion

A model to assess composition noise as part of indirect combustion noise mechanism is proposed. It is based on the decomposition of the linearized specific entropy into contributions related to the specific entropy fluctuations of each pure species given by $\hat{s}_n$ and to the species mass fractions fluctuations through the mixture fraction space fluctuation $\hat{Z}$. Contrarily to previous models (Magri *et al.* 2016; Magri 2017), this provides an independent set of variables that describes an ideal, non-reacting gas mixture, and unambiguously separates temperature and mixture composition contributions. As a result, the linearized Gibbs' energy equation is also simplified. Moreover, when considering quasi one-dimensional flow in nozzles, the resulting linearized Euler equations yield a system of equations similar to previous models ignoring the gas mixture composition (Duran & Moreau 2013) and show a new one-way coupling between composition waves and both acoustic and entropy waves. Two solutions of the resulting system of equations are investigated: on the one hand, a compact solution is deduced; on the other hand, a non-compact formulation is proposed following the methodology based on the Magnus expansion. The latter is used to predict composition transfer functions.

Consequently, composition noise is found to be generated by the acceleration/deceleration of fluctuations of species mass fractions fluctuations Y_k' and can be linked to a single equation like the mixture fraction space fluctuations Z' or the equivalence ratio fluctuation ϕ'. Furthermore, a new entropy wave definition $\hat{s}_n$ is introduced in order to be independent of the composition fluctuations and corresponds to the former definition of the entropy wave when assuming homogeneous composition mixture flows. Entropy noise is caused by the acceleration/deceleration of the entropy wave defined in equation (3.35) (excess density), as previously found by Lapeyre (2015).

This new model has been validated by comparing analytical predictions with direct numerical simulations of nozzle inviscid flows (Euler's equations) considering an air-kerosene mixture in a choked and subsonic nozzle flows Goh & Morgans (2011), in which composition fluctuations have been pulsed. In order to properly handle boundary conditions when the flow is multi-species, the Navier Stokes Characteristics Boundary Conditions (Poinsot & Lele 1992; Daviller *et al.* 2019) have been extended to account for the properly defined entropy wave $\hat{s}_n$. In order to inject properly composition fluctuations into the simulations, a new non-reflecting boundary condition has been developed. In addition, two-dimensional flow effects are also evidenced in both nozzle test cases, distorting the composition wave front. In Goh's choked nozzle, they are caused by shocklets at the nozzle throat; in Magri's nozzle, by the strong cross-section variation as previously found by Emmanuelli *et al.* (2020). Note that the model has been validated for two different types of species mixture flow where $\hat{\gamma} \neq 0$ (core of the text) and $\hat{\gamma} = 0$ (in appendix C).

Finally, a parametric study based on an air-kerosene mixture stresses two important features of the indirect combustion noise mechanism in the framework of an ideal one-dimensional flame front unilaterally coupled to a compact nozzle. First, for lean combustion, composition noise can reach a maximum of 10% of the entropy noise when the nozzle flow is choked and decreases below 3% for subsonic nozzle flow. On the contrary, for a rich combustion, composition noise and entropy noise reaches almost similar levels. This explains why Lapeyre (2015); Livebardon (2015); Livebardon *et al.* (2016); Férand *et al.* (2019); Rahmani *et al.* (2022) found entropy noise is the dominant indirect combustion noise mechanism.

Acknowledgments

This project has received funding from the Clean Sky 2 Joint Undertaking (JU) under grant agreement No. 886554. The JU receives support from the European Union's Horizon 2020 research and innovation programme and the Clean Sky 2 JU members other than the Union. This work was granted access to the HPC resources of IDRIS under the allocation 2022-[A0112B10157] made by GENCI. The authors would also like to thank Luca Magri and Michael Bauerheim for insightful exchanges on compositional noise.

Declaration of Interests

The authors report no conflict of interest.

Appendix A. Specific entropy of a mixture of ideal gases and linearization

A.1. *Specific entropy of an ideal gas: s_i*

Differentiating the specific entropy of a pure species $s_i(T,P)$ yields:

$$\mathrm{d}s_i = \left(\frac{\partial s_i}{\partial T}\right)_p \mathrm{d}T + \left(\frac{\partial s_i}{\partial p}\right)_T \mathrm{d}p \tag{A 1}$$

Since a perfect gas is considered,

$$\left(\frac{\partial s_i}{\partial T}\right)_p = \frac{C_{p,i}}{T}, \quad \left(\frac{\partial s_i}{\partial p}\right)_T = -\frac{r_i}{p} \tag{A 2}$$

Integrating ds_i from a reference state (T°, p°), gives:

$$s_i = C_{p,i} \log\left(\frac{T}{T^\circ}\right) - r_i \log\left(\frac{p}{p^\circ}\right) \tag{A 3}$$

A.2. *Specific entropy of a mixture of ideal gases: s*

When considering a mixture of ideal gases, the specific entropy of the mixture is given by equation (3.9). Introducing equation (A 3) in equation (3.9) yields:

$$s = C_p \log\left(\frac{T}{T^\circ}\right) - r \log\left(\frac{p}{p^\circ}\right) - \sum_{i=1}^{N} r_i \log\left(X_i\right) Y_i \tag{A 4}$$

Replacing the expression of T using the perfect gas equation (3.2), the specific entropy can be reformulated as follows:

$$s = s^\circ + C_v \log\left(\frac{p}{\rho^\gamma}\right) - \sum_{i=1}^{N} r_i \log\left(X_i\right) Y_i \tag{A 5}$$

where $s^\circ = -C_v \log\left(\dfrac{p^\circ}{\rho^{\circ\gamma}}\right)$

A.3. *Linearization of s*

Linearizing equation (A 5) using variables given in equations (3.19) yields:

$$\hat{s} = \hat{s}^\circ - \left(\hat{r} - \hat{C}_p\right)\frac{\bar{\gamma}-1}{\bar{\gamma}}\log(\bar{p}) + (1-\bar{\gamma})\hat{p} + \hat{r} + \hat{T} - \frac{1}{\bar{C}_p}\sum_{i=1}^{N} r_i \log\left(\bar{X}_i\right)\hat{Y}_i \tag{A 6}$$

where $\hat{s}^\circ = -\hat{C}_p \log\left(T^\circ\right) + \dfrac{\bar{\gamma}-1}{\bar{\gamma}}\hat{r}\log\left(p^\circ\right)$

Using equations (3.18) of the mean flow leads to:

$$d\left[\frac{\bar{\gamma}-1}{\bar{\gamma}}\log(\bar{p})\right] = -d\left[\log\left(2 + (\bar{\gamma}-1)\bar{M}^2\right)\right] \tag{A 7}$$

$$\hat{s} = \hat{s}^\circ + \left(\hat{r} - \hat{C}_p\right)\log\left(2 + (\bar{\gamma}-1)\bar{M}^2\right) + (1-\bar{\gamma})\hat{p} + \hat{r} + \hat{T} - \frac{1}{\bar{C}_p}\sum_{i=1}^{N} r_i \log\left(\bar{X}_i\right)\hat{Y}_i + Q^\circ\left(\hat{r} - \hat{C}_p\right) \tag{A 8}$$

where Q° is an integration constant.

Appendix B. Comparison with the model of the literature

Developing the specific enthalpy h_i of each species i^{th} in equation (3.14) yields:

$$\mathrm{d}h = C_p\,\mathrm{d}T + \left(T - T^\circ\right)\,\mathrm{d}C_p + \sum_{i=1}^{N} \Delta h^\circ_{f,i}\mathrm{d}Y_i \tag{B 1}$$

Introducing the mixture fraction Z, $\mathrm{d}Y_i = (\mathrm{d}Y_i/\mathrm{d}Z)\,\mathrm{d}Z$ and $\mathrm{d}C_p = (\mathrm{d}C_p/\mathrm{d}Z)\,\mathrm{d}Z$ in equation (3.3) and dividing it by C_pT provide the following expression for Gibbs' differential equation:

$$\frac{\mathrm{d}s}{C_p} = \frac{\mathrm{d}T}{T} - \left(\frac{\gamma-1}{\gamma}\right)\frac{\mathrm{d}p}{p} + \left[\frac{T-T^\circ}{C_pT}\frac{\mathrm{d}C_p}{\mathrm{d}Z} - \frac{1}{C_pT}\sum_{i=1}^{N}\left(\frac{\mu_k}{W_k} - \Delta h^\circ_{f,k}\right)\frac{\mathrm{d}Y_k}{\mathrm{d}Z}\right]\mathrm{d}Z \tag{B 2}$$

where the perfect gas law equation (3.21) has been used in conjunction with $r = C_p\,(\gamma-1)/\gamma$. Introducing the chemical potential function gives:

$$\psi = \frac{1}{C_pT}\sum_{i=1}^{N}\frac{\mu_k}{W_k}\frac{\mathrm{d}Y_k}{\mathrm{d}Z} \tag{B 3}$$

$$\frac{\mathrm{d}s}{C_p} = \frac{\mathrm{d}T}{T} - (\gamma-1)\frac{\mathrm{d}p}{\gamma p} + \left[\frac{T-T^\circ}{C_pT}\frac{\mathrm{d}C_p}{\mathrm{d}Z} - \psi\right]\mathrm{d}Z. \tag{B 4}$$

This corresponds to equation (2.1c) in Magri *et al.* (2016) and equation (14) in Rahmani *et al.* (2022) when considering $T^\circ = 0$ K and provided sensible variables are used instead of the present specific ones. If, in this Gibbs' differential energy equation (B 4), pressure and density are used instead of pressure and temperature, the following expression is obtained:

$$\frac{\mathrm{d}s}{C_p} = \frac{\mathrm{d}p}{\gamma p} - \frac{\mathrm{d}\rho}{\rho} - \frac{\mathrm{d}\gamma}{\gamma(\gamma-1)} - \frac{T^\circ}{T}\frac{\mathrm{d}C_p}{C_p} - \psi\,\mathrm{d}Z \tag{B 5}$$

Since γ and C_p are only mixture-dependent, their variations $\mathrm{d}\gamma$ and $\mathrm{d}C_p$ can be linked to the mixture fraction space elemental variation dZ as:

$$\frac{\mathrm{d}\gamma}{\gamma(\gamma-1)} = \frac{\mathrm{d}\log\gamma}{(\gamma-1)} = \frac{1}{(\gamma-1)}\left(\sum_{i=1}^{N}\frac{\mathrm{d}\log(\gamma)}{\mathrm{d}Y_i}\frac{\mathrm{d}Y_i}{\mathrm{d}Z}\right)\mathrm{d}Z \tag{B 6}$$

$$\frac{\mathrm{d}C_p}{C_p} = \mathrm{d}\log(C_p) = \left(\sum_{i=1}^{N}\frac{\mathrm{d}\log(C_p)}{\mathrm{d}Y_i}\frac{\mathrm{d}Y_i}{\mathrm{d}Z}\right)\mathrm{d}Z \tag{B 7}$$

Introducing equations (B 6) and (B 7) in equation (B 5), the differential equation (2.7) in Magri (2017) can be obtained:

$$\frac{\mathrm{d}s}{C_p} = \frac{\mathrm{d}p}{\gamma p} - \frac{\mathrm{d}\rho}{\rho} - (\psi + \aleph)\,\mathrm{d}Z \tag{B 8}$$

with the heat-capacity factor $\aleph$:

$$\aleph = \sum_{i=1}^{N}\left(\frac{1}{(\gamma-1)}\frac{\mathrm{d}\log(\gamma)}{\mathrm{d}Y_i} + \frac{T^\circ}{T}\frac{\mathrm{d}\log(C_p)}{\mathrm{d}Y_i}\right)\frac{\mathrm{d}Y_i}{\mathrm{d}Z} \tag{B 9}$$

According to Magri (2017), linearizing and integrating equation (B 8), the dimensionless density fluctuation $\hat{\rho}$ is linked to the other fluctuations as the mixture fraction space fluctuation $\hat{Z} = Z'$:

$$\hat{\rho} = \hat{p} - \hat{s} - \left(\bar{\psi} + \bar{\aleph} + \bar{\phi}\right)\hat{Z} \tag{B 10}$$

where $\bar{\phi}$ is defined as:

$$\bar{\phi} = \frac{\mathrm{d}\log(\bar{\gamma})}{\mathrm{d}Z}\log\left(\bar{p}^{1/\bar{\gamma}}\right) \tag{B 11}$$

As shown in section 3.2, γ is mixture-dependent only and constant. Therefore, $\bar{\phi} = 0$.

By injecting the expression of $\hat{\rho}$ (equation (B 10)) in the system of equation (3.22) leads to a system recast into an invariant formulation (Magri 2017) as follows:

$$2\pi \mathrm{i} He \boldsymbol{B}(\eta)\boldsymbol{J} = \frac{\mathrm{d}\boldsymbol{J}}{\mathrm{d}\eta} \tag{B 12}$$

where He is the Helmholtz number, η is the dimensionless position such that $\eta = x/L_n$, $\boldsymbol{B}(\eta)$ is a 4x4 matrix and $\boldsymbol{J}$ is the fluctuation invariant vector, which can be linked to the wave vector noted $\boldsymbol{V}$ using a 4×4 passage matrix noted $\boldsymbol{D}$ such that: $\boldsymbol{J} = \boldsymbol{DV}$. According to the note of caution in (Magri 2017), the strengths $\bar{\psi}$ and $\bar{\aleph}$ are corrected such that there are mixture-dependent and temperature-independent. Since the mean mixture fraction space $\bar{Z}$ and the mixture fraction space fluctuations $\hat{Z}$ are conserved along the nozzle, the strengths $\bar{\psi}$ and $\bar{\aleph}$ are thus constant and are given by $\bar{\psi} = -8.4$ and $\bar{\aleph} = -1.1$. Considering that $|\bar{\psi}| >> |\bar{\aleph}|$, which is true at first order, the terms $\bar{\aleph}\hat{Z}$ are dropped within the system of equations (B 12). Consequently, the solution of the system of equation (B 12) reduces to the solution of Duran & Moreau (2013) by simply replacing the entropy invariant noted $\hat{\mathcal{I}}_s$ by:

$$\hat{\mathcal{I}}_s = \hat{s} + \bar{\psi}\hat{Z} \tag{B 13}$$

Thus, the mixture-fraction space fluctuation $\hat{Z}$ produces noise through the same mechanism as the entropy fluctuation $\hat{s}$.

Yet, when linearizing equation (B 8) using equations (3.19) yields:

$$\mathrm{d}\left(\hat{s} - \hat{p} + \hat{\rho}\right) = -\left(\bar{\psi} + \bar{\aleph}\right)\mathrm{d}\hat{Z} - \frac{\hat{\gamma}}{\bar{\gamma}}\frac{\mathrm{d}\bar{p}}{\bar{\gamma}\bar{p}} \tag{B 14}$$

In general, the coefficients $\left(\bar{\Psi} + \bar{\aleph}\right)$ are actually not constant and vary along the nozzle. They are functions of temperature and pressure and can be recast as follows:

$$\left(\bar{\psi} + \bar{\aleph}\right)\hat{Z} = -\sum_{i=1}^{N} \frac{s_i^\circ}{\bar{C}_p}\frac{\mathrm{d}Y_i}{\mathrm{d}Z}\hat{Z} + \frac{1}{\bar{C}_p}\sum_{i=1}^{N} r_i \log\left(\bar{X}_i\right)\frac{\mathrm{d}Y_i}{\mathrm{d}Z}\hat{Z} + \frac{\bar{\gamma}-1}{\bar{\gamma}}\hat{r}\log\left(\frac{\bar{p}}{p^\circ}\right) + \frac{\hat{\gamma}}{\bar{\gamma}(\bar{\gamma}-1)} \tag{B 15}$$

where $s_i^\circ(T^\circ)$ corresponds to the specific entropy of the i-th species at the reference temperature T°. Differentiating equation (B 15) gives:

$$\left(\bar{\psi} + \bar{\aleph}\right)\mathrm{d}\hat{Z} = \mathrm{d}\left[\left(\bar{\psi} + \bar{\aleph}\right)\hat{Z}\right] - \left[\frac{\bar{\gamma}-1}{\bar{\gamma}}\hat{r}\mathrm{d}\log\left(\bar{p}\right)\right] \tag{B 16}$$

Introducing equation (B 16) in equation (B 14) and integrating it from a reference state (p°, T°) to (p, T) yields:

$$\hat{s} = \hat{p} - \hat{\rho} - \left(\bar{\psi} + \bar{\aleph}\right)\hat{Z} + \frac{\bar{\gamma}-1}{\bar{\gamma}}\hat{r}\int_{(T^\circ,p^\circ)}^{(T,p)} \mathrm{d}\log\left(\bar{\mathrm{p}}\right) - \frac{\hat{\gamma}}{\bar{\gamma}}\frac{1}{\bar{\gamma}}\int_{(\mathrm{T}^\circ,\mathrm{p}^\circ)}^{(\mathrm{T},\mathrm{p})} \mathrm{d}\log\bar{\mathrm{p}} + \mathrm{K}_0 \tag{B 17}$$

where K_0 is an integration constant. Then, it simplifies as follows:

$$\hat{s} = \hat{p} - \hat{\rho} - \left(\bar{\psi} + \bar{\aleph}\right)\hat{Z} + \frac{\bar{\gamma}-1}{\bar{\gamma}}\hat{C}_p\log\left(\frac{\bar{p}}{p^\circ}\right) + K_0 \tag{B 18}$$

To obtain the value of K_0, the fluctuation of $\hat{s}$ is expressed similarly to equation (A 6) by replacing the value of equation (B 15) in equation (B 18):

$$K_0 = \frac{\hat{\gamma}}{\bar{\gamma}(\bar{\gamma}-1)} + \frac{\bar{\gamma}-1}{\bar{\gamma}}\hat{C}_p\log(p^\circ) \tag{B 19}$$

Note that $\mathrm{dK}_0 = 0$ and that $s_i^\circ = -\bar{C}_{p,i}\log\left(T^\circ\right)$.

Finally, using equation (B 19) to replace the value of K_0 in equation (B 18) gives:

$$\hat{s} = \underbrace{\hat{p} - \hat{\rho} - \left(\bar{\psi} + \bar{\aleph}\right) \hat{Z}}_{(1)} + \underbrace{\frac{\bar{\gamma}-1}{\bar{\gamma}} \hat{C}_p \log\left(\bar{p}\right) + \frac{\hat{\gamma}}{\bar{\gamma}(\bar{\gamma}-1)}}_{(2)} \tag{B 20}$$

Equation (B 20) can be rearranged as:

$$\hat{s} = \hat{p} - \hat{\rho} + K_Y \hat{Z} \tag{B 21}$$

where

$$K_Y = -\chi \log\left(T^{\circ}\right) + \frac{\bar{\gamma}-1}{\bar{\gamma}} \Lambda \log\left(p^{\circ}\right) - \frac{\bar{\gamma}-1}{\bar{\gamma}} (\Lambda - \chi) \log(\bar{p}) \tag{B 22}$$

$$-\frac{1}{\bar{C}_p} \sum_{i=1}^{N} r_i \log\left(\bar{X}_i\right) \frac{\mathrm{dY_i}}{\mathrm{dZ}} \tag{B 23}$$

When comparing equations (B 10) and (B 21), the weighting of the mixture fraction space fluctuation appears different. The model in (Magri (2017)) yields $K_M = -\Psi - \aleph = -9.5$ meanwhile the present model gives $K_Y = -0.73$ using the diffusion flame structure given in figure 8.

In (Magri (2017)), equation (B 10) is used to replace the fluctuation of density $\hat{\rho}$ in the linearized system of equation (3.22). Since the weighting of the composition fluctuation is overestimated by a factor $\kappa_2 = K_M/K_Y \approx 13$, the acoustic predictions due to composition fluctuations can also be expected to be overestimated by a factor 13. Furthermore, in (Magri (2017)), the composition-to-acoustic transfer functions are evaluated when imposing an incident unitary composition fluctuation $\hat{Z} = 1$ and no other fluctuations: $\hat{p} = \hat{u} = \hat{T} = \hat{s} = 0$. According to both equations (B 10) and (B 21), when imposing such fluctuation fields, the entropy fluctuation $\hat{s}$ is equal to either $K_M + \Lambda$ or $K_Y + \Lambda$ respectively. As a consequence, the composition-to-acoustic transfer functions of the literature are not accounting for the overall impact of composition fluctuations. It explains why a greater overestimation factor $\kappa_1 = 60$ is found as least between the simulation results and the results of the literature as shown in figure 11.

Appendix C. Simplified model

C.1. *Theoretical model*

When γ is constant ($\hat{\gamma} = 0$ in equation (3.20)), which corresponds to a particular fluid mixture for which

$$\frac{\bar{W}}{W_i} = \frac{\bar{C}_{p,i}}{\bar{C}_p} = \frac{r_i}{\bar{r}} \tag{C 1}$$

equation (3.24) becomes:

$$\left[\frac{\partial}{\partial t} + \bar{u}\frac{\partial}{\partial x}\right] \sum_{i=1}^{N} \frac{\bar{C}_{p,i}}{\bar{C}_p} \bar{Y}_i \hat{s}_i = 0 \qquad \text{and} \qquad \frac{\partial \bar{s}_i}{\partial x} = 0 \tag{C 2}$$

In the first term (1) of equation (3.23), a new 'entropy' fluctuation termed $\hat{s}_n$ is defined and given by:

$$\hat{s}_n = \sum_{i=1}^{N} \frac{\bar{C}_{p,i}}{\bar{C}_p} \bar{Y}_i \hat{s}_i \tag{C 3}$$

Note that this fluctuation $\hat{s}_n$ is linked to the entropy fluctuations of each species $\hat{s}_i$ that are only varying with temperature and pressure fluctuations. The second term (2) of equation (3.23) only depends on the mixture composition fluctuations $\hat{Y}_i$. As a consequence, this decomposition allows a proper separation of the two possible contributions to indirect combustion noise.
Introducing equations (3.19) into Gibbs' energy equation (3.17) and integrating it yield:

$$\hat{\rho} = \hat{p} - \hat{s}_n - \Lambda \hat{Z} \tag{C 4}$$

Finally, by replacing the fluctuation of $\hat{\rho}$ using equation (C 4) in the linearized equations (3.22*a*) and (3.22*b*), using the linearized entropy equation (C 2) and introducing the mixture fraction space fluctuation conservation equation (3.31*a*), the quasi-one dimensional linearized Euler Equations for non-reacting and multi-species flow can be written as follows:

$$\left[\frac{\partial}{\partial t} + \bar{u}\frac{\partial}{\partial x}\right] \left(\hat{p} - \hat{s}_n - \Lambda \hat{Z}\right) + \bar{u}\frac{\partial \hat{u}}{\partial x} = 0, \tag{C 5a}$$

$$\left[\frac{\partial}{\partial t} + \bar{u}\frac{\partial}{\partial x}\right] \hat{u} + \frac{\bar{c}^2}{\bar{u}}\frac{\partial \hat{p}}{\partial x} = \left[(\bar{\gamma} - 1)\hat{p} + \hat{s}_n + \Lambda \hat{Z} - 2\hat{u}\right] \frac{\mathrm{d}\bar{u}}{\mathrm{d}x}, \tag{C 5b}$$

$$\left[\frac{\partial}{\partial t} + \bar{u}\frac{\partial}{\partial x}\right] \hat{s}_n = 0, \tag{C 5c}$$

$$\left[\frac{\partial}{\partial t} + \bar{u}\frac{\partial}{\partial x}\right] \hat{Z} = 0 \tag{C 5d}$$

As a direct consequence of the remarkable symmetry observed in equations (C 5) and of the conservation of Λ, the dimensionless fluctuations $\hat{s}_n$ and $\Lambda \hat{Z}$ can be summed up to form a new dimensionless fluctuation noted $\hat{\sigma}$ such that:

$$\hat{\sigma} = \hat{s}_n + \Lambda \hat{Z} = (\hat{p} - \hat{\rho} - \Lambda \hat{Z}) + \Lambda \hat{Z} = \hat{p} - \hat{\rho} \tag{C 6}$$

Note that the dimensionless density fluctuation $\hat{\rho}$ undergoes the impact of temperature fluctuations as well as the impact of composition fluctuations. The system of equations (C 5) can be recast into a system of equations similar to equations (3.4-3.6) in Duran & Moreau (2013):

$$\left[\frac{\partial}{\partial t} + \bar{u}\frac{\partial}{\partial x}\right] (\hat{p} - \hat{\sigma}) + \bar{u}\frac{\partial \hat{u}}{\partial x} = 0, \tag{C 7a}$$

$$\left[\frac{\partial}{\partial t} + \bar{u}\frac{\partial}{\partial x}\right] \hat{u} + \frac{\bar{c}^2}{\bar{u}}\frac{\partial \hat{p}}{\partial x} = \left[(\bar{\gamma} - 1)\hat{p} + \hat{\sigma} - 2\hat{u}\right] \frac{\mathrm{d}\bar{u}}{\mathrm{d}x}, \tag{C 7b}$$

$$\left[\frac{\partial}{\partial t} + \bar{u}\frac{\partial}{\partial x}\right] \hat{\sigma} = 0 \tag{C 7c}$$

When the mean velocity is constant (homogeneous flow), i.e. $d\bar{u}/dx = 0$, three decoupled equations called the characteristic equations are obtained for a multi-species flow:

$$\left[\frac{\partial}{\partial t} + (u+c)\frac{\partial}{\partial x}\right] w^+ = 0, \tag{C 8a}$$

$$\left[\frac{\partial}{\partial t} + (u-c)\frac{\partial}{\partial x}\right] w^- = 0, \tag{C 8b}$$

$$\left[\frac{\partial}{\partial t} + u\frac{\partial}{\partial x}\right] w^\sigma = 0 \tag{C 8c}$$

with

$$w^+ = \hat{p} + \bar{M}\hat{u}, \qquad w^- = \hat{p} - \bar{M}\hat{u}, \qquad w^\sigma = \hat{\sigma} \tag{C 9}$$

The variables w^+, w^- and w^σ are called *waves* and propagate at the convection speed: $u+c$, $u-c$, and u respectively. These definitions are consistent with that of Duran & Moreau (2013). When the mean flow velocity is not constant, i.e. $d\bar{u}/dx \neq 0$, the three waves are coupled through the mean flow gradient. Therefore,the entropy wave w^σ can generate acoustic waves through this coupling term dM/dx. As in Duran & Moreau (2013), indirect noise is defined by the noise produced from the acceleration/deceleration of the entropy wave w^σ. Nevertheless, this entropy wave w^σ can be split here into two independent waves: a composition wave, noted w^z and a new defined entropy wave, noted w_h^s such that:

$$w^\sigma = w_h^s + \Lambda w^z \qquad \text{where} \qquad \begin{cases} w_h^s = \hat{s}_n, \\ w^z = \hat{Z} \end{cases} \tag{C 10}$$

Consequently, noise generation mechanism due to composition fluctuations can be simply described by the acceleration/deceleration of composition waves w^z. Finally, according to this decomposition (C 10), the acceleration of an incident entropy wave w_h^s generates as much noise as the acceleration of an incident composition wave w^z to within a scaling factor Λ. Given the similarity of the system of equations (C 5) with that derived by Duran & Moreau (2013) for a homogeneous mixture, the same exact non-compact solution (again termed *Non-compact)* can be obtained using the Magnus expansion.

The entropy invariant term $\hat{\mathcal{I}}_s$ is now linked to the 'excess' density wave $\hat{\sigma}$ as shown in equation (C 6) such that:

$$\hat{\mathcal{I}}_s = \hat{\sigma} = \hat{s}_n + \Lambda\hat{Z} \tag{C 11}$$

Between the two different equations (B 13) and (C 11), two main differences can be noticed: the definition of the dimensionless entropy fluctuation and the weighting of the mixture fraction space fluctuation $\hat{Z}$. As emphasized in section 3, the decomposition wave vector in Magri (2017) is not a basis of independent variables since its entropy fluctuation $\hat{s}$ can be generated by composition fluctuations. Since the composition-to-acoustic transfer functions in Magri (2017) do not take into account the associated entropy wave, the gap between the two models can be quantified by simply comparing the weighting factor of the composition fluctuations $\hat{Z}$ in the two entropy invariant equations (B 13) and (C 11). The ratio of the two weighting term noted κ_3 is given by:

$$\kappa_3 = \frac{|\psi|}{|\Lambda|} \sim \frac{|8.4|}{|0.1154|} \sim 73 \tag{C 12}$$

Consequently, an overestimation by the factor κ_3 can be expected between the acoustic prediction of the model (Magri 2017) and that of the present results obtained with the solution of Duran & Moreau (2013) as presented in figure 21.

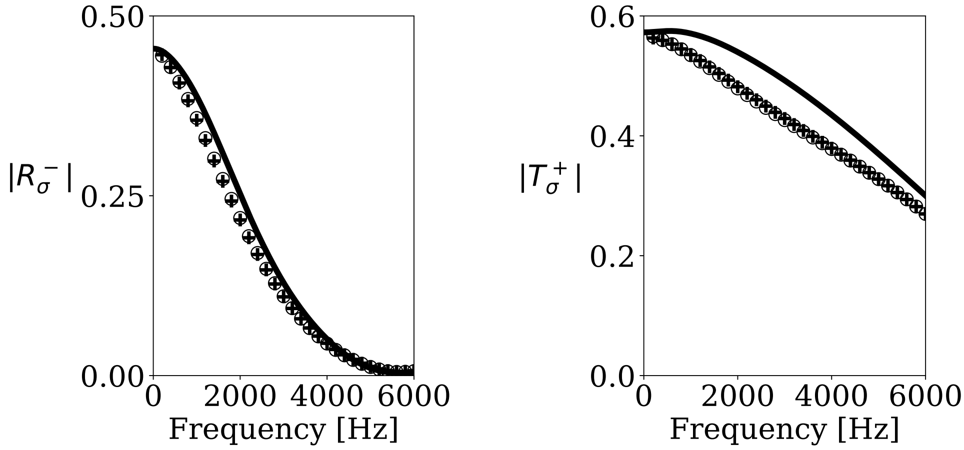

Figure 20: (a) Modulus of the reflection acoustic transfer function (b) Modulus of the transmission acoustic transfer function. *Non-compact* (——) , AVBP-Composition (○), AVBP-Entropy (+)

C.2. *Results*

To numerically investigate the propagation of composition wave w^z and entropy wave w_h^s through the nozzle, incident waves are pulsed in the system of equations (C 7) as in section 4, and transfer functions are determined as the ratio between the nozzle outgoing waves to the incident pulsed waves. Assuming that subscripts 1 and 2 correspond to the inlet and the outlet nozzle positions respectively, the reflection R_σ^- and transmission T_σ^+ transfer functions are defined as follows:

$$R_\sigma^- = \frac{w_1^-}{w_1^\sigma} \qquad \text{and} \qquad T_\sigma^+ = \frac{w_2^+}{w_1^\sigma} \tag{C 13}$$

Note that these definitions of acoustic transfer functions (C 13) allow verifying that composition-to-acoustic and entropy-to-acoustic transfer functions are similar to within a scaling factor Λ. Moreover, to be comparable with equation (C 13), the composition-to-acoustic transfer function results of Magri (2017) must be multiplied by $2/\Lambda$.

C.2.1. *Noise composition from kerosene-air inhomogeneity*

The first test case with the choked nozzle described in section 5.1, is simulated again with composition and temperature fluctuations pulsed separately . The resulting acoustic transfer functions are compared with the *Non-compact* solution of the quasi-one-dimensional linearized Euler equations (Duran & Moreau 2013) in figure 20. Both transfer functions R_σ^- and T_σ^+ are identical for both pulsations confirming the interpretations of section C.1. In both figures 20 (a) and (b), the modulus of the reflection and transmission transfer functions are retrieved by the *Non-compact* solution compared to the AVBP simulation results with a 14% mean relative difference. The remaining difference is most likely explained by the two-dimensional nature of the present choked flow, as already described in section 5.1.

C.2.2. *Noise composition from methane-air inhomogeneity*

The second test case described in section 5.2, is simulated again with superimposed composition waves only. Figure 21 shows the reflection R_σ^- and transmission T_σ^+ composition-to-acoustic transfer functions. The *Non-compact* solution is compared with the results from

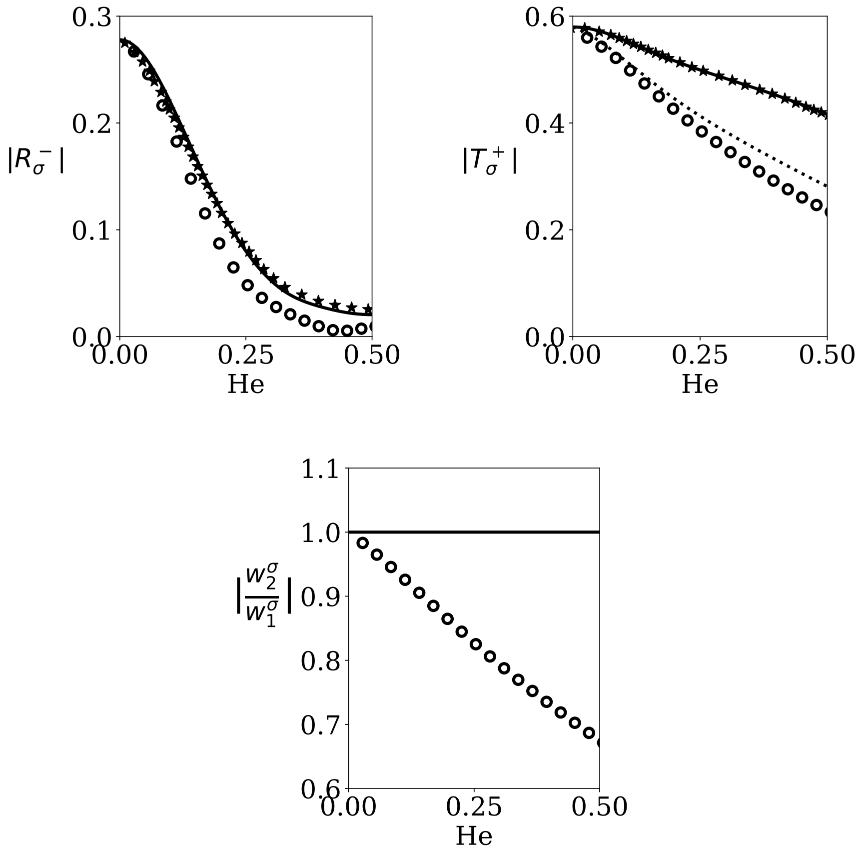

Figure 21: (a) Modulus of the composition-to-acoustic reflection transfer function (b) Modulus of the composition-to-acoustic transmission transfer function. (c) Modulus of the composition-to-composition transmission transfer function. *Non-compact* (——), AVBP (○), *Magri*/κ_3 (Magri 2017) (⋆) and *Non-compact* corrected with the attenuation from the simulation (⋯⋯)

the simulation and from the previous analytical model (Magri 2017) (again termed *Magri*) corrected by a factor κ_3 defined above.

For both acoustic transfer functions, the *Non-compact*, AVBP and *Magri*/κ_3 predictions converge at low frequencies to the same values, which is in agreement with theory (Duran & Moreau 2013). Reflection transfer functions predictions R_σ^- correspond between the *Non-compact* analytical model and AVBP over the whole frequency range. On the contrary, a drastic and increasing gap in modulus is observed for T_σ^+ between the *Non-compact* and AVBP over the considered discrete perturbation frequencies. By correcting the *Non-compact* acoustic transmission transfer function T_σ^+ with the attenuation function (w_2^σ/w_1^σ) from the simulation presented in figure 21(c) allows getting closer results to AVBP, in the same way as described in section 5.2.3.

REFERENCES

Bailly, C., Bogey, C. & Candel, S. 2010 Modelling of Sound Generation by Turbulent Reacting Flows. *International Journal of Aeroacoustics* **9** (4-5), 461–489.

Bake, F., Richter, C., Mühlbauer, B., Kings, N., Röhle, I., Thiele, F. & Noll, B. 2009 The Entropy Wave Generator (EWG): A reference case on entropy noise. *Journal of Sound and Vibration* **326** (3-5), 574–598.

Bauerheim, M., Duran, I., Livebardon, T., Wang, G., Moreau, S. & Poinsot, T. 2016 Transmission and reflection of acoustic and entropy waves through a stator–rotor stage. *Journal of Sound and Vibration* **374**, 260–278.

Blanes, S., Casas, F., Oteo, J. A. & Ros, J. 2009 The Magnus expansion and some of its applications. *Physics Reports* **470** (5-6), 151–238.

Cumpsty, N. A. & Marble, F. E. 1977 Interaction of Entropy Fluctuations With Turbine Blade Rows; a Mechanism of Turbojet Engine Noise. *Proc R Soc London Ser A* **357** (1690), 323–344.

Daviller, G., Oztarlik, G. & Poinsot, T. 2019 A generalized non-reflecting inlet boundary condition for steady and forced compressible flows with injection of vortical and acoustic waves. *Computers and Fluids* **190**, 503–513.

De Domenico, F., Rolland, Erwan O. & Hochgreb, S. 2019 A generalised model for acoustic and entropic transfer function of nozzles with losses. *Journal of Sound and Vibration* **440**, 212–230.

DeHoff, R. T. 1993 *Thermodynamics in Material Science*. McGraw-Hill.

Duran, I. & Moreau, S. 2013 Solution of the quasi-one-dimensional linearized Euler equations using flow invariants and the Magnus expansion. *Journal of Fluid Mechanics* **723**, 190–231.

Duran, I. & Morgans, A. S. 2015 On the reflection and transmission of circumferential waves through nozzles. *Journal of Fluid Mechanics* **773**, 137–153.

Emmanuelli, A., Zheng, J., Huet, M., Giauque, A., Le Garrec, T. & Ducruix, S. 2020 Description and application of a 2D-axisymmetric model for entropy noise in nozzle flows. *Journal of Sound and Vibration* **472**, 115163.

Fattahi, A., Hosseinalipour, S. M. & Karimi, N. 2017 On the dissipation and dispersion of entropy waves in heat transferring channel. *Physics of Fluids* **29** (8), 087104:1–17.

Férand, M., Livebardon, T., Moreau, S. & Sanjosé, M. 2019 Numerical Prediction of Far-Field Combustion Noise from Aeronautical Engines. *Acoustics* **1** (1), 174–198.

Giusti, A., Magri, L. & Zedda, M. 2019 Flow Inhomogeneities in a Realistic Aeronautical Gas-Turbine Combustor: Formation, Evolution, and Indirect Noise. *Journal of Engineering for Gas Turbines and Power* **141** (1), 1–11.

Giusti, A., Worth, N. A., Mastorakos, E. & Dowling, A. P. 2017 Experimental and numerical investigation into the propagation of entropy waves. *AIAA Journal* **55** (2), 446–458.

Goh, C. S. & Morgans, A. S. 2011 Phase prediction of the response of choked nozzles to entropy and acoustic disturbances. *Journal of Sound and Vibration* **330** (21), 5184–5198.

Goodwin, D. G., Speth, R. L., Moffat, H. K. & Weber, B. W. 2021 Cantera: An object-oriented software toolkit for chemical kinetics, thermodynamics and transport processes. https://www.cantera.org, version 2.5.1.

Ihme, M. 2017 Combustion and Engine-Core Noise. *Annual Review of Fluid Mechanics* **49** (August), 277–310.

Lapeyre, C. 2015 Etude numérique de la stabilité, la stabilisation et le bruit de flamme dans un bruleur tourbillonnaire en conditions amorcées. PhD thesis, Institut National Polytechnique de Toulouse (INP Toulouse).

Leyko, M., Duran, I., Moreau, S., Nicoud, F. & Poinsot, T. 2014 Simulation and modelling of the waves transmission and generation in a stator blade row in a combustion-noise framework. *Journal of Sound and Vibration* **333** (23), 6090–6106.

Leyko, M., Nicoud, F. & Poinsot, T. 2009 Comparison of direct and indirect combustion noise mechanisms in a model combustor. *AIAA Journal* **47** (11), 2709–2716.

Livebardon, T. 2015 Modélisation du bruit de combustion dans les turbines d'hélicoptères. PhD thesis, Institut National Polytechnique de Toulouse (INP Toulouse).

Livebardon, T., Moreau, S., Gicquel, L., Poinsot, T. & Bouty, E. 2016 Combining LES of combustion chamber and an actuator disk theory to predict combustion noise in a helicopter engine. *Combustion and Flame* **165**, 272–287.

Magri, L. 2017 On indirect noise in multicomponent nozzle flows. *Journal of Fluid Mechanics* **828**, 1–14.

Magri, L., O'Brien, J. & Ihme, M. 2016 Compositional inhomogeneities as a source of indirect combustion noise. *Journal of Fluid Mechanics* **799**.

Marble, F. E. & Candel, S. M. 1977 Acoustic disturbance from gas non-uniformities convected through a nozzle. *Journal of Sound and Vibration* **55** (2), 225–243.

Moase, W. H., Brear, M. J. & Manzie, C. 2007 The forced response of choked nozzles and supersonic diffusers. *Journal of Fluid Mechanics* **585** (2007), 281–304.

MORGANS, A. S. & DURAN, I. 2016 Entropy noise: A review of theory, progress and challenges. *International Journal of Spray and Combustion Dynamics* **8**, 285–298.

MORGANS, A. S., GOH, C. S. & DAHAN, J. A. 2013 The dissipation and shear dispersion of entropy waves in combustor thermoacoustics. *Journal of Fluid Mechanics* **733**, R2:1–10.

POINSOT, T. J. & LELE, S. K. 1992 Boundary conditions for direct simulations of compressible viscous flows. *Journal of Computational Physics* **101** (1), 104–129.

RAHMANI, E., FATTAHI, A., KARIMI, N. & HOSSEINALIPOUR, S. M. 2022 A comparative analysis of the evolution of compositional and entropy waves in turbulent channel flows. *Physics of Fluids* **34** (1).

SCHØNFELD, T. & RUDGYARD, M. 1999 Steady and unsteady flow simulations using the hybrid flow solver AVBP. *AIAA journal* **37** (11), 1378–1385.

SHAO, C., MAEDA, K. & IHME, M. 2020 Analysis of core-noise contributions in a realistic gas-turbine combustor operated near lean blow-out. *Proceedings of the Combustion Institute* **000**, 1–9.

SHAO, C. X. & IHME, M. 2020 Effect of operating conditions on core noise for a realistic gas-turbine combustor. *Center for Turbulence Research Annual Research Briefs 2020* .

STOW, S. R., DOWLING, A. P. & HYNES, T. P. 2002 Reflection of circumferential modes in a choked nozzle. *Journal of Fluid Mechanics* **467**, 215–239.

TSIEN, H. S. 1952 The Transfer Functions of Rocket Nozzles. *Journal of the American Rocket Nozzle Society* pp. 139–162.

ULLRICH, W. C., SATTELMAYER, T. & KINGS, N. 2015 Numerical investigation of indirect noise generation by accelerated vorticity. *21st AIAA/CEAS Aeroacoustics Conference* pp. 1–15.

YEDDULA, S. R., GUZMÁN-IÑIGO, J., MORGANS, A. S. & YANG, D. 2022 A Magnus-expansion-based model for the sound generated by non-plane entropy perturbations passing through nozzles. *28th AIAA/CEAS Aeroacoustics Conference, 2022* .

Journals with peer review

[1] N.C.W. Treleaven, D. Laera, J. Carmona, N. Odier, Y. Gentil, J. Dombard, **G. Daviller**, L. Gicquel, and T. Poinsot. Coupling of combustion simulation with atomisation and filming models for les in swirled spray flames. *Flow, Turbulence and Combustion*, 2022.

[2] A. Veilleux, G. Puigt, H. Deniau, and **G. Daviller**. Stable spectral difference approach using raviart-thomas elements for 3d computations on tetrahedral grids. *Journal of Scientific Computing*, 91(7), 2022.

[3] A. Veilleux, G. Puigt, H. Deniau, and **G. Daviller**. A stable spectral difference approach for computations with triangular and hybrid grids up to the 6th order of accuracy. *Journal of Computational Physics*, 449:110774, 2022.

[4] D. Lamidel, **G. Daviller**, M. Roger, and H. Posson. Numerical prediction of the aerodynamics and acoustics of a tip leakage flow using large-eddy simulation. *International Journal of Turbomachinery Propulsion and Power*, 27(6), 2021.

[5] R. Biolchini, **G. Daviller**, C. Bailly, and G. Bodard. Temperature effects on the noise source mechanisms in a realistic subsonic dual-stream jet. *Computers and Fluids*, 213, 2020.

[6] **G. Daviller**, J. Dombard, G. Staffelbach, J. Herpe, and D. Saucereau. Prediction of flow separation and side-loads in rocket nozzle using large-eddy simulation. *International Journal of Computational Fluid Dynamics*, 34(7-8):622–632, 2020.

[7] **G. Daviller**, G. Oztarlik, and T. Poinsot. A generalized non-reflecting inlet boundary condition for steady and forced compressible flows with injection of vortical and acoustic waves. *Computers & Fluids*, 190:503 – 513, 2019.

[8] C. Pérez Arroyo, **G. Daviller**, G. Puigt, C. Airiau, and S. Moreau. Identification of temporal and spatial signatures of broadband shock-associated noise. *Shock Waves*, 29:117 – 134, 2018.

[9] E. Kaiser, M. Morzynski, **G. Daviller**, J.N. Kutz, B.W. Brunton, and S.L. Brunton. Sparsity enabled cluster reduced-order models for control. *Journal of Computational Physics*, 352(supplement C):388 – 409, 2018.

[10] C. Pérez Arroyo, **G. Daviller**, G. Puigt, and C. Airiau. Hydrodynamic - acoustic filtering of a supersonic under-expanded jet. In Dimokratis G.E. Grigoriadis, Bernard J. Geurts, Hans Kuerten, Jochen Fröhlich, and Vincenzo Armenio, editors, *Direct and Large-Eddy Simulation X*, pages 79–84, Cham, 2018. Springer International Publishing.

[11] **G. Daviller**, M. Brebion, P. Xavier, G. Staffelbach, J.-D. Müller, and T. Poinsot. A mesh adaptation strategy to predict pressure losses in les of swirled flows. *Flow, Turbulence and Combustion*, 99:93–118, 2017.

[12] S. Le Bras, H. Deniau, C. Bogey, and **G. Daviller**. Development of compressible large-eddy simulations combining high-order schemes and wall modeling. *AIAA Journal*, 55(4):1152–1163, 2017.

[13] J. Kasten, J. Reininghaus, I. Hotz, H.C. Hege, B. Noack, **G. Daviller**, and M. Morzinski. Acceleration feature points of unsteady shear flows. *Archives of Mechanics*, 68(1):55–80, 2016.

[14] **G. Daviller**, J.-F. Boussuge, M. Montagnac, H. Deniau, M. Gazaix, and C. Bogey. Jet-noise reduction by fluidic active control. *Journal of Sound and Vibration*, 340 - Aeroacoustics research in Europe: The CEAS-ASC report on 2013 highlights:44–45, 2015.

[15] A. Fosso Pouangué, M. Sanjosé, S. Moreau, **G. Daviller**, and H. Deniau. Subsonic jet noise simulations using both structured and unstructured grids. *AIAA Journal*, 53(1):55–69, 2015.

[16] E. Kaiser, B. Noack, L. Cordier, A. Spohn, M. Segond, M. Abel, **G. Daviller**, Morzynski M., J. Östh, S. Krajnović, and R. K. Niven. Cluster-based reduced-order modelling of shear flows. *AIP Conference Proceedings*, 1636:151–158, 2014.

[17] E. Kaiser, B. R. Noack, L. Cordier, A. Spohn, M. Segond, M. Abel, **G. Daviller**, J. Östh, S. Krajnović, and R. K. Niven. Cluster-based reduced-order modelling of a mixing layer. *Journal of Fluid Mechanics*, 754:365–414, 2014.

[18] P. Jordan, **G. Daviller**, and P. Comte. Doak's momentum potential theory of energy flux used to study a solenoidal wavepacket. *Journal of Sound and Vibration*, 332(17):3924–3936, 2013.

[19] L. Cordier, B. Noack, G. Tissot, G. Lehnasch, J. Delville, M. Balajewicz, **G. Daviller**, and R. Niven. Identification strategies for model-based control. *Experiments in Fluids*, 54(8):1580–1601, 2013.

[20] A. V. G. Cavalieri, **G. Daviller**, P. Comte, P. Jordan, G. Tadmor, and Y. Gervais. Using large eddy simulation to explore sound-source mechanisms in jets. *Journal of Sound and Vibration*, 330(17):4098–4113, 2011.

Conference proceedings

[1] L. Drozda, P. Mohanamuraly, Y. Realpe, C. Lapeyre, A. Adler, **G. Daviller**, and T. Poinsot. Data-driven taylor-galerkin finite-element scheme for convection problems - the symbiosis of deep learning and differential equations. In *35th Conference on Neural Information Processing Systems (NeurIPS 2021), Sydney, Australia - Virtual conference*, 2021.

[2] Lamidel. D., **G. Daviller**, M. Roger, and H. Posson. Numerical investigation of the tip leakage vortex of an isolated plate/airfoil t-junction with gap. In *Proceedings of 14th European Conference on Turbomachinery Fluid dynamics & Thermodynamics*, Gdansk, Poland, 12-16 April 2021.

[3] M. Férrand, **G. Daviller**, S. Moreau, S. Poinsot, and C. Sensiau. Using les for combustion noise propagation to the far-field by considering the jet flow of a dual-stream nozzle. In *24nd AIAA/CEAS Aeroacoustics Conference*, Atlanta, USA, 25-29 June 2018.

[4] Z. Fu, A. Agarwal, A. V. Cavalieri, P. Jordan, G. Lehnasch, and **G. Daviller** Jet noise reduction through filtering small-scale structures. In *22nd AIAA/CEAS Aeroacoustics Conference*, Lyon, France, 30 May - 1 June 2016.

[5] E. Kaiser, B. R. Noack, A. Spohn, L. N. Cattafesta, M. Morzynski, **G. Daviller**, B. W. Brunton, and S. L. Brunton. A probabilistic approach to modeling and controlling fluid flows. In *APS Division of Fluid Dynamics*, 2016.

[6] S. Le Bras, **G. Daviller**, H. Deniau, and C. Bogey. Wall-modeled large eddy simulations with high-order numerical approach for aeracoustic applications. In *21st AIAA/CEAS Aeroacoustics Conference, Aviation Forum 2015*, Dallas, USA, 22-26 June 2015.

[7] C. Pérez Arroyo, **G. Daviller**, G. Puigt, and C. Airiau. Shock-cell noise of supersonic underexpanded jets. In *ERCOFTAC WORKSHOP DLES*, volume 10, Limassol, Cyprus, May 2015.

[8] S. Le Bras, H. Deniau, C. Bogey, and **G. Daviller** Modélisation de paroi pour la simulation des grandes échelles avec une approche numérique d'ordre élevé. In *XXII ème Congrès Français de Mécanique*, Lyon, France, Août 2015.

[9] C. Pérez Arroyo, **G. Daviller**, G. Puigt, and C. Airiau. Modal structure of a supersonic under-expanded jet. In *XXII ème Congrès Français de Mécanique*, Lyon, France, Août 2015.

[10] E. Kaiser, B. Noack, L. Cordier, A. Spohn, M. Segond, M. Abel, **G. Daviller**, and R. K. Niven. Cluster-based reduced-order modelling of a mixing layer. In *MaxEnt 2013 33rd International Workshop on Bayesian Inference and Maximum Entropy Methods in Science and Engineering*, Canberra, Australia, December 15-20 2013.

[11] E. Kaiser, B. Noack, L. Cordier, A. Spohn, M. Segond, M. Abel, **G. Daviller**, and R. K. Niven. Cluster-based reduced-order modelling of a mixing layer. In *66th Annual Meeting of the APS Division of Fluid Dynamics*, Pittsburgh, PA USA, November 24-26 2013.

[12] **G. Daviller**, G. Lehnasch, and P. Jordan. Numerical investigation of the influence of upstream conditions on properties of shock noise in shock/mixing layer interaction. In *8th International Symposium on turbulence and shear flow phenomena*, Poitiers, France, August 28 - 30, 2013 2013.

[13] P. Kan, J. Lewalle, and **G. Daviller** Comparison of near field events and their far-field acoustic signatures in experimental and numerical high speed jets. In *Eighth International Symposium on Turbulence and Shear Flow Phenomena (TSFP-8)*, Université de Poitiers, France, August 28 - 30 2013.

[14] J. Kasten, J. Reininghaus, I. Hotz, H. C. Hege, B. R. Noack, P. Comte, and **G. Daviller** Temporal evolution of the vortex skeleton in a compressible jet. In *Selected Entry, 29th Gallery of Fluid Motion, American Physical Society, Division Fluid Dynamics*, 2011.

[15] A. V. G. Cavalieri, **G. Daviller**, P. Comte, and P. Jordan. Using les to explore the effect of temperature on sound-source mechanisms in jets. In *Procedia Engineering : IUTAM Symposium on Computational Aero-Acoustics for Aircraft Noise Prediction*, volume 00, University of Southampton, UK, March 31 2010.

[16] **G. Daviller**, P. Jordan, and P. Comte. Toward source analysis of turbulent coaxial jets in large-eddy simulation. In *XIX ème Congrès Français de Mécanique*, Marseille, France, Août 2009.

[17] **G. Daviller**, P. Jordan, and P. Comte. Flow decomposition for the study of source mechanisms. In *15th AIAA/CEAS Aeroacoustic Conference and Exhibit (30th AIAA Aeroacoustics Conference)*, Miami, Florida, May 11-13 2009.

Invited lectures

[1] B. Noack, E. Kaiser, T. Duriez, L. Cordier, J.-C. Laurentie, V. Parezanovic, A. Spohn, J.-P. Bonnet, M. Segond, M. Abel, **G. Daviller**, and R. K. Niven. Turbulence modelling and control using entropy principles. In *MaxEnt 2013 33rd International Workshop on Bayesian Inference and Maximum Entropy Methods in Science and Engineering*, Canberra, Australia, December 15-20 2013.

[2] N. Gourdain, J.-F. Boussuge, F. Crevel, **G. Daviller**, L.Y.M. Gicquel, and F. Sicot. High-Performance Computing and CFD: the state-of-the-art technology for jet engine simulations. In *CEAS 2013 Air and Space Conference, Innovative Europe*, Linköping, Sweden, September 2013.

[3] **G. Daviller**, M.-F. Shahab, G. Lehnasch, P. Jordan, Gatski, T.-B., and P. Comte. Investigating Compressibility Effects in Jets and Supersonic Boundary Layers using HF-LES and DNS. In *Onera Scientific Days : A New Age for Turbulence: DNS, LES, URANS, ...*, Onera Châtillon, France, December, 2 2011.

Other Conferences (no proceedings)

[1] **G. Daviller** and G. Staffelbach. Simulation de la phase d'allumage complet du moteur *Vulcain*®2.1 en utilisant une approche de simulations dites "aux grandes Échelles". In *Journée CCRT 2022*, TGCC - Bruyère le Châtel, 2022.

[2] A. Veilleux, H. Deniau, **G. Daviller**, and G. Puigt. Towards a multi-element-shape extension for the spectral difference method. In *North American High Order Methods Conference*, San Diego, USA, 2019.

[3] P. Roy, **G. Daviller**, J.-C. Jouhaud, and B. Cuenot. Uncertainty quantification-driven robust design assessment of a swirler's geometry. In *4ème Colloque du réseau d'INitiative en Combustion Avancé (INCA)*, Palaiseau, France, 2017. SAFRAN TECH.

[4] C. Pérez Arroyo, **G. Daviller**, G. Puigt, and C. Airiau. Shock-cell noise of supersonic underexpanded jets. In *50th 3AF International Conference on Applied Aerodynamics*, Toulouse, France, March 30-31 2015.

[5] **G. Daviller**. Recent and future developments in elsa: LES and CAA applications. In ***elsA** User's Workshop*, ONERA Châtillon, France, October, 9-10 2014.

[6] E. Kaiser, B. Noack, L. Cordier, A. Spohn, M. Segond, M. Abel, **G. Daviller**, and R. K. Niven. Cluster-based reduced-order modelling of shear flows. In *Seminar Aristote: ROC & ROM - CEA*, 2014.

[7] **G. Daviller**, P. Jordan, and P. Comte. Etude numérique des effets de température sur la turbulence et l'acoustique rayonné dans les jets. In *GDR "Phénoménologie de la Turbulence"*, Poitiers, France, October 15-17 2012.

[8] P. Jordan, **G. Daviller**, and P. Comte. Doak's momentum potential theory of energy flux used to study a solenoidal wavepacket. In *GDR "Phénoménologie de la Turbulence"*, Poitiers, France, October 15-17 2012.

[9] **G. Daviller**, Jordan P., Comte P., George W.K., and Wänström M. Searching for sound-source mechanisms in the flow equations. In *Ercoftac Symposium on sound source mechanisms in turbulent shear-flow*, Poitiers, France, July 7-9 2008.

[10] P. Comte, A. Shams, F. Daude, **G. Daviller**, C. Brun, and P. Jordan. Acoustic coupling, compressibility effects and noise sources from les. In *International Workshop on Compressible Turbulent Flow Research for the Next Generation of Air Vehicles*, IUSTI, Marseille, France, March 17-18 2008.

[11] **G. Daviller**, P. Jordan, and P. Comte. LES of coaxial jets and analysis of sound source mechanisms. In *DFG/CNRS Workshop Noise Generation in Turbulent Jet Flows*, Lyon, France, March 3-4 2008.

Appendix

1 Curriculum Vitae

Guillaume Daviller

Ph.D. in Fluid Mechanics

49 rue de la vieille église, App. 13
31270 Cugnaux, France
☎ *+33(0)0561193110*
✉ *guillaume.daviller@cerfacs.fr*
Nationality: french
40 year old, 1 child

Research interests

- Turbulence & compressible flows
- Aerodynamic & aeroacoustics
- Computational fluid dynamics
- Numerical methods & signal processing
- High performance computing

Professional background

Since 2016 **Research Scientist**, *CERFACS*, Toulouse.
"Research and applications in fluid mechanics and numerical acoustics"

- Computational AeroAcoustics (noise source mechanisms, code coupling & high-fidelity numerical methods)
- Setting-up, coordination & execution of CFD team research projects
- Head of Acoustic Research Group at CERFACS
- In charge of the training session "Fundamentals to understand and analyze high fidelity compressible Large Eddy Simulation"
- Software development

2015–2016 **Research Scientist CNRS**, *IMFT*, Toulouse.
"Introducing Exascale Computing in Combustion Instabilities Simulations"
In collaboration with T. Poinsot & L. Selle
- Simulations LES HPC instationnaires multiphysiques (turbulence, combustion, acoustique)
- Adaptive Mesh Refinement
- Software development (***AVBP, AVSP***, **Antares**)

2013–2014 **Postdoctoral fellow**, *CERFACS*, Toulouse.
"Shock cell noise, installation effect & high order numerical methods"
In collaboration with J.-F. Boussuge, G. Puigt, M. Montagnac & H. Deniau
- Management of research programs in coordination with CERFACS partners (AIRBUS, SAFRAN, ONERA)
- GENCI project manager "Simulation numérique de systèmes multi-composant et multi-physique pour les ensembles propulsifs"
- Head of Acoustic Research Group at CERFACS
- LES, HPC & multiphysics (turbulence, aeroacoustics...)
- Software development (***elsA***, **Antares**)

2011–2012 **Postdoctoral fellow**, *Institut Pprime*, Poitiers.
"HPC simulations of internal and external supersonic flows"
In collaboration with Prof. P. Comte, P. Jordan, T. Gatski & G. Lehnasch
- Aeroacoustics studies of supersonic flows
- DNS/LES studies of shock waves/mixing layer interaction
- A priori and a posteriori analysis of subgrid-scale models for LES & compressible flows
- Study of geometric curvature effects on shock wave/turbulent boundary layer interaction
- Development of hybrid schemes for shock capturing & aeroacoustics
- Parallel Input/Output Optimization

2010 **Research & teaching assistant**, with J. Tartarin.
IUT GTE Poitiers - Institut Pprime
Teaching : fluid mechanics, acoustics & heat transfer

2006–2009 **Research fellow**, *ISAE-ENSMA, Institut Pprime*, Poitiers.
"Temperature effect on noise radiated form free shear flows"
Advisors: Prof. P. Comte & P. Jordan
- Development of a massively parallel compressible Navier-Stokes solver
- 2D/3D numerical investigations using DNS & LES
- Identification of noise source mechanisms

2006 (6 month) **Research training**, *Institut Pprime*, Poitiers.
"Numerical study of an impact problem using SPH method"
Advisor: Prof. S. Huberson
- Development of an Euler equations solver
- Evaluation of SPH method capabilities

Education

2006–2010 **Ph.D. in Fluid Dynamics**, *ISAE-ENSMA, Institut Pprime*, Poitiers.
"Numerical study of temperature effects in single and coaxial jet flows".
Advisor: **Pierre Comte** (Prof. ISAE-ENSMA, Institut Pprime)
Co-advisor: **Peter Jordan** (CR CNRS, Institut Pprime)

2005–2006 **Master of Science**, *Université de Poitiers, UFR Sciences Fondamentales et Appliquées*, Mechanics, Energetic and Engineering - Specialities : Fluids, Acoustics et Energetic.

2004–2005 **Maîtrise**, *Université de Poitiers, UFR Sciences Fondamentales et Appliquées*, Mechanics, Energetic and Engineering.

2003–2004 **Licence**, *Université d'Orléans, U.F.R sciences, Antenne scientifique de BOURGES*, Engineering Sciences and Technologies.

2001–2003 **DEUG**, *Université d'Orléans, U.F.R sciences*.
Engineering Sciences and Technologies

2000 **Baccalauréat Scientifique**, *Lycée Marceau, CHARTRES (28)*.
Speciality: Mathematics

2012 **Formation GPGPU**, *Institut Pprime*, Poitiers, Architecture, CUDA & OpenCL programming.

2006 **Formation MPI**, *Institut Pprime*, Poitiers, Architecture & MPI programming.

Languages

French native

English fluent

Computer skills

Programing C, C++, Fortran(77...2008), MPI, OpenMp, Unix Shell, Python

Software *AVBP, AVSP, AVLP, Antares, JAGUAR, elsA, CODA, ProLB*

Activities and Interests

Music Drums, percussions & guitar, composer

Sport Swimming, cycling, snowboard

Reading Heroic fantasy & science fiction

Miscellaneous fishing, role play

2 Research supervision

Since 2013, I am involved in the supervision of different trainees, PhD student as well as post-docs given below.

Ph.D. students currently supervized:

- Luciano Drozda Dantas Martins: Cerfacs thesis, Learning data-driven discretizations, with P. Mohanamuraly, C. Lapeyre and T. Poinsot (25%)
- Yann Gentil: Cerfacs thesis / EU project CIRRUS, Improved aeroacoustics models for combustion noise prediction, with S. Moreau (advisor, 50%)

Ph.D. students having defended:

- David Lamidel (2022): CIFRE SAE, Modelisation of rotor tip-leakage vortex broadband noise in turbofans, with M. Roger (co-advisor, 50%)
- Adèle Veilleux (2021): Cerfacs/ONERA thesis, Extension of the Spectral Difference method to simplex cells and hybrid grids, with G. Puigt and H. Deniau (co-advisor, 30%)
- Gorkem Oztarlik (2020): ERC INTECOCIS, Numerical and experimental investigations of combustion instabilities of swirled premixed methane-air flames with hydrogen addition, with L. Selle and T. Poinsot (30%)
- Pamphile Roy (2019): Cerfacs thesis, Uncertainty Quantification in High Dimensional Problem, with J.C. Jouhaud and B. Cuenot (30%)
- Mélissa Ferrand (2018): CIFRE SAE, Numerical modeling of far-field turbofan-engine combustion noise, with S. Moreau and T. Poinsot (30%)
- Romain Biolchini (2017): CIFRE SAE, Temperature effects on jet noise using LES, with C. Bailly (co-advisor, 50%)
- Carlos Pérez Arroyo (2016): FP7 Marie Curie Action Aerotranet2, Large Eddy Simulations of a dual stream jet with shock-cells and noise emission analysis, with G. Puigt and C. Airiau (30%)
- Sophie Le Bras (2016): Cerfacs thesis, Wall modeling and no-matched mesh interfaces treatment for aeroacoustics simulations, with G. Puigt, H. Deniau and C. Bogey (30%)
- Maxence Brebion (2016): ERC INTECOCIS, Joint numerical and experimental study of thermoacoustic instabilities, with L. Selle and T. Poinsot (30%)

Post-docs:

- Nikola Sekularac (2022): CleanSky CIRRUS, LES of realistic combustion chambers for combustion noise prediction
- Nadir Messai (2022): Cerfacs funding, Development of shock capturing methodologies within the Spectral Difference method
- Carlos Montilla (2022): DGAC MAMBO, Acoustic analogies for turbomachinery noise prediction
- Alexia de Brauer (2021): FRAE 3C2T - H2020 DJINN, Jet noise simulation using high-order methods
- Nicholas Treleaven (2021): CleanSky CIRRUS, Improved LES prediction of turbulent combustion noise sources terms
- Romain Biolchini (2018): Cleansky SCONE, Simulations of CROR and fan broadband noise with reduced order modeling
- Sophie Le Bras (2016): FP7 X-Noise JERONIMO, Installation & flight effects on jet noise
- Pradip Xavier (2015): ERC INTECOCIS, Mesh adaptation strategy to predict pressure losses in LES of swirled flows

Trainees:

- Ugo Tena (2023): Flow separation and side loads in rocket nozzle
- Stéphane Broutin (2022): Aeroacoustic simulations of cavity noise
- Joël Petit (2021): Implementation of a shock capturing methodology within the Spectral Difference method
- Yann Gentil (2020): Prediction of combustion noise in aircraft engines
- Thomas Naess (2019): Large-eddy simulation of e thrust reversal systems
- Nicolas Cazard (2018): Shock detection & deep learning
- Soufiane Cherkaoui (2018): Adaptive mesh refinement
- Nicolas Urien (2018): Evaluation of LBM for sliding mesh simulation in turbomachinery
- Vincent Bouillin (2017): Development of inlet boundary condition for compressible flows
- Pierre Pineau (2015): Flight effect on shock cell noise

3 Research evaluation

As an author, I am frequently asked by editors of various journals to review papers (8 reviews). I am also involved in expertises of ANR projects (2 reviews).

- Journal of Sound and Vibration
- International Journal of Heat and Fluid Flow
- Computers and Fluids
- Combustion and Flame
- International Journal of Ambient Energy
- Journal of Fluids Engineering
- ASME Journal of Turbomachinery

4 Collective Responsabilies

CSE: I am currently a full member and treasurer of the Social and Economic Committee (CSE) of CERFACS since 3/09/2018.

ARG: Within the framework of the research activity related to acoustics in general at CERFACS, I founded and have been in charge of the Acoustic Research Group (ARG) since 2017. As such, I organize one to two meetings per year, in order to present the current activities, the work of trainees, PhD and post-doctoral students involved in the subject. The objectives of this exchange, including our consultants (S. Moreau, P. Sagaut, F. Nicoud and M. Bauerheim), are to discuss problems encountered in our simulation solvers and to share recent numerical developments in the field of acoustics.

Scientific Council: From 2008 to 2009, I was the PhD students' representative at the scientific council of the *Centre d'Études Aérodynamiques et Thermiques* de l'Institut Pprime - Université de Poitiers.

5 Academic and industrial collaborations

Since the beginning of my PhD in 2006 until today I have participated in many national and European projects (ANR, FRAE, RTRA, FUI, DGAC, CleanSky...). In this section, I summarize the main projects I have been involved, citing my role in terms of execution, supervision, participation in the set-up and management. I am currently the leader of the CIRRUS (Cleansky) project at CERFACS for which I am responsible for two Work Packages.

National and European projects

- European projects
  - CleanSky CIRRUS (2020-2023): Core noIse Reduction foR Uhbr engineS - participation in the set-up, work package leader of two work packages, execution & supervision (1 PhD, 2 post-docs)
  - H2020 DJINN (2020-2023): Decrease Jet INstallation Noise - participation in the set-up, management, execution & supervision (2 post-docs)
  - H2020 TILDA (2015-2018): Towards Industrial LES/DNS in Aeronautics – Paving the Way for Future Accurate CFD - participation in the set-up, execution & supervision (2 post-docs)
  - CleanSky SCONE (2017-2020): Simulation of CrOr and fan broadband NoisE with reduced order modeling - participation in the set-up, execution & supervision (2 post-docs)
  - CleanSky INNOSTAT (2019-2023): Innovative Stator - participation in the set-up, execution & supervision (2 post-docs)
  - CleanSky AMICAL (2020-2023): Advanced Modeling Capabilities For UHBR Low Noise Fan Technology, participation in the set-up, execution & supervision (2 post-docs)
  - ERC INTECOCIS (2013 - 2017): Introducing Exascale Computing in Combustion Instabilities Simulations - execution & supervision (1 PhD, 1 post-doc)
  - FP7 Marie Curie Action Aerotranet2 (2012-2016): Aeronautical Training Network in Aerodynamic Noise from Widebody Civil Aircraft - supervision (1 PhD)
  - FP7 X-NOISE JERONIMO (2012-2016): JEt noise of high bypass RatiO post-docs: Installation, advanced Modelling and mitigatiOn - execution & supervision (2 post-docs)
  - GDR DFG/CNRS 056 (2006-009): Noise generation in turbulent flows - execution

- National projects
  - 3C2T (2017-2019): RTRA STAE - Control of compressible, transitional and turbulent boundary layer - supervision (1 post-doc)
  - OSCAR (2006-2008): FRAE - Optimisation de Systèmes de Contrôle Actif pour la Réduction du bruit de jet - execution
  - REBECCA (2009-2011) FUI/IROQUA - REduction du Bruit motEur avion par des ConCepts technologiques Avancés - execution
  - JESSICA (2009-2011): ANR - Jets supersoniques choqués et couplages aéroacoustiques - execution
  - SPICEX (2007-2009): ANR - Simulations numériques hautes performances d'une interaction onde de choc / couche limite en écoulement externe - execution
- PRACE
  - JNFLAC (2013) - Jet Noise reduction by FLuidic Active Control - participation in the set-up, execution
- Grands Challenges Scientifiques
  - OCCIGEN (2015) - CINES/GENCI - Simulation aéroacoustique de jet subsonique et réduction de bruit par micro-jets - participation in the set-up, execution
  - TOPAZE (2020) - CCRT/CEA - Study of Ariane 6 Vulcain 2.1 engine ignition using high-fidelity simulation - participation in the set-up, management, execution
- DGAC
  - MAMBO (2020-2024) - Méthodes Avancées pour la Modélisation du Bruit moteur et aviOn - participation in the set-up, management, execution, supervision (1 post-doc)
  - LAMA (2021-2022) - Logiciel Avancé de Mécanique des fluides pour l'Aéronautique - participation in the set-up, supervision (1 post-doc)

Because of its status, CERFACS allows me to maintain privileged collaborations with its shareholders, but also with the CNRS. Here are the lists of my main academic and industrial partners:

Academic collaborations

- IMFT:
  T. Poinsot, L. Selle, T. Schuller, C. Airiau
- LMFA:
  C. Bailly, C. Bogey, M. Roger
- Pprime Institut:
  P. Jordan
- DynFluid:
  J.-C. Robinet
- LAUM:
  G. Gabard
- ISAE SUPAERO:
  M. Bauerheim
- M2P2 - University of Aix-Marseille:
  P. Sagaut, P. Boivin
- IMAG - Umiversity of Montpellier:
  F. Nicoud
- University of Sherbrooke:
  S. Moreau
- Imperial College London:
  S. Spencer
- Poliba - DMMM:
  D. Laera
- Queen Mary University:
  J.-D. Mueller

EPIC

- CNES (J. Herpe, C. Bonhomme, L. Prevost)
- ONERA (H. Deniau, G. Puigt, F. Gand)
- INRIA (L. Giraud)
- CEA (P. Kestener)

Industrial collaborations

- Airbus
- Safran
- ArianeGroup
- EDF
- GDtech
- Vibratec
- PSA3
- Free Field Technologies

6 Teaching

CERFACS training course
I am in charge of a CERFACS training course, ”Fundamentals of unsteady CFD” since 2017. On the first day of this training, I give classes divided into two parts:

- Numerical simulation of the Navier-Stokes equations
- High-fidelity numerical schemes for LES

Research & teaching assistant
As a full-time research & teaching assistant in the Génie Thermique et Energie (G.T.E.) department of the Institut Universitaire de Technologie of Poitiers during the academic 2009-2010 year, I have taught 192 hours. My courses covered fluid mechanics, fundamental aerodynamic, acoustics and heat transfer (mainly tutorials and practical works):

- external aerodynamic
- aeroacoustic, active noise reduction, soundproofing
- heat exchangers

Supply Teacher
During the six years (2006-2012) spent at Pprime Institut, I have gave approximatively 80 hours of teaching as supply teacher at ISAE-ENSMA engineering school. Within this framework I took part on two aspects:

- **Practical work:**
  - Numerical application of the Prandtl lifting line theory
  - Experimental study of subsonic flow around cylinder and NACA profile
- **Fortran projects:** I have developed six projects that solve different physical problems using the Fortran programming language. The students were able to develop the code from scratch, test its performance, and analyze the results.

Bibliography

[1] M. J. Lighthill. On sound generated aerodynamically I: General theory. *Proceedings of the Royal Society A: Mathematical, Physical and Engineering Sciences*, 211(1107):564–587, 1952.

[2] M. J. Lighthill. On sound generated aerodynamically II: Turbulence as a source of sound. *Proceedings of the Royal Society A: Mathematical, Physical and Engineering Sciences*, 222(1148):1–32, 1954.

[3] D. I. Blokhintsev. *Acoustics of NonHomogeneous Moving Medium.* NACA, 1946.

[4] J. E. Ffowcs Williams and D.L. Hawking. Sound generation by turbulence and surfaces in arbitrary motion. *Philosophical Transactions of the Royal Society A: Mathematical, Physical and Engineering Sciences*, 264(1151):321–342, 1969.

[5] M. E. Goldstein. *Aeroacoustics.* McGraw-Hill, 1976.

[6] A. Powell. Theory of vortex sound. *Journal of the Acoustical Society of America*, 36(1):177–195, 1964.

[7] M. S. Howe. The dissipation of sound at an edge. *Journal of Sound and Vibration*, 70(3):407–411, 1980.

[8] M. S. Howe. *Theory of Vortex Sound.* Cambridge Texts in Applied Mathematics. Cambridge University Press, 2002.

[9] W. Claus, T. Huttl, and S. Pierre. *Large-Eddy Simulation For Acoustics.* Cambridge University Press, 2007.

[10] L. Leylekian, M. Lebrun, and P. Lempereur. An overview of aircraft noise reduction technologies. *Aerospace Lab*, 7:1–15, 2014.

[11] S. Moreau. Turbomachinery noise predictions: Present and future. *Acoustics*, 1(1):92–116, 2019.

[12] C. K. W. Tam. Jet noise: Since 1952. *Theoretical and Computational Fluid Dynamics*, 10(1-4):393–405, 1998.

[13] P. Jordan and Y. Gervais. Subsonic jet aeroacoustics: Associating experiment, modelling and simulation. *Experiments in Fluids*, 44(1):1–21, 2008.

[14] P. Jordan and T. Colonius. Wave packets and turbulent jet noise. *Annual Review of Fluid Mechanics*, 45(1):173–195, 2012.

[15] N. Peake and A. B. Parry. Modern challenges facing turbomachinery aeroacoustics. *Annual Review of Fluid Mechanics*, 44:227–248, 2011.

[16] H. S. Tsien. The transfer functions of rocket nozzles. *Journal of the American Rocket Nozzle Society*, pages 139–162, 1952.

[17] F. E. Marble and S. M. Candel. Acoustic disturbance from gas non-uniformities convected through a nozzle. *Journal of Sound and Vibration*, 55(2):225–243, 1977.

[18] S. Piantanida, V. Jaunet, J. Huber, W. R. Wolf, P. Jordan, and A. V. G. Cavalieri. Scattering of turbulent-jet wavepackets by a swept trailing edge. *The Journal of the Acoustical Society of America*, 140(6):4350–4359, 2016.

[19] W. E. Zorumski and B. J. Tester. Prediction of the acoustic impedance of duct liners. Technical Report NASA TM X-73951, 1997.

[20] S. Moreau and M. Roger. Advanced noise modeling for future propulsion systems. *International Journal of Aeroacoustics*, 17(6-8):576–599, 2018.

[21] W. Dobrzynski. Almost 40 years of airframe noise research: What did we achieve? *Journal of Aircraft*, 47(2):353–367, 2010.

[22] T. J. Heffernon. *Aircraft Noise Installation Effect*. PhD thesis, University of Southampton, 2013.

[23] D. Casalino, F. Diozzi, R. Sannino, and A. Paonessa. Aircraft noise reduction technologies: A bibliographic review. *Aerospace Science and Technology*, 12(1):1–17, 2008.

[24] J. C. Hardin and M. Y. Hussaini. *Computational Aeroacoustics*. Springer-Verlag, 1993.

[25] T. Colonius and S. K. Lele. Computational aeroacoustics: Progress on nonlinear problems of sound generation. *Progress in Aerospace Sciences*, 40(6):345–416, 2004.

[26] M. Wang, J. B. Freund, and S. K. Lele. Computational prediction of flow-generated sound. *Annual Review of Fluid Mechanics*, 38(1):483–512, 2006.

[27] S. K. Lele and J. W. Nichols. A second golden age of aeroacoustics? *Philosophical Transactions of the Royal Society A: Mathematical, Physical and Engineering Sciences*, 372(2022), 2014.

[28] C. P. Arroyo, J. Dombard, F. Duchaine, L. Gicquel, B. Martin, N. Odier, and G. Staffelbach. Towards the large-eddy simulation of a full engine: Integration of a 360 azimuthal degrees fan, compressor and combustion chamber. Part I: Methodology and initialisation. *Journal of the Global Power and Propulsion Society*, 2021(Special Issue):1–15, 2021.

[29] C. P. Arroyo, J. Dombard, F. Duchaine, L. Gicquel, B. Martin, N. Odier, and G. Staffelbach. Towards the large-eddy simulation of a full engine: Integration of a 360 azimuthal degrees fan, compressor and combustion chamber. Part II: Comparison against stand-alone simulations. *Journal of the Global Power and Propulsion Society*, 2021(Special Issue):1–14, 2021.

[30] E. Fares, B. Duda, and M. R. Khorrami. Airframe noise prediction of a full aircraft in model and full scale using a Lattice Boltzmann approach. *22nd AIAA/CEAS Aeroacoustics Conference, 2016*, pages 1–21, 2016.

[31] S. Moreau. The third golden age of aeroacoustics. *Physics of Fluids*, 34(2022), 2022.

[32] D. G. Crighton. Basic principle of aerodynamic noise generation. *Progress in Aerospace Sciences*, 16(1):31–96, 1975.

[33] C. K. W. Tam. Computational aeroacoustics: Issues and methods. *AIAA Journal*, 33(10):1788–1796, 1995.

[34] S. K. Lele. Computational aeroacoustics: A review. AIAA Paper 97-0018. In *35th Aerospace Sciences Meeting and Exhibit*, 1997.

[35] S. W. Rienstra and A. Hirschberg. An introduction to acoustics, 2021.

[36] M. L. Shur, P. R. Spalart, M. K. Strelets, and A. K. Travin. Towards the prediction of noise from jet engines. *International Journal of Heat and Fluid Flow*, 24(4):551–561, 2003.

[37] H. Xia, P. G. Tucker, and S. Eastwood. Large-Eddy Simulations of chevron jet flows with noise predictions. *International Journal of Heat and Fluid Flow*, 30(6):1067–1079, 2009.

[38] G. Brès, J. W. Nichols, S. K. Lele, and F. E. Ham. Towards best practices for jet noise predictions with unstructured Large-Eddy Simulations. In *42nd AIAA Fluid Dynamics Conference and Exhibit*, number AIAA 2012-2965, pages 1–21, 2012.

[39] D. Casalino. An advanced time approach for acoustic analogy predictions. *Journal of Sound and Vibration*, 261(4):583–612, apr 2003.

[40] F. Farassat and G.P. Succi. A review of propeller discrete frequency noise prediction technology with emphasis on two current methods for time domain calculations. *Journal of Sound and Vibration*, 71(63):399–419, 1980.

[41] A. Najafi-Yazdi, G. Bres, and L. Mongeau. An acoustic analogy formulation for moving sources in uniformly moving media. *Proceedings of the Royal Society A: Mathematical, Physical and Engineering Sciences*, 467(2125):144–165, 2011.

[42] W. Béchara, C. Bailly, P. Lafon, and S. Candel. Stochastic approach to noise modeling for free turbulent flows. *AIAA Journal*, 32(3):455–463, 1994.

[43] R. Ewert and W. Schröder. On the simulation of trailing edge noise with a hybrid LES/APE method. *Journal of Sound and Vibration*, 270(3):509–524, 2004.

[44] C. Weckmüller, S. Guerin, J. Wellner, and U. Michel. Ffowcs Williams & Hawkings formulation for the convective wave equation and permeable data surface. *16th AIAA/CEAS Aeroacoustics Conference*, pages 1–13, 2010.

[45] M. Gruber, T. Lonfils, C. Dumont, L. Vion, A. Dubois, and T. Delteil Mc Williams. On the fast prediction of open rotor tonal interaction noise. In *Proceedings of ASME Turbo Expo 2015: Turbine Technical Conference and Exposition*, number GT2015-42579. American Society of Mechanical Engineers, 2015.

[46] M. Daroukh, S. Moreau, N. Gourdain, J.-F. Boussuge, and C. Sensiau. Tonal noise prediction of a modern turbofan engine with large upstream and downstream distortion. *Journal of Turbomachinery*, 141(2):021010, 2018.

[47] Christopher K. W. Tam. *Computational Aeroacoustics - A wave number approach*. Cambridge University Press, 2012.

[48] P. R. Spalart. Detached-Eddy Simulation. *Annual Review of Fluid Mechanics*, 41:181–202, 2009.

[49] C. Mockett. *Go4Hybrid: Grey Area Mitigation for Hybrid RANS-LES Methods*, volume 134 of *Notes on Numerical Fluid Mechanics and Multidisciplinary Design*. Springer International Publishing, 2018.

[50] G. Brès and S. K. Lele. Modelling of jet noise: a perspective from Large-Eddy Simulations. *Philosophical Transactions of the Royal Society A: Mathematical, Physical and Engineering Sciences*, 377(2159), 2019.

[51] C. Bogey. Grid sensitivity of flow field and noise of high-Reynolds-number jets computed by large-eddy simulation. *International Journal of Aeroacoustics*, 17(4-5):399–424, 2018.

[52] C. Bogey and O. Marsden. Identification of the effects of the nozzle-exit boundary-layer thickness and its corresponding Reynolds number in initially highly disturbed subsonic jets. *Physics of Fluids*, 25(5), 2013.

[53] G. Brès, P. Jordan, V. Jaunet, M. Le Rallic, A. V.G. Cavalieri, A. Towne, S. K. Lele, T. Colonius, and O. Schmidt. Importance of the nozzle-exit boundary-layer state in subsonic turbulent jets. *Journal of Fluid Mechanics*, 851:83–124, 2018.

[54] P. Jordan. *Coherent structures and turbulent jet aeroacoustics.* Habilitation à Diriger des Recherches - University of Poitiers, 2016.

[55] A. Veilleux, G. Puigt, H. Deniau, and **G. Daviller**. Stable Spectral Difference approach using Raviart-Thomas elements for 3D computations on tetrahedral grids. *Journal of Scientific Computing*, 91(7), 2022.

[56] **G. Daviller**, M. Brebion, P. Xavier, G. Staffelbach, J.-D. Müller, and T. Poinsot. A mesh adaptation strategy to predict pressure losses in les of swirled flows. *Flow, Turbulence and Combustion*, 99:93–118, 2017.

[57] **G. Daviller**, J. Dombard, G. Staffelbach, J. Herpe, and D. Saucereau. Prediction of flow separation and side-loads in rocket nozzle using large-eddy simulation. *International Journal of Computational Fluid Dynamics*, pages 1–12, 2020.

[58] D. Lamidel, **G. Daviller**, M. Roger, and H. Posson. Numerical prediction of the aerodynamics and acoustics of a tip leakage flow using large-eddy simulation. *International Journal of Turbomachinery Propulsion and Power*, 27(6), 2021.

[59] **G. Daviller**, G. Oztarlik, and T. Poinsot. A generalized non-reflecting inlet boundary condition for steady and forced compressible flows with injection of vortical and acoustic waves. *Computers and Fluids*, 190:503 – 513, 2019.

[60] T. Poinsot and Sanjiva K. Lele. Boundary conditions for direct simulations of compressible viscous flows. *Journal of Computational Physics*, 101(1):104–129, 1992.

[61] S. Le Bras, H. Deniau, C. Bogey, and **G. Daviller** Development of compressible Large-Eddy Simulations combining high-order schemes and wall modeling. *AIAA Journal*, 55(4):1152–1163, 2017.

[62] S. Le Bras, **G. Daviller**, H. Deniau, and C. Bogey. Wall-modeled large eddy simulations with high-order numerical approach for aeracoustic applications. In *21st AIAA/CEAS Aeroacoustics Conference, Aviation Forum 2015*, Dallas, USA, 22-26 June 2015.

[63] R. Biolchini, **G. Daviller**, C. Bailly, and G. Bodard. Temperature effects on the noise source mechanisms in a realistic subsonic dual-stream jet. *Computers and Fluids*, 213, 2020.

[64] C. Pérez Arroyo, **G. Daviller**, G. Puigt, C. Airiau, and S. Moreau. Identification of temporal and spatial signatures of broadband shock-associated noise. *Shock Waves*, 29:117 – 134, 2018.

[65] Y. Gentil, **G. Daviller**, S. Moreau, N.C.W. Treleaven, and T. Poinsot. Theoretical analysis and numerical validation of the mechanisms controlling composition noise. *Submitted to Journal of Fluid Mechanics*, 2022.

[66] D. A. Kopriva and J. H. Kolias. A conservative staggered-grid Chebyshev multidomain method for compressible flows. *Journal of Computational Physics*, 125(1):244–261, 1996.

[67] Y. Liu, M. Vinokur, and Z. J. Wang. Spectral difference method for unstructured grids I: Basic formulation. *Journal of Computational Physics*, 216(2):780–801, 2006.

[68] Z. J. Wang, Y. Liu, G. May, and A. Jameson. Spectral difference method for unstructured grids II: Extension to the Euler equations. *Journal of Scientific Computing*, 32:45–71, 2007.

[69] G. May and A. Jameson. A spectral difference method for the Euler and Navier-Stokes equations on unstructured grids. In *44th AIAA Aerospace Sciences Meeting and Exhibit, 9-12 January, Reno, Nevada, AIAA Paper 2006-304*, 2006.

[70] Y. Sun, Z. J. Wang, and Y. Liu. High-order multidomain spectral difference method for the Navier-Stokes equations on unstructured hexahedral grids. *Communications in Computational Physics*, 2(2):310–333, 2007.

[71] K. Van den Abeele, C. Lacor, and Z. J. Wang. On the stability and accuracy of the spectral difference method. *Journal of Scientific Computing*, 37:162–188, 2008.

[72] A. Balan, G. May, and J. Schöberl. A stable high-order spectral difference method for hyperbolic conservation laws on triangular elements. *Journal of Computational Physics*, 231(5):2359–2375, 2012.

[73] P. Raviart and J. Thomas. A mixed finite element method for 2nd order elliptic problem. *Lecture Notes in Mathematics*, 606:292–315, 1977.

[74] A. Veilleux, G. Puigt, H. Deniau, and **G. Daviller**. A stable Spectral Difference approach for computations with triangular and hybrid grids up to the 6th order of accuracy. *Journal of Computational Physics*, 449:110774, 2022.

[75] A. Veilleux. *Extension of the Spectral Difference method to simplex cells and hybrid grids*. PhD thesis, University of Toulouse, 2021.

[76] M. Vinokur. Conservation equations of gasdynamics in curvilinear coordinate systems. *Journal of Computational Physics*, 14(2):105–125, 1974.

[77] H. Viviand. Conservation forms of gas dynamic equations. *In its Aerospace Research*, 1974(1974-1):153–159, 1975.

[78] J. Proriol. Sur une famille de polynômes à deux variables orthogonaux dans un triangle. *Compte Rendus de l'Académie des Sciences*, 257:2459–2461, 1957.

[79] T. Koornwinder. Two-variable analogues of the classical orthogonal polynomials. In R. Askey, editor, *Theory and Applications of Special Functions*, San Diego, 1975.

[80] M. Dubiner. Spectral methods on triangles and other domains. *Journal of Scientific Computing*, 6(4):345–390, 1991.

[81] M. Li, Z. Qiu, C. Liang, M. Sprague, M. Xu, and C. A. Garris. A new high-order spectral difference method for simulating viscous flows on unstructured grids with mixed-element meshes. *Computers and Fluids*, 184:187–198, 2019.

[82] D. M. Williams, L. Shunn, and A. Jameson. Symmetric quadrature rules for simplexes based on sphere close packed lattice arrangements. *Journal of Computational and Applied Mathematics*, 266:18–38, 2014.

[83] R. Vichnevetsky and J. B. Bowles. *Fourier Analysis of Numerical Approximations of Hyperbolic Equations*. Society for Industrial and Applied Mathematics, 1982.

[84] L. Shunn and F. Ham. Symmetric quadrature rules for tetrahedra based on a cubic close-packed lattice arrangement. *Journal of Computational and Applied Mathematics*, 236(17):4348–4364, 2012.

[85] R. J. Spiteri and S. J. Ruuth. A new class of optimal high-order strong-stability-preserving time discretization methods. *SIAM Journal on Numerical Analysis*, 40(2):469—-491, 2002.

[86] C. Bogey and C. Bailly. A family of low dispersive and low dissipative explicit schemes for flow and noise computations. *Journal of Computational Physics*, 194:194–214, 2004.

[87] C. Carton de Wiart, K. Hillewaert, M. Duponcheel, and G. Winckelmans. Assessment of a discontinuous Galerkin method for the simulation of vortical flows at high Reynolds number. *International Journal for Numerical Methods in Fluids*, 74:469–493, 2014.

[88] 5th International Workshop on High-Order CFD Methods. `https://how5.cenaero.be/`.

[89] M. Brebion. *Joint numerical and experimental study of thermoacoustic instabilities*. PhD thesis, University of Toulouse, 2017.

[90] D. Barré, M. Kraushaar, G. Staffelbach, V. Moureau, and L. Y. M. Gicquel. Compressible and low Mach number LES of a swirl experimental burner. *Comptes Rendus Mécanique*, 341:277–287, 2013.

[91] H. Ying and Y. Vigor. Dynamics and stability of lean-premixed swirl-stabilized combustion. *Progress in Energy and Combustion Science*, 35(4):293–364, 2009.

[92] L. Y. M. Gicquel, G. Staffelbach, and T. Poinsot. Large-Eddy Simulations of gaseous flames in gas turbine combustion chambers. *Progress in Energy and Combustion Science*, 38(6):782–817, 2012.

[93] S. V. Apte, K. Mahesh, P. Moin, and J. C. Oefelein. Large-Eddy Simulation of swirling particle-laden flows in a coaxial-jet combustor. *Int. J. Multiphase Flow* , 29(8):1311–1331, 2003.

[94] M. Falese, L. Y. M. Gicquel, and T. Poinsot. LES of bifurcation and hysteresis in confined annular swirling flows. *Comput. Fluids* , 89:167–178, 2014.

[95] J. D. Denton. Loss Mechanisms in Turbomachines. *Journal of Turbomachinery*, 115:621–656, 1993.

[96] D. Lengani, D. Simoni, R. Pichler, R.D. Sandberg, V. Michelassi, and F. Bertini. Identification and quantification of losses in a LPT cascade by POD applied to LES data. *International Journal of Heat and Fluid Flow*, 70:28–40, 2018.

[97] M. Harnieh, N. Odier, J. Dombard, F. Duchaine, and L. Y. M. Gicquel. Loss predictions in the high-pressure film-cooled turbine vane of the factor project by mean of wall-modeled large eddy simulation. In *Proceedings of ASME Turbo Expo*, number GT2020-14232, 2020.

[98] C. Dapogny, C. Dobrzynski, and P. Frey. Three-dimensional adaptive domain remeshing, implicit domain meshing, and applications to free and moving boundary problems. *Journal of Computational Physics*, 262:358–378, 2014.

[99] N. Odier, A. Thacker, M. Harnieh, G. Staffelbach, L.Y.M. Gicquel, F. Duchaine, N. Garcia-Rosa, and J.-D. Mueller. A mesh adaptation strategy for complex wall-modeled turbomachinery LES. *Computers and Fluids*, 214:104766, 2021.

[100] Hip Development Team. Pyhip 0.3.2, 2021.

[101] T. Poinsot and D. Veynante. *Theorical and Numerical Combustion.* 3rd edition, 2012.

[102] E. Garnier, N. A. Adams, and P. Sagaut. *Large-Eddy Simulation for compressible flows.* Springer-Science, 2009.

[103] L. S. G. Kovasznay. Turbulence in supersonic flow. *Journal of the Aeronautical Sciences*, 20(10):657–682, 1953.

[104] T. Poinsot and S. Lele. Boundary conditions for direct simulations of compressible viscous flows. *Journal of Computational Physics*, 101(1):104–129, 1992.

[105] T. Colonius. Modelling artificial boundary conditions for compressible flow. *Annual Review of Fluid Mechanics*, 36:315–345, 2004.

[106] L. Selle, F. Nicoud, and T. Poinsot. The actual impedance of non-reflecting boundary conditions: implications for the computation of resonators. *AIAA Journal* , 42(5):958–964, 2004.

[107] W. Polifke, C. Wall, and P. Moin. Partially reflecting and non-reflecting boundary conditions for simulation of compressible viscous flow. *Journal of Computational Physics*, 213(1):437–449, 2006.

[108] R. Prosser. Improved boundary conditions for the direct numerical simulation of turbulent subsonic flows I: Inviscid flows. *Journal of Computational Physics*, 207:736–768, 2005.

[109] N. Guezennec and T. Poinsot. Acoustically nonreflecting and reflecting boundary conditions for vorticity injection in compressible solvers. *AIAA Journal* , 47:1709–1722, 2009.

[110] S. Bocquet, P. Sagaut, and J. Jouhaud. A compressible wall model for large-eddy simulation with application to prediction of aerothermal quantities. *Physics of Fluids*, 24:065103, 2012.

[111] S. T. Bose and G. I. Park. Wall-modeled Large-Eddy Simulation for complex turbulent flows. *Annual Review of Fluid Mechanics*, 50:535–561, 2018.

[112] M. Catchirayer. *Wall-modeling in large-eddy simulations for turbomachinery flows.* Phd thesis, Aix Marseille Université - Ecole Doctorale: Sciences pour l'ingénieur, 2019.

[113] S. Kawai and J. Larsson. Wall-modeling in Large-Eddy Simulation: Length scales, grid resolution, and accuracy. *Physics of Fluids*, 24:015105, 2012.

[114] G. Lodato, P. Castonguay, and A. Jameson. Structural wall-modeled LES using a high-order Spectral Difference scheme for unstructured meshes. *Flow, Turbulence and Combustion*, 92(1-2):579–606, 2014.

[115] A. Fosso, H. Deniau, F. Sicot, and P. Sagaut. Curvilinear finite-volume schemes using high order compact formulation. *Journal of Computational Physics*, 229(13):5090–5122, 2010.

[116] S. K. Lele. Compact finite difference schemes with spectral-like resolution. *Journal of Computational Physics*, 103:16–42, 1992.

[117] C. Bogey and C. Bailly. Computation of a high Reynolds number jet and its radiated noise using large eddy simulation based on explicit filtering. *Computers and Fluids*, 35(10), 2006.

[118] D. J. Bodony and Sanjiva K. Lele. Current status of jet noise predictions using Large-Eddy Simulation. *AIAA Journal*, 46(2):364–380, 2008.

[119] A. Fosso Pouangué, M. Sanjosé, S. Moreau, **G. Daviller**, and H. Deniau. Subsonic jet noise simulations using both structured and unstructured grids. *AIAA Journal*, 53(1):55–69, 2015.

[120] H. Reichardt. The fundamentals of turbulent heat transfer. *Archiv fuer die Gesamte Waermetechnik,(West Germany)*, 6:129–143, 1951.

[121] B. A. Kader. Temperature and concentration profiles in fully turbulent boundary layers. *International Journal of Heat and Mass Transfer*, 24(9):1541–1544, 1981.

[122] E. R. van Driest. Turbulent boundary layer in compressible fluid. *Journal of the Aeronautical sciences*, 18(3):145–160, 1951.

[123] M. V. Morkovin. *Effects of compressibility on turbulent flows*, pages 367–380. Favre, A. (ed.), Mecanique de la Turbulence. CNRS, 1962.

[124] S. Hoyas and J. Jiménez. Scaling of the velocity fluctuations in turbulent channels up to $Re_\tau = 2003$. *Physics of fluids*, 18:011702, 2006.

[125] K. M. Aikens, N. S. Dhamankar, C. S. Martha, S. Yingchong, G. A. Blaisdell, A. S. Lyrintzis, and Z. Li. Equilibrium wall model for Large-Eddy Simulations of jets for aeroacoustics. In *AIAA SciTech, 52nd Aerospace Sciences Meeting*, number AIAA paper 2014-0180, 2014.

[126] A. V. G. Cavalieri, P. Jordan, T. Colonius, and Y. Gervais. Axisymmetric superdirectivity in subsonic jets. *Journal of Fluid Mechanics*, 704, 2012.

[127] S. Le Bras, **G. Daviller**, H. Deniau, and C. Bogey. Wall-modeled Large-Eddy Simulations with high-order numerical approach for aeracoustic applications. In *21st AIAA/CEAS Aeroacoustics Conference, Aviation Forum 2015*, Dallas, USA, 22-26 June 2015.

[128] Antares Development Team. Antares Documentation Release 1.20.0, 2022.

[129] C. Bogey and C. Bailly. Influence of nozzle-exit boundary-layer conditions on the flow and acoustic fields of initially laminar jets. *Journal of Fluid Mechanics*, 663:507–538, 2010.

[130] K. B. M. Q. Zaman. Effect of initial condition on subsonic jet noise. *AIAA Journal*, 23(9):1370–1373, 1985.

[131] K. B. M. Q. Zaman. Effect of initial boundary-layer state on subsonic jet noise. *AIAA Journal*, 50(8):1784–1795, 2012.

[132] J. Huber, G. Drochon, C. Bonnaud, A. Pintado-Peno, F. Cléro, and G. Bodard. Large-scale jet noise testing, reduction and methods validation "EXEJET": 1. Project overview and focus on installation. In *20^{th} AIAA/CEAS Aeroacoustics Conference*, number AIAA 2014-3032, pages 1–17, 2014.

[133] F. David, J. M. Jourdan, F. Cléro, M. Koenig, and J. Huber. Large-scale jet noise testing, reduction and methods validation "EXEJET": 4. - Flows characterization with PIV in the CEPRA19 anechoic wind tunnel of Onera. In *20^{th} AIAA/CEAS Aeroacoustics Conference*, number AIAA 2014-3035, pages 1–11, 2014.

[134] J. Lau. Effects of exit Mach number and temperature on mean-flow and turbulence characteristics in round jets. *Journal of Fluid Mechanics*, 105(1):193–218, 1981.

[135] K. Schneider, M. Farge, and N. Kevlahan. *Spatial intermittency in two-dimensional turbulence: a wavelet approach*, pages 302–328. Series on Knots and Everything - Woods Hole Mathematics. World Scientific, 2004.

[136] C. Bogey. A study of the effects of temperature on velocity and density fluctuations in high-subsonic jets. In *52^{nd} Aerospace Sciences Meeting*, number AIAA 2014-0524, pages 1–15, 2014.

[137] C. Bogey. On noise generation in low Reynolds number temporal round jets at a Mach number of 0.9. *Journal of Fluid Mechanics*, 859:1022–1056, 2019.

[138] A. Towne, A. V. G. Cavalieri, P. Jordan, T. Colonius, O. Schmidt, V. Jaunet, and G. Brès. Acoustic resonance in the potential core of subsonic jets. *Journal of Fluid Mechanics*, 825(1):1113–1152, 2017.

[139] T. Suzuki and T. Colonius. Instability waves in a subsonic round jet detected using a near-field phased microphone array. *Journal of Fluid Mechanics*, 565(1):197–226, 2006.

[140] A. Powell. On the mechanism of choked jet noise. *Proceedings of the Physical Society. Section B*, 66(12):1039, 1953.

[141] M. Harper-Bourne and M. J. Fisher. The noise from shock waves in supersonic jets. In *Advisory Group for Aerospace Research and Development*, number AGARD-CP-131, 1973.

[142] M. Wong, P. Jordan, I. Maia, A. V. G. Cavalieri, R. Kirby, T. Fava, and D. Edgington-Mitchell. Wavepacket modelling of broadband shock-associated noise in supersonic jets. *Journal of Fluid Mechanics*, 918:A9, 2021.

[143] C. K. W. Tam. On the spectral shape and a second component of broadband shock-cell noise. *Journal of Sound and Vibration*, 541:117335, 2022.

[144] **G. Daviller**, P. Jordan, and P. Comte. Etude numérique des effets de température sur la turbulence et l'acoustique rayonné dans les jets. In *GDR "Phénoménologie de la Turbulence"*, Poitiers, France, October 15-17 2012.

[145] **G. Daviller**, G. Lehnasch, and P. Jordan. Numerical investigation of the influence of upstream conditions on properties of shock noise in shock/mixing layer interaction. In *8th International Symposium on turbulence and shear flow phenomena*, Poitiers, France, August 28 - 30, 2013 2013.

[146] C. Pérez Arroyo, **G. Daviller**, G. Puigt, and C. Airiau. Hydrodynamic - Acoustic filtering of a supersonic under-expanded jet. In Dimokratis G.E. Grigoriadis, Bernard J. Geurts, H. Kuerten, J. Fröhlich, and V. Armenio, editors, *Direct and Large-Eddy Simulation X*, pages 79–84. Springer International Publishing, 2018.

[147] C. E. Tinney and P. Jordan. The near pressure field of co-axial subsonic jets. *Journal of Fluid Mechanics*, 611:175–204, 2008.

[148] A. V. G. Cavalieri, **G. Daviller**, P. Comte, P. Jordan, G. Tadmor, and Y. Gervais. Using Large-Eddy Simulation to explore sound-source mechanisms in jets. *Journal of Sound and Vibration*, 330(17):4098–4113, 2011.

[149] R. Camussi, J. Grilliat, G. Caputi-Gennaro, and M. C. Jacob. Experimental study of a tip leakage flow: wavelet analysis of pressure fluctuations. *Journal of Fluid Mechanics*, 660:87–113, 2010.

[150] D. Guariglia, A. R. Carpio, and C. Schram. Design of a facility for shock-cells noise experimental investigation on a subsonic/supersonic coaxial jet. In *22nd AIAA/CEAS Aeroacoustics Conference*, number AIAA paper 2016-2983, Lyon, France, 2016.

[151] C. Pérez Arroyo, G. Puigt, J.-F. Boussuge, and C. Airiau. Large-Eddy Simulation of shock-cell noise from a dual stream jet. In *22nd AIAA/CEAS Aeroacoustics Conference*, number AIAA paper 2016-2798, Lyon, France, 2016.

[152] C. Pérez Arroyo. *Large Eddy Simulations of a dual stream jet with shock-cells and noise emission analysis*. Phd thesis, University of Toulouse - Ecole doctorale MEGeP, 2016.

[153] **G. Daviller** and H. Deniau. High-Order methods for aeroacoustic in ***elsa*** software: Large-Eddy Simulation issues. Technical report, Cerfacs, Toulouse, France, 2018.

[154] M. Férand. *Numerical modeling of far-field turbofan-engine combustion noise*. PhD thesis, Université de Toulouse, INP Toulouse - École doctorale MEGeP, 2018.

[155] C. E. Hughes. *NASA Collaborative Research on the Ultra High Bypass Engine Cycle and Potential Benefits for Noise, Performance, and Emissions*. National Aeronautics and Space Administration, Glenn Research Center, 2013.

[156] R. E. Longhouse. Control of tip-vortex noise of axial flow fans by rotating shrouds. *Journal of Sound and Vibration*, 58(2):201–214, 1978.

[157] F. Kameier and W. Neise. Experimental study of tip clearance losses and noise in axial turbomachines and their reduction. *Journal of Turbomachinery*, 119(3):460–471, 1997.

[158] M. Sanjosé, M. Daroukh, W. Magnet, J. de Laborderie, S. Moreau, and A. Mann. Tonal noise prediction and validation on the ANCF rotor-stator configuration. *Noise Control Engineering Journal*, 63(6):552–562, 2015.

[159] I. Gonzales-Martino. Design sensitivity of a 1-1/2 stage unshrouded high work turbine using Very-Large-Eddy simulations. In *Proceeding of ASME Turbo Expo*, number GT2022-84281, Rotterdam, Netherland, 2022.

[160] M. C. Jacob, E. Jondeau, and B. Li. Time-resolved PIV measurements of a tip leakage flow. *International Journal of Aeroacoustics*, 15(6-7):662–685, 2016.

[161] R. Koch, M. Sanjosé, and S. Moreau. Large-Eddy Simulation of a single airfoil tip-leakage flow. *AIAA Journal*, 59:2546–2557, 2021.

[162] J. Boudet, A. Cahuzac, P. Kausche, and M. C. Jacob. Zonal Large-Eddy Simulation of a fan tip-clearance flow, with evidence of vortex wandering. *Journal of Turbomachinery*, 137(6):061001, 2015.

[163] W. C. Strahle. On combustion generated noise. *Journal of Fluid Mechanics*, 49:399–414, 1977.

[164] S. M. Candel, D. Durox, S. Ducruix, A.L. Birbaud, N. Noiray, and T. Schuller. Flame dynamics and combustion noise: progress and challenges. *International Journal of Aeroacoustics*, 8(1 & 2):1–56, 2009.

[165] A. P. Dowling and Y. Mahmoudi. Combustion noise. *Proceedings of the Combustion Institute*, 35(1):65–100, 2015.

[166] A. S. Morgans and I. Duran. Entropy noise: A review of theory, progress and challenges. *International Journal of Spray and Combustion Dynamics*, 8:285–298, 2016.

[167] L. Magri, J. O'Brien, and M. Ihme. Compositional inhomogeneities as a source of indirect combustion noise. *Journal of Fluid Mechanics*, 799, 2016.

[168] F. A. Williams. *Combustion theory.* CRC Press, 2018.

[169] I. Duran and S. Moreau. Solution of the quasi-one-dimensional linearized Euler equations using flow invariants and the Magnus expansion. *Journal of Fluid Mechanics*, 723:190–231, 2013.

[170] C. S. Goh and A. S. Morgans. Phase prediction of the response of choked nozzles to entropy and acoustic disturbances. *Journal of Sound and Vibration*, 330(21):5184–5198, 2011.

[171] T. Lee and K. T. Kim. Combustion dynamics of lean fully-premixed hydrogen-air flames in a mesoscale multinozzle array. *Combustion and Flame*, 218:234–246, 2020.

[172] K. Duraisamy, G. Iaccarino, and H. Xiao. Turbulence modeling in the age of data. *Annual Review of Fluid Mechanics*, 51(1):357–377, 2019.

[173] G. E. Karniadakis, L. G. Kevrekidis, L. Lu, P. Perdikaris, S. Wang, and L. Yang. Physics-informed machine learning. *Nature Reviews Physics*, 3:422–440, 2021.

[174] L. Drozda, P. Mohanamuraly, L. Cheng, C. Lapeyre, **G. Daviller**, Y. Realpe, A. Adler, G. Staffelbach, and T. Poinsot. Learning an optimised stable taylor-galerkin convection scheme based on a local spectral model for the numerical error dynamics. *Submitted to Journal of Computational Physics*, 2022.

[175] L. Drozda, P. Mohanamuraly, Y. Realpe, C. Lapeyre, A. Adler, **G. Daviller**, and T. Poinsot. Data-driven taylor-galerkin finite-element scheme for convection problems - the symbiosis of deep learning and differential equations. In *35th Conference on Neural Information Processing Systems (NeurIPS 2021), Sydney, Australia - Virtual conference*, 2021.

[176] O. Colin and M. Rudgyard. Development of high-order Taylor-Galerkin schemes for LES. *J. Comp. Physics*, 162(2):338–371, 2000.

[177] A. Roux, L. Gicquel, S. Reichstadt, N. Bertier, G. Staffelbach, F. Vuillot, and T. Poinsot. Analysis of unsteady reacting flows and impact of chemistry description in large eddy simulations of side-dump ramjet combustors. *Combustion and Flame*, 157(1):176 – 191, 2010.

[178] Virginie Daru and Christian Tenaud. Numerical simulation of the viscous shock tube problem by using a high resolution monotonicity-preserving scheme. *Computers and Fluids*, 38(3):664–676, 2009.

[179] Christophe Bogey, Nicolas de Cacqueray, and Christophe Bailly. A shock-capturing methodology based on adaptative spatial filtering for high-order non-linear computations. *Journal of Computational Physics*, 228(5):1447–1465, 2009.

[180] C. Lapeyre, A. Misdariis, N. Cazard, D. Veynante, and T. Poinsot. Training convolutional neural networks to estimate turbulent sub-grid scale reaction rates. *Combustion and Flame*, 203:255–264, 2019.

[181] **G. Daviller** and G. Staffelbach. Simulation de la phase d'allumage complet du moteur *Vulcain*®2.1 en utilisant une approche de simulations dites "aux grandes Échelles". In *Journée CCRT 2022*, TGCC - Bruyère le Châtel, 2022.